INERTIAL CONFINEMENT FUSION

Lawrence Livermore National Laboratory

ICF Annual Report

1997

The Cover: Much of the ICF/NIF Program's work this year has been in direct pursuit of finalizing systems or components that are part of the National Ignition Facility (NIF) design. The **top left photo** shows a KDP crystal grown using the rapid-growth technique that the NIF will employ. The **top right photo** shows an assembled prototype NIF amplifier that is 4 slabs high by 2 wide by 1 long. The **bottom photo** shows a prototype NIF plasma electrode Pockels cell. These technologies are discussed more fully where the photos appear in the Program Overview in this *Annual Report* (pages xxiii, xvii, and xix, respectively).

The **central photo** shows the status of the NIF construction effort in September 1997, which marks the end of the fiscal year reported in this *Annual Report*. By the end of FY 1997, an engineering and support team with almost 400 members drawn from Lawrence Livermore National Laboratory, Sandia National Laboratories, Los Alamos National Laboratory, and the University of Rochester's Laboratory for Laser Energetics was approximately halfway through Title II (final) design, with nearly 90% of all requirements and interfaces under configuration control. NIF structural design reached 100% levels in many areas, and by year's end excavation was almost complete, with concrete being poured. Five of the eight conventional facilities construction packages were awarded for site preparation, site excavation, target building mat, laser bay foundations, laser building shell, and the Optics Assembly Building. The NIF will occupy a building that is 704 feet long, 403 feet wide, and 85 feet tall, about the size of a football stadium. The NIF is twice as tall, long, and wide as LLNL's Nova laser facility.

The NIF will be a 192-beam inertial confinement fusion laser facility for demonstration of fusion ignition and modest energy gain in the laboratory. It will be used primarily for research associated with the U.S. Department of Energy's Stockpile Stewardship Program. It will also be a valuable instrument in many fields, such as astrophysics and plasma physics. In addition, the NIF will establish the scientific basis for electric power generation by inertial confinement fusion. Although the NIF will be fully operational in 2003, partial operation will begin in 2001. The third 1997 *Quarterly Report* is dedicated to the NIF Title I Design and Title II Activities; the third-quarter articles also appear on pages 95 to 222 of this *Annual Report* (minus the original foreword and preface) and is available on the World Wide Web (see "On the Web").

On the Web: The progress of the NIF construction effort is captured regularly in a photo catalogue on the Web at *http://lasers.llnl.gov/lasers/nif/building*. In addition, NIF construction is reported with other noteworthy topics in the ICF/NIF Program's new *Monthly Highlights*, which began in September of 1997. The monthly highlights, quarterly reports, and annual reports are all available on the Web at *http://lasers.llnl.gov/lasers/inertial.html*; the inaugural issue of the *Monthly Highlights* is also reprinted in this *Annual Report*.

Questions and comments relating to the technical content of the journal should be addressed to the ICF Program Office, Lawrence Livermore National Laboratory, P.O. Box 808, Livermore, CA, 94551, or to kauffman2@llnl.gov.

INERTIAL CONFINEMENT FUSION

1997

ICF

Annual

Report

FOREWORD

The *ICF Annual Report* provides documentation of the achievements of the LLNL ICF Program during the fiscal year by the use of two formats: (1) an Overview that is a narrative summary of important results for the fiscal year and (2) a compilation of the articles that previously appeared in the *ICF Quarterly Report* that year. Both the Overview and *Quarterly Report* are also on the Web at http://lasers.llnl.gov/lasers/pubs/icfq.html.

Beginning in Fiscal Year 1997, the fourth quarter issue of the *ICF Quarterly* was no longer printed as a separate document but rather included in the *ICF Annual*. This change provided a more efficient process of documenting our accomplishments without unnecessary duplication of printing. In addition we introduced a new document, the *ICF Program Monthly Highlights*. Starting with the September 1997 issue and each month following, the *Monthly Highlights* will provide a brief description of noteworthy activities of interest to our DOE sponsors and our stakeholders.

The underlying theme for LLNL's ICF Program research continues to be defined within DOE's Defense Programs missions and goals. In support of these missions and goals, the ICF Program advances research and technology development in major interrelated areas that include fusion target theory and design, target fabrication, target experiments, and laser and optical science and technology.

While in pursuit of its goal of demonstrating thermonuclear fusion ignition and energy gain in the laboratory, the ICF Program provides research and development opportunities in fundamental high-energy-density physics and supports the necessary research base for the possible long-term application of inertial fusion energy for civilian power production. ICF technologies continue to have spin-off applications for additional government and industrial use. In addition to these topics, the *ICF Annual Report* covers non-ICF funded, but related, laser research and development and associated applications. We also provide a short summary of the quarterly activities within Nova laser operations, Beamlet laser operations, and National Ignition Facility laser design.

LLNL's ICF Program falls within DOE's national ICF program, which includes the Nova and Beamlet (LLNL), OMEGA (University of Rochester Laboratory for Laser Energetics), Nike (Naval Research Laboratory), and Trident (Los Alamos National Laboratory) laser facilities. The Particle Beam Fusion Accelerator (Z) and Saturn pulsed-power facilities are at Sandia National Laboratories. General Atomics, Inc., develops and provides many of the targets for the above experimental facilities. Many of the *ICF Annual Report* articles are co-authored with our colleagues from these other ICF institutions.

Questions and comments relating to the technical content of the journal should be addressed to the ICF Program Office, Lawrence Livermore National Laboratory, P.O. Box 808, Livermore, CA 94551.

Jason Carpenter
Publication Editor

Don Correll
Managing Editor

ACKNOWLEDGMENTS

CONTENTS

Supernova Hydrodynamics Experiments on the Nova Laser   1

The unstable hydrodynamics of supernovae bear a striking resemblance to those encountered in ICF implosions, and may be examined in experiments on the Nova laser. We see agreement between Nova experiments that emulate behavior of a supernova explosion (by following a sinusoidally perturbed unstable interface well into the nonlinear regime) and simulations using the supernova code PROMETHEUS. We present initial results from Nova experiments designed to mimic supernova remnant collection.

Characterization of Laser-Driven Shock Waves Using Interferometry   11

This article describes a new diagnostic used to characterize both the initial state of a sample being compressed by a laser-driven shock wave (the level of preheating) and the structure of the shock wave itself (the shock planarity). This is essential for absolute equation of state measurements, which rely on accurate determination of the initial state of the material as well as the passage of a reasonably uniform shock wave.

Absolute Equation of State Measurements of Compressed Liquid Deuterium Using Nova   16

The equations of state (EOSs) of hydrogen and its isotopes at high pressures are essential components of the physics of high-density matter. In this article, we describe the first absolute EOS measurements of D_2, which show the importance of molecular dissociation.

Low-Density–Foam Shells   22

Low-density resorcinol-formaldehyde foam shells with 2-mm-diam and 100-µm-thin walls have been produced using microencapsulation techniques. The foam density is from 50 to 75 mg/cm^3, and the foam cell size is less than 0.1 µm.

Tetrahedral Hohlraums   31

Tetrahedral hohlraums are a new form of indirect drive for ICF. They have some symmetry advantages over the conventional cylindrical hohlraums. Experiments are now under way on the Omega laser at the Univeristy of Rochester's Laboratory for Laser Energetics.

The Rosseland Mean Opacity of a Composite Material at High Temperatures   36

The dominant energy-loss mechanism in the indirect-drive approach to ICF is x-ray absorption in the hohlraum walls. By modifying the composition of these walls, we can reduce the energy loss. This paper describes measurements that validate the favorable energetics associated with these composite materials envisioned for advanced hohlraums.

Direct-Drive Capsules for NIF   43

It appears feasible to achieve ignition on NIF capsules driven by direct laser illumination. This article presents designs for direct-drive capsules and discusses capsule sensitivity to illumination nonuniformity, laser imprint, and Rayleigh–Taylor instability.

Taking Average-Power, Diode-Pumped, Solid-State Lasers beyond the Nd^{3+} Ion   52

New developments in the technologies used for packaging and radiance conditioning of semiconductor laser-diode arrays have enabled high-average-power (HAP), diode-pumped, solid-state lasers (DPSSLs) that rely on other than Nd^{3+} as their active laser ion. This has many important implications for applications requiring high average power or wavelengths other than one micron. Examples of HAP DPSSLs using Tm^{3+} and Yb^{3+} as their active laser ion are described.

ICF FY 1997 PROGRAM OVERVIEW

J. D. Kilkenny

B. A. Hammel

H. T. Powell

L. J. Atherton

J. A. Paisner

J. D. Lindl

Introduction

The continuing objective of Lawrence Livermore National Laboratory's (LLNL's) Inertial Confinement Fusion (ICF) Program is the demonstration of thermonuclear fusion ignition and energy gain in the laboratory and to support the nuclear weapons program in its use of ICF facilities. The underlying theme of all ICF activities as a science research and development program is the Department of Energy's (DOE's) Defense Programs (DP) science-based Stockpile Stewardship Program (SSP). The mission of the U.S. Inertial Fusion Program is twofold: (1) to address high-energy-density physics issues for the SSP and (2) to develop a laboratory microfusion capability for defense and energy applications. In pursuit of this mission, the ICF Program has developed a state-of-the-art capability to investigate high-energy-density physics in the laboratory. The near-term goals pursued by the ICF Program in support of its mission are demonstrating fusion ignition in the laboratory and expanding the Program's capabilities in high-energy-density science. The National Ignition Facility (NIF) project is a cornerstone of this effort.

One of the more important aspects of ICF research is the national nature of the program. LLNL's ICF Program falls within DOE's national Inertial Confinement Fusion Program, which includes the Nova and Beamlet (LLNL), OMEGA (University of Rochester, Laboratory for Laser Energetics [UR/LLE]), Nike (Naval Research Laboratory [NRL]), and Trident (Los Alamos National Laboratory [LANL]) laser facilities. The Particle Beam Fusion Accelerator (Z) and Saturn pulsed-power facilities are at Sandia National Laboratories (SNL). In addition, General Atomics, Inc. (GA) develops and provides many of the targets for the above experimental facilities.

LLNL's ICF Program's research and development activities fall principally into two broad program elements and two main laser facilities: (1) target physics and technology (experimental, theoretical, and computational research) and (2) laser science and optics technology. Experiments on the Nova laser primarily support target ignition and high-energy-density physics research. Experiments on LLNL's Beamlet laser support laser and optics science and technology development.

The target physics and technology activities are directed to ensure the success of achieving ignition on the NIF and supporting the science mission of the DP SSP. The activities fall into three main areas: Nova target ignition physics, code development and theory, and NIF target area technology development. The ICF Program and scientists in LLNL's A Division, B Division, V Division, and H Division, as well as high-energy-density scientists from LANL, collaborate on high-energy-density physics experiments on Nova.

The laser science and optics technology activities are directed towards providing laser and optics technology developments, validated performance models for the NIF, and advanced ICF laser systems. Laser developments have non-ICF spin-offs that are also valuable to Stockpile Stewardship, other national programs, and U.S. industry. Many of these spin-offs, which have then been advanced by other sponsors, are now being applied to ICF needs (i.e., spin-backs). The ICF Program is strengthened by this synergistic exchange of information between these diverse activities.

In addition, ICF sciences and technologies, developed as part of the DP mission goals, continue to support other DOE objectives. These objectives are to achieve diversity in energy sources through inertial fusion energy (IFE) research and to maintain a competitive U.S. economy through new development of technologies of interest for government and industrial use, including those developed through the Laboratory Directed Research and Development program.

This overview is divided into the following sections: Target Physics and Technology, Laser Science and Optics Technology, the National Ignition Facility Project,

Inertial Fusion Energy/New Technology Applications, and Program Resources and Facilities. These sections summarize the findings within the many articles written for refereed journals and the ICF FY97 Quarterly Reports and also summarize important results from FY 1997 that have not been covered explicitly in the articles. Because of the national collaborations, many of the articles are coauthored with colleagues from other laboratories.

Target Physics and Technology

The Target Physics and Technology Program includes: (a) target ignition physics on Nova at LLNL and the OMEGA laser at the University of Rochester, (b) Nova high-energy-density experiments, (c) applications of ultrahigh intensities lasers, (d) code development and theory, and (e) NIF target area technology development. A small number of shots (approximately 10% of Nova shots) are devoted to the Science (University) Use of Nova Program in support of Stockpile Science.

Target Ignition Physics

During the past year LLNL, LANL, SNL, UR/LLE, and NRL have begun the development of a detailed plan to reach ignition on the NIF. This National Ignition Plan, which has been incorporated into a Work Breakdown Structure (WBS), is divided into four subject areas—WBS1: Hohlraum Energetics, WBS2: Hohlraum Symmetry, WBS3: Capsule Optimization, and WBS4: Ignition Implosions/NIF Target Design. Although this plan is still under development, it has been effective in delineating high-priority activities in target design and fabrication and near-term Nova and OMEGA experiments. This WBS is used in our internal resource planning and Nova shot allocation.

Hohlraum Energetics

In the areas of Hohlraum Energetics and Hohlraum Symmetry, we have made significant advances in our understanding and control of laser/target interaction using "smoothed" laser beams. At the beginning of FY97, we installed kinoform phase plates (KPPs) and activated temporal smoothing by spectral dispersion (SSD) on all 10 beams of Nova. In collaboration with the Commissariat a L'Energie Atomique (CEA), we conducted a series of experiments with gas-filled hohlraums that were designed to emulate conditions encountered in NIF targets. In these experiments, we demonstrated a dramatic decrease in backscattered laser light in gas-filled hohlraums, resulting from stimulated Raman scattering (SRS) and stimulated Brillouin scattering (SBS), and a corresponding improvement in laser/target coupling. When these targets were driven with shaped laser pulses reaching peak intensities of 4×10^{15} W/cm^2, total laser

backscatter losses were reduced from 18% for unsmoothed laser beams to the 3% level for KPPs plus SSD. Peak-power losses were as small as 5%. Consistent with the increased laser power delivered into the hohlraum, we observed that the radiation temperatures increase by ~15 eV for smoothed laser beams, as shown in Figure 1.

For gas-filled hohlraums driven with laser pulse shape no. 22 (PS 22) at 1.8 terawatts (TW) peak power, we observed peak radiation temperatures in excess of 210 eV, and for PS 26 (2.6 TW peak power), radiation temperatures larger than 230 eV were measured. The radiation temperatures of both gas-filled and empty hohlraums were seen to compare well to each other and follow the Marshak scaling for ablative heat waves. In addition, the temporally resolved measurements of the x-ray production in gas-filled hohlraums is reasonably well described by radiation hydrodynamic LASNEX code modeling when the laser scattering losses are included in the simulations. The experimental peak temperatures agree with the LASNEX
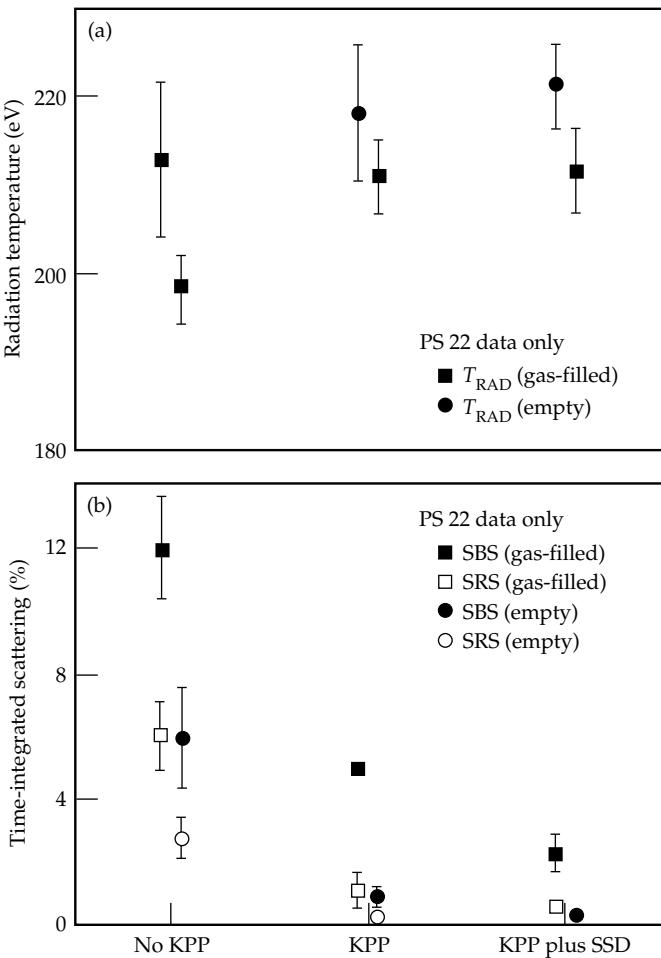
FIGURE 1. A comparison of radiation temperatures and time-integrated scattering percentages for laser beams without KPP (no smoothing), with KPP, and with KPP and SSD. (08-00-0598-1093pb01)

modeling, with a standard deviation of 4 eV, thus increasing our confidence in calculations for future inertial confinement fusion experiments.

We made several advances in the area of hohlraum characterization during FY97. We used Thomson scattering to measure electron and ion temperatures and macroscopic plasma flow in the low-Z plasma of hohlraums, driven by unsmoothed heater beams. We also developed a new 4ω Thomson scattering probe beam that will be used to study plasma conditions in hohlraums driven with smoothed Nova beams in FY98. In addition, we developed a spectroscopic technique to infer the time-dependent, hot-electron fraction in gas-filled hohlraums. These spectroscopic measurements are in good agreement with hot-electron measurements inferred from absolute measurement of SRS and bremsstrahlung emission.

Hohlraum Symmetry

The Hohlraum Symmetry Project achieved advances in two areas—symmetry improvements in gas-filled hohlraums and symmetry control by beam phasing.

Beam smoothing on Nova, described above, was shown to have a positive impact on hohlraum radiation symmetry in gas-filled hohlraums. Previous measurements using unsmoothed Nova beams had showed evidence of laser beam deflection, leading to an outward "shift" in the beam spots on the hohlraum wall and an overall asymmetry in the time-averaged radiation drive on the capsule.[1] Although these experiments had shown that this asymmetry could be corrected by repointing the beams to account for the deflection, an understanding of, and a method to reduce or eliminate the deflection, was desirable. Theoretical work at LANL[2] and LLNL had suggested that the deflection was the result of beam filamentation in a flowing plasma. Using a 3D laser filamentation and propagation code called F3D, we predicted that beam smoothing should reduce filamentation and significantly reduce the beam deflection. This prediction was confirmed by a series of experiments led by LANL, in which capsule distortion was measured in gas-filled hohlraums driven by smoothed laser beams (KPPs only). The deflection was reduced by a factor of ~4 compared with the unsmoothed beam results.[3]

A crucial component of the Hohlraum Symmetry Project is the control of time-dependent flux asymmetries imposed on the imploding capsule.[4,5] During this past year, we began experiments to demonstrate continuous symmetry control on the Nova laser using a two-ring-pair NIF-like illumination geometry. Time-dependent symmetry was principally inferred from the distortions imposed on a backlit foam ball acting as a capsule surrogate.[6] The results demonstrated mitigation of the two lowest-order Legendre harmonic distortion coefficients (a_2 and a_4) relative to traditional

single-ring pair irradiation, in agreement with simulations. A simpler, rudimentary demonstration of time-dependent control of the lowest-order flux asymmetry in hohlraums was also performed on the OMEGA laser facility. The flux asymmetry was inferred from the shapes of x-ray images of imploded cores[7] and from backlit foam balls. By minimizing the symmetry swing, the second-order Legendre distortion a_2 was kept below 2 ± 1 μm at all times. The ±1 μm accuracy is sufficient to detect distortion levels acceptable for ignition capsules. Future campaigns in 1998 will concentrate on using the technologies developed in 1997 to reduce random and intrinsic hohlraum flux asymmetries to demonstrate improved implosion performance.

Capsule Optimization

Correct timing of the ablatively driven shocks in the target is critical in achieving ignition on the NIF. This activity is primarily devoted to the development of techniques for this measurement on the NIF. A secondary goal of this project is to test and improve the physical databases [equation of state (EOS), opacity] of the ablator materials and fuel. More accurate knowledge of this information will allow for improved numerical simulations, thereby potentially reducing the amount of time required to achieve ignition on the NIF. In FY97, we continued work, begun the previous year, to test the accuracy with which we can follow shocks in D_2 and to map out the D_2 EOS near the first shock state of the NIF. We have developed and refined several techniques for these measurements, and in collaboration with the Laboratory's weapons program, have measured the shock velocity, particle velocity, density, temperature, and reflectivity of D_2 on the principle Hugoniot up to 2.4 Mbars (see Nova High-Energy-Density Experiments section). These measurements, which confirmed the higher compressibility of D_2 observed in our previous experiments, resulted in enhancing the "safety" margin in the NIF ignition designs due to the increased fuel compression.

Ignition Implosion/NIF Target Design

The majority of the efforts in Implosion Physics have been directed towards further advances in computational design work and fabrication techniques for the NIF. In the area of NIF target design work, we performed a systematic study that compared the effects of hydrodynamics instabilities seeded by three dimensional (3D) multimode surface perturbations on three similar NIF ignition capsule designs, each driven at 300 eV. The principal difference in these designs is the choice of ablator material that sits outside the deuterium-tritium (DT) ice layer: Br-doped plastic, polyimide ($C_{22}H_{10}N_2O_4$), and Cu-doped beryllium (Be). The computational tool used for this study is the 3D radiation hydrodynamic plus thermonuclear burn

code named HYDRA. Multimode perturbations were applied (modes l = 15 to 120) on both the inner surface of the DT ice layer and on the outer surface of the ablator. All three capsules ignited and burned, resulting in near-1D yields for initial surface finishes equal to the best achieved to date on a Nova capsule ablator and on cryogenic DT ice. The beryllium ablator design is most tolerant of increased initial surface roughness. These 3D calculations were done in a wedge-shaped region that was 12 degrees wide in each angle. As the 3D code is further parallelized and Accelerated Strategic Computing Initiative (ASCI) class machines progress in their capabilities, full capsule simulations can proceed that include the effects of longer wavelength modes from both hydrodynamic instability growth and drive asymmetries.

The effort to identify NIF target designs driven at 250 eV using lower laser intensity and less laser energy than the 300 eV designs discussed above continued this year. These designs offer potentially improved safety margins with respect to laser–plasma instabilities as well as laser energy performance. Thus far, the target that successfully ignited in these integrated calculations was driven with only 900 kJ of energy and a peak power of 250 TW, half the nominal energy and power for the NIF. Rayleigh–Taylor (RT) analysis of this design shows that it will require surface finishes that are beyond current demonstrated capabilities.

This year, we continued our work in support of identifying a beam arrangement on the NIF that allows the baseline hohlraum geometry as well as tetrahedral hohlraum geometry with direct drive. This work concentrated on designing a capsule implosion driven by a tetrahedral hohlraum experiment at UR/LLE's OMEGA laser. Once again, the 3D code HYDRA with its new 3D ray tracing postprocessors (to simulate the x-ray emission data) was used to successfully design and analyze the effect of the tetrahedral hohlraum drive asymmetry on the imploding capsule. Changes in tetrahedral hohlraum geometry (e.g., hohlraum wall radius, size of laser entrance holes, etc.) led to a change from a decidedly triangular shaped x-ray image of the capsule implosion to a round one, as per predictions.

Nova High-Energy-Density Experiments

In FY97, we fielded several diagnostics on Nova to test the precision with which we can follow shocks in D_2 and to map out the D_2 EOS near the first shock state of the NIF. In collaboration with A Division, B Division, and the Physics Directorate, we measured the shock velocity, particle velocity, density, temperature, and reflectivity of D_2 compressed on the principle Hugoniot up to 2.4 Mbar. These experiments were performed in the Nova two-beam facility and used a KPP to produce planar shocks. The compression, shock speed, and par-

ticle speed were measured to a few percent accuracy with a high-resolution Kirkpatrick–Baez microscope. The temperature was measured to about 10% with the multichannel pyrometer. Shock emission intensity, I, is also a sensitive probe of shock steadiness since $I \approx v^8$. Finally the shock velocity (measured to 1 to 3% accuracy) and the reflectivity of shocked deuterium were measured with a velocity interferometer (VISAR).

The compression measurements revealed that liquid D_2 compresses nearly sixfold for a 1-Mbar shock; this is significantly more than most models predict. The first shock for a NIF implosion occurs near this maximum in fuel compression. The shock temperature, which is a good probe of the fuel entropy, is also lower than standard EOS tables (i.e., SESAME) predict. Finally, VISAR clearly shows that D_2 shocked to 1 Mbar has a high reflectivity (~60%). Thus the low-shock temperature and high-shock compression result as the unshocked molecular-insulating phase transforms to the shocked atomic-conducting phase. We are analyzing these data and working with the Physics Directorate to incorporate these data into a new EOS table for D_2. Finally, we are analyzing the optical emission and reflectivity data to determine fuel electron ion equilibration rates that have impact on thermal conduction mechanisms for the shocked fuel.

In collaboration with A Division, Physics, and LANL, we have made single-shock absolute EOS measurements on CH and Be at pressures above 10 Mbar using indirect drive and a preliminary EOS measurement on beryllium near the first shock of the NIF using direct drive. The Be experiments overlap well with quotidian equation of state (QEOS) and previous measurements of Nellis et al. nuclear tests. The CH experiments overlap with QEOS but deviated significantly from the standard preferred EOS table. These data caused a new preferred EOS table for CH to be constructed.

High-Intensity Laser–Matter Interaction

High-intensity laser–matter interaction was given significant emphasis in FY97. The Nova laser had previously been adapted to operate with chirped-pulse amplification (CPA) for ultrashort pulse generation on two such beamlines. The 100-TW beamline, routed to the Nova two-beam target chamber, was capable of delivering a maximum energy of 40 J in a pulse length of ~0.45 ps, producing focused intensities on target of up to 4×10^{19} Wcm^{-2}. The "Petawatt" (PW) (quadrillion-watt) beamline, utilizing Nova's beamline 6, was modified to operate with 70-cm-diam compression gratings, capable of delivering up to 500 J in 0.5 ps and thus a record 1-PW power. This significant milestone was reached in December 1996 and was the prelude to the first experiments with the exciting and unique PW laser. A dedicated target irradiation chamber in which the PW

beam was focused with an f/3 on axis parabolic mirror was constructed for this purpose, and the first target irradiation shots were fired in April 1997.

Science with the 100-TW and PW beamlines in FY97 emphasized two main themes. The first was fast ignition, a new approach to inertial fusion using short-duration, high-intensity laser pulses to ignite a DT target via an ignition spark formed at the focal spot of the laser on the surface of the compressed DT fuel.[8] Valuable results were obtained on the characteristics of the hot electron source and on the heating effect of the hot electrons.

The second was MeV radiography using the energetic electrons produced at a high-intensity focus to generate MeV x rays in collisions with high-Z nuclei. The uniquely intense MeV photon source created in this way has the potential to provide multiaxis, multipulse MeV radiographs of great interest for advanced hydrodynamics research and to be competitive with MeV relativistic electron beam generators more conventionally used for this purpose. The intensity and spectrum of the x-ray source were measured, and test radiographs were recorded through massive lead objects.

FY98 will see significant improvement of the Petawatt to reduce the focal spot to near-diffraction-limited quality using deformable optics. The aim then will be to carry out new experiments to more definitely determine both the short-term feasibility of MeV radiography and the longer-term feasibility of fast ignition.

Code Development and Theory

Work in the area of advanced code development continues in support of the overall Stockpile mission. As described above, the capsule-only 3D radiation hydrodynamics code HYDRA has had new physics algorithms as well as postprocessors added to it. In addition, it had been extensively modified and enhanced to run on distributed memory platforms.

New finite element diffusion operators have been added to enable simulations on more general multiblock meshes in both 2D and 3D. This multiblock mesh structure, plus future additions of a laser deposition package, will enable integrated hohlraum simulations.

A complementary code development approach, funded principally by the ASCI Program, is the general purpose 3D radiation hydrodynamics design code named Kull. This code will use many of the physics modules that have been developed as part of its precursor project, ICF3D. During this past year, the ICF3D hydrodynamics has undergone intense validation testing against a suite of analytic and other well-known test problems. Progress has also been made on its mesh generator.

The main-line ICF design code LASNEX has also undergone important new developments. New magnetic field treatments have allowed us to do simulations of the effects of such fields on the plasma conditions in

hohlraums. With new automated continual rezoning schemes, we have also done simulations of more complicated flows, such as those that occur in hohlraums and in many other applications—laser medical tissue modeling, for example. We have also implemented material strength models for studying low- to moderate-energy-density physics this year. This new modeling capability in LASNEX is important not only to the SSP, but to industrial applications and spin-offs as well.

The new plasma code bZOHAR had many diagnostic capabilities added to it, which helped when it was used in production mode this year. It is a fluid electron, particle ion version of the 2D fully particle in cell (PIC) ZOHAR code. It was used to study the nonlinear saturation behavior of Brillouin scattering including effects of 2D versus 1D ion-wave-coherence collapse, in which it identified an ion-decay instability that facilitates this collapse. Direct comparison of this code's predictions for Brillouin scatter for cross-beam experiments was carried out as well, with good agreement with the measurements.

The 2D fully PIC ZOHAR code was used in studies of fast-ignitor channeling. New diagnostics such as particle trajectories were added that greatly elucidated the physics of the channeling process.

The 3D laser filamentation and propagation code F3D also underwent important new developments. The first models of Raman–Brillouin scattering instability competition were implemented and showed promising results, namely trends of competition that are similar to the observed ones. In addition, relativistic effects were included in the code to allow a study of fast-ignitor channeling on longer-scale lengths and time intervals than those of which the PIC codes are capable. The most important application of the F3D code was in its predictive capability of the role that beam smoothing such as binary phase plate and KPP beams play in the remediation of beam deflection in flowing plasmas. This has been confirmed by Nova experiments.

NIF Target Area Technology

The NIF target area systems include the 48 indirect-drive final optics assemblies, the target chamber, the target positioner, the target diagnostics, and various structures such as mirrors and beam tubes. These target area systems must provide optomechanical stability, incorporate the required target diagnostics, manage the laser light at all three frequencies, protect the optics, and provide radiation shielding. Also included in the target area technologies is the fabrication of the ignition target (hohlraum and capsule), including smooth cryogenic layers of DT as the inner capsule layer.

NIF Diagnostics Developments

A number of diagnostic instruments have been developed both for target physics experiments at

OMEGA and as prototypes for NIF instruments. The Neutron Temporal Diagnostic (NTD) on Nova was reconfigured to operate as a standard diagnostic on the OMEGA target chamber. The NTD at OMEGA now provides a reaction history measurement for implosion experiments and will become a crucial platform for developing a NIF reaction history instrument based on the 16.7-MeV DT gamma-ray. A conceptually new neutron time-of-flight (nTOF) array has also been developed for experiments on OMEGA. Neutron sensitivity is achieved by adjusting the detector volume at a common location relative to the target chamber rather than by adjusting the target-detector distance as is done on Nova. In this way, it is hoped that yield and temperature uncertainties from background sources can be minimized. Finally, an assessment of readout systems for a charged particle spectrometer has been completed in parallel with the fabrication and detailed mapping of two spectrometer magnets. The dynamic range of the new charged particle spectrometers includes both DD alphas (<1-MeV) as well as DT tertiary protons (<30-MeV).

Additional prototype instruments have been tested to assess technology applicable for NIF instrumentation. A new version of a threshold Cherenkov gamma-ray spectrometer has been developed that employs a small magnet to eliminate low-energy Compton electrons before the Cherenkov radiator. Work also continued on the development of new technologies for neutron spectroscopy at the NIF. A prototype silicon-based instrument has been developed at OMEGA for testing in 1998, and an assessment of the resistive plate counter efficiency and response uniformity is under way at LLNL.

A number of new diagnostics have been developed for the PW fast-ignitor and radiography experiments. These include pin-diode and scintillator/photomultiplier tube-based instruments for measuring the intensity and angular distribution of hard photons emitted from the PW targets. Radiochemical techniques have also been applied to study the activation of target materials in the PW experiments. Additional radiochemical techniques (e.g., gas sampling) are also being evaluated as future NIF diagnostics.

Finally, direct neutron damage has been measured in a charge-coupled device (CCD) camera for NIF-relevant fluences at the rotating target neutron source. A total neutron flux of 10^{13} n/cm^2 demonstrated that single-shot damage is likely in an unshielded camera just outside the NIF target chamber. Indeed, single-event upsets were observed for flux rates as low as 10^9 n/cm^2/second. Future analysis and experiments should clarify the shielding requirements for reliable CCD operation inside the NIF target bay.

NIF Ignition Capsules

We have continued to develop a variety of technologies for fabricating NIF ignition capsules. We completed investigating whether interfacial polymerization reactions between components dissolved in a spherical fluid drop and a supporting immiscible medium could produce high-quality plastic shells. Shells of the proper size were easily prepared, but the complexities of the interfacial chemistry made control of the surface structure difficult. We also adapted microencapsulation techniques, long used in the ICF community for submillimeter shells, to the production of NIF-quality 2-mm-diam shells and investigated the effects of processing parameters on the shell quality. We increased our effort to develop Be shells and worked to optimize the surface finish of Cu-doped Be-ablator sputter deposited onto plastic mandrels. Using bias-deposition techniques, thick coatings of this material with surface finishes better than 50 nm rms have been produced, with improvements over unbiased coatings as seen in Figure 2. By incorporating small quantities of boron in sputtered coatings, we have produced smooth, glassy films on flat substrates, which may lead to improved surface and bulk structures on coated spheres. We initiated a program to develop NIF-thickness, high-strength polyimide plastic coatings using vapor deposition techniques that were pioneered in the microelectronics industry for very thin (~1 µm) coatings. Thicker polyimide coatings on spherical mandrels, if strong enough and resistant enough to the beta decay, would allow for the room-temperature handling of the capsules with DT gas fills (~1000 atm) sufficient to produce the required 80-µm DT ice layer when cooled to cryogenic temperatures in the target chamber. This would consid-

6-µm Be on a CH mandrel
No bias
rms roughness ~150 nm

9-µm Be on a CH mandrel
120-V bias
rms roughness ~40 nm
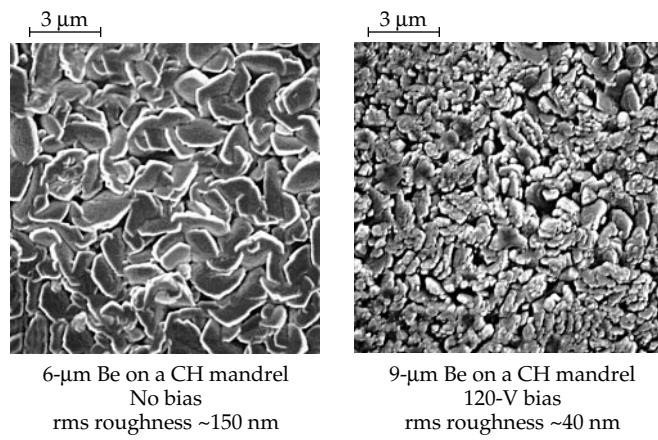
FIGURE 2. A comparison of bias-deposition coatings with unbiased coatings on plastic mandrels. (08-00-0598-1094pb01)

erably simplify the cryogenic fielding of the targets.

Cryogenic Technologies

All known NIF single-shell ignition target designs require smooth cryogenic layers of DT as the inner capsule layer. In 1997, we demonstrated for the first time that ~100-μm-thick DT layers can be formed with surface roughness rms ~1 μm on the inside of millimeter-scale plastic spherical shells. These smooth layers (Figure 3) were formed by a new nucleation and growth process and did not require external enhancement techniques such as joule or infrared heating. We also demonstrated for the first time that by infrared heating the collision-induced molecular vibration absorption in solid HD (which has no natural beta layering), ~100-μm-thick HD layers can be formed with surface roughness rms ~1.5 μm, again on the inside of millimeter-scale plastic shells. From crystal growth experiments on flat substrates we found that surfaces of hydrogen crystals are significantly different than other van der Waals solids such as the rare gas solids. Typically, rare gas solids have no stable facets at temperatures higher than 0.8 times their triple point temperature. We observe that two different crystal orientations have stable facets at temperatures higher than the triple point temperature. Understanding the physics of these surfaces is important to assessing our ability to control the fuel surfaces in ignition targets. Finally, we have designed and analyzed thermal characteristics of cryogenic hohlraums for beta-layering fuel in ignition capsules and are nearing completion of a cryogenic test system for development of cryogenic hohlraums.

NIF Target Chamber Development

A protection scheme for the target positioner was validated by modeling and experiments in collaboration with the French CEA. The concept uses a thin centimeter-diameter B_4C disk backed by a crushable aluminum foam to reduce ablated mass and the intensity of the shock wave to acceptable levels. More stringent outgassing requirements caused a reevaluation of plasma-sprayed B_4C as the first-wall material. Only minor reduction of the outgassing was achieved by potential vendors. Although progress was made reducing the cost of hot-pressed B_4C, which would meet outgassing requirements, more significant was a discovery that a thin Ni-free, stainless-steel first wall would meet neutron activation requirements. Consequently, louvered stainless steel designs are being evaluated for both first-wall and beam-dump applications. Laboratory-scale to NIF-scale tests of beam dump concepts indicate that stainless-steel louvers, as in Figure 4, provided the best compromise for minimizing cost, mass of ablated material, and risk of catastrophic failure, compared to teflon-covered B_4C and silica-covered absorbing glass. Neutronics calculations continued to support construction design and material choice. They also showed that the current chamber-shielding design meets prompt neutron dose limits for operational personnel, and they were used to develop a retrofit plan for additional shielding if needed.

180-μm DT

FIGURE 3. Smooth DT layers formed by a new nucleation and growth process without external enhancement techniques. (08-00-0598-1095pb02)
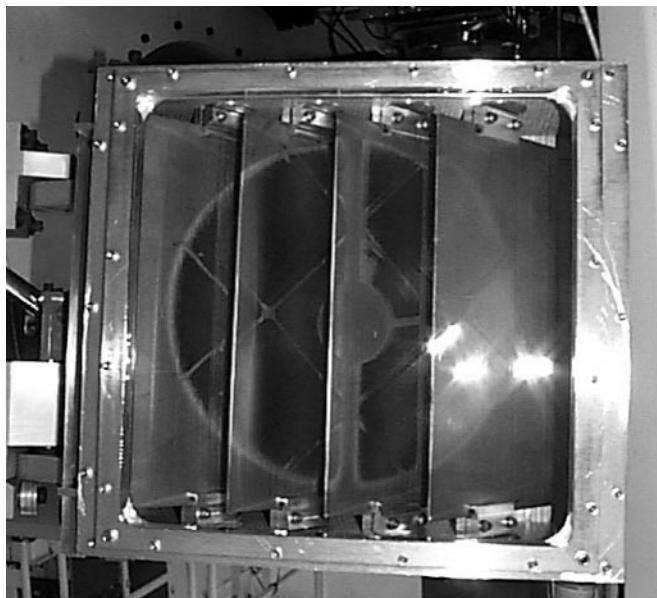
FIGURE 4. Tests showed that stainless-steel louvers provided the best compromise for beam-dump applications. (08-00-0598-1126pb01)

Science (University) Use of Nova

The Science Use of Nova Program is intended to make the Nova facility available to the outside scientific community for high-energy-density science investigations; 1997 was the second year that this program has been in place. As in the previous year when the program was referred to as the University Use of Nova, a call for proposals for Nova use was sent to scientists interested in the field of laser–matter interaction and high-energy-density physics, primarily at U.S. universities and to the membership of the Division of Plasma Physics of the American Physical Society. We received a total of 29 proposals from over 70 researchers at 33 different institutions. The proposals covered a diverse range of topics in high-energy-density science, including astrophysics, hydrodynamics, material science, and atomic physics. The proposals were reviewed and ranked by an external advisory committee made up of senior scientists from outside laboratories and universities. Based on their recommendation, the LLNL ICF Program accepted eight of the proposals for Nova shots. During FY97, approximately 10% of Nova shots were in support of these experiments.

Astrophysicists have shown strong interest in Nova experiments in the Science Use of Nova Program. Researchers from the University of Colorado and the University of Michigan are conducting experiments on the Nova laser to benchmark astrophysical codes used to model the radiative hydrodynamics of supernova remnant (SNR) evolution. Of particular interest is the SNR now developing around SN1987A. The ejecta from this supernova is on a collision course with its circumstellar ring nebula, with impact expected within five years. The astrophysics codes being used to predict the outcome of this extragalactic collision are being benchmarked with experiments on the Nova laser, where 1 ns (from the laser experiment) scales to 1 year for the SNR, 100 km/s to 10^4 km/s, and 100 µm to 0.03 light years. Initial experiments were conducted in 1D, to observe ejecta plasma flowing into a low-density ambient plasma, forming a classic forward shock-reverse shock system, much like in the astrophysical SNR. These first experiments are described in a preliminary overview paper[9] with details given in a set of recently submitted follow-up papers.[10] The group is now planning 2D experiments to study the RT instability predicted to occur at the contact discontinuity between the forward and reverse shocks. Such RT-induced clumping could change the nature of the much awaited collision from a smooth, 1D sweeping up of the ring, to something more akin to "hydrodynamic bullets" impacting the ring, in radiative bursts or "sparkles."

Researchers from the University of Arizona continue to develop experiments using the Nova laser at LLNL to answer specific questions about hydrodynamic instabilities, in particular the RT instability, as is relevant to the evolution of core-collapse supernovae. In particular, the high velocities of the core elements Ni, Co, and Fe in SN1987A are still unexplained (3000 km/s observed, versus predictions of about half that) and may have a bearing on the observed light curve. In collaboration with ICF researchers from LLNL, the Arizona researchers conducted experiments on the Nova laser to test the hydrodynamics of the supernova code PROMETHEUS. Initial 2D experiments have been successfully completed and are described in several papers and conference proceedings.[11] The group is now turning to the crucial question of how the instability evolution in 3D differs from that predicted in 2D. This dimensionality could hold the key to unlocking answers to some of the remaining questions surrounding SN1987A. If the velocities of RT spikes in 3D are significantly larger than 2D predictions (note, 3D star calculations are still beyond current computational capabilities), this could enhance the mixing in the exploding star and help explain the observed light curve from SN1987A. Furthermore, any progress in advancing our understanding of the time-dependent mixing could shed light on the mechanism by which supernovae explode at all. Initial experiments to compare RT-induced mixing in 3D versus 2D in a hydrodynamic setting similar to an exploding SN are planned for the coming year.

NIF Laser Science and Optics Technology

In the Laser Science and Optics Technology (LS&T) area in 1994, we wrote a detailed "Core Science and Technology Plan for Indirect Drive ICF Ignition," which described the developments needed over the next four years to ensure the success of the laser and optics technology utilized in the NIF. In 1997, the third year of this plan, developments have been successful and are on schedule for completion in 1998. Also in 1994, the Beamlet laser was completed to provide an integrated test bed of the NIF optical design. During the past three years, many performance features of Beamlet have been tested including power and energy limits, focal quality, failure modes, and some NIF prototype hardware. It is also anticipated that Beamlet's mission will be completed in 1998 and that the facility will be converted to a NIF amplifier assembly and staging area in 1999.

NIF Laser Component Development

NIF laser component development continued in 1997 on the optical pulse generator, the main amplifier, power conditioning, the plasma electrode Pockels cell, the beam control systems including alignment and wavefront control, laser diagnostics, and the Beamlet and Optical Sciences laser test facilities.

The NIF optical pulse generation system consists of an optical-fiber-based master oscillator, fiber amplitude and frequency modulators for pulse shaping, and a fiber amplifier network that delivers nanojoule-level inputs to the 48 preamplifier modules (PAMs). The PAMs include a regenerative amplifier and a multipass rod amplifier that, to meet NIF specifications, must generate 22-J output energy with stringent specifications on amplitude stability, temporal pulse distortion, and beam quality. The 4-pass amplifier has been redesigned using the 50-mm Nova-type rod amplifier. In 1997, we assembled an optical fiber ring oscillator with improved amplitude and wavelength stability and a smaller overall footprint. A set of three commercially developed fiber amplifiers were assembled in series into an optical circuit with an overall gain of 300. We tested a commercial arbitrary waveform generator that will be used to shape the optical signal into the appropriate ignition pulse. This electronic pulse-shaping system, which was designed and developed at LLNL, creates a 25-ns signal from summing 96 impulses that are 250 ps apart. We evaluated several advanced approaches for improving the regenerative amplifier and modified the optical cavity to utilize a larger volume of the gain medium, reducing temporal pulse distortion. One advanced design results in twice the output energy with no increase in temporal distortion. We also demonstrated >25 J output from a 50-mm-diam, 4-pass rod amplifier system shown in Figure 5 with good beam quality and reduced temporal pulse distortion, which

FIGURE 6. NIF OPG developmental system meets requirements. (40-00-1297-2585pb02)

exceeded specifications for the NIF (see Figure 6). The major goal for 1998 is to demonstrate the performance of a fully integrated, prototype optical pulse generation system.

We have constructed and commissioned a facility to test full-scale amplifiers for the NIF (see Figure 7). The worker in the background of Figure 7 gives an idea of the

FIGURE 5. A 50-mm-diam, 4-pass rod amplifier system. (70-00-0598-1096pb01)

FIGURE 7. NIF prototype amplifier under test in AMPLAB. (70-00-0997-1885#9pb01)

scale of the device. The Amplifier Module Prototype Laboratory (AMPLAB) will provide essential information about amplifier assembly, maintenance, and cleanliness requirements, as well as provide a key test bed for verifying the gain, gain uniformity, wavefront quality, and thermal recovery required for the NIF. The AMPLAB construction began in 1996, with assembly, cleanliness, and initial gain and wavefront measurements beginning in 1997. The facility is capable of testing a $4 \times 2 \times 3$ module array (four slabs high by two slabs wide by three slabs long), with an automated cart for loading cassettes of amplifier slabs while maintaining clean-room conditions and class-100 clean-room facilities for assembly and refurbishment.

The assembly and initial handling tests verified that proposed NIF cleanliness levels were achievable with this bottom-loading design. Slab and flashlamp cassettes were successfully loaded and unloaded from the frame assembly unit as pictured in Figure 7, transported to the clean-room facility, and refurbished as required, demonstrating the viability of each of those operations. Initial full-aperture gain measurements were performed on a $4 \times 2 \times 1$ configuration, with results in good agreement with our design codes and meeting the 5%/cm gain coefficient required for the NIF. A large-aperture diagnostic system (LADS) was assembled for these gain measurements in collaboration with our French CEA colleagues and was initially activated with a Twyman–Green interferometer for wavefront measurements (see Figure 8). To properly

FIGURE 8. Control console for U.S.-French large-aperture diagnostic system.   (70-00-1197-2406pb01)

characterize the wavefront quality of the three-amplifier-long system, the LADS will be retrofitted with a high-resolution ($\lambda/100$) phase-shifting interferometer that is being provided by our CEA partners.

To increase the NIF's shot rate, it will be necessary to actively cool the amplifier flashlamps to reduce the time required for thermal distortions in the amplifier slab to diminish. We have conducted extensive tests on Beamlet to connect temperature rise with wavefront quality, developed detailed thermal models of the amplifier system, instrumented the AMPLAB facility with a thermal data acquisition system, and are now activating a flashlamp cooling system on AMPLAB. Very preliminary results from the AMPLAB tests verify the results obtained on Beamlet and small-scale off-line amplifier experiments regarding flashlamp and amplifier slab temperatures. Additional investigations will verify our ability to effectively cool the flashlamp cassettes and measure the relationship between slab temperature and wavefront quality for comparison with our analytical models.

The NIF employs over 7000 flashlamps, which are 1.8 m long with a 4.3-cm bore, the largest commercial lamps ever produced. In 1997, we completed initial testing of such flashlamps from several vendors and determined that the use of a doped electrode in the anode as well as the cathode appears to significantly reduce anode sputtering, a source of premature flashlamp failure. Although some flashlamps have been tested for more than 20,000 shots, three lamps from one manufacturer failed catastrophically on initial AMPLAB gain experiments. These flashlamps were determined to have a flawed base assembly design. We have worked with the vendor to develop a design solution that will be implemented on future generation lamps.

The power-conditioning design for the NIF consists of approximately 200 modules, each supplying 1.7 MJ of energy. The development of this hardware is shared with SNL. During 1997, we activated a 22-station capacitor test facility and completed initial testing of capacitors from five different commercial vendors. Multiple vendors have been found that can meet NIF capacitor specifications. The NIF specification for the charging power supply was determined to be 25 kJ/s, and three commercial vendors produced prototype supplies that passed acceptance tests at that level. The NIF switch is required to handle 500 kA of current, and the switch test stand at SNL was used to measure various candidates. The NIF baseline spark gap, when fitted with a steel housing, displayed promise of meeting the requirement of 1000 shots before refurbishment. Although tests on a commercial rotating-arc-gap switch demonstrated superior performance, it will be necessary to reduce the cost of this device in order to meet NIF goals. Initial testing of a complete prototype power-conditioning module shown in Figure 9 has begun at SNL.
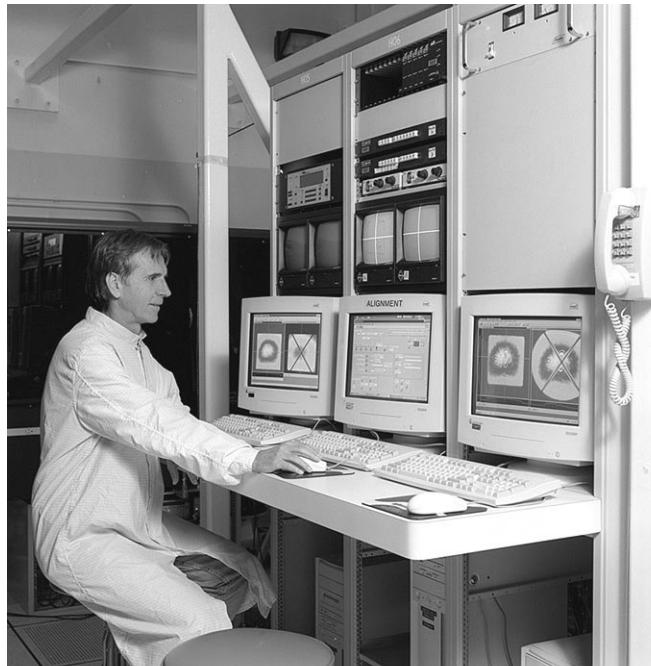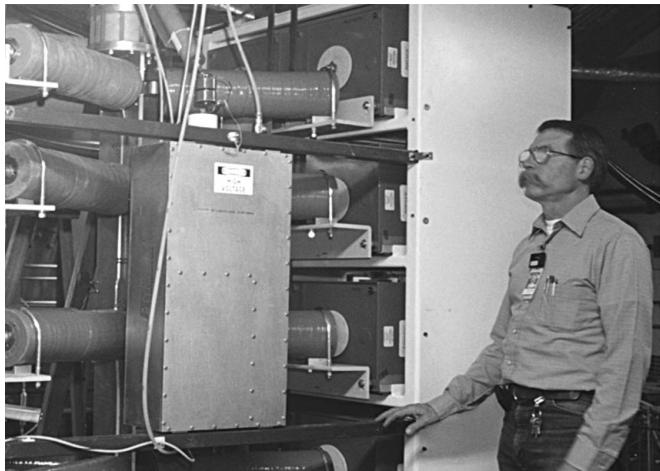
FIGURE 9. A complete prototype power-conditioning module at SNL. (70-00-0598-1097pb01)

The plasma electrode Pockels cell (PEPC) for the NIF is a 4×1 module that is electrically composed of two 2×1 modules that are stacked end-to-end as shown in Figure 10. During 1997, we demonstrated a 2×1 prototype module that greatly exceeded the NIF performance requirements with respect to average and minimum extinction ratio as measured from the residual unrotated polarization. A technique dubbed "magnetic spreading," whereby an external current was used to more uniformly spread the plasma across the electrode region, was beneficial in improving PEPC performance and will be incorporated into the NIF design. The development also verified the use of an anodized metal housing and a grounded cathode.

These features have been incorporated into the prototype 4×1 design, which has been procured and is now being assembled. We also developed a commercial vendor for both the switch and plasma power supplies that will be utilized on the testing of the 4×1 module. Successful testing of this prototype in 1998 will complete the PEPC development effort.

Aligning and controlling the 192 beamlines for the NIF in a cost-effective manner is quite challenging, requiring many new concepts and techniques. In 1997, a complete automatic alignment sequence was successfully executed on our 1/10 scale optical layout of a NIF beamline, verifying that the system has the required degrees of freedom to achieve the required beamline alignment time and precision for the various alignment steps. Both 1ω and 3ω alignment light sources and distribution networks have been developed, as well as precision positioners for alignment light sources and pinholes.

To achieve efficient frequency conversion and a high-quality focal spot on target, it is necessary to actively control the wavefront of the laser. We developed a 40-cm deformable mirror (see Figure 11) with 39 actuators, and in 1997 we installed and tested the device on Beamlet. Despite concerns, there was no degradation or evidence of prompt effects due to flashlamp light or electromagnetic interference. In addition, the advanced mirror controller was successfully integrated into Beamlet with only minor problems. However, the observed beam quality fell short of requirements due to residual error resulting from mirror fabrication problems. These issues are well understood and should be corrected in mirror rebuilding planned for 1998. In the meantime, we have been working with multiple vendors to produce prototype
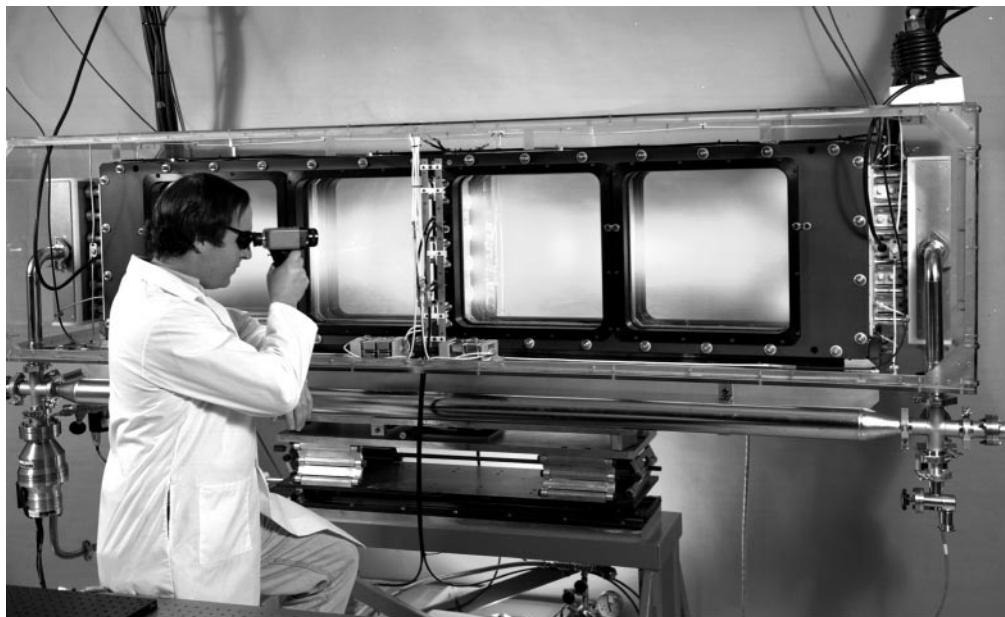
FIGURE 10. The plasma electrode Pockels cell for the NIF. (70-00-1297-2596#8pb01)

Figure 11. A 40-cm deformable mirror.   (02-01-0897-1511#22pb01)

large-aperture mirrors using different methods of actuation. These mirrors will be tested at LLNL in 1998.

Special diagnostic systems related to power balance and optical damage detection are being developed for the NIF. The NIF requires a high degree of amplitude stability among all the beamlines, specified as <8% rms difference during a 2-ns window for each of the 192 beams. In order to measure the power in a cost-effective manner, we are developing 1ω and 3ω optical fiber systems to deliver the light from various points in the optical chain to photodiodes in a temporally multiplexed manner. In 1997, we collaborated with Russian colleagues at the Vavilov Institute to develop special ultraviolet optical fiber that meets stringent requirements for attenuation (<300 dB/km) and dispersion (0.25 ps/m). For 1ω bundles, where acceptable fiber is readily available, our efforts have concentrated on developing inexpensive techniques to reproducibly measure fibers to within ±4 mm to produce bundles up to 70 m in length. Initial tests using an encoded wirelength measurement system verify that we are close to meeting that specification. The monitoring of the many costly optical components will be an important aspect of operations for the NIF. An on-line damage detection technique, which uses a dark-field Schlieren diagnostic to readily view the high spatial frequency portions of the beam produced by various optics in the chain, was designed and will be implemented on Beamlet.

Development of the NIF computer control system has concentrated on the overall system architecture and supervisory software framework. In 1997, we initiated a simulation of the integrated computer control system to assess behavior using models of controlled equipment. The simulation will operate on a computer test bed to evaluate distributed performance under various configurations using emulations of actual control points. We also developed a prototype of the NIF integrated timing system, which successfully demonstrated the most critical aspects of the system, including 25-ps rms short-term timing jitter.

System Integration Tests on Beamlet

The major goals of Beamlet and the much smaller Optical Sciences laser are to validate the analytical models that we have developed to design the NIF laser system and to test laser designs and performance levels that are planned for the NIF. In 1997, several important Beamlet campaigns were completed. The 1ω portion of the laser system was optimized for wavefront quality using the small 7-cm deformable mirror positioned at the front end, resulting in a far-field spot radius <12 μr (80% energy containment). The large-aperture deformable mirror was installed, but due to excess residual error caused by assembly problems, the spot radius increased to 24 μr. Measurements performed on the transport spatial filter revealed onset of beam propagation effects at 10^{-3} Torr, resulting in the specification of a safe operating pressure for the NIF of 10^{-4} Torr. We also designed and tested several advanced pinhole designs. Measurements revealed that a ±150-μr stainless-steel conical pinhole passes a temporally shaped, 21-ns ignition pulse with no sign of closure during the pulse and with acceptable back

reflections more than 20 times less than those observed with "washer" or "leaf" designs. The backscatter growth was linear with output shot energy, and its far-field profile indicated that simple reflections that were from the pinhole annulus were responsible for backscatter rather than nonlinear laser interaction processes from the blowoff plasma. Additional effort will concentrate on optimizing the pinhole shape or using alternate materials in an attempt to provide even tighter spatial filtering. We performed experiments using 1D SSD to improve the uniformity of the focal spot and to minimize unwanted plasma scattering in hohlraum targets. To remain within a safe operating regime, these experiments were limited to B-integral values up to 70% of the NIF limits, and they revealed system behavior consistent with our analytical models.

Assembly, activation, and testing of the new final optics configuration was a major campaign in Beamlet as shown in Figure 12. Dubbed the "test mule," this hardware is intended to confirm several concepts for the NIF: use of a 1ω input window with the frequency conversion crystals and 3ω focusing lens mounted inside the vacuum, color separation and beam sampling gratings, and the general design techniques planned for the final optics hardware. Efficient conversion of the 1ω light to 3ω is a key laser performance specification for NIF. Initial tests in 1997 measured both 2ω and 3ω frequency conversion and revealed that both material homogeneity and stress due to mounting the crystals were sources of the observed spatially nonuniform conversion. Also, initial thermal testing and analysis indicated that the design would result in acceptable recovery time for the crystals between shots. Finally, we installed an optical damage inspection system on all vacuum-loaded lenses and windows and a fail-safe bandwidth system to ensure safe operation and control-stimulated transverse Brillouin scattering in the optics.

Laser Modeling and Optimization

Having completed the cost-optimized laser design of the NIF in 1996, we spent most of this year refining the designs of specific components and carrying out the calculations needed to support the NIF Title I Design Reviews and baseline design changes. This work required numerous code improvements, extensive data evaluation, and extensive "number crunching," as well as close cooperation with the NIF engineering team.

In the main amplifier design effort, we completed pumping, storage, and parasitic codes needed to improve the predicted gain margin. A new 3D multi-wavelength code was brought on-line and was used to analyze improved reflector designs and blast shield treatments. A fast and efficient version was provided to the power-conditioning engineers to allow them to optimize their circuits for highest stored energy.
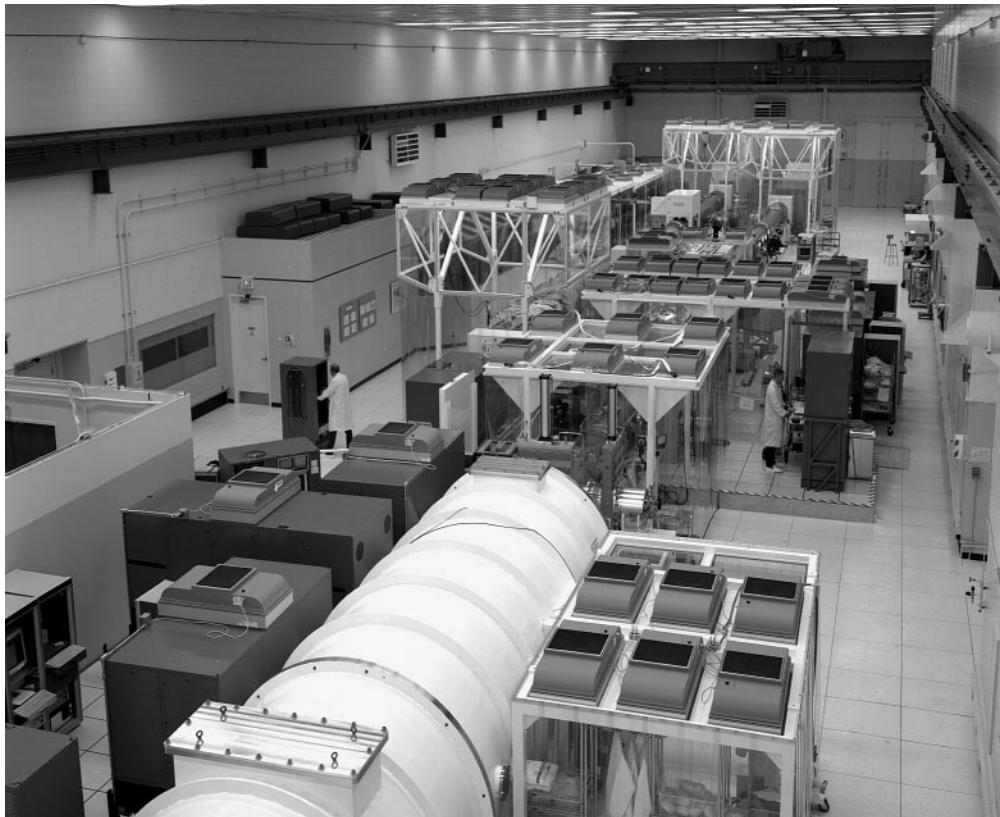
FIGURE 12. The Beamlet laser showing the full-aperture focusing diagnostic in the foreground and the "test mule" for testing, with the final optics design just upstream.
(70-50-1297-2574#3pb01)

The laser modeling team worked closely with the optical pulse generation engineers and used their propagation codes and optics database to supply designs with no temporal overlap and with acceptable output wavefront distortion. A high-fill-factor, small-spot-size beam shaper design was produced.

The calculation of risk due to point defects in the optics at various points in the chain was made practical by streamlined computational methods to carry out the extensive scans needed. Initial runs confirmed our ability to quantify the danger, and we are now carrying out a comprehensive analysis for all NIF optics.

The detailed specification of laser system optics, using spatial-frequency characterization of the phase aberrations, continued in close collaboration with vendors and the NIF optics team. The level of allowable distortion in various spatial frequency bands was refined to assure that the NIF meets its system design requirements.

Our adaptive optics simulation models have been continuously upgraded to simulate the sensing system, control algorithms, and actuator response more accurately. We have determined the optimal number of actuators to meet NIF specifications as a function of the quality of the optical components and supplied this information to the design engineers.

We performed analysis of the nonuniform frequency conversion results with large crystals on Beamlet and ruled out many potential sources of the problem as well as supplied the required instrument sensitivities needed to determine the real cause. The effect of conversion crystal mounting errors, gravitational sag, temperature differentials, and residual stress were evaluated to set specifications on the NIF crystal assemblies.

Propagation of beams through plasma near the spatial filter pinhole was added to our propagation codes to allow accurate analysis of pinhole blowoff. This capability will be used in conjunction with the existing ability in modeling beam profiles to determine the optimum size of various pinholes in the NIF laser chain.

NIF Optics Manufacturing

We are continuing the four-phase program started in 1995 to meet the NIF optics requirements: development, facilitization, pilot production, and production. Progress in development continues to be good in all areas, consistent with the NIF schedule. In parallel with program-funded development, most of the major optics manufacturing facilitization contracts funded by the NIF Project were awarded in 1997. Some of the equipment from these facilitization contracts has been utilized in the development program to permit demonstration of NIF prototype technologies at full size. Most of the facilitization will be complete in 1998 along with the development activities, leading to the pilot production runs in 1999.

Laser Materials: Phosphate Laser Glass, KDP/KD*P Crystals, and Fused Silica

In partnership with the French CEA, we continued working with two companies to develop continuous melting technology of platinum-free phosphate laser glass—Schott Glass Technologies in Duryea, PA, and Hoya Optics in Fremont, California.

Following Schott's efforts with LLNL in 1996 in developing an improved laser glass composition, LG-770, the primary focus in 1997 was preparing for a full-scale development run in the NIF melting facility constructed in 1997. The building and the furnace were designed and constructed in 1997 as part of the NIF Project facilitization effort. In parallel with these efforts, we worked with Schott to refine the material preparation process for efficient melting and to better understand the phase diagram in the vicinity of the NIF baseline composition to ensure the absence of devitrification in the melter. The raw materials for the development run were ordered and processed for the campaign anticipated in late 1997. The melter was heated up to its operating temperature without glass to ensure that the heaters and control system were operating properly. The results of the development run will be evaluated in early 1998 and used to modify the melter in preparation for the pilot production campaign in 1999.

Hoya worked with LLNL and CEA to evaluate phase interferograms of the half-scale laser slabs produced in 1996. These interferometry data were used by Hoya to modify the melter design to improve the homogeneity by roughly 2× the level needed to meet the NIF specifications. The modified melter was built and shipped from Japan to Hoya's Fremont facility for a final demonstration melting campaign in early 1998. During 1997, Hoya also completed their full-scale melter design, ordered the long-lead equipment, and built the production facility in Fremont. The NIF laser glass melter at Hoya will be constructed during 1998 and modified as needed based on the results of the final half-scale demonstration run in preparation for its pilot production run in 1999.

We also built, tested, and installed platinum laser damage testers at both Schott and Hoya for raster-scanning each piece of laser glass to qualify it for meeting the NIF platinum inclusion specification. These laser damage testers will be used to test the laser glass produced during Schott's and Hoya's development work in 1998.

In 1996, the potassium dihydrogen phosphate/ potassium dihydrogen phosphate (deuterated analog) (KDP/KD*P) rapid growth program jointly sponsored by DOE and CEA produced the first boule large enough to yield Pockels cell plates for the NIF, with an approximate 43 to 48 cm^2 cross section. Plates fabricated from these boules met all the NIF optical specifications for the Pockels cell; four of these plates have

been installed in the 1×4 prototype plasma electrode Pockels cell. The primary issues remaining at the end of 1996 were the size needed for the second harmonic generation (SHG) plates, approximately 51 to 55 cm in cross section; the height of these boules expressed as an aspect ratio, which is height divided by lateral dimension; and the formation of solvent inclusions on the prismatic and pyramidal faces, which limit the yield of usable plates. Significant progress was made in 1997 on all three of these issues.

We grew several boules exceeding the NIF size requirement for the SHG plates, ranging from 53 to 58 cm in cross section. These results were enabled by further improvements of the original platform design based on Lucite, as well as by a new design based on aluminum with a Teflon-like fluorocarbon coating to prevent solution contamination. This aluminum design has replaced Lucite as the baseline rapid growth platform. Aluminum has two significant advantages over Lucite. First, at KDP growth temperatures, it is about thirty times stronger than Lucite, so the platform is significantly stiffer. Second, the thermal expansion coefficient is a nearly perfect match to KDP, so the thermal stresses induced in the boule as the temperature is reduced during the growth process are eliminated.

The SHG boules of KDP need to be approximately 51 to 55 cm tall to allow for several plates to be fabricated. Our standard initial growth temperatures of approximately 65°C tends to produce crystals that are somewhat shorter than these requirements due to the relative growth kinetics of the prismatic and pyramidal

faces. Higher initial growth temperatures of approximately 75°C favors fallen growth, but the use of Lucite platforms had precluded routine operation in this regime due to significant softening of the material. Aluminum platforms now allow us to operate at these higher temperatures. We have modified the seed regeneration conditions to further favor pyramidal growth by minimizing the number and strength of the prismatic dislocations. Shown in Figure 13 is a crystal grown under these conditions; this boule is approximately 52×53 cm laterally and 51 cm tall, limited in this case by the platform geometry. Our new aluminum platforms will allow the growth of boules up to 60 cm wide and tall, exceeding the NIF requirements. Most of this work has been performed with undeuterated KDP crystals, but similar findings are expected for KD*P in 1998.

The damage threshold of rapid growth KDP crystals significantly exceeds the NIF requirements in the infrared. In 1996, we found that continuously filtered KDP grown in our small tanks had a damage threshold at 351 nm, within about 20% of the NIF goal. This work was extended in 1997 and demonstrated that the use of high-purity salt coupled with continuous filtration leads to a 3ω damage threshold in rapid growth equivalent to the traditional manner, both of which exceed the NIF requirement. These results will be confirmed in a full-size boule grown in our large tanks in 1998.

Development activity is continuing to reduce the production cost of high-quality fused silica. Initial modeling and single-burner experimental efforts at Corning in 1996 to optimize their fused silica deposition process indicated that an improved burner should
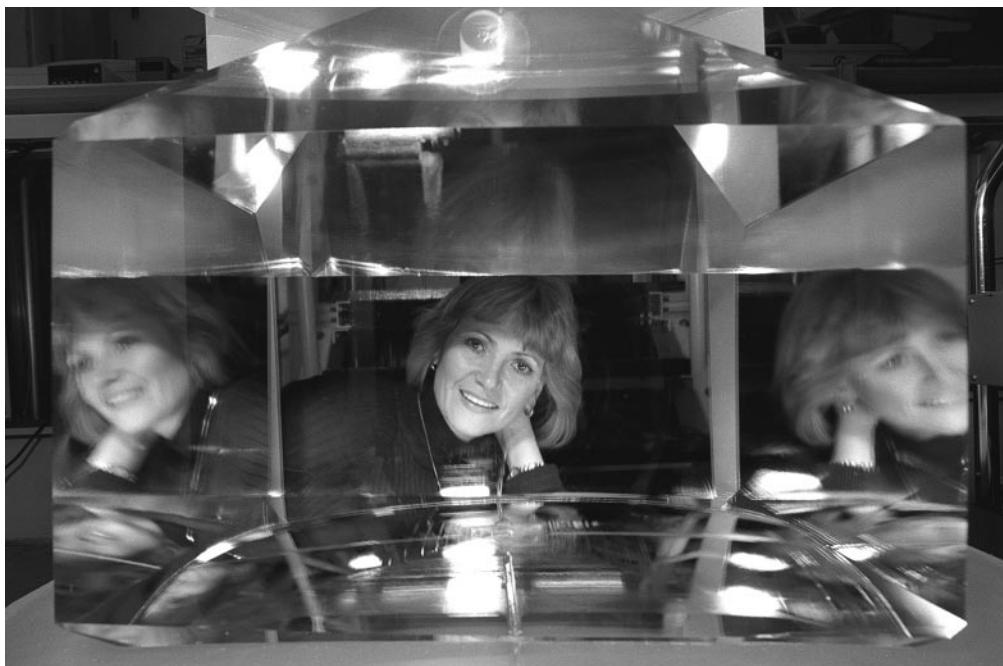
FIGURE 13. KDP crystal.
(40-00-0198-0133#19pb01)

allow for increased deposition rate and boule thickness. Tests in 1997 with the new burner installed in a large furnace confirmed these expectations, providing greater confidence in the Corning cost estimates for NIF fused silica production.

Polishing technology developed at LANL was successfully applied for grinding and polishing full-size Corning boules. This technique improves the inspection capabilities for bubbles and inclusions and enables the use of the polished homogeneity (PHOM) approach for refractive index uniformity instead of oil-on plates.

Damage tests at 351 nm on fused silica with inclusions between 10 and 80 µm indicated that the specification on inclusions (currently 80 µm) may need to be tightened for some of the fused silica optics, particularly the focus lens and phase plate. In 1998, we will extend this study to refine our understanding of damage and its evolution with repeated high-fluence shots in bulk fused silica to refine the inclusion specification and inspection requirements.

Optics Fabrication: Flats, Lenses, and Crystals

Development activities in optics fabrication matured significantly in 1997. In plano optics (flats) and lenses, we continued to work with three companies—Eastman Kodak in Rochester, NY; Tinsley Laboratories in Richmond, CA; and Zygo in Middlefield, CT. We expect all three companies to play a major role in NIF optics fabrication. Facilitization contracts were awarded in 1997, which established the lead suppliers for each optic type. Zygo was selected as the lead supplier for amplifier slabs and mirrors, and Tinsley was selected for windows and lenses. Kodak is expected to provide a significant quantity of both flats and lenses as a secondary supplier to Zygo and Tinsley; their facilitization contract should be awarded in early 1998.

In 1996, Kodak improved its small-tool figuring capability, developed originally for classified and space programs, to meet the NIF power spectral density (PSD) specification. Kodak also demonstrated advanced continuous polishing (CP) technology on a subscale machine to improve the figure of the optical surface prior to small-tool final figuring. In 1997, Kodak completed the design and fabrication of full-size components needed to retrofit their large CP machine. This work was put on hold to permit Kodak to finish most of the large optics needed for the NIF interferometers. The CP retrofit is now scheduled to be completed in 1998. Two NIF-size spatial filter lenses were fabricated at Kodak; these lenses will be tested in 1998 to determine if they meet the NIF PSD requirement.

In 1997, Tinsley built and tested full-size prototypes of every finishing machine with the exception of the CP; the CP is scheduled to be completed in mid-1998. Prototype plano and lens optics fabricated on these machines met all NIF optical specifications except for surface roughness. Reducing the roughness will be addressed in 1998. Tinsley completed four Beamlet spatial filter lenses that will be installed on Beamlet for testing in 1998.

In 1996, Zygo demonstrated each major processing step in its plano fabrication process on equipment ranging from half- to full-size. Improvements to Zygo's CP technology in 1996 significantly increased the determinism of the process, which will require fewer iterations in final figuring. In 1997, Zygo demonstrated a proprietary approach to improve this technology even further, providing much greater confidence in their NIF optics fabrication cost projections. This technology has been designed into the NIF CP machines currently under construction. A full-size electrolytic in-situ dressing grinding machine was also designed and constructed. Zygo also designed, built, and qualified the NIF cladding process fixtures.

The primary remaining technical issue in optics fabrication is the surface damage threshold at 351 nm. In 1997, we extended our finishing damage development activities in several ways. First, a two-pronged study was initiated at LLNL to investigate the impact of finishing parameters on 3ω damage. One thrust focused on the use of a different slurry composition for final polishing, the second focused on a postpolish hydrofluoric acid etch of parts polished using traditional polishing slurry. Both approaches emphasized extreme care in removing residual subsurface damage from prior grinding and polishing steps. Work on small substrates indicated that both approaches can be used to fabricate fused silica optics that exceed the NIF requirement.

In parallel with the LLNL activities, several vendors executed development campaigns to extend their own proprietary finishing technologies with the goal of demonstrating robust processes for 3ω damage. While the details are proprietary, in general these processes involve both traditional processes as well as postpolish etching. Kodak, Tinsley, and Zygo all participated in this work, as well as two French companies, REOSC and SESO, that are working with the CEA. Work was performed with 15- to 20-cm optics to provide better feedback on scaleup as well as on full-size lenses and plano optics. All five of these companies produced optics at the 15- to 20-cm size or larger that were at or near the NIF 3ω specification, and two companies made optics that significantly exceeded the NIF damage requirement. Those companies are currently fabricating NIF-size focus lenses as well as NIF-size plano optics prototypes for testing in 1998. These results will be used to choose the NIF suppliers of focus lenses and 3ω plano optics for final facilitization in 1998/99.

Efforts in 1997 to develop improved diagnostics for damage threshold testing and damage mapping were also very successful. Of particular note is the

demonstration of a mapping system that uses fiber-optic illumination, a megapixal camera for detecting artifacts as small as 5 μm, both in the surface and the bulk, and a long-focal-length camera to resolve these defects. This system has been adapted to our large-area damage testing system to permit real-time feedback on damage morphology and density for more rapid interpretation of 3ω finishing development.

Investigations into damage thresholds using total internal reflection microscopy started in 1996 were continued in 1997. In this effort, we are attempting to correlate the damage susceptibility of surface or near-surface artifacts produced during polishing by comparing pre-illumination images with those after exposure to the high-fluence laser. Although this work is not completed, there is a definite correlation of "clean" surfaces with high-damage thresholds, while surfaces with a high density of artifacts tend to have low-damage thresholds. However, depending on the vendor, some surfaces with a moderate density of fabrication artifacts have high-damage thresholds, and some have quite low thresholds. Work is continuing in 1998 to better understand the nature of these defects and the associated damage mechanism(s).

In KDP/KD*P crystal finishing, development activities continued to make good progress. The current crystal finishing process at Cleveland Crystals, Inc. (CCI), based on single-point turning, produces crystals that meet the NIF specifications, but they are undersized for the NIF 41-cm crystals because they were originally designed for Nova 27-cm crystals. To meet the NIF requirements, we are working closely with CCI to modify the finishing process and to design and build the needed machine tools and metrology instruments. Of particular importance are the tools for establishing the crystal flatness, the final diamond turning machine that determines transmitted wavefront and surface roughness and the crystal orientation measurement system (COMS) for verifying the proper orientation of the crystal axes relative to the surface normal.

In 1997, we completed the conceptual design of the crystal flatness machine prototype and acquired most of the major components. The final design will be done in early 1998, and the machine will be assembled and ready for testing in the middle of 1998. A diamond-turning prototype machine, being built by Moore Tool, is approximately 75% designed with all the long-lead items on order. The design will be done in early 1998, and the machine is scheduled to be complete in late 1998. A conceptual design of a new COMS was completed in 1998. In the present COMS, the crystal orientation is measured at only two points on the crystal. This approach provides extremely little information about the variation throughout the crystal of the crystallographic axes with respect to the surface normal. Hence, the uniformity of frequency conversion cannot be ascertained. A newly designed NIF COMS that will allow for scanning over the entire surface to produce a map of the variation of the crystal axes with respect to position is scheduled to be operational in mid-1998.

Optical Coatings: Mirrors, Polarizers, and Debris Shields

The primary coating development activities concerned defect reduction in 1996, stress reduction in 1997, and spectral control in 1998. Defect reduction for damage threshold improvement was accomplished by development of a starting material, metal hafnium, that has minimum source ejection during deposition. The coating stress has been reduced by optimization of the oxygen pressure during deposition. Improved spectral control will be accomplished by the development and installation of proprietary deposition process control instrumentation, improved deposition stability, and improved thickness calibration. Laser conditioning studies in 1997 were aimed at reducing the laser conditioning costs by minimizing the number of conditioning steps needed to meet the laser damage threshold.

In 1997, three groups successfully used the metal hafnium process to produce full-size mirrors for testing on Beamlet: Optical Coating Laboratory, Inc. in Santa Rosa, California; Spectra-Physics in Mountain View, California; and the UR/LLE in Rochester, New York. Further, these mirrors were also conditioned to the required damage threshold in a single step, rather than the six steps used for the original Beamlet coatings or the two- to three-step process envisioned last year.

Both Spectra-Physics and UR/LLE worked to produce full-size polarizer coatings in 1997. The polarizer coatings require much tighter control of the thicknesses of the individual layers to meet the spectral requirements. Even though this control is improved using metal hafnium source material rather than hafnium oxide, it is still extremely difficult. This difficulty impacts the yield and hence the cost of the process, rather than the performance. Both groups have identified the conceptual approaches they will use to improve the thickness control through the use of improved spectral monitoring with appropriate feedback to the coater. These technologies are scheduled to be demonstrated in development contracts in 1998. Nonetheless, Spectra-Physics and LLE were both nearly on schedule to produce their polarizers by the end of 1997 utilizing their existing technologies.

Damage testers were installed at the coating vendors to enable them to more rapidly evaluate the damage performance of their coatings for quicker process optimization during the remainder of development through completion of NIF production.

While not required until the NIF begins operating at high fluence with substantial target yields, work has started to identify concepts for protecting the final

surface of the debris shield or for using an inexpensive film in place of a debris shield. Many types of potential strippable coatings were evaluated. All organic polymer coatings failed at x-ray fluences well below that required, even though their laser damage thresholds were adequate. A few inorganic coatings were also tested. By far the best was a sol-gel silica material prepared from tetraethylsilicate in a similar manner to our antireflective (AR) coating, except that acid hydrolysis was used. This resulted in a high-purity silica coating that was approximately 95% dense and that had a refractive index almost equal to the dense silica substrate. This coating can be applied using the same facilities as the standard sol-gel AR and is removed by etching in HF/NH4F solution or warm 10% sodium hydroxide solution. Initial experiments indicate no degradation of the surface damage threshold. The primary drawback to this approach is that the coating thickness is limited to about 1 μm, so some damage to the debris shield from target shrapnel can still be expected.

In parallel with the protective coating concept, we began an effort to identify a low-cost "disposable" debris shield. We screened several materials for x-ray damage, small-beam laser damage threshold, shrapnel penetration, thermal/laser decomposition products, optical transmission, and wavefront. A commercial DuPont fluoropolymer (FEP 100A) met all criteria except transmitted wavefront. We established a working relationship with DuPont to identify suitable ways to improve the wavefront of FEP 100A or find an alternative material.

Large Optics Cleaning/Sol-gel Coatings and Diffractive Optics

We performed experiments at the NIF-scale to define the cleaning and drying scheme for the NIF; these results were used to establish specifications for the NIF equipment. These experiments included slow-pull (capillary) drying speed as a function of temperature, particulate contamination levels achievable with our existing prototype cleaning system, bath contamination levels required to achieve NIF cleanliness specifications, and optics angle and fixture design for drip-free drying and sol-gel coating.

We demonstrated the NIF baseline aqueous cleaning processes for laser glass, dielectric-coated BK-7 glass, and fused silica on subscale optics using the LLE automated cleaning system and particulate cleanliness measurement tool. We also validated at full-scale the NIF ultrasonic-assisted laser glass cleaning process.

For KDP, we demonstrated the NIF cleaning process utilizing ultrasonic agitation on crystals for a refurbished Nova array. There was no degradation to the surface damage threshold, no fogging, or any enhancement of pre-existing scratches and digs. We have also demonstrated key elements of the NIF KDP crystal spin-coating process on an 18-crystal Nova array. The NIF process requires development of high-damage threshold, slow-evaporation-rate colloidal silica sol-gel AR coating solutions. These lower-evaporation-rate solutions, in combination with spin-coater design advances, allow replacement of the current dip-coat process with a process capable of tailored coatings for each surface of the conversion crystals. Based on this work, we awarded the contract for the NIF KDP spin coater to be delivered in mid-1998.

Three diffractive optic elements are required for the NIF design. A color separation grating (CSG) is used to separate the residual first and second harmonic from the third harmonic energy exiting the KDP crystals. A beam sampling grating (BSG) steers a small fraction of the beam entering the final optics package, about 0.3%, into a calorimeter for diagnostics. Finally, a kinoform phase plate (KPP) homogenizes the beam and shapes it into a super-Gaussian at the target focal plane.

In 1997, we fabricated ten KPPs for Nova on debris shields larger than the NIF diffractive optics plate. These KPPs focused about 93% of the 3ω energy into a $400\text{-} \times 260\text{-}\mu\text{m}$-diam spot, as compared with the NIF specification of 95% into a $1000\text{-} \times 500\text{-}\mu\text{m}$ spot. We will fabricate a full-size NIF prototype KPP in 1998 for tests on Beamlet. There are advantages in utilizing continuous contour phase plates (CPPs) rather than KPPs on the NIF. The primary advantage comes from the use of single-step ion etching of a continuous contour gray-scale mask rather than the four-mask process used to etch the NIF baseline KPP. This simpler process could reduce the manufacturing cost. However, this approach requires the development of a large-ion etch capability with good uniformity over the full NIF aperture. To demonstrate the feasibility of this approach, we fabricated a 15-cm CPP using reactive ion-beam etching that delivered 97% of the light into a NIF-sized target spot.

We also fabricated and characterized the first NIF-size CSGs in 1997. The full-sized CSGs had excellent performance equivalent to the subscale parts demonstrated in 1996. Prior to sol-gel AR coating, the gratings transmitted 90% of 3ω light in the zeroth order. The blocking at 1ω and 2ω exceeded expectations with transmissions of <1%. Fabrication of the full-scale NIF prototype uncovered a problem with AR coating. We have demonstrated that the physical geometry of the CSG is incompatible with conventional sol-gel dipcoating. In FY98, we will field a CSG prototype on Beamlet without an AR coating on the grating surface while evaluating alternative AR coatings, including spin-coated sol gel and physical vapor-deposited coatings.

We have also demonstrated the lithographic process to produce full-aperture BSGs with focusing power. These gratings are made holographically, by exposing a photoresist-coated substrate to two coherent, spherically propagating laser beams—one that simulates the

NIF main beam going to target focus and another equal-intensity beam that simulates the sampling beam going to focus at the calorimeter. The distances, angles, and orientations of the target focus, diffractive optic plate, and calorimeter focus are laid out on the exposure system exactly as on a NIF beamline, except that a wavelength correction is required due to the fact that our exposure laser operates at 413 nm, while the NIF third harmonic is 351 nm. The two writing beams illuminating the resist-coated substrate set up a series of interference fringes that imprint a latent grating in the resist layer. Development of this pattern results in a photoresist grating which, if properly constructed, provides a mask with which to transfer-etch this pattern into the fused silica substrate by wet hydrofluoric acid etching. This grating, when "played back" by illuminating the optic with a NIF 3ω beam going to target focus, sends off a portion of laser to the calorimeter focus at a location given by the geometry of the beam used to create it, corrected for the playback wavelength. The amount of energy sent to the calorimeter is determined to leading order by the depth of the etched grating grooves. To successfully manufacture this grating, the photoresist grating mask must be cleared to the substrate (to allow acid contact to the fused silica in between) and must have the same duty cycle (ratio of resist grating linewidth to period) across the part to assure spatial diffraction uniformity. Controlling the writing beam balance, spatial uniformity, and fringe stability during exposure are the most difficult process steps. We successfully demonstrated uniform writing of a full-size resist grating mask to illuminate a diagnostic plane 1.5 m away and to the side of the beam. In FY98, we will demonstrate a full-aperture wet-etched BSG at NIF geometry.

National Ignition Facility Project

The National Ignition Facility (NIF) Project has made significant progress since completing its Title I design in October of 1996. The NIF is the largest and most complex laser project of its kind and the most challenging laser–target interaction system ever constructed. With a primary requirement to deliver 1.8 million joules (MJ) of ultraviolet laser energy at a peak power of 500 trillion watts (TW), the NIF will exceed the Nova laser at LLNL and the OMEGA laser at UR/LLE, currently the world's largest ICF experimental tools, by factors of 40 in energy and over 10 in peak power.

The NIF is a key component of DOE's science-based Stockpile Stewardship Program. High-energy-density science spans the gamut from weapons physics studies to planetary geoscience and astrophysics. Researchers from all over the globe have begun to plan NIF experiments. They can learn about the NIF and its progress by accessing the informational Web pages provided on the Internet (http://lasers.llnl.gov). Figure 14 shows an isometric

CAD drawing of the NIF Title I (preliminary) design, described in detail in the *ICF Quarterly Report* for July–September 1997. The Project received the fiscal year (FY)97 and FY98 funding ($191.1 million and $229.1 million respectively) required to maintain its Title I baseline. Together with the DOE Secretarial level National Environmental Policy Act Record of Decision/LLNL site selection on December 19, 1996, and Critical Decision 3 (approval to begin construction) on March 7, 1997, the Project is positioned to produce first bundle operations by the end of FY01 and be complete by the end of FY03.

By the end of FY97, we had filled NIF Project management and staff positions to the planned levels. An engineering and support team with almost 400 members, drawn from LLNL, SNL, LANL, and UR/LLE, was approximately halfway through Title II (final) design by year's end, with nearly 90% of all requirements and interfaces under configuration control. In addition, we had completed the NIF structural design to 100% levels in many areas, and excavation was almost complete with concrete being poured, as the photograph in Figure 15 illustrates. We had awarded five of the eight Conventional Facilities construction packages for site preparation, site excavation, target building mat and laser bay foundations, laser building shell, and the Optics Assembly Building. The NIF will occupy a building that is 704 feet long, 403 feet wide, and 85 feet tall, about the size of a football stadium (e.g., the NIF would just fit inside the New Orleans Superdome). The NIF is twice as tall, long, and wide as LLNL's Nova facility.

In 1997, we placed major Project facilitization contracts with commercial vendors (i.e., for finishing of flats, mirrors, lenses, laser slabs, KDP crystals, and fused silica production) to ensure an adequate optics production capability that meets the NIF cost goals. The NIF laser will contain 33,000 square feet (three-quarters of an acre) of highly polished precision optics, such as glass laser amplifier slabs, lenses, mirrors, and crystals. This is more than 40 times the total precision optical surface area in the Keck telescope in Hawaii, the largest telescope in the world. We also implemented new slab production technologies based on continuous pour of laser glass to meet NIF cost goals (almost a 20-fold improvement compared to Nova). By year's end, we had development runs under way addressing the many production issues that needed to be resolved to produce optical components of the quality required by NIF specifications. We prepared far more precise optical component drawings, which had to conform to the ISO10110 international standard, than earlier laser projects required. The volume of precision optics required for the NIF challenges the existing capacity of skilled opticians working inside the United States. In this era of fiber optics communication, skilled optics fabricators are already much in demand. Consequently, the NIF's optical procurement group initiated an opticians training program at Monroe Community College in Rochester, New York.
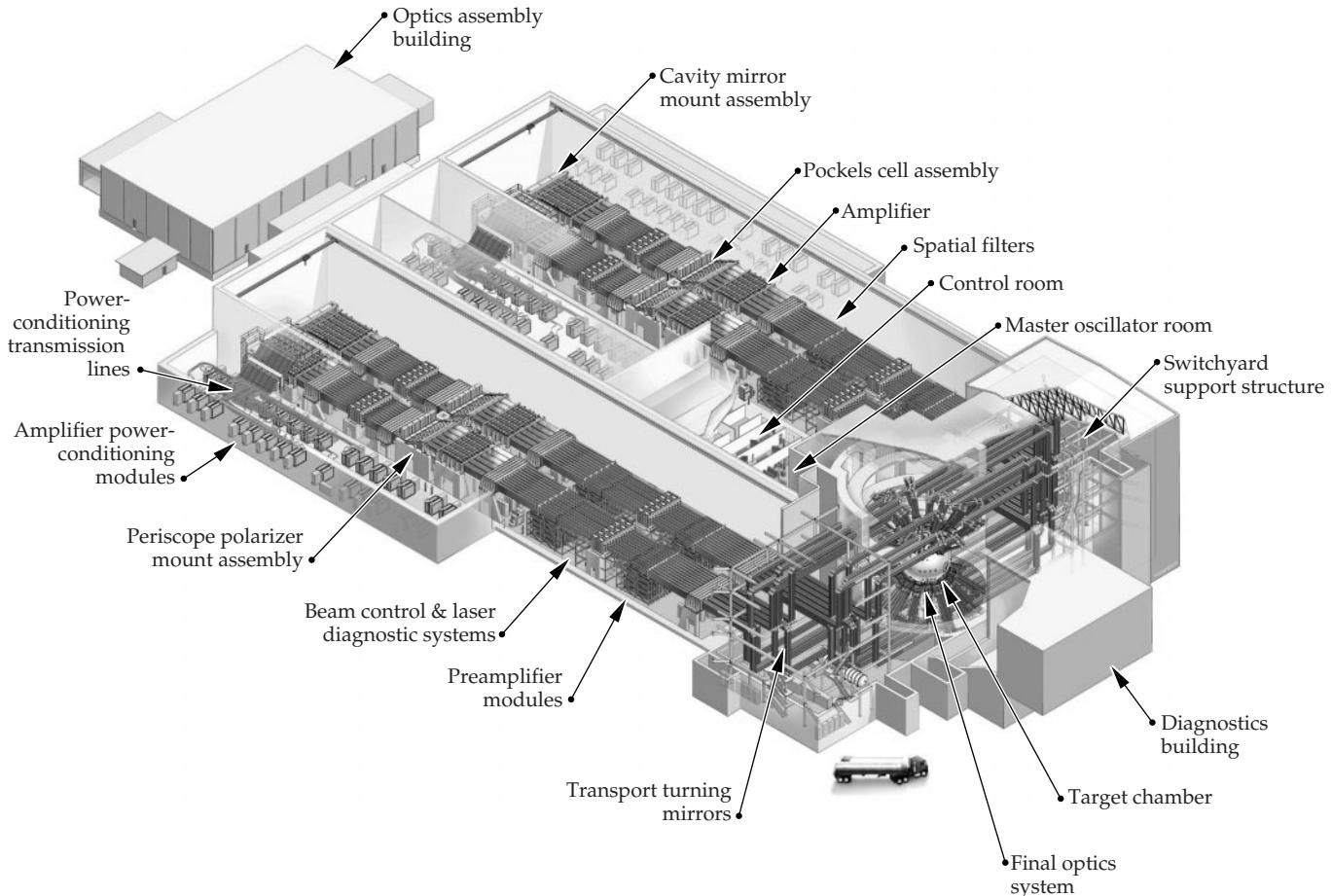
FIGURE 14. NIF Title I design.   (40-00-0996-2100Apb04).

The NIF's Title II design depends on the production of thousands of interdependent, accurate computer-aided designs, beginning with laser system simulations, which combine specialized software packages developed at LLNL, such as PROP92, with commercial software packages such as IDL, GLAD, Code V, and ASAP. We main-

FIGURE 15. Excavation and forms for the NIF target area at year's end. (40-60-1197-2342#1pb01).

tained the technical basis of the NIF design and updated it throughout the year as improved component information became available. In addition to NIF Council reviews, NIF 65% Title II Reviews, and ICF Programmatic reviews, the NIF Project Scientist established a Scientific Panel to oversee the progress of NIF technology development. ICF Program restructuring early this year combined NIF Special Equipment and NIF Development into a single organization to complete the core science and technology activities and transition into the final design phase of this Project. This resulted in significant progress on the Optical Pulse Generation System, or OPG; the accelerated activation of the NIF Amplifier Laboratory, AMPLAB; and the beginning of prototype testing.

Concurrent with these technology development activities, we reviewed and updated the documents that provide a hierarchy of the NIF design requirements, including *System Design Requirements* and the laser system design/performance baseline. Change Control boards, established last year, meet regularly each week. NIF Engineering Services employs over 200 advanced workstations to generate the thousands of detailed drawings required. As

these (mostly ProE and AutoCAD) drawings are completed, they pass through a sign-off and checking process before being placed under change control. We selected and implemented the commercial Sherpa Product Data Management system to provide a project-wide centralized document, engineering drawing, and configuration control capability. We also conducted regular cost and schedule reviews to track progress. The NIF Associate Project Engineer for Special Equipment held weekly engineering status meetings to assure that each System Engineering group was kept up to date on all aspects of the NIF Project. Monthly and quarterly progress reports were also prepared and distributed.

Throughout 1997, we utilized project controls developed and implemented the previous year, including the *NIF Project Control Manual,* the *Configuration Management Plan*, the *Integrated Project Schedul*e, *Cost Account Plans*, and the DOE-approved *Quality Assurance Plan*. The NIF underwent a full DOE Safety Management Evaluation late in the year and was judged to be a model project. During the excavation of the NIF site, for example, buried capacitors leaking detectable levels of polychlorinated biphenyls were uncovered. Safety response and cleanup teams were prompt and professional in dealing with each hazard. As a result, construction delays were minimized.

At the end of FY97, the NIF Project was on schedule and on budget, and its staff was confident in its commitment to meet all of the NIF's requirements.

Inertial Fusion Energy/New Technology Applications

Inertial Fusion Energy

ICF science and technology developed as part of the DP mission goals, in conjunction with Laboratory Directed Research and Development (LDRD) and research sponsored by the DOE Office of Fusion Energy Science, support the development of inertial fusion energy (IFE) as a possible long-range energy source. Work at Livermore supports the development of an IFE driver based on both a heavy-ion induction accelerator (HIF) and a diode-pumped solid-state laser (DPSSL).

In HIF research, LLNL has a broad-spectrum program, including heavy-ion target design, systems analysis of heavy-ion drivers and power plant chambers, and experiments with space-charge-dominated heavy-ion beams, with supporting theory and simulation of beam physics for present and future accelerators. The LLNL work on beam theory supports experiments both at LLNL and at Lawrence Berkeley National Laboratory (LBNL). Over the last year, we completed a high-gain heavy-ion target design,

modeled a multibeam linac driver meeting the requirements for that target, conducted LDRD experiments in beam bending through 90 degrees, and performed 3D beam particle simulations for those experiments.

We completed integrated calculations for a distributed radiator heavy-ion target design. This target ignited and produced 390 to 430 MJ of yield when driven with 5.8 to 6.5 MJ of 3-4 GeV Pb ions. The target has cylindrical symmetry with disk endplates. The ions uniformly illuminate these endplates in a 5-mm-radius spot. We used low-density hohlraum walls in approximate pressure balance with internal low-Z fill materials. Radiation symmetry was determined by the position of the radiator materials and particle ranges, with early time pressure symmetry influenced by radiation shims.[12] Future work will consider higher ion range, scaling to lower input energy and/or to lower beam power and more realistic beam-focusing geometries.

A systems model for a multibeam linac driver was completed to study cost and design optimizations for drivers capable of meeting the requirements of the target described above. The model integrates all accelerator subsystems from the ion source to the target, including drift-pulse compression and final focusing, using analytic models for beam physics and engineering constraints. Modifications of the model to treat recirculators, solenoid linacs, and higher ion charge states are in progress to permit future comparisons of different accelerator architectures.

We have completed the second year of a three-year LDRD experiment on heavy-ion beam bending and control, jointly supported by the Lasers, Physics, and Engineering directorates. Our goal is to address the critical scientific and technical challenges of bending, steering, and pulse-shape control of a space-charge-dominated heavy-ion beam. At present, experiments have been conducted through 45 degrees of bend; experiments on a 90-degree bend with five production modulators have begun.

LLNL's leading candidate for a laser driver for IFE is based on a DPSSL. The Mercury laser, which is an LDRD strategic initiative project, is intended to be 10% efficient, provide 100 J of energy in nanosecond pulses, and operate at 10 Hz. The critical technologies upon which Mercury is based are diode array pumps (instead of the flashlamps used in the NIF), Yb:S-FAP crystals (that replace the Nd:glass used in the NIF), and gas-cooled laser heads.

Figure 16 contains pictures of the key technologies of Mercury that are under development—a completed 40-bar laser diode array and a full-diameter Yb:S-FAP laser crystal. Figure 17 is a sketch of the laser architecture that will be used. Each diode array is referred to as a "tile," and 40 tiles will be needed for each of the four 160-kW peak-power diode arrays that will be deployed in

FIGURE 16. Photograph of an Yb:S-FAP laser crystal and laser diode array tile.   (70-17-0695-1699Cpb01)

Front end

Beam out

Laser diode pump head

Gas-cooled crystalline amplifier head
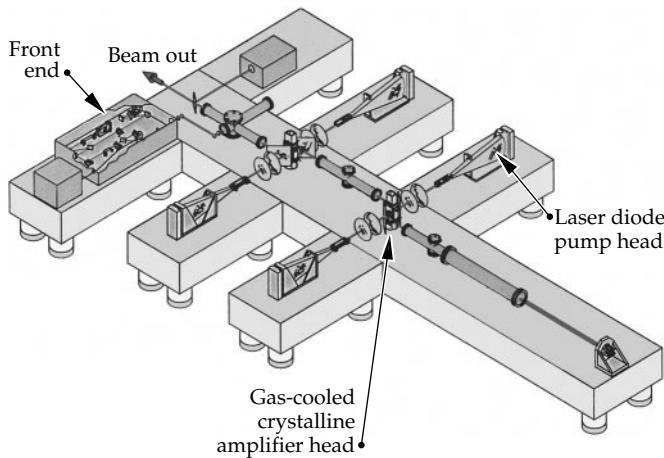
FIGURE 17. Schematic design of the Mercury laser system. (70-00-0497-0657pb01)

Mercury. Most aspects of the heatsink and fabrication technology of the diode arrays have been developed, and we are currently finalizing the structure of the epitaxially grown semiconductor wafers that are processed into the laser bars. We have successfully grown laser crystals that are free of cracks and "smoke," and are in the process of eliminating the core defects that collect near the center of the boule. The design of the laser system has been modeled and optimized by including technical considerations as diverse as the diode spectral chirp and power sag caused by heating and diode array light delivery to the

laser crystal limited by the measured array brightness, pump absorption, extraction efficiency with optical losses, damage and B-integral limits, thermal distortions, and required helium flow conditions. The system has been modeled to a level of detail to have confidence that we will be able to generate 100 J at 10 Hz with 10% efficiency. Beyond Mercury, we envision a sequence of the DPSSLs—Venus (1 kJ), Terra (15 kJ), and Helios (MJ-scale), that could enable improved means of meeting Stockpile Stewardship objectives and ultimately a fusion energy power plant. Importantly, Mercury and subsequent lasers will also have important uses in developing the target technologies needed for IFE.

New Technology Applications

LLNL has a history of initiating research on a broad range of applications of technology developed in the ICF Program. These applications include high-average-power solid-state lasers, Extreme Ultraviolet Lithography (EUVL), and Micropower Impulse Radar (MIR), which have grown into independent programs within the Laser Directorate at LLNL.

A major initiative of the LS&T Program over the past year has been to develop high-average-power femtosecond (fs) lasers for use in the SSP. Thus, technology that grew out of the Petawatt projects has returned to the point in which a 12-W, 100-fs laser-cutting workstation (LCWS) is now being developed for the Y12 plant. The LCWS, being developed jointly with the Weapons Program, will be delivered to Y12 in 1998. LS&T laser technology has also been applied to the DOE-sponsored Caliope Project for remote sensing of chemicals associated with nuclear materials proliferation. A rapidly tunable DPSSL-based optical parametric oscillator operating in the moderate infrared range was tested at the Nevada Test Site in 1997 and proven to detect small concentrations of chemicals at relevant distances. Multishot averaging of atmospheric fluctuations was proven to be quite effective.

High-power laser spin-offs from ICF have also been valuable to DOE. LS&T is now completing the Advanced Imaging Testbed (AIT) laser based on Zig-Zag slab technology, which produces exceptionally coherent 50-J 2ω beams operating at 3 Hz. The AIT laser is scheduled for delivery to the Startive Optical Range at the Philips Laboratory in 1998. In 1997, LS&T also began the development of a heat capacity laser for tactical missile defense planned for use at the High Energy Laser Strategic Test Facility under Army support. In addition, LS&T has been working with an aerospace partner on DPSSL-based illuminators for use with the Airborne Laser, a NIF-scale project of national importance under Air Force sponsorship.

A recent thrust has been the development of applications to medicine including: (1) modeling laser–tissue

interactions, (2) establishing a medical photonics laboratory for developing a host of new medical technologies, and (3) developing user-defined laser diodes and DPSSLs for medical procedures (e.g., port-wine stain removal, tattoo removal, and laser surgery).

The application of computer modeling to medicine uses the LATIS computer program. LATIS is a time-dependent, two-dimensional program. It considers four categories of physical processes and their nonlinear coupling: laser propagation, thermal response, material response, and hydrodynamical response. Because of similarities to ICF modeling in the physical processes, the mathematical equations, and the numerical methods to solve the equations, we have been able to build on the 25 years of experience in ICF modeling to develop LATIS.

One of the main differences between medicine and fusion is the temperature scale (≤ 1 eV vs several KeV). Because of this and the different materials involved, we have had to obtain special data such as opacity, conductivity, equation-of-state, and chemical reaction rates.

During the last year, the modeling project has made several important contributions. In laser tissue welding, we concluded that water diffusion and evaporation play an important role in setting the tissue surface temperature. We also modeled the temperature profiles achieved in animal vessel repair experiments done in collaboration with University of California at Los Angeles Medical School. In particular, we studied the effect of using a feedback control system in these experiments. The models provided an explanation of the difference in weld quality achieved with and without feedback control.

We have applied LATIS to the study of laser-generated vapor bubbles as part of a project to develop a device for breaking up blood clots that cause strokes. We found that although bubbles appear rather spherical in experimental photographs, 1D spherical simulations overestimated the size and duration of the bubbles by about 50%. We developed a new rezoning method to enable the creation of 2D simulations over the long time period of the bubble expansion and collapse. We found very good agreement between the 2D results and experiment. Such simulations have been used to help design a device that is now in animal trials by an industrial partner.

We also developed a model for laser absorption in the multiphoton-initiated plasma regime and applied it to simulations of ultra-short-pulse high-precision tissue ablation. In comparison to experimental measurements of the ablation of dental enamel, we have found good agreement in the ablation threshold and the sharp peak in ablation efficiency just above threshold. The model including only direct vaporization of the enamel underpredicts the amount of material removed. We explored alternate mechanisms, such as melting and

pressure-induced material failure and believe that they may play an important role in ultrashort pulse ablation.

We have found many mutual benefits between laser medicine and ICF modeling. We found it quite effective to build on the ICF experience in first developing the basic laser medicine capability. There has also been a spinback from our medicine experience to ICF. In particular, errors in laser photon Monte-Carlo tracking have been found and corrected. The material strength and failure packages developed to model tissue spallation have been recently applied to design and analyze RT experiments. We also expect that the rezoning scheme recently developed for the stroke treatment project will find use in ICF simulations.

Program Resources and Facilities

Resources

In FY 1997, financial resources for the LLNL ICF Program totaled $84.5 million in DOE operating funds and $2.1 million in DOE capital equipment allocations. At LLNL, the NIF Project managed $59.2 million in new DOE operating funds and $131.9 million in new construction funds for FY 1997. The average LLNL full-time employee equivalent count over the year was 255.3 for the ICF Program and 264.9 for the NIF Project. Supple-mental contract labor personnel were used in clerical, design, and engineering positions, as well as for Nova operators. The ICF Program employed approximately 53.0 supplemental labor personnel, and the NIF Project employed approximately 51.2 supplemental labor personnel in FY 1997.

Figure 18 shows the resources available to the ICF Program over the past 16 years and compares the operating funds provided by DOE in then-year dollars vs the same funding discounted to reflect 1982 dollars. The figure illustrates that the real purchasing power for DOE funding, as related to FY 1982, has remained fairly constant and is expected to remain so in FY 1998. These resources enabled the ICF Program to continue its support of research and development of high-energy-density physics, laser component development, optics technology development, and optics pilot production.

Table 1 illustrates the NIF Project national funding profile as provided during the FY 1999 Field Budget Submission to DOE. As of FY 1997, 22.5% of the total project funding had been obligated by DOE.

The resources provided to the NIF Project in FY 1997 provided for the start of facility construction, including site preparation and extensive site excavation, as well as for the continuation of final design activities across the Project. Major contracts were awarded for the facilitization of optics manufacturers and supply of structural steel.

FIGURE 18. Resources available to the ICF Program over the past 16 years compared with operating funds provided by DOE in then-year dollars. (05-00-0598-1131pb01)
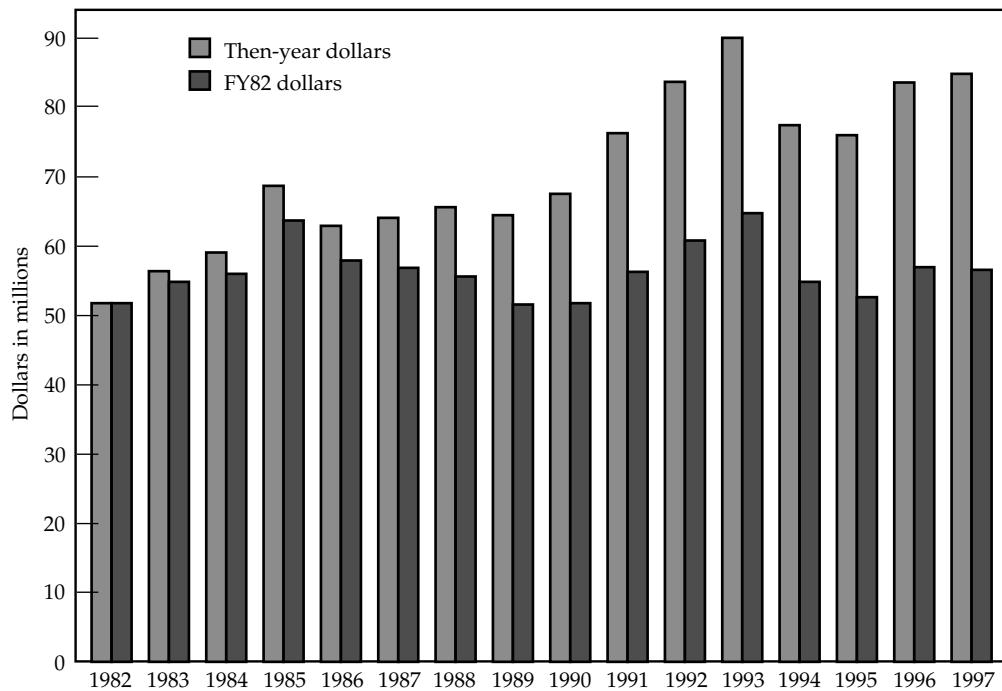
TABLE 1. NIF Project national funding profile.

Funding type ($M)	Prior years	FY97	FY98	FY99	FY00	FY01	FY02	FY03
Operating (Other project costs)	41.8	59.2	31.3	6.8	10.0	1.8	1.4	0.9
Construction (Line item)	37.4	131.9	197.8	284.2	248.1	74.1	65.0	7.2

Facilities

The 1997 facilities activities addressed both support of ongoing operations and buildup of the Title II engineering staff and the beginning of NIF construction. The major activities included: (1) maintaining and providing selected upgrades to the existing Nova, Beamlet, AMPLAB, and development facilities to support demanding experimental schedules; (2) providing space and infrastructure such as networking to accommodate the increased engineering staff for the NIF Title II design; (3) completing use agreements and acquiring construction and laydown areas on the LLNL site in preparation for the beginning of NIF construction; (4) completing a first round of detailed planning for transitioning existing Nova/Beamlet-centered facilities to the NIF and beginning designs in support of this transition.

The ICF Program comprises 54 facilities including laboratories, offices, and support areas totaling 638,000 gross sq ft. Figure 19 shows the locations of these ICF facilities within the Laser Programs and the Laboratory.

Specific activities and accomplishments are described below:

• Building and support system (e.g., low-conductivity water) maintenance were reviewed, prioritized, and updated or corrected as necessary in the key on-line Nova, Beamlet, AMPLAB, and development facilities to assure continuing a high level of experimental operations.

• Several upgrades and modifications to key laboratory- and building-related equipment totaling $2.7M were completed. These included a B481 power feeder upgrade; B298 utility and air-conditioning upgrade; B392 heating, ventilating, and air-conditioning upgrade; and various laboratory, office, and support area modifications.
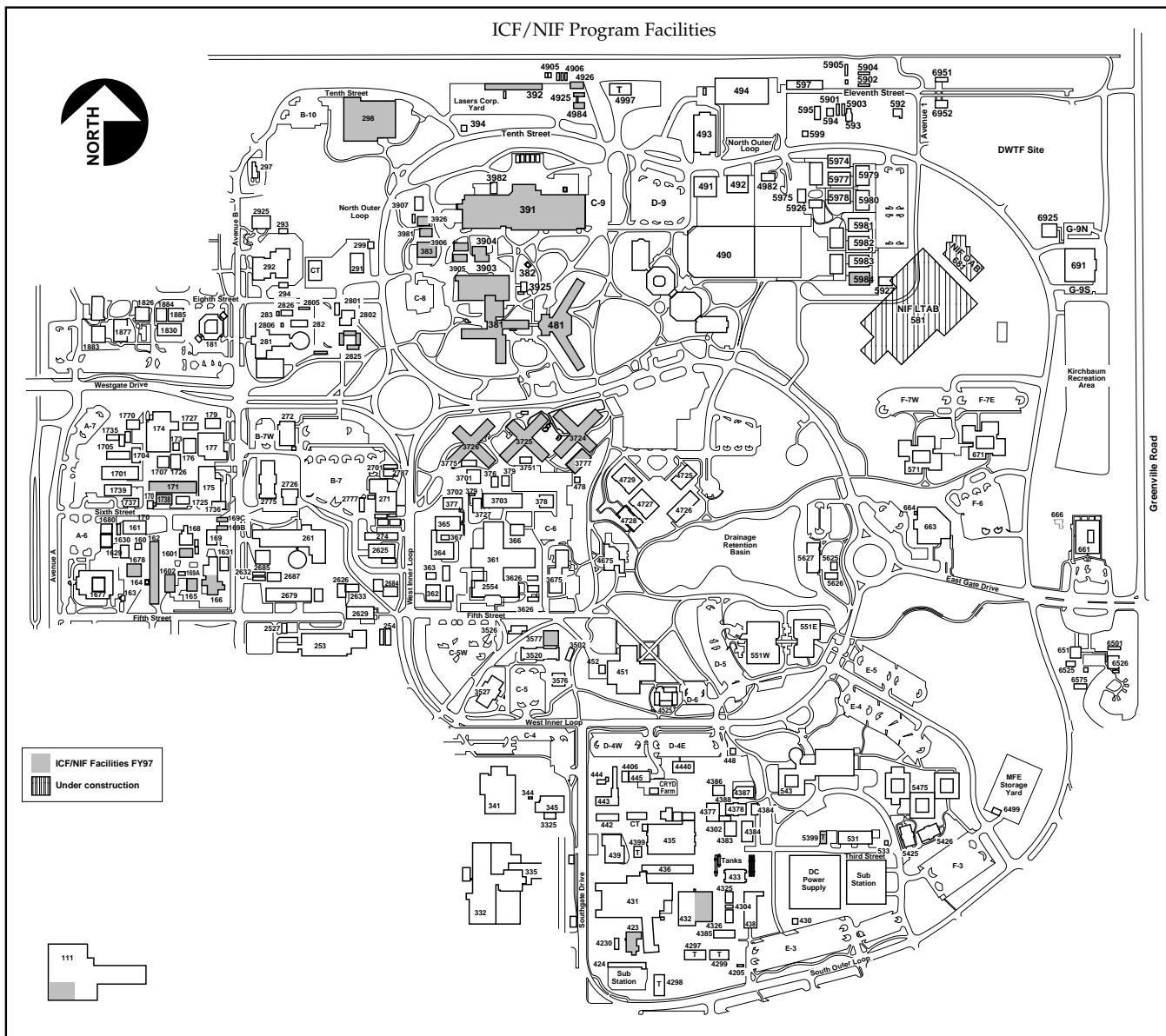
Figure 19. Locations of ICF Program facilities at LLNL. (05-00-0497-0547pb02)

- One of the outcomes of having the Laboratory selected as the official site for the NIF was the increased need to provide additional access to the NIF staff. In support of this need, B481 was converted from a limited (Q) to an administrative controlled (P) status. Although the security level was lowered, proprietary activities within the building still require continued alarm and access control. This access is controlled through the existing CAIN booths at the building entrances. All red badge employees that need access must contact one of the Program Area Access Requesters for access privileges.
- The continuing need for classified meetings for integrating the numerous science, engineering,

technical, and administrative activities within the ICF Program and the NIF Project led to conversion of the B381 Auditorium to a permanent limited (Q) status to provide additional capability for large classified briefings.
- The growth in office/design space (~200 spaces) for the NIF engineering teams was largely accommodated through the use of existing facilities. Temporary lease arrangements with organizations outside the program were arranged for the remaining space. Collocation of engineers/designers primarily within the core ICF/NIF facilities maximized worker efficiency.
- A space utilization program was implemented. Approximately 15% of the total ~200

spaces required for growth in the NIF engineering teams came from improved space utilization, thereby avoiding substantial space-related expenses. Additional areas of increased utilization have been identified and are being implemented.

- Agreements (~20) between the ICF Program and various organizations including LLNL, DOE, and the University of California pertaining to building and land use (e.g., construction areas) were completed in preparation for the beginning of NIF construction. This documentation was catalogued and entered into the Quality Assurance library.

- The support facilities needed for NIF buildup and operations were estimated based on the NIF design, Nova/Beamlet operational data, and detailed inputs from the special equipment engineering staff. Existing space use was reviewed, areas were selected as conversion candidates, and cost estimates were prepared. The support laboratory space for the ICF/NIF Program will be approximately double that of the ICF/Nova Program by using existing Nova/Beamlet space (Figure 20).

- In support of the facility transition effort, a number of feasibility and conceptual design and cost studies were completed addressing conversion or upgrade of existing space to that required for the NIF.

- The ICF Program is completing its current use of the west end of Building 391 as the Two-Beam area. Following analysis and review, this area was designated as the Optics Processing Development Area (OPDA) and will be modified as a laboratory to develop techniques for the cleaning and coating of large-aperture optics. Planning for dismantling of the existing Two-Beam special equipment started, and design for conversion to the OPDA is nearly complete. Construction is scheduled to begin second quarter FY98.

- A preliminary design was completed for conversion of a portion of the Beamlet Hi-bay to a facility for construction of the NIF amplifier frame assembly units following Beamlet shutdown tentatively scheduled for third quarter FY98.

- Various smaller ICF laboratories have been transitioned for use in NIF development and eventual NIF support. Overall, ~35,000 sq ft (~15%) of total ICF experimental space is now in transition.

- The NIF Project has need for ~50,000 sq ft of warehouse space starting third quarter FY98 and for the project duration to accommodate special equipment construction. The availability of on-site space was evaluated with the Laboratory, and no available on-site space meets the requirements. Procurement was requested to begin a survey of off-site warehouse space for cost and availability with preference given to that in close proximity to the Laboratory site.

- Planning has started for the next phase in transitioning office/designer space following completion of the NIF Title II design.

Figure 20. NIF support laboratory space using the existing Nova/Beamlet space. (40-00-0497-0575pb01)
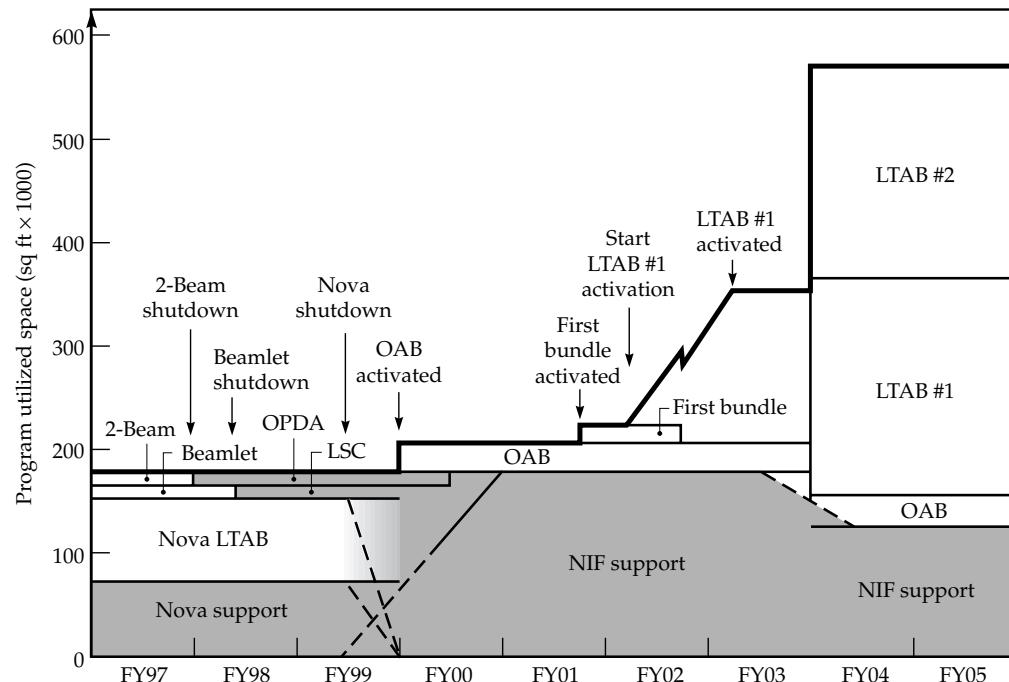
Environment, Safety, and Health (ES&H)

A number of steps were taken in FY97 to improve the ES&H Program to ensure continuing safety of the ongoing operations and to be consistent with an increase in level of activity resulting from the selection of the Laboratory as the NIF site. This selection led to the beginning of site preparation and the beginning of construction. A continuing strong self-assessment program provides the basis for evaluation and improvement.

The ICF ES&H activities encompass 15 major facilities located throughout LLNL with 75 individual laboratories and experimental areas. There are currently 44 Operational Safety Procedures (OSPs) and 3 Facility Safety Procedures (FSPs) pertaining to program operations. Specific activities and accomplishments include:

- A Safety Advisory Group consisting of program personnel from a range of disciplines was reinstated. This group, reporting to the Deputy Associate Director for ICF/NIF/High-Energy-Density Experimental Science, provides an independent evaluation of safety in the design, construction, operation, and maintenance of existing NIF laser and laser-related systems.
- The program ES&H team now includes a Program Laser Safety Officer. This individual provides expertise and support on evaluation and control of laser hazards in all program elements consistent with the applicable laser safety standard ANSI Z136.1. Included is responsibility for installation, checkout, and maintenance of all safety interlocks.
- A Red Team review of the 44 OSPs and 3 FSPs was completed to determine the adequacy of the OSP/FSP and the consistency of the OSP/FSP and the work being performed. Included was a Laboratory walkthrough by the review team with the Responsible Individuals (RIs). The findings and comments were reviewed and documented. Laboratory specific deficiencies were corrected by the RIs. General OSP deficiencies, most of which are procedural, are being corrected as the OSPs are reviewed and approved.
- RI roles/responsibilities information was updated, and mandatory training for all RIs was completed and is current. The training included a component on Integrated Safety Management (ISM).
- Training matrices have been added to all OSPs/FSPs for improved tracking of training. Classes are scheduled in coordination with the Laser Assurance Training Coordinator. Training compliance was reviewed and improvements were made as required.

- The 1997 self-assessment program was completed as scheduled and all laboratories and facilities are current. A total of 256 laboratories and experimental areas were assessed with 297 noted deficiencies. A review of the data shows a close resemblance to previous years in both number and types of findings with the most hits assigned to the "general" category (e.g., exit signs, locker labels, seismic restraints). The assessment identified no imminent hazards, and corrections are under way. DefTrack is used to track completion of these deficiencies and analyze trends.
- The LLNL/DOE Work Smart Standards process was supported with work/hazard identification on selected facilities. Standards verification is under way consistent with the LLNL/DOE schedule.
- Facility deactivation has been formalized with development of a Shutdown Surveillance and Maintenance Plan for the Two-Beam area in B391. This plan will address the removal of special equipment by program personnel following a Two-Beam shutdown scheduled for first quarter FY98. This plan will serve as a model for the future Beamlet and Nova close-out and overall facility transition safety management.
- An activity authorization section was added to all OSPs. This section serves as a reminder for the Approving Individual that he/she is responsible for pre-start and readiness requirements as outlined in the LLNL *Health and Safety Manual*.
- A start-up procedure has been developed and implemented for all new and revised experimental activities. The procedure is used by the RI in conjunction with ES&H Assurances and Hazards Control to ensure that applicable ES&H requirements have been reviewed and integrated into the activity before the start-up is authorized. The procedure includes program management's approval to begin the new or revised activity.
- ES&H roles and responsibilities information was updated and communicated to all program personnel. Included were revisions of the program organization charts showing recent changes. Emphasized are the organizational elements involved in managing and implementing ES&H in the Program, including line management, ES&H support, coordination and oversight, and ES&H technical support. Also identified are the OSP Approvers, RIs, the associated OSPs/FSPs, and program cost centers.
- The NIF Project Management System is documented in the *Project Execution Plan*, *Project*

Management Descriptions, *Project Control Manual*, *Integrated Project Schedule*, *Cost Account Plans*, *Quality Assurance Program Plan*, and supporting documents. The management system was evaluated by the DOE OAK and found to be complete and operational.

- The NIF primary criteria and functional requirements were developed according to the DOE process and Work Smart Standards. These criteria have been approved by DOE and incorporated into the contract between DOE and the University of California.

- The NIF Specific Analysis is Appendix I of the *Programmatic Environmental Impact Statement* (PEIS) for the SSP. This document provides the detailed environmental impacts for the construction and operation of the NIF. The *Mitigation Action Plan* issued in February 1997 presents the activities needed to mitigate the impacts described in the PEIS. A full set of environmental permits were applied for and approved (e.g., Storm Water Pollution Prevention Plan, etc.) for the construction of the NIF and support facilities (e.g., B391W).

- The NIF *Preliminary Safety Analysis Report* was approved in October 1996, and then as design evolved, a set of amendments evaluating these new features and a set of audits of the final Title II design were conducted to ensure that safety commitments were met. These activities form the basis for the *Final Safety Analysis Report* (FSAR) that will be started in FY98.

- The NIF *Construction Safety Program* was approved, and then subtier safety plans were prepared. Training was conducted, and the safety plan implemented at the NIF construction site. The DOE Safety Management Evaluation review of LLNL included the review of construction safety. The NIF was thoroughly reviewed, and the resulting conclusion of the evaluation report was that "...NIF safety management is a model of integrated safety management with respect to construction."

- The NIF Construction Safety Team continues their weekly meetings to coordinate site construction, safety audits, and environmental issues for NIF construction. The NIF Environmental and Safety Working Group continued their biweekly meetings to coordinate ES&H documents and evaluations like the *NIF Risk Management Plan*, *Waste Minimization and Pollution Prevention Plan*, and the FSAR.

- Quality Surveillances and Audits have been conducted for a broad range of Project activities (e.g., design, configuration control, concrete work, etc.). These reviews are all documented, and any action items are tracked to completion in the Project tracking system.

- A safety feature audit of B39 W, Optics Development Facility, was completed. All required safety features for facilities were found to be present in the design modifications and the remaining parts of B391.

References

1. Delamater et al., *Phys. Plasmas* **3**, 2002 (1996).
2. Delamater et al., submitted to *Phys. Rev. Lett.* (1998).
3. H. A. Rose et al., *Phys. Plasmas* **3**, 1709 (1996).
4. J. D. Lindl, *Phys. Plasmas* (1995).
5. S. W. Haan et al., *Phys. Plasmas* (1995).
6. P. Amendt et al., *Phys Plasmas* (1997).
7. A. Hauer, N. Delamater et al., *Rev. Sci. Instrum.* (1995).
8. Tabak et al., *Phys Plasmas* **1**, 1626 (1994).
9. B. A. Remington et al., *Phys. Plasmas* **4**, 1994 (1997).
10. R. P. Drake et al., submitted to *Phys. Rev. Lett.* (1997) and to *Ap. J* (1997).
11. J. Kane et al., *Ap. J.* **478**, L75 (1997) and B.A. Remington et al., *Phys. Plasmas* **4**, 1994 (1997).
12. M. Tabak and D. Callahan-Miller, "Design of a Distributed Radiator Target for Inertial Fusion Driven from Two Sides with Heavy Ion Beams," to be published in *Physics of Plasmas*, May 1998.

Supernova Hydrodynamics Experiments on the Nova Laser

B. A. Remington

J. Castor

R. McCray[*]

K. Estabrook

R. London

E. Liang[**]

S. G. Glendinning

D. H. Munro

D. Arnett[***]

R. P. Drake[†]

L. J. Suter

B. Fryxell[††]

J. Kane[***]

R. J. Wallace

A. Rubenchik[†††]

Introduction

In studying complex astrophysical phenomena, such as supernovae (SNs), investigators do not have the luxury of setting up well controlled experiments at some distant location in the universe to test the physics of their models and theories. A surrogate environment to serve as an experimental astrophysics testbed would be highly beneficial. Sophisticated, modern research lasers have been developed largely as a result of the world-wide effort in inertial confinement fusion. Such lasers offer the potential for creating just such an experimental testbed using well controlled, well diagnosed laser-produced plasmas.

On February 23, 1987, at 0735 UT, the blue supergiant Sanduleak located in the Large Magellanic Cloud, a dwarf galaxy at a distance of 50 kpc from earth, exploded as a core-collapse Type II supernova (SN).[1] This event was marked by a prodigious outburst of neutrinos followed ~3 h later by the ultraviolet (UV) flash as the shock broke through the surface of the star. Thus began what will certainly be recorded as the most significant astrophysical event of the decade.

By February 23, 1997, SN1987A will have been studied for 10 years, and our understanding has progressed enormously. One example is the consensus that strong hydrodynamic mixing of the heavier core elements outward into the lower-density envelope is needed to explain a wide range of observables. Figure 1(a), which shows the results from a two-dimensional (2-D) simulation of SN1987A at 3.6 h after explosion, is an image of density to illustrate such mixing.[2] However, new mysteries continue to emerge. Despite considerable effort worldwide, simulations still predict that the mixing front progresses significantly more slowly than is actually observed.[3–8]

SN1987A is now evolving into the early remnant stage. Figure 1(b) shows an optical image taken in February 1994 with a wide-field camera on the Hubble Space Telescope (HST).[9] The expanding SN ejecta corresponds to the central bright spot, surrounded by what appears to be an assembly of three rings. The origin of these ring nebulae remains a mystery.[10] There is general agreement, however, that the SN ejecta is expanding at a much greater velocity (~10^4 km/s) than the nebular rings (10–20 km/s), with the ejecta expected to impact the inner ring in 5 to 10 years.[10–16] We stand poised to witness a colliding plasma "astrophysics experiment" of a spectacular nature. Simulations offer enticing glimpses of what may happen, as shown by the density–pressure plots in Figures 1(c) and 1(d) (reproduced from Ref. 16). Apart from cosmic pyrotechnics, this collision may shed light on the nature of the circumstellar ring nebula.

Both of these phases of SN evolution—the core hydrodynamic mixing at intermediate times (10^3–10^4 s), and colliding plasmas during remnant formation—are areas rich with possibilities for supporting laboratory experiments. This article describes two such experiments using the Nova laser[17] at LLNL to create the relevant plasma environment. First, we discuss hydrodynamic instabilities in the context of core-collapse SNs (in particular, SN1987A) and the corresponding laser experiment. Next, we describe the early stages of SN1987A remnant formation and the corresponding laser experiment. We conclude with an outlook for the future.

* University of Colorado, Boulder, Colorado.
** Rice University, Houston, Texas.
*** University of Arizona, Tucson, Arizona.
† University of Michigan, Ann Arbor, Michigan.
†† George Mason University, Fairfax, Virginia.
††† University of California, Davis, California.

(a) Simulation 3.6 h after explosion

(b) Hubble image 7 y after explosion

FIGURE 1. (a) Result, in terms of density, from a 2-D simulation of the hydrodynamic mixing in SN1987A (reproduced from Ref. 2). The initial velocity perturbation was $\delta v/v = 10\%$. (b) Image of SN1987A obtained by the Hubble Telescope in February 1994 (reproduced from Ref. 9). The expanding SN ejecta is the central dot. The inner, yellow ring is a planetary nebula of uncertain origin. The outer rings are also part of the nebular structure. The emissions have now faded but are expected to resume in a few years when the ejecta strike the inner ring. (c) Simulations of the collision of SN ejecta with the inner ring nebula two years after initial impact (from Ref. 16). The top half represents density; the bottom half is pressure. (d) Same as (c), except 23 years after initial impact. (40-00-1296-2753pb01)

(c) Simulation 2.1 y after impact

(d) Simulation 23 y after impact
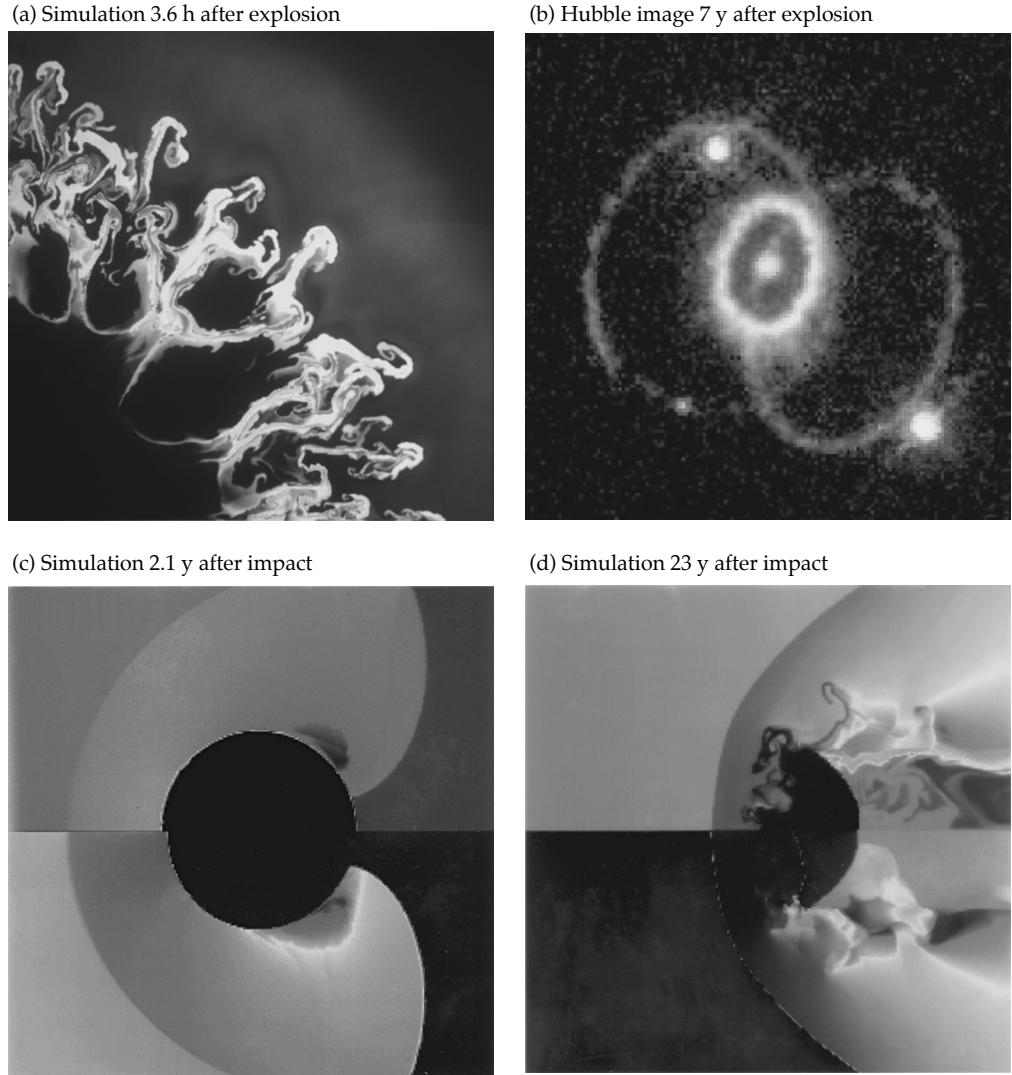
Hydrodynamics of SN1987A

The first hints that all was not well with a spherically symmetric, one-dimensional (1-D) model of SN1987A came from the light curve (total luminosity vs time). A secondary maximum was observed, but it was considerably earlier (~20 days) and broader than expected.[18] Then came the "Bochum event," a spectroscopic anomaly starting at day ~25 and suggesting an auxiliary heat source.[19] The observation of the core elements ^{56}Ni, ^{56}Co, and ^{56}Fe poking out through the surrounding hydrogen envelop six months earlier than expected, however, proved conclusive.[10,20] The 1-D models of SNs were largely abandoned, and modeling in 2D commenced in earnest. From the Doppler broadening of the infrared and gamma spectral lines of Fe, Ni, and Co, core velocities as great as 3000 km/s were inferred.[20] Modeling (done primarily in 2D) predicts significantly lower peak velocities.[2,3] It would be highly beneficial to be able to experimentally test the hydrodynamic instability modeling of the SN codes.

Current uncertainties notwithstanding, the following picture has emerged for SN1987A. A 1-D stellar evolution calculation gives the density profile for the 19-$M_\odot$ mass progenitor,[21] shown in Figure 2(a), where $M_\odot$ represents one solar mass. An inner Fe core, $M_r/M_\odot < 1.6$, is surrounded by a layer of Si, Ne, O, and C in the region corresponding to $1.6 < M_r/M_\odot < 2.3$, where M_r is the mass out to a radius r. This layer is followed by a mostly He layer at $2.3 < M_r/M_\odot < 6$, ending in a hydrogen envelope for $M_r/M_\odot > 6$, which extends out to a radius of $R_0 = 2.2 \times 10^{12}$ cm. The SN explosion is triggered when the Fe core collapses to form a 1.6-$M_\odot$ neutron star. When the core reaches the density of nuclear degenerate matter, the core rebounds, which launches an exceedingly strong radial shock propagating outward through the star, corresponding to a release of 1–2×10^{51} ergs of energy, which effectively blows the star apart. The mass cut—that is, the division between what collapses into the neutron star versus what is ejected—is believed to lie somewhere within the oxygen layer.

(a) SN1987A progenitor

(b) He–H interface velocity

(c) $t = 4000$ s

(d) $t = 3.6$ h, $\delta v/v = 1\%$

(e) $t = 3.6$ h, $\delta v/v = 5\%$
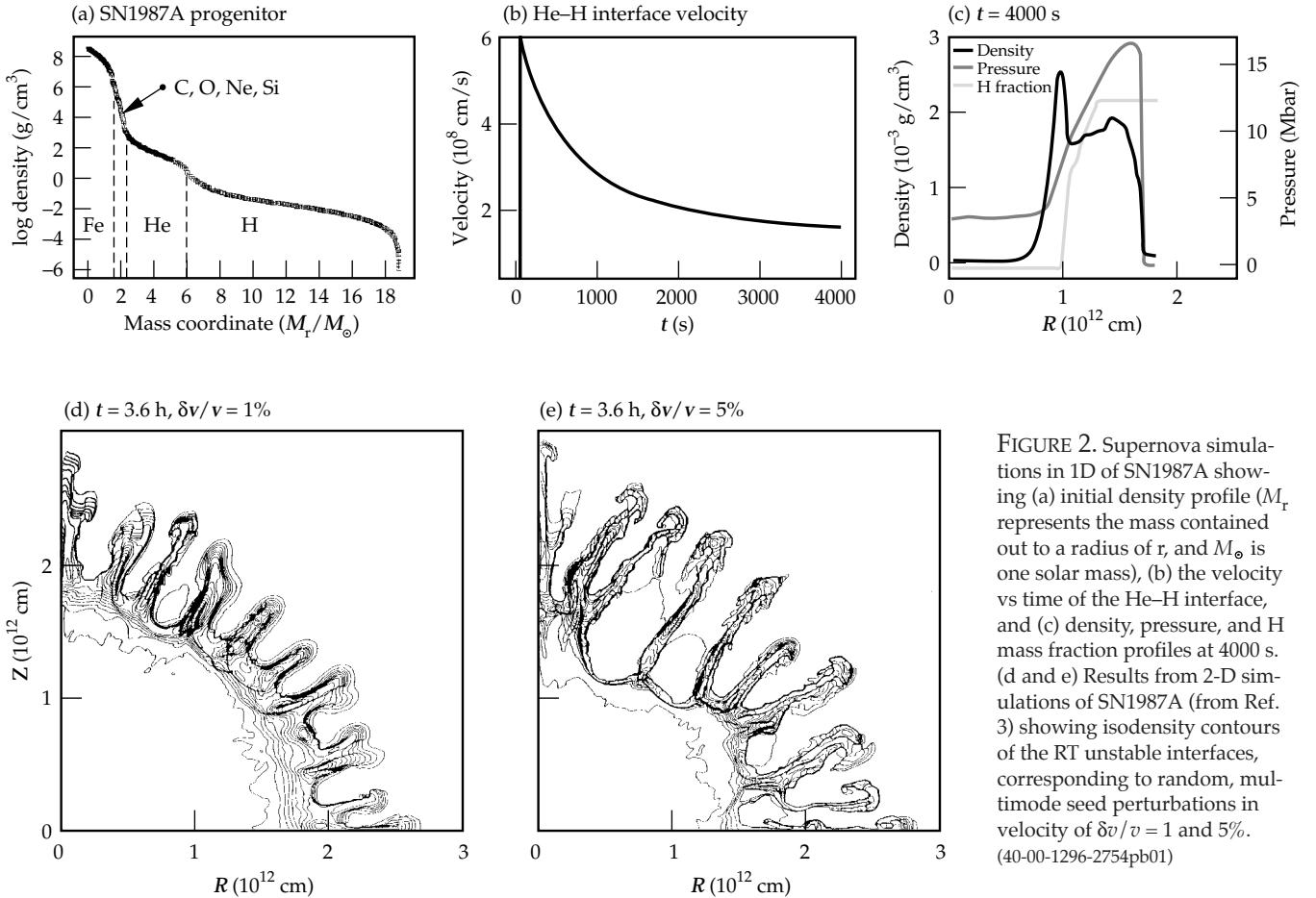
FIGURE 2. Supernova simulations in 1D of SN1987A showing (a) initial density profile (M_r represents the mass contained out to a radius of r, and $M_\odot$ is one solar mass), (b) the velocity vs time of the He–H interface, and (c) density, pressure, and H mass fraction profiles at 4000 s. (d and e) Results from 2-D simulations of SN1987A (from Ref. 3) showing isodensity contours of the RT unstable interfaces, corresponding to random, multimode seed perturbations in velocity of $\delta v/v = 1$ and 5%. (40-00-1296-2754pb01)

We start with a progenitor similar to that shown in Figure 2(a) and calculate the hydrodynamic evolution using the SN hydrodynamics code PROMETHEUS.[3,22] In this work, we focus on instabilities at the He–H interface. To economize computing time, we model only $M_r/M_\odot \geq 5$, depositing the explosion energy, $E = 1.5 \times 10^{51}$ ergs, as a mix of thermal and kinetic energy at the inner boundary ($M_r/M_\odot = 5$). This launches a strong radial shock that reaches the He–H interface ($M_r/M_\odot = 6$) after a transit time of about 100 s. At this point, the initial density, pressure, temperature, and velocity at the interface are 2.3 g/cm^3, 75 Gbar, 6 keV, and 6×10^8 cm/s, respectively. Figure 2(b) shows the velocity of the He–H interface as a function of time, and Figure 2(c) shows the density and pressure profiles at a time of 4000 s. By 4000 s, the shock has traveled about halfway out of the star. Note that at the He–H interface ($R \approx 1.0 \times 10^{12}$ cm), the pressure and density gradients are crossed, that is, $\nabla\rho\cdot\nabla P < 0$, such that the He layer is being decelerated by the H layer. This situation is unstable to the Rayleigh–Taylor (RT) instability,[23] and perturbations at the interface grow in time.

The evolution of compressible, nonlinear, multimode RT instability is an unsolved theoretical problem, and detailed numerical simulations are required. An example of a typical 2-D SN simulation is shown in Figures 2(d) and 2(e) by the isodensity contours corresponding to a time of 3.6 h (Ref. 3). The two cases shown here differ only in the magnitude of the initial multimode velocity perturbation: $\delta v/v = 1\%$ and 5%. [Note that the calculation shown in Figure 1(a) is similar, except that the resolution is higher by a factor of 2, and $\delta v/v = 10\%$]. Strong instability growth is evident, with spikes of the heavier He falling radially outward through the lower-density H layer. The following observations are noteworthy. First, the instability has evolved well into the nonlinear regime for all the calculations, with characteristic peak-to-valley amplitudes larger than characteristic wavelengths, $\eta_{PV} \geq \lambda_{char}$, and the perturbations taking on the classic RT bubble-and-spike shape. Second, the final result at 3.6 h is still sensitive to the "initial conditions" because increasing the seed amplitudes increases the growth. Third, there appears to be a characteristic dominant mode of mode number $l = 2\pi R/\lambda \approx 20$, although the starting configuration was a random multimode pattern. Fourth, the peak velocities of the Ni spikes penetrating into the hydrogen envelope in these calculations are not appreciably different, with $v_{max} \leq 2000$ km/s.

Experiments of Supernova Hydrodynamics

Figure 3(a) shows the experimental configuration, described extensively elsewhere,[24–26] for our laser experiments. Eight of the ten Nova laser beams at a duration of 1 ns and total energy of 12 kJ are focused into a 3.0-mm-long, 1.6-mm-diam Au hohlraum (cylindrical radiation cavity) converting to a ~190-eV thermal x-ray drive. The experimental package is planar, with an 85-μm Cu ($\rho = 8.9$ g/cm^3) foil backed by 500 μm of CH$_2$ ($\rho = 0.95$ g/cm^3). A sinusoidal ripple with wavelength $\lambda = 200$ μm and amplitude $\eta_0 = 20$ μm is imposed at this embedded interface. The package is mounted across a diagnostic hole in the hohlraum wall so that the inner (smooth) side of the Cu sees the x-ray drive. Diagnosis of the interface is through side-on, x-ray radiography using the remaining two Nova beams focused onto an Fe backlighter disk to generate a 5-ns pulse of He-α x rays at 6.7 keV. In this side-on view, the opaque Cu appears as a shadow, and the CH$_2$ is essentially transparent.

We model the laser experiment using a combination of codes. Figures 3(b) through 3(d) show the results of modeling in 1D with HYADES,[27] CALE,[28] and PROMETHEUS.[3,22] HYADES is a 1-D Lagrangian code with multigroup radiation transport and tabular equation of state (EOS); CALE is a 2-D ALE code with tabular EOS; and PROMETHEUS is a 2-D Eulerian PPM code using (here) an ideal-gas EOS. We use a measured radiation temperature, $T_r(t)$, as the source input to HYADES. Figure 3(b) shows the velocity of the Cu–CH$_2$ interface as simulated in HYADES. Note the impulsive shock acceleration, followed by a protracted deceleration, similar to that of the He–H interface in the SN shown in Figure 2(b). We do a high-resolution HYADES run, including multigroup radiation transport, for the first 2.45 ns, at which time the shock approaches the Cu–CH$_2$ interface. We then map the results to either 1-D or 2-D CALE and PROMETHEUS. (We do not have radiation transport in the versions of these 2-D codes that we are using.) We compare the results for pressure and density at 20 ns from a continuous 1-D HYADES run including radiation transport versus that from CALE [Figure 3(c)] and PROMETHEUS [Figure (3d)]. The mapping works very well for both codes. Note that the pressures for the Nova experiment, 1–2 Mbar, are not too different from those of the SN (10–15 Mbar), as shown in Figure 2(c), although the SN densities are lower by a factor of about 10^3.
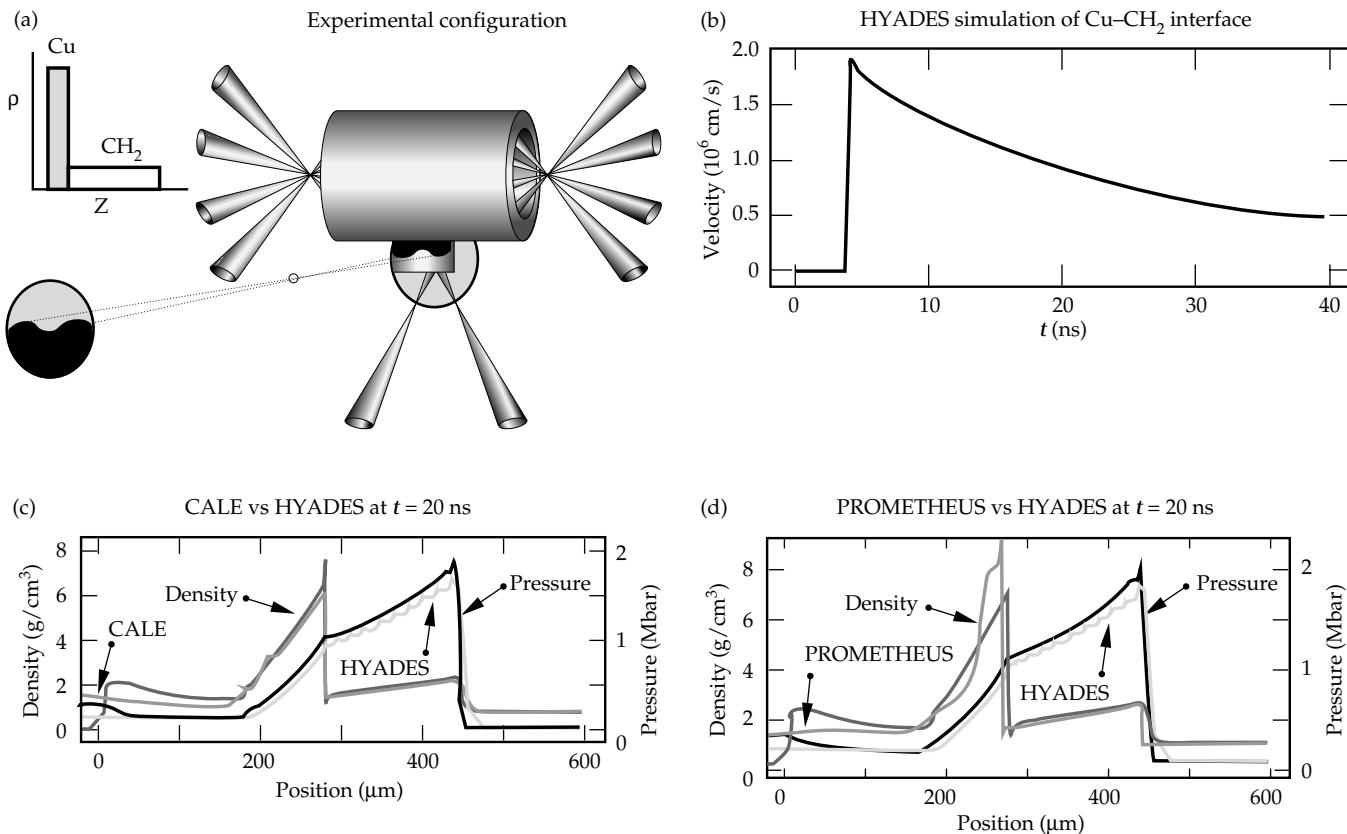
FIGURE 3. SN hydrodynamics experiment using the Nova laser. (a) Experimental configuration. (b) Velocity versus time of the Cu–CH$_2$ interface from a 1-D HYADES simulation. (c) 1-D simulation showing density and pressure profiles at 20 ns using the codes HYADES and CALE. (d) Same as (c) except using PROMETHEUS instead of CALE.   (40-00-1296-2755pb01)

The difference of scales between the SN and the Nova experiment needs to be addressed. We assume the mixing is dominated by the RT instability. In the nonlinear regime, fluid flow can be characterized by a spatial scale on the order of the perturbation wavelength λ, and velocity on the order of the perturbation terminal bubble velocity $v_B \propto (g\lambda)^{1/2}$. Here, g corresponds to the acceleration, and we assume a constant Atwood number. A hydrodynamic time scale is then given by $\tau = \lambda/v_B \propto (\lambda/g)^{1/2}$, and the hydrodynamics equations are invariant under the scale transformation[29] $\lambda \to a_1\lambda$, $g \to a_2 g$, and $\tau \to (a_1/a_2)^{1/2}\tau$. We illustrate this transformation, using characteristic scales taken from the simulations shown in Figures 2 and 3. At 4000 s for the SN, the deceleration of the He–H interface is $g_{SN} = -1.5 \times 10^4$ cm/s^2, the density gradient scalelength is $L_{SN} = \rho/\nabla\rho = 8 \times 10^{10}$ cm, and the dominant perturbation wavelength is approximated to be $\lambda_{SN} \approx 10 L_{SN} = 8 \times 10^{11}$ cm. For the Nova experiment at 20 ns, $g_{Nova} = -2.5 \times 10^{13}$ cm/s^2, $\lambda_{Nova} = 2 \times 10^{-2}$ cm, and the characteristic time interval is $\tau_{Nova} = 5$ ns. The scale transformation is given by $a_1 = \lambda_{SN}/\lambda_{Nova} = 4 \times 10^{13}$, and $a_2 = g_{SN}/g_{Nova} = 6 \times 10^{-10}$. The corresponding hydrodynamically equivalent time interval for the SN is then given by $\tau_{SN} = (a_1/a_2)^{1/2}\tau_{Nova} = 1.3 \times 10^3$ s, which is an appropriate time scale for the SN instability evolution that we are investigating. (Similar scale transformations across vastly different scales have been demonstrated experimentally before.[30]) Hence, the Nova experiment investigates nonlinear compressible

hydrodynamics similar to that at the He–H interface of a Type II SN at intermediate times (10^3–10^4 s).

Figure 4(a) shows a 2-D image from the experiment at 33 ns. These results can be compared with those from the 2-D simulations at 30 ns [Figures 4(b) and 4(c)], both before and after smearing to resemble the effect of the instrumental spatial resolution. The experimentally observed perturbation has evolved into the classic, nonlinear, RT bubble-and-spike shape with peak-to-valley amplitude $\eta_{PV} \approx \lambda$. Faint indications of Kelvin–Helmholtz roll-ups are visible at the tip of the spike and along its sides. For the simulations, we use the same mapping scheme in 2D as we did in 1D, only now the Cu–CH$_2$ interface has a sinusoidal ripple with wavelength $\lambda = 200$ μm and amplitude $\eta_0 = 20$ μm. The run is started at $t = 0$, corresponding to when the drive lasers turn on. By 10 ns, a strong (~15-Mbar) shock has passed through the interface, and the ripple in the Cu has inverted phase due to the Richtmyer–Meshkov instability.[31] By 30 ns, the perturbation has grown with the opposite phase to an overall peak-to-valley amplitude of $\eta_{PV} \approx 180$ μm $\approx \lambda$, as shown in Figures 4(b) and 4(c). The shape of the perturbation has changed from sinusoidal to bubble-and-spike, indicating that the interface has evolved well into the nonlinear regime. Thus, by 30 ns, we access roughly the same degree of nonlinearity in the laser experiment as that shown for the SN in Figure 2(d) for the 1% velocity perturbation.

The gross features of the experiment are reproduced by both CALE [Figure 4(b)] and PROMETHEUS

(a) Data at 33 ns

(b) CALE at 30 ns

(c) PROMETHEUS at 30 ns

(d) Evolution of bubble and spike fronts
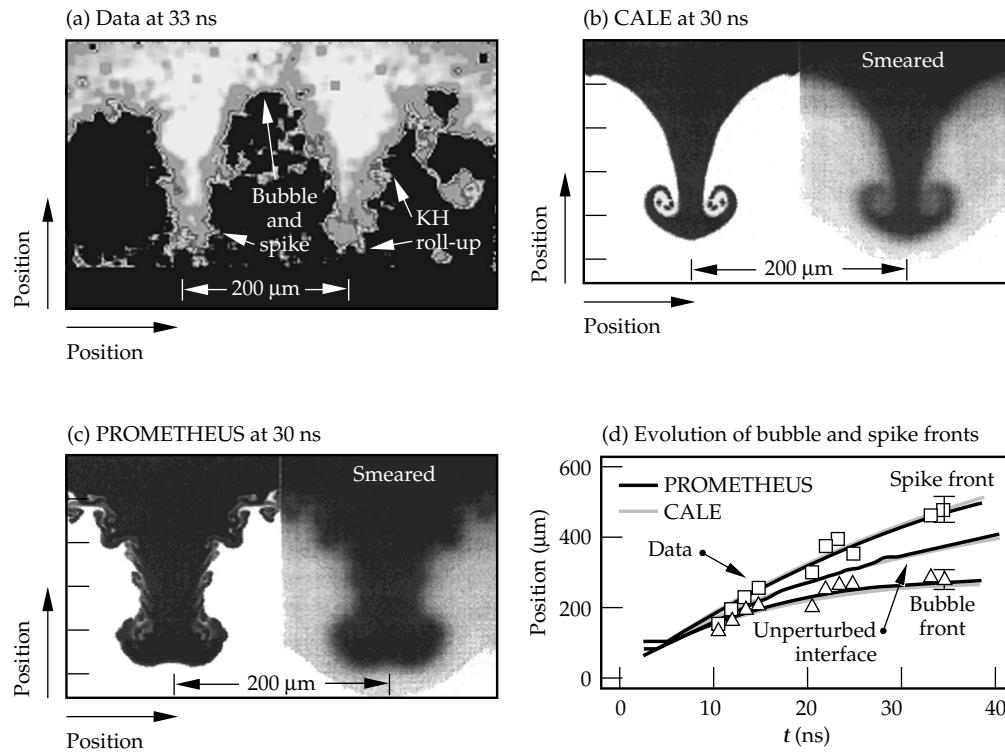
FIGURE 4. Comparison of (a) data at 33 ns with (b) simulations using CALE at 30 ns and (c) PROMETHEUS. The results labeled "smeared" have been convolved with the experimental instrument resolution function. (d) Comparison of the bubble-and-spike front trajectories observed in the data and from the simulations. (40-00-1296-2756pb01)

[Figure 4(c)] simulations. However, the PROMETHEUS simulation contains more fine structure. When CALE is run in pure Eulerian mode with ideal-gas EOS (not shown), that is, in nearly the same manner as the PROMETHEUS simulation, the two codes give similar results. However, there is still somewhat less fine structure in the CALE result due to interface tracking. Figure 4(d) shows the evolution of the bubble-and-spike fronts, compared with the predictions from both codes. The locations of the 2-D bubble front and spike front are reproduced very well by both hydrodynamics codes. In the frame of reference of an unperturbed interface, both the spike and bubble converge to nearly the same constant terminal velocities, $v_b \approx v_s \approx 3.5$–$4.0$ $\mu m/ns$. We compare this with the theoretical asymptotic velocities for the RT instability predicted by Hecht and Alon,[29] namely, $v_{b,s} = [(1/6\pi)2A/(1 \pm A)g\lambda]^{1/2}$, where the + and – in the denominator refer to bubble and spike, respectively. For our conditions of $g \approx 0.35$ $\mu m/ns^2$, $A \approx 0.64$, and $\lambda = 200$ μm, the predicted velocities are $v_b = 1.7$ $\mu m/ns$ and $v_s = 3.6$ $\mu m/ns$. Our spike velocities agree with the Hecht–Alon semi-infinite fluid theory, but our bubble velocities are considerably higher. This most likely is due to the finite thickness of the Cu layer. The Cu spike falls into an essentially infinite reservoir of CH_2 plasma, whereas the bubble of CH_2 rises into a thin layer of Cu (thickness ≈ 60 $\mu m << \lambda = 200$ μm), the result of which would be higher bubble velocities.

The study of hydrodynamic instabilities in Type II SNs has broader significance than simply checking a detail in a hydrodynamics calculation. Type II SNs are used in the Expanding Photosphere Method (EPM) for determining the Hubble constant (H_0).[32] This method holds great promise because SNs are bright, allowing a single method to be used to determine distances from tens of kpc to hundreds of Mpc. The basic premise of the EPM is that the light curve—that is, the total emitted flux as a function of time—of a Type II SN can be calculated absolutely, albeit in 1D. By comparing observed brightness of the SN with calculated brightness, one can infer the distance. Applying the EPM to several different SNs at varying distances (D), together with red-shift measurements of the recession velocity (v_{rec}) allows a plot of v_{rec} versus D to be constructed, whose slope is the Hubble constant, H_0. Note, however, that any RT-induced mixing of the radioactive ^{56}Ni and ^{56}Co core outward into the envelope serves as a heat source, potentially altering the light curve.[18] Furthermore, any coupling between the mixing front at the He–H interface and the photosphere could cause the photosphere to become crenulated. The initial blast wave itself may, in fact, have a distorted shape due to Vishniac instabilities,[33] thereby distorting the photosphere from the very beginning. A crenulated photosphere could have a significantly larger surface area than predictions from a 1-D spherical calculation. Furthermore, for a dominant mode $l \geq 20$, as suggested in Figures 1(a) and 2(e), the surface area would look statistically similar regardless of the angle from which the SN were viewed. In other words, *all* Type II SNs with crenulated photospheres would be brighter than assumed based on 1-D spherical calculations. Consider the implications. For a given recession velocity, if SNs were brighter than assumed, they would be further away. This effect decreases the slope of the v_{rec} versus D plot, reducing H_0. Because the age of the universe varies inversely as the Hubble constant ($\tau_{Univ} \sim 1/H_0$), the result of crenulated photospheres due to hydrodynamic instabilities would be an older universe. Experimentally testing any piece of the puzzle, in this case modeling of the SN hydrodynamic instabilities, is indeed a worthwhile pursuit.

Supernova Remnant Formation

SN remnant formation is one of the classic problems of astrophysics, leading to such spectacular objects in the sky as the Crab nebula. With SN1987A, we have the first opportunity to watch the time-dependent dynamics of the early stages of such evolution [see Figure 1(b)].

Figure 5(a) is a schematic of the remnant formation process (taken from Ref. 12). High-velocity SN ejecta sweep up the surrounding ambient plasma, which is left over from the stellar wind of the SN progenitor. At the contact discontinuity (the place where the two plasmas meet), shocks are launched forward into the ambient plasma ("forward shock") and backward into the SN ejecta ("reverse shock"), as illustrated with the 1-D density profile shown in Figure 5(b) (from Ref. 12). When radiation transport and radiative cooling are included in the plasma hydrodynamics, a much higher density is formed in the compressed SN ejecta. The radiation carries heat away, lowering the temperature and pressure, thus making the shocked SN ejecta more compressible. This steepens the density gradient at the contact discontinuity [compare the dashed and solid curves in Figure 5(b)]. At the contact discontinuity, pressure and density gradients cross, $\nabla P \cdot \nabla \rho < 0$, with the lower-density shocked ambient plasma at higher pressure and decelerating the higher-density shocked SN ejecta plasma. Such a situation is hydrodynamically unstable due to the RT instability. This is illustrated in Figure 5(c) (from Ref. 12), which shows strong RT growth at the contact discontinuity. The simulations assumed a $\rho \propto r^{-n}$ ejecta density profile ($n = 6, 12, 20$) flowing into a uniform ambient plasma. Note that qualitatively different mixing evolves, depending on the density profile of the ejecta. The details of what to expect when SN ejecta impact the ring nebula depend on the structure of both the ring and the projectile assembly. Figure 5(d) shows the

(a)

(b)

(c)

$\rho_{\text{ejecta}} \sim r^{-n}$, $n = 6$ $n = 12$ $n = 20$

(d)

$t = 12$ y
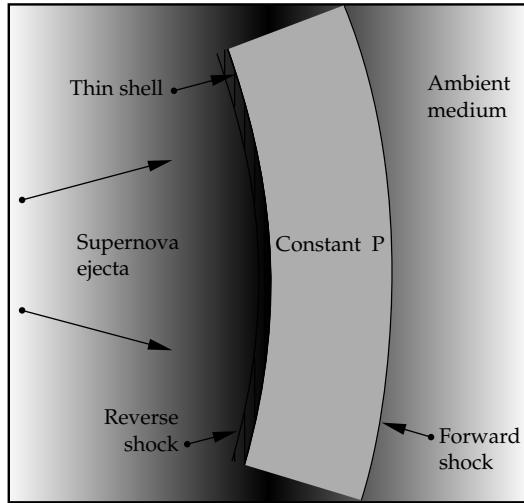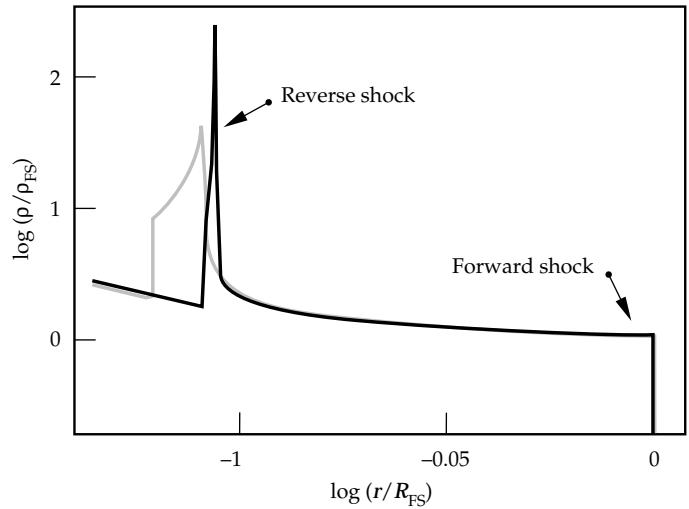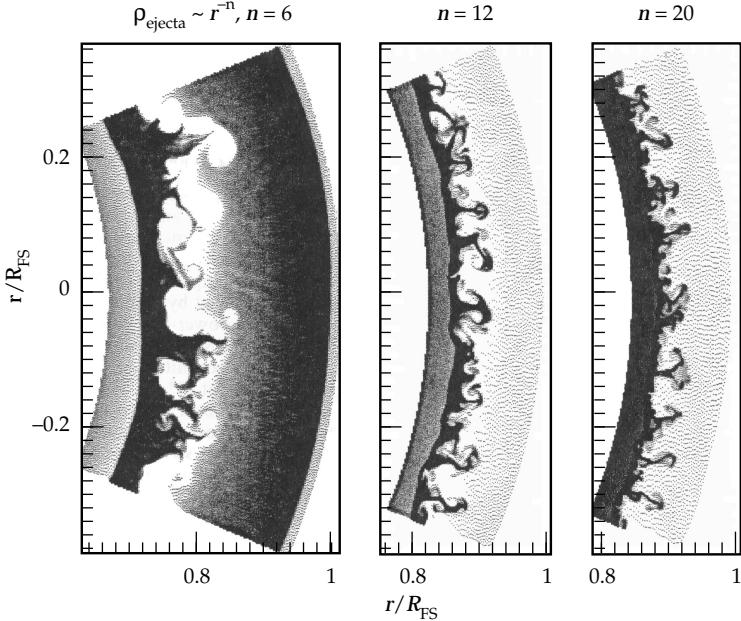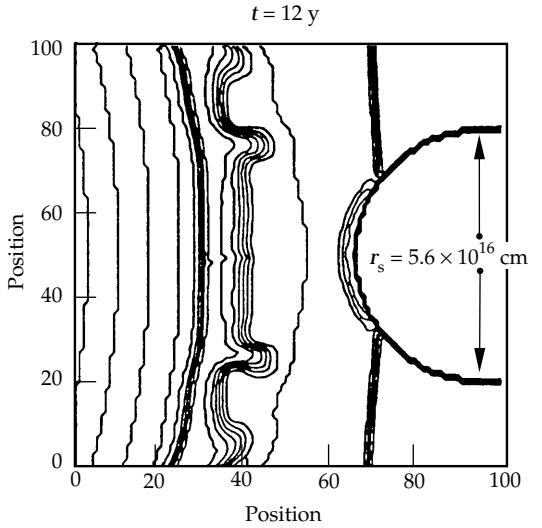
FIGURE 5. (a) Schematic showing the dynamics of SN remnant formation (reproduced from Ref. 12). (b) Structure of a generic SN–stellar-wind interaction (reproduced from Ref. 12). The gray curve shows the structure for small radiative power loss. With larger radiative losses, the stagnated ejecta should collapse to higher density, as the solid curve illustrates. (c) 2-D simulations (from Ref. 12) showing the effect of the ejecta density profile, $\rho_{\text{ejecta}} \propto r^{-n}$, on ensuing RT growth at the contact discontinuity. The axes are radius (r) normalized to the position of the forward shock (R_{FS}). (d) 2-D simulation result showing RT instability growth at the contact discontinuity and the imminent collision with the ring (reproduced from Ref. 11).   (40-00-1296-2757pb01)

results of a 2-D simulation from a different model (from Ref. 11). Clearly, what transpires depends on whether the contact discontinuity looks like Figure 5(a), 5(c), 5(d), or something completely different. It would be highly beneficial to be able to test these models experimentally prior to the awaited collision.

Hence, our second experiment is focused on testing our understanding of the colliding plasma

dynamics in a situation qualitatively similar to that of the ejecta of SN1987A. Our goal is to develop the experiment and model it with the astrophysics codes used to make predictions such as those shown in Figures 1(c), 1(d), 5(c), and 5(d). This work should improve our ability to quantitatively interpret the results of the upcoming pyrotechnics predicted for shortly after the year 2000.

Supernova Remnant Experiment

Our initial approach to experimentally simulate the ejecta–wind interaction hydrodynamics[34] is shown in Figure 6(a). We use about 20 kJ of laser energy at a laser wavelength of 0.35 μm, in a 1-ns pulse, to heat a 3-mm-long by 1.6-mm-diam cylindrical Au cavity (a hohlraum) to a temperature of about 220 eV. The x-ray flux ablates a CH plug, doped with Br to reduce the transmission of higher-energy x rays, which is mounted in a 700-μm-diam hole in the hohlraum. The ablation drives a very strong (~50-Mbar) shock through the CH(Br), ejecting plasma at about 30 eV from the rear of the plug. This plasma (the ejecta) expands and cools. The leading edge of the expansion is a high-Mach-number plasma flow (about Mach 10), although it is at well below solid den-

sity. The ejecta impact a 700-μm-diam cylinder of aerogel foam located 150 μm away and having a density of 40 mg/cm^3. In response, the flowing ejecta stagnate, and a shock is driven into the foam, as well as back into the ejecta.

We diagnose these experiments by x-ray backlighting at 4.3 keV (Sc He$_\alpha$) to obtain radiographs of the shocked matter. Figure 6(a) is a 1-D, streaked radiographic image of the target. We show profiles of –ln(exposure) $\propto$ density from the data in Figure 6(c) and from a LASNEX[35] simulation in Figure 6(d), both at $t = 6$ ns. In both the data and simulation, we observe a clear forward shock in the foam, a reverse shock in the ejecta, and a contact discontinuity in between. From the simulations, the shock breaks out of the CH(Br) at about 2 ns, at which time the back edge of
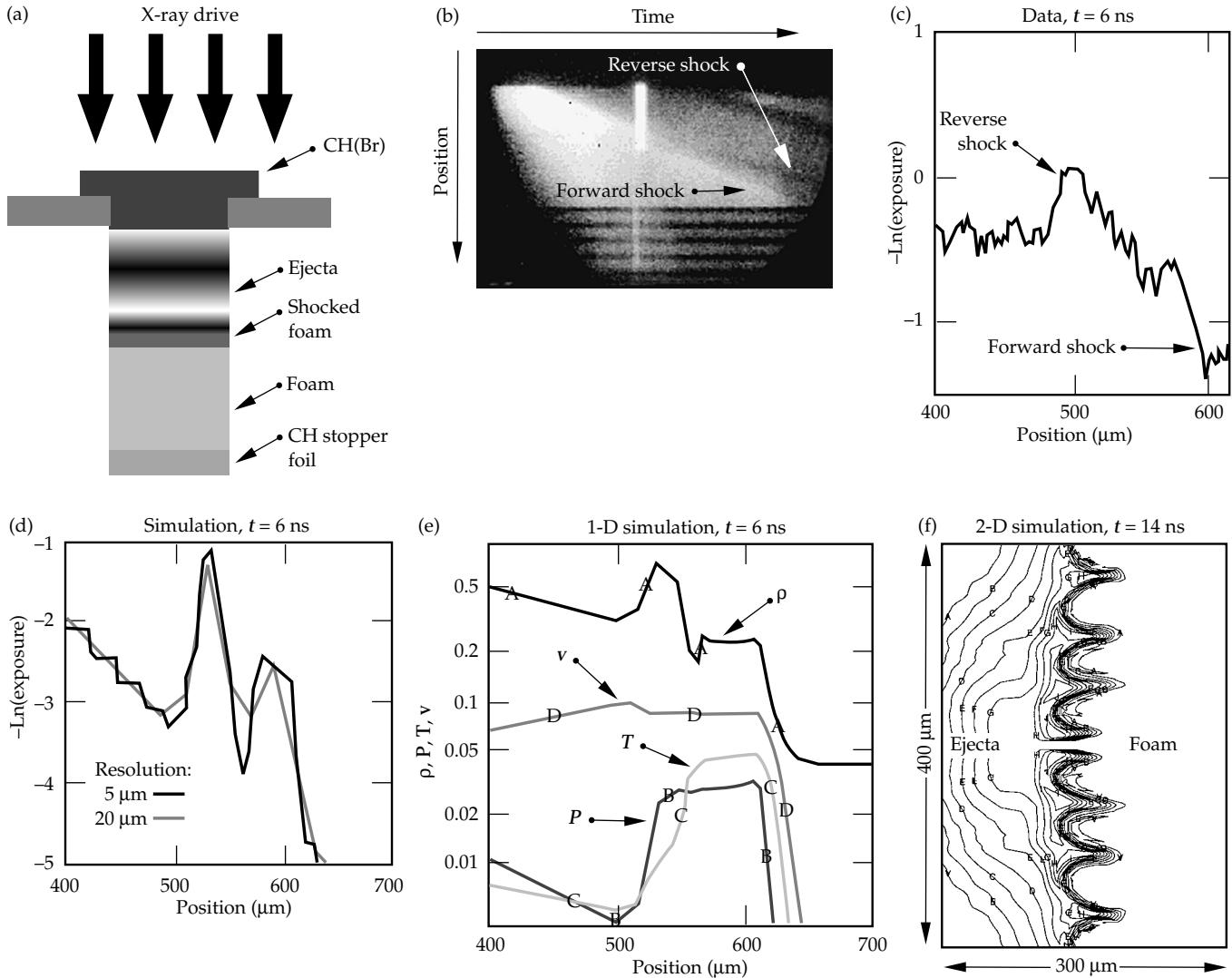
FIGURE 6. (a) Schematic of the laser experiment. (b) Raw streaked image from the experiment. (c) A lineout at 6 ns from the data shown in (b). (d) Same as (c) except based on a 2-D simulation using LASNEX. The solid and gray lines represent different levels of resolution (5 versus 20 μm). (e) Profiles from the simulation at 6 ns showing density (g/cm^3), pressure (Mbar), temperature (keV), and velocity ($\times 10^8$ cm/s). (f) Isodensity contours at 14 ns from a 2-D LASNEX simulation, showing perturbation growth due to RT instabilities at the contact discontinuity. Ejecta flow into the foam from left to right. (40-00-1296-2758pb01)

the CH(Br) is at a density of about 2 g/cm^3 (compression of ~2), pressure of 45 Mbar, and temperature of 30 eV. The foam is impacted by the ejecta about 1 ns later, suggesting that the high-velocity tail of the ejecta is moving at ~150 μm/ns = 150 km/s. Figure 6(e) shows the density, pressure, temperature, and velocity of the ejecta–foam assembly from the LASNEX simulation at 6 ns, that is, about 3 ns after the ejecta first start sweeping up the foam. The contact discontinuity is located at a position of about 560 μm in both the data and the simulation, and the peak densities from the simulation on either side of the contact discontinuity in the ejecta (foam) are 0.65 g/cm^3 (0.25 g/cm^3). The pressure is continuous across the contact discontinuity, at a peak value of 0.035 Mbar, the peak temperature is about 50 eV, and the velocity of the projectile assembly is about 1×10^7 cm/s. Both here and in SN1987A, the forward shock driven by the ejecta is a strong shock; that is, the shocked matter is maximally compressed [by a factor of $(\gamma + 1) / (\gamma - 1)$ for a γ-law gas].

The region near the contact surface at the front of the ejecta is RT unstable, as illustrated in Figure 5(c) for SN1987A, and in Figure 6(f) for the laser experiment. In the latter, a seed perturbation of wavelength $\lambda = 50$ μm and initial amplitude $\eta_0 = 1$ μm was imposed on the surface of the foam. By 14 ns, strong RT growth of the perturbation well into the nonlinear regime is visible, due to the $\nabla P \cdot \nabla \rho < 0$ configuration at the contact discontinuity. The growth bears some semblance to the RT growth shown in Figures 5(c) and 5(d) for the SN ejecta. We intend to apply this experiment to test theories and models being used to predict the behavior of SN1987A well in advance of the upcoming impact of SN ejecta with the ring nebula. Our efforts should facilitate the interpretation of data expected to emerge from the impact.

Conclusions and Future Outlook

We are developing experiments to investigate (1) hydrodynamic instabilities relevant to core-collapse SNs at intermediate times (10^3–10^4 s), and (2) plasma-flow dynamics relevant to the SN ejecta–ambient plasma interactions during the initial stages of remnant formation. Initial results from both experiments look promising. Expanding the first experiment to 3D is the most critical next step to take because RT growth in a supernova is clearly 3D, and growth in 3D is expected to be larger than in 2D.[36] Extending the second experiment into the radiative regime is equally critical because the remnant formation hydrodynamics relevant to SN1987A is clearly radiative.

Beginning such astrophysics experiments now on the Nova laser and other lasers worldwide[33,37,38] is important. With the construction in the U.S. of the

~2-MJ National Ignition Facility laser,[39] and the similar Laser MegaJoule laser[40] planned to be built in France, it is crucial that we acquire experience now with developing laser–plasma astrophysics experiments. Such groundwork will better allow us to plan discriminating astrophysics experiments for the "superlasers" scheduled for completion around the year 2002. This date is just about the time that SN1987A ejecta are predicted to impact the surrounding nebular ring. Dedication ceremonies for the two superlasers may be consummated with a fitting celestial *son et lumière*.

Acknowledgments

Notes and References

1. W. D. Arnett, J. N. Bahcall, R. P. Kirshner, and S. E. Woosley, *Ann. Rev. Astron. Astrophys.* **27**, 629 (1989); W. Hillebrandt and P. Höflich, *Rep. Prog. Phys.* **52**, 1421 (1989).
2. E. Müller, B. Fryxell, and D. Arnett, *Astron. Astrophys.* **251**, 505 (1991).
3. B. Fryxell, W. Müller, and D. Arnett, *Astrophys. J.* **367**, 619 (1991).
4. I. Hachisu et al., *Astrophys. J.* **368**, L27 (1991).
5. A. Burrows and B. A. Fryxell, *Astrophys. J.* **418**, L33 (1993).
6. M. Herant and S. E. Woosley, *Astrophys. J.* **425**, 814 (1994).
7. M. Herant, W. Benz, and S. Colgate, *Astrophys. J.* **387**, 294 (1992); *Astrophys. J.* **435**, 339 (1994).
8. H. Bethe, *Rev. Mod. Phys.* **62**, 801 (1990); *Astrophys. J.* **412**, 192 (1993).
9. A. P. S. Crotts et al., *Astrophys. J.* **347**, L61 (1989); E. J. Wampler et al., *Astrophys. J.* **362**, L13 (1990); L. Wang and E. J. Wampler, *Astron. Astrophys.* **262**, L9 (1992); P. Jacobsen et al., *Astrophys. J.* **369**, 63 (1991); and on the internet at web site <http://www.stsci.edu/pubinfo/jpeg/SN1987A_Rings.jpg>.
10. R. McCray, *Ann. Rev. Astron. Astrophys.* **31**, 175 (1993).
11. R. McCray and D. N. C. Lin, *Nature* **369**, 378 (1994); D. Luo and R. McCray, *Astrophys. J.* **379**, 659 (1991); *Astrophys. J.* **430**, 264 (1994).
12. R. A. Chevalier, J. M. Blondin, and R. T. Emmering, *Astrophys. J.* **392**, 118 (1992); R. A. Chevalier and J. M. Blondin, *Astrophys. J.* **444**, 312 (1995).
13. J. M. Blondin and P. Lundqvist, *Astrophys. J.* **405**, 337 (1993).
14. C. L. Martin and D. Arnett, *Astrophys. J.* **447**, 378 (1995).
15. T. Suzuki, T. Shigeyama, and K. Nomoto, *Astron. Astrophys.* **274**, 883 (1993).
16. K. J. Borkowski, J. M. Blondin, and R. McCray, *Astrophys. J.* (in press).
17. J. D. Kilkenny, *Rev. Sci. Instrum.* **63**, 4688 (1992); E. M. Campbell, *Laser Part. Beams* **9**, 209 (1991).
18. T. Shigeyama and K. Nomoto, *Astrophys. J.* **360**, 242 (1990).
19. R. W. Hanuschik and J. Dachs, *Astron. Astrophys.* **192**, L29 (1987); V. M. Blanco et al., *Astrophys. J.* **320**, 589 (1987).
20. F. Witteborn et al., *Astrophys. J.* **338**, L9 (1989); J. Tueller et al., *Astrophys. J.* **351**, L41 (1990); R. McCray, *Ann. Rev. A. Ap.* **31**, 175 (1993).

21. D. Arnett, *Supernovae and Nucleosynthesis* (Princeton Univ. Press, Princeton, NJ, 1996).

22. B. A. Fryxell, E. Müller, and W. D. Arnett, Max Planck Institut für Astrophysik Report 449 (1989).

23. Lord Rayleigh, *Scientific Papers II* (200, Cambridge, England, 1900); Sir Geoffrey Taylor, *Proc. R. Soc. London* **A201**, 192 (1950).

24. B. A. Remington et al., *Phys. Plasmas* **2**, 241 (1995).

25. J. Kane et al., submitted to *Astrophys. J. Lett.* (November 1996).

26. S. G. Glendinning et al., in proceedings of the *Workshop on Laboratory Astrophysics Experiments with Large Lasers*, Eds., B. A. Remington and W. H. Goldstein (February 26–27, 1996), LLNL Rept. No. CONF-960297, p. 18.

27. J. T. Larsen and S. M. Lane, *J. Quant. Spect. Rad. Trans.* **51**, 179 (1994).

28. R. Tipton (author of CALE), private communication (1996).

29. J. Hecht et al., *Phys. Fluids* **6**, 4019 (1994); U. Alon et al., *Phys. Rev. Lett.* **74**, 534 (1995).

30. E. M. Campbell, N. C. Holmes, S. B. Libby, B. A. Remington, and E. Teller, submitted to *Laser Part. Beams* (September 1996); UCRL-JC-124258, Rev. 2 (1996).

31. R. D. Richtmeyer, *Commun. Pure Appl. Math.* **13**, 297(1960); E. E.Meshkov, *Izv. Akad. Nauk SSSR Mekh. Zhidk.Gaza* **4**, 151 (1969) [*Izv. Acad. Sci. USSR Fluid Dynamics* **4**, 101 (1969)].

32. B. P. Schmidt et al., *Astrophys. J.* **395**, 366 (1992); *Astrophys. J.* **432**, 42 (1994).

33. J. Grun et al., *Phys. Rev. Lett.* **66**, 2738 (1991); G. Schappert et al., in proceedings of the *Workshop on Laboratory Astrophysics Experiments with Large Lasers*, Eds. B. A. Remington and W. H. Goldstein (February 26–27, 1996), LLNL Rept. No. CONF-960297, p. 164.; Ryu and Vishniac, *Astrophys. J.* **313**, 820 (1987); *Astrophys. J.* **368**, 411 (1991); Mac Low and Norman, *Astrophys. J.* **407**, 207 (1993).

34. R. P. Drake et al., in proceedings of the *Workshop on Laboratory Astrophysics Experiments with Large Lasers*, Eds. B. A. Remington and W. H. Goldstein (February 26–27, 1996), LLNL Rept. No. CONF-960297, p. 31.

35. G. B. Zimmerman and W. L. Kruer, *Comments Plasma Phys. Controlled Fusion* **2**, 51 (1975).

36. M. M. Marinak et al., *Phys. Rev. Lett.* **75**, 3677 (1995); G. Tryggvason and S. O. Unverdi, *Phys. Fluids A* **2**, 656 (1990); J. P. Dahlburg et al., *Phys. Fluids B* **5**, 571 (1993); J. Hecht et al., *Laser Part. Beams* **13**, 423 (1995).

37. B. H. Ripin et al., *Laser Part. Beams* **8**, 183 (1990).

38. Y. P. Zakharov et al., in *Plasma Astrophysics* (ESA, 1986), Vol. SP-251, p. 37.

39. J. A. Paisner, E. M. Campbell, and W. J. Hogan, *Fusion Technology* **26**, 755 (1994).

40. CHOCS No. 13, Avril 1995, *Revue Scientifique et Technique de la Direction des Applications Militaires*, CEA; M. Andre, "Conceptual Design of the French LMJ Laser," *First Annual International Conference on Solid State Lasers for Application to ICF*, Monterey, CA, May 31–June 1 (1995), SPIE proceedings.

CHARACTERIZATION OF LASER-DRIVEN SHOCK WAVES USING INTERFEROMETRY

K. S. Budil

P. Celliers

G. W. Collins

L. B. Da Silva

R. Cauble

R. J. Wallace

G. Chiu[*]

A. Ng[*]

Introduction

The behavior of materials at high pressures and densities is of great practical interest in a wide variety of fields, from astrophysics to inertial confinement fusion and other related fields where such conditions are routinely encountered. Compression of matter to such extreme conditions requires strong, multi-megabar shock waves for which only a limited number of drivers exist, including nuclear weapons.[1–5] In a laboratory setting, high-power lasers offer great promise for generating the requisite pressures and densities, although the transient nature of the shock wave greatly complicates such experiments.

Researchers first generated multi-megabar, laser-driven shock waves in the 1970s,[6–8] and this early work has been followed by numerous experiments using both direct[9–11] and indirect[12–14] laser drives. These experiments are often criticized because of the nature of laser-driven shock waves: typically, the duration of the laser pulse is quite short (several nanoseconds), so that the steadiness of the shock wave in time is questionable. The starting conditions of the experiment could be changed if the material being targeted were preheated by the x rays or hot electrons from the high-temperature, laser-deposition region well in advance of the arrival of the shock wave. The spatial structure of the shock may not be accurately diagnosed, and there is the possibility that the shock front may either be severely curved or carry small-scale spatial modulations imparted by the laser driver. Thus, accurate characterization of the spatial and temporal characteristics of the shock wave generated by a laser driver is critically important for calculating high-precision equations of state (EOSs) for the target materials.[15]

* University of British Columbia, Vancouver, B. C., Canada.

EOS of Cryogenic D_2

When our project was begun to make a high-precision EOS measurement for cryogenic D_2 in the 1- to 3-Mbar regime, accurate characterization of the laser-driven shock wave was required to ensure that errors were small enough to differentiate between the two proposed EOS models. Because those measurements relied on solving the Hugoniot equations using the initial state of the material prior to arrival of the shock, any change in this state, particularly due to preheat, would have a large impact on the result. Thus, it becomes important to accurately characterize the shock and initial state of the D_2. The results of these measurements are described in the article "Absolute Equation of State Measurements of Compressed Liquid Deuterium Using Nova" on p. 16 of this *Quarterly* and in the literature.[16]

We compressed liquid D_2 with a shock wave generated using one beam of the Nova laser (Figure 1). The laser drive directly irradiates a polystyrene-coated Al flat, ablatively launching a shock wave into the Al "pusher." The shock breaks out the rear surface of this Al pusher and begins to compress the liquid D_2. We used temporally resolved, side-on radiography to diagnose the position of the Al–D_2 interface and the position of the shock front in the D_2. This yielded direct measurements of shock and particle velocities and compression. To accurately characterize the experimental system, we employed a diagnostic technique using interferometry to probe both the initial state of the liquid D_2 (the level of preheating) and the structure of the shock driving the experiment (the shock planarity). The interferometric probe beam was incident through a sapphire window placed at the end of the reservoir containing the liquid D_2, and the rear surface of the Al pusher was diagnosed.
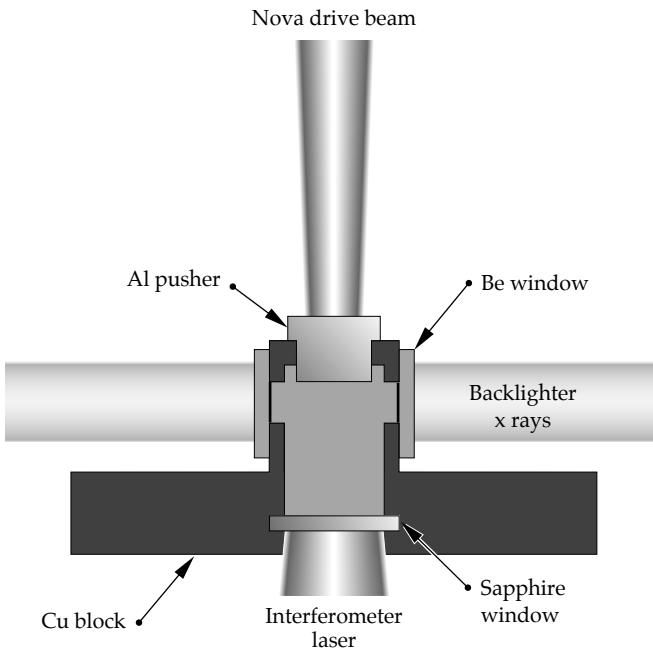
FIGURE 1. Schematic of the cryogenic cell target. One Nova beam is used to ablatively launch a shock wave into a polystyrene-coated Al flat. The shock breaks out the rear surface of this Al pusher and begins to compress the liquid D_2. A laser used as an interferometric probe beam is incident through a sapphire window placed at the end of the reservoir containing the liquid D_2. (08-00-0197-0007pb02)

Interferometric Characterization

Interferometry provides many advantages for characterizing a laser-produced shock wave. Interferometers can be designed with very good spatial resolution and very high temporal sensitivity, allowing extremely accurate measurements of the characteristics of the shock wave. Also, interferometers that measure displacement (the Michelson system)[17] or velocity (Velocity Interferometer System for Any Reflector, VISAR)[18] can be devised to allow investigation of both spatial (shock planarity and preheating) and temporal (shock steadiness) properties. We concentrated on displacement interferometry for our experiments.

Displacement Interferometry

When an unperturbed pulse of light traveling a fixed distance (the reference arm) and a pulse that is reflected from a target surface (the probe arm) are allowed to coherently interfere, the fringe pattern produced provides a measure of the phase difference between the two light paths. If this phase difference changes (for instance, the length of the probe arm begins to increase or decrease because of target motion), a fringe shift will be observed. Therefore, by temporally resolving the output signal from the interferometer with a streak camera, a one-dimensional

image of the position of the surface being probed as a function of time is produced. For example, if the pusher is heated in advance of the arrival of the shock wave, the rear surface of the sample will thermally expand, and the initially static fringe pattern will shift. The velocity and extent to which this surface moves can then be correlated to the temperature of the material by comparing our results with numerical simulations of the thermal expansion process.

This same diagnostic also provides a very sensitive probe of the planarity of the shock wave when it breaks through the rear surface of the material. The passage of the strong shock wave results in the formation of a plasma at the rear surface of the target. This causes a dramatic drop in the reflectivity of this surface to the probe beam, which results in a very rapid (50–100 ps) loss of fringe visibility upon shock breakout. The relative timing of the shock breakout across the face of the target then gives a measure of the planarity of the shock wave at this instant in time. Additionally, any spatial modulations imparted to the shock wave by the laser driver will be seen as variations in the shock breakout time across the target.

Experimental Configuration

To determine the level of preheat at the rear surface of the Al pusher and the planarity of the shock wave, we designed an interferometer to probe the target while radiographic measurements were taken. Figure 2 shows a schematic of the Michelson interferometer used in these experiments.

We used a Q-switched Nd:YAG laser operating at the third harmonic (355 nm) with a pulse duration (full
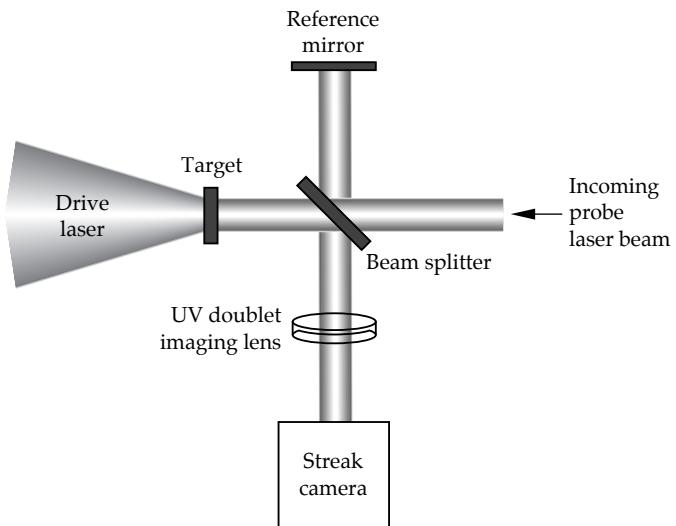
FIGURE 2. Schematic of the Michelson interferometer system showing the reference and target probe arms. The recombined beams are imaged by a UV-doublet lens, and the resulting interference pattern is temporally resolved using a streak camera. (08-00-0197-0013pb01)

width at half maximum) of ~15 ns and ≤1 mJ pulse energy as the probe beam. An f/5 imaging objective (an UV doublet lens combination) was placed external to the interferometer components and imaged the target surface and reference surface simultaneously. The signal generated by the two interfering beams was relayed onto a UV streak camera to provide both spatial and temporal information.

Very small changes in the position of the surface being probed can be detected because a 90° phase shift between the two arms of the interferometer corresponds to a spatial displacement at the target of only $0.5\lambda = 177.3$ nm, and a small fraction of one fringe shift (0.2 fringe shift) is readily detectable. The system was operated at 20× magnification, yielding a spatial resolution of ~10 μm at the target.

Preliminary Experiments

We performed a series of preliminary experiments to demonstrate the utility of this diagnostic. In our first experiment, a 250-μm-thick silicon flat coated with 100 nm of Al on the drive side was irradiated with one Nova laser beam at 2ω (532 nm). The drive-laser spatial profile was spatially smoothed by a kinoform phase plate[19] and was ellipsoidal with major and minor axes of 900 and 600 μm, respectively. The drive laser had an 8-ns, temporally square profile with a rise time of 100 ps, producing an intensity of ~8×10^{13} W/cm^2 at the target. Figure 3(a) shows the data from this experiment. Motion is detected about 1.3 ns before the shock breaks through the rear surface of the Al fringe, which corresponds to an expansion velocity of ~3×10^4 cm/s. The predicted shock breakout time for this irradiance according to calculations using the LASNEX code was ~9.9 ns. Observations indicate that this predicted breakout time is correct to within the error in the experimental timing, which is ±500 ps.

In our second experiment, an Al target consisting of side-by-side steps 50 and 100-μm thick, respectively, with a 15-μm-thick polystyrene ablator coated onto the drive side, was irradiated at an intensity of ~7.7×10^{13} W/cm^2. As seen in Figure 3(b), fringe motion is detected prior to shock breakout on the 50-μm step of Al, but no motion is detected at the rear surface of the 100-μm step. The observed shock breakout times are about 2.2 ns for the 50-μm step and 4.3 ns for the 100-μm step, which are in good agreement with our predictions. A small amount of fringe motion on the 100-μm step immediately adjacent to the step's edge is attributed to edge effects brought on by the earlier breakout of the 50-μm step, not preheating of the sample through the bulk Al. Here, the expansion velocity is about 3.5×10^4 cm/s. The shock velocity in the Al is 26 μm/ns based on the relative breakout times for the two steps compared to a predicted shock velocity of 25 μm/ns with LASNEX simulations.

Because the expansion velocity is two orders of magnitude below the shock velocity, we can indeed attribute the expansion to preheat. The source of the preheat for the Al step target is likely x rays with energies just under the Al k-edge at 1.56 keV. Because the temperature in the laser deposition region is 1 to 2 keV, there is a significant x-ray flux at this frequency.

Characterization of the Cryogenic Cell Targets

Figure 1 shows the design of the cryogenic cell targets. The Al pusher was machined in a "tophat" geometry so that the rear surface of the pusher would always protrude exactly the same distance into the

(a) 250-μm Si coated with 1000 Å Al.

(b) 100-μm Al step; 50-μm Al step.

1.3 ns
Shock breakout time
t (ns)
1.9 ns
0.5 ns
Timing fiducial
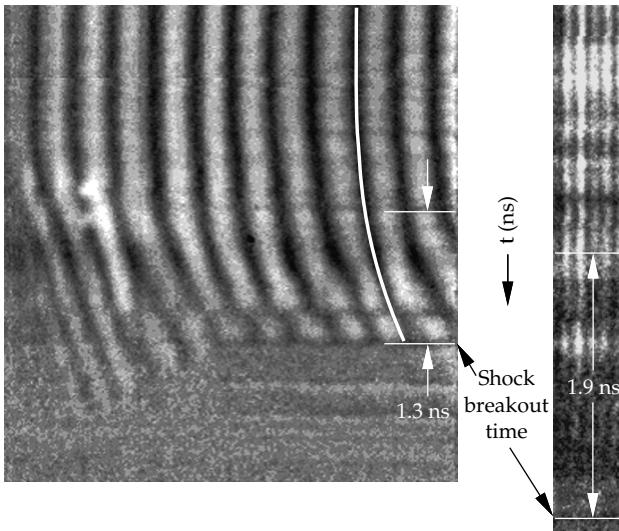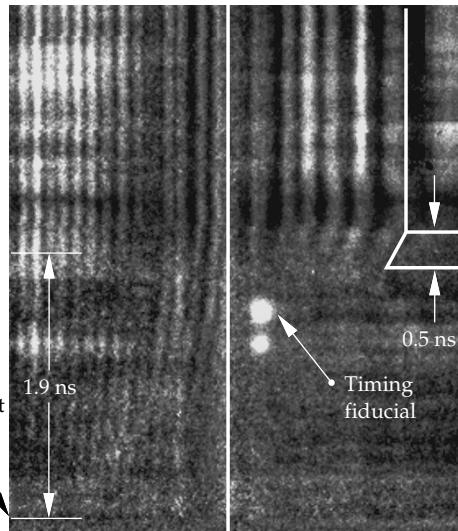
FIGURE 3. Streak camera records of the shock passing through (a) a 250-μm-thick silicon flat coated with a 1000-Å Al layer, where motion of the rear surface in advance of the shock wave is clearly observed, indicating that this surface is preheated; (b) a target with a 100-μm Al step placed next to a 50-μm Al step, where minimal or no fringe motion is detected on the 100-μm Al step side of the image, while preheat-induced thermal expansion is clearly observed on the 50-μm Al step side.
(08-00-0197-0008pb01)

cryogenically cooled D_2 reservoir regardless of the pusher's thickness. Thus, the side of the pusher where the Nova drive beam was incident was more reentrant for thinner pusher geometries. The Al thickness was varied between 100, 180, and 250 μm, and the Al pushers were 1 mm in diameter. The pusher was coated with 20 μm of polystyrene as an ablator, which was subsequently overcoated with 100 nm of Al to prevent direct laser shine through the polysterene at the onset of the drive laser pulse. The probe laser beam was reflected off the rear surface of the Al pusher after passing through a sapphire window and a 0.5-mm-long reservoir filled with liquid D_2, and the entire cell assembly was cooled to a temperature of 19.4 to 19.8 K.

Figure 4(a) shows the interferogram generated when a 100-μm-thick pusher with a 20-μm-thick polystyrene ablator was driven at about 1.5×10^{14} W/cm^2. Motion of the D_2–Al pusher interface is clearly observed beginning ~2 ns prior to shock breakout. A simple thermal expansion model estimates the temperature at this surface to be ~1000 K. The shock breakout was predicted to occur ~4.3 ns after initiation of the drive laser pulse for these conditions, so some preheating of the Al occurs early in the 8-ns-duration, laser-driven pulse. Because any high-energy x rays that penetrate the pusher are unlikely to be absorbed in the D_2, any heating of the D_2 is a consequence of thermal conduction from the Al. Any such D_2 preheat is negligible for the strong shocks considered in these experiments. The shock is planar over the central 400 μm of the target, with rarefaction waves moving inward from the edges causing the observed curvature.

When the intensity on this target was turned down to about 8.5×10^{13} W/cm^2, no evidence of preheating

was observed, as shown in Figure 4(b). Again, the shock is planar over ~400 μm; however, a second region of shock curvature is observed. This structure is attributed to the reentrant nature of the Al pusher design. Al plasma generated by the drive laser beam moves into the path of the beam during its 8-ns duration, effectively reducing the intensity of the drive pulse on the outer perimeter of the Al pusher and slowing down the shock considerably at the target's edges.

Interferograms of the thicker pushers (180 and 250 μm) showed no fringe shifts, indicating that there was no motion at the rear surface. For a detection limit of 0.2 fringe, which corresponds to movement of 30 nm at the pusher surface, the maximum surface temperature of the pusher for these targets prior to shock breakout is estimated to be <400 K.

Future Directions

To produce stronger shocks and investigate both direct- and indirect-drive schemes for generating shock waves, we are planning future investigations of a variety of materials for the Nova ten-beam facility. This will allow multiple drive laser beams to be overlapped in a direct-drive geometry and will allow the use of hohlraum drivers to produce stronger shocks and higher pressures. Preheating is a significant concern, particularly in the case of indirectly driven targets where large quantities of Au M-band x rays ($E > 2$ keV) are generated. We are currently integrating this interferometric characterization diagnostic onto the ten-beam facility. To avert potential problems with background radiation from the Nova drive

FIGURE 4. (a) Intensity of ~1.5 $\times 10^{14}$ W/cm^2 incident on a 100-μm-thick Al pusher coated with 20 μm of polystyrene and 100 nm of Al. Expansion of the rear surface due to preheating is clearly observed. (b) Intensity of ~8.5×10^{13} W/cm^2 incident on the same target described in (a). Here, no motion of the rear surface is observed prior to shock breakout. The shaping of the breakout may be caused by Al plasma generated on the drive laser side of the target moving into the path of the drive beam. (08-00-0197-0009pb01)
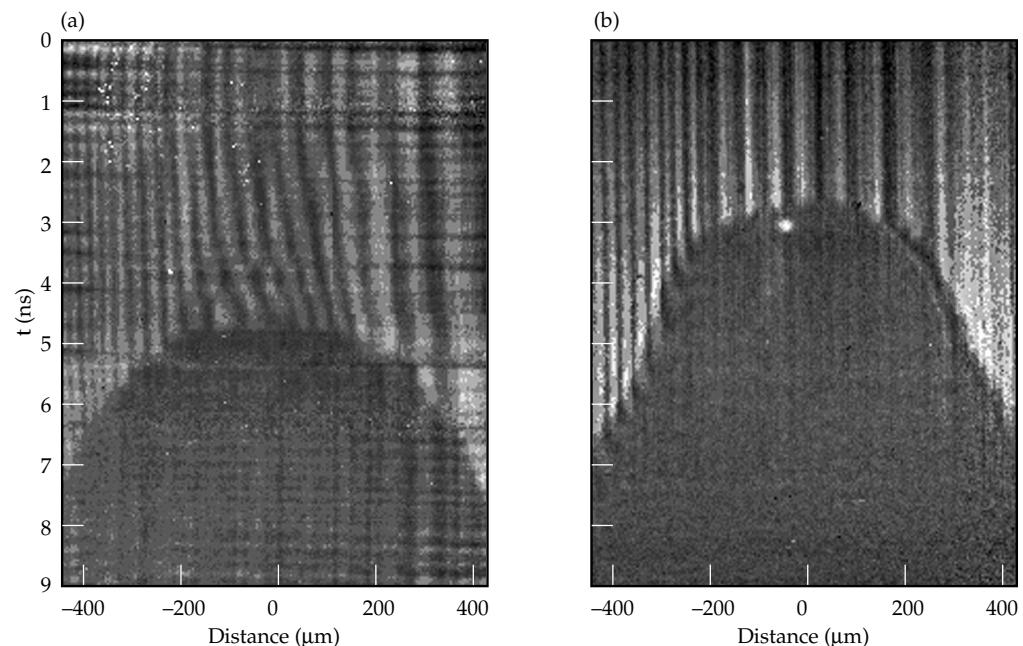
beams, the laser system used will be an injection-seeded, Ti:Sapphire regenerative amplifier operating at a wavelength ($\lambda = 403$ nm) anharmonic relative to standard Nova frequencies. This wavelength is produced by frequency-doubling the 807-nm fundamental of the Ti:Sapphire. We have designed an f/3 imaging system to relay the probe laser beam to the target and image the evolving target system. The first phase of activation incorporates only displacement interferometry, but we are planning an upgrade to a VISAR system.

Conclusions

Interferometric techniques provide an accurate method for determining both the spatial and temporal characteristics of laser-driven shock waves. We used a Michelson interferometer in situ on the two-beam facility at Nova to evaluate both the level of preheating present under a variety of conditions and the spatial uniformity and planarity of the incident shock wave. Using the interferometer, we were able to determine that there were insignificant levels of preheat due to the laser drive and that the driver was shown to generate a shock that remained planar over approximately the central one-third of the target throughout the experiment. With further modeling efforts, the motion of the target's rear surface in advance of the shock breakout could be directly correlated to the temperature of this surface, thus providing a very accurate preheat diagnostic for laser-driven shock experiments. This technique is currently being integrated into the suite of diagnostics available in the ten-beam facility at Nova. The first demonstrations of interferometric characterization of shock-driven targets were conducted in December 1996.

Acknowledgments

Notes and References

1. C. E. Ragan III, M. G. Silbert, and B. C. Diven, *J. Appl. Phys.* **48**, 2860–2870 (1977).
2. C. E. Ragan III, *Phys. Rev. A* **29**, 1391–1402 (1984).
3. A. Vladimirov, N. P. Voloshin, V. N. Nogin, A. V. Petrovtsev, and V. A. Simonenko, *JETP Lett.* **39**, 82–85 (1984).
4. E. N. Avrorin, B. K. Voldolaga, N. P. Voloshin, V. F. Kuropatenko, G. V. Kovalenko, et al., *JETP Lett.* **43**, 308–311 (1986).
5. A. C. Mitchell, W. J. Nellis, J. A. Moriarty, R. A. Heinle, N. C. Holmes, et al., *J. Appl. Phys.* **69**, 2981–2986 (1991).
6. L. R. Veeser and S. C. Solem, *Phys. Rev. Lett.* **40**, 1391–1394 (1978).
7. R. J. Trainor, J. W. Shaner, J. M. Auerbach, and N. C. Holmes, *Phys. Rev. Lett.* **42**, 1154–1157 (1979).
8. C. G. M. van Kessel and R. Sigel, *Phys. Rev. Lett.* **33**, 1020–1023 (1974).
9. S. P. Obenschain, R. R. Whitlock, E. A. McLean, B. H. Ripin, R. H. Price, et al., *Phys. Rev. Lett.* **50**, 44–48 (1983).
10. F. Cottet, J. P. Romain, R. Fabbro, and B. Faral, *Phys. Rev. Lett.* **52**, 1884–1886 (1984).
11. K. A. Tanaka, R. Kodama, K. Nishihara, M. Kado, A. Nishiguchi, et al., in *Shock Waves*, K. Takayama, Ed. (Springer-Verlag, Berlin, 1992), p. 863.
12. T. Löwer, R. Sigel, K. Eidmann, I. B. Földes, S. Hüller, et al., *Phys. Rev. Lett.* **72**, 3186–3189 (1994).
13. A. M. Evans, N. J. Freeman, D. Graham, C. J. Horsfield, S. D. Rothman, et al., *Lasers Part. Beams* **14**, 113–123 (1996).
14. R. Cauble, D. W. Phillion, T. J. Hoover, N. C. Holmes, J. D. Kilkenny, and R. W. Lee, *Phys. Rev. Lett.* **70**, 2102–2105 (1993).
15. R. Cauble, L. B. Da Silva, S. G. Glendinning, S. M. Lane, T. S. Perry, and D. W. Phillion, *1993 ICF Annual Report*, **6**(4)131–136, Lawrence Livermore National Laboratory, Livermore, CA, UCRL-LR-105820-93 (1993).
16. L. B. Da Silva, P. Celliers, G. W. Collins, K. S. Budil, N. C. Holmes, et al., *Phys. Rev. Lett.* **78**, 483 (1997).
17. L. M. Barker and R. E. Hollenbach, *Rev. Sci. Instrum.* **36**, 1617–1620 (1965).
18. L. M. Barker and R. E. Hollenbach, *J. Appl. Phys.* **43**, 4669–4675 (1972).
19. S. Dixit, Lawrence Livermore National Laboratory, Livermore, CA, private communication (1996).

Absolute Equation of State Measurements of Compressed Liquid Deuterium Using Nova

R. Cauble

L. B. Da Silva

P. Celliers

G. W. Collins

K. S. Budil

N. C. Holmes

B. A. Hammel

J. D. Kilkenny

R. J. Wallace

A. Ng*

Introduction

The equations of state (EOSs) of hydrogen and its isotopes at high pressure are essential components of the physics of high-density matter.[1,2] For example, the internal structure of Jovian planets is very sensitive to and largely determined by the hydrogen EOS in the pressure range of 1.0 Mbar to 10.0 Mbar.[3] Further, the performance of deuterated inertial confinement fusion (ICF) capsules relies on shock timing and efficient compression, which are critically dependent on the EOSs.[4] In ICF, a "softer," or more compressible, EOS of the deuterium–tritium (DT) fuel is advantageous for ignition. For these reasons, a number of theoretical models of the EOS of hydrogen have been proposed.[5–7]

An important question in the EOS of H_2, as well as of D_2, has been the transition from a diatomic to a monatomic fluid. A continuous dissociative transition has been suspected, but theoretical predictions of molecular dissociation have been complicated by the presence of electronic transitions and possible ionization near pressures required for dissociation (~1.0 Mbar).[8] In spite of the expected simplicity of the element, there is no inclusive theory for a strongly coupled mixture of hydrogen ions, atoms, and molecules. In the following, we describe results of the first measurements of the principal Hugoniot (i.e., a curve in the EOS that will be defined subsequently) of liquid deuterium compressed with pressures as great as 2.1 Mbar. These absolute EOS data reveal a substantially enhanced compressibility that is an indicator of dissociation.

High-Pressure Hydrogen EOS and ICF

The EOS of the hydrogen-isotope fuel governs the reaction of an ICF capsule to outside pressures to compress the capsule. The fuel must be highly compressed in order to ignite.[4] To reach a high final density, the fuel must be compressed without excessive heating because the more internal energy the fuel has, the more difficult it is to compress and confine it. To compress ICF capsules without excessive heat, a series of progressively stronger shocks is envisioned. In the point-design ignition capsule to be used for the National Ignition Facility (NIF), three main shocks are used, the first of which is delivered to the DT fuel at 0.9 Mbar.[9]

It has been shown that the more compressible the hydrogen EOS is at this pressure, the higher will be the expected yield from the capsule[10] (a greater compressibility means a higher density of the fuel at a given pressure). The higher yield is primarily the result of the capsule fuel's higher final density when the fuel ignites. It is also due to a lower predicted Rayleigh–Taylor instability growth rate. Additionally, the greater the compressibility of the EOS, the less sensitive the calculated yield is to the exact pressure of the first shock.

Molecular dissociation of deuterium can be a source of enhanced compressibility and has been expected to occur in the pressure regime near 1.0 Mbar. Dissociation is an energy sink (it takes energy to break the molecular bonds), so some of the energy transmitted to the NIF capsule fuel from the first shock will be used for this process. The more energy required for dissociation, the lower the temperature of the shocked fluid and, consequently,

the higher the shocked density. The experiments described subsequently were undertaken to evaluate compression of liquid deuterium in the 1.0-Mbar pressure regime.[11]

EOS data for hydrogen in the pressure regime greater than 0.1 Mbar have been obtained by dynamic shock compression and by static compression in diamond-anvil cells. The latter method is used to study static, isothermal properties of solid hydrogen at pressures as great as 3.0 Mbar at very low temperatures.[12] Shock compression produces higher temperatures than does static compression. In shock compression, the most accurate data have been produced using light gas guns.[13–15] While both methods access equilibrium states of matter, the final-state densities and temperatures obtained by shock compression are directly applicable to ICF.

Shock-wave experiments are the only practical technique for measuring high-pressure EOSs. The final state of a shocked material is simply related to the initial state through the Hugoniot relations. These relations are derived by applying conservation equations across the shock front. Conservation relations require that two independent parameters be measured to obtain an *absolute* EOS data point (nonabsolute comparative data are often used to assess the EOS of one material with respect to another). The shock speed U_s, the particle (or pusher) speed U_p, the pressure P, and the final density ρ are related by

$$P - P_0 = \rho_0 U_s U_p \tag{1}$$

and

$$\rho / \rho_0 = U_s / (U_s - U_p) \tag{2}$$

where ρ_0 is the initial density, P_0 is the initial pressure, and ρ / ρ_0 is the compression.[16] Equations (1) and (2) are two of the Hugoniot relations (a third relation, which entails conservation of energy, was not considered).

Temperature is not a quantity in the Hugoniot relations. In an experiment to obtain data on the Hugoniot, the change in internal energy can be determined, but the partition of energy, and thus the temperature, cannot. Separate measurements are required to determine temperatures of shocked matter.

Early EOS experiments on H_2 and D_2 [Ref. 13] were well described by a model that neglected molecular dissociation.[6] However, recent measurements revealed a significantly lower temperature than predicted for pressures greater than 0.2 Mbar.[14] This was interpreted as dissociation of the molecular fluid at high density and temperature. A new model, referred to subsequently as the dissociation model, was formulated to incorporate this effect.[14] The dissociation model is not an *ab initio* theory; it is based on the ideal mixing of molecular states (using a soft-sphere perturbation theory) and monatomic states (using a one-component plasma model) and includes a single adjustable parameter set to agree with all shock-wave and shock-temperature data for H_2 and D_2.[13,14] The inclusion of molecular dissociation leads to a prediction of the compressibility, in the 0.2-Mbar to 5.0-Mbar pressure regime, that is significantly higher than that of the earlier model.[6] For example, the density of D_2 on the Hugoniot at 1.0 Mbar is 50% greater than calculated from the earlier model[6] and from the D_2 table included in the widely used Sesame EOS library.[17]

Equation of State Measurements Using Lasers

It has long been known that lasers are capable of driving very strong shocks into targets.[18] However, the production of EOS data in the megabar regime using lasers with uncertainties of less than 10% is virtually nonexistent. There are four challenges that must be confronted when attempting such experiments.

1. The shock produced must be spatially uniform. A modulated shock has a range of pressures and densities along the shock front; this is unsuitable for measurements. This issue can be addressed by target design and smoothing of the beam.[19] The shock should also be planar; producing a strong shock with a laser of high intensity obtained by focusing to a small spot may succeed only in driving a spherical, rather than planar, shock wave into the target, thus making difficult interpretation of the experiment. A laser spot that is too small will also be subject to edge effects; i.e., rarefaction waves releasing from the perimeter of the spot and moving radially inward. If the spot diameter is small, these rarefactions can reach the center of the spot on the timescale of the measurements, thus compromising the results.

2. The shock should be steady in time. A constant drive will produce a shock moving at a constant speed; e.g., a declining drive produces a decaying shock that must be characterized carefully. As will be shown subsequently, a constant

shock speed offers the possibility of obtaining data with small uncertainties.

3. Preheat has always been a concern in laser-produced EOS measurements. Penetrating x rays or hot electrons produced in the laser-interaction region (generally near 1 keV in temperature) can be absorbed in the sample being measured prior to the sample being shocked. The result is a change in the initial conditions of the sample, including the initial density ρ_0. Because measurements of the Hugoniot determine compression (ρ/ρ_0) rather than the final density (see Eq. 2), a change in ρ_0 means an error in the final density.

4. Typical spatial scales for megabar-regime laser experiments are micrometers, and timescales are a few tens of picoseconds. The diameter of the Nova laser spot used in the described experiment was less than 1 mm, and typical shock speeds in the deuterium were 30 km/s. Instrumentation and diagnostics appropriate for conditions such as these are necessary to produce meaningful data.

All of these challenges were addressed in the experiments described herein; hence, there is considerable confidence in the results.

Nova Experiments to Measure the EOS of Liquid Deuterium

To obtain absolute EOS data, we compressed liquid D_2 with a Nova-laser-driven shock wave launched from an Al pusher. Using temporally resolved radiography, we followed the propagation of the Al/D_2 interface and the shock front in the D_2 and measured the pusher speed, shock speed, and compression. We then determined the pressure by using Eq. (1).

A schematic of the cryogenic target cell is shown in Figure 1. Liquid D_2 was contained in a 1-mm-diam, 0.45-mm-long cylindrical cell machined into a Cu block. One end of the cell was sealed with an Al disk that served as the shock pusher; the opposite end of the cell was sealed with a 0.5-mm-thick sapphire window. The pusher was 100, 180, or 250 μm thick, depending on the experiment, and had a rear-side mean surface roughness of 30 nm rms. The pusher was coated with 15 to 25 μm of polystyrene external to the cell, and the polystyrene was overcoated with a 100-nm layer of Al. The thickness of the polystyrene layer was chosen to prevent direct laser ablation of the Al pusher, thus minimizing x-ray emission and consequent preheat of the pusher from x rays produced in the plasma. The Al overcoating eliminated direct optical laser shine through the plastic at onset of the laser pulse before an absorbing plasma formed. To accommodate radiography through the sides of the

cell, a 500-μm-diam window was drilled into each side of the cell and sealed with a 5-μm-thick Be foil.

Liquid D_2 requires temperatures of approximately 20 K, so a cryostat was constructed for the two-beam facility at Nova, making this series the first cryogenic experiments ever fielded on Nova. The D_2 was loaded into the cell and pressurized to a few hundred torr. Temperatures were monitored to within 0.05 K. D_2 densities were determined from the saturation curve[20] and varied between 0.170 and 0.172 g/cm^3. The initial density ρ_0 for each experiment was known with an uncertainty of less than 0.1%.

One beam of the Nova laser ($\lambda = 527$ nm) was focused onto the target. Ablation of the polystyrene layer drove a shock wave through the Al and into the D_2. Side-on radiography of the D_2 revealed propagation of the Al/D_2 interface and the shock front. To ensure a spatially planar and uniform shock front, a kinoform phase plate[21] was inserted into the Nova beam to generate a smooth laser irradiance profile. The laser spot at the target plane was elliptical, with major and minor diameters as great as 900 and 600 μm, respectively, depending on focusing. Drive irradiances ranged from 5×10^{12} to 2×10^{14} W/cm^2. The Nova drive beam had an 8- or 10-ns temporally square profile with a rise time of 100 ps.

The results of the measurement depend on knowing the initial state of the D_2 (i.e., ρ_0) prior to shock arrival. This made it necessary to determine the preheat level of the pusher/D_2 interface at the time the shock arrived. The position of the rear pusher surface was monitored, with a Michelson interferometer,
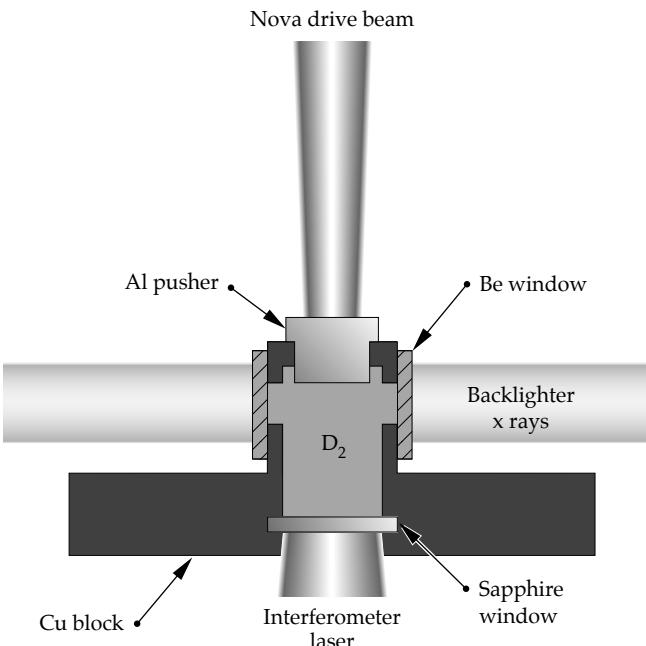
FIGURE 1. Schematic diagram of a cryogenic cell for laser-driven shock compression of liquid D_2. (08-00-0197-0007pb01)
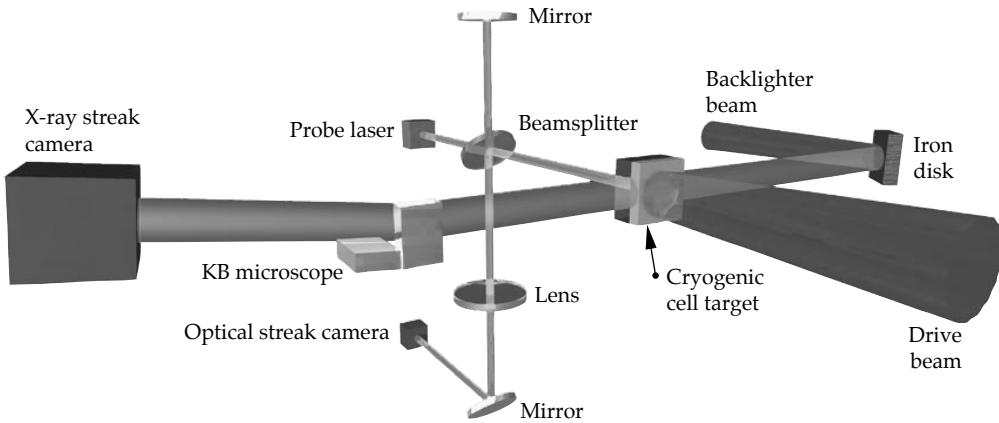
FIGURE 2. Schematic diagram of the experimental setup for simultaneous side-on radiography and end-on interferometry of a cryogenic cell with three laser beams: a smoothed Nova beam to drive a shock in the cell; an oppositely directed Nova beam to provide an x-ray backlighter; and a probe beam for the interferometer. (70-00-0297-0250pb01)

through the sapphire window. This provided the additional advantage of verifying the planarity of the shock at breakout. The interferometer-probe beam was a 10-ns-FWHM, 355-nm laser pulse appropriately time-delayed from the Nova drive beam that generated the shock wave. (The interferometer and results from the diagnostic are described in an article by K. S. Budil on page 11 of this *Quarterly*.) Using this instrument, we were able to confirm that the shock front in the D_2 was sufficiently planar for measurements and that the preheat levels in the D_2 were negligible. The arrangement for the experiment is shown in Figure 2.

Streaked radiography of the shocked D_2 was performed using a plasma x-ray source produced by focusing a second beam of Nova onto an Fe disk (10 ns at 6×10^{13} W/cm^2). The backlighter was placed 12 cm from the target cell to eliminate possible heating of the cell by the backlighter plasma. At that distance, the backlighter x rays produced a near-collimated source. The effective source size in the imaging direction was approximately 150 μm and was set by the width of the laser focal spot. Using the interferometer, we observed that the x-ray backlighter had no effect on the D_2 in the cell. X rays transmitted through the target cell were imaged by a Kirkpatrick–Baez (K-B) microscope onto a streak camera. The K-B microscope's bandpass was 750–840 eV, and the collection half-angle was 2.5 mrad. Two calibrated magnifications were used: 33× and 82×. The resolution of the K-B microscope in this geometry was found to be better than 3 μm over a 300-μm-wide field of view. The microscope imaged a strip 300 μm long by 5 to 30 μm high, depending on magnification and configuration.

An example of a streaked radiograph of shock-compressed D_2 is shown in Figure 3. The drive irradiance was 10^{14} W/cm^2 over 8 ns. The bright area in the figure is the view through the side windows of the cell. Because the pusher is opaque and the liquid transparent, the Al/D_2 interface is the boundary between the light and dark regions. In the figure, the interface is stationary prior to 2 ns. At 2 ns, the laser-driven shock

crosses the interface, and the pusher surface accelerates to a steady speed (the particle speed). A shock front can be seen moving ahead of the interface as the shock wave is driven into the D_2. The shock front, which appears as the dark line, is made visible because of refraction of backlighter x rays at the density jump across the shock front. X rays grazing the shock-front interface are refracted to angular deflections greater than 2.5 mrad and, therefore, out of the angular field of the K-B microscope (x rays impinging at nongrazing angles are internally reflected, so there is transmission between the Al/D_2 interface and the shock front). The detection of the shock front by refraction is similar to the Schlieren technique for detecting density gradients. The steady propagation of both the shock front and the interface is demonstrated by their linear trajectories until ~6 ns, when a stronger shock enters the D_2. The second shock is caused by shock reverberations in the pusher. (In this example, no data after 6 ns were used.) The shock and particle speeds U_s and U_p can be evaluated from the slopes.

The single shock compression can be determined by Eq. (2) using the individually derived shock and pusher speeds. It also can be measured directly from
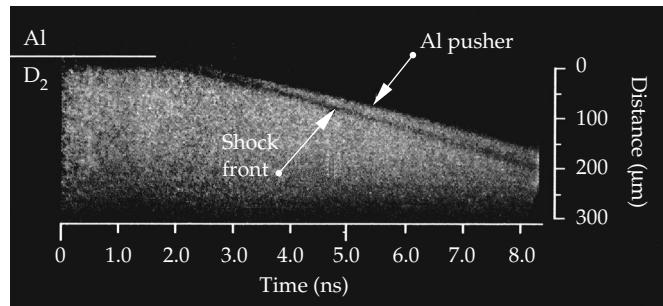
FIGURE 3. A time-resolved, side-on radiograph of a laser-shocked D_2 cell. The bright area views the D_2 through Be windows bounded by the x-ray-opaque Al pusher above. The pusher is seen advancing after breakout at 2 ns; the shock is the dark line in front of and moving faster than the pusher–D_2 interface. (70-00-0297-0249pb01)

the film as long as U_s and U_p are constant (in the experiments, U_s and U_p were constant to better than 1%). At any time t, the compression is equal to the ratio of two lengths: the distance between the shock front $X_2(t)$ and the initial interface position X_0, which is the thickness of a layer of uncompressed D_2, and the distance between the shock front and the interface $X_1(t)$, which is the thickness of the now-compressed layer. Thus $\rho/\rho_0 = [X_2(t) - X_0]/[X_2(t) - X_1(t)]$. Because all of the measurements are made on one piece of film in the streak camera, uncertainties in ρ/ρ_0 due to magnification and sweep speed are canceled in this ratio. In the experiments, we observed a steady shock for 4 to 8 ns with no measurable change in speed of the Al/D_2 interface. Comparison with Eq. (2) provides an internal consistency check on ρ/ρ_0.

The shock position that we observed in the radiograph is the leading part of the shock front that emerged from the center of the pusher. In some experiments, the apparent Al/D_2 interface position at $t = 0$ on film was not identical to the actual value of X_0 because the rotation of the cell about the axis perpendicular to both the backlighter path and the shock path (the axis looking into the page in Figure 1) could be controlled only to within 3 mrad. This resulted in the center of the pusher being shadowed by an edge of the pusher before the shock front emerged from the pusher. In these cases, the shock and interface trajectories did not converge on the film. Extrapolation of the trajectories, however, revealed X_0 as the intersection of the two paths. Alternatively, shock and interface positions taken at two different times were used to determine X_0. This resulted in correcting, by as much as 10%, the compression obtained using the *apparent* position X_0 on film and increased the uncertainty in ρ/ρ_0 from approximately ±3% to approximately ±5%.

The Al/D_2 interface is subject to the Richtmyer–Meshkov hydrodynamic instability (RM). However, using the measured pusher finish of 30 nm, we calculated that the largest perturbation expected from RM is less than 0.5 μm during the times of observation, approximately 1% to 2% of the compression.

Figure 4 shows the pressures and final densities determined from the known initial densities and measured compressions. As explained previously, the error bars are governed predominantly by accuracy in determining the slopes of the shock and interface trajectories in the radiographs. The figure plots curves of the Hugoniot from the dissociation model[14] and the Sesame EOS table.[17] The gas-gun observations[13] are also shown. At the lowest compression, our data are in agreement with the earlier results; at higher compressions, the data deviate from the Sesame prediction. The data point at 0.25 Mbar is significant because it overlies the more accurate gas-gun data,
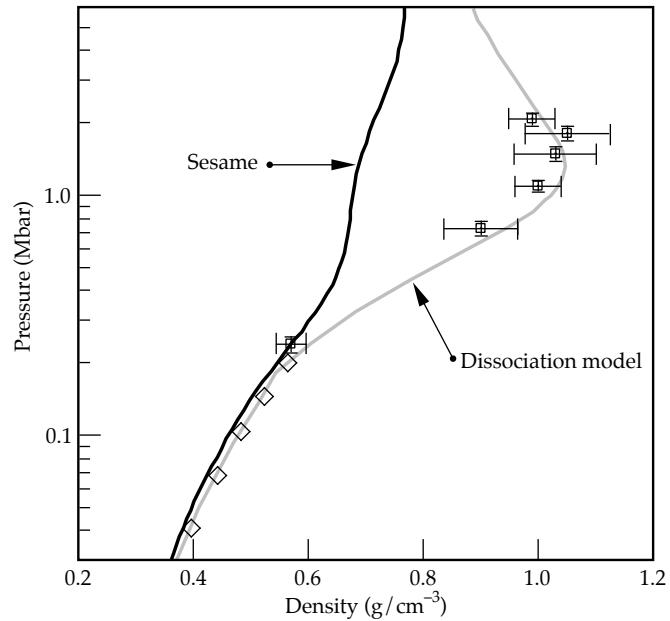
FIGURE 4. The measured data are shown as squares with error bars compared with Hugoniots derived from the Sesame EOS library,[17] which is similar to an EOS without dissociation,[6] and the proposed dissociation model of Ref. 14. The diamond shapes depict gas-gun data.[13] (70-00-0297-0248pb01)

lending confidence to our results. The laser data evince an enhanced compressibility comparable to that of the dissociation model in the region where occurrence of strong dissociation was predicted. We conclude from this that molecular dissociation is indeed significant in hydrogen isotopes compressed near 1.0 Mbar.

Conclusion

These are the first measurements of the density, shock speed, and particle speed in D_2 at pressures greater than 0.2 Mbar. The range of pressures measured extended from 0.25 to 2.1 Mbar, encompassing the regime of the first shock prescribed by the NIF point-design ignition capsule. These absolute data of Hugoniot strongly indicate a dissociative transition from the diatomic to the monatomic fluid state. Because an accurate model of the dissociation was not incorporated in previous EOS theories for hydrogen, the data provide an important benchmark for a revised theory for hydrogen and its isotopes in a regime relevant to high-energy-density physics and ICF. The more compressible EOS of hydrogen indicated by these data offers higher performance and improved margin for NIF ignition capsules. Finally, the experiments demonstrate that laser-driven shocks can effectively and confidently be used for EOS studies at pressures beyond those attainable by traditional techniques.

Acknowledgments

The authors would like to thank R. M. More, F. J. Rogers, M. Ross, D. A. Young, and J. D. Johnson (Los Alamos National Laboratory) for advice on the theory and S. N. Dixit for designing the kinoform phase plate.

Notes and References

1. S. Ichimaru, H. Iyetomi, and S. Tanaka, *Phys. Rep.* **149,** 91 (1987).
2. N. W. Ashcroft, *Phys. World* **8** (7), 43 (1995).
3. R. Smoluchowski, *Nature* **215,** 691 (1967); V. N. Zharkov and V. P. Trubitsyn, *Jupiter,* T. Gehrels, Ed. (University of Arizona Press, Tucson, 1976), pp. 135–175; W. B. Hubbard, *Science* **214,** 145 (1981); W. J. Nellis, M. Ross, and N. C. Holmes, *Science* **269,** 1249 (1995).
4. J. D. Lindl, *Phys. Plasmas* **2,** 3933 (1995).
5. W. B. Hubbard, *Astrophys. J.* **152,** 745 (1968).
6. M. Ross, F. H. Ree, and D. A. Young, *J. Chem. Phys.* **79,** 1487 (1983).
7. D. Saumon, G. Chabrier, and H. M. Van Horn, *Astrophys. J. Supp.* **99,** 713 (1995).
8. W. R. Magro, D. M. Ceperley, C. Pierleoni, and B. Bernu, *Phys. Rev. Lett.* **76,** 1240 (1996).
9. S. W. Haan, S. M. Pollaine, J. D. Lindl, L. J. Suter, et al., *Phys. Plas.* **2,** 2480 (1995); W. J. Krauser, N. M. Hoffman, D. C. Wilson, B. H. Wilde, et al., *Phys. Plas.* **3,** 2084 (1996).
10. S. W. Haan, LLNL Y Division, Livermore, CA, private communication (August 1995).
11. L. B. Da Silva, P. Celliers, G. W. Collins, K. S. Budil, et al., "Absolute Equation-of-State Measurements of Shocked Liquid Deuterium up to 200 Gpa (2 Mbar)," to appear in *Phys. Rev. Lett.* (1997).
12. H. K. Mao and R. J. Hemley, *Rev. Mod. Phys.* **66,** 671 (1994).
13. W. J. Nellis, A. C. Mitchell, M. van Theil, G. J. Devine, et al., *J. Chem. Phys.* **79,** 1480 (1983).
14. N. C. Holmes, M. Ross, and W. J. Nellis, *Phys. Rev. B* **52,** 15835 (1995).
15. S. T. Weir, A. C. Mitchell, and W. J. Nellis, *Phys. Rev. Lett.* **76,** 1860 (1996).
16. Y. B. Zel'dovich and Y. P. Raizer, *Physics of Shock Waves and High-Temperature Hydrodynamic Phenomena* (Academic Press, New York, 1966).
17. G. I. Kerley, *A Theoretical Equation of State for Deuterium*, Los Alamos Scientific Laboratory Report LA-4776 (New Mexico, January 1972).
18. R. J. Trainor, J. W. Shaner, J. M. Auerbach, and N. C. Holmes, *Phys. Rev. Lett.* **42,** 1154 (1979).
19. R. Cauble, L. B. Da Silva, S. G. Glendinning, S. M. Lane, et al., *Inertial Confinement Fusion, 1993 ICF Annual Report,* Lawrence Livermore National Laboratory, Livermore, CA, UCRL-LR-105820-93, 131–136 (1994).
20. P. C. Souers, *Hydrogen Properties for Fusion Energy* (University of California Press, Berkeley, 1986).
21. S. N. Dixit, M. D. Feit, M. D. Perry and H. T. Powell, *Opt. Lett.* **21**, 1715 (1996).

Low-Density–Foam Shells

R. C. Cook

G. E. Overturf, III

G. Wilemski

S. A. Letts

S. M. Lambert*

D. Schroen-Carey**

Introduction

Future inertial confinement fusion (ICF) targets at the University of Rochester Laboratory for Laser Energetics and at Lawrence Livermore National Laboratory's (LLNL's) planned National Ignition Facility will require 1- to 2-mm-diam spherical organic-polymer shells, each having an 80- to 100-μm-thick cryogenic liquid or solid layer of deuterium–tritium (DT) on its inside surface.[1,2] A potential means of fulfilling this requirement is to line the inside of the plastic capsule with a layer of low-density (~50 mg/cm^3), low-atomic-number foam to help support and symmetrize the fuel.[3] The foam layer also provides the opportunity to dope the DT fuel, which permeates it, with mid-Z elements incorporated in the foam that may be useful in providing spectroscopic diagnostics of the implosion.[4,5] In the case of solid DT layers, Collins[6] has shown that DT ice grown on top of foam has a smoother surface finish, presumably because the small cell size of the foam leads to more finely grained crystal sizes. This paper describes fabrication of this inner foam mandrel via the microencapsulation of resorcinol–formaldehyde (RF) aerogel, a foam material developed at LLNL during the past decade for defense and commercial purposes.[7]

Preparation of foam shells by microencapsulation was first developed by Takagi et al.[8–12] using a methacrylate-based chemistry. Shells of this type, filled with cryogenic liquid D$_2$, have been used in the Japanese ICF program.[10] In that scheme, an aqueous drop is enclosed in an immiscible organic-solvent shell that contains an approximately 5% concentration of a multifunctional methacrylate monomer; this compound drop is, in turn, submerged in an aqueous phase. After the compound drop is formed, a polymerization reaction is initiated in the organic phase to create a cross-linked polymer network (gel) that occupies the volume of the organic phase and provides a solid, gelatin-like state to ensure stability. When polymerization is complete, the water core and the organic solvent permeating the gel are exchanged with a mutually miscible solvent, which is then replaced with liquid CO$_2$. Dry foam shells are obtained by removing the CO$_2$ as a supercritical fluid. This drying route is necessary because standard air-drying would cause the foam's very fine cell structure to collapse due to surface forces associated with the vapor/liquid interface. Because the initial organic phase had only approximately 5% solids, the resulting foam has a density of approximately 50 mg/cm^3 (full density is approximately 1 g/cm^3).

This work[8–12] and subsequent work performed at LLNL on methacrylate-based foam shells[13] revealed two important features of the encapsulation technique:

- The polymerization and related gelation of the shell phase must occur quickly to stabilize the inherently unstable compound drop.
- The densities of the inner aqueous droplet and of the nonaqueous shell phase containing the polymerizable compound must be carefully matched to eliminate buoyancy effects that can further destabilize the compound drop and lead to nonuniform shell-wall thickness.

The impetus to pursue RF aerogel shells was realizing an optical transparency considerably greater than that of methacrylate-based foams.[14] The opacity of methacrylate foams is due primarily to the scattering of light by the relatively large (i.e., 1- to 3-μm) cell structure.[15] RF aerogel, on the other hand, has a cell size of approximately 0.1 μm and is therefore significantly more transparent. This allows us to optically monitor the state of the cryogenic DT that fills the shell and, most importantly, to measure the surface finish of the inside DT ice layer, a critical parameter for capsule performance.[1,2]

*   Soane Technologies, Hayward, CA
** W. J. Schafer Associates, Livermore, CA

The preparation of RF foams differs considerably from that of methacrylate-based foams, and these differences profoundly affect the encapsulation process. One important difference is that the typical gelation time of conventional RF aerogel formulations is many hours.[7,16–21] Because successful encapsulation is possible only if gelation of the shell phase occurs within 15 to 20 minutes, a means of accelerating the gelation—that can maintain the desired foam properties (e.g., transparency and low density)—is needed. Another important difference is that, in the case of the RF system, polymerization occurs in an aqueous medium rather than in an organic (oil) medium. As a result, an oil-in-water-in-oil system, rather than the water-in-oil-in-water system used for methacrylate foam shells, is needed to create RF aerogel shells.

RF Aerogel Chemistry

The use of RF resin chemistry to form low-density microcellular materials was pioneered by Pekala et al.[7,16–21] In basic aqueous solutions at elevated temperatures (60–95°C), resorcinol and formaldehyde react to form cross-linked, nanometer-sized particles. After the initial particle-formation and -growth stage, which can take several hours, the colloidal particles begin to aggregate and assemble into a stiff, interconnected structure locally resembling a string of pearls that fills the original volume of the aqueous solution. This process of particle growth, followed by aggregation and gelation, is shown schematically in Figure 1.

RF formulations are characterized by three quantities related to the initial composition of the aqueous solution:

1. The first is the molar ratio of formaldehyde to resorcinol (F/R). A ratio of 2 has been used in all previous studies,[7,16–21] but we have investigated the effect of increasing it to 3. Increasing F/R should increase the average number of reactions per resorcinol and, ultimately, the degree of cross-linking.

2. The second quantity is the molar ratio of resorcinol to catalyst (R/C). The catalyst in this reaction is sodium carbonate, which activates a small fraction of the resorcinol molecules to act as sites for the growth of RF particles. Reducing R/C (i.e., increasing the catalyst concentration) produces more particles of smaller size. Investigation here is limited to R/C ratios of 100 and 200 because it is known that these yield the lowest density and most optically transparent foams.[7,16–18]

3. The last quantity is the theoretical dry-foam density, which is determined from the concentration of polymerizable reactants (resorcinol and formaldehyde) in the initial aqueous solution. A solution containing a combined 5 wt% of resorcinol and formaldehyde will have a theoretical density of approximately 50 mg/cm^3. Due to some shrinkage of the gel upon drying, actual foam densities are usually slightly higher than the theoretical densities. We have worked primarily with RF formulations that produce foams with theoretical densities of 50 and 75 mg/cm^3.
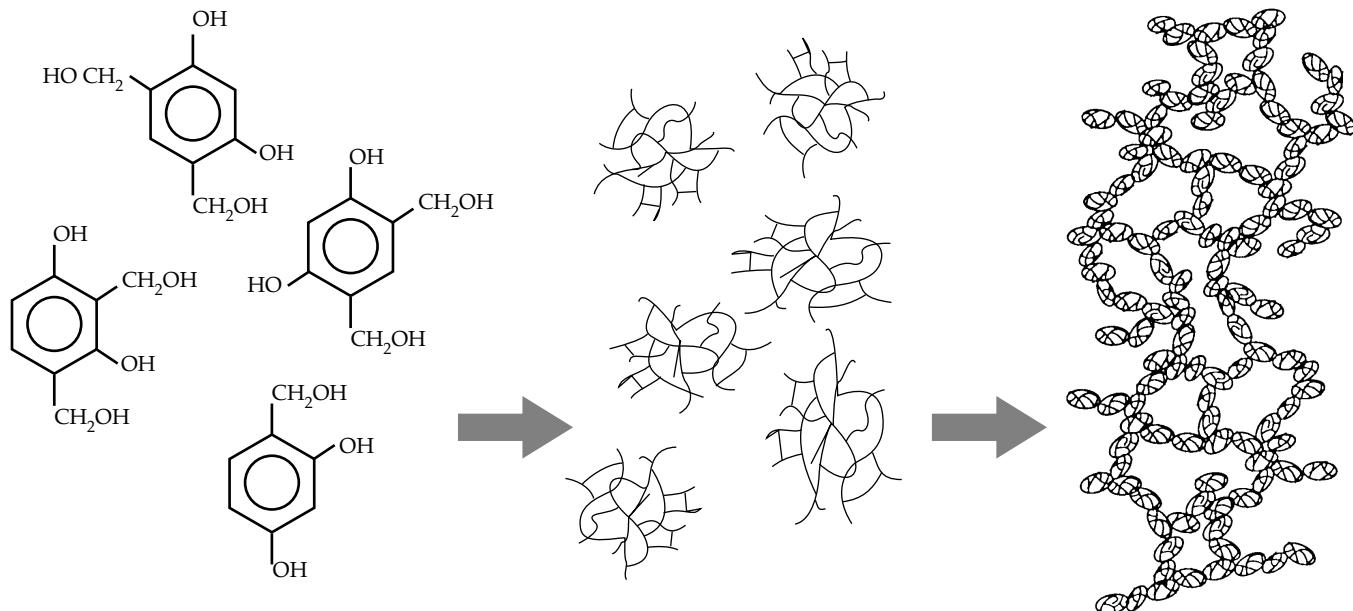
FIGURE 1.   Left: Substituted resorcinol is formed by the initial reaction between resorcinol and formaldehyde. Center: These substituted resorcinol moities react to form cross-linked clusters. Right: Finally, the cross-linked clusters condense into extended "chain-of-pearls" cross-linked molecules, forming a gel-like material.   (02-32-0688-1671pb01)
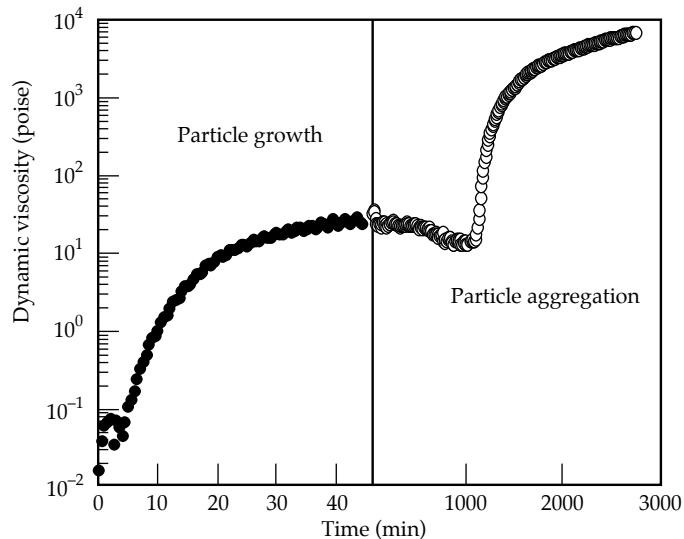
FIGURE 2. Dynamic viscosity of an RF solution (30 mg/cm^3 theoretical foam density, $F/R = 2$, $R/C = 100$) at 70°C. The first regime corresponds to particle growth. The second regime corresponds to particle aggregation to form the stiff gel. Note change in time scale between regimes on the horizontal axis. From Letts et al.[18]
(70-00-0197-0149pb01)

Letts et al.[18] have shown, by dynamic viscosity measurements, that the base-catalyzed RF reaction at 70°C is initially dominated by particle growth that typically ceases after approximately 1 h. In Figure 2, this is illustrated by the dynamic vicosity's initial rise and plateauing at a relatively low value. At some point many hours later (note change in scale), a second large increase in the dynamic viscosity signals the aggregation of particles to form a stiff gel. Titration measurements[19] show that most of the formaldehyde is consumed within the first half hour. These results, coupled with light scattering studies,[20,21] provide convincing evidence that particle growth is completed well before aggregation begins.

We have found that the reactions taking place during the particle-growth stage slowly increase the acidity of the reacting medium. After particle growth has stopped due to the depletion of formaldehyde, the acid-catalyzed reactions between the surfaces of particles create links between particles to form chemical bridges. Nuclear magnetic resonance studies[17] support this difference between intra- and interparticle chemical structures. Because the solution is typically only slightly acidic after particle growth, aggregation proceeds at a slow rate. We reasoned that artificially lowering the pH by adding acid should more rapidly aggregate the particles to the point of gelation.

We confirmed this hypothesis experimentally. Figure 3 shows the effect on the dynamic viscosity of increasing the acidity by a factor of 10 by adding benzoic

acid after 1 h of conventional base-catalyzed reaction. After a short period, the dynamic viscosity rapidly increases and plateaus at gel-like values. This result has led to the two-step procedure for preparing RF gels that is outlined in Figure 4. First, the reactants are mixed together and base-catalyzed at 70°C for 1 h. The solution is then cooled for several minutes in an ice-water bath, and benzoic acid is added to increase the acidity. The compound droplets are then formed in a 70°C oil bath, as will be described subsequently, and this increase in temperature of the now acid-catalyzed RF solution results in rapid gelation of the shells.
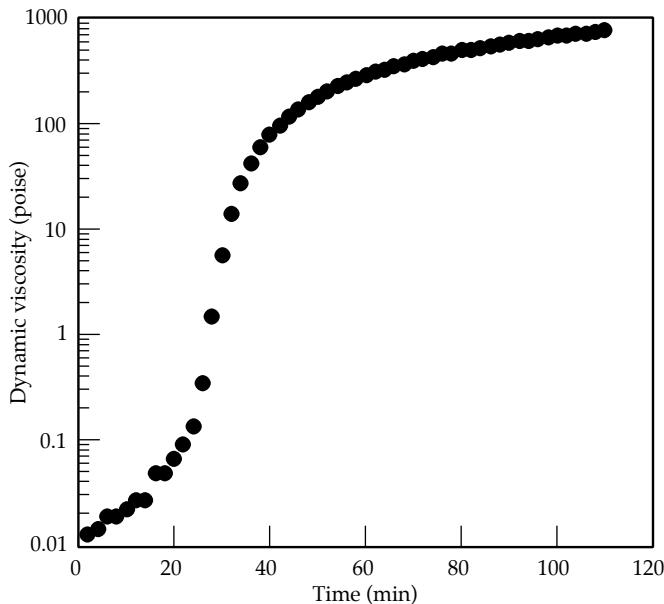
FIGURE 3. Dynamic viscosity of an RF solution (50 mg/cm^3 theoretical foam density, $F/R = 2$, $R/C = 200$) at 70°C that has been spiked with 0.026 wt% benzoic acid following 1 h conventional base-catalyzed reaction. (70-00-0197-0151pb01)
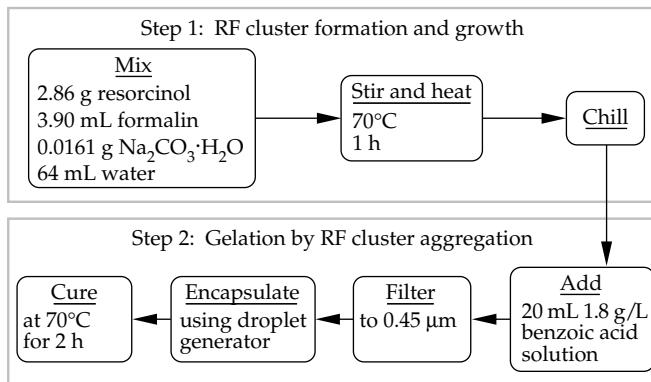
FIGURE 4. The two-step process for preparing acid-accelerated RF gels (50 mg/cm^3 theoretical foam density, $F/R = 2$, $R/C = 200$).
(70-00-0197-0152pb01)

To optimize this two-step RF polymerization process, we studied the effects of modifying the R/C ratio, the length of the initial base-catalysis period, and the amount of benzoic acid added. For all solutions, $F/R = 2$. The goals of this study were to decrease the gelation onset time (some indication of how long it takes the gel to set and thus stabilize the compound droplet) and to maximize the dynamic viscosity of the gel after curing for 2 h (to give an indication of the strength and stiffness of the gelled material).

Figure 5 shows the effect of varying the acid content on the dynamic viscosity of formulations with different values of R/C. Both the $R/C = 100$ and the $R/C = 200$ solutions were base-catalyzed for 1 h. For

both values of R/C, increasing the acid concentration set the gels more rapidly and increased the plateau viscosity. Understanding the effect of changing R/C for a given amount of benzoic acid is not as straightforward. R/F solutions become more basic as R/C is decreased. Because of the increased basicity, more of the added acid will be used to neutralize the carbonate rather than to promote aggregation. As a result, a given amount of acid will be less effective in promoting gelation in low-R/C solutions than it will in high-R/C solutions. This is most evident in Figure 5(a) when 0.036 g benzoic acid is added; as R/C decreases, the gelation onset time begins later. Despite delay in the onset of gelation, gels with lower R/C plateau at a slightly higher viscosity. As shown in Figure 5(b), with solutions having higher acid contents, the effect of differences in R/C become less distinguishable.

Figure 6 shows the effect of varying the length of the initial base-catalysis period. The viscosity behavior is significantly affected within the first hour; after 0.5 h, particle growth is probably still occurring. The increases in gelation rate and plateau viscosity when base-catalysis time is extended beyond 1 h are probably due to continued intraparticle cross-linking and the start of some aggregation before acid addition. Increasing the base-catalysis time has an effect similar to that of increasing acid content; hence, for longer base-catalysis periods, less acid is needed to accelerate gelation.

FIGURE 5. Dynamic viscosity of RF solutions (50 mg/cm³ theoretical foam density, $F/R = 2$) during cure at 70°C as a function of R/C and the amount of benzoic acid added. (70-00-0197-0153pb01)
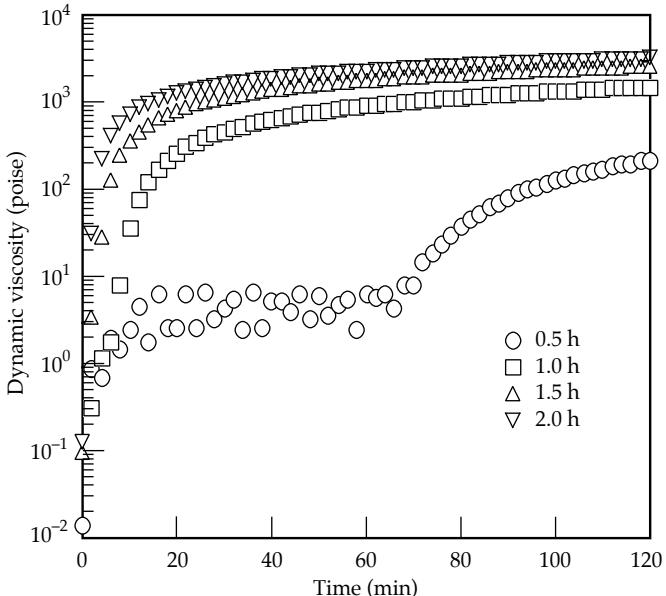
FIGURE 6. Dynamic viscosity of RF solutions (50 mg/cm³ theoretical foam density, $F/R = 2$, $R/C = 200$, 0.036 g benzoic acid added) during cure at 70°C as a function of base-catalysis time. (70-00-0197-0154pb01)

Swelling of RF Gels in Isopropanol

To produce dry foams, one must replace the water solvating the gel with isopropanol (IPA) before subsequently replacing IPA with liquid CO_2, which is then supercritically vented. IPA was chosen as the intermediate solvent because it is miscible with both water and liquid CO_2. When gels were cured (reacted) for 2 h and then exchanged into IPA, we observed macroscopic swelling (which is detrimental to useful shell formation) that suggested the material was not sufficiently cross-linked. Because of the colloidal nature of the gel structure, there are two types of cross-links: intraparticle cross-links (within the nanometer-sized particles making up the gel matrix) and interparticle cross-links. Swelling most likely emanates from the former because swelling is indicative of a molecular-level interaction between the polymer and solvent. The most obvious way to increase intraparticle cross-linking is simply to increase the curing time.

Consequently, the degree of swelling of bulk RF gels in IPA was measured as a function of cure time. We also investigated the influence of R/C and F/R on swelling. The results are presented in Figure 7 in terms of the degree of swelling:
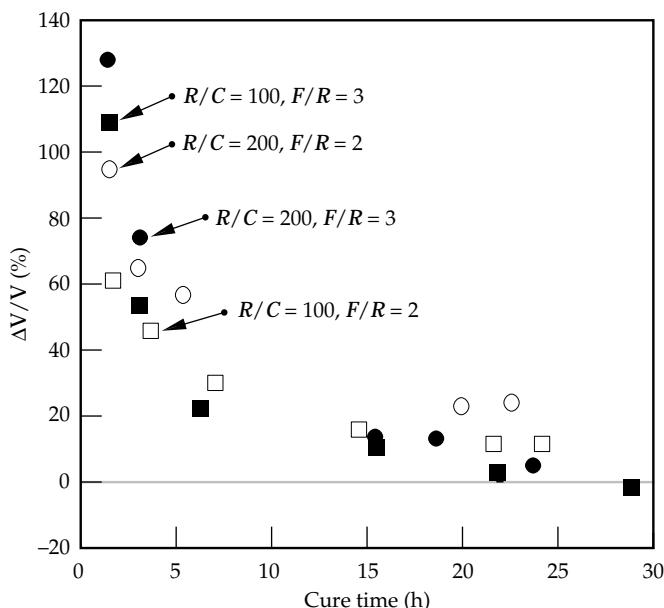
$$\frac{\Delta V}{V} \equiv \frac{V_{\text{IPA}} - V_{\text{W}}}{V_{\text{W}}} \quad , \qquad (1)$$

where V_{W} and V_{IPA} are the volumes of the gel piece before (V_{W}) and after (V_{IPA}) exchanging into IPA. The most important observation was that significant changes in gel dimensions after exchanging into IPA can only be avoided by curing the gel for at least 20 h, rather than the 2 h suggested by the dynamic viscosity measurements. R/C and F/R also influence swelling to a lesser extent. For a given F/R, gels prepared with $R/C = 100$ swell less than gels with $R/C = 200$. Lowering R/C results in the growth of smaller particles, which are probably more cross-linked. For a given R/C and long curing times, swelling can be reduced further by increasing F/R from 2 to 3, which also promotes intraparticle cross-linking.

In summary, this study of RF chemistry, viscometry, and swelling provided important information needed to successfully encapsulate the RF material to form shells. By spiking the RF solutions with an appropriate amount of acid following the base-catalyzed particle-growth stage, the gelation times can be reduced from many hours to less than 20 min. However, although the macroscopic interparticle gel structure gels in minutes, additional annealing of the gel is needed for as long as 20 h to maximize intraparticle cross-linking and thus minimize swelling in the IPA exchange solvent.

Encapsulation Method, Solvents, and Curing

Encapsulation of RF solutions to form a spherical shell is accomplished by using a triple-orifice droplet generator. The generator and compound RF droplets (called preforms) are shown schematically in Figure 8. A preform consists of an interior-oil-phase droplet surrounded by the ungelled aqueous RF solution. This compound drop is formed from two concentric orifices that are inserted into a tube (the third orifice) through which flows a second, exterior-oil phase. The droplets are stripped off the inner orifices by the axial flow of the exterior-oil phase. The delivery tube (~10 cm in length) is made of Teflon® to provide a hydrophobic surface that is wetted only by the exterior-oil phase and not by the aqueous RF solution droplets. The diameter of the compound droplet is roughly determined by the diameter of the delivery tube. More precise adjustment of the diameter is achieved by adjusting the exterior-oil-phase flow rate. The shell's wall thickness is determined by the ratio of the interior-oil-phase flow rate to the RF solution flow rate.

The preformed shells flow down the delivery tube into a gently stirred, heated beaker containing approximately 150 mL of the exterior-oil phase. Agglomeration and coalescence of the preforms are reduced by adding surfactant to the exterior-oil phase. Each batch created

FIGURE 7. Degree of swelling of bulk RF gels (50 mg/cm³ theoretical foam density) in isopropanol as a function of cure time at 70°C for several combinations of F/R and R/C. (70-00-0197-0156pb01)

Interior-oil
phase

Ungelled RF
solution

Exterior-oil
phase

Exterior-oil
phase
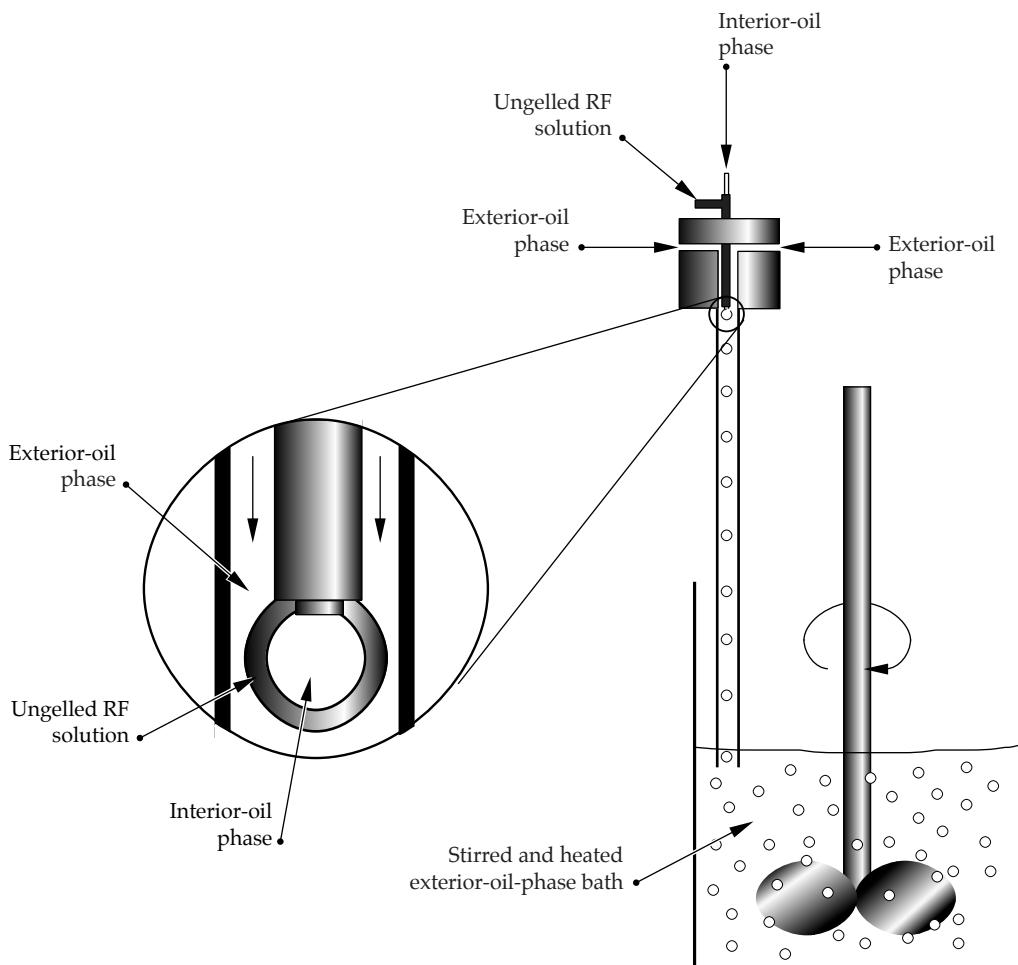
FIGURE 8. Schematic diagram
of the triple-orifice droplet gen-
erator.   (70-00-0197-0157pb01)

Exterior-oil
phase

Ungelled RF
solution

Interior-oil
phase

Stirred and heated
exterior-oil-phase bath

by the droplet generator has approximately 200 to 300 shells, of which one-third to two-thirds survive the curing step.

The choice of appropriate interior- and exterior-oil phases was not immediately obvious. The only initial requirements were that they be immiscible with water and that the interior phase be closely matched in density to the aqueous RF phase to minimize wall-thickness nonuniformity due to buoyancy effects. Dibutyl phthalate was chosen initially for the exterior-oil phase because it was used for the preparation of methacrylate foam shells.[12,13] For reasons of density matching, 1-methyl naphthalene was chosen as the interior-oil phase. The density of the exterior-oil phase is also important, but for a different reason: to help keep the compound drops suspended (but not at the surface) without applying vigorous agitation, the density of the exterior-oil phase should be only slightly less than that of the compound drops.

In retrospect, dibutyl phthalate was a poor choice for the exterior-oil phase. Initial results[14] showed that shell walls thinned during cure because of a loss of water from the aqueous phase. This dehydration

resulted in shells with foam densities that were two to three times greater than the theoretical foam density. Although dibutyl phthalate is immiscible with water, we found that it, in fact, had enough capacity to dissolve much of the water present in the preformed shells. The solubility of water in dibutyl phthalate at 25°C is 0.46 wt%.[22] The dibutyl phthalate (as received) was determined to already contain 0.12 wt% water. Hence, 150 mL of dibutyl phthalate (a typical bath volume) has the capacity to absorb approximately 0.5 g water, which is about half the water present in 100 compound drops. This situation is exacerbated at the higher temperatures needed to cure the RF gel. Attempts to saturate the exterior-oil phase with water before attempting encapsulation failed because doing so severely reduced the effectiveness of the surfactant and resulted in shell agglomeration.

Using a model for convectively enhanced mass-transfer from an isolated aqueous shell suspended in an agitated nonaqueous solvent, we examined factors that control the transport of water from the shell into the exterior-oil phase. We found that the rate of water lost from the shell can be written as[23]

$$\frac{df}{dt} \propto \frac{k_{s}T^{2/3}\omega^{1/2}}{\delta\mu^{5/6}} \qquad (2)$$

where f is the fraction of water removed from the shell, t is time, k_{s} is related to the solubility of water in the oil phase, T is temperature, ω is related to the degree of solution agitation, δ is the shell-wall thickness, and μ is the viscosity of the exterior-oil phase.

Equation (2) points out the desirable properties and processing conditions that help reduce shell dehydration:

- As expected, the rate of water transport out of the shell is directly proportional to the solubility of water in the organic-oil phase.
- Equation (2) suggests we should cure at lower temperatures with reduced agitation.
- Oil phases with higher viscosity will retard water transport out of the shell.

This analysis led us to consider using a grade of mineral oil commonly known as Nujol oil. This fluid has a very low water solubility (0.0038 wt% at 25°C), which is more than two orders of magnitude smaller than that of dibutyl phthalate. It also has a higher viscosity. A major drawback, however, is that its density (0.85 g/cm^3 at 25°C) is too low to keep the shell preforms adequately suspended. This problem can be circumvented by sacrificing some of the higher viscosity of the mineral oil by mixing it with approximately 40 wt% carbon tetrachloride, which has a high density and a comparatively low water solubility (1.59 g/cm^3 and 0.011 wt% at 25°C). We found that shells cured in this oil-phase mixture at 70°C for 1.5 h to 2 h would form stiff-gelled preforms that were significantly less dehydrated than shells cured under the same conditions in dibutyl phthalate. However, although 1.5 h to 2 h is enough time to stabilize and stiffen the shell preforms, we found that water evaporation from the heated system became the dominant mechanism for additional water loss over the remaining 20–22 h of cure needed to maximize intraparticle cross-linking.

To avoid this dehydration of the shells over longer times, the gelled shells were annealed in the configuration shown schematically in Figure 9. After the initial 1.5 h to 2 h of curing, the preforms had hardened enough that agitation was no longer required. Additional carbon tetrachloride was added until the shells floated near the surface. Water was then placed on top of the denser oil phase, saturating it and preventing further dehydration. The beaker was covered and placed in a 70°C constant temperature bath for an additional 20–22 h to finish the cure.
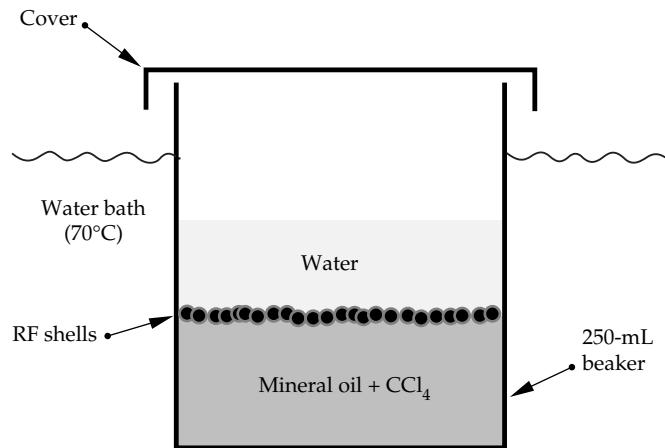
FIGURE 9. Configuration for annealing-gelled RF shells for long periods. (70-00-0197-0158pb01)

Solvent Exchange, Drying, and Characterization

During this final annealing period, the shells eventually sank to the bottom of the beaker because the dense carbon tetrachloride from the exterior-oil phase preferentially permeated the aqueous layer to replace the 1-methyl naphthalene interior-oil phase. This helped separate shells from residual RF debris (broken and collapsed shells), which tends to remain at the oil–water interface; this separation allowed decanting of the water, RF debris, and most of the oil phase, leaving the shells behind. Surviving shells were soaked in IPA to dissolve excess exterior-oil phase, to replace the water solvating the gel, and to replace the interior-oil phase. After numerous exchanges with fresh IPA, the shells were ready to be dried by means of the supercritical drying technique.

The consistency of shell dimensions and wall thickness within a batch is illustrated in Figure 10. The droplet generator has the capacity to make shells that, in IPA, have diameters ranging from 1.6 mm through 2.3 mm and wall thicknesses ranging from 100 μm through 200 μms. The deviations of diameters and wall thicknesses within a batch of shells is typically ±0.03 mm and ±10 μm, respectively.

The measured foam densities of shells were found to be slightly greater than those of bulk RF aerogel samples prepared with the same formulation (shown in Table 1). This is a likely indication that some unavoidable dehydration of the shells by the oil-phase solvents was still occurring. Further, shells and bulk samples prepared with $R/C = 100$ had higher densities
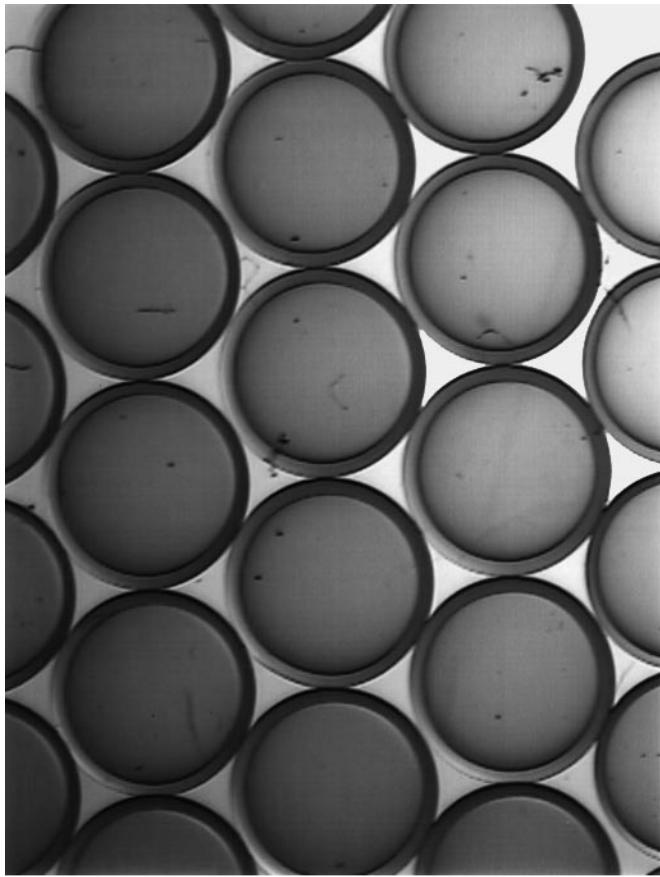
FIGURE 10. A typical batch of RF shells after exchange into iso-propanol; for this batch, the average diameter was 2.3 mm, and the average wall thickness was 145 μm. (70-00-0197-0159pb01)

TABLE 1. Measured dry-foam densities of RF shells and bulk RF aerogel as a function of R/C and F/R (the theoretical density of all samples is 50 mg/cm^3).

Sample Description	Measured Density (mg/cm^3)
$R/C = 100$, $F/R = 2$	
Bulk	73
Shells	80
$R/C = 100$, $F/R = 3$	
Bulk	55
Shells	65
$R/C = 200$, $F/R = 2$	
Bulk	47
Shells	64
$R/C = 200$, $F/R = 3$	
Bulk	48
Shells	60

than did samples prepared with $R/C = 200$. This observation is consistent with an earlier finding[7] that $R/C = 100$ gels shrink more upon drying than $R/C = 200$ gels. Lastly, when F/R was increased from 2 to 3, the gels swelled less in IPA. Therefore, with respect to final foam density and reduced dimensional changes during processing, RF formulations with $F/R = 3$ and $R/C = 200$ are optimal.

Dry foam shells were also examined by optical and scanning electron microscopy (SEM). Figure 11 is a photo of a dry shell placed on top of a millimeter scale. This photo clearly demonstrates the optical transparency of the aerogel and provides a visual indication of the uniformity and sphericity of the wall that can be achieved. SEM analyses of a fractured shell wall indicate that the density of the foam is uniform throughout and that the foam shows the same submicrometer cell structure as RF aerogel prepared by conventional means.
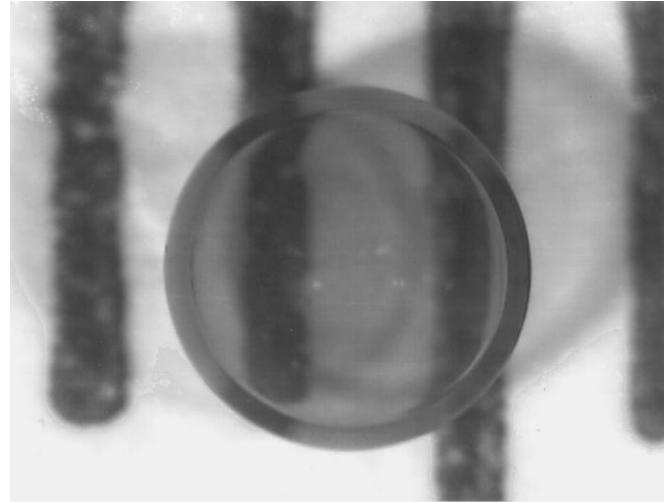
FIGURE 11. Photograph of a dry RF foam shell; diameter is 1.90 mm, wall thickness is 120 μm, and density of the shell is 63 mg/cm^3. (70-00-0197-0160pb01)

Summary

We have successfully developed a process to fabricate hollow spherical shells from low-density RF aerogel. The most notable accomplishments of this work are reduction in gelation time and decreased shell dehydration. The time required to set the macroscopic interparticle gel structure was reduced from several

hours to several minutes by adding acid following the base-catalyzed particle-growth stage. However, additional annealing of the gel for at least 20 h is needed to maximize intraparticle cross-linking and to minimize swelling in exchange solvents. Increasing the molar ratio of formaldehyde to resorcinol from 2 to 3 also helps reduce swelling and reduce the shrinkage of the gel upon supercritical-CO_2 drying. Dehydration of the shells during cure was drastically reduced by prudent selection of immiscible oil phases and by saturating the exterior-oil phase with water during the annealing process. The resulting foam shells have densities that approach their theoretical value and the measured density of bulk aerogel of the same formulation.

When considering the use of these shells as potential fuel containers for ICF experiments, two important issues remain:

- The factors that control shell wall-thickness uniformity must be explored. The only control employed here was density matching, which essentially limited the position of the interior-oil droplet to a random walk within the aqueous RF droplet. We are not cognizant of any naturally occurring centering forces, and artificial ones[24] appear difficult to implement.

- ICF target specifications require that the outside of the shells be coated with a transparent, smooth, full-density polymer layer 5–200 μm thick. We have explored two methods for overcoating shells. The first is deposition of the layer from the vapor phase onto a dry shell using plasma-polymerization techniques;[25–27] in a limited number of experiments, we found that this method produced an unacceptably rough surface. The second method is the use of an interfacial polycondensation technique in the liquid phase (prior to drying); this is similar to that developed by Takagi et al.[10] for methacrylate foam shells. Work in this area has shown some positive results, but additional work is still necessary to meet the surface specifications for the National Ignition Facility.

Acknowledgments

Notes and References

1. S. W. Haan, et al., *Phys. Plasmas*, **2**, 2480 (1995).
2. S. Lindl, *Phys. Plasmas*, **2**, 3933 (1995).
3. R. A. Sacks and D.H. Darling, *Nucl. Fusion*, **27**, 447 (1987).
4. C. J. Keane, et al., *Rev. Sci. Inst.*, **66**, 689 (1995).
5. C. J. Keane, et al., *J. Quant. Spectrosc. Radiat. Transfer*, **54**, 207 (1995).
6. G. Collins, LLNL Lasers, Livermore, CA, private communication (1995).
7. R. W. Pekala, C. T. Alviso, and J. D. LeMay, "Organic Aeorgels: A New Type of Ultrastructured Polymer," in *Chemical Processing of Advanced Materials*, L. L. Hench and J. K. West, eds., (John Wiley & Sons, NY, 1992), pp. 671–683.
8. C. Chen, T. Norimatsu, M. Takagi, H. Katayama, T. Yamanaka, and S. Nakai, *J. Vac. Sci. Technol. A*, **9**, 340 (1991).
9. M. Takagi, T. Norimatsu, T. Yamanaka, S. Nakai, and H. Ito, *J. Vac. Sci. Technol. A*, **9**, 820 (1991).
10. M. Takagi, M. Ishihara, T. Norimatsu, T. Yamanaka, Y. Izawa, and S. Nakai, *J. Vac. Sci. Technol. A*, **11**, 2837 (1993).
11. T. Norimatsu, C. M. Chen, K. Nakajima, M. Takagi, Y. Izawa, T. Yamanaka, and S. Nakai, *J. Vac. Sci. Technol. A*, **12**, 1293 (1994).
12. M. Takagi, T. Norimatsu, Y. Izawa, and S. Nakai, *MRS Symp. Proc.*, **372**, 199 (1995).
13. D. Schroen-Carey, G. E. Overturf, III, R. Reibold, S. R. Buckley, S. A. Letts, and R. Cook, *J. Vac. Sci. Technol. A*, **13**, 2568 (1995).
14. G. E. Overturf, III, R. Cook, S. A. Letts, S. R. Buckley, M. R. McClellan, and D. Schroen-Carey, *Fusion Tech.*, **28**, 1803 (1995).
15. R. B. Stephens, *Fusion Tech.*, **28**, 1809 (1995).
16. R. W. Pekala, *J. Mat. Sci.*, **24**, 3221 (1989).
17. R. W. Pekala, C. T. Alviso, F. M. Kong, and S. S. Hulsey, *J. Non-Cryst. Solids*, **145**, 90 (1992).
18. S. A. Letts, S. R. Buckley, F. M. Kong, E. F Lindsey, and M. L. Sattler, *Mat. Res. Soc. Symp.*, **177**, 275 (1990).
19. R. W. Pekala, F. M. Kong, *Rev. Phys. Appl. Sup.*, **4**, 24 (1989).
20. P. M. Cotts, R. W. Pekala, *Polym. Preprints*, **32**, 451 (1991).
21. P. M. Cotts, "Static and Dynamic Light Scattering from Solutions and Gels of RF Particles," in *Synthesis, Characterization, and Theory of Polymeric Networks and Gels*, S. M. Aharoni, ed., (Plenum Press, NY, 1992), pp. 41–51.
22. J. A. Riddick, W. B. Bunger, and T. K. Sakano, *Organic Solvents: Physical Properties and Methods of Purification*, (John Wiley & Sons, NY, 1986), p. 442.
23. S. M. Lambert, G. E. Overturf, III, G. Wilemski, S. A. Letts, D. Schroen-Carey, and R. Cook, *J. Appl. Poly. Sci.* **65**, 2111 (1997).
24. C. P. Lee and T. G. Wang, *J. Fluid Mech.*, **188**, 411 (1988).
25. G. W. Collins, S. A. Letts, E. M. Fearon, R. L. McEachern, and T. P. Bernat, *Phys. Rev. Lett.*, **73**, 708 (1994).
26. S. A. Letts, D. E. Miller, R. A. Corley, T. M. Tillotson, and L. A. Witt, *J. Vac. Sci. Technol. A*, **3**, 1277 (1985).
27. S. A. Letts, D. W. Myers, and L. A. Witt, *J. Vac. Sci. Technol. A*, **19**, 739 (1981).

Tetrahedral Hohlraums

S. M. Pollaine

J. D. Schnittman*

Introduction

Inertial confinement fusion (ICF) has two main approaches: indirect drive[1] and direct drive.[2] In direct drive, a laser directly irradiates the capsule; in indirect drive, the laser is directed into a hohlraum containing the capsule, generating secondary x rays that irradiate the capsule. Either way, the outer layers of the irradiated capsule are ablated, causing high pressures that compress the deuterium–tritium (DT) fuel, and raising the density and temperature to the point at which a runaway nuclear fusion reaction occurs. In both cases, it is imperative that the shell remain spherical up to the point of ignition, and this requirement, in turn, demands a very uniform flux on the shell. The capsule must be compressed by a factor of 30 to 40 (Ref. 3), so that drive asymmetry can be no more than about 1%. In indirect drive, flux uniformity is achieved by transport of x rays from the hohlraum wall to the capsule.

Drive asymmetry can be expanded as

$$f(\theta,\phi) = \sum_{l,m} a_{lm} Y_{lm}(\theta,\phi) \quad , \qquad \text{1(a)}$$

where $Y_{lm}(\theta,\phi)$ are the spherical harmonics,

$$\iint Y_{lm}(\theta,\phi) Y_{l'm'}(\theta,\phi) \sin(\theta) \ d\theta \ d\phi = \delta_{ll'} \ \delta_{mm'} \quad , \qquad \text{1(b)}$$

l ranges from zero to infinity, and m ranges from $-l$ to $+l$. If the asymmetry is azimuthally symmetric, then $a_{lm} = 0$ for $m \neq 0$, and it becomes convenient to expand the asymmetry in Legendre polynomials:

$$f(\theta,\phi) = \sum_{l} a_{l} P_{l}(\cos \ \theta) \quad , \qquad (2a)$$

where

$$\int_{-1}^{1} P_{m}(x) \ P_{n}(x) \ dx = \frac{\delta_{mn}}{n + 1/2} \quad . \qquad (2b)$$

In the usual indirect-drive geometry, the hohlraum has the shape of a cylinder with laser entrance holes (LEHs) at the ends of the cylinder, and the laser beams are arranged in rings on the hohlraum wall. In Nova, ten beams illuminate the hohlraum wall in two rings of five beams each, one ring on each side of the hohlraum. In the National Ignition Facility (NIF), 48 clusters of four beamlets each will illuminate the hohlraum wall in two rings per side: an inner ring on the waist plane at 90°, and an outer ring at about 50° from the hohlraum axis, as shown in Figure 1. Because of azimuthal symmetry and left/right symmetry, the capsule flux asymmetry consists of the even Legendre polynomials. As the hohlraum walls move inward, the location of the rings on the walls changes. The second Legendre polynomial P_2 of the capsule flux asymmetry can be eliminated in a time-varying way by varying the relative power between the inner and outer rings. The fourth moment P_4 can be averaged to zero by choosing a suitable hohlraum length. Higher moments are small because of the smoothing effect of x-ray transport between the walls and the capsule.[4]

Tetrahedral Hohlraums

Tetrahedral hohlraums are a new form of indirect drive.[5,6] The hohlraum is spherical instead of cylindrical. Instead of two LEHs, four LEHs are arranged in a tetrahedral configuration, leading to greater radiation losses but some symmetry advantages, as explained below. Instead of distinct rings on the hohlraum wall, the beams are scattered. In all formulations considered to date, an identical pattern of beams goes through

*   University of Rochester's Laboratory for Laser Energetics, Rochester, New York.

Capsule

Outer ring
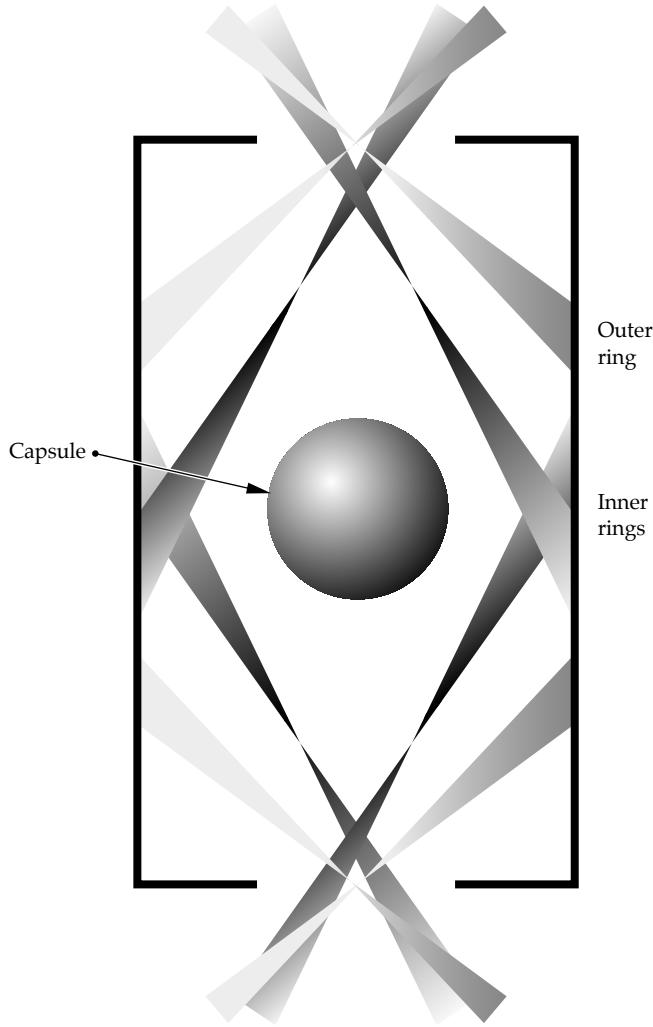
Inner rings

FIGURE 1. NIF cylindrical hohlraum, showing the inner rings on the hohlraum symmetry plane and the outer rings towards the laser entrance holes. The relative power in the inner and outer beams is varied to maintain good symmetry.   (50-04-0197-0162pb01)

FIGURE 2. Typical tetrahedral hohlraum with four holes and 12 beams. The rear hole with its beams is hidden from view. (50-04-0197-0163pb01)

each of the four holes. Figure 2 shows a tetrahedral hohlraum with some of its beams.

If the beams are arranged properly, exact tetrahedral symmetry can be maintained.[5] Each beam through an LEH is characterized by its opening angle θ, and its azimuthal angle ϕ. The opening angle θ is the angle that the beam makes with the normal to the LEH. The azimuthal angle ϕ is the angle about the normal, where $\phi = 0$ is along the great circle connecting one LEH with another LEH (which one is arbitrary). Tetrahedral symmetry is maintained if the beams come in sets of 12, with three beams per LEH, each at the same opening angle θ and at the azimuthal angles ϕ, $\phi + 120°$ and $\phi + 240°$. Thus, there are two free parameters, θ and ϕ, for each set of 12 beams, which may be varied without breaking tetrahedral symmetry.

With tetrahedral symmetry, the flux asymmetry hitting the capsule cannot have any spherical harmonic components with mode numbers $l = 1$, 2, or 5 at any time. This is true even when the effects of spot motion, refraction of the beams, or absorption of laser light along the beam path are included because all such effects will occur in a tetrahedrally symmetric way. In addition, only one component of $l = 3$ and one component of $l = 4$ can exist. The LEHs contribute the $l = 3$ and $l = 4$ components in a fixed ratio, independent of hohlraum wall albedo. Thus, one set of 12 beams with the correct ratio of $l = 3$ to $l = 4$ can eliminate these components from the flux asymmetry. As the albedo of the hohlraum wall increases, the relative contribution (or lack of flux) from the LEHs requires increasing power in these 12 beams to eliminate the $l = 3$ and $l = 4$ components. With two sets of 12 beams—one set containing no $l = 3$ or $l = 4$ components and the other containing the $l = 3$ and $l = 4$ components in the correct ratio—we can vary the relative power in the two sets of beams to compensate for the LEH at all times, leaving $l = 6$ as the first nonvanishing moment in addition to $l = 0$. This point is discussed in detail in Reference 5.

The beam angles on the NIF have been chosen to maximize the flexibility of the cylindrical hohlraum design and to accommodate direct drive. Thus, the beam angles are not situated properly for tetrahedral symmetry. Each of the four holes has an identical configuration of beams passing through them. However, the beams through any given hole do not come in sets of the triplets ϕ, $\phi + 120°$, and $\phi + 240°$. This weaker symmetry on NIF results in the spherical harmonic modes $l = 2$ and 5, as well as extra components of $l = 4$. The extra modes require that we vary the power independently in each

beam going through a given hole, with the corresponding beams through other holes having the same power.

On Omega—the 30-kJ laser at the Laboratory for Laser Energetics (LLE) at the University of Rochester—the beams are arranged in a stretched soccer-ball pattern. This arrangement allows for a hohlraum with exact tetrahedral symmetry.

Constraints

Three constraints govern which beams can go through a given hole. If the opening angle θ is too small, the beams will hit the capsule. If θ is too large, the beams will enter the hohlraum at a very shallow angle and travel near the hohlraum wall, where blowoff from the wall will absorb the beam energy via inverse bremsstrahlung. In addition, beams with large θ will have less clearance through the hole. These two constraints limit θ from about 20° to about 60°.

The third constraint is that the beams not come too close to another hole. If part of a beam exits the hohlraum through another hole, its energy will be lost to the hohlraum. On the Omega laser, the beam could enter a beam port on the opposite side of the chamber, damaging the laser. Moreover, if a beam comes too close to another hole, material around that hole will heat and expand into the path of the beams entering that hole, causing those beams to lose energy and refract.

The NIF has 72 beam ports arranged in ten lines of latitude. The standard indirect-drive cylindrical hohlraums will use the 48 ports located on latitudes 23.5°, 30°, 44.5°, 50°, 130°, 135.5°, 150°, and 156.5°. Direct-drive targets will use the 48 ports located on latitudes 23.5°, 44.5°, 77.5°, 102.5°, 135.5°, and 156.5°. Because of the three constraints, tetrahedral hohlraums will use only 44 of the available 48 beams. These beams will come from a set of ports located on all latitudes
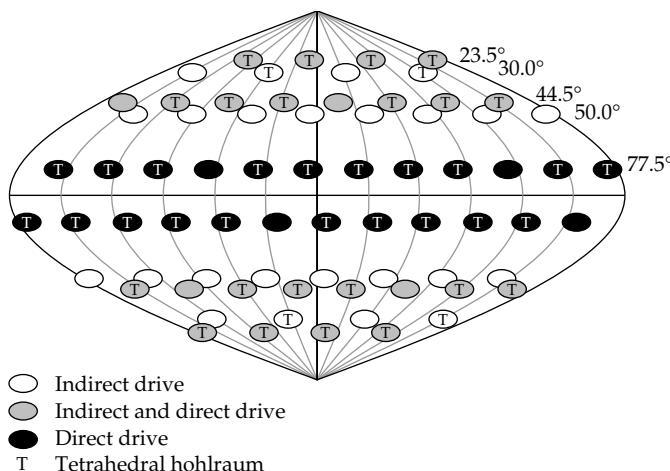
except those at 50° and 130°. Figure 3 shows which of the 72 ports are used for the three ICF applications.

The Omega laser has 60 beams arranged in a stretched soccer-ball pattern. The symmetry of Omega allows full tetrahedral symmetry with all 60 beams. Of these beams, 24 have an opening angle of 23.2°, 24 have an opening angle of 47.8°, and 12 have an opening angle of 58.8°. In the absence of refraction, the beam centers land anywhere from 32° to 46° away from the closest LEH.

Symmetry

Radiation flux on the capsule consists of three components: one from the hohlraum wall, which is completely symmetrical; a second from the LEHs, which is negative and has tetrahedral symmetry; and a third from laser hot spots. The relative contribution of these three sources depends on the wall albedo α and can be computed by considering the power balance inside the hohlraum. The x-ray power generated by the laser must equal radiation losses into the capsule, losses into the hohlraum wall, and losses out the laser entrance holes.[7] The fraction of total power received by the capsule from the wall, LEHs, and laser hot spots is $\alpha(1-f_c)$, $-\alpha(1-f_c)f_h$, and $1-\alpha(1-fc)(1-f_h)$, respectively, where f_c is the area of the capsule divided by the area of the wall, and f_h is the total area of the LEHs divided by the area of the wall.

The next step is to expand the flux asymmetry of each of the three components in terms of spherical harmonics, and, for each mode, to add the contribution from the components weighted by the fraction of total power received by the capsule, as listed in the previous paragraph. Because flux from the wall is uniform, it contributes only to the $Y_{0,0}$ mode. The modal contribution of the four holes is the sum of $Y_{lm}(\theta,\phi)$ evaluated at each hole times a reduction factor R based on the mode number l and the angular radius β of the hole:

Indirect drive
Indirect and direct drive
Direct drive
T Tetrahedral hohlraum

FIGURE 3. Beam ports on the NIF. Cylindrical indirect drive uses the ports shown in dark blue and light blue; direct drive uses the ports shown as light blue and green; tetrahedral hohlraums use the ports identified with a "T." (50-04-0197-0164pb01)

$$R_l(\beta) = \frac{P_{l-1}(\cos \beta) - P_{l+1}(\cos \beta)}{(2l+1)(1-\cos \beta)} \quad . \qquad (3)$$

The modal contribution of the laser hot spots to each spherical harmonic mode Y_{lm} is the sum of $Y_{lm}(\theta,\phi)$ evaluated at each hot spot and weighted by the power of that hot spot. If the hot spots are large, then each mode is reduced by the same reduction factor $R_l(\beta)$.

The last step in computing capsule flux asymmetry is to compute for each mode the effect of x-ray transport from the hohlraum wall to the ablating capsule surface. Because the hohlraum and capsule are spherical, the spherical harmonics are the normal modes, so that flux asymmetry at the capsule is equal to the flux asymmetry at the wall times a smoothing factor $T_l(r)$ that depends only on the mode number l and the ratio r of the capsule ablation radius to the wall radius:[4]

$$T_l(r) = 2 \int_r^1 \frac{(x-r)(1-rx)}{\left(1-2rx+r^2\right)^2} \; P_l(x) \; dx \quad . \tag{4}$$

Thus, the spherical harmonic decomposition of the capsule flux asymmetry is readily calculated. When this is done, we find that the capsule flux asymmetry is dominated by the mode $Y_{3,2}$.

This procedure for calculating the capsule flux asymmetry assumes that we know the location of laser hot spots on the hohlraum wall. The location of hot spots in the absence of refraction is readily calculated from geometry; however, calculating the effects of refraction, absorption, and spot motion requires a detailed model of the plasma conditions inside the hohlraum. We have used plasma density profiles obtained from hydrodynamic simulations to estimate the effects of refraction on the location of laser hot spots.

It is interesting to compare the flux asymmetry of tetrahedral hohlraums with that of cylindrical hohlraums. Because cylindrical hohlraums break the spherical symmetry, cross coupling arises between the modes, and a view factor code is needed to calculate how the various modes at the hohlraum wall couple to the modes of the capsule flux asymmetry. Schnittman wrote such a code, BUTTERCUP, that can calculate capsule symmetry in both tetrahedral and cylindrical hohlraums.[6] Figure 4 is a comparison between the two when applied to the NIF. For various times, the effects of wall motion, capsule implosion, and changing albedo were included in symmetry calculations. For each time, the relative power in the various beams was varied to minimize asymmetry on the capsule. For cylindrical hohlraums, this amounted to adjusting the relative power between the inner and outer rings of beams to zero out the second Legendre moment P_2. For tetrahedral hohlraums, the power in 11 independent sets of four beams each was varied to minimize the rms flux asymmetry at the capsule while keeping the total power fixed to maintain drive temperature. Then, for both cylindrical and tetrahedral hohlraums, each beam was moved an rms average of 50 μm to simulate beam-pointing errors, and the power in each beam was varied by an average of 5% rms to simulate power imbalance. Figure 4 shows that the tetrahedral hohlraum was less sensitive to pointing and power-balance errors than the cylindrical hohlraum.

Figure 5 shows a similar analysis for Omega, where albedo is explicitly varied. Note that the cylindrical hohlraum is more sensitive to changes in albedo than was the tetrahedral hohlraum. Cylindrical hohlraums need beam phasing (defined as changing the relative power between the beams as a function of time) to reduce time-dependent swings in flux asymmetry. Tetrahedral hohlraums may get by without beam phasing.
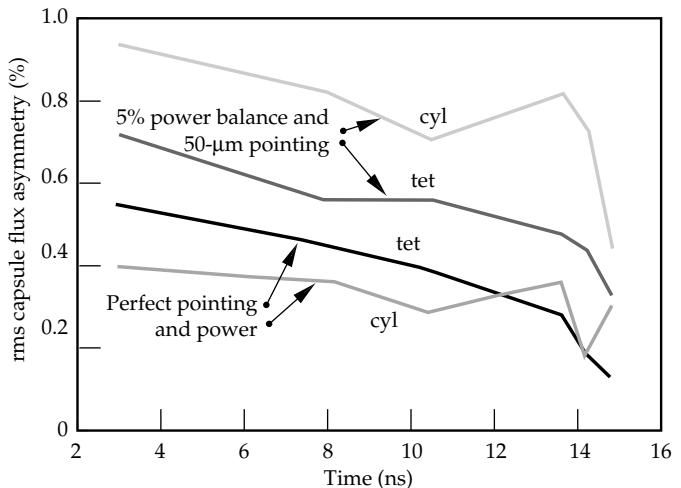
FIGURE 4. Comparison of cylindrical and tetrahedral hohlraums on the NIF. The rms capsule flux asymmetry versus time is shown for perfect beams and for 50-μm pointing errors and 5% power imbalance.   (50-04-0397-0422pb01)
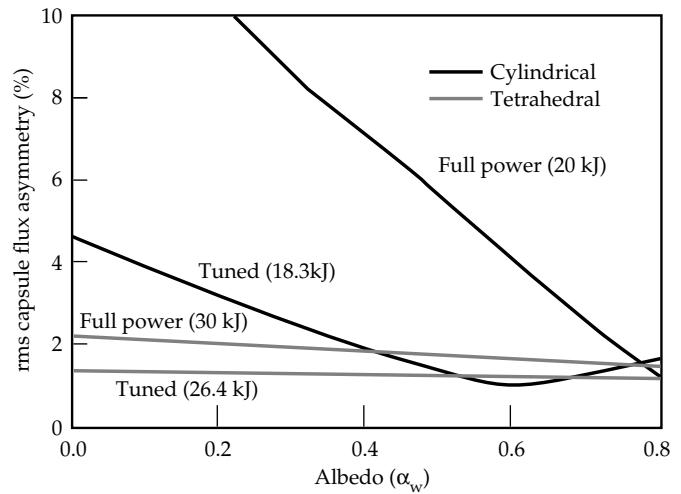
FIGURE 5. Comparison of cylindrical and tetrahedral hohlraums on Omega. The rms capsule flux asymmetry is shown versus wall albedo. Curves marked "full power" have equal beam energies, and curves marked "tuned" are optimized at an albedo of 0.8.
(50-04-0397-0423pb01)

Experiments

In March 1997, researchers from Los Alamos National Laboratory, Lawrence Livermore National Laboratory, and LLE Rochester will have conducted the first experiments using tetrahedral hohlraums on the Omega laser. This first set of experiments will use thin-walled hohlraums to determine where the beams land, providing information on refraction and absorption inside the hohlraum. Radiation flux asymmetry, expected to be mainly in the spherical harmonic mode $Y_{3,2}$, will be measured using symcaps[8] and reemission

balls.[9] The initial set of experiments is expected to prove that tetrahedral hohlraums will work and deliver good symmetry. The next set of experiments in August 1997 will diagnose asymmetry using foam balls.[10] Ultimately, Omega experiments will pave the way for possible tetrahedral ignition experiments on the NIF in the year 2003 and after.

Conclusion

Tetrahedral hohlraums represent a third ICF alternative to cylindrical hohlraums and direct drive. They have the potential to provide better flux symmetry on the capsule than that provided by cylindrical hohlraums in the presence of pointing errors, power imbalance, and changes in albedo. Spherical symmetry allows analytic modeling that is not possible for cylindrical hohlraums. The first experiments to test the proof of principle will have been completed in March 1997.

Acknowledgments

Don Phillion was the first to recognize and quantify the symmetry advantages of tetrahedral hohlraums.[5] Much of the design work was done by Jeremy Schnittman,[6] a summer student at LLNL and LLE, currently a sophomore at Harvard University. We have had many helpful discussions with S. Haan, S. Weber, and M. Tabak at LLNL, and with S. Craxton and T. Boehly at LLE.

Notes and References

1. J. D. Lindl, *Phys. Plasmas* **2**, 3933–4024 (1995).
2. C. Verdon, *Bull. Am. Phys. Soc.* **38**, 2010 (1993).
3. J. D. Lindl, op. cit., p. 3934.
4. S. W. Haan, *Radiation Transport Between Concentric Spheres,* Lawrence Livermore National Laboratory, Livermore, CA, UCRL-ID-118152 (1994); D. Kershaw, private communication.
5. D. W. Phillion and S. M. Pollaine, *Phys. Plasmas* **1**, 2963–2975 (1994).
6. J. D. Schnittman and R. S. Craxton, *Phys. Plasmas* **3**(10), 1–12 (1996).
7. L. J. Suter, *Laser Program Annual Report 1988*, Lawrence Livermore National Laboratory, Livermore, CA, X-Div-90-0054, 21–32 (1988).
8. A. Hauer et al., *Phys. Plasmas* **2**, 2488 (1995); A. Hauer et al., *Rev. Sci. Inst.* **66**, 672 (1995); N. Delamater et al., *Phys. Plasmas* **3**, 2022 (1996).
9. N. Delamater et al., *Phys. Rev. E* **53**, 5240–5248 (1996); G. R. Magelssen et al., *Phys. Rev. E* (in press).
10. P. Amendt et al., *Phys. Rev. Lett.* **77**, 3815–3818 (1996).

The Rosseland Mean Opacity of a Composite Material at High Temperatures

T. J. Orzechowski   H. N. Kornblum   R. J. Wallace

M. D. Rosen   L. J. Suter   L. J. Porter*

A. R. Thiessen

Introduction

The indirect-drive approach[1] to inertial confinement fusion (ICF)[2] relies on thermal x-ray radiation to drive the implosion of the fuel capsule. This radiation is generated by the interaction of intense beams—either lasers[3] or particles[4]—with the interior wall of a high-Z cavity or hohlraum. The radiation is usually described by a blackbody spectrum with a temperature of about 250 eV. This high-temperature radiation not only drives the fuel pellet compression, but it also heats and ablates the hohlraum wall. In this article, we describe a method for making the hohlraum wall more opaque to the drive radiation. This leads to lower losses and more energy available to implode the fuel.

The interaction of the radiation with the hohlraum wall is characterized by multiple absorption and reemission of the x rays.[5–7] The ratio of the reemitted flux to the incident flux is referred to as the albedo, α. The efficiency with which the radiation couples to the capsule depends on the albedo; increasing the albedo improves the drive efficiency. The incident flux is the sum of the reemitted flux plus the x-ray flux lost to the wall. The flux lost to the wall propagates through the wall in the form of a diffusive ablative heat wave.[8] Figure 1 shows how radiation propagates through the high-Z wall material. The details of this radiation flow will be discussed in the next section. The rate of diffusion is (approximately) inversely proportional to the square root of the Rosseland mean opacity,[9] which is used to describe radiation transport in optically thick materials when the matter and radiation are in thermodynamic equilibrium. It is defined as a weighted harmonic mean of the frequency-dependent opacity:

$$\frac{1}{\kappa_R} \equiv \frac{\displaystyle\int_0^\infty \kappa_\nu^{-1} \frac{\partial B_\nu}{\partial T}\, d\nu}{\displaystyle\int_0^\infty \frac{\partial B_\nu}{\partial T}\, d\nu} \quad . \tag{1}$$

Here, κ_R is the Rosseland mean opacity, κ_ν is the frequency-dependent opacity, B_ν is the blackbody spectrum, and T is the radiation and material temperature. This mean opacity is dominated by the minima in the frequency-dependent opacity. Increasing the Rosseland mean opacity reduces the radiation energy lost to the walls, thereby increasing the drive temperature and improving the coupling efficiency of the radiation to the fuel pellet for a given laser power (and x-ray conversion efficiency).

Typically we use pure Au hohlraums heated to ~250 eV. Figure 1 shows a frequency-dependent opacity for Au at a density and temperature relevant to these experiments. This opacity was calculated using a very simple average atom model[10] for Au at 1.0 g/cm³ and a temperature of 250 eV. There are significant windows in the opacity at energies around the peak of the blackbody spectrum. The gross structure of the opacity in Figure 2(a) is dominated by the bound-free (photoelectric) absorption coefficient; the sharp increases in opacity correspond to the photoionization of the atomic shells (K, L, M…). Figure 2(a) also shows the weighting function $\partial B_\nu / \partial T$ used in the definition of the Rosseland mean opacity for a 250-eV blackbody distribution. The peak of the weighting function is fairly broad (~1 keV FWHM), and it occurs at about 1 keV, which is near the minimum in the opacity between the N- and O-band absorption edges. To improve the efficiency of the hohlraum, we need to

* Sandia National Laboratories, Albuquerque, New Mexico
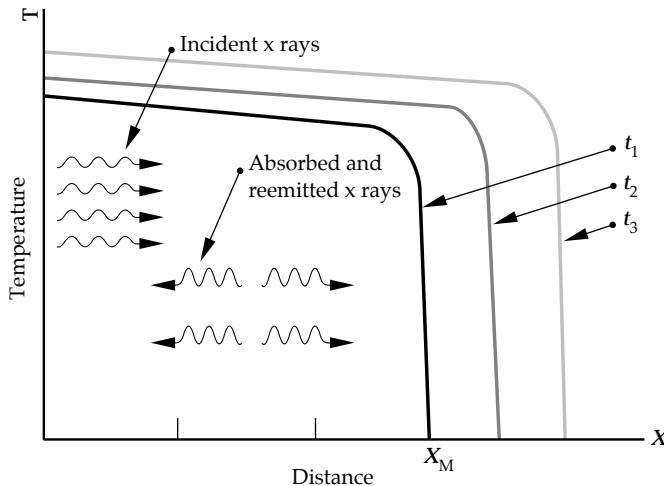
FIGURE 1. Schematic of radiation diffusion (Marshak wave propagation) into high-Z material. Blackbody radiation is incident on the material at $X = 0$. The front of the heat wave at any given time t is indicated by X_M. In this schematic, the temperature is a weakly increasing function of time. (70-00-0197-0143pb01)

blend-in materials whose high-opacity regions complement the low-opacity regions of the original material.[11] Figure 2(a) also shows the calculated frequency-dependent opacity for gadolinium at $T = 250$ eV at a density of 1.0 g/cm^3. Gd was chosen because its high-opacity regions occur around the same frequency as the holes in the Au opacity. For the frequency-dependent opacities shown here, the Rosseland mean opacity for Au is 823 cm^2/g and 455 cm^2/g for Gd. In a properly designed material containing both atoms, the radiation samples the combined opacity of both materials resulting in a higher Rosseland mean opacity. Using the opacity model employed in generating Figure 2(a), the Rosseland mean opacity of a 50:50 mixture of gold and gadolinium, with density 1 g/cm^3 and temperature 250 eV, is 1390 cm^2/g. The frequency-dependent opacity of this composite material is shown in Figure 2(b). A more sophisticated opacity model, XSN,[12] wherein bound-bound transitions play a more central role in determining opacity, would give $\kappa_R = 1500$ cm^2/g for Au, 1300 cm^2/g for Gd, and 2500 cm^2/g for the 50:50 Au/Gd mixture at the same density and temperature.

Analytic Model of Radiation Flow through High-Z Material

In order to determine the Rosseland mean opacity of a material, we measure the propagation time of a radiation heat wave (also referred to as a Marshak wave) through a well characterized sample of that material and compare the measurement to analytic[13–15] and numerical
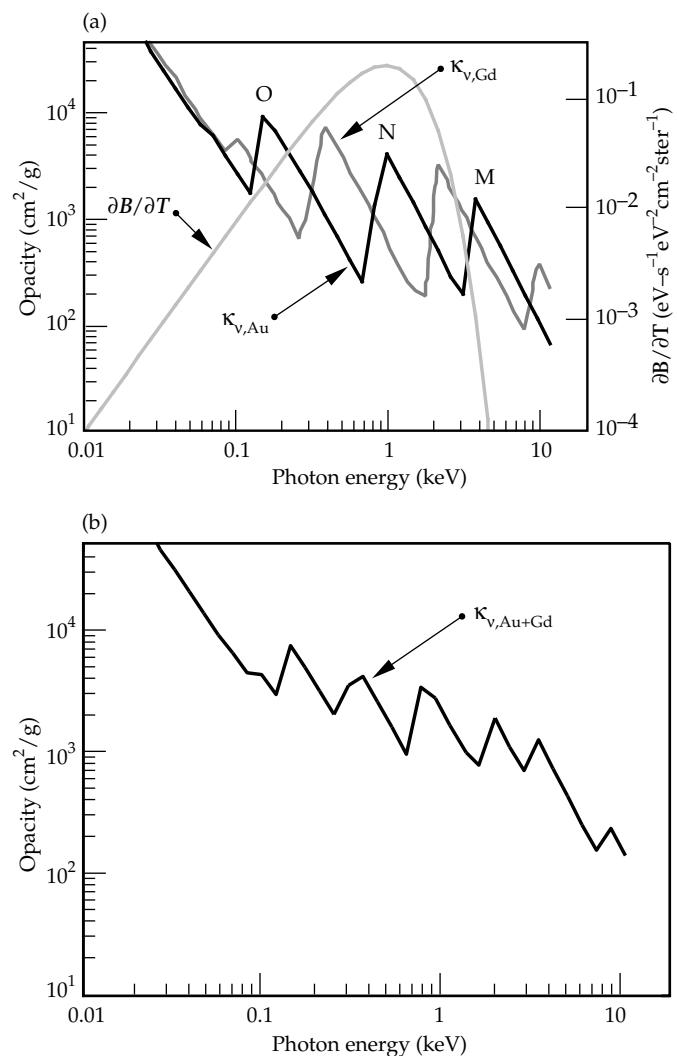
FIGURE 2. (a) Frequency (energy)-dependent opacity of Au and Gd. Also shown is the weighting function ($\partial B/\partial T$) used in the definition of the Rosseland mean opacity corresponding to a 250-eV Planckian distribution. (b) Frequency (energy)-dependent opacity of a 50:50 mixture of Au and Gd at a density of 1 g/cm^3 and a temperature of 250 eV. (70-00-0197-0144pb01)

solutions. The nonlinear diffusion equation that governs the Marshak wave behavior involves the specific energy density and the Rosseland mean opacity of the material. For the experiments discussed here, it can approximately be written as:

$$\frac{\partial}{\partial t}(\rho \varepsilon) = \frac{\partial}{\partial x}\left(\frac{4\sigma}{3\rho \kappa_R} \frac{\partial}{\partial x} T^4 \right) \quad , \qquad (2)$$

where ρ is the material density, ε is the specific energy density of the material, and σ is the Stefan-Boltzmann constant. Using the XSN opacity model, the Rosseland mean opacity for Au in the temperature range of 100 to 300 eV is found to scale as $\kappa_R = \kappa_0 \rho^{0.33} T^{-1}$, where κ_R is in

cm^2/g, κ_0 is 3500 when ρ is in g/cm^3, and T is in heV (10^2 eV). The energy density of the material is approximated as $\varepsilon \approx \varepsilon_0 T^{1.5}$. With these analytic models for κ_R and ε, the self-similar solution for the diffusion equation gives the energy lost to the wall and the position of the Marshak wave front as a function of time and temperature:[6]

$$E_w \propto T^{3.0} t^{0.62} \kappa_0^{-0.4} \tag{3}$$

$$\rho X_M \propto T^{1.7} t^{0.55} \kappa_0^{-0.45} \quad . \tag{4}$$

These solutions were derived for a constant temperature. In a more general case, the boundary temperature itself can vary in time, thus changing the temporal dependence of E_w and ρX_M. For example, in the case of a constant absorbed x-ray flux on the wall, $\dot{E}_w = const(\propto t^0)$, and from Eq. (3), we would have the temperature scaling as $T \propto t^{0.12}$. In this case, the position of the Marshak wave would scale as $t^{0.78}$. This is the sort of behavior one would expect for a constant laser power and a constant x-ray conversion efficiency. In fact, the x-ray conversion efficiency increases slowly in time. We will assume that $\eta_{c.e.} \propto t^{0.2}$, although measurements[16] from Au disks indicate that the conversion efficiency could be significantly higher ($\eta_{c.e.} \propto t^{0.4}$). Using this temporal behavior for the x-ray flux (and hence wall loss), we find the temperature to scale as $t^{0.18}$ and the Marshak wave position to scale almost linearly with time for constant laser power:

$$\rho X_M \propto t^{0.9} \kappa_0^{-0.45} \quad . \tag{5}$$

The time dependence of the Marshak wave position is very close to that observed experimentally[14] for Au foils of varying thickness exposed to the same hohlraum drive in these experiments ($\rho X_M \propto t$). We will also see below that this temporal dependence of the hohlraum temperature is close to that observed experimentally. Therefore, this model is probably the best representation of the experiment described here.

Measurement of Radiation Flow through High-Z Material

To measure the propagation of the heat wave through a given material, we expose the sample to the near Planckian radiation distribution generated inside a standard Nova hohlraum.[17] The sample materials are attached to the side of the hohlraum wall (Figure 3, top). Figure 3 (bottom) is a photograph of an actual sample patch on the side of the hohlraum. The standard Nova hohlraum consists of a 2700-μm-long-cylindrical cavity with a diameter of 1600 μm. The laser entrance holes (LEHs) on the ends of the hohlraum are 800 μm in diameter. The Nova laser beams, five from each end,
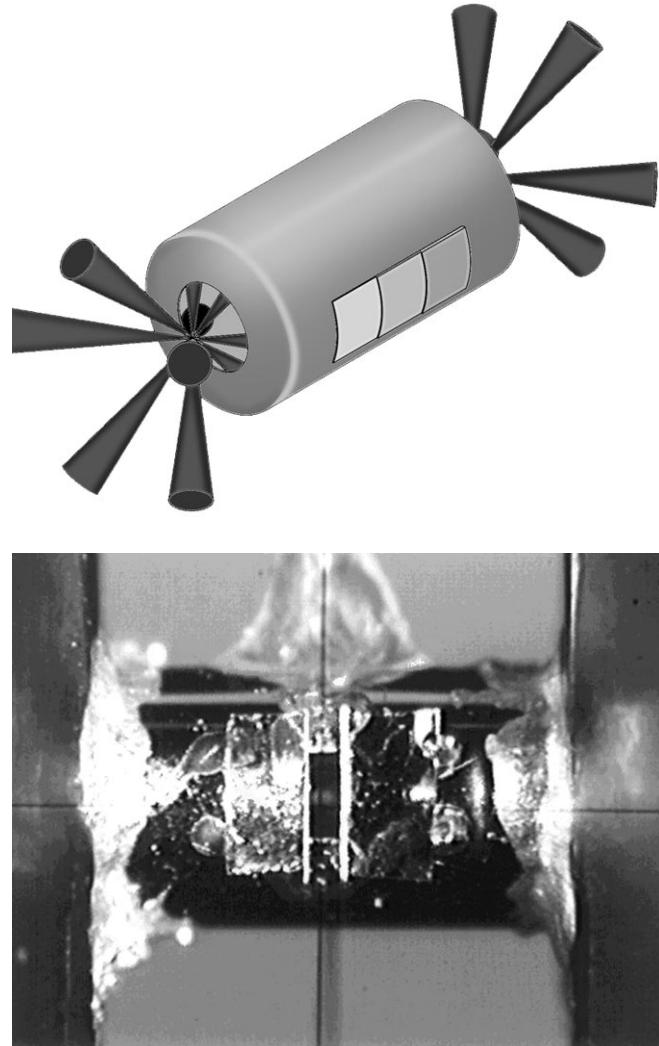
FIGURE 3. Schematic of hohlraum showing laser illumination scheme and sample package mounted on side of hohlraum (top); photograph of foils mounted on hohlraum (bottom). The region between the foils looks directly into the hohlraum and serves as a temporal fiducial. (70-00-0197-0145pb02)

enter the hohlraum through the LEHs and strike the inside of the hohlraum at 40° to the surface normal. The laser beams illuminate an annular region that is centered about 900 μm from the hohlraum midplane on each end of the hohlraum. For the experiments described here, the total laser energy is about 27 kJ, and the laser pulse duration is 1 ns. The five beams on each end intersect in the LEH and are focused 1000 μm in front of the LEH. The laser beam illumination on the hohlraum wall is roughly a 400-μm-x-600-μm ellipse. Thus the average laser intensity on the wall is about 10^{15} W/cm^2.

The hohlraum wall temperature is monitored with an absolutely calibrated multiple-channel soft x-ray spectrometer, DANTE.[18] This diagnostic views a portion of the interior hohlraum wall through a small hole in the hohlraum. Care is taken that DANTE does not view a

laser spot. In Figure 4, we show the temporal profile of the total laser power and the hohlraum temperature. The laser pulse rises rather sharply (~100 ps) and exhibits a small oscillation (±5%) during the "flat-top" region of the pulse. The corresponding hohlraum temperature rises more slowly, reaching a temperature of about 200 eV at 300 ps. Beyond this point, the hohlraum temperature rises more slowly with time (~$t^{0.15}$) during the nominal constant laser power. This is characteristic of the Marshak wave behavior in a material absorbing a constant flux as opposed to a material at constant temperature. The test sample package covers a 600-μm-high, 1200-μm-long slot that is cut in the hohlraum wall and is centered about the hohlraum midplane (see Figure 3). Various test materials cover portions of this slot with one section left uncovered to provide a fiducial signal at $t = 0$ (the beginning of the drive pulse). The sample package usually contains a pure Au sample and a sample of the mixture. The fiducial is located in the center and the burnthrough foils are mounted on either side of it to mitigate any possible effects of hohlraum temperature nonuniformity in the axial direction (i. e., higher hohlraum temperature closer to the laser spots). The radiation inside the hohlraum drives the Marshak wave into the material. Sample thicknesses are usually on the order of one to a few microns so that the radiation propagates through the sample before the drive (i. e., the laser beams) turns off.

In the measurements described here, we investigate the transport of the thermal wave through pure Au foils and Au/Gd mixtures. Two methods of fabricating the mixture are to cosputter the elements resulting in an amorphous material of Au/Gd, or to alternate layers of the constituent elements. A Au/Gd foil that was fabricated by cosputtering the Au and Gd atoms onto a substrate was found to be unacceptable because the

internal stresses generated by this fabrication technique resulted in an extremely fragile material.

In the latter method of fabrication, the areal density of each layer must be optically thin to the radiation, so that the radiation samples both elements simultaneously and averages over the opacity of two elements. In this experiment, the Au/Gd samples are formed by depositing alternate layers of the two elements on a substrate, which is later removed to provide a free standing sample. Two different samples (of the multi-layer variety) corresponding to different atomic fractions of Au and Gd were fabricated. One composite comprises 200 layer pairs of Au and Gd. The thickness of each Au layer is 75 Å, and the thickness of each Gd layer is 75 Å. This sample is 33% Gd and 67% Au by atom. The overall thickness is 2.22 μm, and the areal density of this sample is equivalent to 1.6 μm of Au (i. e., 3.15 mg/cm^2). The second sample comprises 146 layer pairs; the thickness of each Au layer is 35 Å, and the thickness of each Gd layer is 116 Å. In this case, the sample is 67% Gd and 33% Au. The overall thickness of this second sample is 3.02 μm, again corresponding to an equivalent areal mass of Au of 3.15 mg/cm^2. In either of these samples, the individual thickness of each layer of either the Au or the Gd is much less than the range of a photon (100–1000 eV) in these materials. For example, the cold opacity of Au to x rays between 100 and 1000 eV is between 0.5 and 1.5×10^4 cm^2/g. For solid density, then, the range of a photon is $(\kappa \rho)^{-1}$ or about 1000 Å, which is much larger than the typical layer thickness (~10^2 Å) and much less than the typical sample thickness (~10^4 Å).

The thermal radiation corresponding to the hohlraum drive is monitored as a function of time as it burns through the different foils using a streaked x-ray imager (SXI). The SXI images the foil in one direction using a 20-μm-wide imaging slit. The image is dispersed with a transmission grating oriented perpendicular to the imaging slit, and the energy at which we monitor the burnthrough is determined with an offset aperture located behind the transmission grating. All of the data discussed here corresponds to 225-eV radiation. The one-dimensional image is monitored with an x-ray streak camera. Figure 5 shows the streaked image for a sample patch mounted on the side of a hohlraum. The corresponding lineouts of the image (fiducial, pure Au foil and Au/Gd composite foil) are also shown. Figure 5 shows that the radiation burns through the composite foil about 100 ps after it burns through the pure Au foil.

To determine the ratio of the mixture's Rosseland mean opacity to that of Au, we used the results of self-similar solutions [Eq. (5)] and assumed that the two foils are exposed to the same temperature. Independent measurements on the uniformity of the temperature in the region of the test patch indicated that the hohlraum temperature is uniform to within
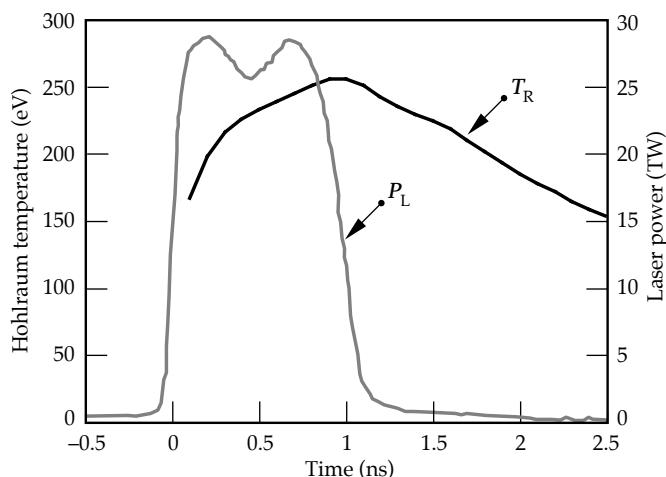
FIGURE 4. Typical 1-ns "square" laser pulse used to drive the hohlraum and the corresponding hohlraum temperature measured with DANTE and albedo corrected.   (70-00-0197-0146pb01)
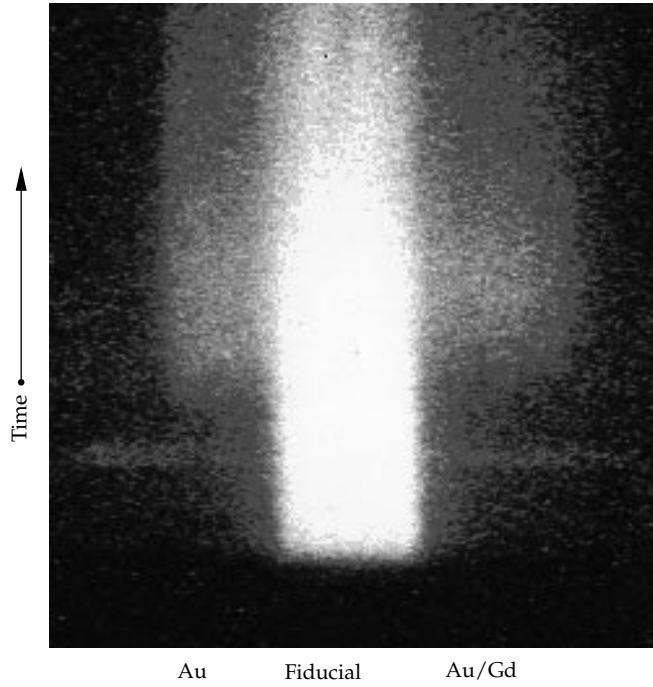
FIGURE 5. Streaked image of test-sample patch monitored at 225 eV (top). The fiducial signal is in the center of the image; the radiation burning through the pure Au sample is on the left of the fiducial, while the radiation burning through the Au/Gd composite sample is on the right. Lineouts of the three sections of the streaked image (bottom). The radiation burns through the Au/Gd composite about 100 ps after it burns through the equivalent areal mass of Au. (70-00-0197-0147pb01)

for the two different concentrations of Gd. The errors associated with the measurement correspond to uncertainties in the streak camera sweep speed (±15 ps) and in errors in determining the precise thickness of the foils (±250 Å). In addition, the measured concentration of Gd is accurate to about ±5%. Figure 6 also shows the calculated Rosseland mean opacity of the Au/Gd mixture as a function of Gd concentration. For these calculations, we used the XSN opacity model and assumed a temperature of 250 eV and a density of 1.0 g/cm^3. The calculations were done for seven different Gd concentrations ranging from 0% to 100%; the solid line is a fit to these seven calculated points. These calculations indicate that the maximum improvement in opacity corresponds to a 50:50 mixture of Au and Gd. The overall improvement in the opacity (over that of pure Au at the same temperature and density) is a factor of 1.7. This curve is normalized to the Rosseland mean opacity of Au at 1.0 g/cm^3 at temperature of 250 eV ($\kappa_R[\text{Au}]) = 1500 \text{ cm}^2/\text{g}$). The opacity of Gd at this temperature and density is $1300 \text{ cm}^2/\text{g}$. An independent series of experiments measured Marshak wave propagation through different thicknesses of Au foil (1–3 μm) and monitored the radiation at two different energies (225 and 550 eV).[14] In these experiments, the hohlraum temperatures were 250 to 265 eV, and they validated the XSN opacity model to within 20% for Au at these temperatures. We indicate the results of those experiments by the datum at the pure Au end of the curve (fraction Gd = 0%).
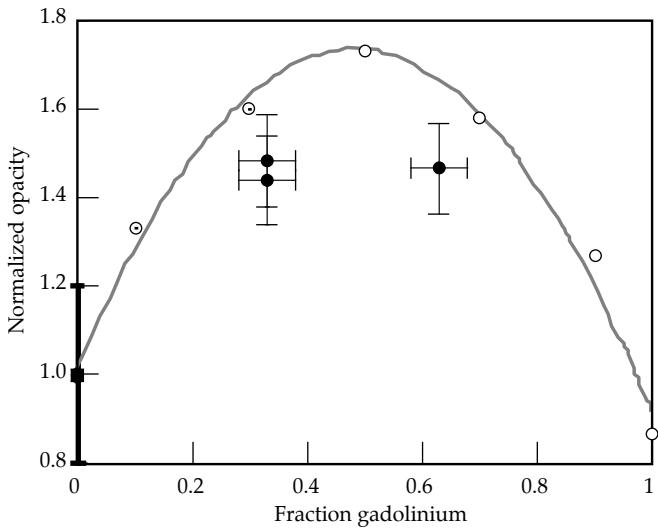
FIGURE 6. Rosseland mean opacity of a Au/Gd composite normalized to that of pure Au at a temperature of 250 eV and a density of 1 g/cm^3. The open points correspond to the results of XSN calculations, and the solid line is a quadratic fit to those points. The solid points show the normalized opacity of the measurements as determined using Eq. (5). The datum at zero concentration of Gd corresponds to earlier work that verified the XSN opacity model. (70-00-0197-0148pb01)

the accuracy of the measurement. The ratio of the Rosseland mean opacities then depends on the ratio of the burnthrough times squared and on the ratio of the areal masses of the foils to the 2.2 power. The foils were fabricated so that this latter quantity is nominally one, but the exact values were used in determining the ratio of opacities. Figure 6 shows the ratio of the Au/Gd foil's Rosseland mean opacities to that of Au

40

The analytic models yield insight into the physical processes that govern the behavior of the Marshak wave propagation and illustrate its sensitivity to the various parameters that affect it (κ_R, T, etc.). However, the real situation is quite complicated. For example, the absorbed laser power may not be constant in time because of parametric instabilities such as SRS, or hohlraum conversion efficiency may behave differently from "disk" conversion efficiency. Furthermore, the opacity calculation in Figure 6 represents one specific density and temperature. In reality, the experiment samples a range of densities and temperatures. In view of the relative simplicity of the model to the actual time dependent phenomenon, the model is remarkably accurate in that the measurements as interpreted by the model are only about 10 to 12% lower than the XSN calculation. Perhaps an even more sophisticated treatment of bound-bound transitions than that XSN employs would account for the discrepancy. The most accurate way of determining the opacity of the composite is to simulate the experiment with a rad-hydro code. Initial LASNEX calculations monitoring a 250-eV photon energy channel yield a burnthrough time in a 2:1 Au/Gd mixture that is 1.3 times longer than that in an equivalent areal mass of pure Au. The measured burnthrough time (at 225 eV) is 1.2 times longer. Similarly, the simulation gives a burnthrough time that is 1.25 times longer than that in an equivalent areal mass of pure Au for a 1:2 Au/Gd mixture while the measured burnthrough time is 1.3 times longer.

Conclusion

By combining the appropriate elements, we have demonstrated that we can produce a composite whose Rosseland mean opacity is higher than that of either of the constituents at a given temperature and density. The elements must be chosen so that the high-opacity regions (in photon energy) of one element overlap with the low-opacity regions of the other. Because the composites have a higher reemission coefficient to the incident radiation, less energy is lost to the wall. For example, in the scale-1 hohlraums used in these experiments, the wall losses account for about 75% of the total energy lost (the remainder goes out through the LEHs; there are no capsule losses in these hohlraums). The observed 50% increase in the opacity of the composite could result in a 15% reduction in wall loss and in 12% less energy required to achieve the same hohlraum temperature. Alternatively, on Nova, the same amount of laser energy could lead to an increase in temperature of about 8 eV (about 12% more flux available to drive a capsule). The reduction in wall loss for the National Ignition Facility, the planned 1.8-MJ laser designed to achieve ignition in an ICF target, is even more dramatic. Here, for the point design ignition target,[19] the energy lost to the hohlraum wall would be reduced by about 160 kJ if the pure Au hohlraum was replaced with a hohlraum made of the 37% Au, 63% Gd composite. For an alternate ICF reactor based on a 10-MJ heavy-ion driver,[4] a reduction of 1.7 MJ in wall loss can be realized with the Au/Gd hohlraum wall.

Acknowledgments

Notes and References

1. Lindl, J. D., McCrory, R. L., and Campbell, E. M., *Physics Today*, **45** (9), p. 32–40 (1992).
2. Nuckolls, J. H., Wood, L., Thiessen, A. R., and Zimmerman, G. B., *Nature*, **239**, p. 139–142 (1972).
3. Lindl, J. D., *Physics of Plasmas*, **2**, p. 3933–4024 (1995).
4. Lindl, J. D., Bangerter, R. O., Mark, J. W.-K., and Pan, Y. L., "Review of Target Studies for Heavy Ion Fusion," *Heavy Ion Inertial Fusion*, M. Reiser, T. Godlove, and R. O. Bangerter, eds., *AIP Conf. Proc. 152* (American Institute of Physics, New York, 1986).
5. Rosen, M. D., "Scaling Law for Radiation Temperature," Lawrence Livermore National Laboratory, Livermore, CA, UCRL-50055-79, 1979 (unpublished).
6. Rosen, M. D., "Marshak Waves: Constant Flux vs. Constant T—a (slight) Paradigm Shift (U)," Lawrence Livermore National Laboratory, Livermore, CA, UCRL-ID 119548, 1995 (unpublished).
7. Pakula, R., and Sigel, R., *Phys. Fluids,* **28**, p. 232–244 (1985); **29**, p. 1340(E) (1986).
8. Marshak, R. E., *Phys. Fluids*, **1**, p. 24–29 (1958).
9. Rosseland, S., *Monthly Notices of the Royal Astronomical Society*, **84**, No 7 (1924).
10. Larsen, J. T., "Hyades—A Radiation Hydrodynamics Code for Dense Plasma Studies," *Radiative Properties of Hot Dense Matter: Proceedings of the 4th International Workshop*, W. Goldstein, C. Hooper, J. Gauthier, J. Seely, R. Lee, eds. (World Scientific, Singapore, 1990).
11. Nishimura, H., Endo, T., Shigara, H., Kato, Y., and Nakai, S., *Bull. Am. Phys. Soc.* **37**(6), p 1383 (1992). Also, *Appl. Phys. Lett.* **62**(12), p 1344 (1993).
12. Lokke, W. A., and Grasberger, W. H., "XSNQ-U, a non-LTE emission and absorption coefficient subroutine," Lawrence Livermore National Laboratory, Livermore, CA, UCRL-52276, 1977 (unpublished).
13. Sigel, R., et al., *Phys. Rev. Lett.*, **65**, p. 587–590 (1990).
14. Porter, J. L., and Thiessen, A. R., "Summary of albedo experiments," Lawrence Livermore National Laboratory, Livermore, CA, CLY-92-059, 1992 (unpublished).
15. White, V. J. L., Foster, J. M., Hansom, J. C. V., and Rosen, P. A., *Phys. Rev E* **49**, p. R4803–R4806 (1994).
16. Ze, F., Kania, D. R., Langer, S. H., Kornblum, H., Kauffman, R., Kilkenny, J., Campbell, E. M., and Tietbohl, G., *J. Appl. Phys.* **66**, p. 1935–1939, (1989).
17. Kauffman, R. L., Suter, L., Darrow, C. B., Kilkenny, J. D., Kornblum, H. N., Montgomery, D. S., Phillion, D. W., Rosen, M. D., Thiessen, A. R., Wallace, R. J., and Ze, F., *Phys. Rev Lett.* **73**, p. 2320–2323 (1994).
18. Kornblum, H. N., Kauffman, R. L., and Smith, J. A., *Rev. Sci. Instrum.* **57**, p. 2179–2181 (1986).
19. Haan, S. W., et al., *Phys. Plasmas* **2**, p. 2480–2486 (1995).

Direct-Drive Capsules for NIF

S. V. Weber   D. Eimerl   J. E. Rothenberg

H. E. Dalhed   M. H. Key   C. P. Verdon*

S. M. Pollaine

_____

Introduction

In inertial confinement fusion (ICF), large amounts of (laser) energy are delivered onto a target containing fusion fuel, usually deuterium–tritium (DT). The rocket-like blowoff of the target shell material compresses the fuel within, leading to fusion.

The direct-drive approach to ICF uses direct laser irradiation to implode the capsule. The indirect-drive approach converts laser energy to x rays in a Au hohlraum, and the x rays are used to implode the capsule. The National Ignition Facility (NIF) has been designed principally for indirect-drive ignition; however, fairly modest enhancements to the facility would make direct-drive ignition achievable as well. The facility requirements were specified in 1995 in a white paper,[1] and the design modifications necessary to meet those requirements were presented in the Advanced Conceptual Design Review.[2] The main requirements for direct drive are a beam configuration that is distributed nearly evenly around the capsule in all directions and a beam smoothing system in the laser front end that meets more stringent requirements than those for indirect drive. The timescale to implement these capabilities on the NIF has not yet been determined.

Background

To illuminate the capsule uniformly requires a different beam geometry than that used to drive a cylindrical hohlraum, as shown in Figure 1. For indirect drive, clusters of four beamlets are distributed in four rings, grouped in two pairs, in each hemisphere. These rings give two cones of illumination that are directed into each end of a hohlraum[3] at angles 23.5°, 30°, 44.5°, and 50° from the chamber axis. For direct drive, suitable illumination may be obtained by steering the beams from the second and fourth rings to a fifth ring at 77.45°, giving an intrinsic illumination uniformity (for perfect pointing and power balance) of 0.2% rms. This is considerably better than the 1% rms in spherical harmonic modes $I < 20$, which is required. However, beam pointing errors and power imbalance will also cause illumination nonuniformity. Pointing accuracy and power balance requirements, which follow from the uniformity specification, are discussed later in this article.

For indirect drive, only a fraction of the laser energy is converted into x rays, and only a fraction of the x rays are absorbed by the capsule, which makes direct drive appear to be a more efficient use of laser energy to implode a capsule. However, there are also several inefficiencies in direct drive, and, by our current understanding of target physics, it appears that about the same energy is needed to obtain ignition by either approach. Only about half of the laser energy is actually absorbed by the capsule in the direct-drive designs we have considered. The laser spot size is chosen to be comparable with the initial target diameter to get adequate illumination uniformity. As the capsule implodes, only the centers of the beams get into dense plasma and are absorbed efficiently. Also, the fraction of absorbed energy converted into implosion kinetic energy, the "rocket efficiency," is lower for direct drive. Direct laser illumination deposits energy into lower-density plasma than indirect x-ray illumination, so a lower mass is ablated at a higher exhaust velocity, which gives a less efficient rocket.

Also, it is necessary to implode a direct-drive capsule shell on a higher adiabat than is the case for indirect drive. The adiabat characterizes the degree of degeneracy of the fuel. The usual definition of the adiabat is $\alpha = P/P_F$, where P is the pressure in the fuel, and P_F is the pressure for Fermi degenerate fuel at the same

* University of Rochester, Laboratory for Laser Energetics, Rochester, NY

FIGURE 1. Beam cluster locations on a map of the target chamber. Ports used for direct drive are shaded. Indirect-drive ports, which are not used for direct drive, are unshaded, with arrows showing how the beams are shifted to the new rings at 77.45° and 102.55°.
(20-03-0397-0432pb01)
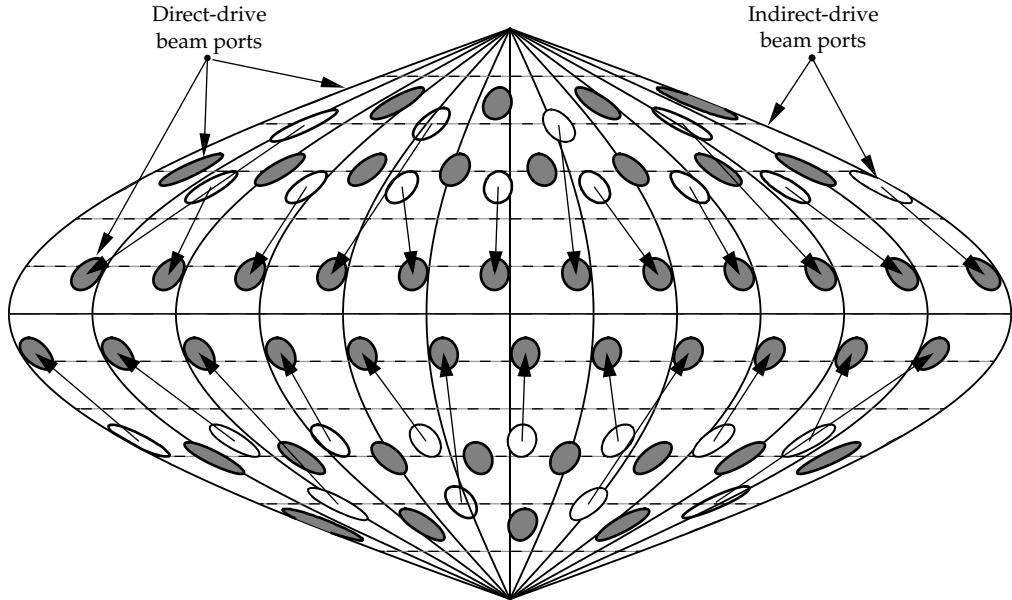
density. Indirect-drive designs with $\alpha \approx 1$ are predicted to have adequate stability;[3] direct-drive designs are predicted to need an increase of the adiabat to $\alpha \approx 2$–4 to prevent the shell from breaking up. The higher the adiabat, the lower the fuel density for a given stagnation pressure resulting from the implosion. This lower density leads to a faster ablation rate and improved stability. However, more implosion energy is needed to achieve ignition, and the gain at a given implosion energy is lower.[4] Lindl presents these energetics scalings in detail.[5]

The physics for the indirect-drive target design have been tested exhaustively in the work specified by the Nova Technical Contract.[6] A significant amount of direct-drive research has also been conducted on Nova and elsewhere, but much more is required. The research program on the Omega[7] laser at the University of Rochester, together with work at the Nike[8] laser at the Naval Research Laboratory, the GEKKO XII[9] laser at Osaka University, and other facilities throughout the world, will make it much more clear in a few years what the probability of success will be for direct drive as a route to ignition on the NIF.

Capsule Designs

We have examined the capsule designs (frozen DT shells surrounding DT gas) developed at the University of Rochester,[10] shown in Figure 2. Practical capsules would require a thin outer layer, such as a few micrometers of CH, for mechanical support, but this layer has been omitted from our simulations. The capsules are driven with 1.5 MJ of 0.35-μm light with pulse shapes as shown in Figure 2. The capsule in Figure 2(a) uses a picket pulse shape; the one in Figure 2(b) uses a continuous pulse

shape. Both pulse shapes are used to adjust the timing of shocks through the shell to set the fuel on the desired adiabat ($\alpha = 3.7$ for the continuous pulse shape and $\alpha = 2.2$ for the picket pulse). Figure 3 shows the time history of the mass-averaged fuel adiabat. Note that most of the entropy for the continuous pulse capsule is created by the first shock, while for the picket capsule most is added by the fourth shock. The capsule yields, in 1D simulations neglecting mix, are 17 and 33 MJ for the continuous and picket designs, respectively.
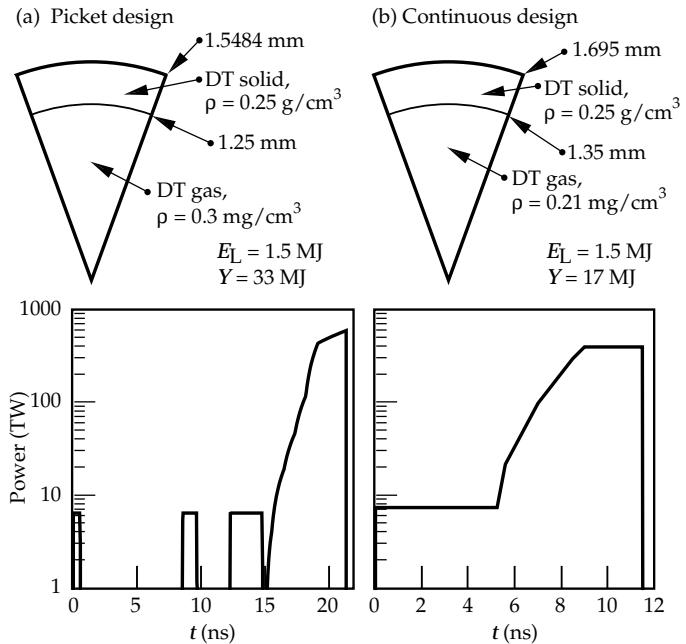
FIGURE 2. Capsule dimensions and pulse shapes for two direct-drive designs: (a) picket-pulse and (b) continuous-pulse shape. E_L is laser energy on target, and Y is fusion yield from the target.
(20-03-0397-0441pb01)
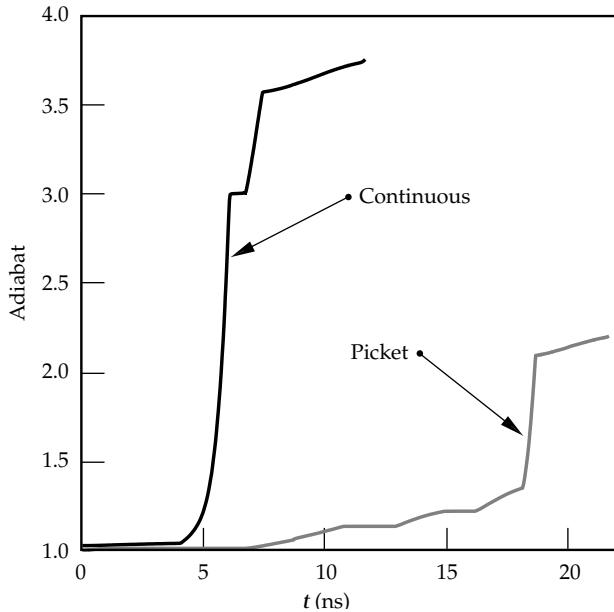
FIGURE 3. Fuel adiabat vs time for picket- and continuous-pulse capsules.   (20-03-0397-0442pb01)
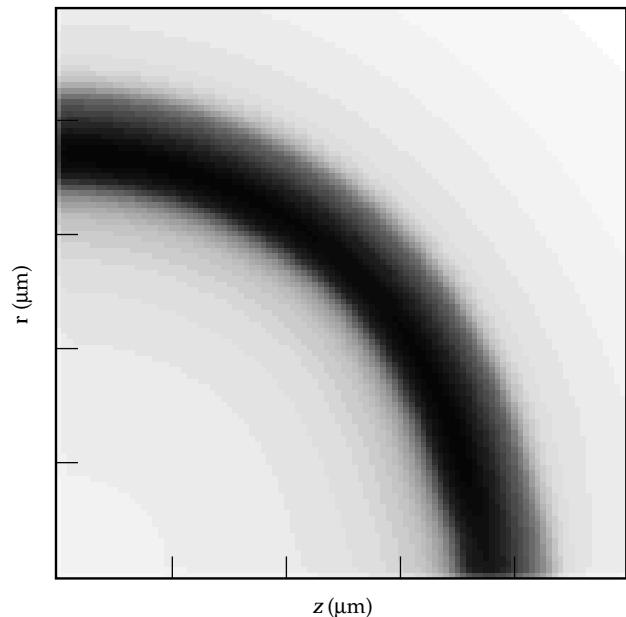
FIGURE 4. Gray scale indicates fuel density near ignition time in a 2D simulation of one quadrant of the continuous-pulse capsule design driven with the NIF beam geometry, assuming perfect pointing and power balance.   (20-03-0397-0443pb01)

Illumination Uniformity

Direct- and indirect-drive capsules require uniformity over the capsule surface to a level of about 1% rms. For direct drive, this must be achieved by the laser. For indirect drive, x-ray transport between the capsule and the hohlraum wall effectively eliminates nonuniformity for approximately $l \geq 10$, while lower modes must be controlled by hohlraum geometry, beam pointing within the hohlraum, and beam phasing. For direct drive, nonuniformity in modes $l \leq 20$ is dominated by contributions from the beam geometry, pointing errors, power imbalance, and gross beam profile. Contributions for $l > 20$ are dominated by substructure within individual beams, which creates target modulations in a process called imprint, discussed later in this article.

2D simulations can examine implosion nonuniformity, resulting from the beam locations, by representing the laser illuminations as cones of beams. Only a full 3D simulation can examine a 3D structure resulting from discrete beams in each cone. Figure 4 shows fuel density at ignition time for a simulation of one quadrant of the continuous pulse design. Nonuniformities in the angular direction are small, and the simulation predicts full yield. We anticipate no significant nonuniformity in direct-drive implosions resulting from the beam configuration.

Beam pointing errors and power imbalance give additional irradiation nonuniformities. Figure 5 shows the level of nonuniformity expected for the pointing and power balance accuracy for which NIF has been
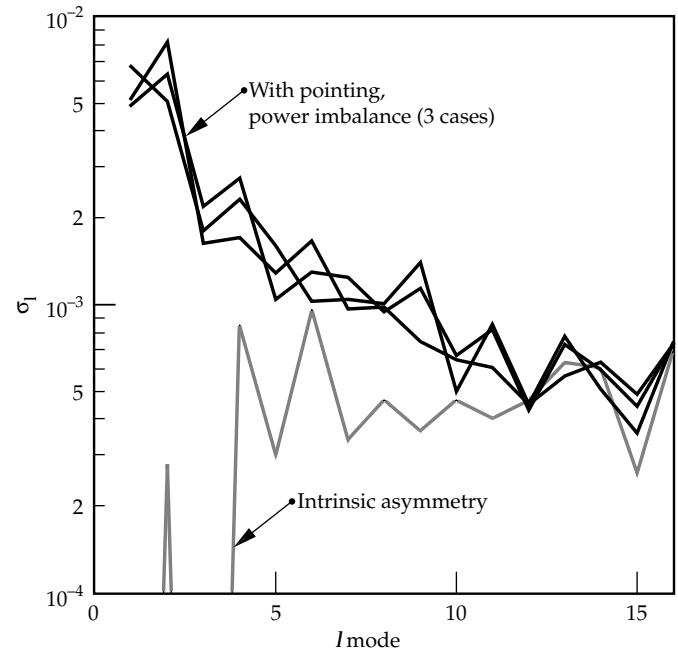
FIGURE 5. The solid lines show illumination nonuniformity (contribution of a given mode to the rms) vs spherical harmonic mode number *l*, for three random choices of pointing error and power imbalance consistent with NIF specifications. The shaded line shows intrinsic nonuniformity from the beam geometry alone. (20-03-0397-0444pb01)

designed—50 μm rms pointing accuracy for each beam cluster and 5% rms power imbalance for each beamlet.[11] These specifications follow the 1% rms illumination uniformity requirement. The white paper[1] gives the derivation of these laser specifications from the uniformity requirement. The nonuniformity has been calculated for three randomly selected sets of errors, and then broken down into spherical harmonic modes, Y_{lm}. The quadrature sum over m of the intensity rms, σ_l, is shown at each l mode. It may be seen that most of the nonuniformity is in modes $l = 1$–4, and that the contribution from pointing errors and power imbalance dominates the intrinsic nonuniformity. At higher modes, the intrinsic component becomes a significant fraction of the total.

Drive nonuniformities from pointing deviations and power imbalance generally are not axisymmetric. To look at these effects in a 2D LASNEX simulation, we consider $m = 0$ for a single l mode at a time. Drive asymmetry is introduced as an angle-dependent energy deposition source, rather than the usual laser ray trace, as this gives better control of the spatial

structure and less numerical noise. Figure 6 shows results of simulations for $l = 2$, 4, 8, and 12 at levels comparable with the predicted values, none of which is very distorted. The capsule is subject to the sum of the distortions over l, which is several times worse than one of the single low l cases, but this should still be tolerable. Thus, the LASNEX simulations support the laser uniformity specifications in the white paper.

Laser Imprint

Illumination nonuniformity on smaller spatial scales, roughly $l > 20$, arises mainly from spatial modulation in individual beams. Imprint is the formation of target perturbations from small-scale intensity nonuniformity. Rayleigh–Taylor (RT) instability causes target perturbations in the range $20 < l < 200$ to grow by large factors during the implosion, so the uniformity must be very good. Beam smoothing is performed with random phase plates (RPPs)[12] and smoothing by spectral dispersion (SSD).[13] RPPs break up the spatial coherence of the beam to give a laser spot with fine speckles

FIGURE 6. Fuel density near ignition time from simulations of single l mode drive asymmetry for (a) $\sigma_2 = 0.012$, (b) $\sigma_4 = 0.0025$, (c) $\sigma_8 = 0.001$, and (d) $\sigma_{12} = 0.0004$. A full quadrant was simulated for $l = 2$, 4, while $l = 8$, 12 were modeled with a wedge between the first peak and valley of the modulation. (20-03-0397-0445pb01)

(a) $l = 2$ $\sigma = 0.012$

(b) $l = 4$ $\sigma = 0.0025$

(c) $l = 8$ $\sigma = 0.001$

(d) $l = 12$ $\sigma = 0.0004$

r (μm)

z (μm)
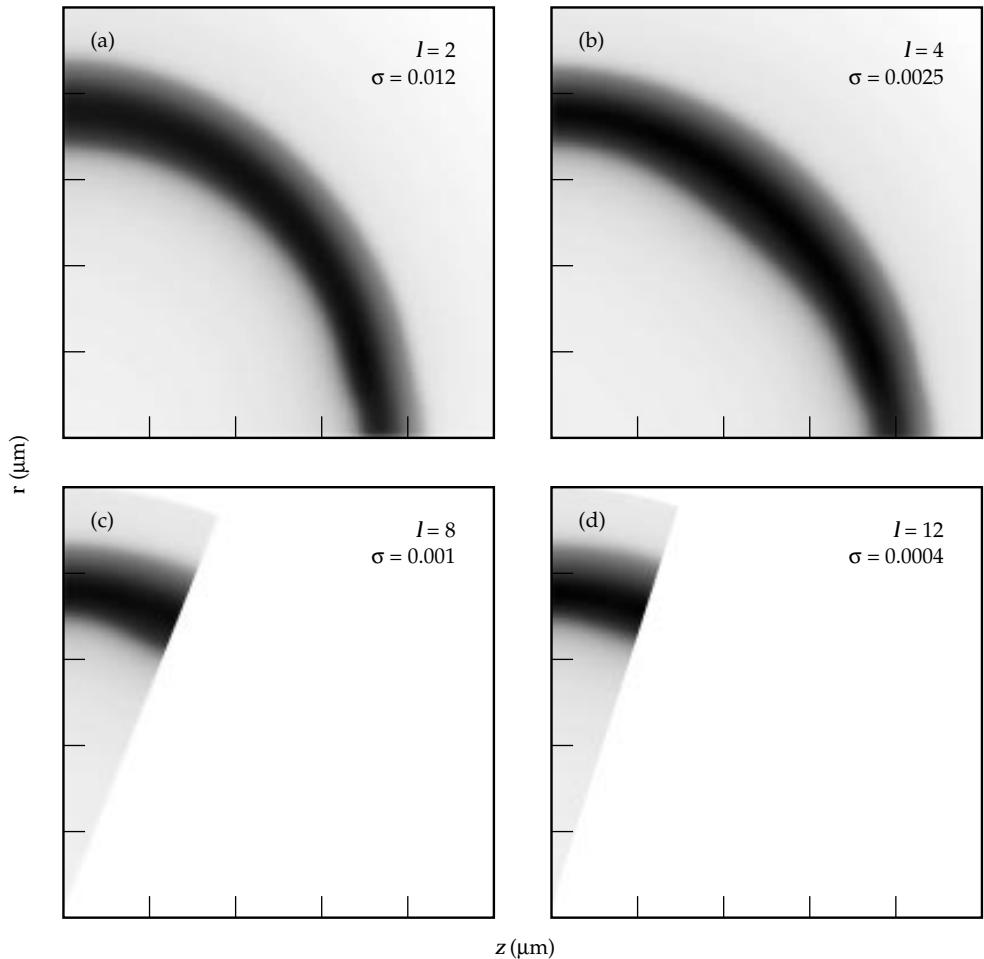
and a smooth envelope. The RPP spot has a total modulation $\sigma_{rms}/I_0 = 1$, where I_0 is the mean intensity, and there is power on all spatial scales larger than the speckle size. SSD reduces the modulation further by introducing bandwidth to the laser beam and dispersing the spectral components with a grating, giving a different speckle pattern every coherence time so that the spot is smoothed in the time average. To get the smoothing level needed for direct drive, $\sigma_{rms}/I_0 < 0.01$, the beam must be dispersed in both directions, which is called 2D SSD. While 1D SSD may help mitigate laser–plasma instabilities for indirect drive, we believe that 2D SSD is needed to meet the more stringent requirements of direct drive. At best, the modulation is reduced to $\sigma_{rms}/I_0 = (t_c/t_{avg})^{1/2}$, where t_c is the coherence time, related to the bandwidth $\Delta\nu$ by $t_c = 1/\Delta\nu$, and t_{avg} is the averaging time. A more detailed description of the effects of the beam smoothing parameters upon the character of the intensity nonuniformity has been presented elsewhere.[14]

We simulated imprint by calculating the target modulation introduced by single-mode time-independent intensity modulations. The structure of a perturbation resulting from laser speckle is found to become indistinguishable from that of a perturbation that started out as a surface bump after some characteristic relaxation time.[15,16] The relaxation time is often the beginning of bulk acceleration of the shell, when perturbations of any origin relax into eigenmodes of the RT instability. Also, the amplitude of the target perturbation is proportional to the size of the intensity modulation. Therefore, it is convenient to relate the imprinted perturbation to a surface finish perturbation that develops into the same size structure after the relaxation time, called the equivalent surface finish, ε_l. Then, we scale out the intensity modulation to get a quantity called the imprint efficiency, $E_l = \varepsilon_l/(\delta I_l/I_0)$, where δI_l is the intensity modulation amplitude in mode l. Figure 7 shows the imprint efficiency calculated for several mode numbers. These simulations were conducted in planar geometry, as convergence effects are small during the imprint timescale, and used a modulated energy deposition source, as described earlier.

Imprint is generally effective for only a limited period of time—intensity nonuniformity has less effect upon a target at later times. One reason is that heat conduction gives thermal smoothing[17] between where the laser energy is absorbed and the ablation front. Modulation of ablation pressure is predicted to be reduced from the modulation in laser intensity as $\delta P/P = e^{-k\Delta r}$, where δP is the ablation pressure modulation, k is the wave number of the transverse intensity modulation, and Δr is the separation between where the laser energy is deposited and the ablation front. Thermal smoothing is greater for shorter wavelengths or higher mode
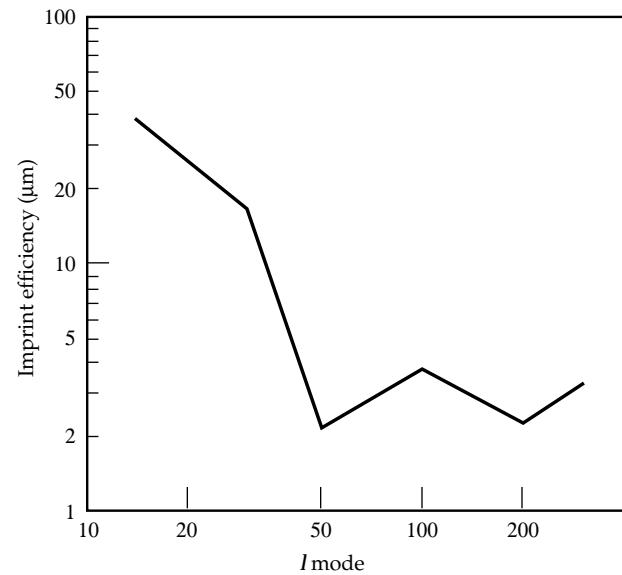
FIGURE 7. Imprint efficiency vs spherical harmonic mode number for the continuous-pulse NIF design. (20-03-0397-0433pb01)

numbers and increases with the thickness of the ablated plasma. Also, once hydrodynamic perturbations are created at the ablation front, they grow by the RT and Richtmyer–Meshkov (RM) instabilities. Over time, additional imprint becomes less and less significant compared with earlier imprint, which has been amplified by growth. Note that the imprint time may not be the same as the relaxation time. Imprint may have terminated before the shell begins bulk acceleration, but the longitudinal structure of the imprinted perturbation may differ from that of a surface finish perturbation until both relax into an RT eigenmode.

A timescale over which imprint occurs has been examined with simulations in which the intensity pattern is switched from modulated to spatially uniform at different times. Figure 8 shows column density modulation, taken from planar simulations of modulation wavelength corresponding to $l = 30$ and $l = 100$, for cases in which the laser was made spatially uniform after 0.25, 0.5, 1, 2, or 4 ns. The later we switch to uniform illumination, the closer the results are to these with constant modulation. We can extract a characteristic time by which 80% of the imprint has occurred (about 1.4 ns for $l = 100$ and 4.9 ns for $l = 30$). Phase oscillations somewhat complicate interpretation of the imprint timescale, especially for the $l = 100$ case.

An equivalent surface finish modal spectrum was obtained by multiplying the imprint efficiency by the predicted spectrum of optical modulation, using a simplified smoothing model in which an independent speckle pattern is generated every laser coherence time. (Reference 14 provides a more complete model.) We took the imprint timescale to be 2 ns, independent of l, and the coherence

FIGURE 8. Column density modulation amplitude from imprint simulations for (a) $l = 30$ and (b) $l = 100$. The heavy solid line shows the case where the intensity is modulated at all times, while the shaded curves show cases in which the laser is made spatially uniform at various times. (20-03-0397-0434pb01)
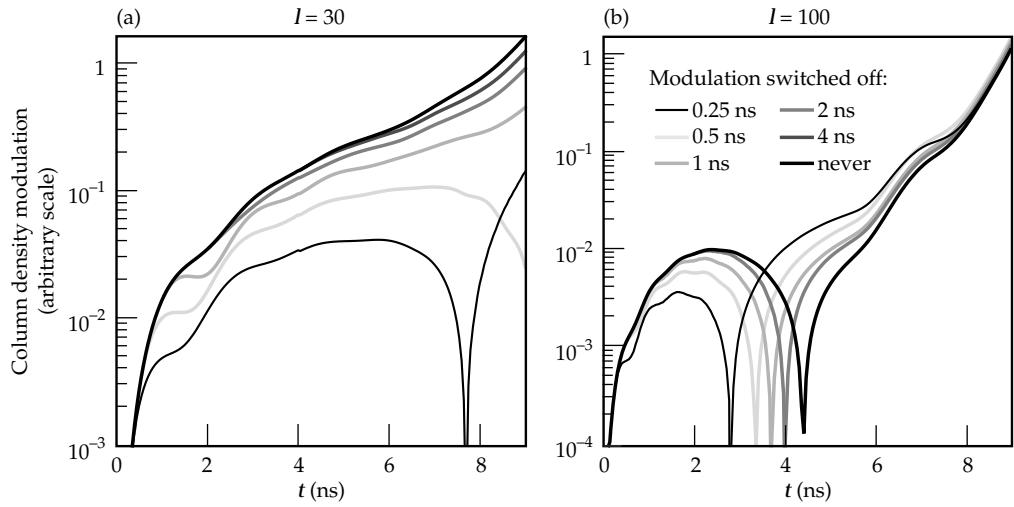
time to be 2 ps, from the NIF direct-drive bandwidth of 0.5 THz. Overlap of 50 beamlets and two polarizations at any spot on the capsule gives an additional smoothing factor of 10. The equivalent surface finish spectrum, shown in Figure 9, is comparable in amplitude with the surface finish from fabrication measured for Nova capsules.[18] The rms modulation from imprint is 11 nm and that from fabrication is 8.4 nm, adding in quadrature to a total effective surface finish of 13.9 nm. These spectra do not include a rise in the fabrication spectrum at low mode

numbers ($l < 16$), neglected in the fit shown here, or intensity modulation in low modes due to beam pointing and power imbalance.

The bandwidth and divergence requirements for beam smoothing stress the laser performance in some respects. Frequency-conversion efficiency decreases with increasing bandwidth, although this effect can be mitigated to some degree with, for example, three crystal conversion schemes. Spatial filter pinhole closure can limit the divergence. Since imprint occurs mainly during the early, low-power phase of the pulse, it seems likely that smoothing requirements at peak power should be less stringent. The beam smoothing specifications in the white paper[1] assume that the bandwidth requirement at peak power can be relaxed a factor of two below that for the foot of the pulse. Further research is needed to refine this estimate.

Ablation Front Perturbation Growth

Growth at the ablation front of perturbations initiated either by imprint or surface finish may be evaluated using the dispersion relation for ablative RT[19,20]

$$\gamma_k = \sqrt{\frac{gk}{1 + kL}} - 3kv_a ,$$ (1)

where γ_k is the growth rate at wave number k, the acceleration $g = 8.5 \times 10^{15}$ cm/s^2, the density gradient scale height $L = 0.5$ μm, and the ablation velocity $v_a = 3.4 \times 10^5$ cm/s. Numerical values are averages over the shell acceleration from a 1D simulation of an implosion. The wave number is related to the mode number by $k = l/r$, where we use $r = 0.1$ cm as

FIGURE 9. Amplitude per spherical harmonic mode number Y_{lm} vs mode number l for imprint modulation expressed as equivalent surface finish, actual surface finish, and total effective initial surface modulation. (20-03-0397-0435pb01)

a mean shell radius for this time interval. LASNEX simulations of linear regime mode growth have been used to check that this dispersion relation is applicable. The peak growth rate is about 2 ns^{-1} at $l \approx 150$. The total linear growth factor to the time of peak inward velocity is

$$GF_{abl}(k) = e^{\gamma_k \Delta t} , \qquad (2)$$

where $\Delta t = 4.66$ ns is the acceleration time. Figure 10 shows the ablation front growth factors from Eq. (1) for the continuous pulse capsule design and for an $\alpha \approx 1$ design. It is clear that raising the adiabat improves stability. The ablation velocity is defined as $v_a = \dot{m}/\rho_{max}$, where $\dot{m}$ is the mass ablation rate and ρ_{max} is the peak density in the shell. The mass ablation rate changes little if the shell adiabat is changed while the laser intensity is held fixed. However, for a given ablation pressure, $\rho_{max} \propto \alpha^{-3/5}$, so a higher α gives a higher v_a, thus more stabilization. The GF_{abl} curve for the $\alpha = 1$ design uses $L = 0.3$ µm and $v_a = 1.8 \times 10^5$ cm/s, with other parameters the same. This gives a peak GF_{abl} that is larger by more than 10^3 than for the higher adiabat design, while the GF_{abl} for $l = 100$ is larger by a factor of about 10.

The modal amplitudes for linear growth were obtained by multiplying the effective surface finish spectrum by the growth factors. Figure 11 shows the ablation front perturbation spectrum at peak shell velocity. According to the multimode saturation theory of Haan,[21] modes with amplitudes greater than $\nu r/l$ will be affected by saturation. We used $\nu = 2$ for the saturation parameter.[22] Modes near the peak of the linear growth spectrum are substantially affected by saturation. After saturation effects are considered, the peak in the amplitude spectrum is shifted down to $l \approx 60$. The total rms amplitude of RT bubbles obtained from this spectrum is 6.4 µm, well under the total shell thickness (to $1/e$ of peak density) at peak velocity of 135 µm. The rms bubble amplitude for the $\alpha = 1$ design is 30 µm with saturation effects included in the same manner, although the rms, based upon linear growth factors, is 5 cm. The total shell thickness at peak velocity is 91 µm for the low adiabat design, but as the peak amplitude is several times the rms, the shell would be penetrated.

The Haan saturation model does not include addition of power to modes through multimode coupling.[23] The high degree of saturation for the most rapidly growing modes in this case causes concern that a turbulent cascade could feed more power into the lower l modes than was obtained by the analysis above, which assumed only growth from the seed amplitude of each individual l

FIGURE 10. Growth factor for ablation front perturbations during inward acceleration vs mode number l from the dispersion relation Eq. (1), for the continuous-pulse capsule design, and for an $\alpha = 1$ design.   (20-03-0397-0436pb01)
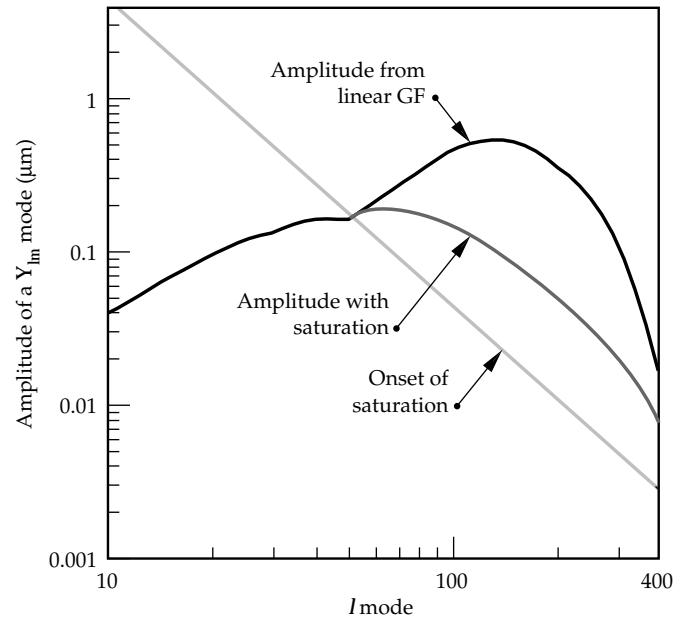
FIGURE 11. Ablation front modulation amplitude at peak velocity vs l mode from linear growth factors, corrected for saturation, and amplitude for onset of saturation.   (20-03-0397-0437pb01)

mode. To address this issue, we used a 2D multimode simulation using finite modal amplitudes, including modes in the range $10 \leq l \leq 200$ in a wedge of a sphere extending from $\theta = \pi/2$ out to the first minimum of the P_{10} Legendre polynomial. The modes were represented as *cosine* harmonics of the lowest mode. Although these modes differ slightly from *spherical* harmonics, as the latter do not match a single reflection boundary in a wedge, the difference should have little effect on the results. The mode amplitudes were adjusted so that the total power in all Y_{lm}, $10 \leq l \leq 200$ was included in the reduced set of modes ($l = 10, 20, ..., 200$; $m = 0$) included in the simulation. We simulated imprint of static speckle with an amplitude corresponding to a 2-ns time-average for the beam smoothing conditions described earlier. The true averaging time varies with mode number, but it is probably within a factor of two of this value for the important modes, so these amplitudes should be accurate to within a factor of $\sqrt{2}$. No surface finish modulation was included in this simulation.

Figure 12 compares the rms modulation of the ablation front radius postprocessed from the 2D multimode simulation with two applications of the Haan quasilinear analysis. One Haan application uses the growth factors from the dispersion relation in Eq. (1) applied to perturbations arising from imprint alone. The other uses linear growth factors from 2D LASNEX single-mode simulations. All three cases agree to within a factor of about two. The Haan application with LASNEX

growth factors should agree identically with the multimode simulation when the perturbations are linear. However, there is some disagreement because the evolution of every included mode was followed in the multimode simulation, while the Haan model application interpolated between a smaller number of discrete l values, which were actually simulated. The multimode simulation shows that the Haan theory gives a reasonably good result even though linear growth factors for this case predict a high degree of saturation.

The Haan theory may be applied to perturbation amplitudes at the inside of the shell as well, where perturbations can feed through from the ablation front, grow during deceleration of the shell, and penetrate into the hot spot that ignites the capsule. Figure 13 shows linear growth factors to the inner surface, defined as the ratio of amplitude at the hot spot boundary at ignition to initial outer surface amplitude. The model for shell feedthrough at deceleration growth is very simplified. The feedthrough factor is $F_{ft} = (1 + 1/\eta)^{-l}$, where $\eta = r/\Delta r = 16$ is an average shell aspect ratio. As much of the deceleration is from a single strong shock, we used for the deceleration growth factor the RM instability expression $GF_d = 1 + \Delta v k A$, where the velocity change $\Delta v = 3.8 \times 10^7$ cm/s, the Atwood number $A = 0.5$, and a radius of 150 μm is used to obtain the mode number k from l. The total linear growth factor to the hot spot boundary is $GF_{hs} = GF_{abl} \times F_{ft} \times GF_d$. Note that the peak GF_{hs} is
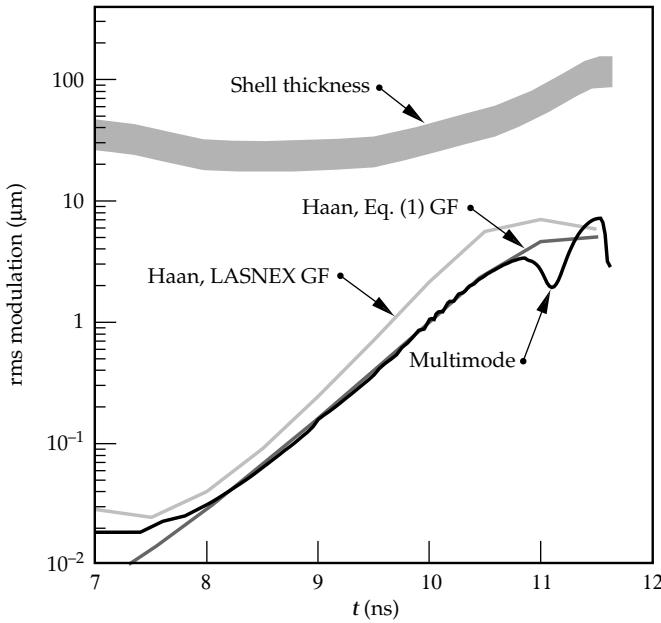
FIGURE 12. Ablation front rms modulation amplitude vs time postprocessed from a LASNEX 2D multimode simulation, from application of the Haan model using linear growth factors from Eq. (1), and from the Haan model using LASNEX single-mode simulations. The approximate shell thickness is also shown. (20-03-0397-0438pb01)
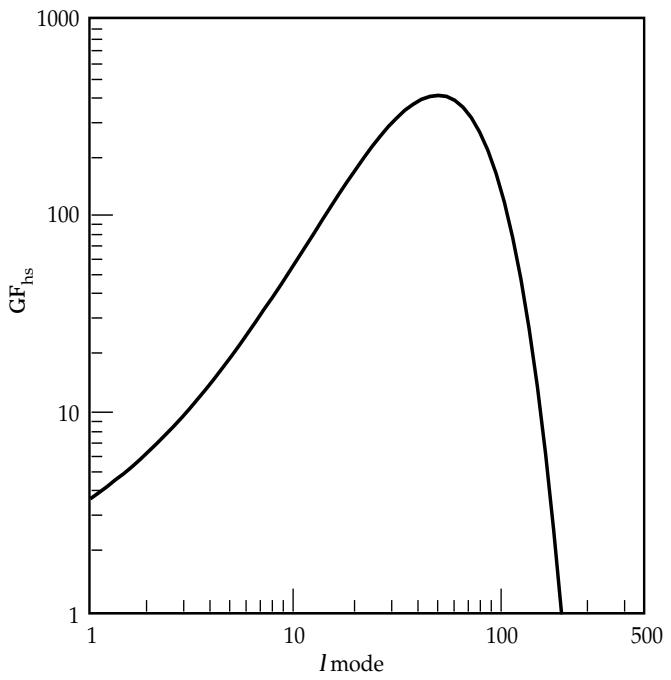
FIGURE 13. Hot spot growth factor vs mode number. The hot spot linear growth factor is the ratio of the amplitude on the outside of the hot spot at ignition time to the initial outer surface amplitude. (20-03-0397-0439pb01)

approximately equal to 400 at $l \approx 50$, which is smaller than the peak GF_{abl}, and peaks at a lower l, because the high modes feed through inefficiently.

Penetration of cold fuel into the hot spot at ignition time was assessed similarly to ablation front penetration. The outer surface initial amplitude spectrum from Figure 9 was multiplied by GF_{hs}; then, saturation effects were applied using the Haan model. Figure 14 shows the resulting hot spot amplitude spectrum. The degree of nonlinearity at the hot spot boundary is more moderate than was the case at the ablation front. The rms bubble amplitude with saturation effects is predicted to be 3.7 µm, while the amplitude resulting from linear growth factors would be 9.6 µm. The spike amplitude, which is 1.5 times larger, is about 10% of the hot spot radius. This analysis predicts that penetration into the hot spot is not great enough to impede ignition or to significantly reduce the capsule yield. We have not yet examined sensitivity to the DT ice roughness, which we assume to be similar to that for indirect drive.

Conclusions

We have examined direct-drive capsule designs that could achieve ignition in NIF. Beam geometry suitable for imploding direct-drive capsules will be provided by steering some of the beams from the indirect-drive configuration to an additional pair of rings near the waist of the chamber. Achievable beam pointing accuracy and power balance is predicted to give satisfactory uniformity to the implosions. Simulations of laser imprint have been used to set the beam smoothing requirements for direct drive. A laser bandwidth of 0.5 THz on the foot of the pulse is predicted to cause target perturbations comparable with those from a surface finish of ~10 nm.

RT growth factors at the ablation front reach several thousand for these designs, which have been tuned to a fuel adiabat of $\alpha = 3–4$, and growth factors for a low adiabat design are much larger. Ablation front modulations for the nominal design are predicted to become substantially nonlinear by peak shell velocity, but when saturation effects are included, the shell is predicted to remain intact. Multimode simulations confirm predictions of the Haan model on the effects of saturation. Similar analysis at the hot spot boundary predicts penetration of about 10% of the hot spot radius. These results give us a basis for believing that ignition can be achieved.

Notes and References

1. D. Eimerl, Ed., "Configuring the National Ignition Facility for Direct-Drive Experiments," Lawrence Livermore National Laboratory, Livermore, CA, UCRL-ID-120758 (1995).
2. R. Sawicki, Ed., "Advanced Conceptual Design Review," Lawrence Livermore National Laboratory, Livermore, CA, NIF-LLNL-96-065, internal document (1996).
3. S. W. Haan et al., *ICF Quarterly Report* **5**(4), 215–225, Lawrence Livermore National Laboratory, Livermore, CA, UCRL-LR-105820-95-4 (1995).
4. J. Meyer-ter-Vehn, *Nucl. Fusion* **22**, 561–565 (1982).
5. J. Lindl, *Phys. Fluids* **2**(11), 3933–4024 (1995).
6. J. D. Lindl and J. D. Kilkenny, *ICF Quarterly Report* **5**(4), 209–214, Lawrence Livermore National Laboratory, Livermore, CA, UCRL-LR-105820-95-4 (1995).
7. T. R. Boehly et al., *Rev. Sci. Instrum.* **66**, 508 (1995).
8. J. D. Sethian et al., *Fusion Technology* **26**(3), 717–721 (1994).
9. C. Yamanaka et al., *J. Quantum Electron.* **QE-23**, 1361 (1987).
10. C. P. Verdon, *Bull. Am. Phys. Soc.* **38**, 2010 (1993).
11. S. M. Pollaine and D. Eimerl, "Modal Analysis of Directly Driven ICF Targets," Lawrence Livermore National Laboratory, Livermore, CA, UCRL-JC-125731; submitted to *Nucl. Fusion Lett.* (1997).
12. Y. Kato, K. Mima, N. Miyanaga, S. Aringa, et al., *Phys. Rev. Lett.* **53**, 1057 (1984).
13. S. Skupsky et al., *J. Appl. Phys.* **66**, 3456 (1989).
14. J. E. Rothenberg, *Proc. Soc. Photo-Opt. Instrum. Eng.* **2633**, 634 (1995).
15. S. G. Glendinning et al., *Phys. Rev. E,* **54**, 4473 (1996).
16. S. V. Weber et al., "Simulations of Laser Imprint for Nova Experiments and for Ignition Capsules," Lawrence Livermore National Laboratory, Livermore, CA, UCRL-JC-124547; *Phys. Plasmas* **4**, 1978 (1997).
17. S. E. Bodner, *J. Fusion Energy* **1**, 221 (1981).
18. R. McEachern et al., *ICF Quarterly Report* **4**(1), 25–30, Lawrence Livermore National Laboratory, Livermore, CA, UCRL-LR-105820-94-1 (1994).
19. H. Takabe, L. Montierth, and R. L. Morse, *Phys. Fluids* **26**, 2299 (1983); H. Takabe, K. Mima, L. Montierth, and R. L. Morse, *ibid.* **28**, 3676 (1985).
20. J. Lindl, *Phys. Plasmas* **2**, 3933 (1995).
21. S. W. Haan, *Phys. Rev. A* **39**, 5812 (1989).
22. M. J. Dunning and S. W. Haan, *Phys. Plasmas* **2**, 1669, (1995).
23. S. W. Haan, *Phys. Fluids B* **3**, 2349 (1991).
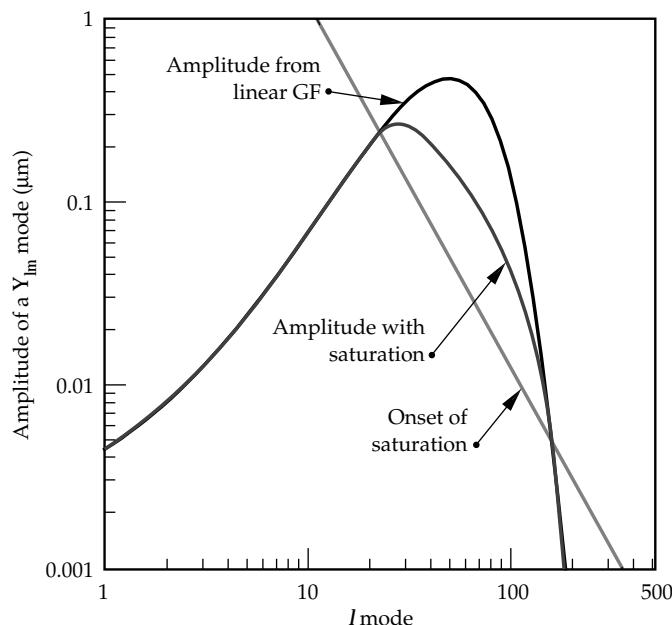
FIGURE 14. Modulation amplitude at the hot spot boundary at ignition time vs *l* mode from linear growth factors, corrected for saturation, and amplitude for onset of saturation. (20-03-0397-0440pb01)

Taking Average-Power, Diode-Pumped, Solid-State Lasers beyond the Nd^{3+} Ion

R. J. Beach

C. Bibeau

E. C. Honea

S. B. Sutton

Introduction

Diode lasers have long been strategically viewed as the ultimate replacement for flashlamp and arc lamp radiation sources used to pump solid-state lasers. Diode semiconductor lasers, first demonstrated in 1963, directly convert electric current into laser photons at a semiconductor junction.[1] Today, such lasers exhibit electrical-to-optical conversion efficiencies in excess of 50% (Ref. 2). By varying the composition of semiconductor materials during growth of the laser diode crystal, emission wavelength can be tuned over a broad range that covers many rare-earth-ion absorption features. The properties of high efficiency and flexible wavelength generation, along with dramatic improvements in performance and device reliability over the last several years, make laser diode arrays viable pump excitation sources for solid-state lasers using rare-earth-ion-doped crystalline gain materials.

The impact of semiconductor lasers on the development of solid-state lasers is most evident in the high-average-power, solid-state laser systems that are finding wide application in the field of materials processing. High-average-power, diode-pumped, solid-state lasers (commonly referred to as HAP DPSSLs) are best characterized as being performance-limited by thermal management issues associated with the solid-state laser crystal or glass. Thermal management issues can manifest themselves in several different forms, such as optical quality aberration of the output laser beam due to thermally induced optical refractive index variations in the crystal and, in extreme cases, fracture of the laser crystal due to buildup of excessive stress in the crystal.

The most common ion/host crystal combination used in HAP DPSSL systems today is Nd^{3+}:YAG (Ref. 3). Of all the well developed laser crystals that can be grown with rare-earth impurities, YAG (yttrium-aluminum-garnet) is the most robust in a thermal sense—i.e., it has the highest thermal conductivity and resistance to fracture. Thus, YAG is the crystalline host of choice for HAP DPSSLs. The wide use of Nd^{3+} as the active ion in nearly all HAP DPSSLs is associated with several fortuitous coincidences between the pump irradiance and wavelength required to efficiently excite it, and the pump irradiance and wavelength that can be conveniently developed by AlGaAs semiconductor 2D laser diode arrays. AlGaAs is the most mature of the semiconductor laser materials in use today.

Although the Nd^{3+} ion now dominates the HAP DPSSL field, the situation could change in the future because of continued technical developments in laser diode arrays. One such development, which has been actively pursued by the Lawrence Livermore National Laboratory's Laser Programs, is a diode array pump technology that enables pump power to be delivered at much higher irradiances than was previously possible.[4] Because many rare-earth-ion-based HAP DPSSLs are only practical if pumped at higher irradiances than the several kW/cm^2 possible with conventional scaled diode array technologies, this approach has opened a path to HAP DPSSLs that rely on ions other than Nd^{3+} as the lasant. We have demonstrated several such systems by taking advantage of the new flexibility in active lasant ion. Two of the systems, which lead the world for average power generation in their respective class, are our HAP Tm:YAG and Yb:YAG DPSSLs, which generate output radiation at 2 and 1 μm, respectively. These two laser systems, along with our end-pumping technology, are the focus of this article.

Scalable Diode End Pumping

The stumbling block in developing a scalable diode end-pumping architecture has been the intrinsically low effective radiance of the 2D emitting apertures constructed from a stack of laser diode array bars. Figure 1 shows the packaging technology developed within the Laser Programs, which uses a silicon, microchannel-cooled, diode-bar heatsink, and is designed to be stacked to build up large emitting apertures.[5] The low effective radiance of arrays results from the fact that the diode radiation is generated in a waveguide structure having at least one transverse dimension approximately equal to the radiation wavelength. The result is a beam of radiation with high divergence angle, up to 60° in one dimension, commonly referred to as the fast axis direction.

The key to overcoming low radiance in the fast axis direction of diode arrays is optical conditioning of the diode radiation from individual bars. A very-high-precision cylindrical microlens developed in our group does just that. The microlens can be produced in quantity at very low cost using a shaped-fiber-pulling technique.[6] Figure 2(a) is a cross-sectional view of one of our Si microchannel-cooled packages with a microlens in place.[7] The radiation, diverging at

(a)

(b)
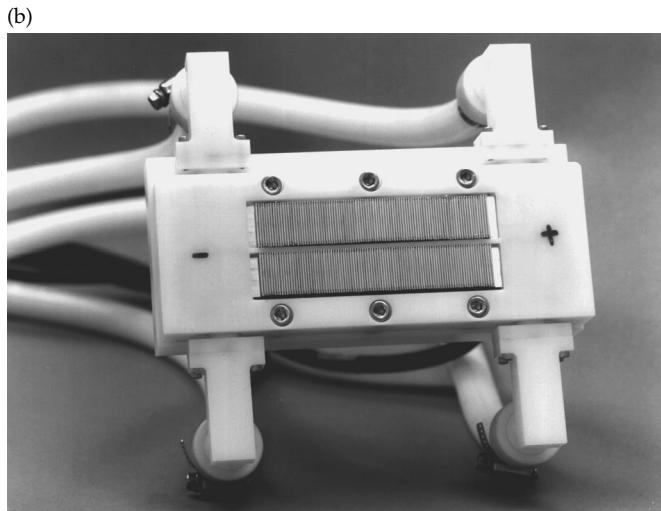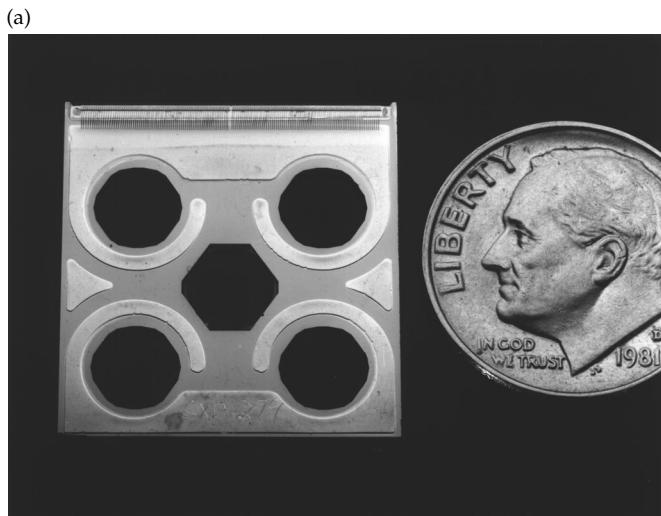
FIGURE 1. (a) Si, microchannel-cooled, laser diode module developed at LLNL. Dime shown for size comparison. (b) 2D stack of Si, microchannel-cooled, laser diode modules developed at LLNL. (99-50-0693-2304pb01)

(a)

(b)
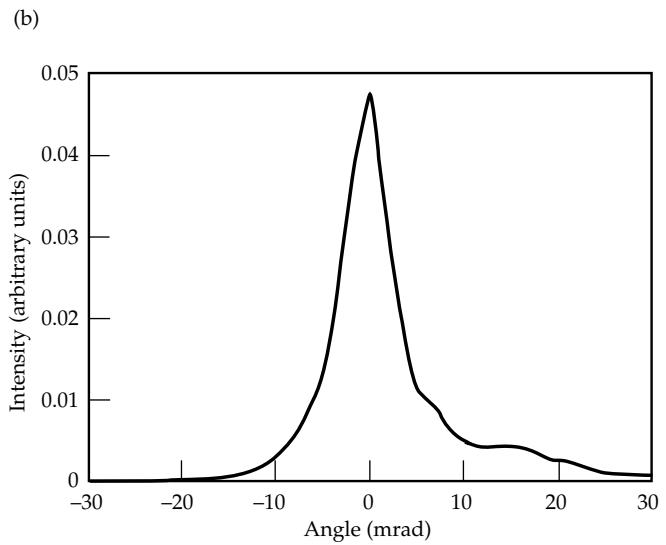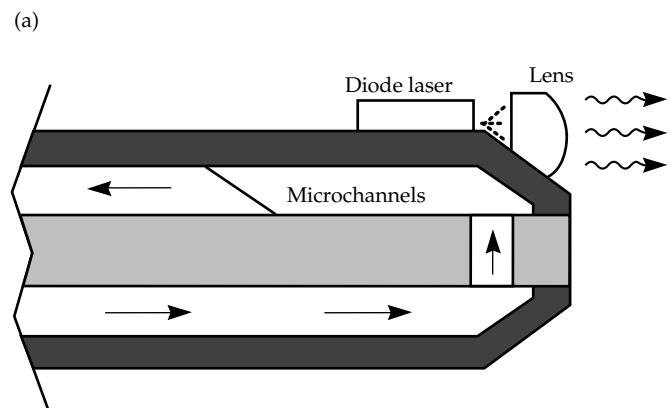
FIGURE 2. (a) Cross-sectional view of the LLNL silicon, microchannel-cooled, laser diode module with a cylindrical microlens. (b) Fast-axis, far-field intensity profile of a microlens conditioned package. (99-50-0595-1257pb02)

FIGURE 3. Schematic of a typical diode end-pumped and Q-switched laser. (99-50-0192-0153pb01)
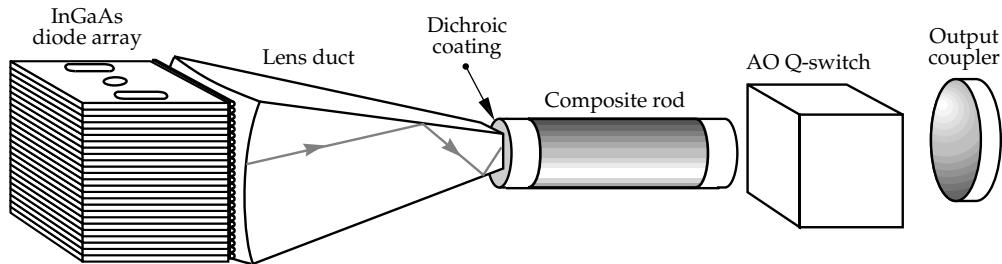
approximately 60° out of the bar, is collected and collimated by the cylindrical microlens mounted on the front of the package. After collimation, divergence of the diode light is reduced to ~0.6°. Using such microlens packages to build up large arrays by stacking leads to overall fast-axis divergences that are reduced by a factor of ~100 compared to values without microlens conditioning. This decrease in divergence, together with the accompanying ability to focus radiation to a smaller spot than if no conditioning had been performed, enables the output of radiation from large, 2D diode stacks to be efficiently delivered to the end of rod lasers. Figure 2(b) is a plot of the variation in angular intensity of a typical laser diode package fitted with a cylindrical microlens.

Figure 3 shows a typical end-pumped laser system using our scalable end-pumping architecture. Pump radiation from the microlens-conditioned stack of laser diode packages is delivered to the laser rod by a device called a lens duct. This optical device delivers the pump radiation to the end of the laser rod with high efficiency and increased intensity. Lens ducts are fabricated from transparent optical materials. They rely on lensing at their curved input face and total internal reflection (TIR) at their canted planar faces to channel the diode pump radiation to the laser rod.[8]

The best way to visualize the operation of a lens duct is to consider a plane wave normally incident on a spherically curved input surface of an optical material, as shown in Figure 4. With the radius of curvature

of the input face r and the index of refraction of the optical material n, the wave comes to a geometric focus at distance l into the material according to

$$l = r \frac{n}{n-1} \quad . \tag{1}$$

For an extended incoherent source, such as a microlens-conditioned, 2D, semiconductor laser diode array, there is no single, well defined geometric focal spot. Rather, the transverse dimensions of the focal region are determined by the angular divergence of the radiation's source function. Unfortunately, with today's microlens-conditioned laser diode arrays, the focal region can easily overfill the aperture of a laser rod for many of the practical laser systems of interest to designers. However, by reshaping the object in Figure 4 to resemble the lens duct in Figure 3, it is possible to deliver most of the diode radiation to the end of a laser rod within the constraints imposed by Etendue invariance.[9] Using Figure 4 as a guide, it might be expected that the optimum design of a lens duct configured to couple diode radiation into a circular laser rod would be to adjust its length l from Eq. (1) and cant in its planar sides so that it has a square output end that just inscribes the circular end of the laser rod to be pumped. In this fashion, many of the rays that would be delivered outside of the rod aperture, without the canting in of the planar sides, could be efficiently channeled to the laser rod by making high-angle (near grazing incidence) TIRs off the planar sides of the lens duct. We find that length l from Eq. (1) is not optimal. Rather, the length should be somewhat shorter,

$$l_d = (0.92) r_d \frac{n_d}{n_d - 1} \quad . \tag{2}$$

The length shortening comes about because the minimum transverse dimension of the focal region occurs somewhat before the geometrical focus shown in Figure 3 and predicted by Eq. (1).

To better understand the optimization of lens ducts, we have developed a geometric "method-of-images" analysis that allows transfer efficiency studies to be performed quickly and easily.[8] When modeling the
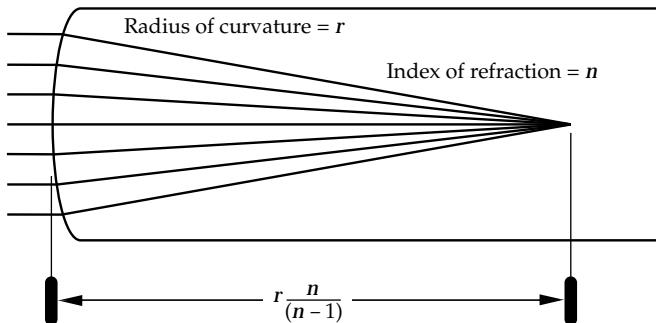
FIGURE 4. Focusing of a normally incident plane wave at a distance $rn/(n-1)$ into a material having an input radius of curvature r and index of refraction n. (99-50-0595-1258pb02)

(a) 2D construction
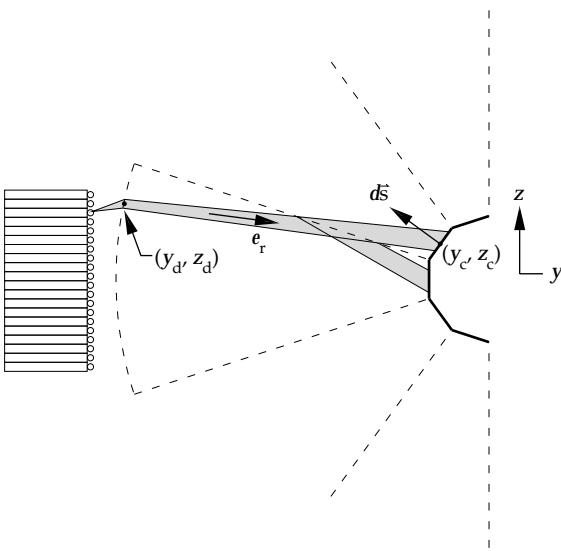
(b) 3D construction
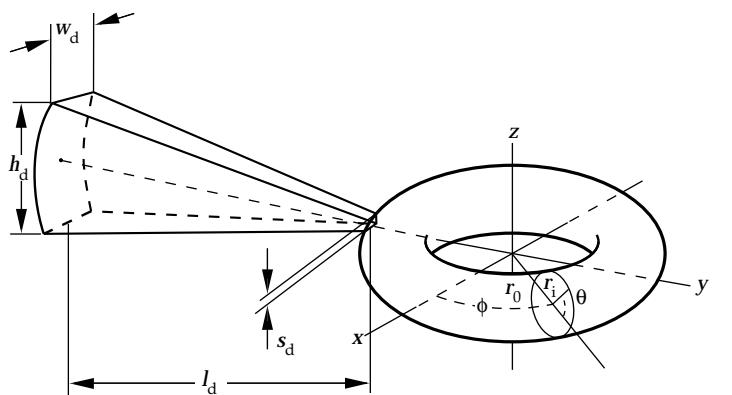
FIGURE 5. (a) 2D view of a lens duct showing the method-of-images construction used in calculating the transfer efficiency of radiation from a diode array into a laser rod. One bundle of rays bounces by total internal reflection off one of the canted planar sides of the lens duct; a related direct bundle of rays is also shown. (b) 3D lens duct and its method-of-images construction for a toroidal surface. (99-50-0595-1259pb02)

transfer efficiency of lens ducts, the front input surface is straightforward to treat because it acts as a simple lens. However, complications arise in modeling the TIR bounces made by pump light off the canted planar sides of the duct. Nevertheless, the TIR bounces can be easily treated by using a simple trick.

Figure 5(a) shows a semicircular surface representing the lens duct output face and the rod pump input face. This illustration was generated using our method-of-images construction (here, we ignore the complication that the semicircular surface is actually faceted). This construction consists of repeatedly reflecting the lens duct about its TIR surfaces as shown. When tracing a particular bundle of rays from the diode array to the end of the lens duct, instead of reflecting the rays at their intersection with one of the canted planar duct sides, the rays can be traced straight through to their intersection with the generated semicircle. To calculate the transfer efficiency of the duct, it is only necessary to track those rays that leave the diode array and propagate along straight-line trajectories that intersect the semicircle. For any such bundle of rays, the transfer efficiency associated with the bundle is determined by reflective losses at the duct input and output surfaces. A complete calculation of transfer efficiency involves a double integral over two surfaces: the diode-array-emitting aperture, and the semicircle representing the output surface of the lens duct.

An extension from two to three dimensions is straightforward. Figure 5(b) shows the 3D method-of-images construction in which a toroidal surface is generated instead of a semicircle. The double integral used to calculate the transfer efficiency is now over the diode array aperture and that section of the 2D toroidal surface that faces the diode aperture. This technique to calculate transfer efficiencies allows quick optimization of lens duct structures and has been useful in defining rules of thumb for their design.

Although our method-of-images construction is an elegant and simple way to calculate transmission efficiencies of a lens duct, it has several practical limitations. The most serious is that the technique is only applicable to lens ducts with output ends that are either square or rectangular. Although these were the shapes in our early work, we have recently used ducts with output ends shaped like octagons. An octagon-shaped output end increases the area of the output end of the duct that must fit within the circular boundary defined by the rod end. An octagon inscribed within a circle has 40% more area than a square inscribed within the same circle. Because we are interested in coupling large diode array apertures into the ends of small rods, and we must respect Etendue invariance or the brightness theorem, the ability to use an octagon-shaped duct output with its larger area reduces the radiance requirements on the diode array.

Figure 6 shows a lens duct with an octagon-shaped output end that is being used in the diode-pumped NIF prototype regenerative amplifier heads.[10] To model these more advanced lens ducts, we have developed a Monte Carlo ray-tracing code that takes a brute-force approach and simply traces rays from the

FIGURE 6. Photograph of a NIF regenerative amplifier head illustrating the compactness of a lens duct and laser diode array. (99-00-0595-1337pb02)

diode aperture through the system, including TIR bounces. Not only can we calculate transfer efficiencies with this code, but we can also calculate pump intensity profiles, both at the end of the lens duct and within the laser rod being pumped. Figure 7 shows the output from a code simulation run for the case of a lens duct used in our Yb:YAG system (discussed below). In addition to showing the pump light intensity profile at the end of the lens duct, this figure also shows the intensity profile at a selected cross-sectional plane within the laser rod, as well as the far-field intensity profile (or angular dependence) of the pump light that emerges from the duct.

After pump light emerges from the lens duct, it enters the laser rod through a dichroic optical coating designed to pass the pump light and act as a high

FIGURE 7. Output from our Monte Carlo ray-tracing code showing the diode-laser-array source function and the diode pump intensity at various locations in an end-pumped rod laser. (10-00-0797-1160pb01)
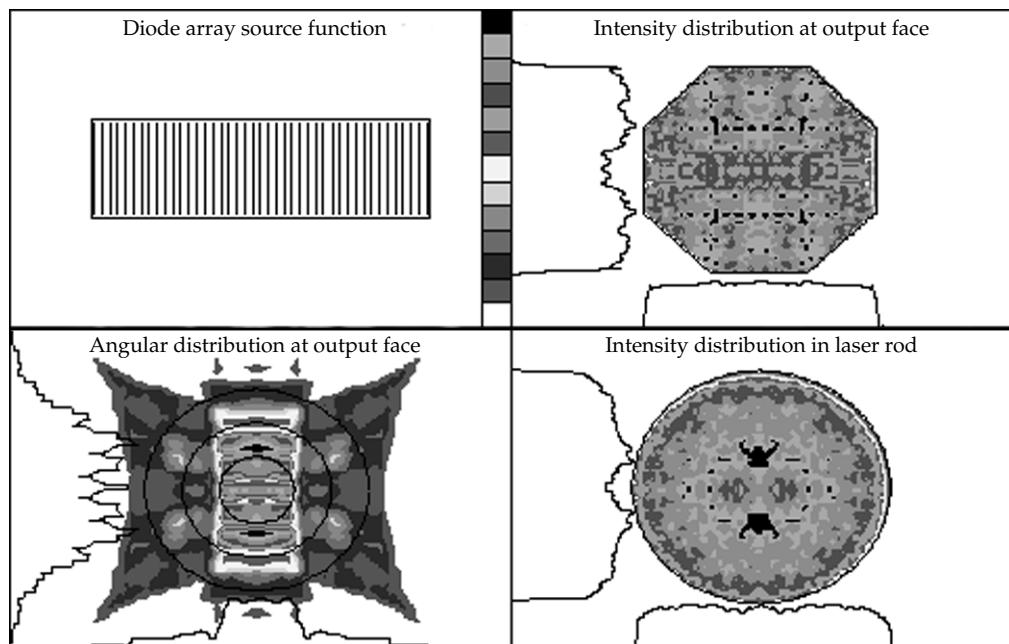
reflector for the laser radiation to be generated. Typically, the rods used in this approach have an optical polish along their barrel and are bathed in a coolant. Once pump light enters the laser rod, it is ducted along the length of the rod and is confined by TIR as it is absorbed. This approach allows the use of rods with light doping concentrations, compared to amounts required in a side-pumped configuration, since the available absorption paths are lengthened in the end-pumping approach. Light doping, in turn, allows the thermal load to be distributed over the entire length of the laser rod, enabling effective thermal management of the gain medium.

One problem in the practical realization of such end-pumped systems is the very high pump-power irradiances incident on the end of the laser rod. For example, in our HAP Yb:YAG DPSSL, the pump irradiance is up to 30 kW/cm^2 on the pump input end of the rod. As a result of high pump irradiances and the generated thermal power density, rod fracture at the pump input end was one of the early, but persistent, problems we encountered in developing our end-pumped system. Other practical problems are associated with cooling the end of the laser rod. Typically, the last few millimeters of a rod end cannot be effectively cooled by the water jacket around the rest of the rod because of the space required for o-ring seals. To address this thermal management problem at the pump input end of the laser rod, we use nonabsorbing or undoped rod sections that are bonded to the doped ends of the laser rod.

Figure 8 shows calculated temperature isotherms in two rods. Figure 8(a) is an ordinary, uniformly doped rod; Figure 8(b) is a composite rod with an undoped end cap. Clearly evident is an alteration of the temperature field near the end of the rod, which has two important effects. The first is related to the sensitivity of the transmission/reflection properties of dichroic coatings to temperature. In the composite rod, the coating temperature is nearly spatially uniform and very near the coolant temperature. The second benefit is associated with surface thermal stresses. The presence of temperature gradients in the rod leads to thermally induced stresses. Generally, the stresses are tensile on the rod surfaces and compressive inside the rod. Tensile stresses on the rod surfaces, where defects may be present, can lead to fracture of the laser rod. The end cap in the composite rod reduces temperature gradients near the rod end faces, thereby reducing tensile stresses and the potential for thermal fracture from face defects. In practice, we have found that such composite laser rods fabricated using a diffusion-bonding technology are extremely beneficial at enhancing the performance of our laser systems.[11] In fact, we now routinely run our systems at average powers that would not be possible without undoped end caps because of rod fracture.

Tm³⁺:YAG HAP DPSSL

The 2-μm radiation produced by the ³F₄–³H₆ transition of Tm³⁺ has many practical applications in medical, commercial, and military technologies. The strong absorption of radiation at this wavelength by water and human tissues is attractive for laser surgery, and the low atmospheric absorption and eye-safe properties make this system useful for materials processing, range finding, remote sensing, and other applications. In addition, 2-μm lasers are useful for pumping mid-infrared optical parametric oscillator materials, for which 1-μm radiation cannot be used. Such applications, together with the potential for efficiency, compactness, and ruggedness, have driven our interest in and the development of a HAP DPSSL Tm:YAG system.[12–18]

Because of the quasi-three-level laser properties of Tm³⁺, intense pump sources are required for efficient operation. A major advantage of 2-μm Tm lasers is the ability to use AlGaAs diodes operating around 0.8 μm as the pump source while maintaining high efficiency and low thermal loading. This is because Tm³⁺ exhibits a beneficial two-for-one cross-relaxation process at high doping levels. The cross-relaxation process can lead to efficient laser operation, as demonstrated by measured slope efficiencies up to 59%, considerably larger than the 39% maximum expected from the quantum defect alone.[19]

(a)	(b)
Conventional	Undoped ends
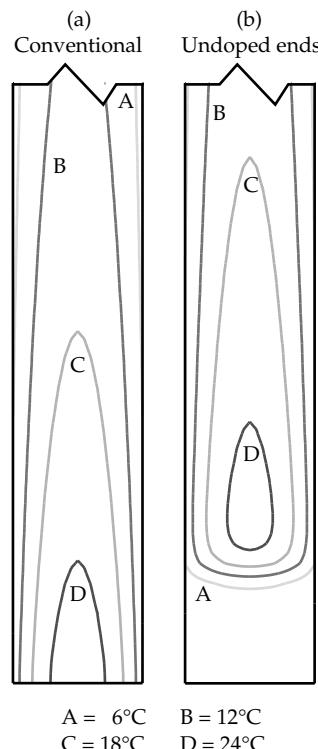
FIGURE 8. Modeled temperature profiles of a laser rod (a) with conventional, uniform doping and (b) with an undoped end cap. (70-00-0896-1881pb01)

A = 6°C   B = 12°C
C = 18°C   D = 24°C

Although the two-for-one pumping efficiency requires high doping levels, lower Tm^{3+} concentrations can be beneficial in distributing the thermal load over a longer length of the rod (for end-pumping as used here), and for reducing ground-state reabsorption losses at the laser wavelength. Therefore, a good laser design must integrate several factors, including sufficiently high dopant concentration, to obtain the best overall laser performance. Our Tm:YAG laser has generated 115 W of continuous-wave (CW) output power at 2.01 μm (multimode).[20] To our knowledge, this is the highest CW power operation achieved to date with a diode-pumped, 2-μm-wavelength laser.

Figure 9 shows the relevant components of the end-pumping technology. The pump source consists of a 2.5-cm-high, 23-module stack of microlens-conditioned, 1-cm, laser diode bars mounted on silicon microchannel coolers and producing up to 460 W of CW power reliably. The measured combined efficiency of the microlenses and lens duct is 78%, resulting in powers of up to 360 W delivered to the laser rod. The lens duct tapers to an octagonal end face to match the laser rod, with a delivered power density of more than 5 kW/cm^2.

The 3-mm-diameter by 55-mm-long laser rod has a polished barrel finish over its length, allowing pump light to be efficiently directed down the length of the rod while being confined by TIR. To decrease thermal stresses at the rod ends, 5-mm-long undoped YAG end caps are diffusion bonded to each end of the central, 45-mm-long, Tm-doped section. The pump end of the rod is coated to obtain high reflectivity at 2.01 μm (the laser wavelength) and high transmission at 0.8 μm (the pump wavelength) over wide angles. The output end of the rod has a coating that has high transmission at 2.01 μm and is a high reflector at 0.8 μm, allowing the pump light to be effectively double-passed up and down the laser rod.

For the end-pumping geometry used here, thermal management issues must be balanced with Tm concentration requirements for efficient cross relaxation. The cross-relaxation process between Tm^{3+} ions, where an ion excited to the $^3H_4$ pump level results in two ions excited to the $^3F_4$ upper laser level, requires high Tm doping levels with typical laser designs using concentrations on the order of a few percent. To incorporate the high doping levels needed for efficient cross relaxation, we use so-called "wing pumping" at 805 nm rather than the peak $^3H_6$–$^3H_4$ absorption feature at 785 nm. This distributes the pump light absorption over a longer rod length, improving pump and thermal dissipation uniformity. A further advantage of the 805-nm pump wavelength is reduced Al concentration in the AlGaAs diodes, increasing output performance and reliability relative to the 785-nm diodes that would be used to pump the Tm^{3+} at the peak of its $^3H_6$–$^3H_4$ absorption.

FIGURE 9. Photographs and sketch of 2-μm Tm:YAG laser. (70-15-0294-0287pb04)

(a)

(b)

(c)

(d)

Output coupler

Rod assembly

Duct assembly

Diode array

Water connector

Electrical connector

3.063"

9.750"
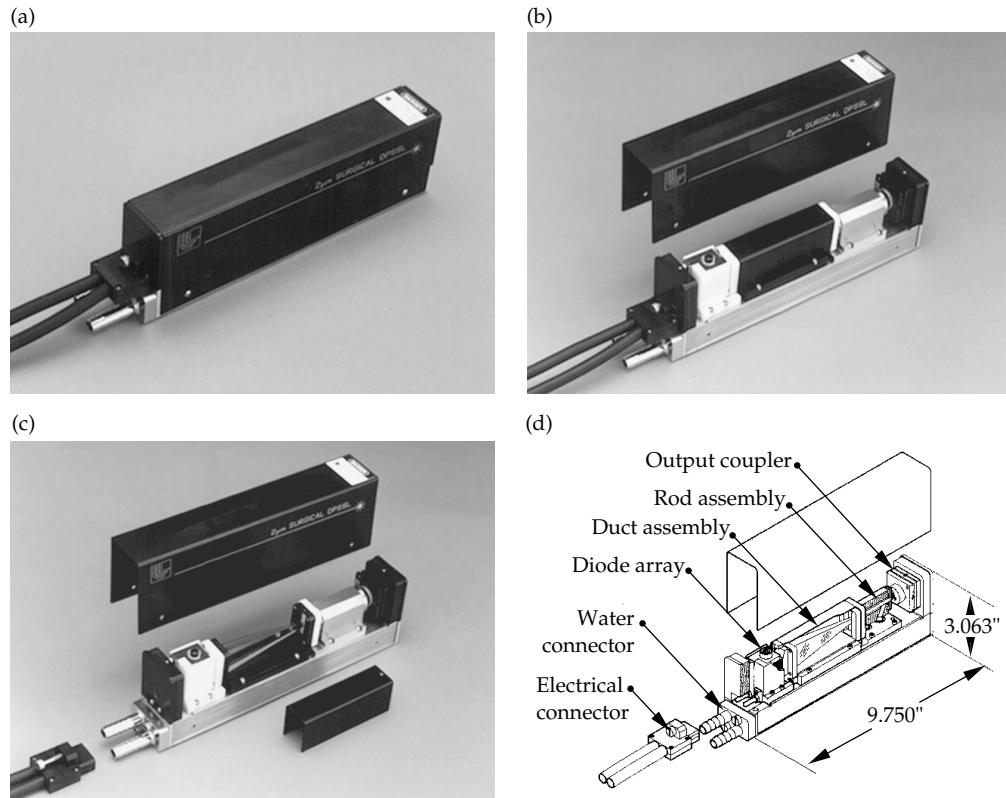
Figure 10 shows laser power vs diode pump power delivered to the Tm:YAG laser rod for 2% and 4% doping levels, obtained with a 95.2%-reflective, 50-cm concave output coupler and a cavity length of 6 cm. The output power for the 2% Tm rod increases up to 115 W for a delivered pump power of 360 W; whereas the 4% rod shows a significantly higher threshold and a maximum power of 74 W. Laser power measurements were also obtained with flat output couplers of various reflectivities, although the maximum power observed (again with the 2% rod) was approximately 10% less than with the concave reflector. The slope efficiencies in Figure 10 are similar for the two doping levels, with the 2% rod yielding an intrinsic slope efficiency of 40% relative to pump power delivered to the rod. A small reduction in slope efficiency occurs at the highest powers, possibly due to thermal effects.

T_{cav} = 0.997. Each value is near the maximum expected, consistent with the high power and efficient operation achieved. Note that η_{QY} is still quite high, although the Tm doping level is only 2%, whereas the high value of η_{mode} reflects the multiple transverse laser modes that nearly fill the rod cross section.

From Figure 11, we see that the model generally overestimates the threshold power. The overestimation is possibly due to nonuniform pump light across the rod cross section because threshold could be reached for some fraction of the rod before the entire rod had sufficient gain to overcome losses. The slope efficiencies are relative to the pump power delivered to the rod, although the fraction of pump energy absorbed, f_{abs}, is estimated to be only 77% for the 2% Tm rod. Therefore, the slope efficiency relative to absorbed pump power is 52% for the 2% Tm data shown in Figure 11, which compares favorably with values reported for lower-average-power systems.[16]

Figure 12 shows the M^2 beam-quality factor against pump power, which is proportional to the square root of the delivered pump power. This observation has been analyzed in terms of a gradient lens model of

FIGURE 10. Tm:YAG laser CW output power at 2 μm vs pump power delivered to the laser rod for 2% and 4% Tm-doped rods. The output coupler is concave with a 50-cm radius of curvature and a reflectivity at 2.01 μm of 95.2%.   (10-00-0797-1158pb01)

We can compare measured laser performance with that predicted by a quasi-three-level laser model developed by our group.[21] By measuring laser power as a function of input power for various output coupler reflectivities, we can determine values for T_{cav}, the one-way cavity transmission, η_{mode}, the mode-fill efficiency, and η_{QY}, the quantum yield, which are difficult to obtain from more direct measurements. Figure 11 shows a set of measurements for the 2% Tm rod, with laser thresholds and slope efficiencies plotted vs output coupler reflectivity. The measurements are compared to a simultaneous least-squares fit using the model to determine η_{mode} = 0.92, η_{QY} = 1.88 and

FIGURE 11. Comparison between best-fit model predictions and measured (a) laser threshold and (b) slope efficiency vs output coupler reflectivity for the 2% Tm-doped rod.   (10-00-0797-1159pb01)
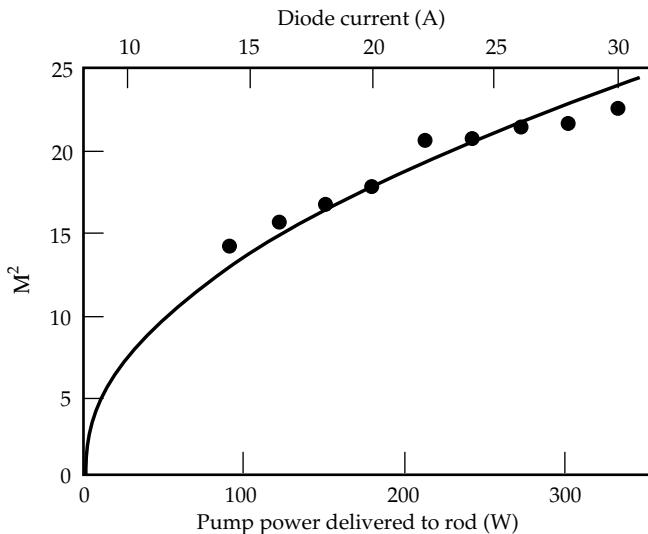
FIGURE 12. Plot of M^2 vs laser diode pump power. (10-00-0797-1157pb01)

thermal focusing in the laser rod, and the expectation that the fundamental beam mode scales as $P^{1/4}$. The model appears to give the correct scaling behavior; however, the measured scaling factor based on the model is 3.1 times greater than the calculated value. Although the measured beam quality is far from diffraction-limited, there are a broad range of applications for which M^2 values of 20 and less are useful.

Yb^{3+}:YAG HAP DPSSL

The Yb^{3+}:YAG system we are presently developing is particularly attractive to many applications now using Nd^{3+}:YAG because the Yb^{3+} ion only generates about one-third the heat of an excited Nd^{3+} ion. The lower heat generation is due predominantly to the lower Stokes shift, or quantum defect, between pump and laser photon energy of the Yb^{3+} ion compared to the Nd^{3+} ion. Because system efficiency of a Yb^{3+}-based system is expected to be approximately the same as that of a Nd^{3+}-based system, the thermal management problems in the Yb^{3+} system should be substantially reduced from those in Nd^{3+} systems of comparable power. The reduced thermal heat load of Yb^{3+} should ultimately allow HAP DPSSL systems with better beam quality and higher average power than are now possible with Nd^{3+}.

In addition to these thermal management issues, the broad pump line at 940 nm makes the Yb:YAG system highly suitable for diode pumping using InGaAs diodes, which are more robust than the AlGaAs diodes used to excite Nd:YAG at approximately 808 nm. Recent results from lifetime tests on LLNL-fabricated 940-nm diode packages have shown projected lifetimes of more than 10,000 hours (with 30% degradation)

when operated at 30 W/cm (Ref. 22). Another advantage of Yb:YAG is that the 940-nm absorption feature is approximately 10 times broader than the 808-nm absorption feature in Nd:YAG; therefore, the Yb:YAG system is less sensitive to diode wavelength specifications. These advantages of Yb over Nd-based systems, together with a broad spectrum of laser applications, have prompted the Laser Programs' interest in developing a Yb^{3+}:YAG HAP DPSSL.[23]

Figure 3 shows our end-pumped Yb:YAG laser system, which is similar to the Tm:YAG system previously described. The pump source consists of a 44-bar stack of 1.5-cm-long InGaAs laser diode bars packaged on microchannel coolers. As in the Tm:YAG laser, the diode light is first conditioned by a shaped cylindrical microlens directly mounted on each diode package, and then delivered to the composite Yb:YAG rod via a lens duct. The Yb:YAG composite rod is coated at the pump end of the rod with a dichroic coating having high reflectance at 1030 nm and high transmission at 940 nm, thus allowing one end of the rod to perform as a flat, high reflector for the laser cavity. A simple, broadband antireflection coating was placed on the opposite or output end of the rod.

We have demonstrated the Yb:YAG laser in both CW and Q-switched operation. The doping concentration for our CW experiments was 0.44%, and the rod diameter was 2 mm with an overall composite length of 60 mm. The laser crystal was housed in a simple aluminum cooling jacket designed to flow coolant along the barrel of the rod. The rod temperature was maintained near 0°C by using a mixture of water and propanol. Approximately 63% of the pump light was transmitted through the microlenses and lens duct into the laser rod. Of the light transmitted into the rod, approximately 80% was absorbed within the laser rod. Figure 13 shows the Yb:YAG CW output power against the power generated at the laser diode array. The maximum CW output power of 434 W more than doubles the average power generated in this type of system by any other research group at this time. Based on our quasi-three-level models, we anticipate generating more than 500 W in the near future with improved optical coatings on the laser rods.

Our Yb:YAG system distinguishes itself from comparable average-power Nd:YAG systems in the output beam quality that is generated. Typically, Nd:YAG rod laser systems in this average power class produce output beams with M^2 values of 30 or larger. Using a conventional stable resonator, the measured M^2 of the Yb:YAG system was 6.5 at an output power level of 190 W. The predominant reasons for better beam quality with the Yb:YAG system are the lower thermal power generated by Yb compared to Nd, and the much smaller rod diameter of the Yb:YAG system relative to a Nd:YAG system. The smaller rod diameter
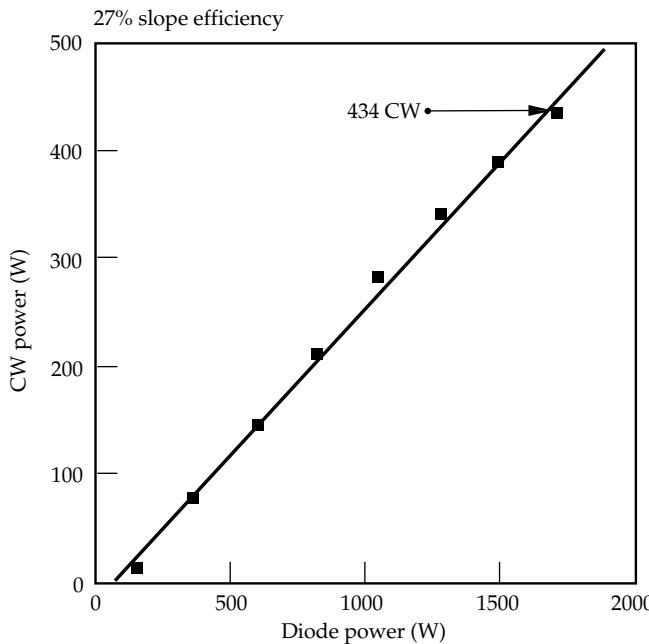
Figure 13. Yb:YAG laser output power at 1 µm vs pump power delivered to the laser rod.   (10-00-0797-1156pb01)
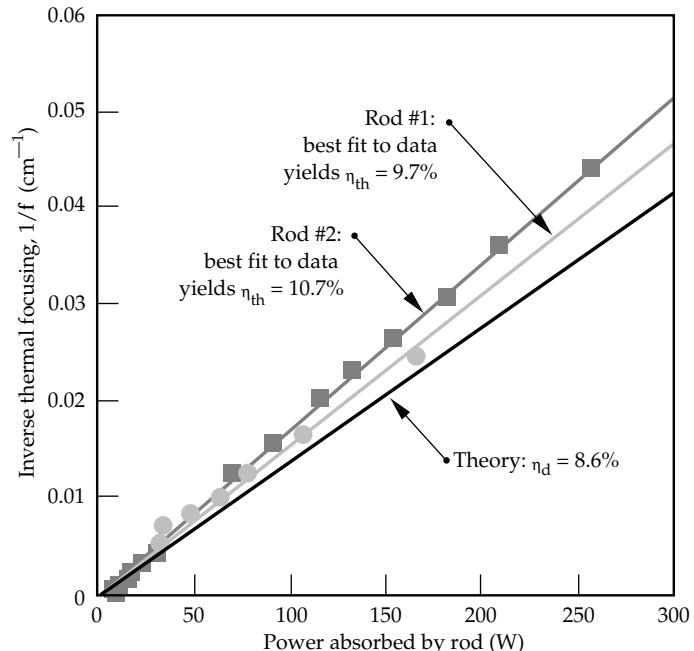
Figure 14. Inverse thermal focusing in Yb:YAG laser rod as a function of absorbed pump power.   (10-00-0797-1155pb01)

essentially limits the number of transverse modes the Yb:YAG laser can support.

To document the thermal-generation properties of the Yb:YAG system, we measured thermal lensing and stress-induced birefringence. Measured thermal-generation rates are in close agreement with values expected using the quantum defect value of 8.6% for Yb:YAG. A probe beam at 632 nm was used to measure the thermal lensing of the laser rod. Two different rods were used in the measurements shown in Figure 14. The best fit to the data yielded an average thermal efficiency factor of 10.2%, where thermal efficiency η_{th} is defined as the percent of pump power dissipated as heat into the rod. Measurements of stress-induced birefringence were made using a 1.03-µm probe beam. The best fit to the data yielded a thermal efficiency factor of 8.74%. The average result from both types of measurements gives η_{th} = 9.5%.

We also generated Q-switched pulses at high repetition rate using an acousto-optic Q-switch. In this work, the laser rod was pumped continuously, as in the CW operation of the system, and the acousto-optic Q-switch was gated off at various repetition rates between 5 and 20 kHz. To date, our best result is an average output power of 285 W at 10 kHz. Based on a Q-switched, quasi-three-level model we have developed, we expect to achieve more than 300 W of Q-switched power with better-performing optical coatings on the laser rod.[24] Under such conditions, the resulting Q-switched pulse width was 26 ns. This Yb:YAG Q-switched pulse width is substantially shorter than values demonstrated with comparable Nd systems and is presently being used to investigate the feasibility of high-average-power, external-cavity harmonic generation.

Summary

We are continuing to develop high-average-power, diode-array, end-pumping technology in an effort to move HAP DPSSL systems beyond the Nd^{3+} ion. To date, most of our work has concentrated on two systems that are perceived to have near-term applications. The first system is based on the Tm^{3+} ion and generates output radiation at 2 µm. To date, we have demonstrated more than 100 W of CW output from a compact, efficient, and reliable diode end-pumped Tm:YAG laser system. Using a quasi-three-level laser model, we find that the cross relaxation in Tm:YAG can be quite efficient at a doping level of 2%. The use of this relatively low doping level, while maintaining efficient cross relaxation, is beneficial to thermal management issues necessary for scaling to high average powers. The second system is based on the Yb^{3+} ion and generates output radiation at 1 µm. To date, we have demonstrated up to 434 W of CW power from an end-pumped Yb:YAG laser system. In addition, at a 10-kHz repetition rate, we have produced up to 285 W of Q-switched power at a 26-ns pulse length. The short pulse widths and better beam quality that can be generated with the Yb:YAG system, relative to comparable average-power Nd:YAG systems, highlight the unique capabilities of the Yb:YAG system.

Acknowledgments

We wish to acknowledge many useful conversations with Steve Payne, Bill Krupke, Rich Solarz, Mark Emanuel, Jay Skidmore, Ralph Page, John Crane, Isaac Bass, Gaylon Erbert, Chris Marshall, and Howard Powell, all of LLNL, during the course of this work. We also acknowledge the expert laser technical assistance of Scott Mitchell and Joel Speth. In addition, we thank Steve Mills, Dennis Maderas, John Lang, Barry Freitas, Chuck Petty, Vic Sperry, Evert Utterback, Kathy Reinhardt, and Larain Dimercurio, all of LLNL, in carrying out various portions of the work reported. We also thank Dr. Helmuth Meissner of ONYX Optics for fabricating the composite laser rods with diffusion-bonded end caps, Ralph Hucheson of Scientific Materials for growing the YAG crystals used in our lasers, and Karl George of Quality Thin Films for supplying the optical coatings used on our laser rods.

Notes and References

1. N. G. Basov, O. N. Krokhin, and M. Popov, "Production of Negative Temperature States in P–N Junctions of Degenerate Semiconductors," *J.E.T.P.* **40**, 1320 (1961).
2. L. J. Mawst et al., "8-W Continuous Wave Front-Facet Power from Broad-Waveguide Al-Free 980-nm Diode Lasers," *Appl. Phys. Lett.* **69**, 132 (1996).
3. W. Koechner, *Solid-State Laser Crystals* (Springer-Verlag, Berlin, 1976).
4. R. Beach et al., "Scaleable Diode-End-Pumping Technology Applied to a 100-mJ Q-Switched Nd³⁺:YLF Laser Oscillator," *Opt. Lett.* **18**, 1326–1328 (1993).
5. R. Beach et al., "Modular Microchannel Cooled Heatsinks for High Average Power Laser Diode Arrays," *IEEE J. Quant. Elect.* **28**, 966–976 (1992).
6. J. Snyder, P. Reichert, and T. Baer, "Fast Diffraction-Limited Cylindrical Microlenses," *Appl. Opt.* **30**, 2743–2747 (1991).
7. R. Beach et al. "Applications of Microlens-Conditioned Laser Diode Arrays," *SPIE* **2383**, 283–297 (1995).
8. R. Beach, "Theory and Optimization of Lens Ducts," *Appl. Opt.* **35**, 2005–2015, (1996).
9. W. T. Welford and R. Winston, *High Collection Nonimaging Optics* (Academic Press, New York, 1989).
10. J. K. Crane et al., *Description and Performance of the Preamplifier for the National Ignition Facility (NIF) Laser System*, UCRL-JC-124517, Lawrence Livermore National Laboratory, Livermore, CA (preprint).
11. ONYX Optics, 6546 Sierra Lane, Dublin, CA 94568, Tel: 510-833-1969.
12. G. J. Kintz, R. Allen, and L. Esterowitz, *Digest of Conference on Lasers and Electro-Optics*, paper FB2 (Optical Society of America, Washington, D.C., 1988).
13. P. Suni and S. Henderson, *Opt. Lett.* **16**, 817–819 (1991).
14. T. S. Kubo and T. J. Kane, *IEEE J. Quant. Elec.* **28**, 1033–1040 (1992).
15. D. C. Shannon, D. L. Vecht, S. Re, J. Alonis, and R. W. Wallace, *Proc. SPIE* **1865**, 164–173 (1993).
16. G. Rustad, H. Hovland, and K. Stenersen, *OSA Proceedings on Advanced Solid State Lasers*, S. Payne and C. R. Pollock, Eds., *Opt. Soc. Amer.* **15**, 315–318 (1996).
17. S. R. Bowman et al., *OSA Proceedings on Advanced Solid State Lasers*, A. Pinto and T. Y. Fan, Eds., *Opt. Soc. Amer.* **15** (1993).
18. I. F. Elder and M. J. P. Payne, *OSA Proceedings on Advanced Solid State Lasers*, S. A. Payne and C. R. Pollock, Eds., *Opt. Soc. Amer.* **15**, 319–325 (1996).
19. R. C. Stoneman and L. Esterowitz, *Opt. Lett.* **15**, 486–488 (1990).
20. E. C. Honea et al., *High Average Power Tm:YAG Diode-Pumped Solid-State Laser*, UCRL-JC-125109, Lawrence Livermore National Laboratory, Livermore, CA (preprint).
21. R. Beach, "CW Theory of Quasi-Three-Level End-Pumped Laser Oscillators," *Optics Comm.* **123**, 385–393 (1995).
22. M. A. Emanuel, J. A. Skidmore, and R. J. Beach, "High-Power Laser Diodes at Various Wavelengths," *SPIE Photonics West 1997 Proc.*, paper 3001-1 (1997).
23. H. Bruesselbach and D. Sumida, "69-W-Average-Power Yb:YAG Laser," *Opt. Lett.* **21**, 480–482 (1996).
24. R. Beach, "Optimization of Quasi-Three-Level End-Pumped Q-Switched Lasers," *IEEE J. Quant. Elec.* **31**(9), 1606–1613 (1995).

Laser-Beam Deflection Induced by Transverse Plasma Flow

D. E. Hinkel

E. A. Williams

C. H. Still

Introduction

Recent experiments[1,2] conducted at Lawrence Livermore National Laboratory (LLNL) using the Nova laser show anomalous deflections of the laser beam in the plasma. In gas-filled hohlraum experiments,[1] the laser spot on the hohlraum wall is 100–150 μm closer to the laser entrance hole (LEH) than in empty hohlraum experiments. This corresponds to a beam deflection of roughly 6° if the deflection occurs near the LEH. In a series of exploding foil experiments,[2] intensity-dependent deflection of a transmitted probe beam is observed.

Simulations by the hydro code LASNEX,[1,3] which accurately model empty hohlraum experiments, do not show beam deflection in gas-filled hohlraums. Neither whole-beam refraction nor differential laser absorption accounts for the experimental results (because the laser makes an angle of 50° with the hohlraum axis, the path length of the innermost portion of the laser beam is longer than that of the outermost portion). In this article, we show that, in the hohlraum plasma, effects of flow transverse to the laser propagation direction on (1) filamentation and (2) forward Brillouin scatter (FBS) can account for this anomalous deflection.

Model for Transverse-Flow–Induced Beam Deflection

Solution of the steady-state filamentation dispersion relation shows that filaments grow in a direction tilted downstream to the initial beam direction.[4] This mechanism was recently proposed[5] as a cause of beam deflection in the aforementioned hohlraum experiments.

In this article, we examine a group of related mechanisms for laser beam deflection. In the presence of a transverse plasma flow, ponderomotively (or thermally) created density depressions form *downstream* from the laser beam's high-intensity regions. Light refracted into the lowered density is thus deflected in the direction of the flow. We use the numerical model F3D to quantify these mechanisms.[6] To illustrate the physics, a highly simplified, steady-state model is used,

$$\left(2ik_0 \frac{\partial}{\partial z} + \nabla_\perp^2 \right)\psi = \frac{\omega_{pe}^2}{c^2}\delta n\, \psi \tag{1a}$$

$$\left[M\frac{\partial}{\partial x}\left(M\frac{\partial}{\partial x} + \kappa \right) - \nabla_\perp^2 \right]\delta n = \left(\frac{v_0}{v_e} \right)^2 \nabla_\perp^2 |\psi|^2 \quad . \tag{1b}$$

Equation (1a) describes the light wave amplitude ψ (vector potential scaled to its mean value) in the paraxial approximation, scattered by the fractional density perturbations δn. Equation (1b) gives the steady-state density response to the ponderomotive force. In these equations, the light is propagating in the $\mathbf{e}_z$ direction, and the density fluctuations propagate only in the transverse direction. Here, k_0 is the vacuum wave number, n_0 is the unperturbed plasma density, ω_{pe} is the electron plasma frequency, and c is the speed of light. Also, $M \equiv u/C_s$ is the Mach number of the flow u in the x direction, with C_s the sound speed, κ the spatial damping rate of ion acoustic waves, v_0 the quiver velocity of an electron in the mean light wave field, and v_e the electron thermal velocity. The density response calculated by F3D in steady state,[6] when thermal effects are neglected, is that given by Eq. (1b). In highly collisional plasmas, thermal effects supplement the ponderomotive potential, thereby increasing filamentation, and might be expected to similarly increase deflection.

Equations of motions for the beam centroid and width can be derived by taking intensity-weighted moments of Eq. (1a). Defining

$$\langle \mathbf{x}_\perp \rangle \equiv \int \psi^* \mathbf{x}_\perp \psi \, d^2 x_\perp , \quad \langle \mathbf{k}_\perp \rangle \equiv -i \int \psi^* \nabla_\perp \psi \, d^2 x_\perp$$

etc., we obtain

$$\frac{\partial^2}{\partial z^2} \langle \mathbf{x}_\perp \rangle = -\frac{\omega_{pe}^2}{2 k_0^2 c^2} \langle \nabla_\perp \delta n \rangle, \tag{2a}$$

$$\frac{\partial^2}{\partial z^2} \left\langle \left(\mathbf{x}_\perp - \langle \mathbf{x}_\perp \rangle \right)^2 \right\rangle = \frac{2}{k_0^2}$$

$$\times \left\{ \left\langle \left(\mathbf{k}_\perp - \langle \mathbf{k}_\perp \rangle \right)^2 \right\rangle - \frac{\omega_{pe}^2}{c^2} \left\langle \left(\mathbf{x}_\perp - \langle \mathbf{x}_\perp \rangle \right) \cdot \left(\nabla_\perp \delta n \right) \right\rangle \right\}. \tag{2b}$$

Equation (2b) is analogous to Eq. (11) of Ref. [7]. Similar equations have also been derived in Refs. [8] and [9].

In Eq. (2a), the transverse density gradient refracts the light toward regions of lower electron density. In Eq. (2b), the beam width is determined by the competition between diffraction [first term on right-hand side (RHS) of Eq. (2b)] and self-focusing [second term on RHS of Eq. (2b)].

When the Fourier transform of Eq. (1b) is substituted into Eq. (2a),

$$\frac{\partial^2 \langle \mathbf{x}_\perp \rangle}{\partial z^2} = -\frac{i \omega_{pe}^2 v_0^2}{2 k_0^2 c^2 v_e^2}$$

$$\times \int \frac{d^2 k_\perp \left| \tilde{\psi}(k_\perp) \right|^2 \left| \tilde{\psi}(-k_\perp) \right|^2 k_\perp^2 \mathbf{k}_\perp}{k_x^2 (M^2 - 1) - i \bar{\kappa} M k_\perp k_x - k_y^2}, \tag{3}$$

where we have defined the wave amplitude damping decrement $\bar{\kappa} \equiv \kappa / k_\perp$. (Setting $\bar{\kappa}$ = constant approximately represents Landau damping.) The y component of the above equation yields $\langle \partial^2 y / \partial z^2 \rangle = 0$, as the integrand is an odd function of k_y. In the absence of flow, then, the beam is not deflected.

In the x direction, for subsonic flow ($M < 1$), only the even portion of the integrand survives, and the

deflection can be seen to be an increasing function of M, and to be proportional to the damping decrement. The deflection (i.e., $\partial^2 \langle x \rangle / \partial z^2$) is greatest for two-dimensional (2D) perturbations with $k_y = 0$, where the denominator is smallest.

In a non-steady-state model, there would have been an additional transient density response over a characteristic time scale $t = a / (1 - M) C_s$, where a is the beam width, even when $\kappa = 0$. This is most significant as $M \to 1$, when the ion acoustic damping is weak.

With supersonic transverse flow ($M > 1$), the integrand in Eq. (3) has a resonant contribution where

$$k_y = k_x \sqrt{M^2 - 1}.$$

This is the matching condition for forward SBS, where different k components of the beam are coupled by ion acoustic waves Doppler shifted to zero frequency. In 2D, the resonance occurs only at $M = 1$.

Substitution of the Fourier transform of δn as determined from Eq. (1b) into the second term on RHS of Eq. (2b) shows that the self-focusing of the beam is proportional to

$$\partial_{k_x} \left\{ k_x k_\perp^2 \big/ \left[k_x^2 (1 - M^2) + k_y^2 \right] \right\}.$$

This expression is always positive definite for M<1, and increases the self-focusing in the flow direction over that experienced by the beam in the nonflow direction.

Numerical Simulations of the Ponderomotive Density Response

We examined the density response of a transversely flowing plasma to a legislated Gaussian laser wave amplitude $\psi = \exp[-(x^2 + y^2)/2\sigma^2]$. We compared the linearized response obtained analytically from Eq. (1b) (with time dependence retained, but with zero damping)[10] to the nonlinear response computed numerically using the Eulerian, 3D hydrodynamics code NH3,[11] in which the plasma is treated as a single, nondissipative, nonconducting fluid. For example, when $M = 1.2$, a ponderomotive potential that drives a maximum linearized density response of $\delta n \sim 25\%$ has a corresponding nonlinear response approximately 20% smaller. However, there is only a 2.5% difference between $\langle \nabla_\perp \delta n_{lin} \rangle$ and $\langle \nabla_\perp \delta n_{nl} \rangle$, i.e., in the centroid deflection as governed by Eq. (2a). Since such large density perturbations are reached only in very localized regions of plasma, we do

not anticipate that the results presented here would be modified by the inclusion of nonlinearity. For more strongly driven systems, this may not be the case.[12]

2D Simulations of a Gaussian Beam

Motivated by the above considerations, we performed a series of 2D and 3D F3D simulations.[6] The plasma parameters chosen are characteristic of LASNEX simulations[1,3] of gas-filled hohlraums near the sonic point in the transverse flow, where the plasma electron density is $n = 0.1n_c$, n_c being the critical density, and the electron temperature is $T_e = 3$ keV. We initially modeled a single hot spot of the Nova beam (a hot spot is a portion of the beam that is more intense; this region of higher intensity is caused by constructive interference between coherent pieces of the beam). In these 2D simulations, the incident laser amplitude is Gaussian with peak intensity $\bar{I}$ and beam width variance $\sigma^2 = a^2$, corresponding to an input wave field $\psi = (x,z = 0) = \exp(-x^2/2a^2)$.

Simulations in 2D with a constant transverse flow and zero damping decrement (but with time dependence retained) were performed where the laser intensity and system length varied. The amount of beam deflection increases approximately linearly with laser intensity (for $1 \times 10^{15} \leq \bar{I} \leq 6 \times 10^{15}$ W/cm^2) and system length (for $0 \leq L \leq 1000\lambda_0$). By varying the width of the Gaussian beam ($2\lambda_0 \leq a \leq 100\lambda_0$), we found that maximum filamentation amplication and beam deflection occurs for $a \approx 10\lambda_0$, corresponding to the peak linear gain rate (without flow) $[\kappa_{fil} = 0.125(v_0/v_e)^2(n/n_c)$ for $a^{-1} = 0.5k_0 (v_0/v_e)(n/n_c)^{1/2}]$.

LASNEX simulations[1,3] of gas-filled hohlraums indicate that the plasma flow transverse to the laser beam is sheared, i.e., $\mathbf{u} \approx u_0(1 + z/L_v)\mathbf{e}_\perp$, with $L_v \approx 500$ µm, and that the transverse flow profile has a sonic point on a long shelf of plasma with density $n = 0.1n_c$. The laser propagation was simulated in the vicinity of the transverse sonic point; i.e., M decreased linearly from a value of 1.1 at $z = 0$ to a value of 0.5 at $z = 1000\lambda_0$, where $\lambda_0 = 0.351$ µm. Figure 1 is a surface plot of the laser intensity with $\bar{I} = 6 \times 10^{15}$ W/cm^2 and $a = 10\lambda_0$ at time $t = 90$ ps. These values of peak intensity and beam width mimic the peak intensity and transverse size of laser hot spots 1 mm beyond best focus for an unsmoothed Nova beam,[13] i.e., near the LEH. The entrance plane ($z = 0$) is at the top of the figure. In this plane, the beam is centered in the middle of the box. At $z = 1000\lambda_0$, the beam is no longer centered. Approximately 70% of the beam energy is deflected
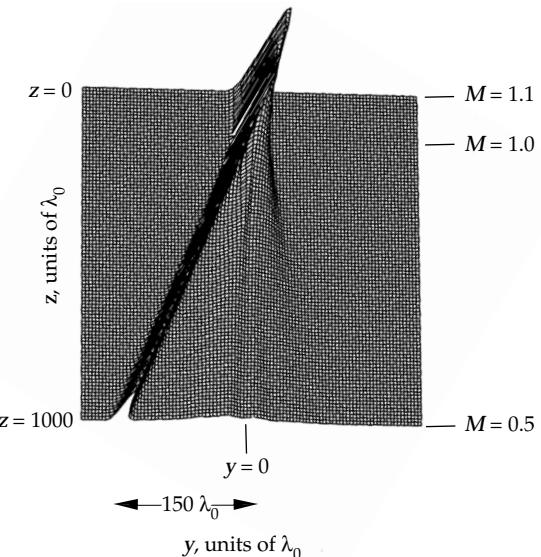
FIGURE 1. A surface plot of the laser intensity of a 2D Gaussian beam at time $t = 90$ ps for $\bar{I} = 6 \times 10^{15}$ W/cm^2, $n = 0.1n_c$, $T_e = 3$ keV, $\bar{v} = 0$, and transverse flow scale length $L = 500$ µm. The initial beam width is $a = 10\lambda_0$, where $\lambda_0 = 0.351$ µm. Approximately 70% of the beam deflects 9°, and self-focuses as well. The remainder of the beam not captured in the filament travels undeflected through the system. (08-00-0697-1094pb01)

in the direction of the flow in the vicinity of the transverse sonic point, at $z = 150\lambda_0$, and the remainder of the beam is undeflected and is also defocused by diffraction.

3D Simulations of an RPP Beam

The 2D simulation described above illustrates the deflection of one hot spot. Near the focal plane, the beam consists of many spots of varying power and size. To model the laser beam more accurately, we performed simulations in 3D with a model of the laser beam at best focus when random phase plates (RPP) are used.[14] The RPP technique produces a large number of beamlets in the laser beam with random phases. The superposition of these beamlets yields spikes (from constructive interference) and depressions (from destructive interference) in the intensity pattern, i.e., speckles. A speckle length is typically $L_s \equiv 8f^2\lambda_0$, where f is the f number of the lens.

We simulated a piece of the RPP Nova beam near peak intensity, where $I_0 = 3 \times 10^{15}$ W/cm^2 in $f/4$ focusing geometry. All other plasma parameters were unchanged, except the damping decrement, $\bar{\kappa} \equiv v/kC_s = 0.1$. Figure 2 depicts the effect of transverse flow on the hot spots of the laser beam. Plotted are contours of laser intensity greater than or equal to $5I_0$. The laser
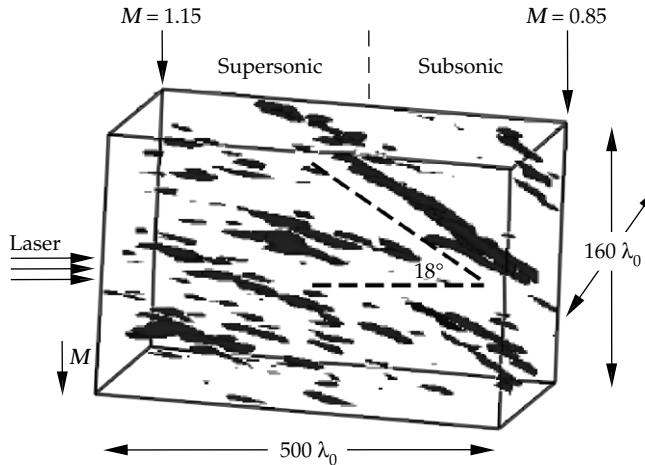
FIGURE 2. A plot of the hot spots of a 3D, RPP laser beam at time $t = 90$ ps for $\bar{I}_0 = 3 \times 10^{15}$ W/cm^2, $n/n_c = 0.1$, $T_e = 3$ keV, $\bar{\kappa} = 0.1$, and transverse flow scale length $L_v = 500$ µm. The speckle length is $L_s = 128\lambda_0$, where $\lambda_0 = 0.351$ µm. Those portions of the laser beam at intensities greater than or equal to $5I_0$ are shown. The hot spots of the laser beam undergo deflection of 18°; the calculated centroid of the beam deflects 6°. In the subsonic region, the hot spots also show evidence of self-focusing. (08-00-0697-1095pb01)

beam enters from the left side of the simulation box, where the downwardly directed transverse flow decreases linearly from $M = 1.15$ to $M = 0.85$ on the right side of the simulation box, with the transverse sonic point located at the center. In contrast to 2D simulations, where deflection is localized at the sonic point, in 3D, beam deflection occurs throughout the supersonic region, where internal FBS between different k components of the beam takes place.

In the subsonic region, the hot spots become wider, indicating that the area of the beam at intensities greater than or equal to $5I_0$ has increased. The beam hot spots are undergoing self-focusing in addition to deflection. The calculated centroid of the laser beam has deflected by 6° at the exit plane, roughly 1/3 of the deflection of the intense parts of the beam (~18°) shown in Figure 2.

A series of 3D RPP simulations was also performed at the above parameters to determine the Mach number scaling. The constant (over the simulation system) transverse flow was increased from $M = 0$ to $M = 1$ in successive simulations, and we found that the deflection approximately scales as $M/(2 - M^2)^2$. This is in agreement with Eq. (3), where, for a circular beam ($k_x \approx k_y$), the calculated deflection is proportional to $M/(2 - M^2)^2$.

We also performed 3D simulations incorporating smoothing by spectral dispersion (SSD),[15] which causes the speckles to move around and appear or disappear as a function of time. (At any given instant, an SSD beam has a sinusoidal variation in frequency with transverse wave number.) SSD is most effective when

there is at least one complete color cycle of the sinusoid. Application of 3 Å of bandwidth to a laser beam dispersed by a grating that provides 1.2 color cycles reduces deflection of the previously described RPP beam from 6° to roughly 2°. Figure 3 is a plot of the hot spots of the laser beam of Figure 2 when SSD with 3 Å of bandwidth is applied.

However, with sufficient bandwidth and dispersion, SSD can *induce* oscillatory (in time) beam deflection, even in the absence of flow. (In a time-averaged sense, i.e., when averaged over many SSD cycles, this deflection approaches zero.) Those k components of the beam that instantaneously have higher frequencies transfer energy to others at lower frequencies when the frequency and wave vector matching conditions for FBS are satisfied. This is the same physical mechanism believed to be responsible for the energy transfer between *separate* beams of different frequency, observed in experiments at LLNL.[16,17]

Figure 3 depicts the laser beam when the downstream edge of the beam is red, i.e., at the time when SSD is adding its maximum contribution to the beam deflection. Comparing Figure 3 to Figure 2, we see clearly that the amount of energy greater than or equal to $5I_0$ is reduced for the SSD beam (i.e., self-focusing is reduced) and that the amount of deflection of the hot spots is greatly reduced as well (~18° in Figure 2 vs ~5° in Figure 3). In simulations without flow, but with 3 Å of bandwidth applied to an SSD beam, the beam
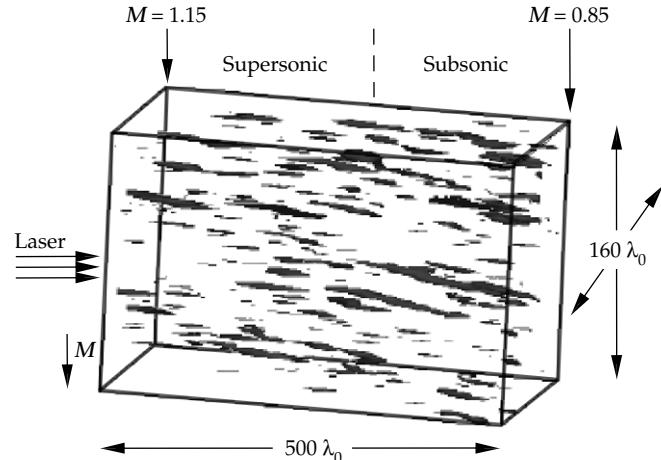
FIGURE 3. A plot of the hot spots of a 3D, RPP laser beam with SSD and 3 Å of bandwidth at time $t = 90$ ps for $\bar{I}_0 = 3 \times 10^{15}$ W/cm^2, $n/n_c = 0.1$, $T_e = 3$ keV, $\bar{\kappa} = 0.1$, and transverse flow scale length $L_v = 500$ µm. The speckle length is $L_s = 128\lambda_0$, where $\lambda_0 = 0.351$ µm. Those portions of the laser beam at intensities greater than or equal to $5I_0$ are shown. The centroid of the beam deflects by 2° at the exit plane, and the hot spots are deflected about 5°. There is less deflection and self-focusing than in Figure 2. (08-00-0697-1096pb01)

centroid deflection (which is caused by the SSD itself) is roughly 2° at the time when the downstream edge of the beam is red (time of maximum deflection). Thus, in Figure 3, the deflection is primarily caused by the SSD itself, and not by the flow.

In a 2D, steady-state model, the linearized density response diverges as $M \rightarrow 1$. This divergence is mitigated by inclusion of 3D effects and/or ion wave damping when $\kappa a > 1 - M$, where a is the beam width. In the absence of these effects, fluid nonlinearity limits the resonance when $v_0 / v_e > 1 - M$.[18] Nonlinear hydrodynamic effects become more significant at higher intensities than considered here, e.g., when $\delta n \rightarrow 1$. In the very near future, this problem will be examined at higher intensity, where the nonlinear aspects of this problem are important, via the incorporation of the nonlinear hydrodynamics package NH3 into F3D.

Summary

Recent experiments in gas-filled hohlraums suggest that laser beams refract more than calculated by the hydrocode LASNEX. We show, from theoretical arguments and three-dimensional simulations with F3D, that transverse plasma flow causes a deflection in the inferred direction of the appropriate magnitude. The physical mechanisms involve filamentation and forward SBS. In each case, the density depressions created by the laser's ponderomotive force are swept downstream by the transverse flow. The displaced depressions then refract the laser energy in the direction of the flow.

Acknowledgments

Notes and References

1. S. G. Glendinning, private communication.
2. J. D. Moody et al., *Phys. Rev. Lett.* **77**, 1294 (1996).
3. G. Zimmerman and W. L. Kruer, *Comments Plasma Phys. Controlled Fusion* **2**, 85 (1975).
4. R. W. Short, R. Bingham, and E. A. Williams, *Phys. Fluids* **25**, 2302 (1982).
5. H. A. Rose, *Phys. Plasmas* **3**, 1709 (1996).
6. R. L. Berger et al., *Phys. Fluids B* **5**, 2243 (1993).
7. C. E. Max, *Phys. Fluids* **19**, 74 (1976).
8. M. V. Goldman, K. Rypdal, and B. Hafizi, *Phys. Fluids* **23**, 945 (1980).
9. J. J. Rasmussen and K. Rypdal, *Phys. Scr.* **33**, 481 (1986).
10. E. A. Williams and D. E. Hinkel, *Bull. Am. Phys. Soc.* **40**, 1824 (1995).
11. C. H. Still et al., *Bull. Am. Phys. Soc.* **40**, 1823 (1995).
12. In F3D there is an imposed saturation of the density perturbations, using log $(l + \delta n)$ in lieu of δn as the linearized density variable. This prevents the nonphysical singularities of the nonlinear Schrödinger equation (NLSE), Eq. (1a), which can occur at higher intensities than used in these simulations. For the F3D simulation results presented in this article, the imposed saturation had negligible effect.
13. P. Wegner, "Measurements and Modeling of Laser Irradiance in the High-Power Third Harmonic Nova Focus," Lawrence Livermore National Laboratory, Livermore, CA, UCRL-ID-110480 (1992).
14. Y. Kato et al., *Phys. Rev. Lett.* **53**, 1057 (1984).
15. S. Skupsky et al., *J. Appl. Phys.* **66**, 3456 (1989).
16. W. L. Kruer et al., *Phys. Plasmas* **3**, 382 (1996).
17. R. K. Kirkwood et al., *Phys. Rev. Lett.* **76**, 2065 (1996).
18. W. L. Kruer and J. H. Hammer, *Comments Plasma Phys. Controlled Fusion* **18**, 85 (1997).

X-Ray Backlit Imaging of Indirect-Drive Capsule Implosions

D. H. Kalantar

S. W. Haan

B. A. Hammel

C. J. Keane

O. L. Landen

D. H. Munro

Introduction

In indirectly driven inertial confinement fusion (ICF),[1] a fusion capsule is bathed in broadband soft x rays created inside a hohlraum. The x-ray drive ablates material from the outer capsule surface, causing the inner wall (pusher) of the capsule to implode and compress the fuel. Both the efficiency of the implosion and the growth of hydrodynamic instabilities at the ablation surface (Rayleigh-Taylor instability)[2] vary with the aspect ratio of the imploding capsule.[3–5]

Capsules illuminated by a broadband soft x-ray drive experience preheat due to the harder component of x rays. To maintain a low adiabat for the fuel and pusher during the implosion, it is necessary to shield them from the harder x rays. This is done by introducing dopants in the capsule ablator material. The dopant added to the ablator prevents the harder x rays from preheating the pusher and, as a result, maintains a higher density as well as a sharper density gradient in the pusher increasing both the implosion efficiency and hydrodynamic instability growth. The doped ablator also has a higher initial aspect ratio because it has a higher initial density and a lower mass ablation rate.

We use x-ray backlighting to measure the in-flight areal density of the pusher in both Ge-doped and undoped x-ray driven imploding capsules. Previous images of an indirectly driven implosion provided a measure of the implosion velocity and low-mode distortion.[6] We recorded large-area backlit images, performed radial intensity lineouts, and unfolded a radial density profile. Postprocessed simulations are in good agreement with the measurements.

X-Ray Backlighting on Nova

We used x-ray backlighting techniques[7] to image an x-ray driven implosion capsule on the Nova laser.[8] The plastic capsules consisted of a 3-μm-thick polystyrene shell, a 3-μm-thick layer of polyvinyl alcohol (PVA), and an ablator layer coated on the outside. The polystyrene ablators were 34 μm thick with 2.5% Ge by atomic fraction, or 50 μm thick with no dopant to match the implosion velocities. The outside diameter of the capsules was about 510 to 530 μm. The capsules were filled to 50 atm pressure with an equal mixture of hydrogen and deuterium.

The backlighter target is shown in Figure 1. The ICF capsule was placed at the center of a cylindrical gold hohlraum that was 1.6 mm in diameter and 2.5 mm long. There were two 650-μm-diam diagnostic access holes in the hohlraum, positioned on opposite sides at the midplane of the hohlraum. These were covered with 150-μm-thick CH foils to fill the hohlraum with a low-mass plasma and restrict the flow of emissive gold plasma into the diagnostic line of sight. A thin foil used for backlighting was positioned approximately 3 mm from the center of the hohlraum, collinear with the capsule diagnostic holes and diagnostic line of sight.

We used eight Nova beams at 0.35 μm to create an x-ray drive in the hohlraum. The beams were pointed inside the hohlraum through the laser entrance holes so that they were distributed symmetrically around the azimuth of the hohlraum with a fourfold rotation symmetry. The 2.2-ns shaped laser pulse had an intensity contrast from the foot to the peak of 1:6 (Figure 2). A total of 25 kJ of laser energy was delivered into the hohlraum, with a peak laser power of 19 TW. The x-ray drive temperature in the hohlraum is shown in Figure 2. It peaks at about 200 eV at 1.8–2.0 ns.
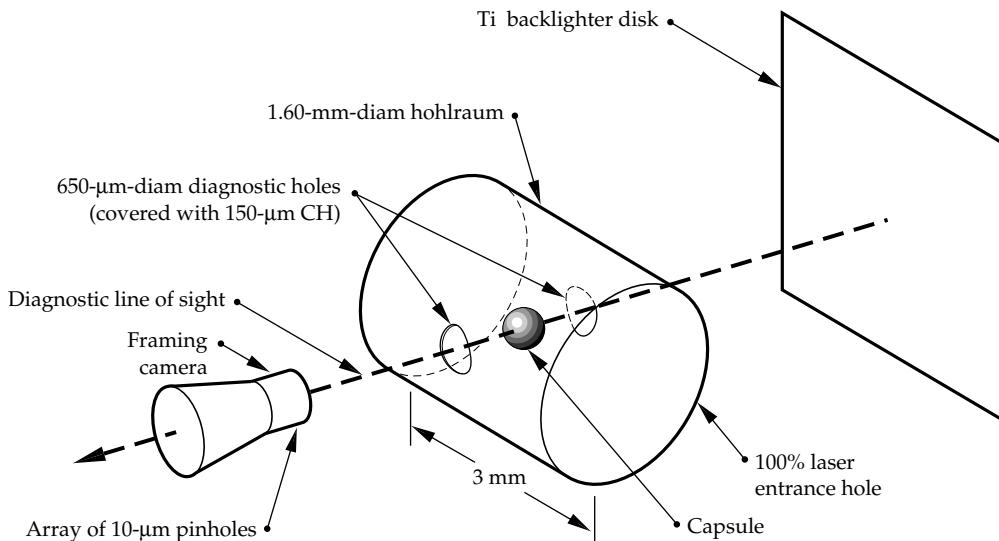
FIGURE 1. Diagram of the backlighter target used on Nova. (20-03-0397-0446pb01)

Two frequency-doubled Nova beams were focused onto the backlighter foil. These were configured with random phase plates and focused to an ~700-μm focal spot on the backlighter foil at about 5×10^{14} W/cm^2 to generate a large-area source of backlighter x rays. The laser pulse shape on these two beams was 2 ns square, which gave us a constant intensity of x rays.

For imaging the Ge-doped capsules, we used a Ti backlighter foil and recorded the images filtered with a 12-μm Ti filter. This provided a nearly monochromatic image, principally in 4.7 keV emission from the 1s2p–1s^2 line of Ti (Figure 3). For the undoped implosion

capsules, we used a Rh backlighter and filtered the images with a 12-μm Sc filter. This provided a narrow-band spectrum at about 3–3.5 keV.

We recorded the radiograph images of the fusion capsule at various times during the implosion using a gated x-ray framing camera.[9,10] The timing of the back-lighter beams was varied in order to record images over approximately 3 ns. The camera had a full width at half maximum gate width of 55 ps. We used an array of 10-μm pinholes at 8× magnification, overlaid with a 250-μm-thick collimator that had 50-μm-diam holes to limit the hard x-ray background in each pinhole image.
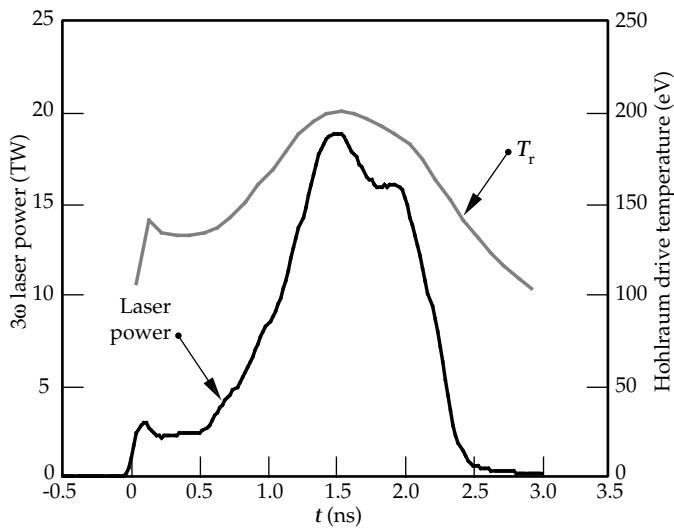
FIGURE 2. Laser power and hohlraum x-ray drive temperature as a function of time. (20-03-0397-0447pb01)
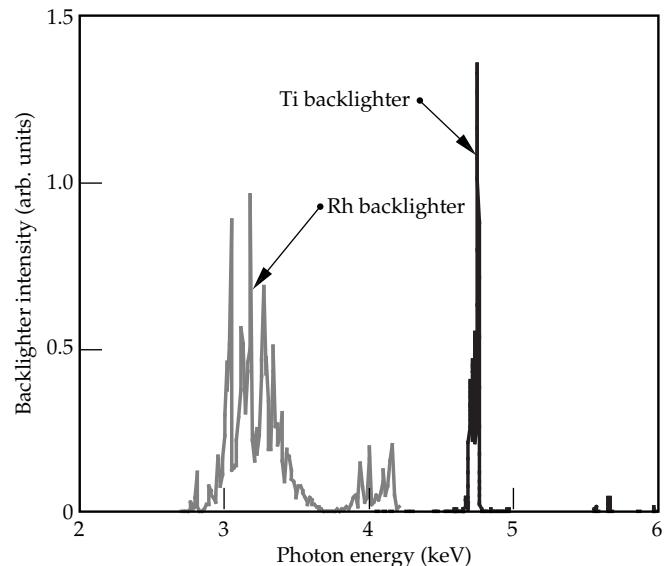
FIGURE 3. Ti and Rh x-ray backlighter spectra. (20-03-0397-0448pb01)
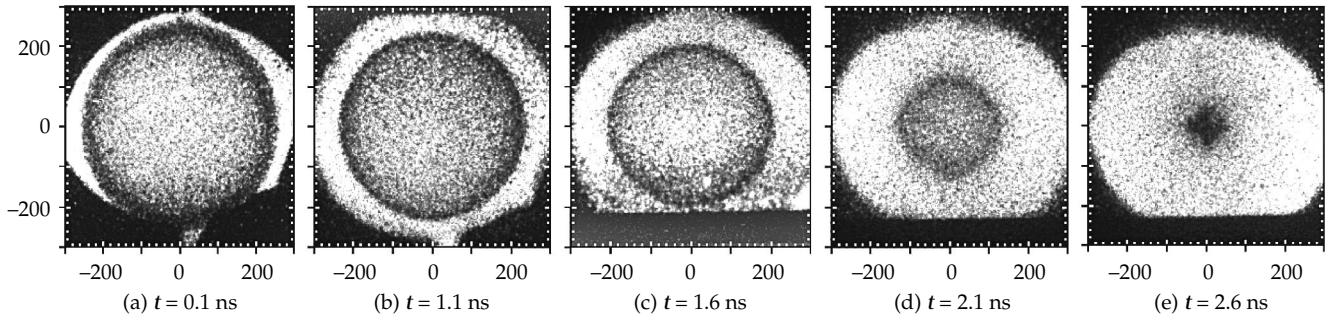
FIGURE 4. Series of x-ray backlit images of a Ge-doped capsule recorded at t = 0.1, 1.1, 1.6, 2.1, and 2.6 ns. The scales are in microns at the target. (20-03-0397-0449pb01)

Backlit Images of a Ge-Doped Implosion Capsule

Figure 4 shows a series of backlit images from Ge-doped capsules. These images are shown corrected for the diagnostic flat-field and for the spatial intensity profile of the x-ray backlighter. These images were obtained on two Nova target shots. For each shot, the capsule had an initial outer radius of 255 μm.

We imaged the backlighter foil from the rear side using a second x-ray framing camera. The Ti backlighter foil was 12 μm thick, so that these images of the foil were filtered identically to the backlit images of the implosion capsule. The flat-field characterization incorporating the gain degradation in each strip line for both framing cameras and the overall backlighter intensity profile were applied to normalize the backlit images.

We tested that the backlit implosion images of Ge-doped capsules were nearly monochromatic by measuring the initial contrast of the undriven capsule shell in the backlighter x rays. We compared the fractional transmission of backlighter x rays through the center of the capsule with the unattenuated backlighter intensity. Based on the composition of the Ge-doped capsule shell, the calculated transmission through twice the total wall thickness is about 0.47. For the image shown above in Figure 4a, we measured a fractional transmitted intensity of 0.45 in the center of the image.

In-Flight Pusher Density Profile

We calculated radial density profiles by performing an Abel inversion of the radial lineouts for each image. Since the late-time images shown in Figure 4 have a P4 asymmetry, the radial lineouts were averaged over 45° segments in the polar direction, as indicated schematically in Figure 5. Up to eight individual lineouts per image were Abel inverted by assuming azimuthal symmetry for each.

Abel-inverted lineouts from Ge-doped capsules are shown at five different times in Figure 6. These are
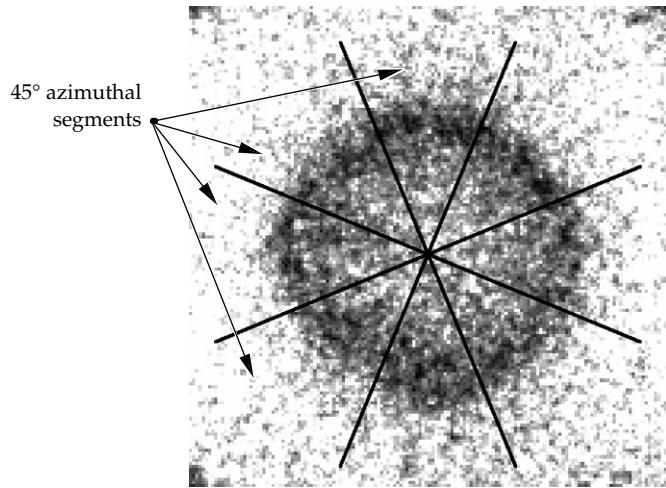
FIGURE 5. Schematic showing the wedge segments that were averaged in the polar direction to perform the radial lineouts of the backlit images. (20-03-0397-0450pb01)

plotted as the product of opacity times density. Since the shock-preheated ablator is at a temperature of <<100 eV, the opacity of the Ge-doped ablator material at the backlighter energy of 4.7 keV (dominated by L-shell Ge and K-shell carbon) is nearly identical to the cold material opacity. Therefore, these lineouts are proportional to the density profile of the capsule pusher. Note that we have smoothed the inverted lineouts at small radius. The polar average smooths the radial lineout at large radii, but noise statistics and speckle of the microchannel plate detector and backlighter profile dominate at small radii.

We used LASNEX[11] to model the implosion of the Ge-doped capsule. The conditions of the pusher in the Ge-doped capsule implosions were calculated, and the output was postprocessed to generate simulated images with the backlighter spectrum shown in Figure 3, at the same times of the images shown in Figure 4. These images were then convolved with the instrument resolution expected of a 10-μm pinhole
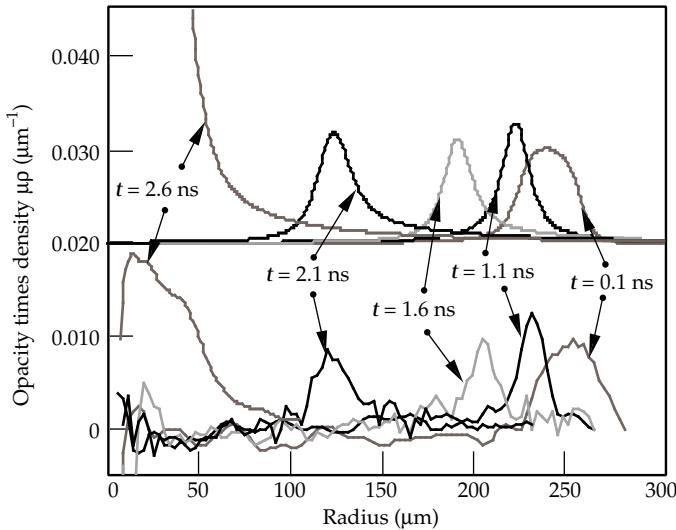
FIGURE 6. Radial density profiles calculated by Abel-inverting radial lineouts of the x-ray transmission through the capsule (bottom curves). Results from postprocessed simulated images are shown for comparison (top curves).   (20-03-0397-0451pb01)

and unfolded by Abel inversion using the same assumptions about spherical symmetry and monochromatic imaging. The resulting Abel-inverted simulated lineouts are shown overlaid in Figure 6. These show a time history similar to the experimental lineouts.

We measured the radius of the half-maximum density on the outer edge of the Abel-inverted lineouts. This is shown in Figure 7, plotted with the aspect ratio

that we calculate as the ratio of the average radius to the full width at half maximum of the radial density profile for each time. Note that the error bars represent the standard error in the mean, based on an average from the 45° lineouts.

The radius and aspect ratio calculated from the postprocessed simulated images are shown in Figure 7 as solid curves. These values were calculated from the Abel-inverted lineouts of the simulated images in the same manner as the values measured in the experiment. The simulations are in good agreement with the measurement.

Undoped Implosion Capsules

X-ray backlit images of undoped capsules were obtained throughout the implosion with a Rh backlighter. We performed radial lineouts over the same 45° segments to obtain radial density profiles at each time. The average radius and aspect ratio, measured as described above, are shown as a function of time in Figure 8.

The results from postprocessed simulated images are shown overlaid in this figure by the solid curves. Note that the undoped capsules are expected to decompress more due to less preheat shielding, which lowers their late-time ($t > 1.5$ ns) aspect ratio, as measured by comparing Figures 7 and 8. The fact that the aspect ratio is lower for the undoped capsules than for the doped capsules early in time is because it was necessary to use an initially thicker undoped ablator to match the implosion velocities for the different cases.
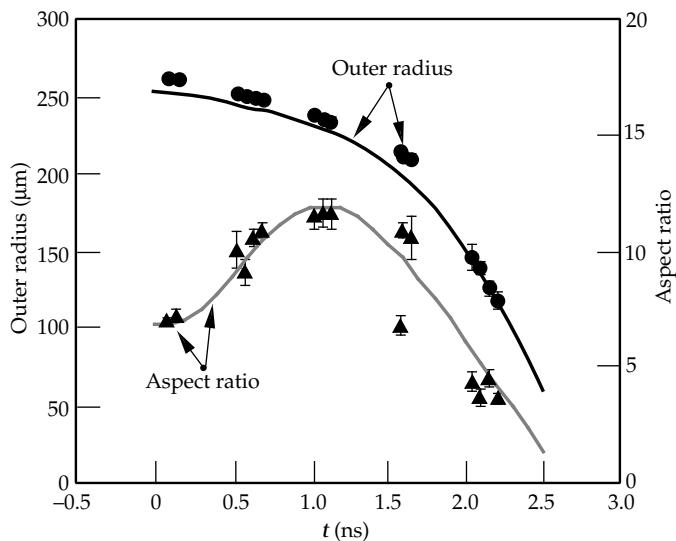
FIGURE 7. Radius and aspect ratio calculated from the Abel-inverted lineouts of Ge-doped backlit images as a function of time (data points). Results from postprocessed simulated images are shown for comparison (curves).   (20-03-0397-0452pb01)
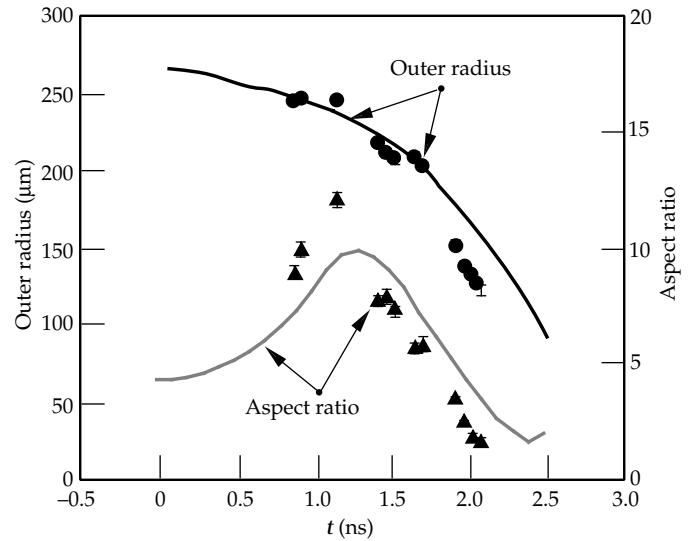
FIGURE 8. Radius and aspect ratio calculated from the Abel-inverted lineouts of undoped backlit images as a function of time (data points). Results from postprocessed simulated images are shown for comparison (curves).   (20-03-0397-0453pb01)

Summary

We have used x-ray backlighting techniques to record images of indirectly driven ICF capsules on Nova. These large-area images provide quantitative information about the in-flight pusher density profile as a function of time. We measure the in-flight aspect ratio of imploding Ge-doped and undoped capsules using an 8-beam pulse-shape–26 drive. The doped results and simulations match well. The results from the undoped capsules do not agree as well. These results should be more sensitive to preheat levels, which would otherwise be difficult to measure. Detailed comparisons with modeling in which the preheat level is varied in the simulations will allow a better characterization of the preheat levels.

Acknowledgments

Notes and References

1. J. Lindl, *Phys.Plasmas* **2**, 3933 (1995).
2. Lord Rayleigh, *Scientific Papers*, Vol. II, p. 200, Cambridge Univ. Press (1900).
3. O. L. Landen, C. J. Keane, B. A. Hammel, W. K. Lovedahl, et al., "Effects of variable x-ray preheat shielding in indirectly-driven implosions," to appear in *Phys. Plasmas* **3**, 2094 (1996).
4. O. L. Landen, C. J. Keane, B. A. Hammel, M. D. Cable, et al., *J. Quant. Spectrosc. Radiat. Transfer* **54**, 245 (1995).
5. C. Keane, G. W. Pollak, R. C. Cook, T. R. Dittrich, et al., *J. Quant. Spectrosc. Radiat. Transfer* **54**, 207 (1995).
6. M. Katayama, H. Shiraga, M. Nakai, T. Kobayashi, and Y. Kato, *Rev. Sci. Instrum.* **64**, 706 (1993).
7. S. G. Glendinning, P. Amendt, K. S. Budil, B. A. Hammel, et al., *Applications of Laser Plasma Radiation II*, edited by M. C. Richardson and G. A. Kyrala, in *Proc. SPIE* (Society of Photo-optical Instrumentation Engineers, Bellingham, WA, 1995), vol. 2523, pp. 29–39.
8. E. M. Campbell, J. T. Hunt, E. S. Bliss, D. R. Speck, and R. P. Drake, *Rev. Sci. Instrum.* **57**, 2101 (1986).
9. D. K. Bradley, P. M. Bell, O. L. Landen, J. D. Kilkenny, and J. Oertel, *Rev. Sci. Instrum.* **66**, 716 (1995).
10. P. M. Bell, J. D. Kilkenny, O. L. Landen, D. K. Bradley, et al., *Ultrahigh and High Speed Photography, Videography, and Photonics '94*, in *Proc. SPIE* (Society of Photo-optical Instrumentation Engineers, Bellingham, WA, 1994), p. 234.
11. G. B. Zimmerman and W. L. Kruer, *Comments Plasma Phys. Controlled Fusion* **2**, 51 (1975).

INTERACTION BETWEEN STIMULATED RAMAN SCATTERING AND ION-ACOUSTIC WAVES IN IGNITION-RELEVANT PLASMAS

R. K. Kirkwood

B. B. Afeyan[**]

K. G. Estabrook

M. A. Blain[***]

B. J. MacGowan

W. L. Kruer

C. A. Back

E. A. Williams

D. S. Montgomery[*]

J. D. Moody

S. H. Glenzer

R. L. Berger

B. F. Lasinski

Introduction

The transport of intense laser beams through large regions of underdense plasmas is important to achieving ignition by indirect-drive inertial confinement fusion (ICF).[1] The energy deposition profile of the laser beam in the target is strongly affected by stimulated scattering from ion-acoustic and Langmuir waves in the plasma created when the target material ionizes. These interactions are most simply modeled by the three-wave decay processes of stimulated Brillouin scattering (SBS) and stimulated Raman scattering (SRS), respectively.[2] The three-wave decay models assume that waves propagating in the plasma do not interact, that is, that the plasma response to the ponderomotive force of the incident and scattered light is linear. However, previous experimental observations[3,4] and theoretical studies[5–13] provide evidence that the Langmuir waves and the ion-acoustic waves are not independent. In fact, in the high-temperature, high-Z plasmas present in indirect-drive targets,[1] secondary decay instabilities can limit the SRS.[9–13] In these secondary processes, the Langmuir wave produced by the SRS process can itself decay into an ion-acoustic wave and either a secondary Langmuir wave (LDI) or a secondary electromagnetic wave (EDI), thus coupling the properties of the Langmuir wave directly to the properties of the ion-acoustic wave. The mechanism for limiting SRS reflectivities by LDI was first described by Karttunen[9] and Heikkinen and Karttunen,[10] and was later invoked to explain the SRS spectrum from Au foil plasmas.[11] These processes were subsequently shown

to occur in numerical simulations.[7,8,12] Recently, Baker[13] suggested that EDI may also result in a limit to the reflectivity.

This article describes the first demonstration that the SRS reflectivity in a plasma can depend directly on ion-wave damping, and finds that under conditions similar to what is expected in ignition experiments, the SRS reflectivity is consistent with Langmuir wave amplitudes that are limited by a secondary decay. The experiments are done in a low-density Xe gas target plasma, in which C_5H_{12} is added as a low-Z impurity.[14] Measurements of x-ray spectra and transmitted light and calculations show that variation of the concentration of impurities below 10% has very little effect on the electron density n_e, temperature T_e, or collisional absorption rate, while calculations indicate that the impurities have a large effect on the ion-wave damping. The SRS reflectivity, or equivalently the Langmuir wave amplitude, is found to depend on the impurity concentration and thus on ion-wave damping, and to track the threshold for decay of the Langmuir wave. The plasmas produced in these experiments mimic the properties of those that form near the wall in a Au hohlraum filled with a low-Z gas, such as will be used in ignition experiments on the National Ignition Facility (NIF) at somewhat lower laser intensity.[1] These open geometry targets also provide a uniform and well characterized plasma. Other experiments in gas-filled hohlraums have also shown a dependence of SRS on ion-wave damping, both when the wall is doped with a Be impurity to mimic the gradients and time dependence of the wall plasma expected in NIF experiments,[15] and when the gas has large fractions of both low- and high-Z material.[16] However, plasma properties vary along the ray path in those experiments, making identification of the physical mechanism difficult.

*   Los Alamos National Laboratory, Los Alamos, NM.
**   University of California at Davis, Davis, CA.
*** Centre D'Etudes de Limeil–Valenton, France.

Experimental Design

The experiments were conducted on the Nova laser in an approximately spherical plasma produced by nine $f/4.3$, $\lambda = 351$ nm beams. These heater beams each produce 2.5 TW of power continuously for 1 ns, with a total power of 22.5 TW. The beams pass through a gas mixture at 1 atm of pressure contained inside a 260-nm-thick spherical polyimide shell with radius $r_0 = 1.3$ mm.[17] The heater beams are aligned to cross at the center of the target. The heaters are defocused such that they are converging with a beam radius that is approximately equal to the target radius, providing spatially uniform heating. The electrons are heated to a temperature of $T_e = 3.6$ keV during the $t = 0.5$- to 1.0-ns period when the plasma parameters are most constant in space and time.[17] The electron density n_e is determined by the initial gas density and the average charge state. At this temperature, Xe has a charge state of about 40,[18] leading to $n_e = 8.5 \times 10^{20}$ cm^{-3}. Since the C_5H_{12} impurity is fully ionized and carries 42 electrons per molecule, n_e is independent of its concentration to within ≤5%. T_e is determined from measurements of x-ray line ratios and x-ray transport modeling as described in Ref. 18 and is in agreement with LASNEX[19] simulations. Measurements of radiated power and beam attenuation by collisional absorption indicate that T_e is also insensitive to impurity concentration. The measured transmission of a beam through the plasma[20] varies only from 1% to 2% when the impurity concentration is varied from 0% to 30%, and is also in agreement with the simulations, similarly indicating that the T_e variations are small ($\leq \pm 6\%$). Measurements of the radiated x-ray power in the photon energy range of 0.2 to 2 keV[21] indicate that the radiated power is also constant within ±15% over the same range of impurity concentration. The lack of dependence of n_e and T_e on impurity concentration indicates that the frequency and damping rate of the Langmuir wave are also constant.

An interaction beam produces 1.5 TW continuously for 1.0 ns with $\lambda = 351$ nm. This beam is delayed 0.5 ns with respect to the heaters and is focused at the plasma center. Reflectivity measurements are made during the 0.5- to 1.0-ns (early) period when the heaters are on, as well as during the 1.0- to 1.5-ns (late) period when the plasma is cooling and less homogeneous. The interaction beam is smoothed by a random phase plate and by 0.7-Å FM bandwidth dispersed across the beam in the near-field that smoothes by spectral dispersion (SSD), so that its peak intensity and spot size in vacuum are 7.0×10^{15} W/cm^2 and 177 μm full width at half maximum (345 μm between first Airy minima). The plasma properties encountered by the interaction beam during the early period are calculated by LASNEX[19] for a 90% Xe, 10%

C_5H_{12} gas mix, indicating a T_e and n_e plateau near the plasma edge, as shown in Figure 1. The classical collisional absorption length for 351-nm light in Xe with a 3.6-keV T_e and 8.5×10^{20}-cm^{-3} n_e is 800 μm. Therefore, the majority of the backscattering occurs outside $r = 0.5$ mm. The downshifted light scattered within 20° of direct backscatter is measured[22] with a streaked optical spectrometer in the visible, with a spectral range of 400 to 700 nm, and a second spectrometer in the ultraviolet, with a spectral range of 346 to 361 nm. The SRS light detected by the long-wavelength spectrometer from an experiment with 5.5% C_5H_{12} impurity is shown in Figure 2. During the early period, the peak of the spectrum is at 575 nm, consistent with scattering from a Langmuir wave propagating in a plasma with an electron density n_e equal to 10% of the critical density n_c and a 3.0-keV T_e comparable to the simulated plasma parameters near $r = 1.2$ mm. After the heaters turn off at 1.0 ns, the peak shifts to the blue, indicating cooling and expansion of the plasma.
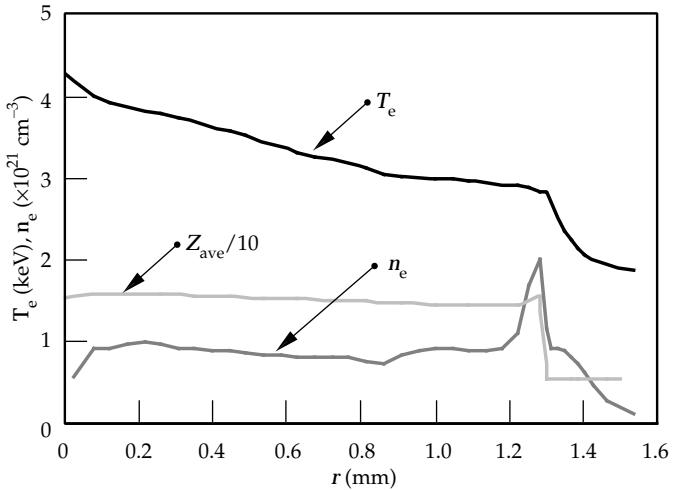
FIGURE 1. Calculated electron density n_e, electron temperature T_e, and averaged ionization state at $t = 0.7$ ns indicate that n_e and T_e scale lengths are long.   (08-00-0797-1243pb01)

Observations of Scattering vs Ion-Wave Damping

Experiments were performed with six different impurity concentrations between 0% and 30% C_5H_{12} and exhibit a strong dependence of the SRS reflectivity on the concentration of C_5H_{12}, which is interpreted as a dependence of Langmuir wave amplitude on the

(a)

(b)

(c)
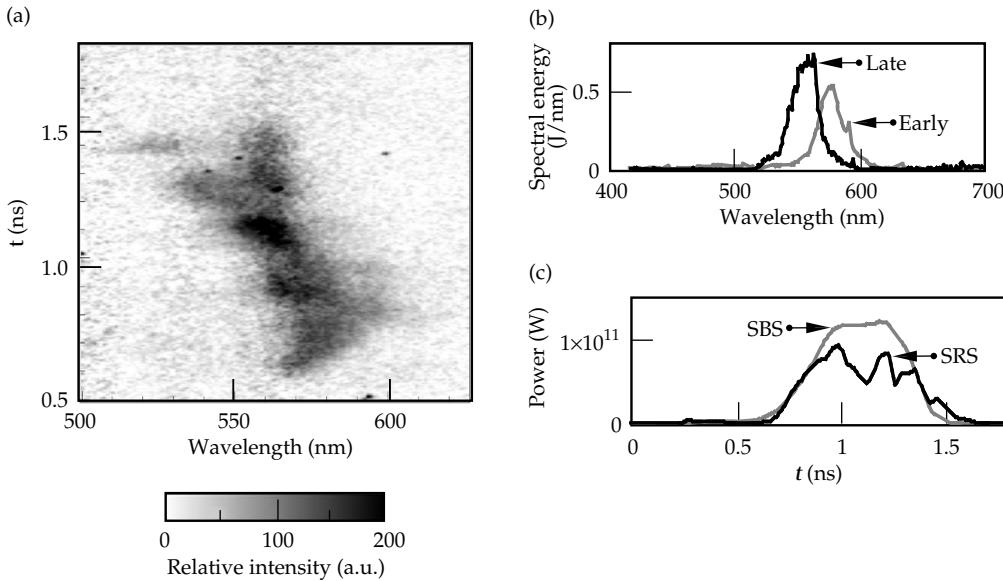
FIGURE 2. (a) A streaked spectrum of the SRS reflectivity from a target with 5.5% impurity concentration shows a narrow line consistent with a flat density profile before 1.0 ns and a decreasing density after 1.0 ns. (b) Time-integrated reflectivity from (a) shows a narrow peak at 575 nm in the 0.5- to 1.0-ns "early" period. (c) The spectrally integrated power collected by the SRS and SBS detectors is shown for the case in (a). (08-00-0797-1245pb01)

damping rate of the ion-acoustic wave. The integrated energies from the two time periods are expressed as percent reflectivities of the incident beam power due to SRS, and are plotted in Figure 3. A similar analysis has been done for backscattered light between 350.5 and 352 nm, which is interpreted as SBS backscatter as
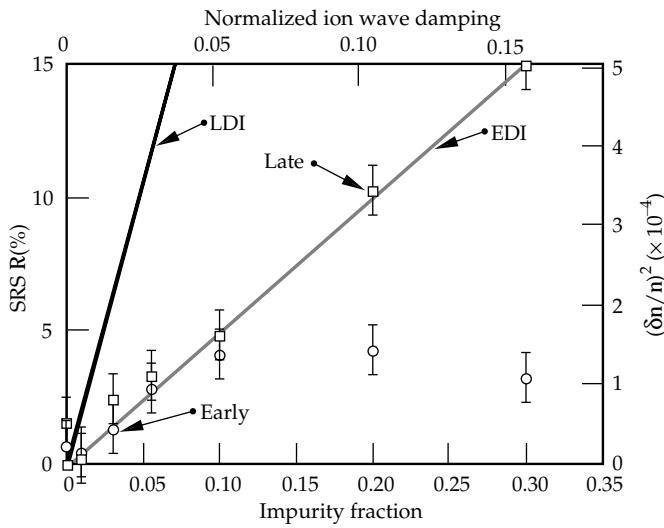
FIGURE 3. SRS reflectivities averaged over the 0.5- to 1.0-ns "early" period and the 1.0- to 1.5-ns "late" period are shown vs impurity concentration. The impurity concentration is interpreted as the ion-wave damping rate (top axis), and the reflectivity is interpreted as the square of the fluctuation amplitude (right axis). Black and gray lines represent the LDI and EDI threshold amplitudes for a uniform beam and parameters relevant to early-time data. The LDI limited reflectivity in a nonuniform beam can be much lower than what is shown (see text). (08-00-0797-1246pb01)

described in Ref. 14. The integrated data clearly show that late-time SRS reflectivities are approximately proportional to the impurity concentration for all concentrations studied. The early-time reflectivities are proportional to concentration up to 10% and become independent, or a mildly decreasing function, of concentration between 10% and 30%. Because the ion-acoustic damping rate is expected to be linear with impurity concentration in this case,[23] a linear dependence of reflectivity on impurity concentration is interpreted as a linear dependence on the damping of the ion-acoustic wave. The possibility that dependence of the reflectivity on ion-wave damping is actually the result of suppression of SRS by large-amplitude ion waves generated by SBS (as discussed in Refs. 3 and 4 and references therein) is unlikely, because the observed dependence of SBS on ion-wave damping is weak in this case.[14]

These observations are the first demonstration of the direct dependence of SRS reflectivity on the damping rate of the ion-acoustic wave. In particular, the early-time reflectivity for concentrations between 1% and 10% demonstrates SRS increasing with ion-wave damping when the electron–ion collision rate, electron temperature, radiated power, and SBS level are essentially constant. In addition, the early-time reflectivity at higher concentration is nearly independent of the ion-wave damping rate, suggesting that the reflectivity falls below the threshold scaling law when the ion-wave damping is strong. Two types of plasma are expected in the NIF: a hot Au plasma near the hohlraum wall and a hot low-Z plasma in the hohlraum interior. These types of plasma correspond to the early-time plasma

conditions at the two extremes of the ion-wave damping axis in Figure 3, which suggests that the SRS will be at correspondingly low levels in the NIF hohlraum.

Comparison with Models of Secondary Decays Involving Ion Waves

A simple model is presented to show how the observed dependence of the reflectivity on ion-wave damping may be explained by secondary decay of the Langmuir wave. In this model, the intensity profile of the beam and filamentation are neglected for simplicity, and the Langmuir wave amplitude is assumed to be in the vicinity of the threshold for the secondary decay. This threshold for decay, expressed in terms of the density fluctuation, is given by Ref. 9 for LDI and by Ref. 13 for EDI,

$$\left(2ik_0\frac{\partial}{\partial z} + \nabla_\perp^2\right)\psi = \frac{\omega_{pe}^2}{c^2}\delta n\,\psi \tag{1a}$$

$$\left[M\frac{\partial}{\partial x}\left(M\frac{\partial}{\partial x} + \kappa\right) - \nabla_\perp^2\right]\delta n = \left(\frac{v_0}{v_e}\right)^2\nabla_\perp^2|\psi|^2 \tag{1b}$$

where k_L is the wave vector of the SRS-generated Langmuir wave, v_{ia}/ω_{ia} is the normalized linear ion-wave damping rate, v_{em} is the linear damping rate of the EDI, v_L is the linear damping rate of the LDI, and λ_{De} is the electron Debye length. The measured SRS light is interpreted as Thomson scattering off density fluctuations in the scattering volume using the following assumptions. For these experiments the rapid collisional absorption rate of the incident and reflected light determines the size of the interaction region that can be viewed by the backscatter diagnostic. The effective length L used is the depth at which the attenuation of an incident 351-nm light times the attenuation of the reflected 580-nm light is equal to $1/e$. L is 300 μm, which in this case indicates that the observed SRS comes primarily from the plasma at radii larger than 1 mm. For perfectly coherent fluctuations, the reflectivity is proportional to this length to the second power,[10] but the finite spectral width observed in Figure 2 ($\Delta k \approx 5.6 \times 10^5\,\mathrm{m}^{-1}$) indicates that in this experiment the maximum distance over which the radiation can be coherent is given by $\ell_{c\,max.} = 1/\Delta k$. A finite correlation length will reduce the reflectivity by a factor of at least $\ell_{c\,max}/L$ (Ref. 8) below the value for coherent

fluctuations, giving the maximum reflectivity R for a uniform beam as

$$R_{max} = \frac{1}{4}\left(\frac{n_e}{n_{c_0}}\right)^2 \; k_0^2 L(\Delta k)^{-1}\left(\frac{\delta n_e}{n_e}\right)^2 \quad, \tag{2}$$

where k_0 and n_{c_0} are the wave number and critical density of the incident beam. This model indicates that the SRS reflectivity is linearly proportional to ion-wave damping if the Langmuir wave amplitude does not grow significantly above the secondary decay threshold. This linear dependence is most clearly observed in the reflectivity data taken at early time when the impurity concentration is less than 10%. For impurity concentrations above 10%, the early-time reflectivity is not very dependent on the ion-wave damping. This is likely due to the convective saturation of the SRS-generated Langmuir wave before it reaches the secondary decay threshold. The secondary decay mechanism will only determine the SRS reflectivity when the primary three-wave process is sufficiently strong to drive the Langmuir wave amplitude to the threshold for the secondary decay. Thus at early time and high impurity concentration (>10%), the secondary decay threshold is sufficiently high that the SRS reflectivity is likely limited by the convective saturation of the three-wave SRS process and is therefore observed to be approximately independent of ion-wave damping. The late-time data show linear dependence of the reflectivity on the impurity concentration up to much higher concentration. This may be because at late time the plasma has cooled and therefore has a higher convective saturation level for the three-wave process, resulting in reflectivities that follow the linear scaling with ion-wave damping up to at least 30%, as shown in Figure 3. However, quantitative analysis of the late-time data is complicated by variations of the plasma properties in time and space.

As an additional check of the model of secondary decay, the density perturbation is estimated from the measured reflectivity at early time using Eq. (2), and is compared with that predicted by Eqs. (1a) and (1b). To evaluate Eqs. (1a) and (1b), the damping rates[24] of the Langmuir and electromagnetic waves are calculated using the distribution function expected in a high-Z plasma illuminated with high-intensity light.[25] The thresholds are evaluated assuming the average beam intensity ($3.0 \times 10^{15}\,\mathrm{W/cm}^2$) exists throughout the interaction region and are shown as black and gray lines in Figure 3. In this case the equilibrium distribution is a super-Gaussian with $n = 3.5$ (where $n = 2$ corresponds to a Maxwellian). The estimate shown for the EDI threshold is not changed significantly by

inhomogeneities in the beam profile (i.e., hot spots), but the estimate for LDI may be significantly reduced by inhomogeneities. This reduction results from the fact that the Langmuir-wave Landau damping is strongly sensitive to intensity, as discussed in Ref. 24, so that in a hot spot the threshold density fluctuation will be much lower and the gain of the three-wave SRS process will be much higher. As a result, in a nonuniform beam, LDI may be significantly affecting the SRS even when the reflectivity is well below the uniform beam threshold. Comparison of these estimates with data indicates that the average fluctuation amplitudes observed in the experiment at early times and when the impurity concentration is between 0% and 10% are large enough to excite EDI over much of the beam profile and LDI in intense regions of the beam.

Conclusion

We have observed that the SRS reflectivity in a high-Z plasma is dependent on the ion-wave damping when the Langmuir wave properties are held constant, implying that SRS is limited by a process involving ion-acoustic waves. Furthermore, the observed reflectivities are linear with ion-wave damping as expected when the electron-wave amplitude is limited by EDI or LDI, and the observed wave amplitudes are near or above the thresholds for those instabilities, indicating that the SRS reflectivity in the NIF is likely to be limited by these secondary decay processes.

Acknowledgments

Notes and References

1. J. Lindl, *Phys. of Plasmas* **2**, 3933 (1995).
2. W. L. Kruer, *The Physics of Laser Plasma Interactions* (Addison–Wesley Publishing Co., Redwood City, CA, 1988).
3. C. J. Walsh, D. M. Villeneuve, and H. A. Baldis, *Phys. Rev. Lett.* **53**, 1445 (1984).
4. H. A. Baldis, et al., *Phys. Rev. Lett.* **62**, 2829 (1989).
5. H. A. Rose, D. F. DuBois, and B. Bezzerides, *Phys. Rev. Lett.* **58**, 2547 (1987).
6. K. Estabrook, W. L. Kruer, and M. G. Haines, *Phys. Fluids B* **1**, 1282 (1989).
7. T. Kolber, W. Rozmus, and V. T. Tikhonchuk, *Phys. Fluids B* **5**, 138 (1993).
8. T. Kolber, W. Rozmus, V. T. Tikhonchuk, *Phys. Plasmas* **2**, 256 (1995).
9. S. J. Karttunen, *Phys. Rev. A* **23**, 2006 (1981).
10. J. A. Heikkinen and S. J. Karttunen, *Phys. Fluids* **29**, 1291 (1986).
11. R. P. Drake and S. H. Batha, *Phys. Fluids B* **3**, 2936 (1991).
12. B. Bezzerides, D. F. DuBois, and H. A. Rose, *Phys. Rev. Lett.* **70**, 2569 (1993).
13. K. L. Baker, Ph.D. Dissertation, University of California, Davis (1996); see also P. K. Shukla et al., *Phys. Rev. A* **27**, 552 (1983).
14. R. K. Kirkwood et al., *Phys. Rev. Lett.* **77**, 2706 (1996).
15. R. K. Kirkwood et al., *Phys. of Plasmas* **4**, 1800 (1997).
16. J. C. Fernandez et al., *Phys. Rev. Lett.* **77**, 2702 (1996).
17. D. H. Kalantar et al., *Phys. of Plasmas* **2**, 3161 (1995).
18. C. A. Back, personal communication.
19. G. Zimmerman and W. Kruer, *Comments in Plasma Phys. and Controlled Fusion* **2**, 85 (1975).
20. J. D. Moody et. al., *Bull. Am. Phys. Soc.* **39**, 1753 (1994).
21. H. N. Kornblum, R. L. Kauffman, and J. A. Smith, *Rev. Sci. Inst.* **57**, 2179 (1986).
22. R. K. Kirkwood et al., *Rev. Sci. Inst.* **68**, 636 (1997).
23. E. A. Williams et al., *Phys. of Plasmas* **2**, 129 (1995).
24. B. B. Afeyan, W. L. Kruer, and A. E. Chou, "New Regimes of Parametric Instabilities in Plasmas with Super Gaussian Velocity Distribution Functions," Lawrence Livermore National Laboratory, Livermore, CA, UCRL-JC-125364; submitted to *Phys. Rev. Lett.*, and in this *Quarterly Report*, p. **XX**.
25. P. Alaterre, J.–P. Matte, and M. Lamoureaux, *Phys. Rev. A* **34**, 1578 (1986); A. B. Langdon, *Phys. Rev. Lett.* **44**, 575 (1980).

Effects of Non-Maxwellian Electron Velocity Distributions on Parametric Instabilities

B. B. Afeyan*

A. E. Chou**

W. L. Kruer

Introduction

It is well known that non-Maxwellian electron velocity distribution functions (VDFs) exist in plasmas where there are sources of energy to sustain the plasma state away from the usual Maxwellian equilibrium. Whether it be nonlinear many-wave interactions, such as described by quasilinear theory for example[1]; turbulence,[2] a high-power laser heating a high-Z plasma,[3–7] or nonlocal heat transport in laser-produced plasmas due to steep temperature gradients,[8,9] non-Maxwellian velocity distributions have long been identified for conditions that are readily accessible in experiments today. A concrete example in laser-produced plasmas occurs when a strong enough laser irradiates a target such that the ionization state Z multiplied by the ratio of the oscillatory energy of the electrons in the field of the laser divided by their thermal energy in the plasma is ≥ 0.1. Dum[2] proposed a family of super-Gaussian distribution functions that can continuously vary from a Maxwellian ($n = 2$) to the saturated ($n = 5$) limit later explored in laser plasmas by Langdon and others.[3–7] In the latter context, when the laser intensity is sufficiently high, electron–ion heating takes place fast enough that electron–electron collisions cannot equilibrate the distribution, giving rise to these novel states. Fokker–Planck simulations have shown that such non-Maxwellian distribution functions retain their shape even in the presence of heat transport and other gradient-driven processes in the plasma.[6,7]

An important area of current research in inertial confinement fusion is the study of high-temperature hohlraums,[10] which have smaller dimensions than scale 1 hohlraums typically used on Nova.[11] These Au hohlraums do not contain fill gases, and the laser intensities used are in the 10^{16}-W/cm^2 or higher range. Clearly, such conditions are ripe for the development of non-Maxwellian distributions in the Au plasma. In addition, the importance of non-Maxwellians has been recently reinforced in two sets of Nova experiments[12,13] that used high-Z plasmas to study the behavior of parametric instabilities[14–16,11] such as stimulated Raman scattering (SRS)—the decay of an electromagnetic wave (EMW) into an electron–plasma wave (EPW) and a scattered EMW—and stimulated Brillouin scattering (SBS)—the decay of an EMW into a scattered EMW and an ion-acoustic wave (IAW). These experiments recorded the reflected levels of SRS and SBS as a function of the fractional composition of a low-Z dopant in the high-Z, Xe plasma. The data show that ion-wave properties do indeed affect SRS reflectivities via modifications of the levels of secondary instabilities.[12,13,17]

All such arguments, however, in order to be made quantitative, require that we know the frequencies and damping rates of their constituent EPWs, EMWs, and IAWs. Secondary instabilities such as the Langmuir decay[18–20] (LDI, the decay of an EPW into another EPW and an IAW) and the electromagnetic decay[21] (EDI, the decay of an EPW into an EMW and an IAW) instabilities have been studied in the past but only under the assumption that the velocity distribution of the electrons is a Maxwellian. Our results indicate that in the Xe experiments,[12,13] LDI has a threshold comparable to that of EDI and not the much higher one that Maxwellian Landau damping would have implied.

In this article, we present the results of the first systematic and not-just-perturbative calculation of the solutions of the plasma-dispersion relation in Dum-Langdon-Matte (DLM) distribution functions.[2,3,6] These are super-Gaussians whose exponents range from 2 to 5. Previous attempts to address EPWs in DLM

*   University of California at Davis, Davis, CA.
** University of California at Los Angeles, Los Angeles, CA.

distributions relied on first-order perturbation-theory evaluation of the damping rate, which our results (see Figure 1) show to be insufficiently accurate for the tasks at hand.[22–24] We also treat IAWs in DLM electron and Maxwellian ion VDFs for the first time and find novel changes in the behavior of IAWs. Strictly Maxwellian models have been routinely used to solve the kinetic dispersion relations for SRS and SBS,[26,27,11] sometimes including laser hot-spot models and additional Maxwellian hot-electron tails in an attempt to bridge the gap between theory and experiment.[24,28,29] We have developed a dispersion relation solver that calculates the Hilbert transform of any differentiable isotropic distribution function. We restrict our attention here to DLM VDFs because they provide an adequate description of smooth transitions from a Maxwellian to flat-top/depleted-tail VDFs as the laser intensity is increased in a moderate- to high-Z plasma.

This article states the plasma dispersion relations to be solved, sketches the solution method, and then shows the frequencies and damping rates of EPWs and IAWs as a function of wave-number and super-Gaussian exponent n. In addition, we use a result obtained via the Fokker–Planck simulations of Matte[5,6] (which is an empirical formula relating plasma temperature, ionization state, and laser intensity and wavelength to a given n super-Gaussian distribution function) to show damping rates of EPWs as functions of these physical parameters. This is strictly a conservative estimate of what would happen in a spatially nonuniform intensity distribution. An RPP (random phase plate)[25] laser model is adopted next and the gain of SRS calculated vs angle for different Z values. We observe that within a hot spot, not only will the laser intensity be higher than average, but the intensity-dependent damping rate of EPWs will be lower as well, making the spatial gain of the instability very much larger, as it is proportional to the exponential of the spatial integral of the ratio of these two quantities. Ramifications of these results for parametric instabilities in moderate- to high-Z plasmas are discussed, and a new model is put forward that seems to capture various seemingly unrelated trends in the many outstanding problems that exist in the interpretation of Raman and Brillouin backscattering experimental observations.

The Theoretical Model

The linear theory of parametric scattering instabilities taking into account kinetic effects was originally presented by Drake et al.[26,15] The dispersion relations to be solved for Raman and Brillouin, for instance, are

$$\frac{1}{\chi_e} + \frac{1}{1 + \Sigma_j \chi_i^{(j)}} = c^2 k^2 \left(\frac{v_0^2}{4c^2} \right) \left(\frac{|\hat{v}_0 \times k_-|^2}{k_-^2 D_-} + \frac{|\hat{v}_0 \times k_+|^2}{k_+^2 D_+} \right) \quad (1)$$

where the electron and ion susceptibilities are

$$\chi_{e,i} = \frac{\omega_{P_{e,i}}^2}{N_{0e,i} k^2} \int \frac{k \cdot \partial f_{0e,i}/\partial v}{(\omega - k \cdot v)} \; dv \quad (2)$$

and the electromagnetic Stokes (–) and anti-Stokes (+) sidebands have the following dispersion relations:

$$D_{\pm} = c^2 (k \pm k_0)^2 - (\omega \pm \omega_0)^2$$
$$+ \omega_P^2 \left[1 - 2iv_{ei}/(\omega \pm \omega_0) \right]. \quad (3)$$

The DLM VDFs may be written in the form

$$f_{0e} = C(n) \frac{N_{e0}}{v_e^3} \; \exp - \left(\frac{|v|}{\alpha_e v_e} \right)^n \; , \quad (4)$$

where v_e^2 is proportional to the electron temperature and the constant $\alpha_e = [3\Gamma(3/n)/\Gamma(5/n)]^{1/2}$ is chosen to ensure the proper definition of temperature in terms of the second moment of the 3D distribution function. The overall normalization factor is

$$C(n) = \left[1/\left(4\pi\alpha_e^3 \right) \right] \left[n/\Gamma(3/n) \right] \; ,$$

chosen so that the zero-order moment of the 3D distribution function reduces to the density, N_{e0}. As the DLM exponent n is increased from the Maxwellian limit of $n = 2$ to the limit where electron–electron collisions are entirely negligible, $n = 5$, the distribution functions have increasingly more flattened cores and depleted tails. The waterbag model is reached in the limit $n \to \infty$. Matte[5,6] has obtained the connection between the exponent n and parameters that characterize the laser-plasma system in steady-state constant-intensity illumination simulations. With the laser intensity I defined in units of 10^{15} W/cm^2, laser wavelength λ_0 in units of 0.35 μm, and the electron temperature T_e in keV, the conversion is

$$\overline{Z} I_{15,W/cm^2} \lambda_{0,\,0.35\mu m}^2 / T_{e,keV} = 44.29 \left[(n-2)/(5-n) \right]^{1.381} \; .$$

The dispersion relation for an EPW in any isotropic VDF is obtained by neglecting the coupling

due to the pump as well as ignoring the (low-frequency) ion susceptibility contribution in Eq. (1):

$$\epsilon = \left(1 + Ak^2\lambda_{De}^2\right) + \sqrt{\pi}\ \zeta_0 I\left(\zeta_0\right) = 0 \quad , \tag{5}$$

where the coefficient A describes the modified Debye shielding properties in non-Maxwellian electron VDFs. It renormalizes the temperature defined by the rule that the average kinetic energy be equal to $(3/2)kT_e$, giving rise to a new effective Debye shielding temperature boosted by this factor A. A is proportional to the ratio of the second to zeroth moments of the VDF:

$$A = \frac{n_{e0}}{2\pi \bar{f}_e} \quad , \tag{6}$$

$$n_{e0} = 4\pi \int_0^\infty f_e(\zeta)\zeta^2\ d\zeta \quad , \tag{7}$$

and

$$\bar{f}_e = \int_{-\infty}^\infty f_e(\zeta)\ d\zeta \quad . \tag{8}$$

Here $\zeta = v/v_{th}$, and the thermal velocity is given by

$$v_{th}^2 = \left(4\pi/3\right)\int_0^\infty v^4 f_e(v)dv \quad . \tag{9}$$

The normalized phase velocity is $\zeta_0 = v_\phi/v_{th}$, while the function $I(\zeta_0)$ is defined in terms of an integral along a Landau contour:

$$I\left(\zeta_0\right) = \frac{1}{\sqrt{\pi}\bar{f}_e}\int_{LC}\frac{f_e(\zeta)\ d\zeta}{\zeta - \zeta_0} \quad . \tag{10}$$

These results are true for any isotropic VDF. Specializing to the case of DLMs, the energy to Debye shielding temperature renormalization factor, A, defined in Eqs. (6–8), becomes

$$A(n) = \frac{3\Gamma^2(3/n)}{\Gamma(1/n)\ \Gamma(5/n)} \quad , \tag{11}$$

while the function I may be expressed as a principal value integral plus a simple pole contribution:

$$I\left(\zeta_0;n\right) = \frac{1}{\sqrt{\pi}}\ PV\left\{\int_{-\infty}^\infty d\zeta\ \frac{\exp\left[-|\zeta|^n\right]}{\zeta - \zeta_0}\right\} + 2i\sqrt{\pi}\ \exp\left[-\zeta_0^n\right]$$

$$= I_R + iI_I + I_{pole} \tag{12}$$

$$I_R = \frac{1}{\sqrt{\pi}}\int_{-\infty}^\infty d\zeta\ \frac{\zeta - \Re(\zeta_0)}{\left[\left(\zeta - \Re(\zeta_0)\right)^2 + \left(\Im(\zeta_0)\right)^2\right]}\exp\left[-|\zeta|^n\right] \tag{13}$$

$$I_I = \frac{1}{\sqrt{\pi}}\int_{-\infty}^\infty d\zeta\ \frac{\Im(\zeta_0)}{\left[\left(\zeta - \Re(\zeta_0)\right)^2 + \left(\Im(\zeta_0)\right)^2\right]}\exp\left[-|\zeta|^n\right] \quad . \tag{14}$$

For DLMs, it is convenient to use $\zeta_0 = (\omega/\omega_p)/[\alpha_e(k\lambda_{De})]$ as the normalized phase velocity of an EPW. The root finder must solve Eq. 5 for ζ_0 given a value of $(k\lambda_{De})^2$. For $n = 2$, the function $I(\zeta_0, n)$ reduces to the Hilbert transform of a Gaussian, and is simply the plasma dispersion function $Z(\zeta_0)$.

For small $k\lambda_{De}$, the integrands in Eqs. (13) and (14) are sharply peaked at the pole location and therefore sensitive functions of $k\lambda_{De}$. This becomes more severe as n increases and the tails become more depleted. For example, in the case of the Maxwellian, the amplitude of the integrand in I_I at the pole varies by a factor of 4.4, as $k\lambda_{De}$ is varied from 0.3 to 0.55, whereas in the same range but for $n = 5$, I_I varies by four orders of magnitude. A strategy is required in order to avoid nonconvergence problems associated with finding zeros of functions defined implicitly via integrals with sensitive dependences on the independent variable.

One such method is to start with small values of $k\lambda_{De}$, such as 0.2, and the Maxwellian VDF. By using the analytic estimate for the root of the dispersion relation found by perturbation theory, one can use a Z-function evaluator to solve the dispersion relation instead of calculating the Hilbert transform integrals directly. Increasing values of $k\lambda_{De}$ can be treated by using the roots at the previous value as a starting guess. Once a $k\lambda_{De}$ of $O(1)$ is reached, the I function evaluator can be used to go to higher n in small increments. When the desired n is reached, one may redescend to smaller values of $k\lambda_{De}$, at that large n, using the latest root as a guess. With this procedure, one may study small $k\lambda_{De}$ values for any n without uncontrolled error accumulation. This "morphing the distribution function" technique is not restricted to DLM VDFs. It would work as well with any non-Maxwellian VDF f_{nM} by the construction of a set of intermediate VDFs including an adiabatic switch ε, which would lead from the easily computable VDF f_0 to $f_0 + \varepsilon(f_{nM} - f_0)$ as $\varepsilon \to 1$. Alternate criteria can be used to choose f_0, such as by holding fixed the mean square error between itself and f_{nM} or by insisting that it be a sum of Maxwellians with particle numbers, widths, and center locations to be optimized to fit the particular VDF. In Figure 1, the frequencies and damping rates of EPWs are plotted vs

$k\lambda_{De}$ for n = 2, 3, 4, and 5. The substantial reduction in damping rates is clearly visible. Note that the first-order perturbation theory results

$$\frac{\omega_{EPW}}{\omega_{pe}} = \sqrt{1 + 3\left(k\lambda_{De}\right)^2} \tag{15}$$

and

$$\frac{\nu_{EPW}}{\omega_{pe}} = -\frac{\pi}{4}\left[\frac{n}{\left(\Gamma(3/n)\alpha_e^3\right)}\right]\frac{1}{\left(k\lambda_{De}\right)^3}$$

$$\exp-\left[\frac{1}{\left(\alpha_e k\lambda_{De}\right)^n} + \left(\frac{3n}{2\alpha_e^n}\right)\frac{1}{\left(k\lambda_{De}\right)^{n-2}}\right] \tag{16}$$

are inaccurate for $k\lambda_{De} > 0.3$ in the Maxwellian case and much earlier for higher-n cases. For values of $k\lambda_{De}$

FIGURE 1. Frequencies and damping rates of EPWs in DLM VDFs normalized to the local plasma frequency ω_p vs $k\lambda_{De}$. The thick dashed curve is the analytic result for Landau damping of an EPW with n = 5, and the solid thick curve is the same for a Maxwellian (n = 2). The dotted curves with diamonds correspond to n = 5, the solid curves with open circles correspond to n = 4, the dotted curves with crosses correspond to n = 3, and the plain solid curves correspond to n = 2. The dot-dashed curve with filled squares is the Bohm–Gross frequency.
(50-00-0797-1177pb01)

of most interest in laser-plasma experiments today (0.2 to 0.5), the actual reduction in damping can be an order of magnitude and thus must be incorporated into any analysis of scattering data, as has been recently deduced.[12,13] In Figure 2, the damping rate of EPWs is plotted vs n for different values of $k\lambda_{De}$. In Figure 3, the damping rate of plasma waves in high-Z plasmas is given vs the relevant laser-plasma parameters. This figure shows that in a speckled laser beam, where hot spots can have 5× the average intensity, the modified distribution functions will reduce the threshold for high-frequency parametric instabilities precipitously. Note, too, that the usual Bohm–Gross frequency, as given in Eq. (9), can be in error by as much as 15%.
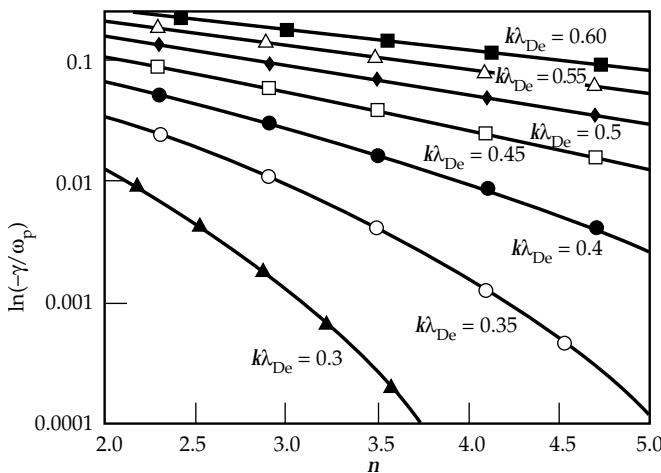
FIGURE 2. Damping rates of plasma waves in DLM VDFs normalized to the local plasma frequency ω_p vs the DLM exponent n for values of $k\lambda_{De}$ ranging from 0.3 to 0.6 in steps of .05.   (50-00-0897-1603pb01)
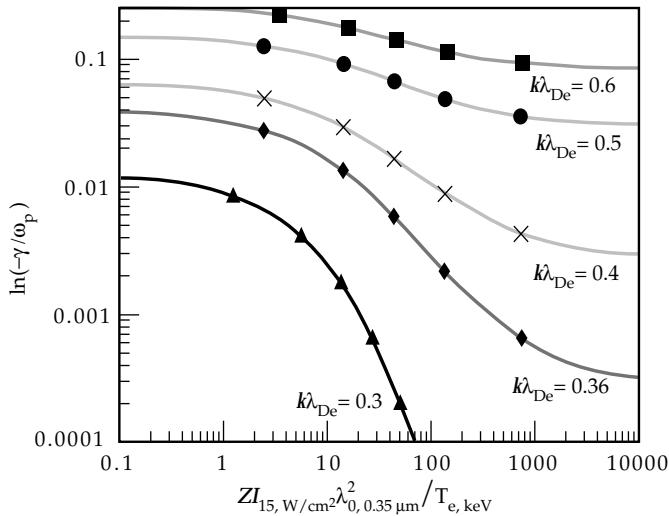
FIGURE 3. Damping decrement of electron–plasma waves normalized to the local plasma frequency ω_p vs $ZI_{15,\,W/cm^2}\lambda_{0,0.35\mu m}^2\big/T_{e,\,keV}$ for various values of $k\lambda_{De}$.   (50-00-0797-1178pb01)

In contrast, IAWs in high-Z plasmas will not have as dramatic a reduction in their damping rates. Instead, it is easily shown that their real frequencies increase with n by roughly twenty percent. The reason for this is the reduced number of cold electrons in higher-n distributions and the concomitant reduction in shielding available to the ions. This is the physical explanation for the parameter A defined in Eqs. (6) and (11). The renormalized sound speed (or the square root of the effective electron temperature) is given by the factor

$$C_{\mathrm{eff}} = \sqrt{3\Gamma^2(3/n)\big/\big[\Gamma(1/n)\Gamma(5/n)\big]} \quad . \tag{17}$$

IAWs in such plasmas will have variable frequencies for the same k as they go in and out of laser hot spots and inhomogeneities of the illumination. This constitutes an additional source of dephasing for SBS, especially if the scattered light is traveling at a large angle with respect to the axes of the speckles. The perturbation theory result for the complex IAW frequency is

$$\omega_{\mathrm{IAW}} = C_{\mathrm{eff}}c_s k\left[\frac{1}{1+C_{\mathrm{eff}}^2 k^2\lambda_{De}^2} + 3\left(\frac{T_i}{ZT_e}\right)\right]^{1/2} \quad , \tag{18}$$

and

$$\frac{v_{\mathrm{IAW}}}{\omega_{\mathrm{IAW}}} = -\sqrt{\frac{\pi}{8}}\left\{\begin{array}{l}\left(\dfrac{\sqrt{2}C_{\mathrm{eff}}}{\alpha_e C_0}\right)\left(\dfrac{Zm_e}{M_I}\right)^{1/2} \\[2mm] + \dfrac{C_{\mathrm{eff}}^3(ZT_e/T_i)^{3/2}}{\big[1+C_{\mathrm{eff}}^2 K^2\lambda_{De}^2\big]^{3/2}} \\[2mm] \exp\left[-\dfrac{C_{\mathrm{eff}}^2(ZT_e/2T_i)^{3/2}}{\big[1+C_{\mathrm{eff}}^2 K^2\lambda_{De}^2\big]}\right]\end{array}\right\} \tag{19}$$

where $C_0 = 2\Gamma(1/n)\big/(n\sqrt{\pi})$, $T_{e,i}$ is the electron/ion temperature, Z is the charge state, c_s is the ion acoustic speed, and $c_s^2 = ZT_e/M_i$. These are compared to the numerical solutions of the IAW dispersion relation in Figures 4 to 6 for different values of the wave number of the ion acoustic wave and different electron to ion temperature ratios.

The effect of changing the sound speed as a function of local laser intensity should be included in convective gain calculations for SBS that take into account flow inhomogeneities and laser nonuniformities.[30] For damping rates of the order of 0.1× the ion-acoustic
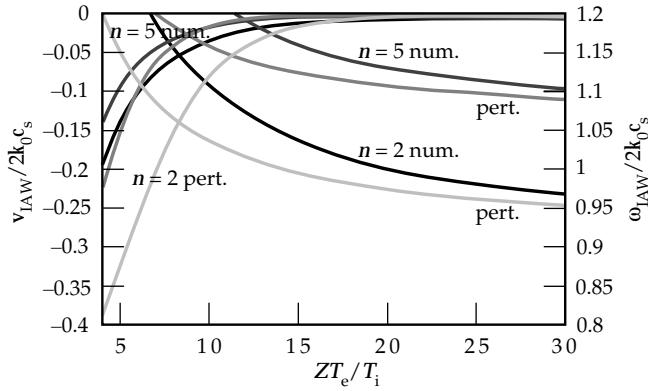
FIGURE 4. Frequencies and damping rates of IAWs in DLM electron and Maxwellian ion VDFs vs ZT_e/T_i for $k = 2k_0$. The $n = 2$ and $n = 5$ cases are plotted together with the results of perturbation theory as given in Eqs. (18) and (19).   (50-00-0797-1179pb01)
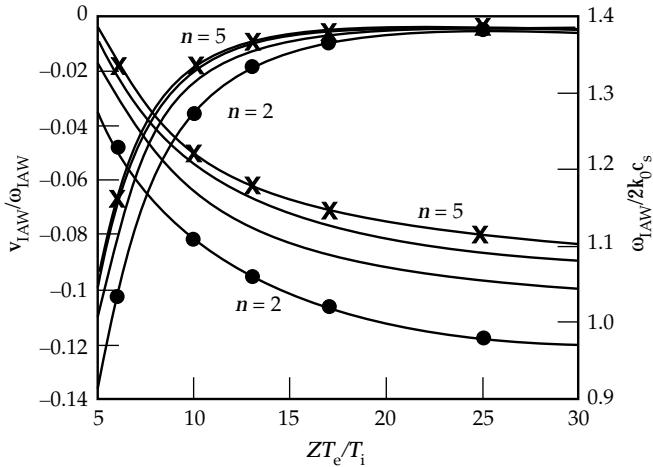
FIGURE 5. Frequencies and damping rates of IAWs in DLM electron and Maxwellian ion VDFs vs ZT_e/T_i for $k = 2k_0$. The $n = 2$, 3, 4 and 5 cases are shown.   (50-00-0897-1602pb01)
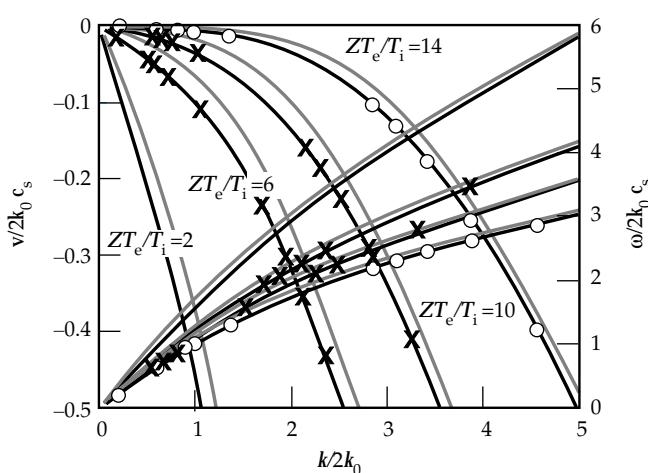
FIGURE 6. Frequencies and damping rates of IAWs in DLM electron and Maxwellian ion VDFs vs $k/2k_0$. ZT_e/T_i = 2, 6, 10 and 14 are plotted together with the approximate expressions given in Eqs. (18) and (19). (50-00-0897-1601pb01)

frequency, velocity fluctuations of order 10 to 20% have been shown to significantly reduce the gain of SBS.[31,30] The intensity-dependent frequency shift causes an additional reduction of the same order, while the angular dependence of this term is independent of and very different from that of the background flow profile. These effects help explain the low crossed beam gains observed in recent Nova experiments.[32,30]

Similar considerations for Raman lead to the picture that intensity-dependent *damping rates* will dictate the angular dependence of Raman gain. The reduction in damping inside hot spots will favor backscattered waves over side, and the ratio of the gain inside and outside hot spots can be many orders of magnitude, with pump depletion levels easily reached inside a single hot spot with only moderate gain outside. To show this, we use a typical $f/4$ hot spot and calculate the SRS gain as a function of angle for a gain length given by the length of the $I = 5I_{ave}$ region. The integrated reflectivity as a function of angle is given by the expression[15,30]

$$\left|a_s\left(L\zeta/2\right)\right|^2 = 1/L\eta \int_{-L\eta/2}^{L\eta/2} d\eta \left|a_s\left(-L\zeta/2, \eta\right)\right| \exp\left[G(\eta)\right] \quad (20)$$

$$G(\eta) = 2\Re\left[\int_{-L\zeta/2}^{L\zeta/2} k(\zeta, \eta)d\zeta\right] \quad (21)$$

$$k^{(\text{SRS})} = -\frac{1}{2}\left(\frac{D_-}{k_{-//}} + \frac{D_s}{k_s}\right) +$$

$$\sqrt{\frac{1}{4}\left(\frac{D_-}{k_{-//}} + \frac{D_s}{k_s}\right)^2 + \frac{\gamma_0^2}{4k_{-//}k_s}} \quad (22)$$

where ζ is the direction along the scattered Raman beam and η is perpendicular to it, the component of the wave vector of the EPW along the scattered light direction is $k_{-//} = \sqrt{\varepsilon}\cos\theta_s - k_s$, the k vector magnitude of the scattered light wave is

$$k_s = \pm\sqrt{1 - 2\sqrt{\frac{n/n_c + 5.87 \times 10^{-3} T_{e,\text{keV}}}{\times\left(\varepsilon - 2\sqrt{\varepsilon}k_s^0 \cos\theta_s + k_s^{(0)^2}\right)}}} \quad ,$$

θ_s is the angle between the pump and scattered light k vectors, $k_s^{(0)} = k_s\left(T_{e,keV} = 0\right)$, $\varepsilon = 1 - n/n_c$, the dispersion relation of the EPW is

$$D_- = \left[\left(\omega_0 - \omega_s\right)v_{EPW}\right]\Big/\omega_0^2 + \left(i/2\right)\left[\left(\omega_0 - \omega_s\right)\delta\big/\omega_0^2 - V_n\right],$$

the frequency of the EPW beyond the Bohm–Gross frequency is δ, the dispersion relation for the scattered light wave is $D_s = \left[v_s/\omega_s\right]\left[n/n_c\right] + i/2V_n$, and potential density inhomogeneities and fluctuations are given by

$$V_n = \left[\omega_P^2(\zeta,\eta) - \omega_P^2(0)\right]\Big/\omega_0^2, \text{ and}$$

$$\gamma_0^2 = \left(1/4\right)\left(v_0^2/c^2\right)\left(n/n_c\right)\,k_-^2 \; .$$

In Figure 7, we plot the gain of SRS as a function of angle for CH, Ti, and Xe, where $\overline{Z} \equiv \left\langle Z^2\right\rangle\big/\left\langle Z\right\rangle = 5$, 21, and 40 respectively, the electron temperature in the plasma $T_e = 3$ keV, the laser wavelength $\lambda_0 = 0.35$ μm, and the average laser intensity $I_{ave} = 10^{15}$ W/cm^2. The gain exponent for straight backscatter through the center of the hot spot where $I > 5I_{ave}$ is ~32 in the case of CH with a density of $0.1n_c$. This is consistent with very strongly collimated SRS emission, which has been observed in recent Nova experiments.[11] The effect for higher-Z materials is even more dramatic, and suggests the picture that steep-temperature-gradient–driven transport off the sides of an intense hot spot, which gives rise to depleted-tail VDFs,[9] will produce electron–plasma waves with significantly lower Landau damping and therefore larger Raman scattering in the hot spot. Large-amplitude plasma waves will be created by SRS inside the hot spots as the instability saturates, and large density and velocity fluctuations will remain in their wake. While quantitative numerical studies are needed to confirm the range of validity of the following scenario, it is hypothesized that such SRS-dominated hot spots will not be amenable to significant SBS growth even in the saturated SRS regime. When these fluctuations have dissipated their energy at typically ion-acoustic transit or ion–ion collision time scales, SRS will return, and the cycle will repeat itself. This model implies that in moderate- to high-Z plasmas with RPP beams, SRS will dominate the hot spots while SBS is forced to occur well outside these regions of highest intensity.

Nonlocal heat transport and vigorous bremsstrahlung heating-modified distribution functions, which as a class are well captured by the DLM VDFs, can play an important role in determining when SRS dominates hot spots and how low in density one must go before SRS is turned off so that SBS can take advantage of hot-spot intensities and grow to larger levels. In fact, a recent experiment by Montgomery[17] has shown that the SBS gain increases by two orders of magnitude in a CH plasma when the density is reduced from $0.1n_c$ to $0.07n_c$. The relative levels of Raman and Brillouin reflectivity measured in that experiment as a function of density are consistent with the picture that at the lower density, Raman is not strong enough to dominate the hot spots, and that Brillouin occurring in hot spots with five times the average intensity overcomes the reduction due to a decrease in density and produces the two orders of magnitude increase in SBS reflectivities seen experimentally. In order to investigate further the hot-electron dynamics and instability development in the presence of nonlocal heat transport and steep temperature gradients in moderate- to high-Z materials, Fokker–Planck transport calculations are required in conjunction with parametric instability models. We hope to address this challenging problem next.[33]

FIGURE 7. $G^{(SRS)}$ vs near-backscattering angles for $T_e = 3$ keV, $I_{ave} = 10^{15}$ W/cm^2, $n/n_c = 0.1$, and (a) $\overline{Z} = 40$ (solid line, and dashed line in the case of fixed damping at the average intensity); (b) $\overline{Z} = 21$ (solid line with x's, and dashed line with x's in the case of fixed damping at the average intensity); (c) $\overline{Z} = 5$ (solid line with circles) and dashed line with circles in the case of fixed damping at the average intensity). (50-00-0797-1180pb01)

Summary

In high-Z plasmas, or in laser hot spots with moderate Z, the damping rate of an electron-plasma wave (EPW) is substantially lower and the frequency of an ion-acoustic wave (IAW) significantly higher than those in a Maxwellian distribution. EPWs and IAWs were analyzed in flat-topped and depleted-tail electron velocity distribution functions that arise due to nonlocal heat transport and vigorous bremsstrahlung heating in high-intensity lasers. In such plasmas, SRS can dominate the most intense laser hot spots, excluding SBS from such hot spots unless the density is low enough to eliminate SRS.

Acknowledgments

Notes and References

1. R. Z. Sagdeev and A. A. Galeev, *Non-Linear Theory of Plasma*, Benjamin, New York, N. Y., 1969.
2. C. T. Dum, *Phys. Fluids* **21**, 945–956 (1978).
3. A. B. Langdon, *Phys. Rev. Lett.* **44**, 575 (1980).
4. R. D. Jones and K. Lee, *Phys. Fluids* **25**, 2307 (1982).
5. P. Alaterre, J. P. Matte, and M. Lamourex, *Phys. Rev. A* **34**, 1578 (1986).
6. J. P. Matte et al., *Plasma Phys. Cont. Fusion* **30**, 1665 (1988).
7. J. M. Liu et al., *Phys. Plasmas* **1**, 3570 (1994).
8. P. Mora, *Phys. Rev. A* **26**, 2259 (1982).
9. J. A. Albritton, *Phys. Rev. Lett.* **50**, 2078 (1983) and **57**, 1887 (1986).
10. T. J. Orzechowski et al., *Bull. Amer. Phys. Soc.*, 1996.
11. B. J. MacGowan et al., *Phys. Plasmas* **3**, 2029 (1996).
12. R. K. Kirkwood et al., *Phys. Rev. Lett.* **77**, 2706 (1996).
13. J. C. Fernandez et al., *Phys. Rev. Lett.* **77**, 2702 (1996).
14. W. L. Kruer, "*The Physics of Laser-Plasma Interactions,*" *Frontiers in Physics* series, No. 73, Addison-Wesley Publishing Co., 1988.
15. C. S. Liu, in *Advances in Plasma Physics*, Vol. 16, ed. A. Simon and W. Thompson, J. Wiley & Sons, New York, N. Y., 1976.
16. H. A. Baldis, E. M. Campbell, and W. L. Kruer, in *Handbook of Plasma Physics*, Vol. 3, ed. A. Rubenchik and S. Witkowski, North-Holland, N. Y., 1991.
17. D. S. Montgomery et al., submitted to *Phys. Rev. Lett.* (1996).
18. S. J. Karttunen, *Phys. Rev. A* **23**, 2006 (1981); J. A. Heikkinen and S. J. Karttunen, *Phys. Fluids* **29**, 1291 (1986).
19. B. Bezzerides, D. F. Dubois, and H. A. Rose, *Phys. Rev. Lett.* **70**, 2569 (1993).
20. T. Kolber, W. Rozmus, and V. T. Tikhonchuk, *Phys. Fluids B* **5**, 138 (1993).
21. K. L. Baker, Ph. D. dissertation, University of California at Davis (1996).
22. R. P. Drake et al., *Phys. Fluids* **31**, 1795 (1988); R. P. Drake et al., *Phys. Fluids B* **1**, 2217 (1989).
23. C. Rousseaux et al., *Phys. Fluids B* **5**, 920 (1993).
24. V. Yu. Bychenlov et al., *Phys. Plasmas* **4**, 1481 (1997); J. Zheng et al., *Phys. Plasmas* **4**, 2736 (1997).
25. S. M. Dixit et al., *Appl. Optics* **32**, 2543 (1993).
26. J. F. Drake et al., *Phys. Fluids* **17**, 778 (1974).
27. S. C. Wilks et al., *Phys. Fluids B* **4**, 778 (1992).
28. W. Seka et al., *Phys. Fluids* **27**, 2181 (1984).
29. D. S. Montgomery et al., *Phys. Plasmas* **3**, 1728 (1996).
30. B. B. Afeyan et al., submitted to *Phys. Plasmas* (1997).
31. W. L. Kruer et al., *Phys. Plasmas* **3**, 382 (1995).
32. R. K. Kirkwood et al., *Phys, Rev. Lett.* **76**, 2065 (1996).
33. B. B. Afeyan et al., submitted to *Phys. Rev. Lett.* (1997).

MODELING OF HIGH-POWER Z PINCHES

J. H. Hammer

J. S. De Groot

A. Toor

M. Tabak

P. Springer

K. Wong

G. Zimmerman

Introduction

Imploding *Z* pinches are powerful sources of x rays with application to weapons physics, weapons effects simulation, and inertial fusion. At drive powers of 20 TW and above, a pinch x-ray source heats materials to black body temperatures of order 100 eV or greater, enabling a variety of high-energy-density applications. Many of these applications, however, would benefit from a higher energy-density than achieved to date with *Z* pinches, placing a premium on understanding and controlling the pinch dynamics that limit the achievable energy density. For example, a factor of ~30 greater power density, as well as control of the x-ray pulse shape, may be required to employ a *Z* pinch as an ICF driver. Recent modeling work has shown the importance of RT instability in limiting the achievable power density of the pinch, and points to possible methods of reducing the effects of instabilities, which can lead to more useful high-power-density sources.

The *Z*-Pinch

Figure 1 is a sketch of the simplest pinch geometry, showing a pinch starting from an annular plasma shell or sheath. The sheath makes contact on each end with planar electrodes, and is created by electrical break-down of an annular gas puff, wire array, cylindrical foil, or low-density foam. High voltage applied across the electrodes causes the breakdown and also causes a large electric current to flow in the direction of the cylindrical or *Z*-axis. The *Z*-current and resulting azimuthal magnetic field produce a radially directed force that implodes the pinch. The Saturn accelerator[1] at Sandia National Laboratories (SNL) drives *Z*-pinch loads at currents up to 10 MA, with a rise time of 50 ns and peak electrical power of 20 TW. The Z accelerator, also at SNL,[2,3] generates currents up to 20 MA with a rise time of 100 ns and peak electrical power of 40 TW.

X rays are produced when the imploding plasma reaches the axis. The implosion converts the electromagnetic energy of the driver into kinetic energy of the plasma, which becomes thermal energy at stagnation where the pinch collides with itself. The pinch is usually composed of a high-atomic-number material, such as W, that efficiently couples the plasma thermal energy to radiation. Saturn W wire-array pinches[4] have generated in excess of 0.5 MJ of x-ray energy at a peak power of 80 TW, while Z has produced 1.9 MJ of x rays at over 200 TW peak power.[5] The x rays can be used to drive an auxiliary experiment, including heating a hohlraum that encloses the *Z* pinch.

Although the energy and power of *Z*-pinch x-ray sources are high, the energy and power densities
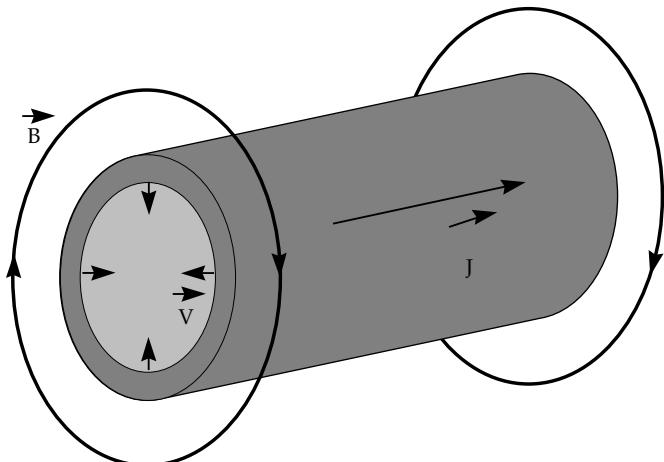
FIGURE 1. Imploding *Z* pinch configuration. B is the azimuthal magnetic field produced by the axial current J. V is the velocity resulting from the J × B force. (50-00-0797-1249pb01)

remain below those of laser-based sources, such as Lawrence Livermore National Laboratory's (LLNL's) Nova laser**.** The energy and power densities inside a hohlraum vary as the fourth power of the radiation temperature T_R, with critical minimum values of T_R required for inertial confinement fusion (ICF) or other high-energy-density experiments. For instance, successful ICF implosions[6] may require $T_R > 250$ eV. T_R is set by a balance between the input power and losses, which scale as the hohlraum area, so the highest T_R is achieved for the smallest-area hohlraum at a given power. T_R also depends on the hohlraum wall reflectivity, or albedo, which increases with T_R and time. In Saturn hohlraum experiments, the W wire-array pinch was surrounded with a gold radiation case (1 cm in radius and 2 cm long), producing peak T_R of 80 eV for a pinch-radiated power up to 80 TW with 4-ns pulse width.[7] At Nova, in comparison, values of T_R greater than 300 eV have been measured for 30 TW of laser power, nanosecond pulse lengths, and millimeter-size hohlraums.[8]

To increase the usefulness of *Z*-pinch x-ray sources, we are interested in increasing the energy density by decreasing the hohlraum size. The minimum *Z*-pinch hohlraum size is set by the initial pinch, radius, power feed gap, and the pinch length. The power feed gap is an annular slot on one end of the hohlraum between the sheath at radius $r = r_{sheath,}$ and the cylindrical hohlraum wall at $r = r_{sheath} + \Delta_{slot}$. Δ_{slot} is typically chosen to be 2 to 3 mm to avoid shorting out from plasma closure. If the sheath radius is not large enough to keep the initial inductance small, power flow is compromised by excessive voltage and current losses in the transmission line system. Saturn loads of 8-mm radius and below were fielded, while Z has required load radii of 10 mm or larger in initial experiments. Pinch lengths of at least 1 cm are thought to be needed to avoid excessive "end effects" where the imploding sheath interacts with the electrodes. Also, lengths of this order are considered necessary for good energy efficiency, which requires that the final pinch inductance (proportional to the length) be comparable with the driver inductance.

Higher currents and pinch energies can partially compensate for large loss areas in the effort to reach high T_R. At a given size, the energy scales approximately as the square of the current I, leading to T_R very roughly proportional to $I^{0.5}$ for similar pulsewidths and hohlraum dimensions. When Z can drive hohlraums similar in size to Saturn hohlraums, an improvement of roughly $(20/10)^{0.5}$ or T_R in the range 130–140 eV is expected and has recently been observed. Larger drivers in the 40–60-MA range are being planned, but it appears unlikely that $T_R > 250$ eV will be possible with this geometry, referred to as a *vacuum* hohlraum.

An alternative to the vacuum hohlraum is the *dynamic hohlraum*,[7] also known as the flying radiation case.[9] In this concept, the imploding pinch serves as the radiation case, trapping x rays produced when the imploding pinch strikes a "soda straw" or on-axis target. The x-ray energy is efficiently trapped if the imploding sheath is many optical depths in thickness. Because of the radial convergence, the dynamic hohlraum area can be dramatically reduced in comparison with the vacuum hohlraum, potentially leading to higher values of T_R.

The dynamic hohlraum places greater demands on our ability to predict and control plasma motion than the vacuum hohlraum. Control of the plasma is made difficult by magneto–Rayleigh–Taylor (RT) instability of the imploding sheath/hohlraum wall. The RT instability can lead to breakup of the hohlraum wall, permitting large losses of x-ray energy through holes and disruption of the symmetry due to the irregularity of the hohlraum wall. Fluid (nonmagnetic) RT instability can also be a problem when the hohlraum wall stagnates against low-density, low-opacity material interior to the dynamic hohlraum**,** causing mixing. Since the hohlraum wall is necessarily very opaque, the mixing could reduce the transport of x rays to a capsule or experiment of interest.

Aside from thermal x-ray sources, *Z*-pinches have also been used to generate K-shell x rays for weapons effects testing.[10] For this application, there is a need for higher-photon-energy (higher-atomic-number) K-shell radiators, which require both high implosion velocity for high temperatures and high stagnation densities to couple efficiently to radiation. As with the dynamic hohlraum, achieving these conditions places greater demands on control of the plasma dynamics, and RT modes in particular, than required for earlier, low-energy x-ray sources. The need for greater control motivates development of better theoretical and experimental understanding of imploding *Z* pinches.

Z-Pinch Modeling

A reliable predictive model for *Z* pinches does not yet exist, although there has been considerable recent progress. RT instability plays a central role in making the modeling difficult, as we can see from a simple argument. An imploding pinch does not have the benefit of ablative stabilization, as in ICF implosions, and resistive diffusion is ineffective at damping the most unstable modes.[11] The growth rate of the most unstable mode is given by the classical RT growth rate $\gamma = (kg)^{0.5}$, where $k = 2\pi/\lambda$, λ is the wavelength, and g the acceleration. For a uniformly accelerating sheath starting at radius r_0 the implosion time is given by $t = (2r_0/g)^{0.5}$, leading to the number of *e*-foldings $N = \gamma t = (2kr_0)^{0.5}$. Pinch simulations with Saturn or Z current

waveforms and "matched" annular loads that couple efficiently to the driver give $N \approx (3kr_0)^{0.5}$. If we take a typical Z initial pinch radius of 15 mm and instability wavelength of 1 mm seen in x-ray framing images, we find $N = 17$. Such a large number of e-folding times indicates that the instability will be far into the nonlinear stage, making effective modeling a challenge.

2D, radiation magnetohydrodynamics (MHD) calculations confirm that strong growth of the RT instability plays a dominant role in the pinch dynamics. If the instability is ignored, as in 1D or under-resolved 2D calculations, the codes predict pinches that are orders of magnitude smaller in spatial extent and radiation output time than observed in experiments. Calculations including RT modes find x-ray pulse widths and magnitudes in reasonable agreement with experiments, as shown in Figure 2 for Saturn Al wire implosions. In all present calculations, however, there are at least two incomplete parts of the physics that limit our predictive capability: early time history and stagnation phase.
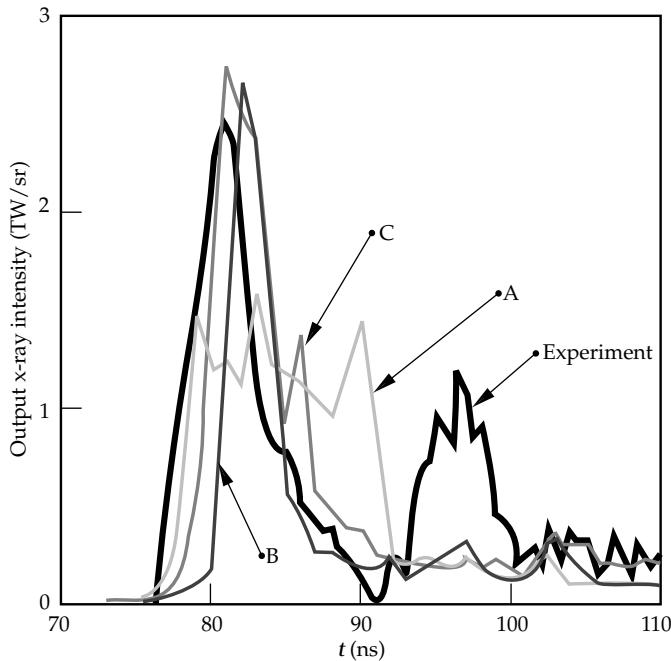
FIGURE 2. Saturn x-ray output power per unit solid angle measured by the bolometer in TW/sr compared with simulations: A, a single-mode density perturbation with amplitude 1% and wavelength 1 mm; B, a 1% random initial density perturbation with periodic boundary conditions and simulation length of 2 mm; C, a 5% random density perturbation with periodic boundary conditions and simulation length of 1 mm.   (50-00-0797-1250pb01)

Early Time History

The first missing piece of physics concerns the early time history or initiation of the pinch. In the calculations, an initial density perturbation level is chosen arbitrarily, varying from 1% to 5% in the cases shown in Figure 2, which can cause a factor of 2 or greater variation in the x-ray pulse width. The pulse width is affected by the radial smearing of the mass from the breakup into RT bubble–spike structures. The RT growth sets the time scale for the stagnation on axis to $t_{stag} = t_{spike} - t_{bubble}$, where t_{spike} and t_{bubble} are the arrival times for the spike tip and bubble, respectively. Because the radiation is produced when kinetic energy is converted to thermal energy, the output radiation pulse also occurs in a time of order t_{stag}.

One approach to understanding the pinch initiation is to do finely zoned calculations modeling a small portion of the pinch. In these calculations, shown in Figure 3, we find that very small density-perturbation levels (~1 part in 1000) are sufficient to trigger large-amplitude RT instability. The modes that are initially excited have short wavelengths (~0.1 mm) and rapidly reach the nonlinear phase, consistent with the $1/\lambda^{0.5}$ scaling of the growth rate. The short wavelengths couple to longer (eventually ~1 mm) wavelength modes, creating a cascade similar to the behavior found in other classically RT unstable systems. After reaching the nonlinear stage, the calculations[12] show self-similar growth of a turbulent layer with width and dominant instability scale growing proportional to gt^2. This behavior is similar to the growth of mix layers in RT unstable fluid systems as described by Youngs.[13] Once the bubbles penetrate the entire sheath, the self-similar growth model breaks down, or at least changes in scaling coefficient. Also, once mode wavelengths approach the scale of the sheath thickness, resistive effects are more important and may cause deviation from the self-similar scaling. The early phase growth starting from short wavelengths may represent an "irreducible" seed for the long-wavelength modes that can ultimately disrupt the sheath. We are exploring ways to use fine-scale calculations to seed larger-scale calculations of the full implosion, as discussed further in the section on dynamic hohlraum modeling.

Wire-array pinches have the additional complication of the initial explosion and merging of the wires, which can create nonuniformities and seed RT modes. Recent experiments on Saturn and Z have found a strong dependence of the x-ray pulse width on the number of wires,[4,5,14] with much shorter pulses and higher power at large wire numbers. It is not known whether the improvement is due to reduced seeding of RT or other effects. The breakpoint in wire number where performance improves is close to the point where the expansion clouds from neighboring wires

Density (g/cm³) at t = 18×10⁻⁸s
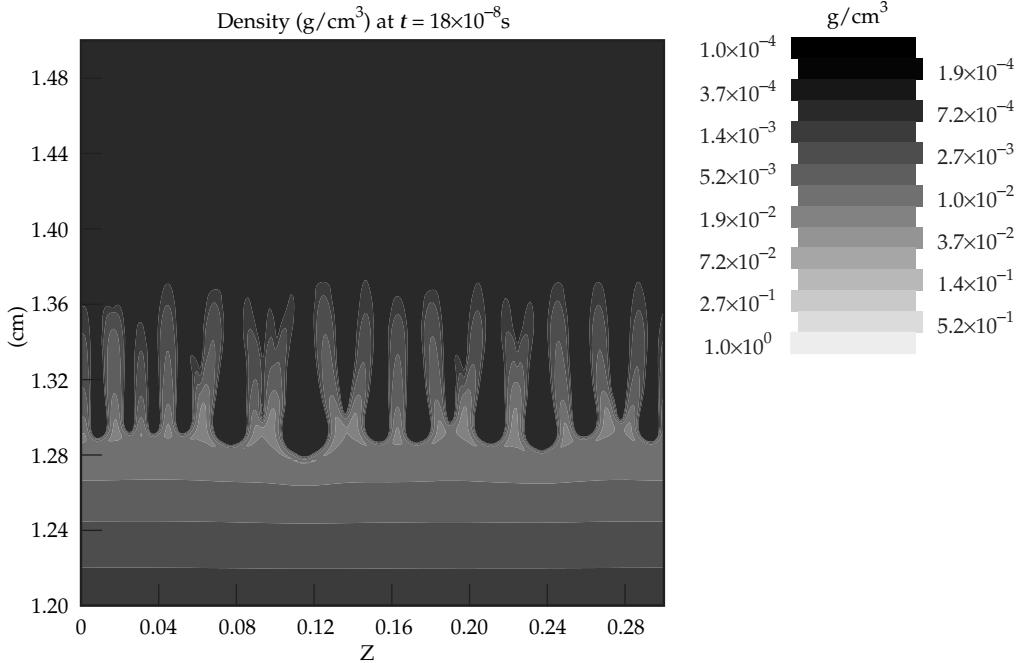
FIGURE 3. Density contours for a W *Z* pinch driven by Z. The problem is finely zoned with 10 × 10-µm zone size and an initial random density perturbation of 0.1%. The sheath was initialized as a nearly uniform block of 1-eV W vapor with a mean radius of 1.5 cm and width of 0.1 cm. (50-00-0707-1251pb01)

are expected to overlap.[14] The initial nonuniformity due to discrete wires is in the azimuthal direction, which is treated as uniform in the 2D RT calculations. Modes varying in the azimuthal direction behave differently because of the "field-line bending" effect that substantially lowers their growth rate. We hope to improve our understanding of wire-array initiation through calculations of the wire explosion and merging phases. Calculations are in progress using the TRAC2 radiation MHD code,[15] and experiments diagnosing wire initiation are planned at the University of Nevada.[16]

The large-wire-number Saturn and Z experiments may be approaching the "2D limit," where the pinch is fairly uniform in azimuth and dominated by rapidly growing azimuthally symmetric modes.

Stagnation Phase

A second missing piece of the physics applies to the stagnation phase. Our comparisons between calculation and experiment show that the radiating region is too dense and radially localized at stagnation, even for strongly RT-unstable pinches. Inclusion of 3D effects will likely be needed to resolve the differences. Because of the high radial convergence (~20), the effect of a relatively small azimuthal perturbation is strongly amplified. For instance, if a portion of the plasma develops angular momentum due to azimuthal nonuniformities, the energy associated with the angu-

lar motion increases as the square of the convergence ratio, making the plasma resistant to large radial compressions. If weak, as expected for large wire numbers and from the stabilization of field line bending, the 3D effects would have a small effect on the x-ray pulse width, yet would have a large effect on the pinch density and spatial scale at stagnation. The 3D effects are more important for self-stagnating than dynamic-hohlraum-type pinches because the latter strike an internal target and have lower convergence ratios.

Saturn Ne–Ar Gas-Puff Hohlraum Experiments

To benchmark and improve the 2D models, experiments were done on Saturn that permitted the first space- and time-resolved measurements of the density and T_e in the stagnating plasma.[17] Gas puff pinches composed of 90% Ne and 10% Ar were used for these experiments, and conditions at stagnation were measured with an absolutely calibrated, high-resolution space- and time-resolving x-ray spectrometer. The T_e was determined from the slope, as a function of photon energy, of the continuum radiation from recombining, fully stripped Ne ions. The ion density was found by measuring the Stark (or density-induced) broadening of spectral lines from He-like Ar ions.

For annular gas puffs (2 cm long, 1.25 cm initial *r*, 0.8 cm thick, and 600 µg total mass), the peak n_e at

stagnation was measured to be 8×10^{20} cm^{-3} with a corresponding peak mass density of 0.0028 g/cm^3, with a peak T_e of 1.2 keV. Figure 4 shows radial and axial profiles of the intensity of emission in two spectral energy bins (approximately proportional to the square of the density) and the radial and axial profile of T_e. The experimental data shown in Figure 4 are from a snapshot in time taken near peak x-ray emission. The axial variation is caused by "zippering" of the pinch where the sheath reaches the axis at different times. The middle of the pinch was observed to radiate first, followed by two localized emission spots that move outward toward the electrodes. The zippering is caused by initial axial variation of the gas puff, which is formed by releasing a supersonic gas jet into the vacuum.

We compared the data with 2D radiation MHD cal-
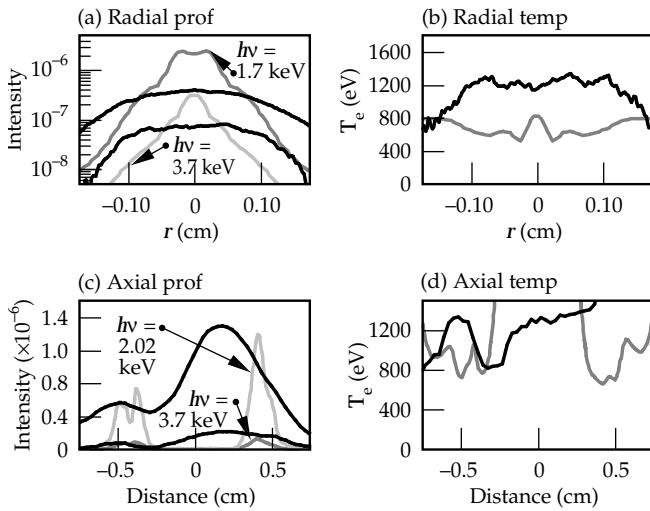
FIGURE 4. Radial and axial profiles of the intensity of emission in two different spectral energy bins near 1.7 keV and 3.7 keV. The intensity data are processed to give the radial and axial temperature profiles, also shown. Experimental data is shown in black, and the 2D non-LTE calculation is represented in gray. (50-00-0797-1252pb01)

culations with an initial large-scale density nonuniformity to simulate the zippering and with a 1% random zone-to-zone density perturbation to seed RT modes. We used two different atomic physics models. The first model assumes local thermodynamic equilibrium (LTE) where the populations of different atomic states are set equal to the values they would have in thermodynamic equilibrium at the local T_e. The second (non-LTE) model solves rate equations for the population of atomic states. Not surprisingly, for a comparatively low-density, hot plasma such as produced in the experiment, the non-LTE model differs markedly

from the LTE model. The LTE model predicts a stagnation density of 0.33 g/cm^3, T_e of 300 eV, and a pinch diameter of 0.02 cm vs the observed pinch diameter of 0.2 cm. The 2D non-LTE model gives an improved stagnation density of 0.018 g/cm^3, a T_e of 700 eV, and a pinch diameter of 0.05 cm. The LTE model predicts stronger coupling to radiation than the non-LTE model, cooling the plasma so that it has less pressure to resist the radial collapse. The calculated intensity and T_e profiles from the 2D non-LTE run are shown in Figure 4 for comparison with the data. Figures 5 and 6 show a series of time snapshots of the plasma density and T_e during the implosion for the non-LTE run. The axial zippering and development of RT bubble-spike features are clearly visible in Figures 5 and 6.

We have also done a series of 1D non-LTE runs to determine whether the remaining differences are due to the atomic physics or other aspects of the modeling. We fix the pinch radius and density and add an ion heat source representing the shock heating at stagnation. At the radius and density of the 2D non-LTE simulation, the 1D runs also give a 700-eV T_e, while at the experimentally observed radius and density we calculate 1.2 keV in agreement with the experiment. These results suggest that the difference between the 2D model and experiment is not in the atomic physics, but in another part of the physics. The 2D hydrodynamic treatment is a likely source of the difference, perhaps requiring 3D as discussed above. Further support for this comes from broadband x-ray framing images of the implosion. The images show hoop-like structures during much of the implosion, as expected when viewing axially symmetric RT bubble–spike structures from an angle. At stagnation, however, the framing images show asymmetric features suggesting that a 3D treatment is needed. For both the 1D and 2D runs, the ion temperature (a few keV) is much lower than the 36-keV measured value from Doppler broadening. On the other hand, the emission-averaged turbulent flow energy from the 2D run is several tens of keV, suggesting that the Doppler-measured temperature actually measures plasma flow.

Z Dynamic Hohlraum Simulations

We have done 2D radiation MHD simulations of a dynamic hohlraum target designed to be driven by Z. In this design, we attempt to reduce the effects of RT modes by using a distributed initial density profile. In earlier work[11], we showed that "tailoring" the initial density profile could reduce the time-averaged sheath acceleration and number of e-foldings of the RT instability. As the sheath moves in radially, fresh material is swept up or "snow plowed," providing a back pres-

Density evolution of Ne-Ar annular pinch
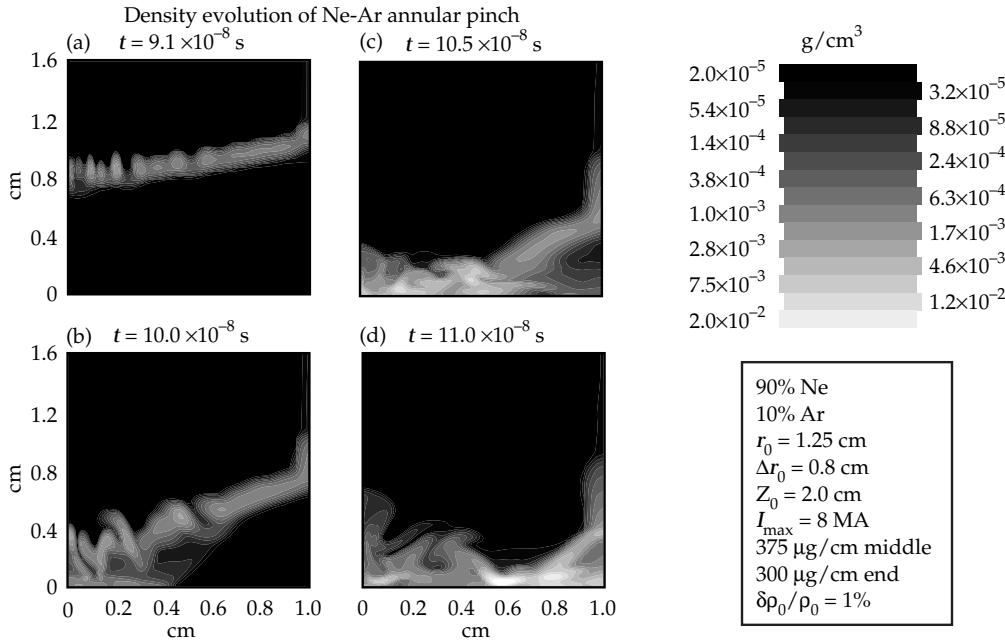
FIGURE 5. Density evolution of Ne–Ar annular pinch. Density contours are shown at times of 91, 100, 105, and 110 ns. (50-00-0797-1253pb01)

90% Ne
10% Ar
$r_0 = 1.25$ cm
$\Delta r_0 = 0.8$ cm
$Z_0 = 2.0$ cm
$I_{max} = 8$ MA
375 µg/cm middle
300 µg/cm end
$\delta \rho_0 / \rho_0 = 1\%$

Te evolution of Ne-Ar annular pinch
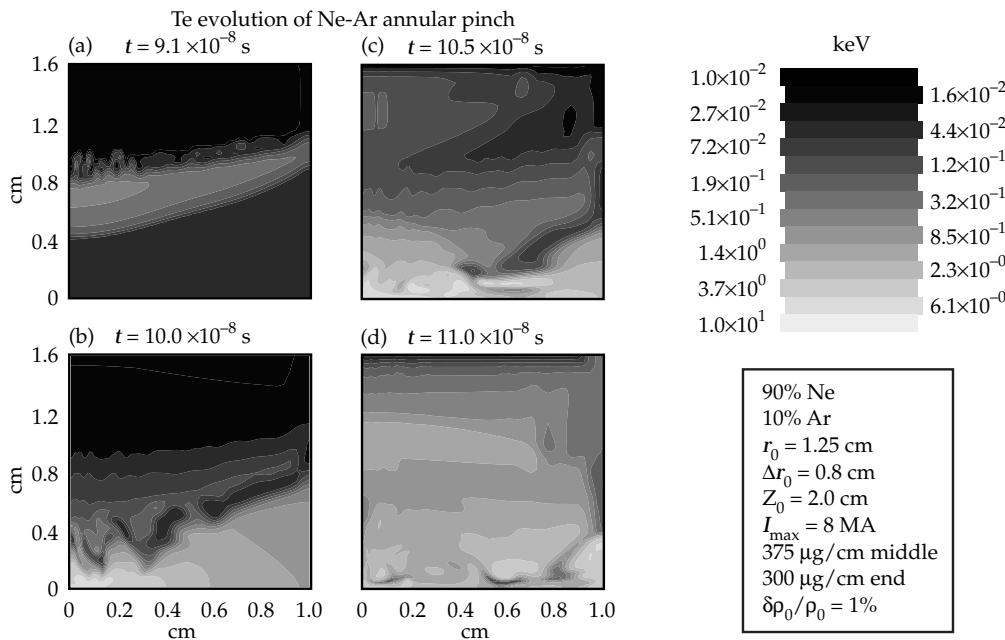
FIGURE 6. Electron temperature T_e evolution of Ne–Ar annular pinch. Temperature contours are shown at times of 91, 100, 105, and 110 ns. (50-00-0797-1254pb01)

90% Ne
10% Ar
$r_0 = 1.25$ cm
$\Delta r_0 = 0.8$ cm
$Z_0 = 2.0$ cm
$I_{max} = 8$ MA
375 µg/cm middle
300 µg/cm end
$\delta \rho_0 / \rho_0 = 1\%$

sure that counters the $\mathbf{J} \times \mathbf{B}$ force.[18] A special profile can be found where the unstable outer surface of the sheath implodes at constant velocity, reducing the classical growth rate to zero, although residual Richtmeyer–Meshkov-type instability (instability of the snow-plow shock front) may be present. In practice, it is hard to create tailored initial density profiles due to the difficulty of machining and otherwise manipulating very-low-density materials. It becomes easier to manufacture these complex targets as the cur-

rent, energy, and load mass increase with large drivers. Z is the first fast-pulse power device with enough energy to consider loads of this type.

The design we have modeled employs a 3-cm-diam, 2-cm-long W wire array of mass 7.54 mg as the high-atomic-number shell material. The wire array implodes on three concentric, annular shells of low-density (10-mg/cm^3) agar foam with a 25-µm layer of Be covering the interior of the central shell, shown in Figure 7. The annular shells, with foam between radii

of 1.1 and 1.15 cm (outer shell), 0.6 and 0.7 cm (middle shell), and 0.25 and 0.3 cm (inner shell), explode under the influence of the x rays emitted by the wire array and outer shells. In the process, they create a rough approximation to the zero-acceleration tailored density profile. The use of multiple shells to control RT insta-bility in Z pinches has been studied previously.[19] Simulations in 1D show the stagnation of the Be at a minimum diameter of about 0.16 cm, with a peak radi-ation temperature of 240 eV and temperatures exceed-ing 200 eV for 7 ns. Figure 8 shows the radii of the different layers and the T_R on the pinch axis. The peak

r = 1.5 cm, W array

r = 1.1–1.15 cm, agar shell, 10 mg/cm^3

r = 0.6–0.7 cm, agar shell, 10 mg/cm^3

r = 0.25–0.3 cm, agar shell, 10 mg/cm^3
25-µm Be shell
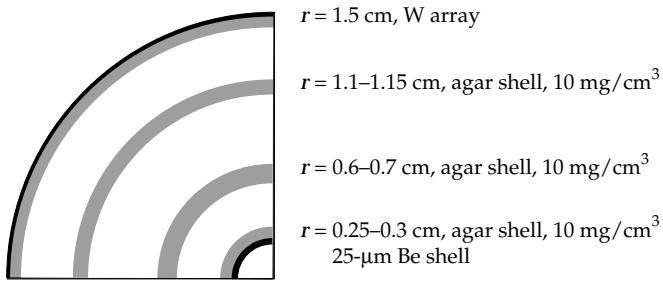
FIGURE 7. Dynamic hohlraum target. (50-00-0797-1263pb01)
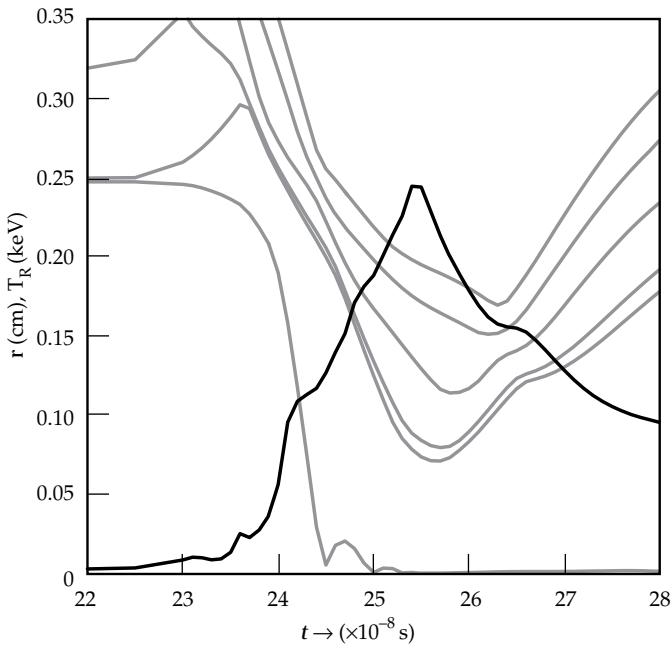
FIGURE 8. T_R (keV) on axis (solid line) and radius (cm) of shells (dashed lines) vs time (ns). (50-00-0797-1263pb01)

temperature occurs 50 ns after the current peaks at 17 MA. In the hot, stagnated Be, the average distance that x-ray photons can travel before being absorbed and re-emitted, the Rosseland mean free path, is several times the pinch diameter, while the agar and W layers have an optical depth of about 20. With these conditions, it is sensible to describe the configuration as a dynamic hohlraum. The Be fills the hohlraum at a density of about 0.1 g/cm^3 and pressure of order 50 Mbar. This type of hohlraum is better suited to driving auxiliary experiments than ICF capsules inside the hohlraum that could be affected by the high plasma pressure. The drive temperature seen by an auxiliary experiment depends on the type of experiment. A highly reflective load on the end sees the full 240 eV, while a highly absorptive load removes significant energy from the hohlraum, dropping the effective drive temperature to 180 eV.

We have also done 2D calculations including the effects of RT modes for this target and similar designs. A calculation for a similar target with a 1% density perturbation and a 2-mm wavelength show significant instability growth in the W, but little perturbation of the inner layers. At stagnation against the inner annu-lus, the bubble–spike formation in the W is partly reversed. The peak temperature drops from 230 eV to ~220 eV, and the hohlraum interior remains optically thin at about the same diameter as the 1D simulation. Simulations of 2D with 5% initial random zone-to-zone density perturbation show larger amplitude growth in the W with less perturbation of the inner shells. The W is sufficiently disrupted that cracks in the radiation case form and allow large radial losses, causing the T_R on axis to drop to 180 eV. Perturbations in the 1% to 5% range have been found to give reasonable pulsewidths for Saturn and Z experiments,[11,20] although the pertur-bation level imposed in this way is zoning-dependent.

To reduce the uncertainty in choosing the perturba-tion level and come closer to a "first principles" RT cal-culation, we have done simulations with a very fine mesh. As discussed above, RT modes at short wave-lengths can grow to nonlinear amplitudes very quickly from small initial perturbations, then seed more destructive long-wavelength modes through a nonlin-ear cascade. To provide a self-consistent instability seed, we have done a finely zoned (10-µm × 10-µm zones) calculation capable of resolving the short wave-lengths that dominate the early phase. This method of initiating RT calculations with a 2D *r-z* code is only valid when there are enough wires in the initial array to merge into an azimuthally uniform sheath before significant RT growth begins. For this calculation, modeling 3 mm of the pinch length with periodic
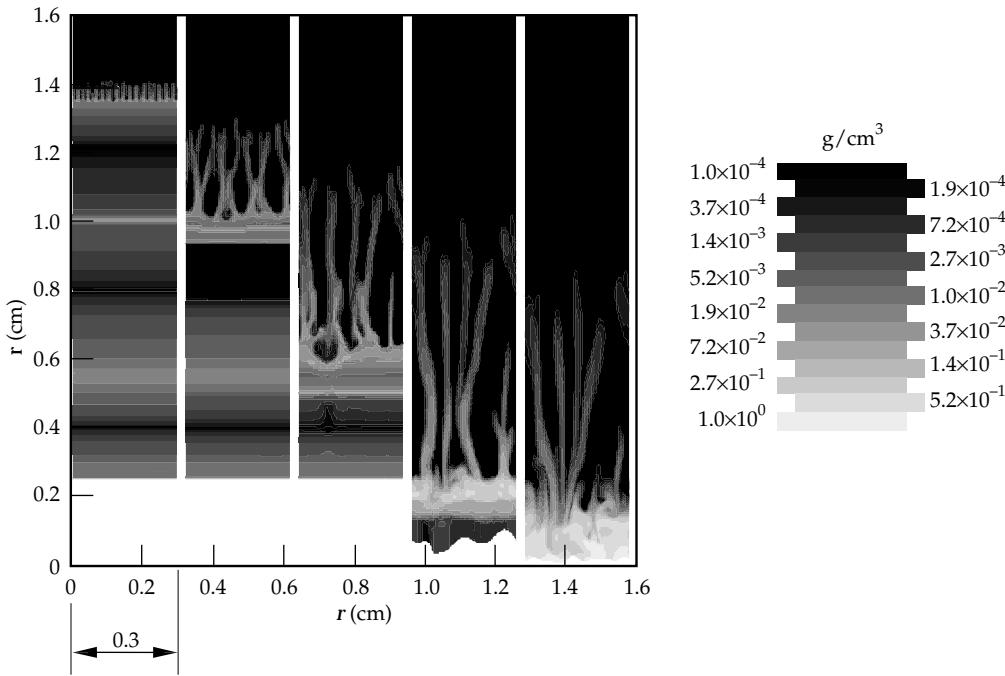
boundary conditions in the *z*-direction, random density perturbations of 0.1% were sufficient to stimulate large-amplitude RT growth. Once the dominant features were several hundred microns in scale, we linked to a coarser mesh (~30-µm zone size) to follow the complete implosion. A series of time snapshots of the plasma density for the multishell agar foam plus Be target are shown in Figure 9. This calculation showed reasonable integrity of the radiation case so that radiation leakage was not a major effect and the radiation temperature was ~220 eV in the hohlraum interior. A plume of optically thick, high-atomic-number material reached the axis at one location, however, which could inhibit energy flow to an adjacent load. If the high-atomic-number plume occurs more than a few mm from the output end, the effect on energy flow should be small. The RT calculations do not include the effect of an x-ray-absorbing load, which would cause an additional drop in the T_R.

All of the calculations show significant breakup of the W sheath before it encounters the outermost stabilizing agar shell. This prompts us to consider an initial state that more closely approximates the zero-acceleration density profile at large radius. At present, it is not practical to extend the profile to larger radius with low-density foams because of our limited ability to machine and handle these extremely fragile materials. An alternative may be to use concentric, nested wire

arrays, with the separation between wires in each shell smaller than the distance the wires expand due to heating by x rays. With this technique, an arbitrary initial density profile of virtually any material may be possible. The first experiments with simpler loads will indicate if these more complex targets are necessary to control RT instability.

Conclusion

Imploding pinches have produced very powerful and energetic x-ray sources, yet our understanding of the basic dynamics of these devices is still at an early stage. The initiation of the pinch, in particular, is critical to the subsequent dynamics but remains poorly understood. Recent modeling work has shown the importance of RT instability in limiting the achievable power density of the pinch and points to possible methods of reducing the effects of instabilities through control of the initial density distribution. Developing efficient, reproducible, high-power-density sources (>250 eV) is likely to require control of instabilities. We anticipate that further research will enable us to develop a better understanding of pinch dynamics, which may lead to higher energy densities of greater use to the Department of Energy's Stockpile Stewardship and Management Program.

Notes and References

1. D. D. Bloomquist, R. M. Stinnett, D. H. McDaniel, J. R. Lee, et al., *Proc. 6th International Electrical and Electronic Engineering Pulsed Power Conference*, Arlington, VA, Eds., P. J. Turchi and B. H. Bernstein (IEEE, New York, 1987), p. 310.

2. R. B. Spielman, et. al., "Paper O–4–3," in *Proceedings of the 10th International Conference on High Power Particle Beams*, Prague, Czech Republic, June 10–14, 1996, Eds., K. Jungwirth and J. Ullschmied, pp. 150–153. (Copies of the conference proceedings can be ordered from *BEAMs96*, Institute of Plasma Physics, Czech Academy of Sciences, Za Slovankou 3, 182 00 Prague, Czech Republic.)

3. R. B. Spielman, G. A. Chandler, C. Deeney, F. Long, T. H. Martin, M. K. Matzen, et al., *Bull. Am. Phys. Soc.* **41**, 1422 (1996).

4. C. Deeney, T. J. Nash, R. B. Spielman, J. F. Seamen, et al., "Power Enhancement by Increasing Initial Array Radius and Wire Number of Tungsten Z Pinches," submitted to *Phys. Rev. E.*

5. R. B. Spielman, Sandia National Laboratory, Albuquerque, NM, private communication (1997).

6. J. Lindl, *Phys. Plasmas* **2**, 3933 (1995).

7. M. K. Matzen, *Phys. Plasmas* **4**, 1519 (1997).

8. R. Kauffman, L. Suter, C. B. Darrow, J. D. Kilkenny, et al., *Phys. Rev. Lett.* **73**, 2320 (1994).

9. J. Brownell, Los Alamos National Laboratory, Los Alamos NM, private communication (1995).

10. C. Deeney, T. Nash, R. R. Prasad, L. Warren, et al., *Phys. Rev. A* **44**, 6762 (1991).

11. J. H. Hammer, J. L. Eddleman, P. T. Springer, M. Tabak, et al., *Phys. Plasmas* **3**, 2063 (1996).

12. J. H. Hammer, J. L. Eddleman, M. Tabak, A. Toor and G. B. Zimmerman, "Sheath Broadening in Imploding Z-pinches due to Large-bandwidth Rayleigh-Taylor Instability," in *Proceedings of the 10th International Conference on High Power Particle Beams*, Prague, Czech Republic, June 10–14, 1996, Eds. K. Jungwirth and J. Ullschmied. (Copies of the conference proceedings can be ordered from *BEAMs96*, Institute of Plasma Physics, Czech Academy of Sciences, Za Slovankou 3, 182 00 Prague, Czech Republic.)

13. D. L. Youngs, *Physica* **12D**, 32 (1984).

14. T. W. L. Sanford, G. O. Allshouse, B. M. Marder, T. J. Nash, et. al., *Phys. Rev. Lett* **77**, 5063 (1996).

15. J. L. Eddleman, J. H. Hammer, C. W. Hartman, A. W. Molvik, and H.S. McLean, *Bull. Am. Phys. Soc.* **34**, 2051 (1989).

16. B. S. Bauer, Department of Physics, University of Nevada, Reno, private communication (1997).

17. K. L. Wong, P. T. Springer, J. H. Hammer, C. A. Iglesias, et. al., "Spectroscopic Characterization of an Argon-Neon Z-Pinch Plasma at Stagnation," in preparation, July 1997.

18. A. L. Velikovich, F. L. Cochran, and J. Davis, *Phys. Rev. Lett.* **77**, 853 (1996).

19. R. B. Baksht, S. P. Bugaev, I. M. Datsko, A. V. Luchinskii, et al., "Dense Z-Pinches, Tjore International Conference," Eds. M. Haines and A. Knight (AIP Conference Proceedings, vol. 299, p. 365, AIP, New York), 1994.

20. D. L. Peterson, R. L. Bowers, J. H. Brownell, A. E. Greene, et al., *Phys. Plasmas* **3**, 368 (1996).

A WALK THROUGH
THE NATIONAL IGNITION FACILITY

J. Murray

---

*T*he National Ignition Facility (NIF) will house the world's most powerful laser system. Figure 1 shows the laser and target area building, as they appear in the Title I Design (see p. vi). The overall floor plan is U-shaped, with laser bays forming the legs of the U, and switchyards and the target area forming the connection. The NIF will contain 192 independent laser beams or "beamlets" that are 40 × 40 cm each. Beamlets are grouped into 2 × 2 "quads," which are stacked two high in 4 × 2 "bundles" (thus eight beamlets per bundle). These bundles are grouped six each into four large "clusters," two in each laser bay, for a total of 192 beamlets (8 beamlets per bundle × 6 bundles per array × 4 clusters. The 192 laser beamlines will require more than 7000 discrete, large optical components (larger than 40 × 40 cm) and several thousand smaller optics. Beams from the laser will strike a series of mirrors, which will redirect them to the large target chamber shown on the right side of Figure 1. The building for the NIF will be about 100 m wide (122 m including the capacitor bays), and about 170 m long.

In the following tour, we track the path of a laser pulse from its beginnings in the master oscillator room (MOR) to the target chamber through the principal laser components.
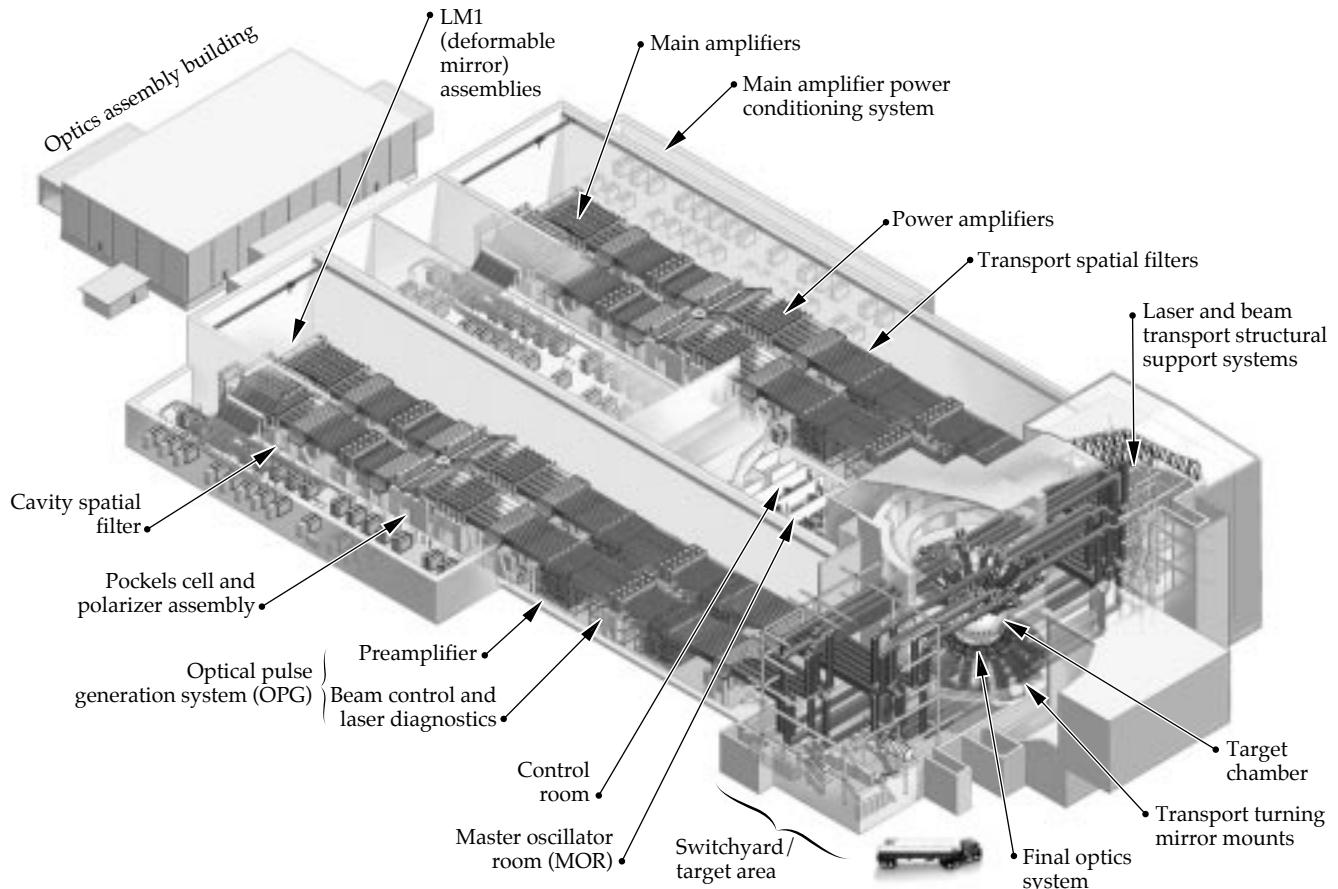
FIGURE 1. Layout of the laser and target area building. Note the two pairs of large beamlet clusters running the length of each laser bay; each of these four clusters is essentially identical to the other. (40-00-0096-2100pb01)

<div style="border:1px solid #000; padding:1em;">

WHY 192 BEAMS?

In deciding how many beams for the NIF, there were two conditions we had to meet. First, there had to be enough beam area facing the target to deliver the required energy. The maximum safe 3ω fluence for an ignition target pulse is about 9 J/cm^2. The maximum practical single beam area is about 1300 cm^2, which would deliver about 11 kJ/beam on the target. At 11 kJ per beam, we need at least 164 beams to put 1.8 MJ on target. Second, we had to consider the conditions required by indirect- (x-ray-) drive targets. These targets (cylindrically symmetric hohlraums) require twice as many beams in the outer cone as in the inner cone, illumination from two directions, and eight or more beam spots per cone. When we multiply these factors together, we find that the beam count must be divisible by 48. The smallest system that satisfies these two conditions is $4 \times 48 = 192$ beams.

It turns out that it is also very convenient to transport these beams in 48 (2×2) clusters, and that this configuration is also compatible with direct-drive uniformity requirements. Finally, 192 beams at 9 J/cm^2 provides 2.2 MJ, a full 20% margin for baseline operation of 1.8 MJ.

</div>

Master Oscillator System

The laser pulse is produced in the master oscillator room, where a fiber ring oscillator generates a weak, single-frequency laser pulse. A phase modulator puts on bandwidth for smoothing by spectral dispersion (SSD) and suppressing stimulated Brillouin scattering. Each pulse is then launched into an optical fiber system that amplifies and splits the pulse into 48 separate fibers. The optical fibers carry the pulses to 48 low-voltage optical modulators very similar to those used in high-bandwidth fiber communication systems. These modulators allow us to temporally and spectrally shape each pulse by computer control. An optical fiber then carries each nanojoule, 1-μm pulse to a preamplifier module (PAM).

Preamplifier Module

Optical fibers carrying the pulses from the master oscillator room spread out to 48 preamplifier modules, located on a space frame beneath the transport spatial filters. Each preamplifier has a regenerative amplifier followed by a flashlamp-pumped four-pass rod amplifier. The preamplifier is a two-stage system, designed as a self-contained assembly, that can be pulled out and replaced as needed. The preamplifier brings the pulse to about 10 J, with the spatial intensity profile needed for injection into the main laser cavity. Before entering the main cavity, the output from the preamplifier is split four ways. These four pulses are injected into the four beams that form each of the 48-beam "quad" arrays.

Main Laser System

Figure 2 shows the layout of the main laser components of a NIF beamlet. These components take a laser pulse from the preamplifier to the final optics assembly. A laser pulse from the preamplifier enters the main laser cavity when it reflects from a small mirror labeled LM0 in Figure 2. This mirror is located near the focal plane of the transport spatial filter. The 40-cm-diam pulse exits the transport spatial filter, traveling to the left, and passes through the power amplifier, containing five amplifier slabs.

The beam then enters the periscope assembly, which contains two mirrors (LM2 and LM3) and a switch (a Pockels cell and a polarizer). The pulse reflects off LM3 and the polarizer before passing through the Pockels cell. It goes through the cavity spatial filter and the 11-slab main amplifier, and then reflects from a deformable mirror with 39 actuators. After once again passing through the main amplifier, the beam comes back through the cavity spatial filter to the periscope assembly. Meanwhile, the Pockels cell has been fired to rotate the polarization, so the beam passes through the polarizer and strikes mirror LM2, which redirects it back through the cavity spatial filter for another double pass through the main amplifier. The beam returns to the periscope assembly, passes through the de-energized Pockels cell, reflects off the polarizer and LM3, and is further amplified by the power amplifier. Now the pulse passes through the transport spatial filter on a path slightly displaced from the input path. The output pulse just misses the injection mirror LM0 and enters the switchyard and beam transport area.
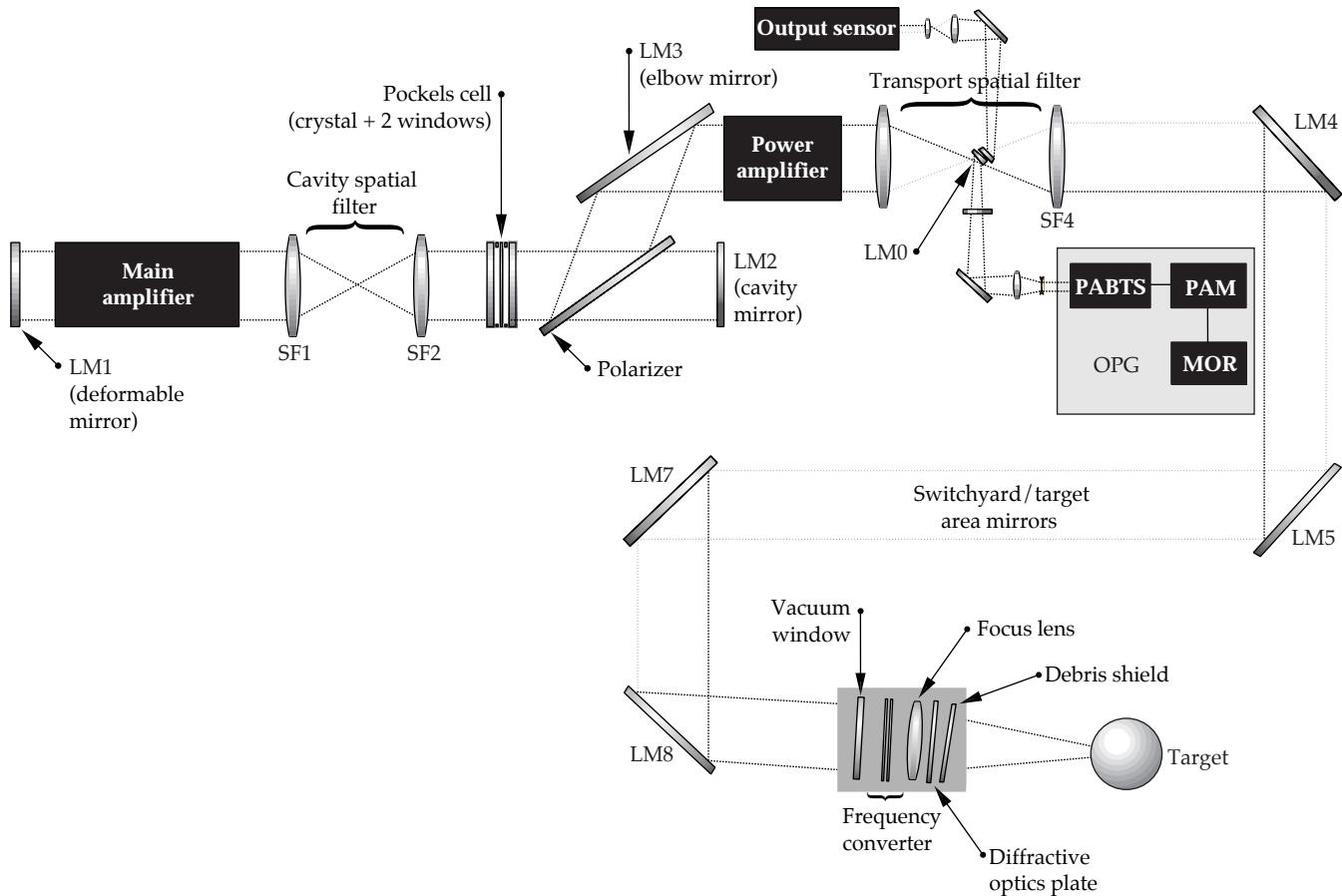
FIGURE 2. Schematic diagram of the NIF laser system.   (40-00-0997-1759pb01)

Switchyard and Beam Transport

Between the switchyards and the target chamber room, the beams are in two 2×2 arrays: The 4×2 bundles are split into 2×2 quads, moving up or down to one of the eight levels of the switchyard (see p. 154). Each pulse now travels through a long beam path, reflecting off of several transport mirrors before reaching the target chamber. The transport mirrors can be moved to create the beam configuration needed for direct- or indirect-drive experiments. For indirect drive, mirrors send the beams straight up or straight down to make the cones coming into the top and the bottom of the target chamber cylinder (Figure 3). For direct drive, we can direct 24 beams to circumferential positions around the target chamber by moving two mirrors in each of these beamlines (Figure 4). Once the beams reach the target chamber, they enter the final optics assembly.

Final Optics Assembly

The final optics assemblies are mounted on the target chamber. Each assembly includes a vacuum window at 1ω, a cell that includes a frequency converter (two plates of potassium dihydrogen phosphate crystal) to convert the pulse to 3ω, and the final focusing lens. The cell tips and tilts to tune the frequency converter, and translates along the beam direction to focus the beam on the target. A debris-shield cassette includes the capability of diffractive optics for spot shaping. Once a pulse travels through this assembly, it proceeds to the target in the target chamber.

FIGURE 3. Beam transport layout for indirect-drive experiments (end view). (40-00-0796-1623pb01)
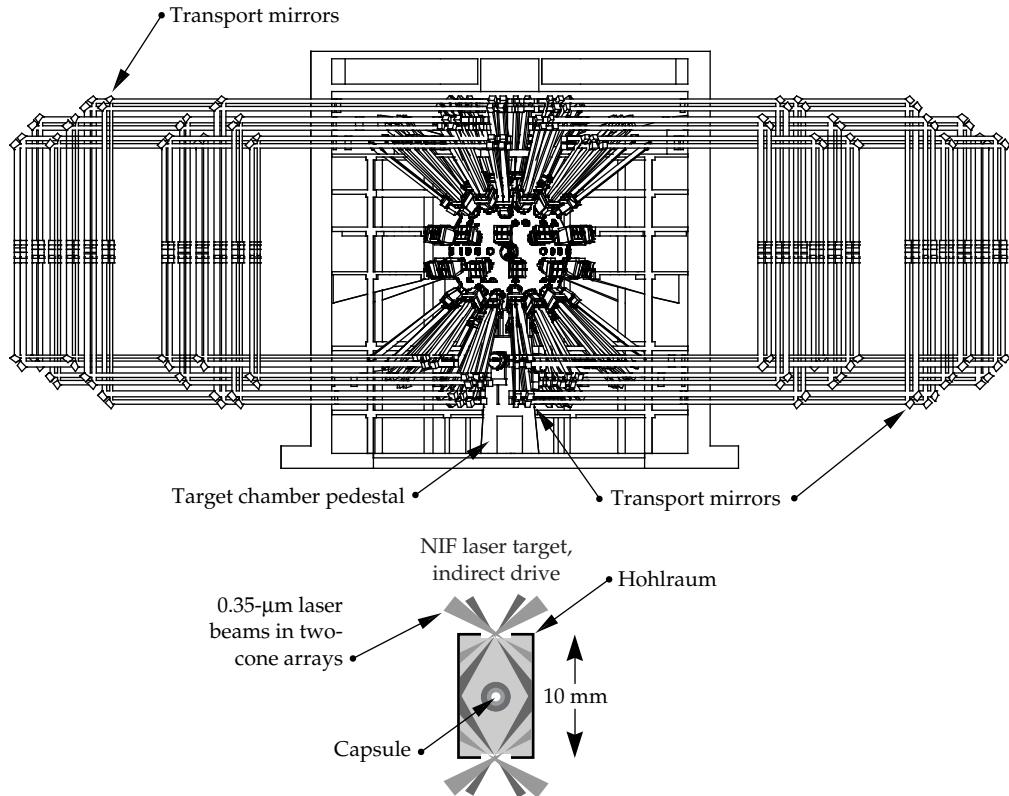
FIGURE 4. Beam transport layout for direct-drive experiments (end view). (40-00-0796-1624pb01)
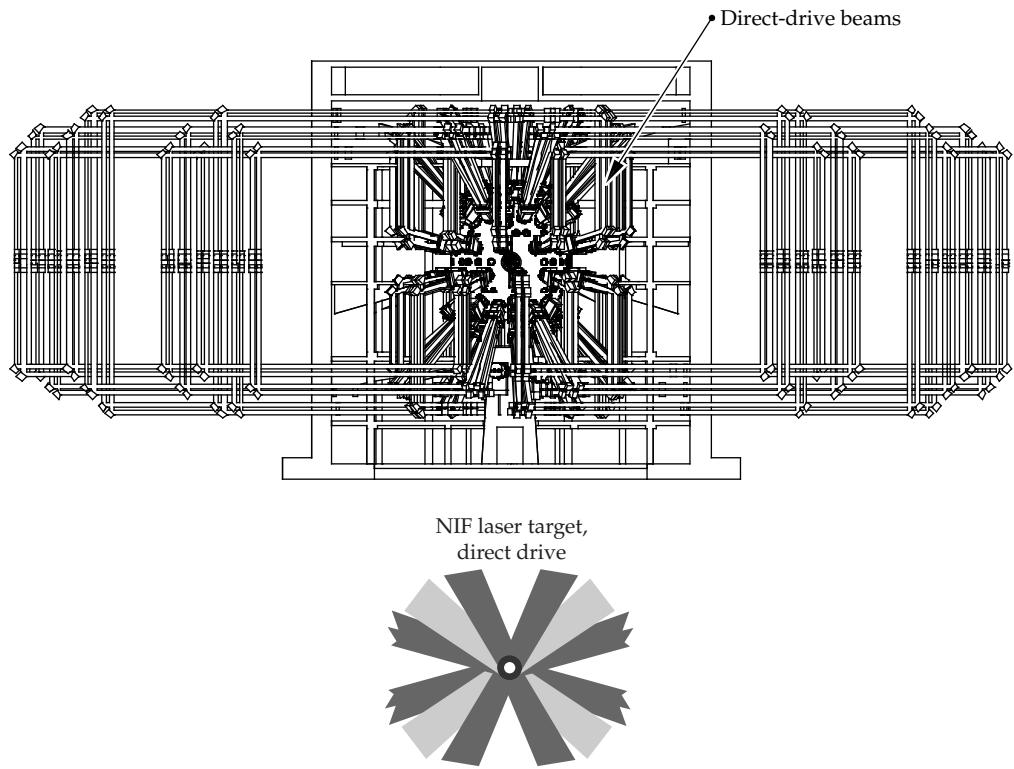
LASER REQUIREMENTS AND PERFORMANCE

J. Murray

J. Auerbach

J. Hunt

K. Manes

R. Sacks

J. Trenholme

W. Williams

*T*he Title I Design for the NIF meets all baseline perfor-mance requirements of our users from the ICF, weapons physics, and weapons effects communities. The Title I Design is a refinement of the NIF conceptual design and includes 16 amplifier slabs for each of the 192 beams and a total of 48 preamplifier modules (for all 192 beams) for the initial configuration. Laser performance for this con-figuration was validated with performance models and Beamlet data.

User Requirements

The Title I Design for the NIF takes into account the requirements and requests of our three main user com-munities. The top-level performance requirements for the NIF were driven by the indirect- (x-ray-) drive, ICF mission. Those requirements are as follows:

- 1.8 MJ of laser pulse energy on target.
- Flexible pulse shaping (dynamic range >50).
- Peak power of 500 TW.
- Pulse wavelength in the ultraviolet (0.35 µm).
- Beam power balance better than 8% over 2 ns.
- Pointing accuracy <50 µm.
- Compatibility with cryogenic and noncryogenic targets.
- Ability to do 50 shots per year, each with a yield of 20 MJ, for a total 1200 MJ annual yield.
- Maximum credible DT fusion yield of 45 MJ.
- Ability to perform classified and unclassified experiments.

In addition to these capabilities, weapons physics users want to have the highest possible peak power for short pulses (>750 TW at 3ω for 1 ns) in order to reach high temperatures and a range of pulse lengths from 0.1 to 20 ns for a wide variety of experiments. These users want bright sources for experiments requiring x-ray backlighting, with small spots at high tempera-tures (half the energy in a 100-µm spot, and about 95%

of the energy at 200 µm). The beams for these back-lighters must be pointed a few centimeters away from the center of the main target chamber.

Weapons effects users want the ability to locate arrays of laser targets several tens of cm from the tar-get chamber center, as well as 1ω and 2ω capability. Their other requirements include access to the cham-ber for large, heavy test objects, a well-shielded diag-nostics area for testing electronic systems, and no residual light on the test objects.

The NIF target chamber will also have ports that allow the beams to be placed in the proper location for direct-drive ICF experiments and for tetrahedral hohlraums as well as for the baseline cylindrical hohlraums. All these requirements mean that the NIF must accommodate experiments spanning a wide range of operating conditions (see Figure 1).
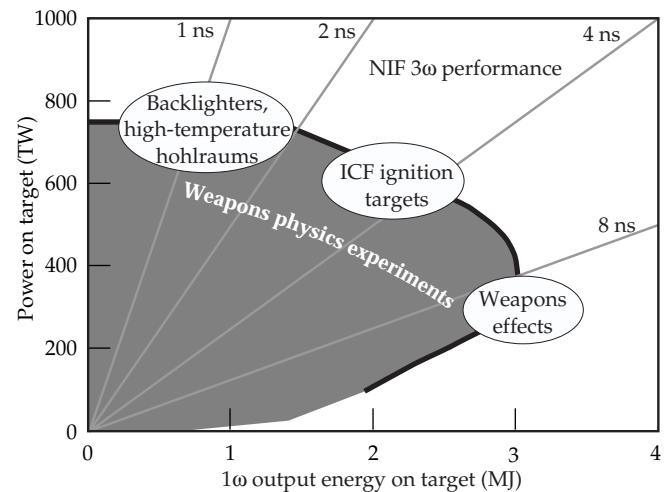
FIGURE 1. NIF users have identified important experiments span-ning a wide range of operating conditions. (40-00-0997-1998pb01)

Laser Design Highlights

The NIF laser system, as it appears in the Title I Design, provides routine operation at 1.8 MJ/500 TW in an ignition-target-shaped pulse and has a wide range of operation to meet other user requirements. The laser uses neodymium glass amplifier slabs, with 192 beams in a multipass architecture. The beams are grouped in 4×2 bundles and have an amplifier clear aperture of 40×40 cm^2. Frequency conversion is to the third harmonic, i.e., 3ω (350 nm). The laser has adaptive optics (deformable mirrors) to control the beam quality and uses kinoforms and smoothing by spectral dispersion (SSD) to control the beam quality on the target.

This design of the NIF laser system is essentially the same as what appears in the Advanced Conceptual Design (ACD) and is modified only slightly from the original conceptual design. However, due to the design-to-cost considerations, some features will not be implemented as part of the initial activation, most notably the 11-7 amplifier configuration and 192 preamplifier modules (PAMs). Instead, the initial NIF system will have an amplifier configuration of 11-5 and 48 PAMs. (This is similar to Beamlet, which is the scientific prototype for NIF.) This configuration can meet all NIF requirements, although with less performance margin than the 11-7 configuration, and it is less expensive to build. The laser and facility design are such that two additional amplifier slabs and 48 more PAMs can be added easily later. Other changes in the laser design include changing the baseline laser bundle size from 4×12 to 4×2 to simplify maintenance and raise the shot rate.

This design does preclude some options. For instance, there cannot be more than one color within each 2×2 beam quad, although different colors in different quads of beams or different cones are still possible. In addition, to bring the system back up to the original 192 preamplifier modules, while possible, would require major modifications to the laser support structure.

Laser Design and Performance

We use three methods to project the NIF laser's performance and safe operating limits. First, we calculate laser performance using simple scaling relations and propagation models. Second, we perform full propagation simulations using fast Fourier transform propagation codes, with simulated phase noise on each component based on measurements of Beamlet components. The codes also incorporate the calculated damage and filamentation risk at each component (Figures 2 and 3), and a full simulation of frequency conversion, including the beam quality and bandwidth. Finally, we compare these predictions to experimental results from Beamlet and Nova to be sure that the codes accurately predict what we expect to see on NIF.

Many of the propagation simulations were for a 2.2-MJ/600-TW pulse, about 20% higher than the 1.8-MJ/500-TW pulse required for routine ignition-target- shaped pulses. This 20% performance margin allows us to maintain the required output energy under less than ideal conditions. Conditions affecting output include looser performance specifications, out-of-specification components, beam balance issues, component degradation over time, and stressing operating conditions, such as broadband SSD for direct-drive targets.
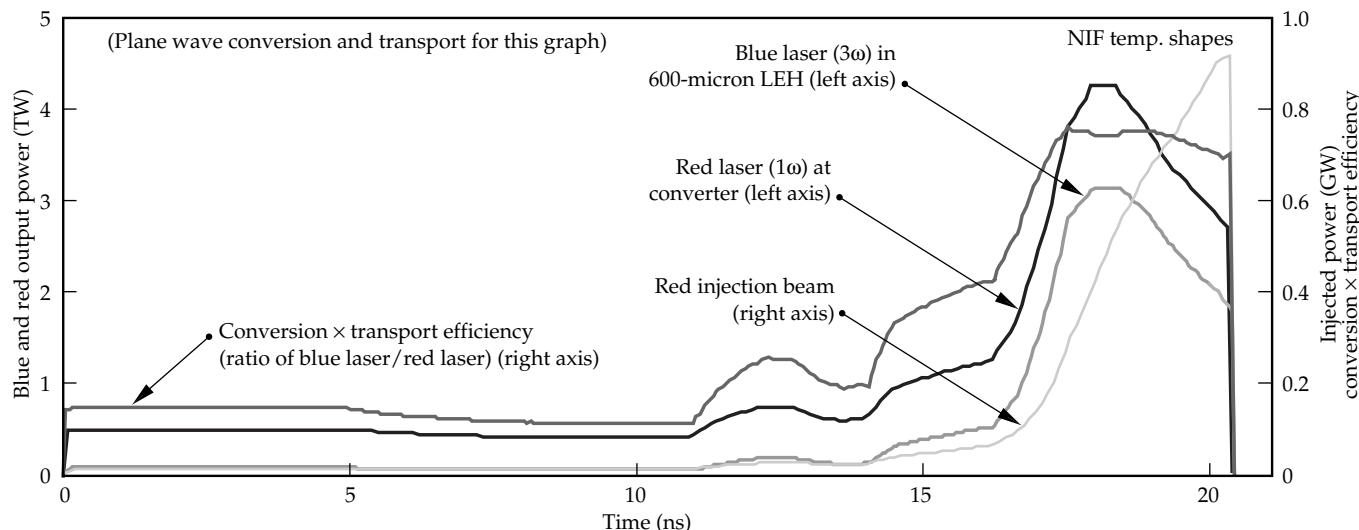
Figure 2. The nominal NIF 3ω ignition target pulse shape and the 1ω pulse shape required at the frequency converter and at the injection mirror (PABTS) to generate that pulse, as evaluated from a full NIF beamline simulation using LLNL propagation codes. Table 1 (on p. 102) summarizes other features of the simulation.   (40-00-0997-1760pb01)

Contrast ratio over center ±7.5 cm:
fluence average: .070
0 − 11 ns average: .154
11 − 14 ns average: .132
14 − 16.25 ns average: .109
16.25 − 17.1 ns average: .087
17.1 − 18 ns average: .066
18 − 18.5 ns average (peak): .061
18.5 − 19.5 ns average: .068
19.5 − 20.45 ns average: .076
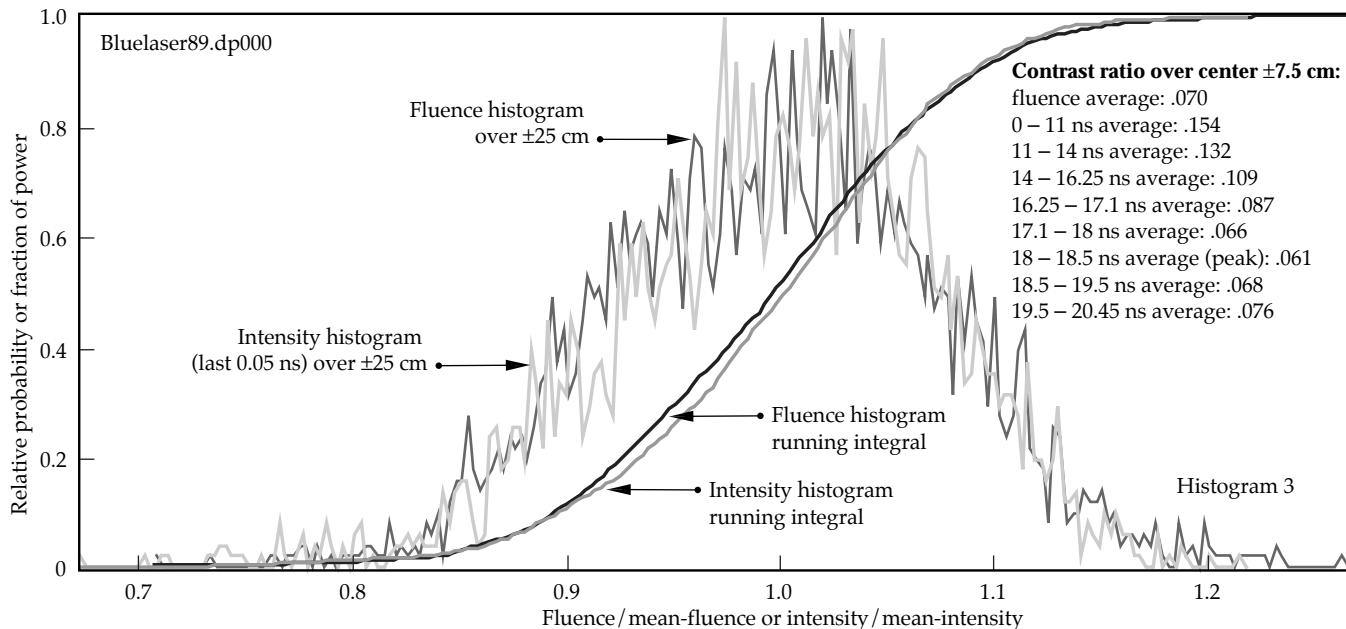
FIGURE 3. Simulated beam fluence and intensity distribution over aperture at frequency converter output (3ω) for an ICF pulse simulation. (40-00-0997-1761pb01)

Selecting the NIF Laser Design

The NIF laser design described in the ACD meets requirements, but—as mentioned above—it was necessary to determine whether a less expensive design could also meet the baseline performance requirements. In this section, we compare the NIF design from the ACD (11-7 slab configuration with 192 preamplifier modules) to less expensive options with fewer slabs and preamplifier modules that can be upgraded to the full ACD configuration.

The most important limit to the irradiance (power per unit area) and fluence (energy per unit area) of a glass laser system is damage to optical components in parts of the beam that have high irradiance or fluence. Because we wish to make the laser as inexpensively as possible, we need the smallest possible beam area—the laser cost for a multibeam system scales proportionally to the total beam area. Inevitably, then, damage to optical components is a major issue. The laser beam must have a highly uniform, flat fluence profile that fills the amplifier aperture as fully as possible. Also, we must minimize intensity noise on the beam, since these local regions of higher intensity may lead to local damage and may also grow due to nonlinear propagation effects in the amplifiers.

Tests on Beamlet, the NIF scientific prototype, and supporting modeling with detailed propagation codes show that nonlinear growth of intensity noise on the beam is small for operating conditions that keep the average nonlinear phase shift between any two spatial filter pinholes to less than 1.8 rad, as shown in Figure 4.

For larger phase shifts, intensity noise grows very quickly. Therefore we use 1.8 rad of nonlinear phase shift between pinholes as the safe operating limit for NIF. For long pulses, there is an additional energy limit. The amplifiers store a limited energy per unit area, and there is a practical limit to the output energy when so much of that energy has been extracted that the input energy to the final stage must rise to a very high value.

These operating limits appear on the power vs energy diagram in Figure 5. The safe operating limits shown are limited by nonlinear noise growth at the top
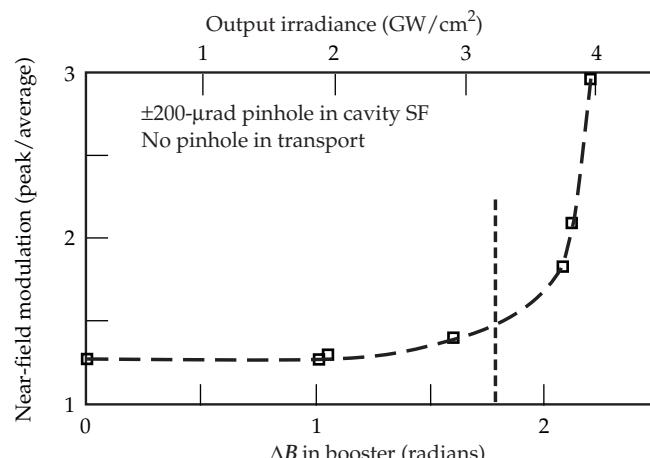
FIGURE 4. Beamlet data show that there is little nonlinear intensity noise growth for ΔB < 1.8 rad. (40-00-0997-1999pb01)
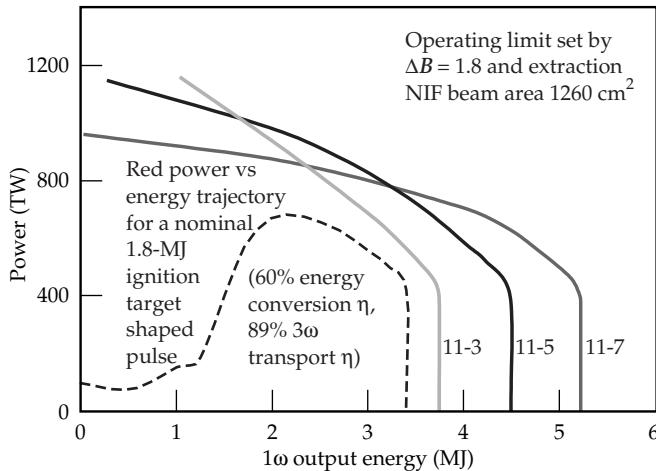
FIGURE 5. An 11-5 amplifier configuration meets the NIF requirements (1.8-MJ shaped pulse), but with less margin than 11-7. (40-00-0997-2000pb01)

FIGURE 6. The 11-7 and 11-5 amplifier configurations have adequate performance with 48 preamplifier modules. (40-00-0997-2001pb01)

of the figure and by energy extraction at the maximum practical energy at the vertical line to the right. A "square" flat-top pulse of constant intensity has a trajectory on this figure that follows a line of constant power from the zero-energy axis on the left to the end of the pulse at time τ, where it drops vertically to zero. The maximum nonlinear phase shift occurs exactly at the end of the pulse, so the closest approach to the laser safe operating limit occurs exactly at the end of the pulse. Square pulses of different power and energy but constant pulse length τ lie on a straight line through the origin of the figure.

The shaped pulses required for fusion have a somewhat more complex behavior, as shown by the power-energy trajectory of a nominal ignition target pulse in Figure 5. The intensity of these pulses can be lower at the end than earlier in the pulse, so the closest approach to the safe-operating-limit line can occur partway through the pulse.

Figure 5 shows that 11-7 and 11-5 laser amplifier configurations can both generate sufficient laser output to meet the requirements of a nominal 1.8-MJ 3ω target-drive pulse that requires about 3.4 MJ of 1ω drive in the shape shown. An 11-3 slab configuration can meet the requirement as well, but the margin is small.

The input drive required from the preamplifier is also important for comparing these systems. The proposed NIF preamplifier module can generate about 10 J, so if there is one module per beam (192 modules), it can safely drive any of these amplifier configurations to the required 3.4-MJ output for the nominal ignition target pulse, as shown in Figure 6. If we have one preamplifier module for four beams (48 modules), then

the module can supply only about 2 J per beam, after inevitable losses. The 11-7 and 11-5 configurations still have adequate input drive under these conditions, but the 11-3 does not.

We must also consider the possible variations in component quality and performance from those assumed in generating these figures, although we believe the nominal assumptions used there are the most probable result for NIF. We might test, for example, the sensitivity of the performance curves to a range of possible performance variations for the NIF amplifiers. Table 1 shows a range of possibilities for these parameters, with those chosen as most probable and assumed for the baseline analysis appearing in white boxes. Figure 7 shows a gray-shaded

TABLE 1. The design models are used to study sensitivity to variations in component performance. Those values assumed for the baseline analysis appear in white boxes.

Sensitivity to amplifier performance				
	Low value			High value
Slab transmission	0.985	0.9945		0.9975
Gain coefficient multiplier	0.95	1.0		1.05
Glass type	all LG770	50:50		all LHG-8
Gain rolloff (fraction of Beamlet value)	1.0	0.75	0.5	

	Values assumed in NIF baseline model

range over which the safe operating limit of an 11-5 NIF amplifier configuration would vary between the best and worst cases generated by combinations of the ranges in Table 1. The 11-5 configuration meets the 1ω drive requirements for the 1.8-MJ 3ω ignition target pulse even in the worst-case combination of these variations. The gray-shaded zone for the 11-3 configuration is of comparable size to the one shown in Figure 7, so that configuration clearly fails to meet the requirements over a wide range of possible component variations. The 11-7 (Figure 8) has more performance margin than the 11-5 and could tolerate a more severe combination of perfor-

mance degradations than assumed in Table 1, which the 11-5 could not.

These amplifier variations also affect the input drive required from the preamplifier module. Figure 9 shows a gray-shaded range of input energy required for the 11-5 configuration over the range of variation in Table 1. The 48-PAM case has adequate input drive to reach the nominal ignition requirements over a fairly wide range of variation, but some unfavorable combinations could require 96 PAMs.

After careful study with analyses such as these, supported by detailed simulations, we decided to
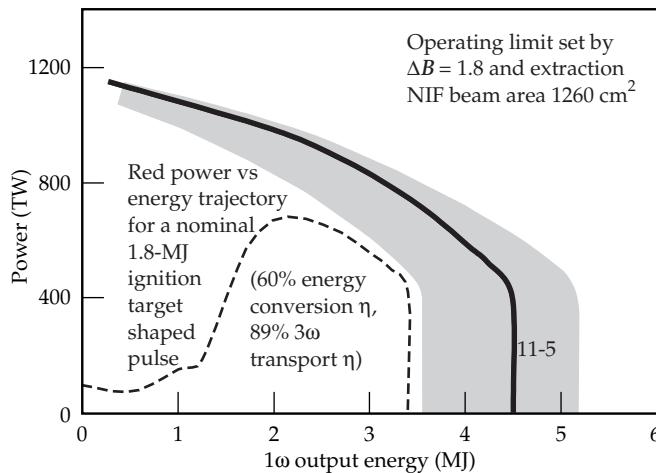
FIGURE 7. An 11-5 NIF has a small performance margin above the requirement over this range of amplifier variation. (40-00-0997-2002pb01)
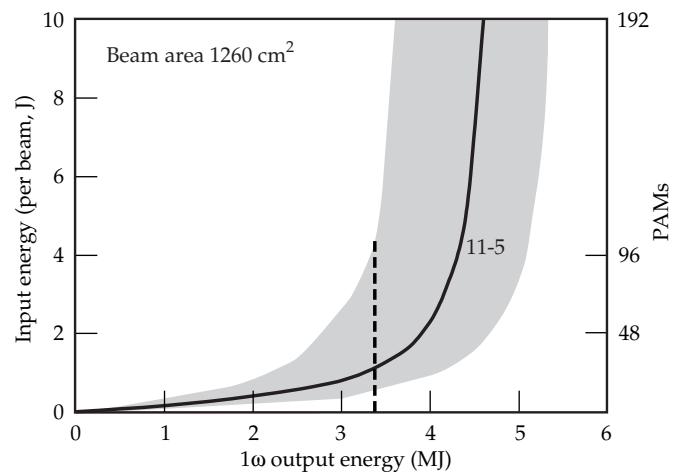
FIGURE 9. The input energy requirements for an 11-5 NIF are acceptable for 48 PAMs over this range of amplifier variation. (40-00-0997-2004pb01)
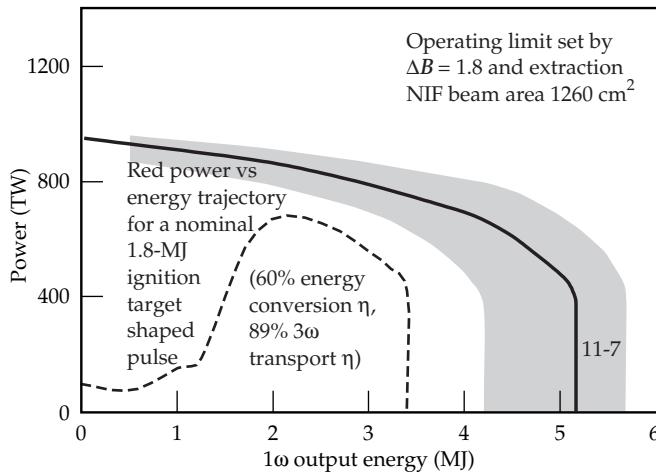
FIGURE 8. An 11-7 NIF has a significantly larger margin than an 11-5 over this range of amplifier variation. (40-00-0997-2003pb01)

reduce the NIF laser hardware cost by changing to an 11-5 amplifier configuration and reducing the PAM count to 48. Since Figure 9 shows there is some risk with 48 PAMs, we chose at Title I to make the system easily upgradable to 96 PAMs. We also plan to revisit the PAM design early in Title II (final design) to see whether the design can be increased in size at modest cost to cover up to the drive energy of roughly 4 J per beam that would be required in a worst case.

With these choices, the NIF laser design is now essentially the same as the design we first chose for the Beamlet scientific prototype for NIF; tests of the Beamlet laser[1] show in detail that the 11-5 laser architecture and performance work. There are minor differences having to do with beam injection and component size and spacing, but the basic performance should be very similar. This assumes, of course, that

we can get components such as laser slabs in quantities of several thousand at the same quality we see in quantities of twenty, which is the point of studying the effect of variations such as those in Table 1. Figure 10 shows that we have operated Beamlet for about 50 shots at or slightly beyond the safe operating limits projected for NIF, with acceptable intensity modulation and damage. Note that the figure scales Beamlet shots to the NIF beam area at constant fluence, which is the important parameter for comparisons of performance. The Beamlet beam area is smaller than NIF (34 to 35 cm^2 vs 37.2 to 37.8 cm^2 at zero intensity), so 192 Beamlet beams would give somewhat less energy than shown on Figure 10.

So far, we have considered only the 1ω performance of the laser. Laser damage thresholds are a factor of two or more lower at 3ω than at 1ω, and the effect of nonlinear propagation is a factor of four worse for a given length of material. Therefore we designed the laser so that the frequency conversion happens as close to the target as possible and so that the optical components that see 3ω light are as thin as possible. Many users want the highest possible peak power from NIF at short pulses. As a result, we changed the final optics package from the original conceptual design to use a

color separation grating rather than a wedged lens, allowing the lens to be about half its original thickness and giving higher peak power with short pulses. The lens was originally the vacuum barrier to the target chamber, as on Nova, but this requires a thicker lens for safety and would severely restrict the short-pulse performance of NIF. Therefore we have changed the design so that the vacuum barrier is a window in the 1ω beam where damage and nonlinear effects are less important.

Beamlet has a frequency conversion package similar to that designed for NIF, and we have studied the performance of this converter and shown that its performance agrees well with simulation codes. Figure 11 shows the projected performance of NIF at 3ω, delivered to target chamber center, with our nominal design assumptions. For short pulses below about 2 ns, the 3ω performance is limited by beam breakup due to nonlinear index effects in the 3ω optics. Pulses from about 2 to 8 ns are limited by nonlinear effects in the 1ω part of the laser and possibly by damage thresholds of the 3ω optics, depending on how successful we are at acquiring consistently high-quality material and finishing. Long pulses are limited by the energy extraction limit of the laser, together with increasingly inefficient
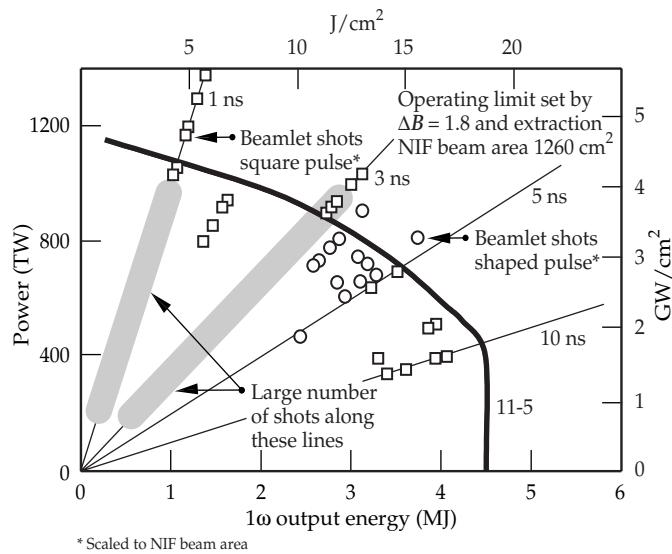
FIGURE 10. Beamlet has fired about 50 shots near or slightly over the 1ω safe operating limits projected for an 11-5 NIF.
(40-00-0997-2005pb01)
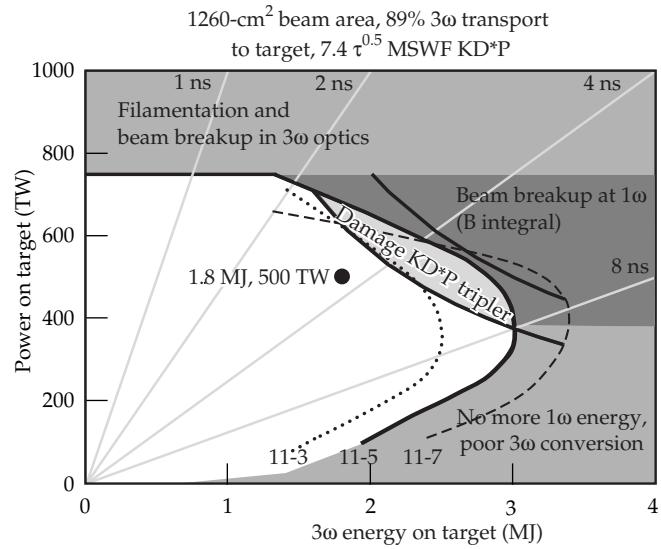
FIGURE 11. NIF 3ω power and energy delivered to target.
(40-00-0997-2006pb01)

frequency conversion as the 1ω laser irradiance decreases.

Beamlet will test a "brassboard" version of the NIF final optics assembly in late 1997. We have, however, studied 3ω optical performance with a configuration using a much thicker wedged lens, like the one appearing in the original conceptual design. Shots at 0.2 to 1 ns and at an irradiance corresponding to 750 TW on target for NIF caused a few (~10) damage spots in the focus lens from self-focusing of local hot spots on the beam. This is an acceptable level of damage, and in addition, the thinner lens in the current NIF design will further reduce filamentation. Several shots at irradiance and fluence corresponding to 600 TW, 1.9 MJ on target caused no damage to the frequency-tripler crystal, which is the component we expect to have the lowest 3ω bulk damage threshold. There were a few damage spots to the surface of the 3ω focus lens, showing the importance of quality control over surface finishing of high-fluence 3ω components. Although components of adequate damage threshold have been fabricated by vendors, this area remains a principal concern of the Project.

Conclusion

The Title I Design for NIF will meet the top-level performance requirements with an 11-5 amplifier configuration and 48 preamplifier modules, according to performance models and data from Beamlet. Tests of the Beamlet laser[1] show that the 11-5 laser arcitecture and performance will meet and support the NIF requirements. The performance margin is less than that for the 11-7 configuration: component performance is more critical and the energy and power is less for stressing operating conditions. However, if a larger performance margin is desired, the design is such that 2 amplifier slabs and 48 additional PAMs can easily be added later.

Reference

1. Van Wonterghem et al., *Applied Optics* **36** (21), 4932 (1997).

For more information, contact
John Murray
Chief Scientist for NIF 1ω Special Equipment
Phone: (925) 422-6152
E-mail: murray5@llnl.gov
Fax: (925) 424-5195

CONVENTIONAL FACILITIES

G. Kugler   P. Kempel

D. Coats   V. Roberts

J. Hands

*T**he NIF Conventional Facilities include the Laser and Target Area Building (LTAB) and the Optics Assembly Building (OAB). The LTAB will be an environmentally controlled facility for housing the laser and target area systems. It has two laser bays, two optical switchyards, a target room, target diagnostic facilities, capacitor areas, control rooms, and a few operations support areas. The OAB includes a loading dock for receiving and inspection, mechanical and optical transfer areas, a mechanical cleaning area, an assembly and alignment area, and a transfer basement and loft for moving completed assemblies from the OAB to the LTAB. The Title I Design scope work for the LTAB includes the building plus utilities to the laser bay perimeter, power distribution to the center of the laser bay slab, and the target bay pedestal in the LTAB. The Title I Design for the OAB includes the building with utilities and operational support equipment associated with the cleaning of mechanical components and assembly of optics components for the LTAB.*

Introduction

The LTAB, shown in Figure 1, consists of two main parts: the Laser Building and the Target Area Building. The Laser Building consists of two laser bays providing a thermally and vibrationally stable environment to house and support the components of the laser system. In addition, it contains a central three-story core structure providing experimental support space on the ground level and mechanical equipment space on the second and third levels.
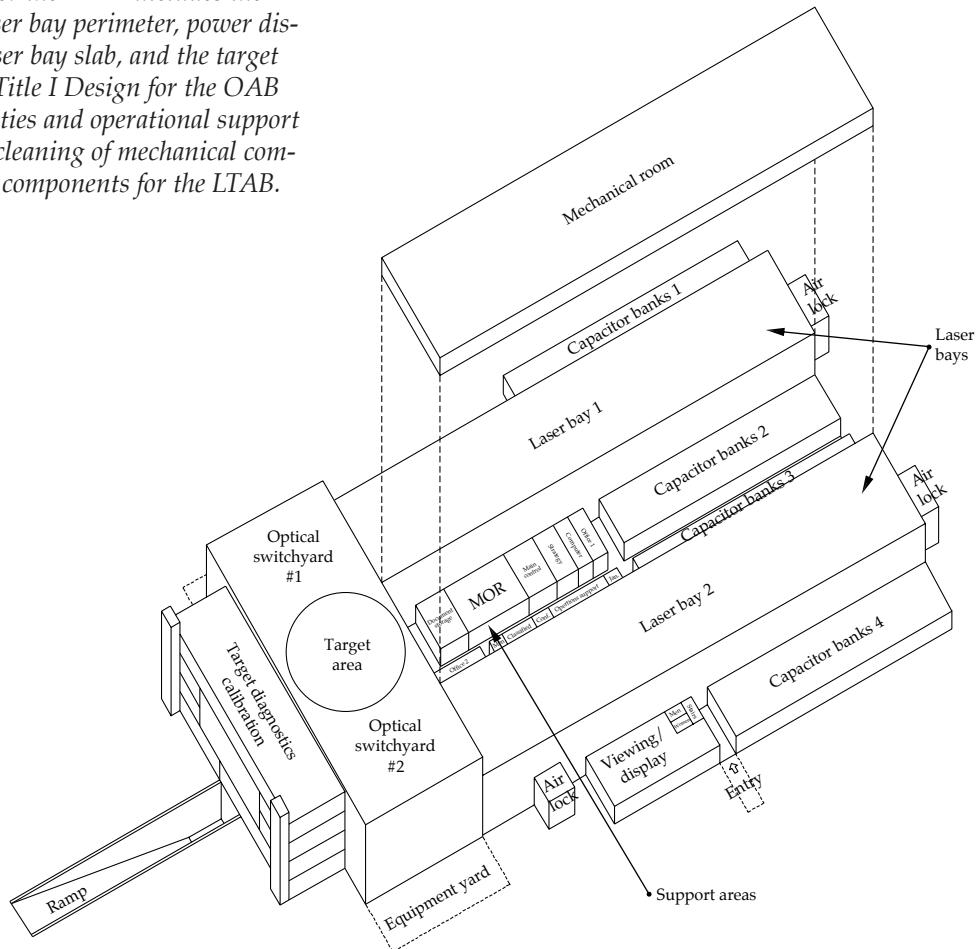
FIGURE 1. Laser and Target Area Building (LTAB).   (40-00-0394-1090pb01)

The Target Area Building is divided into the target area, the switchyards, and the target diagnostic areas. The target bay and switchyards have class 100,000 clean room environments. The switchyards house and support special equipment, such as turning mirrors and chamber, final optics, and target diagnostics. The diagnostics portion houses and supports the diagnostics instruments.

The LTAB floor plan (Figure 2) is based on a U-shaped scheme with the two laser bays forming the legs of the U and the switchyards with target room at the junction. This facility scheme was selected to provide an optimum laser experimental equipment configuration and to permit the addition of a second target room in the future without major disruption to the NIF operation.

The central area between the laser bays will contain the control rooms and facility management areas. Two capacitor banks will be located in the center area between the laser bays, and one capacitor bank will be on the outside of each laser bay.

The largest research areas in the LTAB are the two laser bays at 130.1 m long by 24.4 m wide by 17 m tall, each of which covers 3158.6 m^2. The laser bay floor is a monolithic, reinforced-concrete slab 0.91 m thick resting on compacted earth.

The target building is a cylindrical structure with an inside diameter of 30.48 m and a height of 29.26 m to the base of the domed roof. The concrete wall thickness of 1.82 m is required for radiation shielding. The two switchyards, which connect the laser bays to the target room, are constructed of 1.21-m-thick reinforced-concrete walls. A 0.6-m wall thickness is required as radiation shielding for the beam and diagnostic opening in the target room walls. The switchyards are 24.4 by 30.48 m and 24.68 m high. All of these areas incorporate 1.82-m-thick monolithic slab floors for structural stability and vibration control.

The OAB (see Figure 3) is adjacent to the LTAB and will provide the necessary facilities for assembling the laser subsystem components. Each laser component will be packaged into a line replaceable

LTAB first floor plan
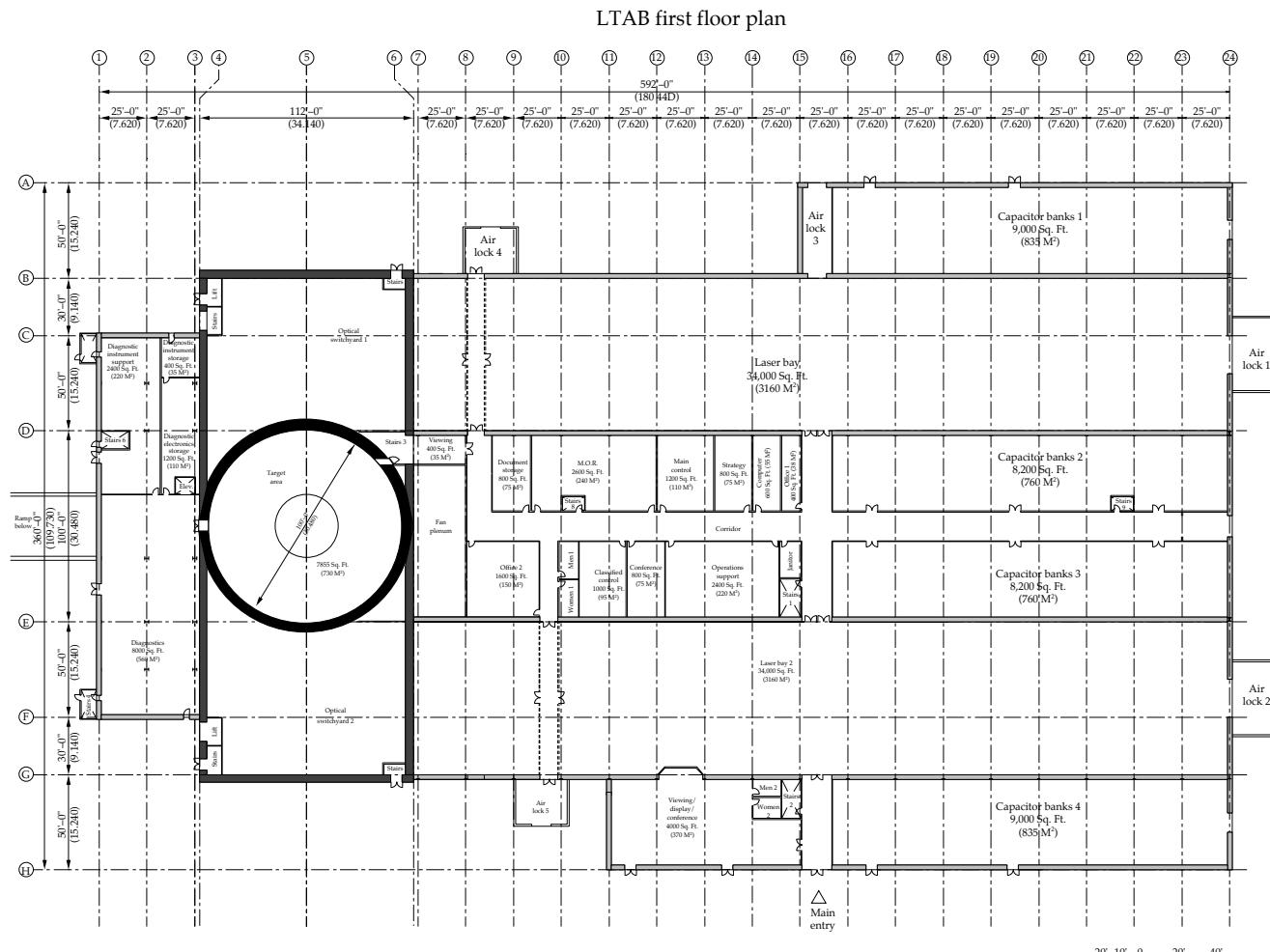
FIGURE 2. LTAB floor plan. (40-00-0394-1093)
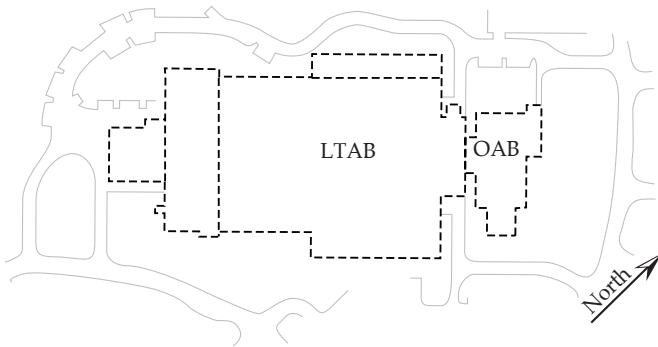
FIGURE 3. The OAB in relation to the LTAB.   (40-00-1097-2229pb01)

unit (LRU) for assembling, transporting, installing, and removing the component in an efficient, safe, and cost-effective manner. Assembling the LRUs will occur in the OAB.

All components arrive at the loading dock and undergo receiving inspection in an enclosed area. Adjacent to this loading/unloading space, mechanical and optical transfer clean rooms are provided in the main part of the building for joining and transfer of optical and mechanical components of LRUs. The transfer areas contain component handling mechanisms, cleaning stations, and a staging area. The mechanical components undergo additional cleaning and partial assembly in the mechanical cleaning clean room. Final assembly, alignment, and testing of the assemblies are performed in the assembly and alignment clean room. A transfer basement and loft are provided for moving completed assemblies out of the OAB assembly area and onto a transporter for delivery through the corridor link to the LTAB.

LTAB Title I Design Functional Scope

The Title I Design functional scope for the LTAB includes all the building components; the utilities to the laser bay, switchyard, and target bay; power distribution to the center of the laser bay slab; and the target bay pedestal, which holds up the target chamber.

An important part of the Title I Design is defining the interfaces between facilities and special equipment to assure that requirements are met. We are also analyzing the performance of proposed designs and closely coordinating design development with the special equipment designers.

In developing the LTAB Title I Design, we are, through various studies, choosing among alternatives

for reasonable compromises between performance and cost. The decisions made are in support of the *Preliminary Safety Analysis Report*, and we are establishing quality levels by system and/or component.

The final Title I Design deliverables include the following:
• Drawings.
• Specifications.
• Basis of design document.
• Code analysis report.
• Calculations.
• Title I construction cost estimate.
• Energy conservation report.
• Environment, safety, and health report.
• Safeguard and security report.
• Preliminary qualification and testing acceptance plan.
• Heating, ventilating, and air conditioning (HVAC) commissioning plan.
• Reliability, availability, and maintainability (RAM) analysis report.
• Fire protection design analysis.
• Major equipment list.
• Computational fluid dynamics analysis report.
• Quality level assignment report.

The drawings and specifications being prepared for the Title I Design must include general arrangements that assure physical integration and accommodation of
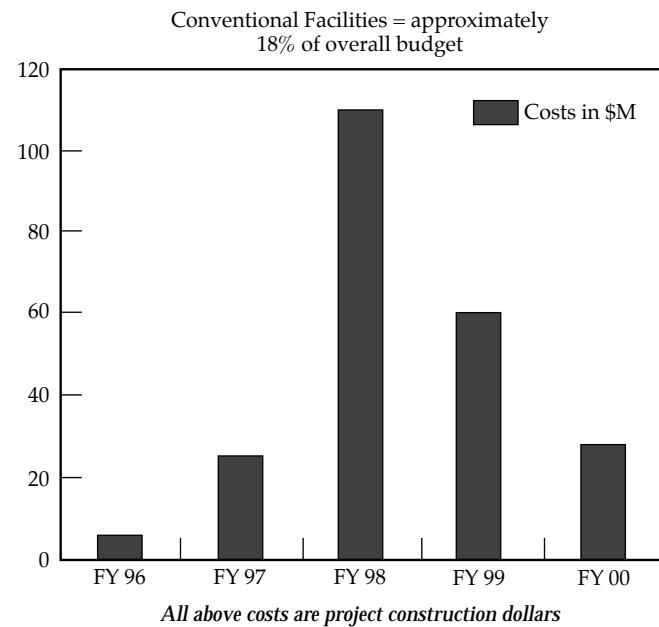
FIGURE 4. Conventional Facilities cost estimates.
(40-00-1097-2230pb01)

operational requirements. They must also show analyses that confirm that requirements can be met in Title II; develop accurate construction cost estimates (Figure 4) and procurement schedules; identify potential needs for long-lead procurements; and form a firm basis for Title II design, construction planning, construction subcontract packaging, and project scheduling.

Foundation, Vibration and Thermal Stability, and Shielding Design

Several high-impact design requirements are being integrated into the Title I Design, including vibration isolation and structural stability; tight spatial temperature control in large-volume critical spaces with complex geometry; neutron shielding sufficient to protect the workers and the public, and to allow for required operation and maintenance activities; and structural position stability in severe weather extremes.

Reinforced-concrete seismic analyses were performed for the laser bay foundation and the target bay and switchyard. Our conclusion from these analyses was that the target area circular floor openings are critical to the final design. In addition, we concluded that torsional support for the target sphere should be developed, laser beam tubes and special equipment should be added, and conflicts between radial beams and the HVAC system must be resolved.

Vibration criteria are critical to the Title I Design. We have several ambient vibration analyses in progress, including the laser bay foundations and pedestals, the target bay and switchyards foundations, the master oscillator room (MOR) foundation, and the preamplifier module maintenance area (PAMMA) foundation. Several vibration analyses have been completed or are in progress. Of the unbalanced fan vibration sources analyses, the steel laser bay structure analysis is complete, while the transmission of footing vibrations to critical structures analysis is in progress. The acoustic-sound pressure-level-sources preliminary analysis of the laser bay foundation has been completed. The flow-induced-vibration-sources analysis of nitrogen cooling lines is in progress.

The allowable air temperature variation according to the Subsystem Design Requirements is 20°C, ±0.28°C. Thermal analyses to meet these criteria are in progress for the laser bay foundation slabs and the target bay structure.

The Title I shielding analysis was performed by LLNL's NIF Project team and reviewed and coordinated with Parsons Infrastructure and Technology Group, Inc., of Pasadena. We concluded from this analysis that a minimum 2-in. cover for all reinforcing should be required. The concrete of the target bay walls must be 1.82 m thick. The switchyard walls will range from 0.83 m to 1.13 m (Figure 5). The target bay concrete roof must be 1.35 m thick, and the switchyard concrete roof should be 2 ft thick.

Recent analysis (to be verified in Title II) has resulted in the following recommendations:
1. HVAC ducts can be of steel, aluminum, or fiberglass.
2. Shield door frames can be of aluminum or stainless steel.
3. Minimum rebar cover must be 2 in.
4. Boration requirements in the target bay floor are unnecessary.
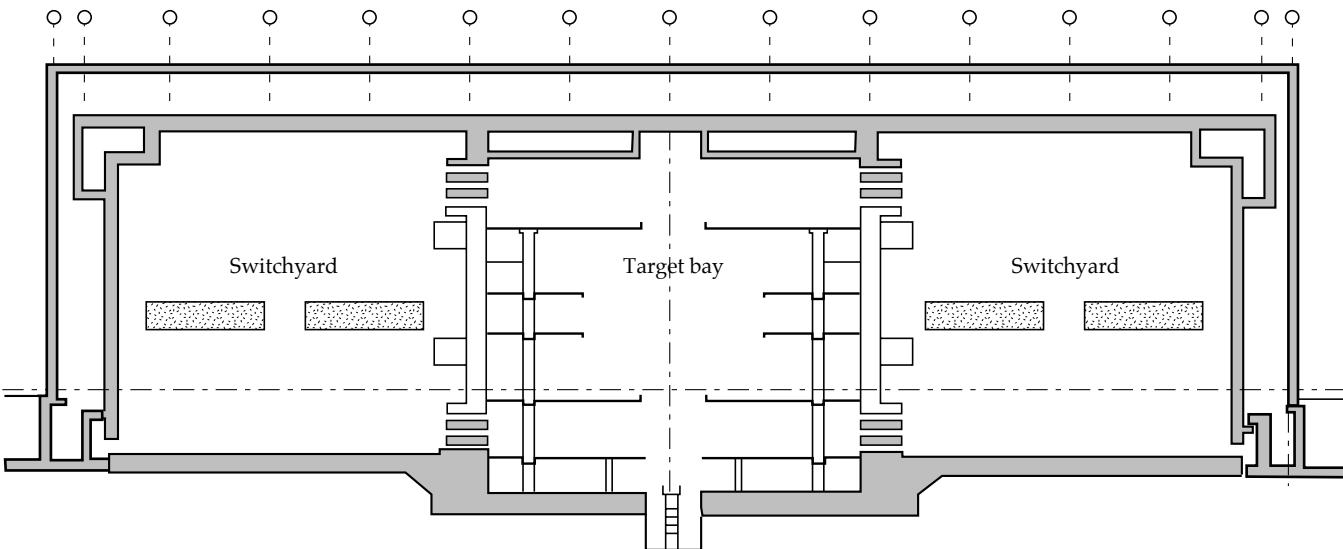
FIGURE 5. Shielding design.   (40-00-1097-2231pb01)

Title II Activities

The target bay floors, pedestal, and lift pit will be designed during Title II. The laser bay interface loads and loading conditions will be provided, and the laser bay support system will be designed during Title II.

In Title II, the construction contract language, general conditions, market survey, contractor prequalification, drawing reviews, and independent cost estimate will be developed.

Title II shielding design activities include investigating whether borated concrete is required and, if so, determining the extent and degree of boration. In addition, we will be investigating whether collimation is required for the laser bay/switchyard beam penetrations.

OAB Title I Design Functional Scope

The Title I Design functional scope for the OAB includes all the building components with utilities, external access, interior spaces, and operational support equipment associated with the cleaning of mechanical components, and assembly of optics components for the LTAB (see Figure 6).

As with the LTAB, we will define the interfaces between OAB facilities and special equipment to assure that requirements are met, analyze the performance of

proposed designs, and closely coordinate the Conventional Facilities design development with user groups in anticipation of the final Interface Control Documents.

The OAB Title I Design definition includes a design development phase for a clean room building to a preliminary level (± 35% design). It also confirms and formalizes user requirements and interfaces; requires drawings, specifications, and other information that assure physical integration of operational requirements; establishes quality levels by system and/or component; performs engineering and other analyses that confirm that requirements can be met in Title II Design; and confirms the budget cost model and considers alternatives for reasonable compromise between performance and cost.

The final Title I OAB Design deliverables include:
- Drawings.
- Outline specifications.
- Cost estimate.
- Engineering calculations.
- Quality Assurance Program Plan.
- Code Analysis Report.
- Fire Protection Design Analysis Report.
- Energy Conservation Report.
- Preliminary Qualification and Testing Acceptance Plan.
- HVAC commissioning plan.
- RAM analysis report.
- "Q" Level Assignments.
- Rendering.
- Materials Sample Board.

FIGURE 6. OAB floor plan with user equipment at start-up. (40-00-1097-2232pb01)
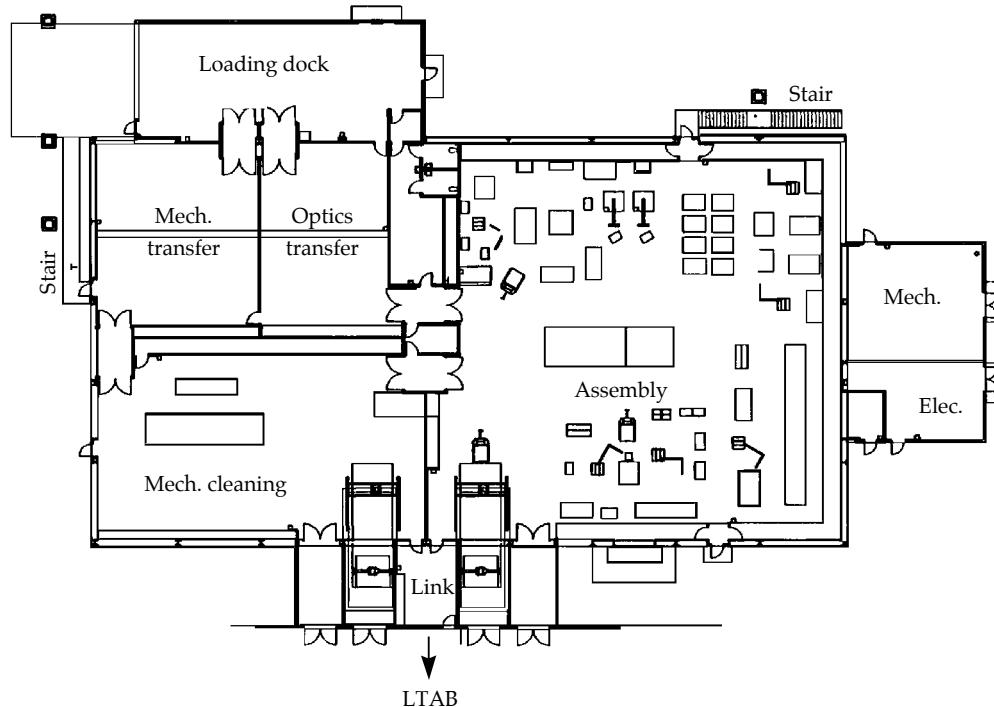
The OAB Title I Design integrates a number of high-impact design requirements, including the maintenance of 24-hour operation for Class 100 and Class 1000 clean rooms, temperature and humidity control, vibration isolation and structural stability, and facilitation of optics assembly transfers to and from the LTAB.

HVAC Systems

The reliability and availability of the HVAC system are critical to the success of the OAB to assure an uninterrupted support of LTAB experiments. Preliminary RAM analysis was performed for the HVAC system serving the Assembly/Alignment, Mechanical Cleaning, and Mechanical/Optics Transfer areas; the availability result was 99.87%.

With outdoor conditions ranging from 37°C in the summer to –5°C in the winter, the indoor conditions for a Class 100 or 1000 clean room must be 20°C ±0.5°C with 45% ±15% RH, and a Class 10,000 clean room must be 22°C ±0.5°C with 45% ±15% RH.

The Assembly/Alignment area is a Class 100 clean room, the Mechanical Cleaning area a Class 1000 clean room, and the Mechanical/Optics Transfer area a Class 10,000 clean room, each with gowning rooms and air locks. Each clean room will have a high-efficiency particulate air (HEPA) filtration system, air circulation, and pressure control.

The Class 100 clean room will have 26 recirculating fans (RFs), raised floor and return air chase, 80% HEPA coverage at the ceiling, pressurization, and vibration and noise control of the RFs. The Class 1000 clean room will have a raised floor and return air chase, 30%+ HEPA coverage at the ceiling, four RFs grouped together, pressurization, and vibration and noise control. The Class 10,000 clean room will have sidewall return, two RFs grouped together for backup, pressurization, 15%+ HEPA coverage at the ceiling, and vibration and noise control.

Title II Activities

In Title II Design, we will design, prototype, and test the assembly station for the common LRU assembly. This includes an optics insertion mechanism, rotating assembly table, and an OAB LRU transporter. Interface Control Documents will be completed and updated as needed. Procurement specifications for vertical lifts and jib cranes will be completed. The design and a prototype will be completed for the bottom-loading and top-loading LRU systems. During Title II, the LRU certification equipment will be identified, and the procurement specification will be completed.

For more information, contact
Gus Kugler
Associate Project Engineer for Conventional Facilities
Phone: (925) 422-2212
E-mail: kugler1@llnl.gov
Fax: (925) 422-0946

Optical System Design

R. E. English, Jr.   J. Miller
C. Laumann   L. Seppala

The optical system for the NIF includes every performance-based piece of glass in the system: many thousands of mirrors, lenses, amplifier slabs, polarizers, crystals, windows, diffractive optics plates, etc. This complex system is divided into six subsystems, each with its own requirements and design issues. In Title I, we have completed preliminary designs for each subsystem. Specifications are well beyond Title I requirements for the large-aperture optics, and we expect to start the procurement process for these optics early in Title II. This section will discuss those ~7000 large-aperture components. Optical design of the 15,000 to 20,000 smaller components will be treated briefly in discussions of specific subsystems.

Introduction

The optical system for the NIF encompasses every performance-based piece of glass in the entire system, including over 7000 pieces with large apertures (Table 1), the 5000 to 10,000 smaller optical components in the front-end of the laser system, and the several thousand small components in the beam alignment and control systems. We divide this system into six areas, as shown in Figure 1:

- The optical pulse generation system.
- The injection system.
- The main laser system.
- The switchyard and target area.
- The final optics assembly.
- The beam control systems.

The optical pulse generation system, injection system, and beam control systems contain smaller components that are in a preliminary state of design. These designs will be developed further in Title II. The preliminary designs for components in the optical pulse generation system and injection system are described in the "Laser Components" article of this *Quarterly* (p. 132). The component designs for the beam control systems are briefly discussed in "Laser Control Systems" (p. 180).

In this article, we describe the optical design and specifications of the large optical components comprising the main laser system, switchyard and target area, and final optics assembly. The optical configuration for these systems is contained in our configuration drawings, which detail the location, orientation, and size of

TABLE 1. NIF contains over 7000 large-aperture optics.

Component	Material	Number
Amplifer slabs	Laser glass	3072
Lenses	Fused silica	960
Deformable mirrors	BK-7	192
Cavity mirrors	BK-7	192
Elbow mirrors	BK-7	192
Transport mirrors	BK-7	816
Polarizers	BK-7	192
Crystals	KDP/KD*P	576
Debris shields	Fused silica	192
Switch windows	Fused silica	384
Vacuum windows	Fused silica	192
Diffractive optics plate	Fused silica	192
Total		**7152**
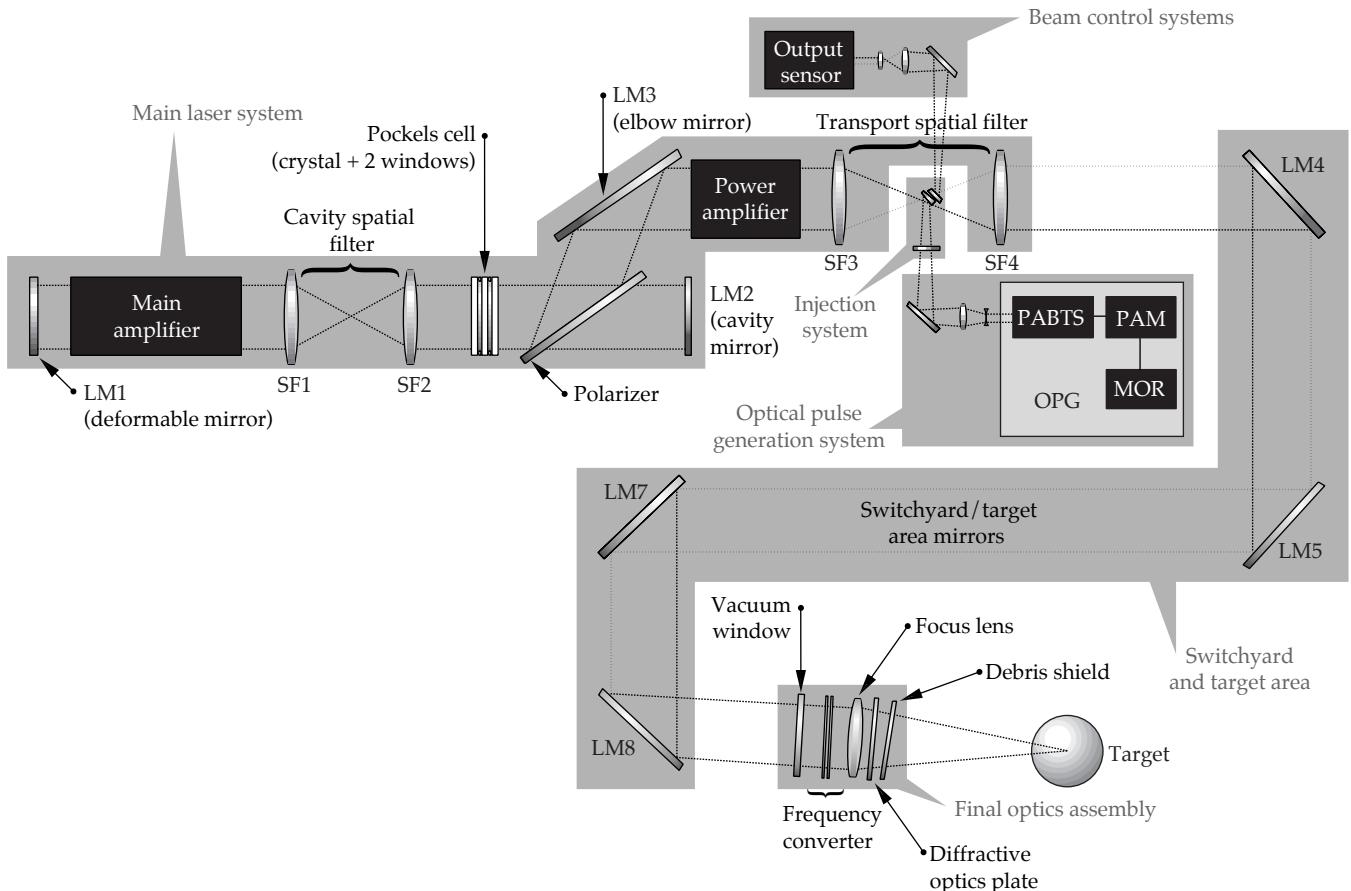
FIGURE 1. The six main optical systems (shaded areas) for the National Ignition Facility. (40-00-0997-2064pb01)

each NIF optical component. These components constitute a major fraction of the cost of the laser hardware and have a very long procurement lead time. The designs and specifications for these components are essentially complete, and we are ready to begin the procurement process. At the end of this section, we include a discussion of the specification process for the NIF large-aperture optics.

Main Laser System

In the main laser system, the large optical components include the amplifiers, the spatial filters, the periscope assembly, and the deformable mirror (Figure 2). In this section, we focus mostly on the optical design and components for the amplifiers and spatial filters, which are key to the design of the main laser. The basic features of the laser design come from laser physics optimization models—as discussed briefly in "Laser Requirements and Performance" (p. 99)—together with the practical

limits on the availability of large optics. At this time, the maximum practical clear aperture for the laser glass slabs used in the amplifiers, as well as for KDP crystals, is roughly 40 cm; we chose a clear aperture of 400×400 mm for the laser slabs. By definition, the amplifier is the limiting aperture in the main laser optical system. The laser optimization model shows that the best configuration to give us a wide operating range for the laser is to make these amplifier slabs 41 mm thick and place 11 in the main amplifier and 7 in the power amplifier. (As discussed in "Laser Requirements and Performance," the cheaper 11-5 configuration has adequate performance, so we chose to build that configuration and leave space in the design to upgrade to the 11-7 configuration, if required.) The actual size of the slab is larger than the 400-mm clear aperture, since there are edge claddings on the slab to absorb amplified spontaneous emission and these become hot enough during laser pumping that a region of about a third to a half of the slab thickness around the edge is unusably
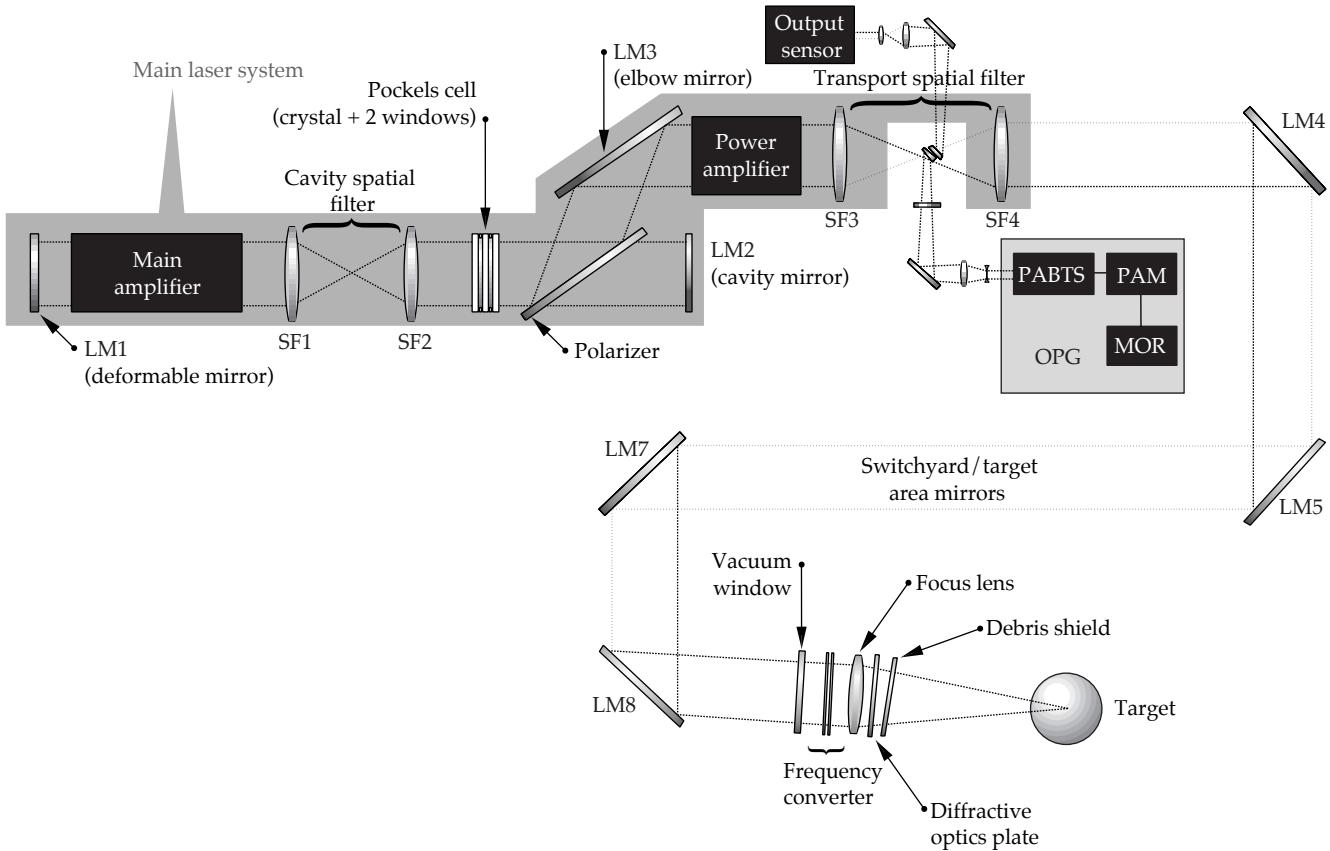
FIGURE 2. The main laser optical system.   (40-00-0997-2065pb01)

distorted. The actual slab size, then, is 456.8×800.2 mm, including the edge cladding thickness. The slab is longer in one dimension because it is placed at Brewster's angle to the beam.

The cavity spatial filter (CSF) length is set by the length of the main amplifier, required ghost standoff distances, component access clearances, and the length of the periscope assembly. These components require a space of 23.5 m. Mirrors LM1 (the deformable mirror) and LM2 (the cavity mirror) both must lie at relay planes of the system, so the CSF length must also be 23.5 m, giving a cavity length of 47 m.

The transport spatial filter (TSF) must form an image of the relay plane near the frequency converters. An exact relay would require a TSF length of about 75 m, but a study with propagation codes shows that there is negligible increase in irradiance noise at the frequency converter for a 60-m-long TSF. We chose this shorter length to reduce cost.

The beams travel at a small angle to the optical axis, and this angle is set by the separation between the injection and output pinholes in the focal plane of the TSF. The required size of the injection mirror, plus necessary mechanical clearances, set a minimum spacing between these pinholes of 35 mm.

The diameter of these pinholes determines the angular content that we allow to propagate through the laser system, or the minimum spatial frequency of noise on the beam. This angle will vary to optimize performance for particular experiments over the range of ± 100 to 200 μrad (6 to 12 mm diameter in the TSF pinhole plane). The clear aperture required for each optical component in the laser falls out directly from these choices, with proper consideration for mounting and alignment tolerances.

The spatial filters are evacuated, so the spatial filter lenses serve as vacuum barriers, and this loading must be considered in the design. Also, the windows of the

Pockels cell must withstand a vacuum load. The Title I design presented here for these components has a maximum tensile stress of 700 psi, consistent with Nova experience. In Title II we shall evaluate the consequences of going to a lower-stress design (i.e., 500 psi), which requires slightly thicker components. The thickness of other components (mirrors and polarizers) is set to the minimum consistent with maintaining the acceptable flatness in the presence of mounting distortions and coating stress.

The maximum beam size is set by the aperture of the amplifier, the transverse motion of the beam in the cavity due to off-axis propagation (vignetting) and alignment and positioning tolerances. The vignetting allowance is ±6 mm, and we allow ±4 mm each for component placement and alignment. This gives a maximum beam size at zero intensity of 372×372 mm. The effective beam area (equivalent area assuming constant fluence across the beam) is about 1230 cm^2, after allowing for the apodized edge region around the beam. This is slightly smaller than pre-Title I estimates because of revisions in component placement tolerances during Title I design.

The clear apertures of other components in the main laser are similarly set by beam size, and by vignetting, alignment, and placement allowances. Actual component dimensions are larger, as required for mounting. Table 2 summarizes the sizes of the main laser components.

Lenses SF1 and SF2 for the CSF are symmetric biconvex lenses with a very slight aspheric correction on one surface. The input lens to the TSF, SF3, is tilted with respect to the axis so that the backward single-reflection ghost (see "Ghost Beams in Large Laser Systems" on p. 116) strikes a beam dump outside the clear aperture of the beamline. This allows the distance between the power amplifier and SF3 to be shorter, saving space, but requires more aspheric correction. The output lens of the TSF, SF4, has an aspheric input surface and a flat output surface. This flat surface provides a diagnostic sample of the output beam for use by a wavefront sensor located near the TSF focal plane. The performance of these lenses, and the effect of the full laser beam propagation path through them, has been verified using the Code V® suite of optical design tools.

Title II Activities

High on the list of Title II optical design activities for the main laser system is to confirm our ghost management solutions. We will complete our ghost analysis, including tolerances, and specify locations for ghost reflection baffles and beam dumps in the main laser system. Also in Title II, we will complete the analysis for changing the lens thickness, based on a peak stress of 500 psi. We will also update the main laser optic system drawings to reflect minor adjustments in component locations and sizes.

TABLE 2. The sizes and apertures for the main laser large-aperture optics are under configuration control.

Optic	Name	Optical clear aperture (mm)	Mechanical hard aperture (mm)	Optics size (mm)
Amplifer slabs	Main / power amplifiers	400×400	401×401	$800.2 \times 456.8 \times 41$
CSF lens	SF1/2	406×406	409×409	$434 \times 434 \times 46$[a]
TSF lens (input)	SF3	410×406	413×409	438[b]$ \times 434 \times 46$[a]
TSF lens (output)	SF4	406×406	409×409	434[b]$ \times 434 \times 46$[a]
Deformable mirror	LM1	392×392	392×392	$449.5 \times 433.7 \times 10/30$
Cavity mirror	LM2	392×392	392×392	$412 \times 412 \times 80$
Elbow mirror	LM3	396×392	397×393	417×740[b]$ \times 80$
Polarizer	PL	396×396	397×397	417×807[b]$ \times 90$
Switch crystal	SC	397×397	398×398	$410 \times 410 \times 10$
Switch window	SW	397×397	398×398	$430 \times 430 \times 30$[a]

[a] Lens thickness change pending approval by Level IV Change Control Board (ECR 66)
[b] Dimensional changes pending approval by Level IV Change Control Board (ECR 69)

GHOST BEAMS IN LARGE LASER SYSTEMS

The surfaces of NIF transmissive optical components are all antireflection coated, but these coatings are never perfect. Each such surface reflects a small fraction of the incident beam, and this weak "ghost" beam propagates through the system. Even a small reflection of a high-energy beam can contain enough energy to damage optical components if those components lie near a position where the ghost beam comes to a focus. The ghost beams can also cause other difficulties. It is extremely important to manage where these beams fall in NIF.

The figure shows, as an example, the ghost reflections from symmetric biconvex lenses in the cavity spatial filter on NIF. A beam traveling from left to right through lens SF1 reflects from the second surface of the lens, propagates back towards the main amplifier, and comes to a focus at 0.233 *f* distance from the lens, where *f* is the lens focal length. If the reflectivity of this surface is 0.5%, the energy in this reflection can be as high as 50 J, and the ghost focus is a serious hazard to any optical component located in that vicinity. If one considers the size of the beam near focus, as well as multiple reflections between this lens and mirror LM1 (which must be considered, since they see the residual gain of the main amplifier), the hazardous zone extends from about 0.19 to 0.28 *f*. For beams going from right to left through the system, there is a double-reflection (reflection from first one, then the other surface of the lens) ghost focus that is hazardous over about 0.14 to 0.16 *f*. For left to right beams, again, there is a triple-reflection lens surface ghost that focuses at about 0.084 *f*. Even this weak a ghost can have a few milli-joules of energy and cause damage if a component is very near the focus, or if antireflection coatings degrade. There are similar sorts of ghosts located near every lens in the system, and tracking their positions and behavior is a major task in the optical design.

Lens ghost focus stay-out zones (in units of focal length *f*) for symmetric biconvex lenses. (40-00-0997-1753pb01)

Expanding beams from these ghosts can also flood the pinholes with light, giving rise to nearly collimated "pencil-beam ghosts" that propagate forward and backward through the system. Generally these are harmless, but they can cause damage if antireflection coatings are badly degraded.
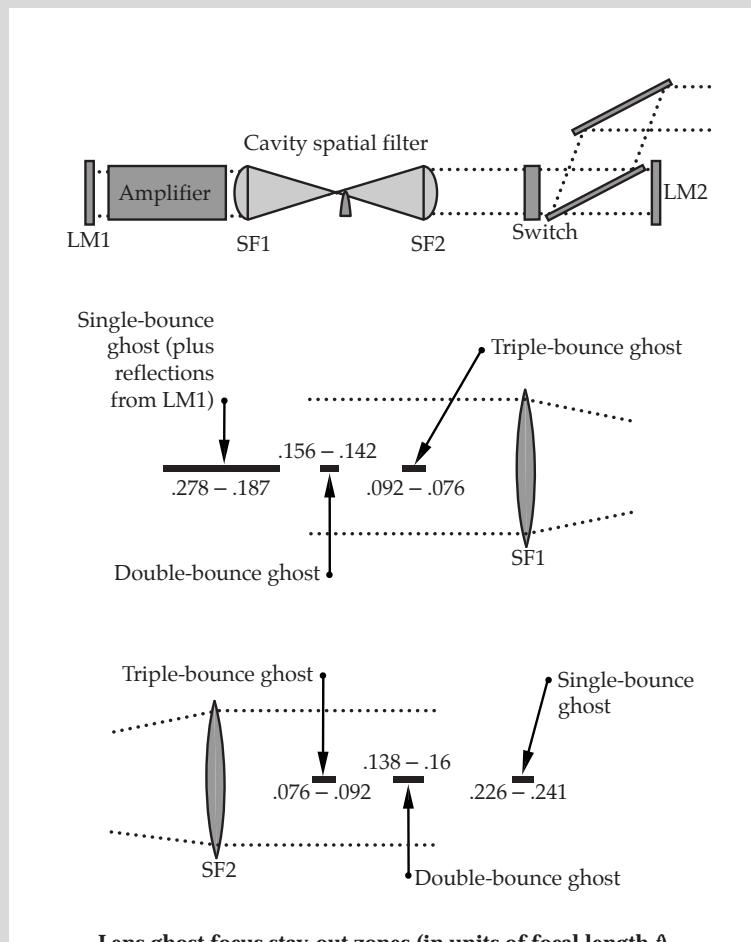
Switchyard and Target Area Mirror System

The function of NIF's switchyard and target area (SY/TA) optical system (Figure 3) is to transport a set of 192 beams grouped into 48 quads from the laser to the final optics assemblies located on the target chamber. These quads are arrayed in cones pointing at target chamber center, with 24 on the top and 24 on the bottom of the chamber. The mirrors must provide sufficient clear aperture for incident beams and reflected diagnostic beams. The aim point of each quad, with respect to target chamber center, can move ±30 mm transverse to the beamline and ±50 mm along the beamline. The pointing is controlled by tilting mirrors, so the mirrors must have adequate aperture to accommodate the changes in beam position required for this pointing. Also, the

mirrors must be sized so that the beam can be centered on the frequency converters using mirror tilts. There are many other design drivers affecting SY/TA mirror sizes that originate elsewhere in the NIF design, such as beam spacing requirements at the final optics location, the requirement for target back-reflection diagnostics, and the line-replaceable unit (LRU) maintenance concept.

There could be as many as 17 distinct mirror types in the system, but it is very costly to have such a wide variety. Consequently, we have grouped the 816 SY/TA mirrors into nine types having similar size requirements and angles of incidence, as shown in Table 3. Each beamline has either four or five SY/TA mirrors, designated as LM4 through LM8; some beamlines lack LM6.

We set the size of these mirrors using a ray-trace analysis tool and a ProE CAD model. The models adjust the tilt of each mirror and determine the beam positions required to accommodate the desired range
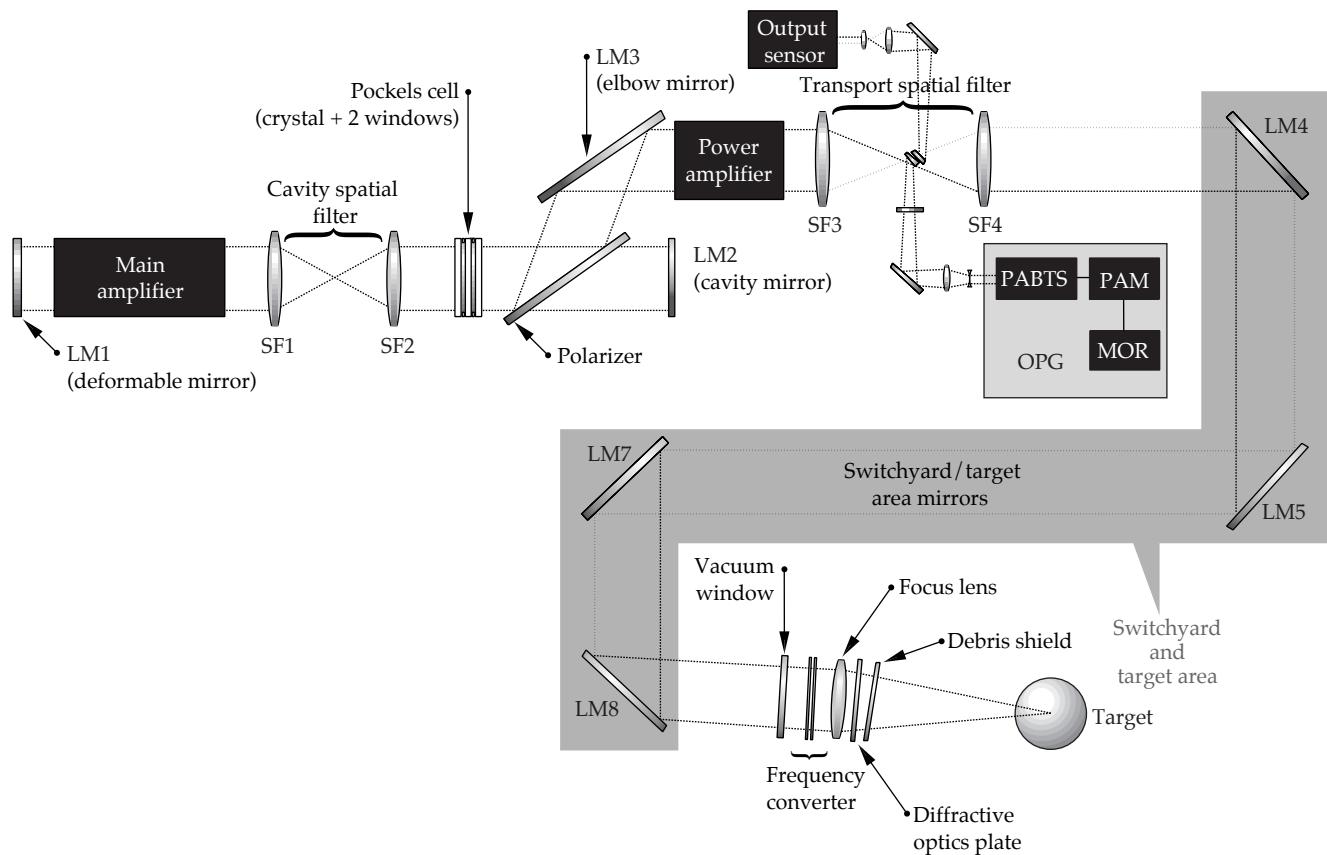
FIGURE 3. The switchyard and target area. (40-00-0997-2066pb01)

TABLE 3. Summary of switchyard/target area mirror characteristics.

NIF mirror position	Angle of incidence	Pol.	X-axis physical size and mechanical hard aperture (mm)	Y-axis physical size and mechanical hard aperture (mm)	Physical size diagonal (mm)	X-axis optical clear aperture (normal to optic) (mm)	Y-axis optical clear aperture (normal to optic) (mm)	Qty.
LM4A	45	S	507.0	595.4	782.0	477.0	565.4	96
LM4B	45	S	507.0	595.4	782.0	477.0	565.4	96
LM5	45	P	673.1	440.8	804.6	643.1	410.8	192
LM6	45	S	501.4	718.6	876.2	471.4	688.6	48
LM7A	14.1 16.9 19.7	S	502.0	524.6	726.1	472.0	494.6	48
LM7B	25.3 28.1 30.9	S	509.8	591.0	780.5	479.8	561.0	48
LM7C	36.6 39.4 42.2	S	503.2	688.0	852.4	473.2	658.0	96
LM8A	20.0 22.8	P	535.6	490.6	726.3	505.6	460.6	128
LM8B	30.0 33.2	P	586.2	483.2	759.7	556.2	453.2	64

of pointing and centering at the target chamber center and final optics assembly. Briefly, LM4 and LM5 move to center the beam on the final optics assembly. LM7 and LM8 move to compensate for any beam rotation in the path, and LM8 controls the final pointing to the target position. LM6, if present, does not have a control function. The ray-trace model quantifies the additional aperture required for each mirror to accommodate pointing the beam off-axis in the target chamber.

Title II Activities

For Title II, we will update the ray-trace model and the model that controls the optical configuration for the SY/TA mirrors to reflect a change in the final optics assembly focal length to 7700 mm. We will also develop a comprehensive model of the beamlines to verify mirror sizes so that we can begin the procurement process.

Final Optics Assembly

The final optics assembly contains four integrated optics modules, one for each beam in a quad. Each module contains a vacuum window, two frequency-conversion crystals, a final focus lens, a diffractive optics plate, and a debris shield (Figure 4). The primary functions of the final optics assembly are to convert the laser light to 3ω and focus it on the target (see "How Frequency Conversion Works" on p. 120). The system also smooths the on-target 3ω irradiance profile, moves the unconverted light away from the target, and provides a vacuum barrier between the laser and the target chamber. The system also has two additional alignment and diagnostic functions: to provide a signal for frequency conversion alignment and to provide a signal for power and energy diagnostics.

A failure of the target chamber vacuum window could have severe consequences because of the high
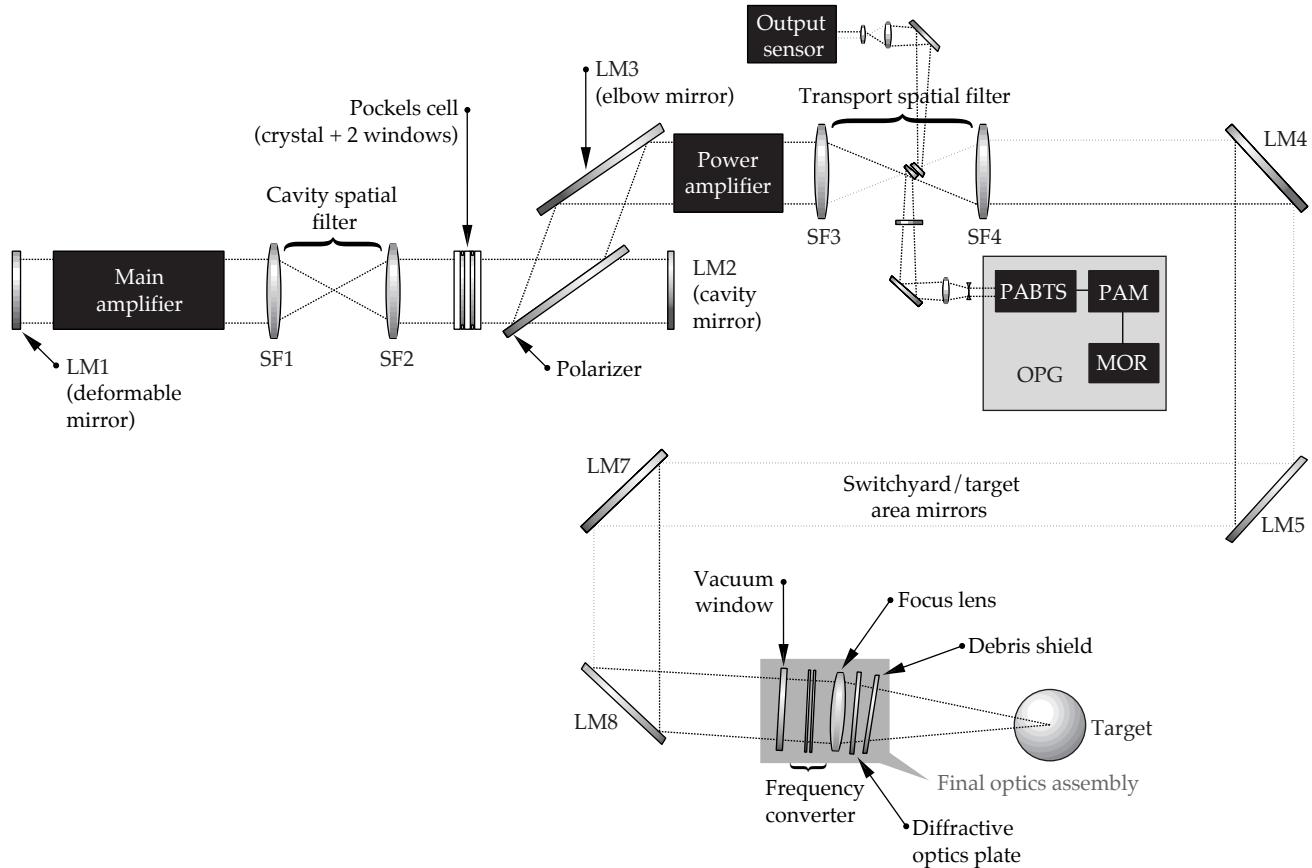
Figure 4. The final optics assembly. (40-00-0997-2067pb01)

value of the equipment in the target chamber and the possible release of tritium gas. Careful studies of fractured lenses on Nova show that a fused silica window will fail with no more than a single full aperture crack if designed to a peak tensile stress less than 500 psi. Therefore, we designed the NIF chamber window to that stress level. The window is thick enough (43 mm) that it would seriously limit the peak power on target if it were in the 3ω beam, so the frequency converters and a thin 3ω target focus lens must be placed in the vacuum environment of the target chamber.

The final optics cell, which holds and positions the two crystals and the focus lens, must have an optical clear aperture of 400 × 400 mm. Title I requires a focal length for the final focus lens of 7000 mm; this will be changed to 7700 mm early in Title II. This new focal length will allow each integrated optics module to be an individually removable LRU. The final optics must

divert the unconverted 1ω and 2ω light at least 3.0 mm from the center of the laser entrance hole (LEH) in an indirect-drive laser ignition target. (The unconverted light is diverted much more in the Title I design because of the use of diffractive optics, as discussed below.) The system must also provide for pointing the focused spot within ±5 cm of target chamber center.

The major design drivers for this system are ghost reflections, damage, optics fabrication, flexibility for different user applications—such as direct-drive experiments—and beam control.

In the Title I design of the final optics, the frequency-conversion crystals and focus lens are mounted together in a final optics cell that allows tip-tilt adjustment for the crystals and translation to move the focal point in the target chamber. The plano-convex focus lens has its flat surface facing away from the target so that the flat first surface

HOW FREQUENCY CONVERSION WORKS

A neodymium glass laser like NIF generates light at a wavelength of about 1 µm in the infrared region. However, we know that inertial fusion targets perform much better when driven with ultraviolet radiation. The NIF laser will convert the infrared (1.05 µm or 1ω) light to ultraviolet (approximately 0.35 µm) using a system of two nonlinear crystal plates: one made of potassium dihydrogen phosphate crystal (KDP), the other of its deuterated analog, KD*P. The figure shows the arrangement of the two crystal plates. The first plate converts two-thirds of the incident 1ω radiation to the second harmonic (2ω) at 0.53 µm. Then the second crystal mixes that radiation with the remaining 1.05-µm light to produce radiation at 0.35 µm, or the third harmonic (3ω). This process has a peak efficiency greater than 80%, and the efficiency can exceed 60% for the complex shapes used to drive ignition targets.

NIF configuration for frequency conversion to 3ω using two KDP crystal plates. (40-00-0997-2071pb01)
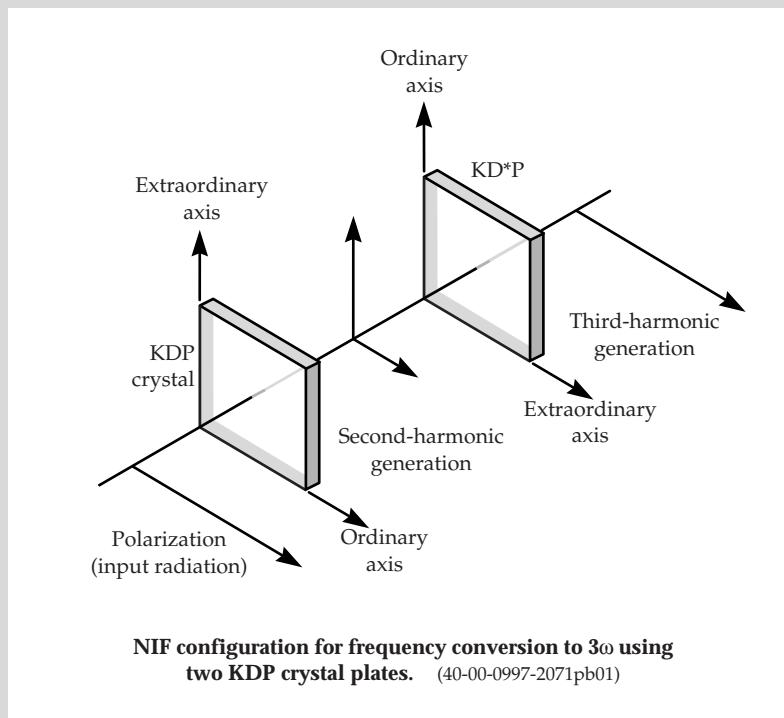
provides a back-reflected beam to alignment sensors and diagnostics located near the focal plane of the TSF. The lens also has a beam sampling grating for providing a diagnostic signal to an energy measurement calorimeter. The beam then goes through a separate diffractive optics plate, which contains a color separation grating and a kinoform phase plate. The grating moves the unconverted light well away from the target by creating multiple diffracted orders. The diffractive optics plate can be customized for various spot sizes and profiles, which provides flexibility for experiments studying indirect drive, direct drive, weapons physics, weapons effects, and other applications. The main beam and the diagnostic beam then pass through the debris shield, which is the last optical element in the system. This 10-mm-thick fused-silica optical element protects the final optics from target debris and

contamination. Table 4 shows the sizes and apertures for the final optics assembly (FOA) components. Some dimensions need to be verified by more detail design during Title II.

The exact relative positions of the optical components in the FOA are determined by careful analysis of the ghost reflections. The ghost analysis is complicated by the 12 surfaces involved, the mechanical restrictions in spacing the optical components, the requirement to accommodate a ±5-cm focus adjustment, and the tolerances involved in fabricating the focus lens. We locate the window and debris shield where they are safe from damage, then tilt them to eliminate potential ghost problems (Figure 5).

NIF uses a new color separation grating (CSG) technology for separating the 3ω light from unconverted 1ω and 2ω light. This grating allows the focus lens to be much thinner than it would be if refraction were

TABLE 4. Title I optics sizes and apertures for the final optics assembly.

Optic	Name	Optical clear aperture (mm)	Mechanical hard aperture (mm)	Optics size (mm)
Focus lens	FL	400×400	401×401	$430 \times 430 \times 25$
Doubler	SHG	400×400	400×400	$410 \times 410 \times 11$
Tripler	THG	400×400	400×400	$410 \times 410 \times 9$
Debris shield	DS	400×400	420×400	$440^c \times 420 \times 10$
TC vacuum window	TCVW	400×400	410×410	$440^c \times 440^c \times 43^c$
Diffractive optics plate	DOP	400×400	420×400	$440^c \times 420 \times 10$

[c] Dimensions need to be verified in detail design during Title II

The window position is set by the lens triple-reflection ghost
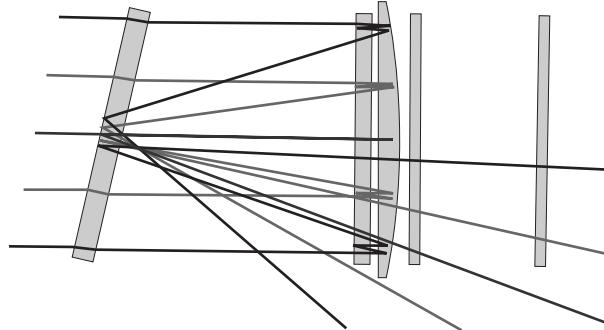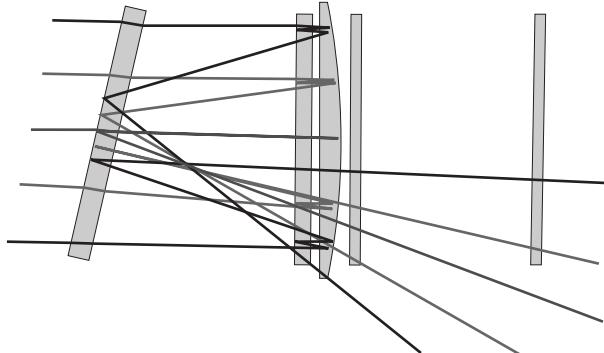
Window and debris shield are tilted to help control ghosts
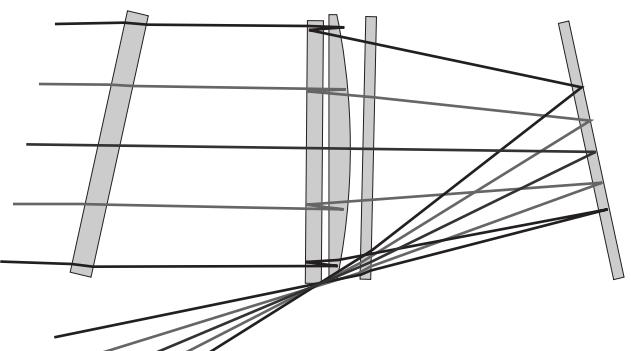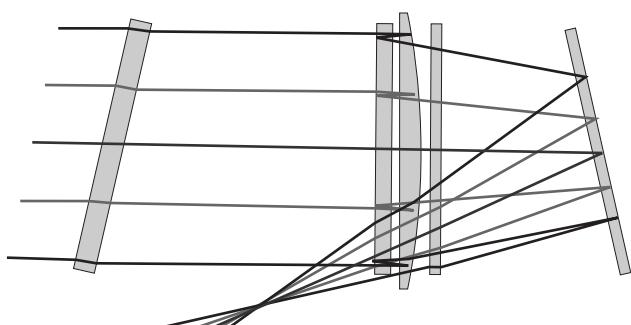
FIGURE 5. Ghost reflection analysis in the final optics. (40-00-0997-2068pb01)

used to remove unconverted light, as was done on Nova. The CSG is a kinoform or diffractive optic structure. On its surface are steps that have an optical path difference of exactly one wavelength at 3ω. These steps diffract the unconverted 1ω and 2ω light out of the beam. The pattern of these steps determines the position of the unconverted light at target chamber center and on the opposite wall of the target chamber. A subscale (12-cm) CSG of this sort has been fabricated; it easily met the minimum NIF specifications for transmitting >95% of 3ω light and <5% of 1ω and 2ω light, to the zero order (Figure 6).

FIGURE 6. Color separation grating performance of a 12-cm part meets minimum NIF specifications. (40-00-0997-2069pb01)
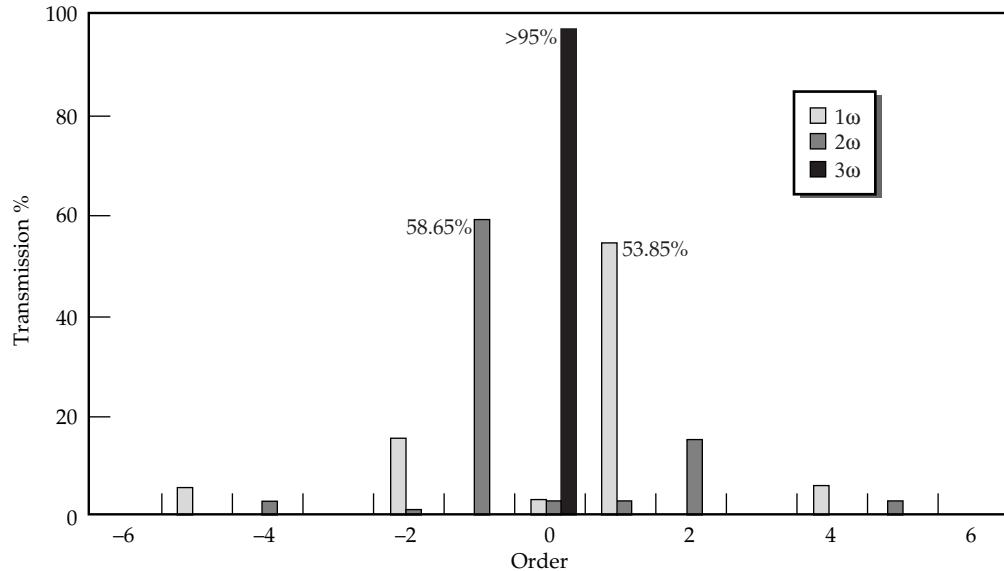
Title II Activities

In Title II, we will complete the analysis to determine the dimensions of the vacuum window, the diffractive optics plate, and the debris shield. We will also verify our ghost management solutions by adding tolerances to our ghost analysis, finalizing window and debris-shield tilt angles, and specifying baffle and absorber locations. We will analyze the unconverted light distribution from the CSG and choose a design that optimizes the placement of unconverted energy both near the target chamber center and on the beam dumps on the opposite wall of the chamber. We will also finalize the kinoform design for user-defined NIF irradiance patterns.

Specifications for Large-Aperture Optics

Each one of the 7000 large-aperture optics in the NIF system must be manufactured by outside vendors. To be certain that we get optics that meet users' requirements at a minimum cost, we are producing a set of detailed specifications. We are iterating these Title I draft specifications with vendors to ensure that, with the final specifications, the optics can be manufactured and that they meet NIF performance requirements.

We divide the specifications into two basic types: optical quality specifications (wavefront error, transmission and reflectance, etc.) and design-related specifications (dimensions, radius of curvature of lenses, etc.). The optical quality specifications are derived using three techniques. First, we follow the flow-down of NIF requirements to ensure that we meet the primary criteria of the system. There are two general

optical requirements: the focal spot required on the target (1.8 MJ of 3ω energy within a 600-μm-diam spot, and a goal of half the short-pulse energy within a 100-μm spot), and the reliability, availability, and maintainability of each optic. We also derive the specifications empirically, tying the NIF design to historical results with Beamlet and Nova optics, thus ensuring the manufacturability of the optics. Finally, we determine measurement limitations, so that the requirements are interpreted in measurable terms. Below, we discuss several important optical quality specification areas: the wavefront error, which is dependent on spatial wavelength regions of varying scale, and discrete defects and coatings, which are independent of the spatial wavelength regions.

Wavefront Error

We define three spatial wavelength regions for wavefront error, where L is the spatial wavelength:
1. Figure, where $L > 33$ mm.
2. Waviness, where 33 mm $> L > 0.12$ mm.
3. Roughness, where $L < 0.12$ mm.

These regions have different effects on the beam, and are discussed separately below.

Figure

We further divide the figure error into three bins based on the ability of the deformable mirror to correct them. Models for the mirror show that it corrects 99% of 0–0.5 cycle error ($L > 800$ mm), 90% of 0.5–1.5 cycle error (800 mm $> L > 267$ mm), and none of the 1.5–12 cycle error (267 mm $> L > 33$ mm). "Cycle" refers to cycles across the 400-mm aperture.

To determine the figure error of a particular element, we track the peak-to-valley (P-V) contributions from the following sources:

- Fabrication. We assume these errors are relatively small: 0.15λ for crystals, and 0.2λ for all other optics.
- Lens misalignments. We assume that a pair of lenses can be aligned to a total wavefront error of 0.25λ of focus, and that the angle tolerance on SF1/SF2 can create 0.2λ of coma. Slight mirror, crystal, or slab misalignments will not affect the wavefront.
- Coating. For mirrors and polarizers, we specify a total reflected wavefront error of 0.3λ at 1ω, for both fabrication and coating.
- Thermal effects. Thermal effects are mainly present in the amplifier slabs, due to instantaneous flashlamp loading and residual temperature gradients. We assume the cumulative effect in the slabs is about 5λ.
- Environment. Coatings respond to changes in humidity, so we are restricting the humidity fluctuations in the laser to those that create <0.125λ wavefront error.
- Structural effects. We assume that the gravity sag from transport mirrors is 0.2λ, and that mounting errors for the transmissive elements are negligible, except for the amplifier slabs at 0.1λ.

We add errors coherently according to how many times the laser beam passes through an element, and add errors incoherently according to the number of elements involved. For example, if the fabrication error for a cavity lens is 0.1λ, and two cavity lenses are multipassed four times, then wavefront error$^2 = 2(4 \times 0.1\lambda)^2$, or wavefront error = 0.566λ.

This analysis shows that the wavefront error in the "figure" spatial frequency range is dominated by pump-induced thermal distortions in the amplifiers. Also, fabrication errors could be relaxed from λ/6 to λ/3 without significantly affecting the total wavefront error. Alignment of the spatial filter lenses strongly affects the accumulated wavefront error. Finally, wavefront errors in the 1.5- to 12-cycle spatial frequency bin are the limiting factor in beam quality and focusability, since they are not corrected but are transmitted through the spatial filter pinholes, which cut off errors at shorter spatial wavelengths.

Figure errors are specified in three ways, namely the P-V wavefront error (the value of λ/3 discussed above), the rms wavefront error (which is usually derived from the P-V error), and a wavefront gradient limit. The gradient limit is used to control the short spatial wavelength region (267 mm > L > 33 mm) that contributes to the minimum focal spot size. A gradient specification of (λ/90)/cm, or (equivalently) 99.8% of slope errors <(λ/30)/cm, will allow us to meet NIF focal spot requirements. The wavefront error budget will be examined and reviewed in even greater detail early in Title II.

Waviness and Roughness

Errors in the "waviness" spatial frequency range (33 mm > L > 0.12 mm) cause irradiance noise on the beam. This noise can also seed the growth of irradiance noise due to the nonlinear index of refraction at high irradiance, and can ultimately lead to beam breakup and filamentation. Errors in this range are reset to zero every time the beam passes through a spatial filter pinhole, at which point they constitute an optical loss. Errors in the "roughness" range (L < 0.12 mm) are not as dangerous for seeding nonlinear growth, except for 3ω optics where seeding of filamentation is important for L a bit smaller than 0.12 mm. Roughness also leads to an optical loss.

We specify waviness and roughness using a not-to-exceed line on a power spectral density (PSD) plot of the optical surface (Figure 7). Tests on many Beamlet and other parts show that the specification shown here is achievable with good manufacturing practice, and will be reasonable for NIF.

Discrete Defects

All optical components contain discrete defects, such as bubbles, inclusions, and scratches. These may lower the damage threshold of the part, and a high concentration of defects can lead to noticeable optical losses. We specify discrete defects using the ISO 10110 standard that is beginning to be used for optical specifications.

Our preliminary specification for defects such as bubbles is 26×0.25, which in ISO notation means less than 26 defects each having a maximum area of $(0.25 \text{ mm})^2$. Any number of smaller defects are allowed by the standard, so long as the total obscured area does not exceed $26 \times (0.25 \text{ mm})^2$. Opaque inclusions generally lead to very low damage threshold, and are not acceptable unless it can be demonstrated that they will not damage at NIF operating fluence. The scratch/dig specification is 100×0.125. The long scratch specification is L1 × 0.03 with a maximum length of 50 mm, where L designates "long," 1 is the number of scratches allowed, and 0.03 is the width of the scratch in mm. Thus, one 30-μm-wide scratch 50 mm in length is allowed (or any combination of narrower scratches that total less than 30 μm width and are shorter than 50 mm).

We expect to refine these specifications in Title II based on further propagation analyses and experiments on damage initiated by defects.

FIGURE 7. Power spectral density specifications assure NIF performance.
(40-00-0997-2070pb01)
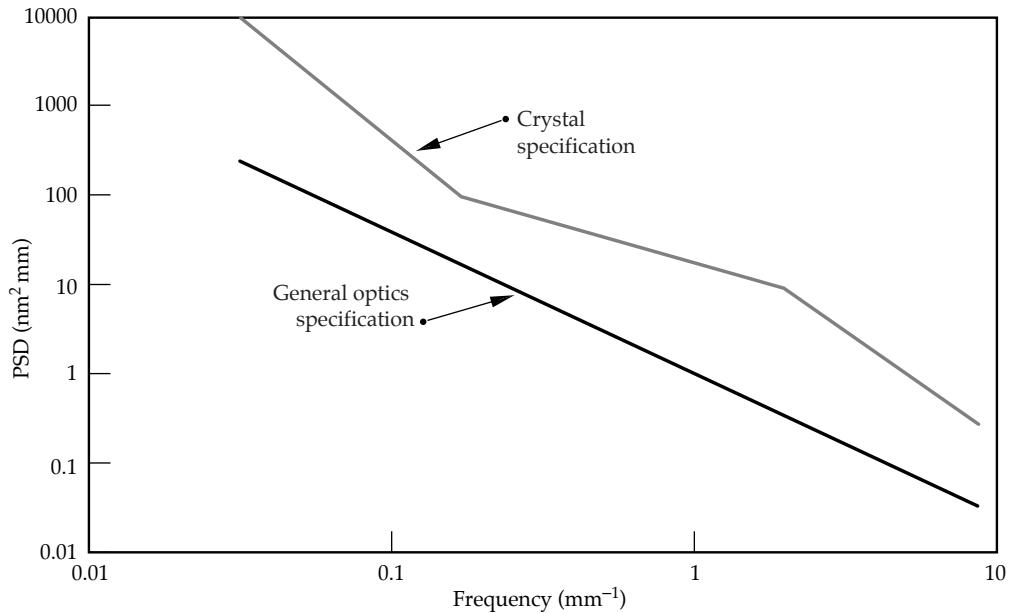
Coatings

Except for the amplifier slabs, all NIF optics have either antireflection coatings (lenses, crystals, and windows) or highly reflecting multilayer dielectric coatings (mirrors and polarizers). The antireflection coatings are deposited by a liquid-dip sol-gel process developed at LLNL. They have high damage threshold and, when new, have a transmission of 0.999 per surface at 1ω and 0.998 per surface at 3ω. There is some degradation with age.

Mirror and polarizer coatings are supplied by commercial vendors. We specify a reflectivity >0.995 for mirrors. Transport mirrors (LM4–LM8) must also have a reflectivity between 0.25 and 0.71 at 2ω, and between 0.31 and 0.71 at 3ω. There are a few other specialized specifications on transmission for some mirrors. Polarizers are specified to have an *S*-polarized reflectivity >0.99 and a *P*-polarized transmission >0.98 at a use angle of 56±0.5° with a bandwidth of 1°.

Title II Activities

Design-related specifications are contained and controlled in our configuration drawings. As part of the Title I reviews, we have completed 82 large-aperture drawings for blanks, finished parts, coatings, etc. The drawings exceed normal Title I standards and include mounting and handling details as well as detailed notes on the specifications. We are now ready to solicit procurement bids for those optics that require a long lead time.

In the optical specifications area, our list of Title II activities contain no critical items. Propagation modeling efforts will provide us with more detailed justification for specifying the rms gradient, PSD limits, and discrete defects for the various optics. Damage experiments could change the specifications for some discrete defects. Design engineers will be providing updates on mounting requirements, part sizes and so on, and vendors will be commenting on our assumptions in the wavefront error budget and providing general feedback on our drawings. We will incorporate the responses from design engineers and vendors as the design and specifications evolve. Another Title II priority is to develop supporting documentation on handling, inspection, and testing.

For more information, contact
R. Edward English, Jr.
Opto-Mechnical Systems Engineer
Phone: (925) 422-3602
E-mail: english2@llnl.gov
Fax: (925) 424-6085

PRODUCING NIF's OPTICS

J. Atherton

D. Aikens

J. Campbell

J. De Yoreo

R. Montesanti

T. Parham

C. Stolz

*T*he NIF will be the world's largest optical instrument. The basic challenge for producing optics for NIF is to establish and maintain high production rates and low costs while meeting tight technical specifications. We are working with industry to develop advanced manufacturing technologies that will help meet this challenge. Our optics development program has been very successful to date: most production process details are finalized, and key results have been demonstrated in many areas. We are on schedule and, as of Title I, are soliciting competitive proposals in most areas, consistent with the overall NIF schedule.

Introduction

Within the NIF optical system, we have more than 7000 large optics that handle the full-sized NIF beam (0.5 to 1 m maximum optical dimension), and about 15,000 to 20,000 smaller optical components. The technical requirements for these optics present many challenges for their production. For instance, most damage thresholds are about three times higher than Nova's, and at or above Beamlet's levels. Other challenges are in the areas of schedule and cost. First, we have an extremely short production schedule. Installation of the optics must begin in FY99 and be completed by the end of FY02. This means that procurement bids must be awarded by mid-FY97 for the start of final facilitization for optics; pilot production must start in late FY98; and production must begin by FY99. The fact that we need thousands of meter-class optics also puts pressure on the schedule. At present, the U.S. optics industry can produce about 200 to 300 meter-class optics per year—about 10 times too low for our needs. As for costs, the extreme technical requirements and tight time restraints work against efforts to keep costs low.

We are working with the U.S. optics industry, as well as with University of Rochester's Laboratory for Laser Energetics (LLE) and Los Alamos National Laboratory (LANL), to develop the technologies needed to meet NIF's goals and requirements within time and budget. Our partnership with industry is nothing new. We have worked with the optics industry since LLNL began researching inertial confinement fusion with large laser systems, beginning with the Janus laser system in 1974. We have helped advance the state-of-the-art in optics manufacturing technology to increase production volume and performance, and to decrease production costs for optics of NIF size.

We and our partners are following a four-part program—development, facilitization, pilot production, and production—to meet NIF's optics performance, schedule, and cost requirements. Figure 1 shows the production areas and the schedule for each.

To date, most of our activities in these areas have been in the development program. This program's goal is to reduce optics cost and improve performance of NIF's significant optical components (Table 1). Our development program has yielded some impressive results to date, particularly in the areas of continuous melting of laser glass, potassium dihydrogen phosphate crystal (KDP) rapid growth, KDP diamond turning, deterministic high-convergence figuring, and coating designs for polarizers. We still have concerns in some areas, but in general, our strategy is to use multiple vendors and backup technologies to minimize risks to production costs and schedules.

As for Title II activities, we are proceeding in a manner consistent with the overall NIF schedule. We are now soliciting competitive proposals in most areas, and final facilitization for optics is scheduled to begin in mid-FY97.

The rest of this section summarizes our activities and future directions for each of the areas listed in Figure 1.

FIGURE 1. Schedule and areas of focus for NIF's optics development, facilitization, pilot production, and production programs. (40-00-0997-2072pb01)

	FY95	FY96	FY97	FY98	FY99	FY00	FY01	FY02	FY03
Laser glass									
KDP growth									
KDP finishing									
Fused silica									
Finish flats									
– Amps									
– HRs, polarizers									
– Windows, debris shields									
Finish lenses									
Coating									
Diffractive optics									

Development
Early facilitization
Final facilitization
Pilot production
Production

First quad to target chamber

Laser bay #1 installed

Laser bay #2 installed
and laser bay #1 activated

TABLE 1. The development program is focusing on the technologies that will improve performance and bring costs down for amplifier slabs, crystal optics (i.e., frequency converters and Pockels cells), polarizers, and lenses.

Optical component	Beamlet actual	NIF production estimate (FY96$)	Development required
Amplifer slabs	$49K	$17.5K	Continuous melting/forming of laser glass High-speed grinding/polishing Deterministic figuring
KDP/KD*P crystals	$34.3K–$73.5K	$15.7K–$25.3K	Rapid growth of KDP/KD*P Low-modulation diamond turning
Polarizers	$43.2K	$19.2K	Improved yields in coatings Reduced defects; increased damage threshold from >12 J/cm^2 to 20 J/cm^2 at 1053 nm
Lenses	$28.5K	$12.3K–$14.1K	Reduced inclusions, NIF boule geometry in fused silica Deterministic figuring of square lenses Maintain large-area damage threshold >14 J/cm^2 at 351 nm

Estimates based on vendor cost studies

Laser Glass

The laser glass effort involves producing the "blanks" of neodymium-doped glass that are later machined into amplifier slabs. The NIF Title I design requires well over 3000 laser glass slabs—11 in the main amplifier and 5 in the power amplifier for each of the 192 beamlines. These neodymium-doped slabs must have certain characteristics for fusion laser applications: they must extract energy efficiently from the flashlamps that pump them, store that energy efficiently and at a high density, and be of high optical quality (i.e., high homogeneity, low nonlinear index, low thermal distortion, high damage threshold, and low losses).

At 80 × 46 × 4 cm, NIF's slabs are slightly larger than Beamlet's slabs, which are roughly twice the size of anything previously produced. To produce laser glass in the size and volume required by NIF, our vendors are developing a "continuous melting" technique to replace the more common "batch melting" technique (see "Melting Methods for Glass" below). There are only two laser glass vendors in the U.S. capable of producing the NIF slabs: Schott Glass Technologies, Inc., and Hoya Corporation/ Hoya USA. They are taking different approaches to solving the technical issues involved with the continuous melting technique. Hoya has designed, built, and operated a subscale continuous melter to study key development issues, whereas Schott has decided to design and build a full-scale continuous melter starting in early 1997, with operation starting in late 1997.

MELTING METHODS FOR GLASS

There are two possible methods for producing the glass needed for NIF's amplifiers: the discontinuous or "batch" method and the recently developed continuous method. In the more common batch process, as shown here, raw materials are first melted and stirred in a quartz vessel. The melt is cooked, broken up, and the fragments or "cullet" are melted, refined, and stirred in a platinum vessel. The contents of the vessel are then poured onto a moving conveyor to form the glass blanks. The batch process has serious drawbacks when applied to NIF. The vessel must have a volume of approximately 50 L to produce a single blank with a volume of about 10 L; hence most of the glass is wasted. In addition, the batch-to-batch variations are greater with a batch melter than with a continuous melter, thereby reducing yield and increasing cost.

In a continuous melting furnace, the raw materials melt and mix in one chamber, then flow as a liquid into refining and homogenizing chambers. A continuous liquid stream of glass runs out of an aperture in the homogenizing chamber. This process, shown here, is much better suited to manufacturing the large volumes of glass that NIF requires.
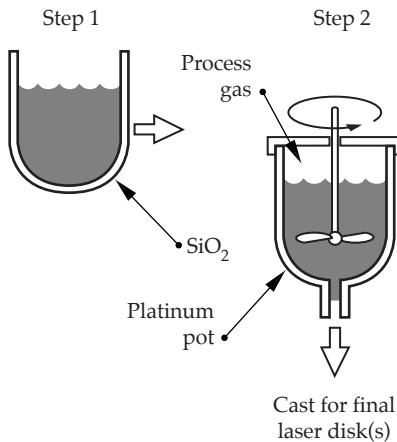
Batch melting process for laser glass
(40-00-0496-0936pb02)
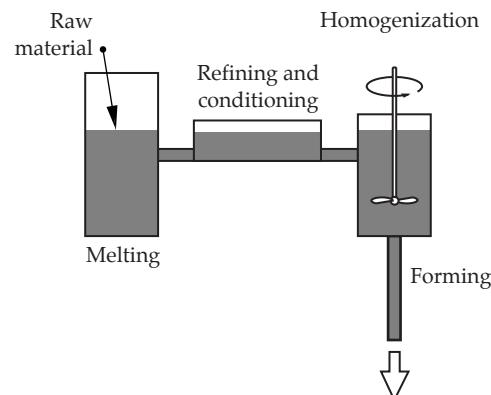
Generic continuous melting process for optical glass
(T. Izumitani, ***Optical Glass***, 1985, Chap. 3)
(40-00-0997-2077pb01)

KDP Growth

NIF requires 600 large-aperture KDP components for optical switches and frequency converters for its 192 beamlines. For NIF, there are three main issues driving KDP development. First is performance, including the threshold for 3ω damage in KD*P, KDP and KD*P wavefront requirements, and surface modulations. Second is risk: using conventional crystal growing methods, it takes longer than two years to grow KD*P crystals of the size needed for NIF. In addition, the yields from the conventional growing process are highly uncertain. Third, we have cost considerations. The average cost of KDP plates for Beamlet was $65K/plate; we hope to bring this cost down considerably. Also driving KDP development efforts are the NIF requirements for the crystals, including sizes, surface finish, and the fact that we need 600 crystals within three years.

We are taking two approaches to meeting these challenges. At LLNL, we have designed, built, and tested a full-scale rapid growth system, while Cleveland Crystals, Inc. (CCI) is improving conventional crystal growing technology as a backup technology for NIF (see "Growing Crystals" below).

We have demonstrated that, with rapid growth, we can meet all NIF crystal requirements at the 15-cm scale and almost all in 41-cm z-plates. For both technologies, we still need to demonstrate full-aperture growth for the doublers and triplers used for frequency conversion. We have two issues to address for large-scale rapid growth: inclusions, which can cause damage, and spontaneous crystallization under certain conditions.

Our Title I strategy for delivering NIF crystals has two parts: one for our rapid growth technology, the second for our CCI backup technology. For rapid growth, we plan to demonstrate the technology at full-scale by mid-FY97, and provide limited optimization in mid- to late-FY97. We will transfer the technology to vendors for NIF production in FY98 and also conduct some pilot production at LLNL as a backup. CCI will begin upgrading their facilities in mid-1997, allowing six years for a NIF pilot plus full production. If CCI uses crystal seeds from our rapid growth efforts, this time could be less. Major issues for this strategy include LLNL being ready to transfer the technology to vendors by early FY98 and determining how many vendors to include in the facilitization, since those costs are high. Finally, the timing for CCI facilitization and seed production is still evolving.

KDP/KD*P Finishing

To get from a crystal boule to a finished piece requires precision machining and finishing. There are two general steps to the finishing process—blank fabrication and final finishing. In blank fabrication, the blanks are sawed from a boule before being processed to a final size and flatness by single-point machining. In final finishing, the final surfaces of the crystals are generated by single-point diamond flycutting. The two major challenges for crystal finishing are the tight specifications and the high production rate.

Three crystal finishing specifications for NIF are particularly difficult to meet: surface roughness, surface waviness, and reflected wavefront. We are making progress in all three areas. Improvements to the diamond flycutting machine at CCI reduced the surface roughness and waviness of crystals by a factor of three. CCI has now met NIF reflected wavefront requirements on a 37-cm Beamlet crystal.

GROWING CRYSTALS

In general, crystals are grown from a seed or "starter" crystal, which is submerged in a melt or solution containing the same material. The final growth, which has the same atomic structure as the seed, is called the boule. Conventional techniques for growing crystals from solution are generally slow; growth rates for conventionally grown KDP are about 1 mm/day. Because of a high density of defects in the material near the seed crystal in KDP, the quality in this region of the crystal is low; and because the seed defects propagate into the final boule, a substantial fraction of the boule is of low quality. A large percentage of crystals that have taken a long time to grow are, in the end, useless for their intended purpose.

LLNL's rapid growth method, which derives from research at Moscow University, uses a small "point" seed and produces only a small number of defects. As a result, even material near the seed is of high quality. The process relies on pretreatment of solutions using high temperature and ultrafiltration. This process destroys any small crystal nuclei that might be present in the solution and allows it to be highly supersaturated without spontaneous crystallization. Of secondary importance to this method are the technique for holding the seed, the temperature profile during growth, and the hydrodynamic regime. The two major advantages of this process—high growth rate and potentially high yields—dramatically reduce cost.

An aggressive production schedule means that finished pieces must be completed at three to four times the current production rate. CCI plans to purchase new equipment and streamline their process to meet NIF's schedule, perhaps running two or three shifts instead of the current 1.5.

The major challenges for production are achieving flatness and diamond flycutting the faces. The current method for achieving crystal flatness was developed for Nova. CCI has developed a proprietary process that produces flatter surfaces. Additional process development is aimed at making the new process more deterministic and faster. The diamond flycutting machine can finish a crystal to NIF specifications, but takes about a week to do it. To meet the production rate of one crystal/day will require a new, state-of-the-art machine. The Laboratory and France's Commissariat a l'Energie Atomique (CEA), which also requires KDP components for its Laser Megajoule (LMJ), have commissioned to build two such machines.

Our outstanding tasks for the future include refining the process for efficient part flow and designing and building equipment for blank fabrication. For final finishing, we need to optimize the process to reduce fogging on

the flycutting machine and to design the new machine. Finally, for facilitization, we need to select the finishing vendor and install and check out equipment.

Substrates for Mirrors, Polarizers, Lenses, and Windows

The eight NIF mirrors and polarizers in each beamline, highlighted black in Figure 2, will be made of a readily available optical glass (BK7™ or a similar equivalent). Ten large aperture lenses and windows, shown gray in Figure 2, will be made of fused silica. Our focus in the area of substrates is on the cost and schedule for the fused silica components rather than the technical requirements.

We are working with Corning Inc. to improve its synthetic fused silica deposition process to increase the yield. First, the boule geometry will be better matched to the NIF blank size to maximize the number of blanks obtained from each boule. Second, the process design and control will be improved to reduce inclusions. Finally, the boules will be more efficiently processed to reduce metrology needed for quality assurance.
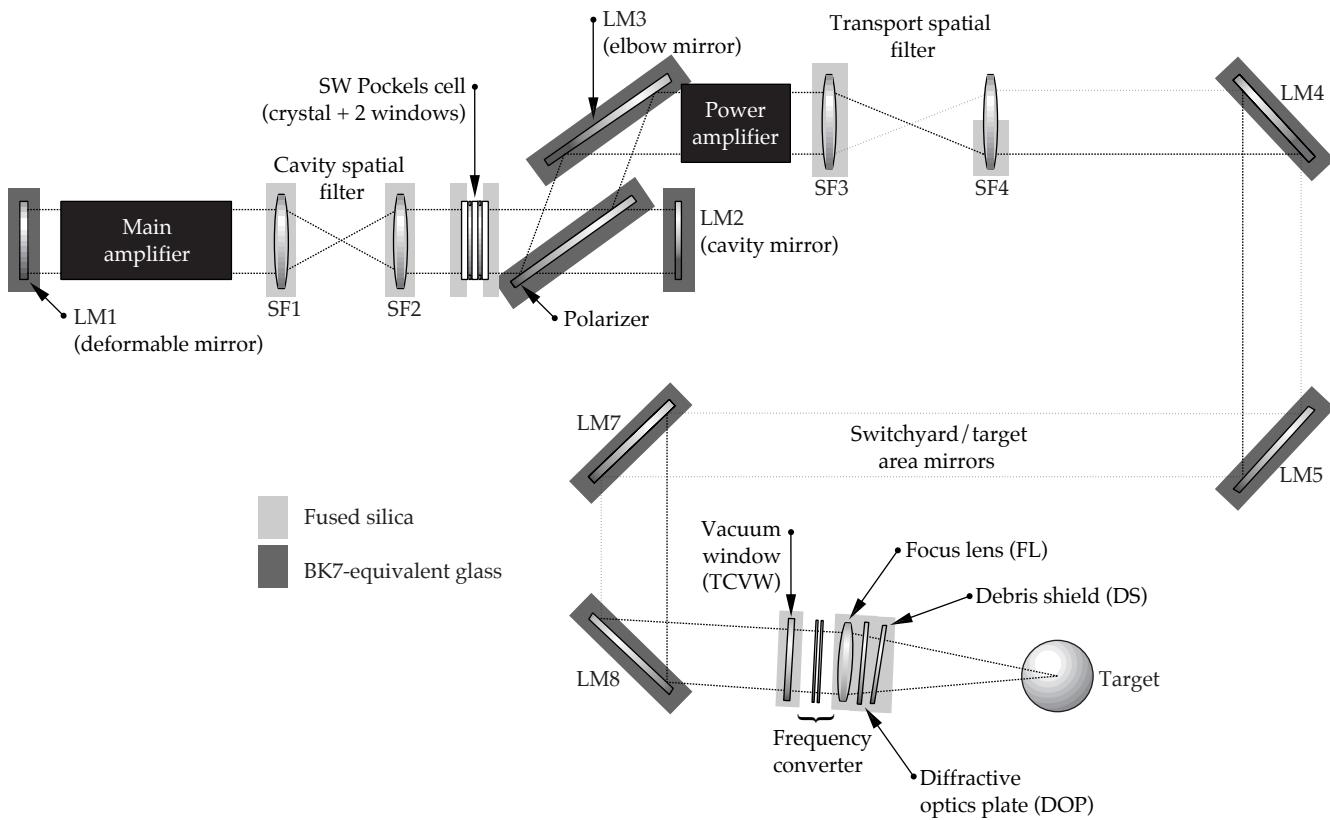
FIGURE 2. Eighteen large-aperture optical components in each NIF beamline, about 3500 total, will be fabricated from glass substrates. The components in black will be based on a BK7™-equivalent glass; the components shown in gray will use fused silica.   (40-00-0997-2073pb01)

In addition to these yield improvement activities, we are also investigating the homogeneity specification of the fused silica blanks. Improved figuring capability at the optics fabrication vendors may allow us to significantly relax the homogeneity requirements of the glass for some of the optics. In this manner, the glass yield can be increased and the cost decreased, without significantly impacting the overall cost of the fused silica optics or the performance of the optics in NIF.

Optics Fabrication for Flats and Lenses

The optics fabrication process takes optics materials—laser glass, fused silica, BK7™—from the raw blanks to polished surfaces. The blanks are shaped with machine tools, similar to those used in metal fabrication. This machining process leaves a significant amount of subsurface damage, which is removed through lapping and polishing. The most expensive, time-consuming fabrication step is iterating to achieve the final figure. To achieve NIF cost targets, this final figuring step needs to be as automated and deterministic as possible.

Most of the functional performance requirements, such as achieving the proper shape and meeting wavefront requirements, have been demonstrated. We have three primary concerns still to address. First, finishing vendors must consistently meet NIF smoothness and ripple requirements. Second, they must establish the capacity necessary to meet NIF's schedule (i.e., completing 30 lenses/month, 90 laser slabs/month, and 80 mirrors and windows/month). Finally, they must demonstrate and consistently achieve high 3ω damage thresholds of 14.1 J/cm^2 (for the focus lens, diffractive optics plate, and debris shield only). To meet the performance requirements and cost targets at the needed throughput will require a highly optimized process, and new and custom machine tools.

In FY97, lens development efforts will focus on meeting specifications as well as throughput and 3ω damage requirements. In flats fabrication, we will be funding development at three companies to broaden the competitive field. All throughput and performance requirements for flats fabrication will be demonstrated at full scale during FY97 and FY98.

Optical Coatings for Polarizers and Mirrors

Each of the large-aperture mirrors and polarizers in the NIF beamline has its own, often very complex, coating requirements. Meeting the fluence requirement for the transport mirrors represents the greatest technical challenge for coatings. As for meeting cost and schedule constraints, our greatest concerns involve the yields and capacity. For instance, poor yields translate to high costs per unit. In addition, NIF is not the only project with optical coating requirements. Competition from other LLNL and Department of Energy programs potentially restricts NIF's access to coating chambers, which could impact the schedule.

Looking at the coating process used on Beamlet, we find that many of the NIF coating technological requirements have already been demonstrated with Beamlet optics. This coating process can be improved without major process modifications, which will increase the yields. This leaves the issue of capacity. Since coating is the last step in the optical manufacturing process, we need extra capacity to compensate for any schedule slips in earlier steps. Vendors are working on ways to increase their capacity and meet NIF's requirement of coating about 10 optics/week. We are also working with other programs that have optical coating needs, to see if their needs can be met with the smaller coating chambers, freeing up the larger ones for NIF. We will minimize the number of test runs and subsequent coating costs by grouping the optics into "campaigns." Finally, we are working with vendors to optimize the metrology to increase the throughput.

Diffractive Optics

We have diffractive structures on two components in NIF's final optics assembly. The final focus lens has a 3ω sampling grating on the flat, incoming surface, and the diffractive optics plate has a color separation grating (CSG) on the incoming surface and a kinoform phase plate (KPP) on the outgoing surface. These diffractive optics are fabricated at LLNL in our diffractive optics lab. We have produced 3ω sampling gratings that meet NIF's requirements. We have also

fabricated KPPs for Beamlet and Nova that meet the NIF energy requirement of 1.8 MJ, but we need to improve the beam divergence. Finally, we have produced a subscale CSG part that meets the minimum performance specifications.

We can meet the Title I performance requirements for diffractive optics with the existing process technology, which is based on interference lithography for the 3ω sampling gratings, and conventional photo-lithographic techniques for KPPs and CSGs (see Figure 3). However, to meet our cost and yield projections, we must complete several activities. First, we must decide by mid-1998 between two techniques for etching patterns into the KPP fused silica substrates: the existing wet etch technique or a reactive ion etching (RIE) technique under development. The RIE involves fewer manufacturing steps, and would improve KPP performance and reduce costs. For the CSG, we must improve the precision of the mask alignment from 2 µm to 1 µm to minimize errors at the shorter ~240-µm period. Finally, we need to upgrade our facilities. We have already begun modifying the facility to provide processing for the 3ω sampling gratings and CSGs. We will add RIE capabilities, if our development effort shows that it would be cost effective to do so.

For more information, contact
L. Jeffrey Atherton
Associate Project Leader for Optics Technology
Phone: (925) 423-1078
E-mail: atherton1@llnl.gov
Fax: (925) 422-1210

(a)

Start with high-quality polished part

Coat with resist and bake

Expose with holographic technique, develop, and rinse

Etch by immersing in HF solution

Wash off resist

(b)

Start with high-quality, fused-silica substrate

Coat with photoresist

Expose through binary mask

Develop resist

Etch pattern into fused-silica substrate

Wash off resist
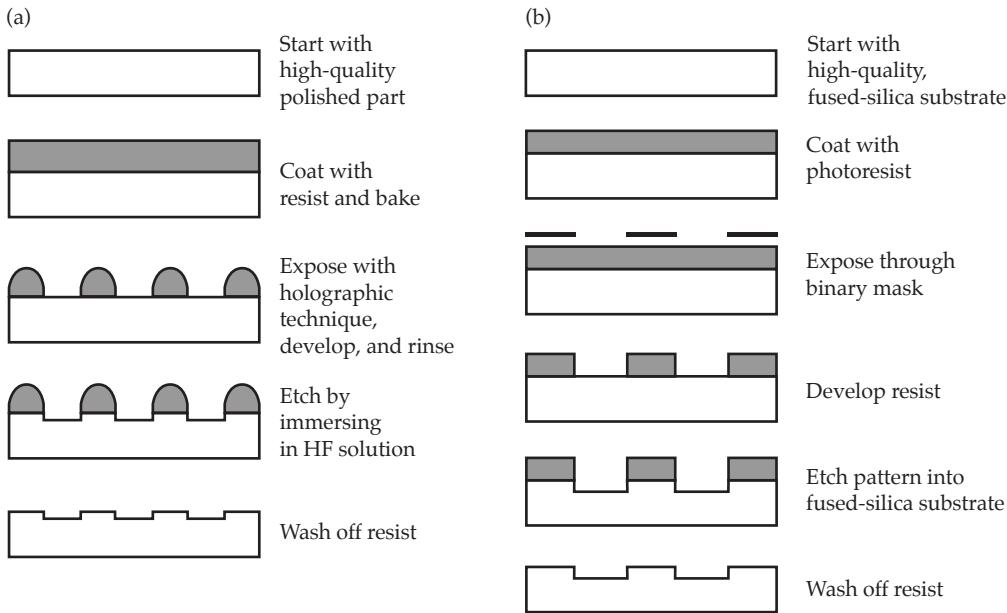
FIGURE 3. The NIF baseline process for producing 3ω sampling gratings and kinoform phase plates (KPPs) and color separation gratings (CSGs) are based on lithographic techniques. (a) The sampling grating uses interference lithography with hydrogen fluoride wet etching. (b) The large-scale features of the KPP and CSG allow us to use conventional photolithographic techniques. (40-00-0997-2075pb01)

LASER COMPONENTS

D. Larson

P. Biltoft

J. Davin

M. Newton

B. Pedrotti

M. Rhodes

M. Wilson*

*T*itle I designs are complete for a number of critical NIF components, including the NIF optical pulse generation system, the amplifiers and their associated power conditioning system, and the Pockels cell. Each of these systems follows the line-replaceable-unit philosophy, modularizing wherever possible. Prototype testing and component evaluations will proceed during Title II (final design), as we continue to look for ways to further simplify designs, optimize costs and performance, and enhance the safety and reliability of these systems.

Introduction

In this article, we review the laser's full-aperture active components—the amplifiers, their associated power conditioning system, and the Pockels cell. We also discuss the optical pulse generation system that prepares the input pulse for injection into the main laser beamlines. System control functions for alignment, positioning, and wavefront correction are covered in a separate article on laser control systems (p. 180).

The hardware for these components resides in the laser bay and capacitor banks. A portion of the optical pulse generation system—the master oscillator room—is in NIF's central operations area.

Each system has a development effort associated with it to address key technologies and design issues. For instance, the Title I amplifier design—a close-packed 4×2 aperture configuration, with a larger number of flashlamps and cassettes and flashlamp cooling—was developed in LLNL's AMPLAB. For the power conditioning system, we are testing and evaluating switches at Sandia National Laboratories and capacitors at LLNL, as well as developing pulsed power components with industrial partners including Primex and American Control Engineering. Similarly, we are completing optical system development for the optical pulse generator's preamplifiers on the Preamplifier

Testbed at LLNL, and completing analysis of our Pockels cell design in a dedicated development lab.

Another common thread is our focus on reliability and failure modes for these components. During Title I, we identified failure modes that could cause significant delays or costs. The most serious for the pulse generation system involved cleanliness, excessive output power or energy, or failure to put the appropriate bandwidth on the output pulse. To address these issues, we will be developing fail-safe systems for beam modulation and power; and energy limiters in detail as part of Title II. For amplifiers, we have modularized the system to the point where the only thing that can cause damage over a large fraction of the laser is an earthquake. Pockels cells are in a similar situation. For power conditioning, the biggest concern is a fault mode or a fire. We are ensuring in Title I and Title II design that none of these issues present credible risks.

There have been many changes to NIF since the conceptual design (CD). Those that have a significant impact on design in these areas are the bundle change from 4×12 to 4×2, the laser architecture change from the 9-5-5 amplifier configuration to 11-5 (not to preclude a change to 11–7), the number of preamplifiers changing to 48 from 192, and the added requirements for active flashlamp cooling in the amplifiers and for smoothing by spectral dispersion (SSD) in the front-end. Finally, for power conditioning, the very large rigid transmission lines that were part of the CD have been replaced by flexible lines to simplify interfaces with the facility and other equipment.

In this article, we describe the Title I design of each of the systems and summarize their Title II activities as well.

Optical Pulse Generation System

The primary function of the optical pulse generation system (OPG) is to generate, amplify, spatially and temporally shape, and inject an optical pulse into the plane

*Sandia National Laboratories, Albuquerque, NM

of the transport spatial filter pinhole, where it enters the amplifier system. The baseline Title I configuration described here is for 192 independent beamlines, although we plan to change the design to a 48-preamplifier module (PAM) system early in Title II to reduce cost. Design drivers include delivering a square-shaped beam of 1.053 μm, with a maximum pulse length of 20 ns to the injection optics. The intensity profile of the beam must be shaped to precompensate for any gain nonuniformities in the large-aperture section of the laser. For a square beam 22.5 mm on a side, the beam pointing stability must be 9.7 μrad. Another design driver is that the OPG optics and other components need to withstand a 25-J back-reflection without damage. Finally, the OPG needs to be able to deliver at least an 8.8-J pulse to the transport spatial filter (TSF).

The OPG system and its Preamplifier Maintenance Area (PAMMA) are centrally located in the Laser Target Area Building (LTAB) (Figure 1). The OPG system includes the master oscillator room (MOR), where the pulse is generated; the PAM, where the beam is initially amplified and shaped; and the preamplifier beam transport system (PABTS) and the injection system, which relay and focus the beam through the TSF in the main laser system (Figure 2). We include the injection system in our discussion, even though it is sometimes considered separate from the OPG system. The input sensor is also located in the OPG area, between the preamplifier and its associated beam transport system. For information about this diagnostic system, see "Laser Control Systems" on p. 180 of this *Quarterly*.

The master oscillator room (MOR) is where the parameters of the beam are determined: wavelength, bandwidth, pulse shape, and pulse timing. We designed the MOR to be highly flexible to accommodate changes in experimental requirements. The MOR uses fiber-optic technology extensively: five fiber-optic subsystems connect optically in a series (Figure 3), before fiber-optic cables deliver the pulses to the preamplifiers. At the start of this optical chain, a fiber-ring oscillator produces a single pulse, on the order of 1 nJ, which then passes through high-frequency wave-guide modulators that apply phase modulation for suppressing stimulated Brillouin scattering (SBS) and for smoothing by spectral dispersion (SSD). A "chopper" then selects a time window for the pulse to avoid overdriving the fiber amplifier chain. The SBS bandwidth is controlled by a four-part, robust, fail-safe system that will preclude optics damage due to SBS. Next, the pulse is amplified by a single-fiber amplifier before entering an array of four-way splitters, dispersion compensators, and fiber amplifiers that split and amplify the single pulse into 192 of equal energy (Figure 4). Each optical pulse is then shaped by an amplitude modulator. The modulator can form a pulse 200 ps to 20 ns long, with 500:1 contrast, 250-ps shaping resolution, and 5-ps timing resolution. Finally, the pulses travel through MOR fiber-distribution racks holding timing fibers, where different timings can be selected for target backlighting, etc. From here, each pulse travels by fiber-optic cable to a PAM in one of the two laser bays.

Center of transport spatial filter (TSF)

Preamplifiers (PAM) and preamplifier beam transport system (PABTS)

Master oscillator room (MOR)

Preamplifier maintenance area (PAMMA)
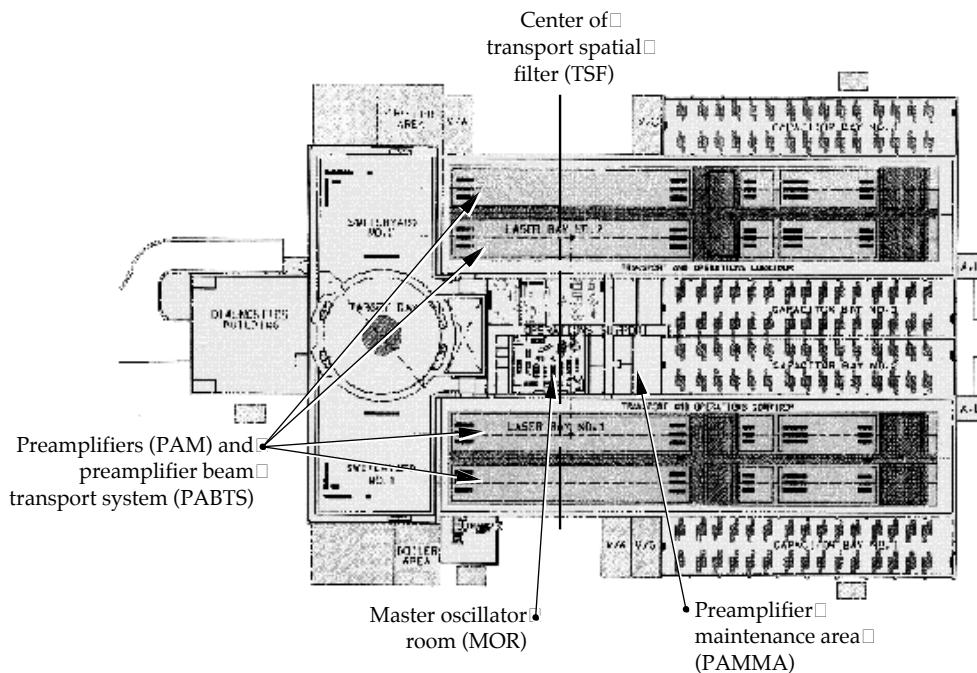
FIGURE 1. The OPG is centrally located in the LTAB (plan view). (40-00-0997-2100pb01)
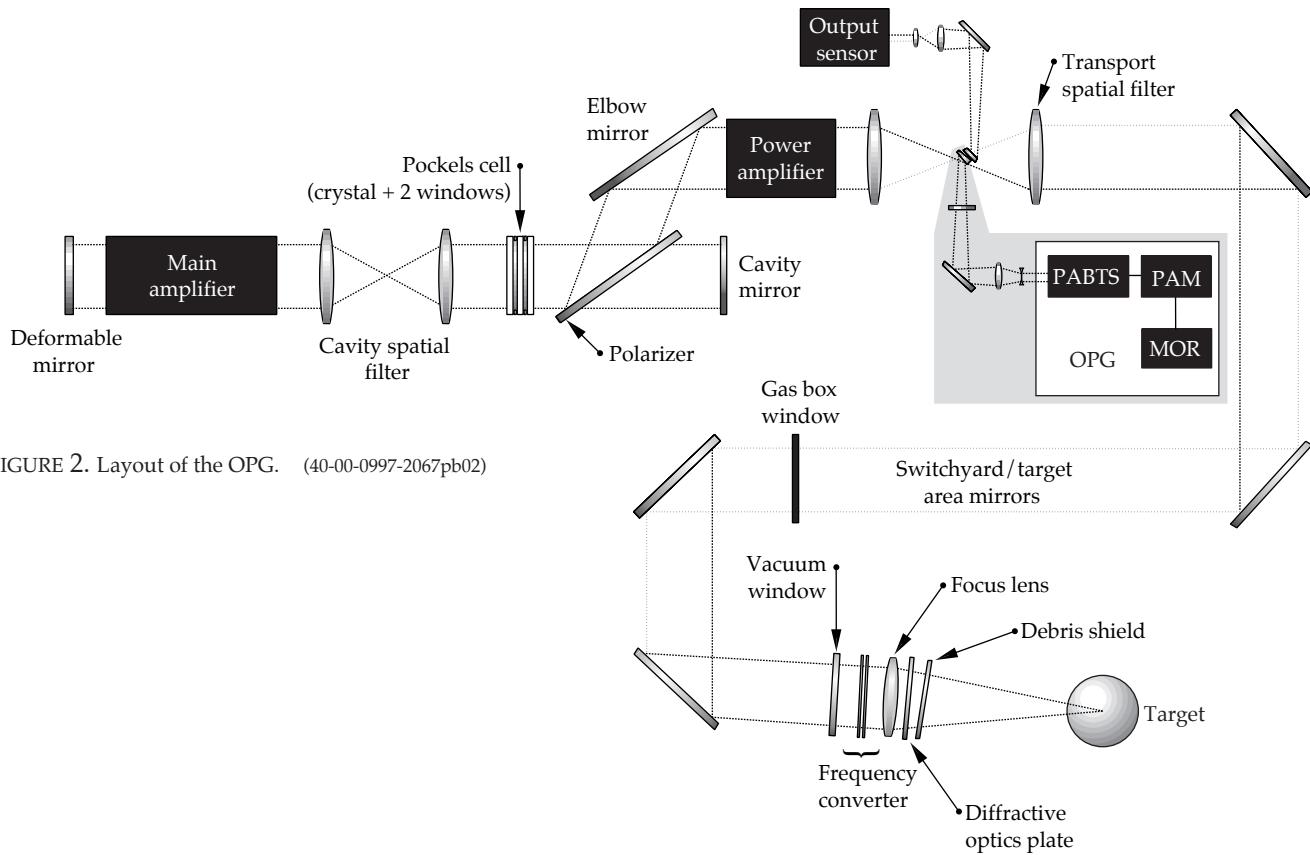
FIGURE 2. Layout of the OPG. (40-00-0997-2067pb02)
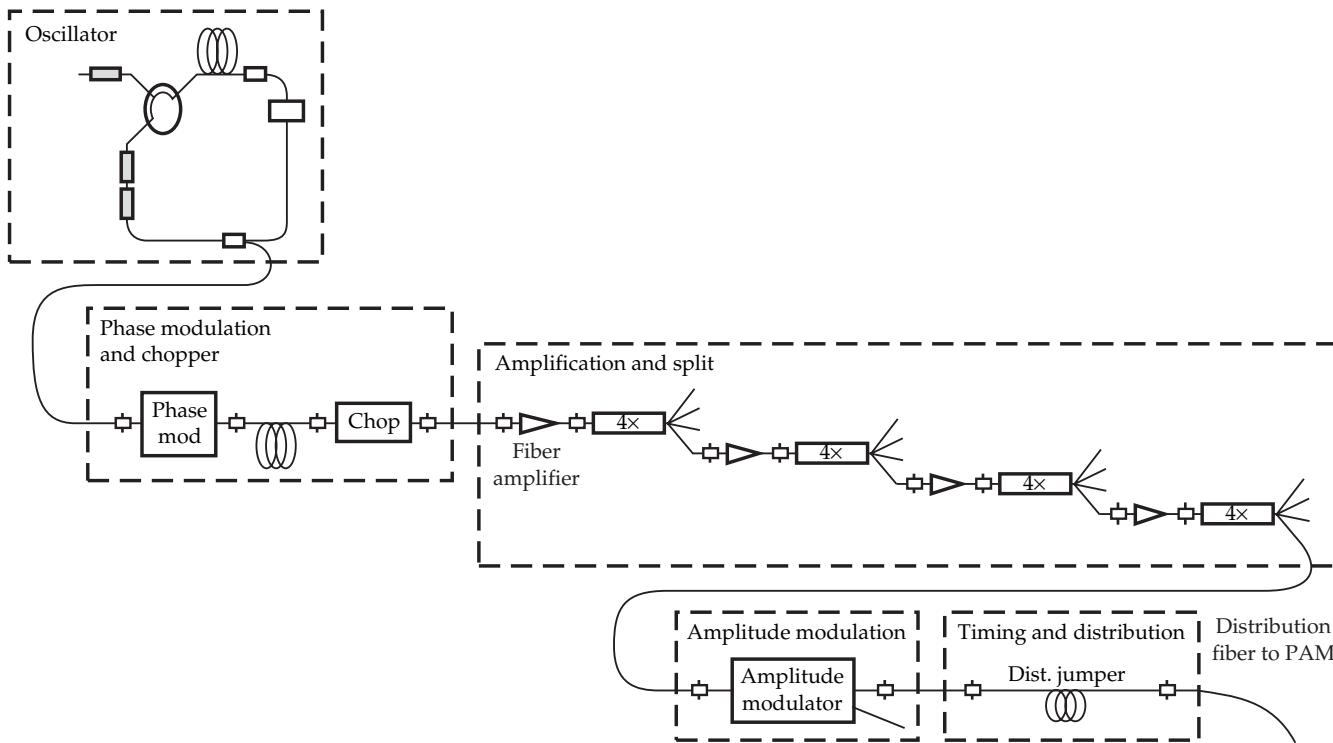
FIGURE 3. The NIF MOR design consists of fiber-optic subsystems in an optical series. (40-00-0997-2102pb01)
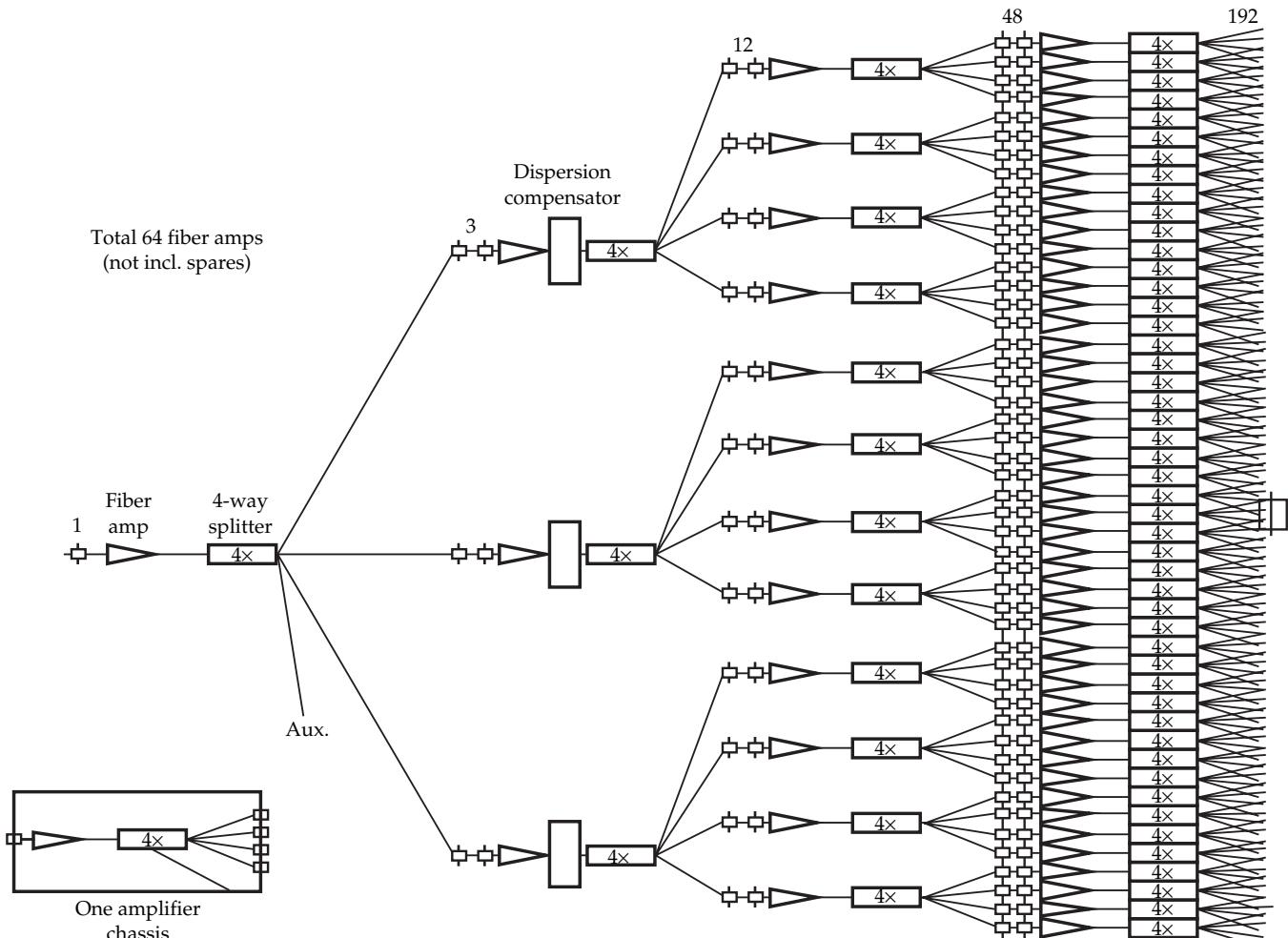
FIGURE 4. Amplifier array for 192 modulators showing dispersion compensators. (40-00-0997-2103pb01)

Each PAM is a line-replaceable unit, providing energy amplification on the order of 10^{10}, spatial shaping, and optional 1D beam SSD for one laser pulse. The PAM is a complicated system comprising the fiber launch, the regenerative amplifier, a beam shaper, the SSD, and a multipass amplifier (Figure 5). The fiber launch takes the MOR fiber-optic output, generates a Gaussian beam, 1.72 mm ($1/e^2$) diameter, and injects that beam as a seed pulse into the regenerative amplifier. Within the regenerative amplifier, the beam's energy is amplified to ~30 mJ using two diode-pumped rod amplifiers. The beam shaper transforms the Gaussian beam's spatial profile as it passes through an expansion telescope, an anti-Gaussian filter, and a quadratic filter, producing a nominally flat-top, 22.5-mm-square output beam. The beam then passes through a serrated aperture at relay plane 0 (RP0) before proceeding to the SSD subsystem. The SSD subsystem modulates the beam's propagation angle

according to the frequency modulation previously imparted on the pulse in the MOR. The current 1D design is such that 2D SSD can be added later, if required. The multipass amplifier provides a 1.2×10^3 gain, increasing the pulse energy to 12.5 J, and uses relay imaging to control the beam's diffraction and walk-off.

Once the pulse leaves the multipass amplifier, it enters the optics that transport a small sample of the beam to the input sensor (see "Laser Control Systems" on p. 180 for the design of the input sensor). The majority of the beam then enters the PABTS, which primarily provides optical relaying and isolation (Figure 6). It optically links the PAM to the beam transport of the transport spatial filter using fully enclosed, nitrogen-filled beam tubes, and it provides an optical output that matches the requirements of the laser optical system. Its vacuum relays (relay telescope #1 and #2) carry the image of the RP0 from the PAM to the spatial filter.
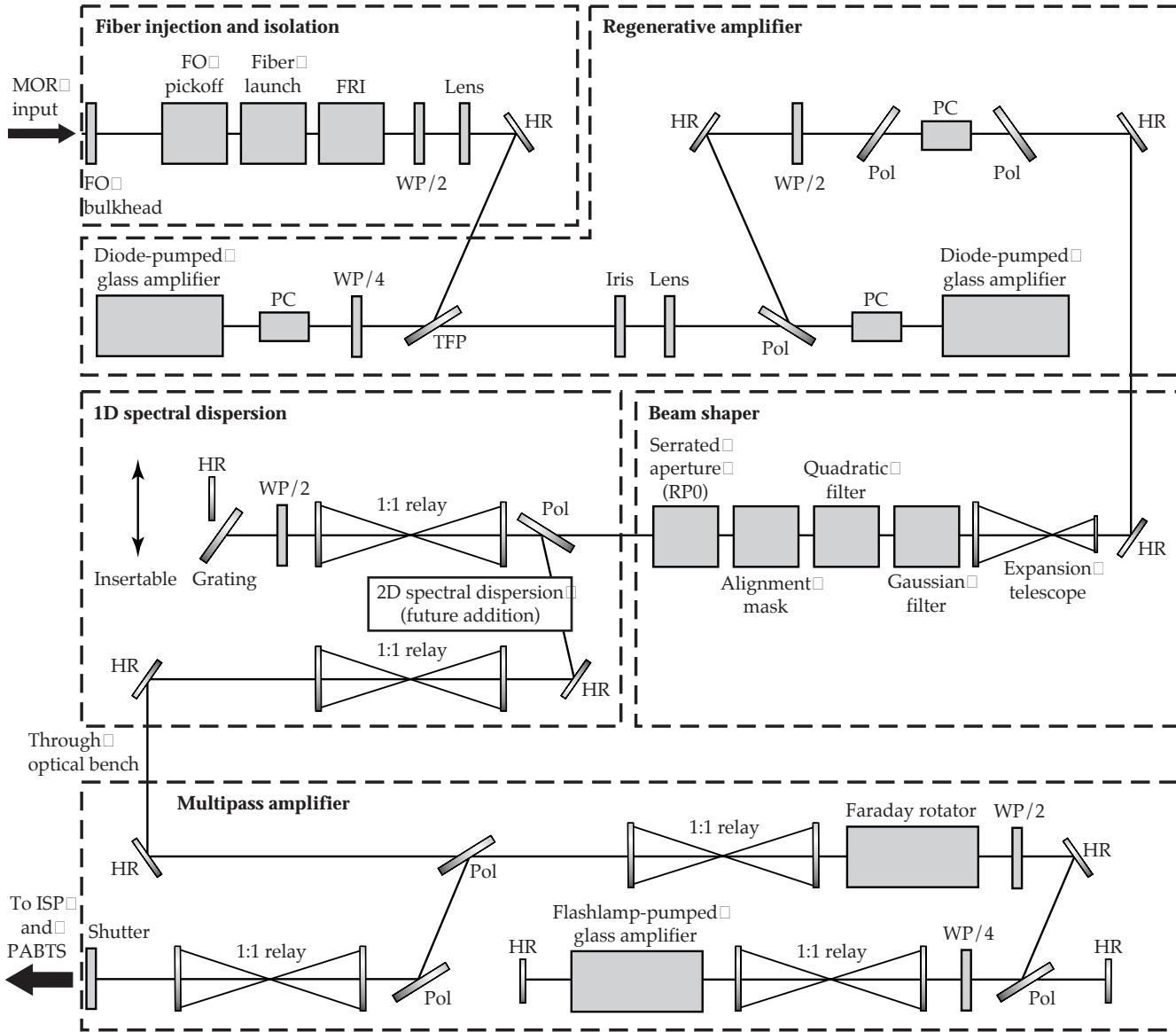
FIGURE 5. Five major sections comprise the PAM optical system.   (40-00-0997-2104pb01)
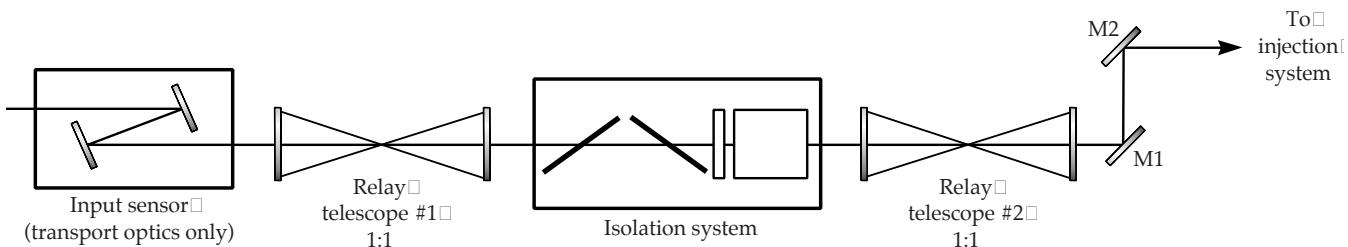
FIGURE 6. The PABTS comprises transport, relay, and back-reflection optics from the input sensor to the TSF support structure.
(40-00-0997-2105pb01)

Between the two relays, an isolation system—consisting of two polarizers, a half-wave plate, and a permanent-magnet Faraday rotator—protects the PAM from back reflections of up to 25 J. Once the pulse leaves the sec-

ond relay telescope, it exits the PABTS and enters the injection system.

The injection system, which comprises a telescope of two fused-silica elements and the injection mirror, focuses

the beam into TSF pinhole #1 and projects the relay plane 16,805 mm past the SF3 lens of the TSF. The telescope design satisfies optical requirements and packaging constraints, and uses spherical fused-silica elements.

Title II Activities

During Title II, we will implement the change from 192 PAMs to 48 PAMs. The split to 192 beamlines will occur in the PABTS, using a 1:4 splitter that is under design (see "Conceptual Design for a 1:4 Beam Splitter in the Preamplifier Beam Transport System" below). We will complete the detailed design of the OPG in Title II, reducing the number of optics where possible. We also will extensively test prototypes and integrated systems operations.

Amplifier System

This section focuses on the two large amplifiers in the NIF laser cavity—the main amplifier and the power amplifier (Figure 7). The functions of these amplifiers are

CONCEPTUAL DESIGN FOR A 1:4 BEAM SPLITTER IN THE PREAMPLIFIER BEAM TRANSPORT SYSTEM

Since mid-Title I, we have changed the architecture to reduce costs and still meet the required laser performance. As part of that change, we are reducing the number of preamplifier modules to 48, with the final split to 192 beamlines occurring in the preamplifier beam transport system (PABTS), instead of in the master oscillator room as set out in the Title I design. We have come up with a conceptual design showing that a 1:4 beam split is feasible in the existing PABTS layout, with some modification in the injection telescope. The split would follow the isolation system, in the area where the second 1:1 relay telescope and two mirrors appear in the Title I design (see figure at right). In the splitter design, the 48 pulses are split twice, using half-wave plates, polarizers, and mirrors. Most of the half-wave plates are motorized and remotely controlled so that we can continuously adjust the energy throughput. The path lengths are equalized using trombones, and the individual beam energies monitored at the output sensor packages. This design allows us to meet packaging requirements and keeps the cost down with a minimum of optical elements. In early Title II, we will continue to study and develop the 1:4 splitter section and modify the injection telescope as required.
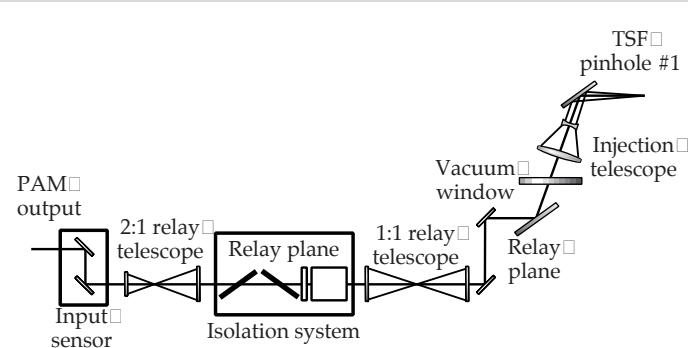
The 1:1 relay telescope and injection telescope design can be modified to accommodate additional path length for the splitter. (40-00-0997-2120pb01)
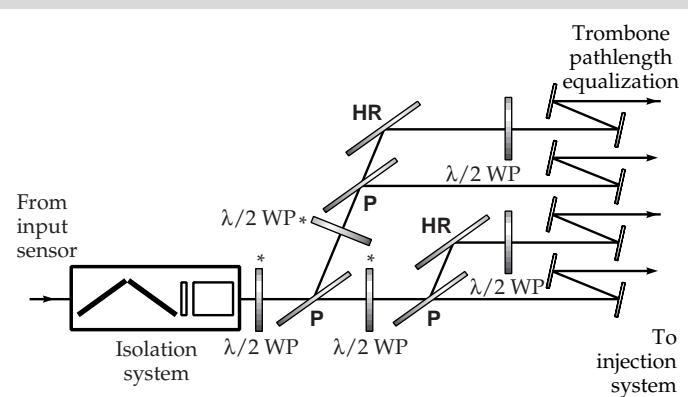
* Denotes remotely controlled motorized device

The 1:4 conceptual design matches path lengths to maintain relay imaging and provides remote continuous adjustability of energy throughput. (40-00-0997-2121pb01)
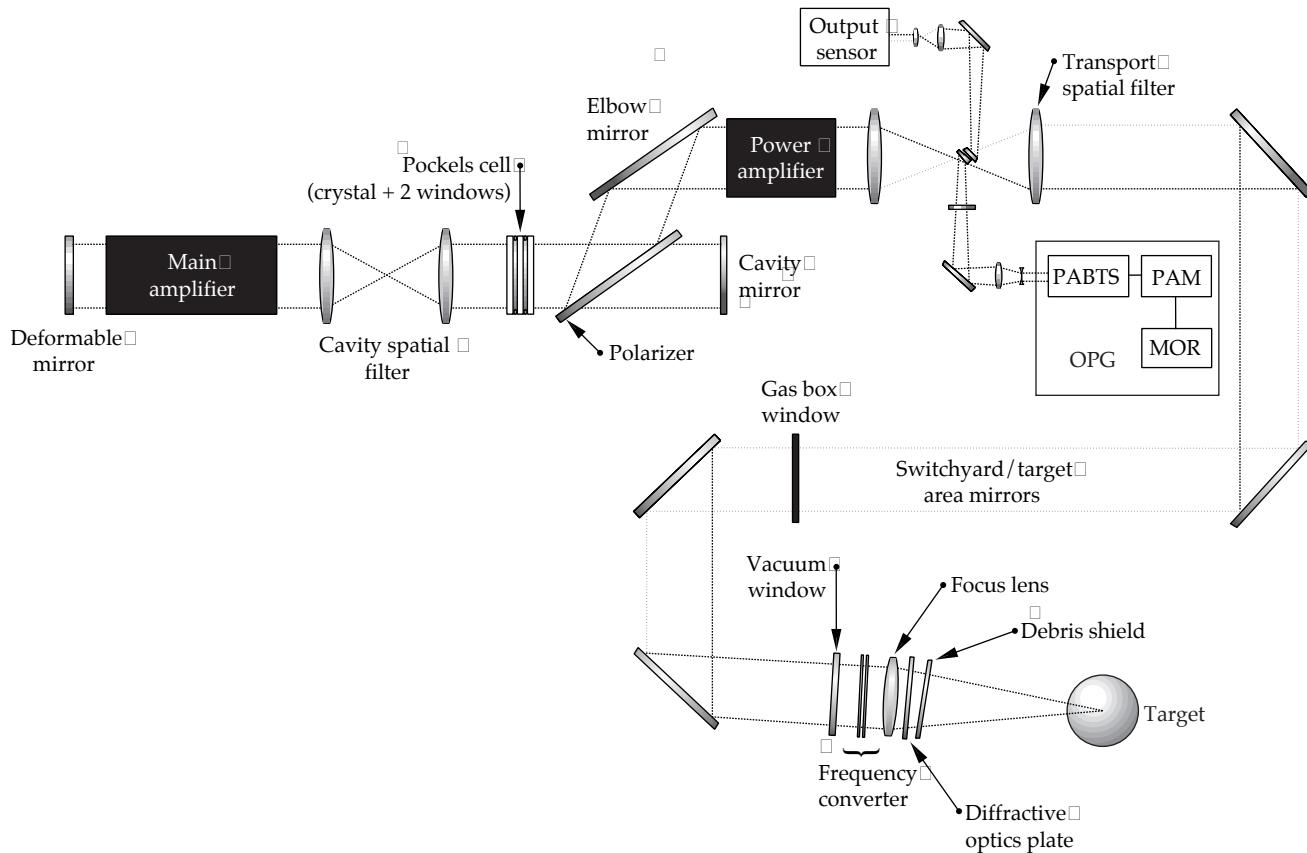
FIGURE 7. The main amplifier and power amplifier are parts of the main laser cavity. (40-00-0997-2067pb03)

to efficiently amplify the 1ω input pulse to its required power and energy, as well as to maintain, within specified limits, its pulse shape, wavefront quality, and spatial uniformity. We also had to design a clean, mechanically stable housing, called the frame assembly unit (FAU), that allows the amplifiers' LRUs to be replaced rapidly without disrupting adjacent components.

The amplifiers are located in the Laser and Target Area Building (LTAB), adjacent to the four capacitor bays (Figure 8). One of the major design challenges for the amplifiers was minimizing their volume to save space in the LTAB while still satisfying requirements. The following discussion summarizes the preliminary design features of the amplifiers, including the optical pump cavity, the bundle configuration, the cluster configuration, and the flashlamp cooling system. (For information about the optical design of the amplifier slabs, see "Optical System Design" on p. 112.) The support structure for the amplifiers, power cables, and utilities are discussed in the article "Beam Transport System" (p. 148).

The NIF amplifiers have a compact pump-cavity design with shaped reflectors. Figure 9 shows a cross

section of the optical pump cavity of a one-slab-long segment. The cavity includes two types of LRUs—a slab cassette and a flashlamp cassette— shaped reflectors, and antireflection-coated blast shields. The glass slabs in the slab cassette are 4.1 cm thick and have an Nd-doping concentration of 3.6×10^{20} ions/cm^3. NIF has a total of 7680 large flashlamps; each amplifier has six flashlamps in two side arrays and eight flashlamps in a central array. These flashlamps are larger and less expensive than those used in previous ICF solid-state lasers (Table 1). The compactness of these amplifier units is limited by NIF's mechanical design requirements, including the requirements for stability, insertion clearances for the LRUs, and the seals.The side flashlamp cassettes have involuted reflectors, which improve pumping efficiency by reducing light reabsorption by the flashlamps. For the central flashlamp cassettes, skewed diamond-shaped reflectors improve gain uniformity by directing pump light to selected regions of the slab. Figure 10 shows the seven components, or basic building blocks, that comprise one amplifier assembly. The LRUs and blast shields slide into FAUs, which come in configurations of $4 \times 2 \times 2$ and $4 \times 2 \times 3$.
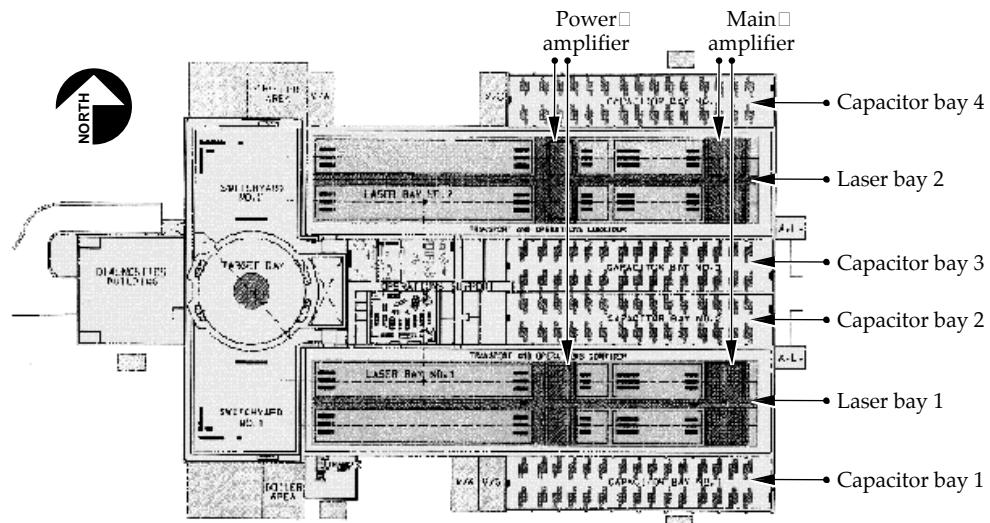
FIGURE 8. The main and power amplifiers are located in the LTAB (plan view). (40-00-0997-2107pb01)
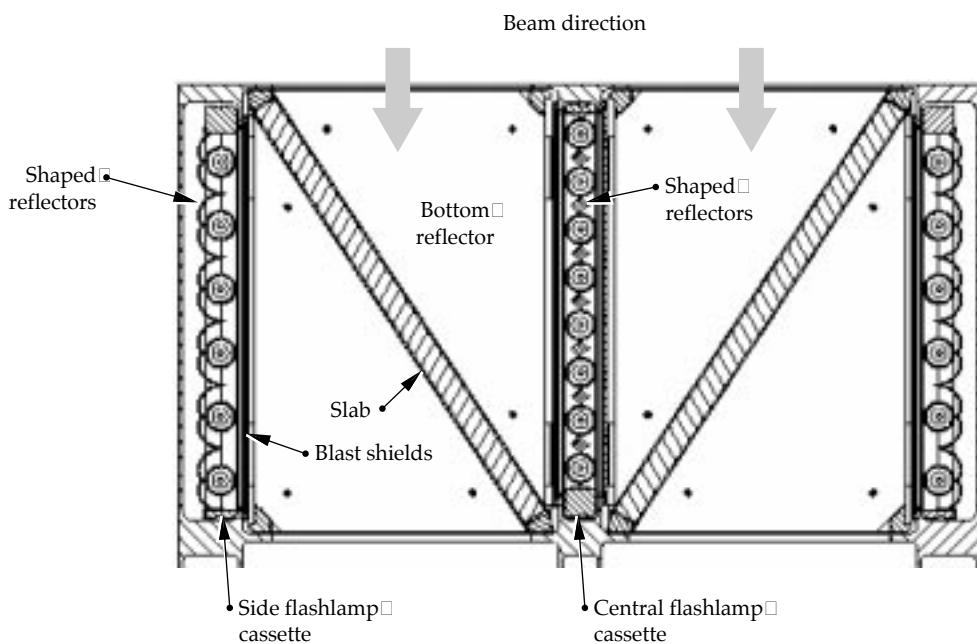
FIGURE 9. Each amplifier has a glass slab cassette, a side flashlamp cassette, and glass blast shields with antireflection coatings. A central flashlamp cassette runs between two beamlines. (40-00-0997-2108pb01)

TABLE 1. Flashlamp parameters for ICF solid-state lasers.

	Nova	Beamlet	NIF	LMJ
Number	5000	512	7680	~10,800
Bore diameter (cm)	2	2.5	4.3	4.3
Arc length (cm)	48	91	180	180
Energy/lamp (kJ)	6	12	34	34
Cost/kJ	~$100/kJ	~$70/kJ	$38/kJ	—

FIGURE 10. (a) Each amplifier is assembled from interchangeable "building blocks": a plenum, top plate, frame assembly unit (FAU), blast shields, a side flashlamp cassette, a slab cassette, and a central flashlamp cassette. The cassettes slide into the FAU, and the FAU and blast shields are removable as well. The plenum and top plate are "fixed" to the structural support. (b) A $4 \times 2 \times 2$ amplifier FAU for eight beamlines. (40-00-0997-2110-pb01)

(a)

(b)

- Plenums
- Top plates
- Frame assembly units
- Blast shields
- Side flashlamp cassette
- Slab cassette
- Central flashlamp cassette
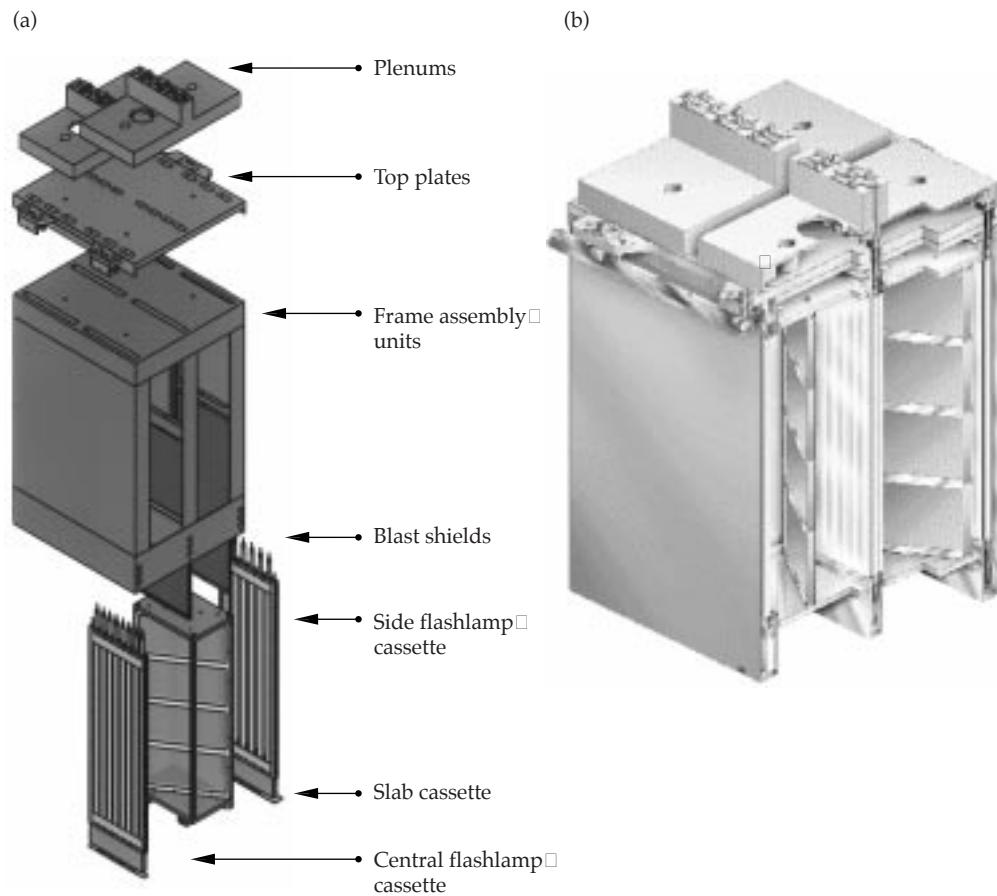
Bundles in the main and power amplifiers include both FAU configurations, as well as other components (Table 2). The bundle, which contains eight beams, is the minimum amplifier operating unit. Each bundle is environmentally sealed from the laser bay and operates independently. Each bundle provides a common amplifier electrical ground, common flashlamp cooling distribution, and a common slab cavity atmosphere.

The amplifier cluster consists of six tightly packed bundles. Table 3 shows the parameters of the two clusters that appear in each of the four laser bays. The cluster configuration allows us to balance many requirements, including minimizing bundle spacing and height to reduce LTAB costs, providing bundle electrical ground isolation to 25 kV, and permitting amplifier cassette LRUs to be loaded from the bottom and clean amplifier bundles to be installed from above.

To meet the requirement of one shot every eight hours, the flashlamps are air-cooled at 20 cfm/flashlamp for 6 to

TABLE 2. Bundle components and parameters.

Components in a bundle	Main amplifier (11 slabs)	Power amplifier (5 slabs)
$4 \times 2 \times 2$ FAU enclosure	4	2
$4 \times 2 \times 3$ FAU enclosure	1	1
FAU mating flange	4	2
End isolators	2	2
Blast shields	44	28
Slab cassettes	22	10
Flashlamp cassettes	33	15
Flashlamps	220	100
Distribution plenums	11	7
Top plate assemblies	5	3

TABLE 3. Cluster components and parameters.

Quantity in each laser bay (i.e., 2 clusters)	Main amplifier	Power amplifier
Number of slabs long	11	5
Number of slabs	1056	480
Number of flashlamps	2640	1200
Number of blast shields	528	336
Number of bundles	12	12
Overall width (mm)	2390	2390
Overall length (mm)	11,074	8034
Centerline above floor	4572	6987
Assembled weight (kg)	110,000	70,000
Bank energy (MJ)	106	48
Cooling gas flow (cfm)	26,400	14,000

7 hours. We chose air instead of nitrogen as the cooling gas to meet cost objectives and have a plan for dealing with the possible degradation of the flashlamps' unprotected silver reflectors.

Title II Activities

During Title II, we will finalize the details of the amplifier design and continue testing prototypes in the LLNL's AMPLAB. We are about to begin the final design of the slab and flashlamp cassettes. The potential risk areas for the cassette designs were identified during prototyping, and we will resolve those risks in the AMPLAB amplifier prototype. Among those risks are flashlamp reliability, thermal recovery, and optical performance. We plan to reduce the costs of these cassettes by simplifying the designs (i.e., combining parts and using part features such as shape, tolerance, and finish).

NIF flashlamps will work as required, but we need to develop them further to meet NIF's failure rate requirements. During Title II, our prototype flashlamps will undergo a 200-flashlamp, 10,000-shot test to qualify vendors. We will also continue thermal tests to demonstrate the air-cooling technology we have chosen for cooling the flashlamps. We also address the degradation of the silver plate on the flashlamp reflectors that arises from air cooling. We have three possible approaches that we will be exploring during Title II.

First, we could overcoat the silver with a protective layer or use an alternative, more stable, reflector material. Second, we could clean the air before it is injected. Third, we could revert to nitrogen cooling.

We will also change the FAU design to increase the rigidity and provide greater design flexibility for the FAU joints. As part of that redesign, the blast shield seal will become a mechanical seal, with a hard-mounted joint. During Title II, we will also choose what glass and antireflection coating to use for the blast shields.

Power Conditioning System

The Title I design for the power conditioning system, which provides energy to the 7680 flashlamps in NIF's amplifiers, is driven by these key laser system design requirements:

- Performance requirements. The laser system must deliver to the target 1.8 MJ in 3ω, with an rms deviation of <8% in the power delivered by each beam.
- Operational requirements. The laser system must have a shot-turnaround time of eight hours, not to preclude a four-hour turnaround, and must be able to fire an arbitrary subset of bundles on each shot.
- Reliability/availability/maintainability requirements. The laser system must have a lifetime of 30 years, shot availability of at least 97.44%, an overall reliability of 82.66%, and no more than 6.8 unplanned maintenance days per year.

The amplitude, pulse shape, and timing of the power delivered by the power conditioning system to the flashlamps depend on the required amplifier gain (see Figure 11). We derived the nominal output specifications for the power conditioning system, based on an average gain coefficient of 5.0%/cm. Using computer models, we determined that the power conditioning system's main pulse must deliver 34 kJ/flashlamp in a critically damped pulse 360 μs long, the preionizing pulse must deliver no less than 500 J/flashlamp in a critically damped pulse 120 μs long, and the energy variations between flashlamps must be less than ±3% rms.

The resulting Title I design for the NIF power conditioning system is a product of the collaborations of LLNL, Sandia National Laboratories (SNL), and industry. In this design, the system occupies four capacitor bays adjacent to each laser cluster (Figure 12). Each capacitor bay contains 48 500-kA "bank modules," which feed one amplifier cluster (Figure 13). Eight modules are needed to power each laser bundle

(a)

Constant pulse duration, variable bank voltage

(b)

Constant voltage, variable pulse shape
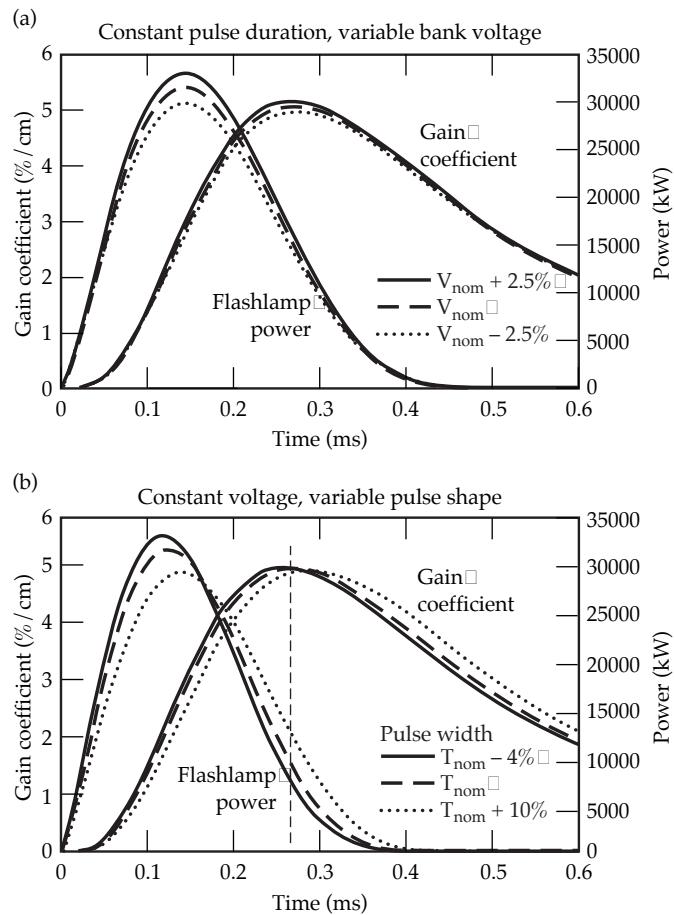
FIGURE 11. Amplifier performance calculations are used to predict the allowable tolerance on the pulsed power output to meet the NIF power balance requirements. (a) Shows a variation in amplitude; (b) shows variations in pulse shape and timing. (40-00-0997-2111pb01)

(see "How Big a Bank?" next page). These bank modules are the heart of the power conditioning system. Each module has a preionization system, a capacitor bank, a switch/ballast assembly, and controls/electronics, and can drive 40 flashlamps configured as 20 series pairs.

A module must deliver three pulses to each flashlamp: a trigger pulse on the order of several kV/μs to trigger the flashlamps, a 500-J, 120-μs preionization pulse, and a 34-kJ, ~360-μs main pump pulse with a peak current of 25 kA to each pair of flashlamps in a series. Two independently switched circuits—one in the preionization bank, the other in the main bank—generate the required flashlamp excitation. Either bank can supply a trigger pulse to the system. During normal operation, the preionization bank supplies the trigger; in a main switch prefire, the main bank delivers the trigger.

For the preionization pulse, a small (30×30-in.^{2}) single-capacitor bank delivers the preionization pulse by coaxial cable to the 40 flashlamps. This small bank consists of a single 100-μF, 30-kV metallized film capacitor; a small, independent charging supply; a sealed gas or vacuum switch; a fuse to isolate it from the main bank; a pulse-shaping inductor; and a dedicated dump circuit. The circuit for this bank comes packaged as a preassembled unit. The bank also has a ballast system, which forces current sharing in the event of a shorted or an open-circuited flashlamp.

A large ($7 \times 5 \times 8$ ft^3), 20-capacitor bank delivers the main current pulse to the flashlamps via coaxial cables roughly 300 μs after the beginning of preionization.

FIGURE 12. Location of the power conditioning system. (40-00-0997-2112pb01)

Capacitor bays

Target chamber

Laser clusters

HOW BIG A BANK?

We determined the size of each individual bank module by examining the trade-offs between cost and performance risk. Larger modules reduce the total cost of the system by reducing the number of power supplies, triggers, controllers, and so on. However, the module size is limited by the availability of reliable, high-current switches. Our preliminary design features a 500-kA switch, which balances cost and performance risks and is a reasonable extrapolation from commercial devices now available.

(a)

Top view

Single bundle

Double segment

Main amplifier
(11 slabs / bundle)

Power amplifier
(5 slabs / bundle)
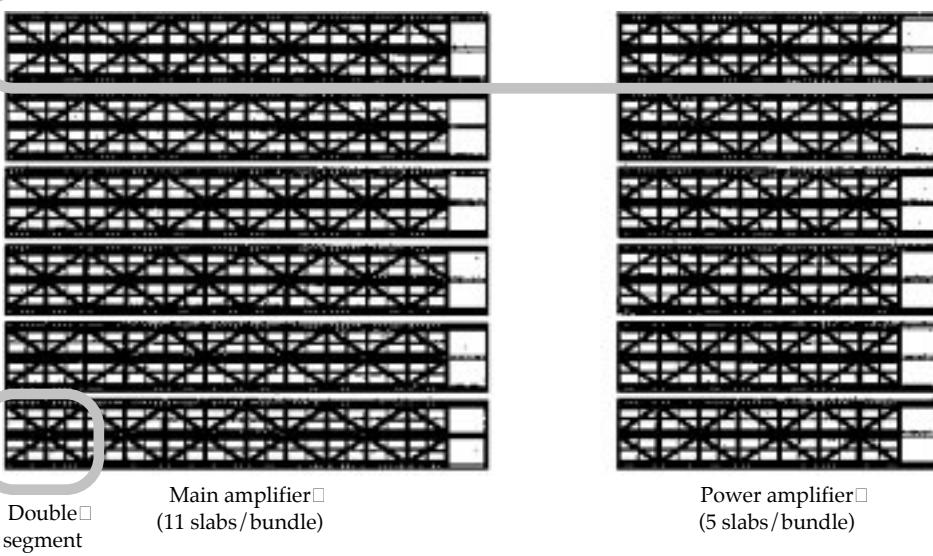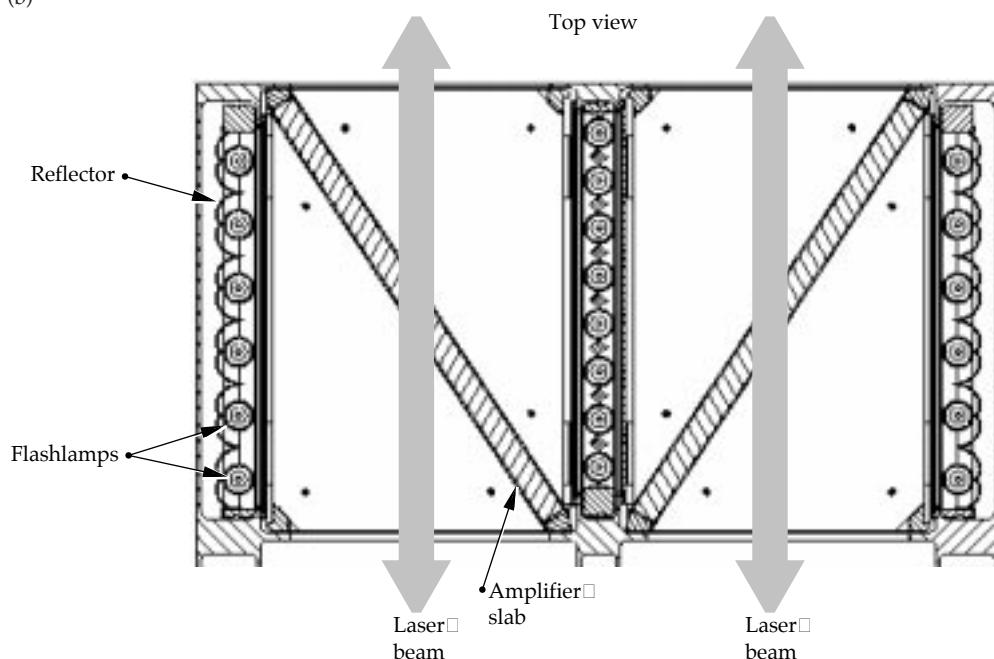
FIGURE 13. (a) A top view of one amplifier cluster, including both the main amplifier and power amplifier. Each cluster contains six bundles of 16 amplifier slabs (11 slabs from the main amplifier and 5 from the power amplifier). (b) The insert shows a scaled-up view of a single 4×2 section of a bundle, with 20 flashlamps arranged in 10 series pairs.
(40-00-0997-2113pb01)
(40-00-0997-2114pb01)

(b)

Top view

Reflector

Flashlamps

Laser beam

Amplifier slab

Laser beam

This large bank consists of 290-μF, 24-kV metallized film capacitors, an independent 25-kW charging supply, a pressurized spark gap, pulse-shaping inductors, dedicated redundant dump circuits, and a ballast system similar to that for the preionization bank.

Each transmission line consists of a bundle of RG-220 coaxial cables. We have 22 cables per bundle: 20 to feed the flashlamp circuits, 1 as a return of reflector fault current, and 1 spare.

Our present design satisfies voltage, energy, and pulse-width requirements. However, using simple models to determine the flashlamp load, we determined that a 90%-efficient preionization circuit is underdamped. Final circuit parameters will be determined in Title II.

Each of the four capacitor bays can be viewed as a "stand-alone" system. The 48 1.6-MJ modules are configured in doublets for seismic stability and access. We have 30 full modules feeding the main amplifier, 12 feeding the power amplifier, and 6 feeding flashlamp cassettes in both amplifiers. The modules are configured such that space is available for more, should the power amplifier be upgraded to a 7-slab configuration. Each bay has a 13.8-kV substation to supply 480 VAC charging power, and each module has its own 100-A circuit breaker. Each bay also has a single front-end processor for communications to and from the NIF control room, as well as its own gas, water, and pressurized air manifolds.

Title II Activities

In our future activities, we have identified several challenges, but see no show-stoppers. For the switching, we have identified a feasible candidate, the Physics International ST-300 spark gap. We will obtain data on switch lifetime, reliability, and performance from SNL's switch test facility, and will continue to investigate other technologies as well. For the capacitors, at least three vendors are pursuing technology enhancements to reduce the costs. The flashlamp operation is well characterized; in Title II, we may recommend some enhancements to increase the safety margin. The design of the power conditioning system module will be refined to further optimize cost and performance, and the final design will be thoroughly demonstrated in experiments on SNL's prototype test bed before construction begins.

Plasma Electrode Pockels Cell

The Pockels cell, located between the cavity spatial filter and the polarizer in the main laser cavity of NIF (Figure 14), rotates the polarization of light transmitted through the cell and works with the polarizer to act as an optical switch. This configuration allows the laser pulse to gain energy efficiently by making multiple passes through the main amplifier (Figure 15). To meet NIF requirements, this Pockels cell must have a 100-ns rise time and a 150-ns flat-top pulse shape, and its switching efficiency must be >99% for both "on" and "off" states.

We are using an LLNL-developed plasma electrode Pockels cell (PEPC), which has distinct advantages over conventional Pockels cells (see "Why a PEPC?" below). We have successfully used this PEPC design for a 37-cm-aperture Pockels cell on Beamlet for two years, with no missed shots. Electrically, the PEPCs are two independent 2×1 Pockels cells, back to back. Mechanically, the NIF PEPCs are designed as a 4×1 LRU that can be bottom-loaded into the periscope structure.

WHY A PEPC?

Pockels cells use electrically induced changes in the refractive index of an electro-optic crystal, such as KDP, to rotate the polarization of light when an electric field is applied along the direction in which the light beam propagates. Conventional ring-electrode cells have high damage thresholds, but require a crystal that is about the same thickness as the beam diameter. A crystal this thick is completely impractical for the NIF's 40-cm beam. Some cells use transparent, conducting films as electrodes, but these have questionable damage thresholds and a high surface resistivity, which causes slow and nonuniform switching.

For NIF, we are using the plasma electrode Pockels cell (PEPC) developed at the LLNL. As shown in Figure 17, a thin plate of KDP is sandwiched between two gas-discharge plasmas. The plasmas serve as conducting electrodes, allowing us to charge the surface of the thin crystal plate electrically in ~100 ns with very high uniformity. These plasmas are so tenuous that they have no effect on the high-power laser beam passing through the cell. The damage threshold of the KDP crystal is unaffected by the plasma or electrical charge.
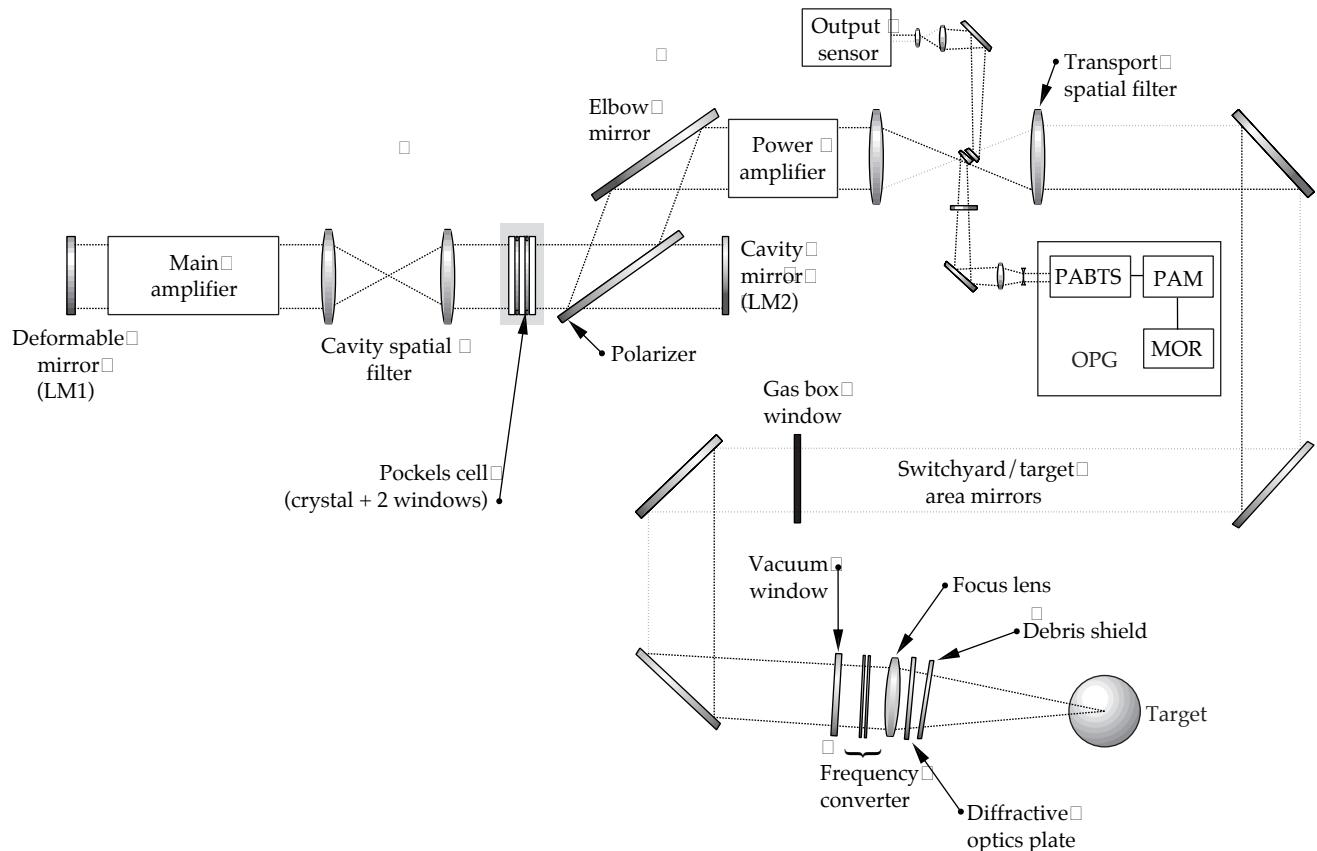
FIGURE 14. Location of the NIF Pockels cell in the beamline (shaded area).   (40-00-0997-2067pb04)
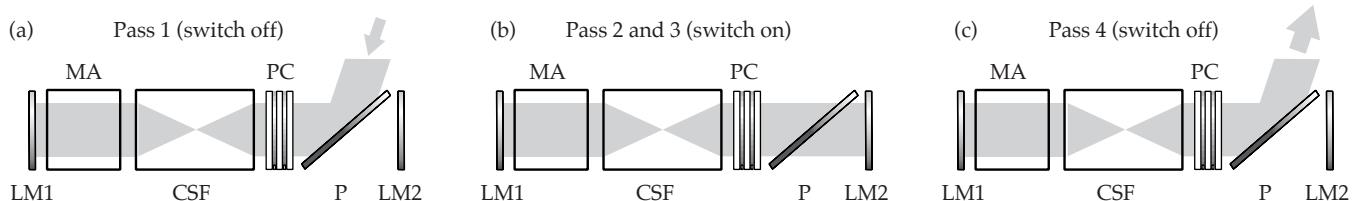
FIGURE 15. The Pockels cell and polarizer work as an optical switch to trap the pulse in the cavity between LM1 and LM2 for four passes, as follows. (a) When the cell is "off," the cavity is open and the beam is injected into the cavity between the deformable mirror, LM1, and the cavity mirror, LM2. (b) When the cell is "on," the cavity is closed and the beam multipasses between LM1 and LM2, through the main amplifier, for four passes. (c) On the fourth and final pass, the cell is switched off, allowing the pulse to switch out of the cavity. (40-00-0997-2116pb01)

The PEPC is a complex opto-mechanical-electrical system including a gas cell, switch pulsers, plasma pulsers, and controls and diagnostics, as well as vacuum, gas, and structural subsystems (Figure 16). In this section, we focus on the design of the pulsers and the gas cell, while briefly addressing the vacuum and gas subsystems and structural design of the housing and window. An overview of controls and diagnostics appears on p. 180 of this *Quarterly*; more information on the structural design of the periscope structure appears in the article "Beam Transport System" (p. 148).

The PEPC is driven by three pulse generators, shown in Figure 17. In each PEPC, two plasma pulsers drive several kiloamperes of discharge current through a low-pressure helium background to create conductive and transparent plasma electrodes. The switch pulser can charge the KDP crystal to a V_π of about 17 kV or discharge it from V_π back to zero volts in ~100 ns,
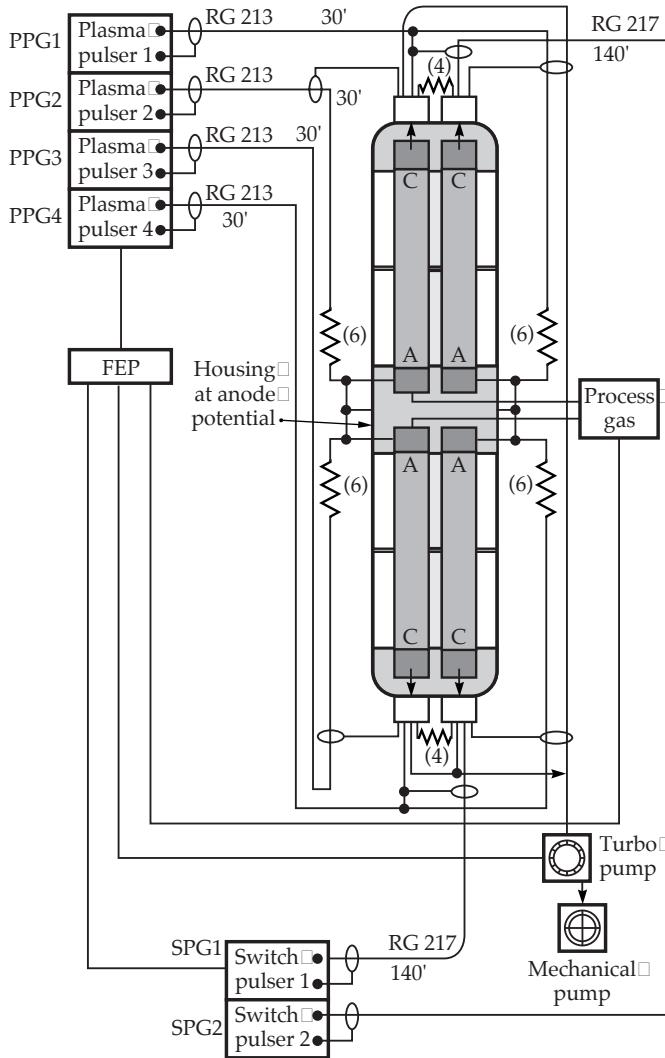
FIGURE 16. The PEPC subsystem schematic.　(40-00-0997-2117pb01)

FIGURE 17. The PEPC includes a KDP crystal, two plasma pulsers, and a switch pulser.　(40-00-0997-2118pb01)

where V_π is the voltage required to rotate the polarization through 90°. Each 4×1 LRU requires two switch pulsers and four plasma pulsers, designed to meet NIF optical switching and reliability, availability, and maintenance requirements. The "on" pulse length is determined passively by an electrical transmission line, which gives very high reliability for the cavity switchout. This is a "fail-safe" feature to protect the laser components in the cavity. Each plasma pulser generates a discharge that spans two apertures on one side of the midplane assembly. The NIF switch pulser and plasma pulser circuits are similar to the Beamlet design but are being reengineered and packaged for low cost and high reliability by Titan-Beta Corporation.

The gas cell integrates several subassemblies and optical elements, including housings, switch windows, a midplane assembly, an anode assembly, a cathode assembly, and a vacuum plenum/baffle assembly

(Figure 18). The cell is designed to meet NIF's optical and cleanliness requirements, beam spacing requirements, and the requirement to provide a switching efficiency >99%. To meet the spacing requirement, we designed a compact 4×1 LRU with insulated aluminum housings, an external frame, and square-edged windows. We also designed the anodes to be back-to-back at the midpoint of the housings and the cathodes, which are larger, to be at the top and bottom of the housings. To meet the switching efficiency, we optimized the plasma channel design to achieve uniform plasma for switching, and optimized the vacuum pump and gas control systems as well. To minimize static birefringence, we designed a rigid aluminum housing with a precise window–housing interface.

Our Title I PEPC 4×1 housing design is based on anodized aluminum construction, and is designed to meet NIF mechanical, electrical, and vacuum requirements at minimum cost. The structural integrity of the housing design is verified by finite-element analysis. The housing and window are designed to minimize shear stress in the window. The PEPC window is a rectangle, 3.5 cm thick, with a tensile stress below 700 psi. The midplane assembly that holds the crystals is 13-mm-thick borosilicate float glass and provides adequate electrical insulation for the PEPC switch operation and low outgassing ($< 7.4 \times 10^{-9}$ Torr-L/s-cm^2) per NIF requirements.

Switch windows

Cathode assembly

Anode assembly

Midplane assembly

Housings

Vacuum plenum/ baffle assembly
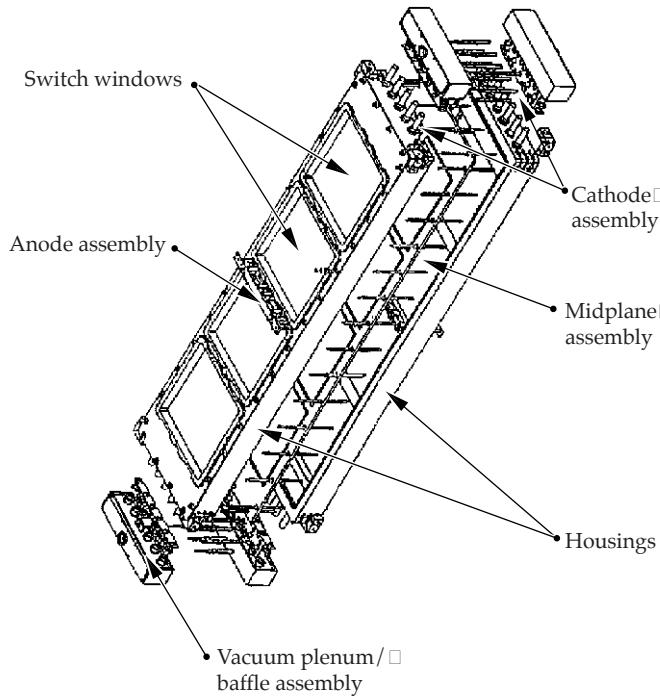
FIGURE 18. Configuration of the PEPC gas cell. (40-00-0997-2119pb01)

The PEPC cathode and anode structures exposed to the plasma are faced with pyrolitic graphite. This facing ensures that any material sputtered from these electrodes will react with the oxygen in the process gas (helium plus 1% O_2) to form CO and CO_2, which are removed by the pump system. This reaction prevents sputtered material from depositing on the crystal or window surfaces. The anode is segmented into six individually ballasted "buttons" to force the plasma to be uniform across the width of the discharge. Process gas enters through ports at the anode. The hollow-cathode assembly contains the vacuum ports and connects to a vacuum baffle structure that prevents discharge current from running through the vacuum lines to other locations.

The gas and vacuum system for each LRU has individual vacuum plenums for each plasma channel. These connect to a vacuum manifold evacuated by a turbomolecular drag pump that is part of the LRU. Foreline pumping is by connection to a foreline pumping system in the laser bay. Each bay has two 50-cfm (cubic feet per minute) foreline pumps, located outside the LTAB on a utility pad. The gas flow at operating pressure (35 mTorr) is 0.23 Torr-L/s, and the base pressure is $< 5 \times 10^{-5}$ Torr.

Each plasma channel has an electrically controlled valve and pressure gauge that provides closed-loop control of the operating pressure through the integrated computer control system. The control system also monitors the electrical performance of each cell during operation to verify that all parameters are within preset limits.

Title II Activities

A 2×1 PEPC, now in construction, will test most of the key features of the NIF design and is the next step towards a full NIF prototype. We are using the 2×1 prototype to demonstrate the full-scale anodized aluminum housing, uniform switching of the two crystals, and uniform plasma production across the double aperture. In FY97, we plan to finish testing the 2×1, validate the 2×1 discharge, procure 4×1 parts based on the Title I design, and begin testing the assembled 4×1. We will use those test results to complete our Title II design early in FY98, then do detailed tests, including life evaluations. The results will be used to update the design for Title III.

For more information, contact
Douglas W. "Doug" Larson
Laser Systems System Engineer
Phone: (925) 422-1524
E-mail: larson8@llnl.gov
Fax: (925) 422-7748

Beam Transport System

J. Bowers

A. Chakradeo

D. Chambers

P. Densley

K. Dutta

M. Eli

M. Gerhard

P. Gursahani

L. Hale

K. Hamilton

M. Johnson

C. Karlsen

J. Meick

S. Mukherji

H. Patton

J. Reed

M. Richardson

G. Shaw

S. Sommer

D. Trummer

C. Vannicola

R. Villesis

E. Wang

The Title I designs for the beam transport system—including the optomechanical systems, the spatial filter vessels and beam enclosures, and the laser bay and switch support structures—are dominated by the NIF's requirements for optical and mechanical stability and physical access. As Title II begins, we are ready to detail thousands of tons of structures, mechanisms, and vacuum vessels and to verify all analyses for detailed designs.

Introduction

The primary mission of the NIF's beam transport system is to support propagation of the laser beams. Our responsibilities include enclosing and supporting laser components up to the target area and positioning all the optics that transport the beam from mirrors LM1 to LM8. We transport the laser pulse through amplification and image-relaying components in the laser bays through the nine-story switchyards and into the target bay, where the pulse converges on the target.

A wide variety of hardware encloses, supports, or positions the major laser systems.[1] For instance, vacuum vessels and beam tubes enclose all beams between the preamplifier injection and the target room in a clean, light-tight environment. Steel and concrete spaceframes provide stable support for the optics and diagnostics in the laser bay and switchyard. Optomechanical systems point and center all full-aperture lenses, polarizers, and mirrors. All in all, we provide mounting and positioning for 768 spatial filter lenses, 768 laser bay mirrors, about 800 switchyard and target bay mirrors, and hundreds of shutters, injection mirrors, beam dumps, fiducials, windows, and 4×1, 2×2, and 2×1 handling cassettes.

Throughout the design, our efforts were dominated by requirements for optical and mechanical stability, physical access, and cleanliness. The stability requirements drove us to an intensive modeling and analysis effort to minimize system costs. Hundreds of hours of design tradeoffs led to the final Title I design of the beam transport system. Our designs accommodate bottom- and top-loading of handling cassettes and minimize structural footprints to allow room for electronic racks, sensor packages, and optics handling transporters.

Our design philosophy was this: simplify everything. For the laser bay structures and vessels, our design goal was to minimize job site activities by modularizing these components into the largest practical subassemblies so that these could be aligned, leak tested, cleaned, and assembled by the fabricators. In the switchyard, we depended on standard building erection techniques and details. For the optomechanical components, we were committed to making the line replaceable unit (LRU) philosophy succeed, to maximizing the use of mass production processes, and to consolidating component designs to use common parts.

Some areas within the facility, however, defy simplification. For instance, the transport spatial filter (TSF) area is a highly congested network of mirrors, light, and structures (Figure 1), and the switchyards are 30-m-high steel jungles encompassing diagnostics, pathways, mirror LRUs, and beam tubes.

---

[1] We do not discuss the auxiliary systems, which are also part of the beam transport system area. Auxiliary systems control the vacuum vessel and argon environments, and local power, lighting, and fire protection systems.
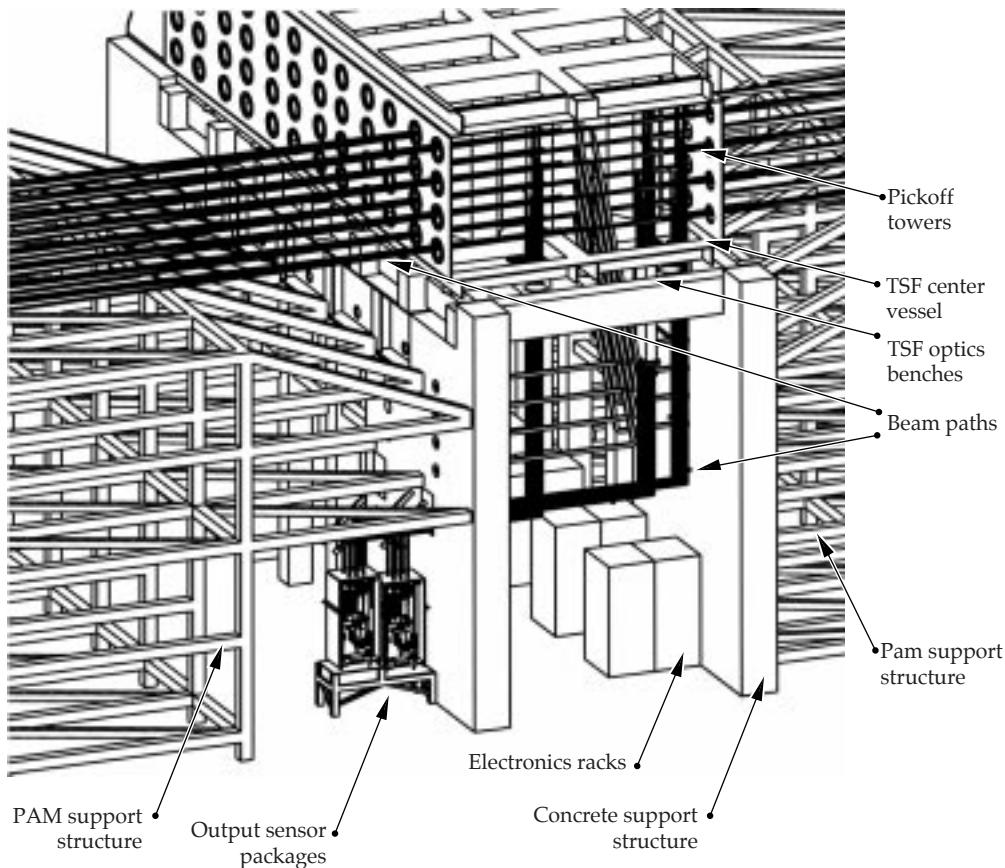
FIGURE 1. The transport spatial filter (TSF) plane area must accommodate numerous needs. (40-00-1097-2291pb01)

- Pickoff towers
- TSF center vessel
- TSF optics benches
- Beam paths
- Pam support structure
- Electronics racks
- PAM support structure
- Output sensor packages
- Concrete support structure

The rest of this article summarizes the design for the following:

- The laser bay and switchyard support structures.
- The vacuum vessels and beam enclosures.
- The spatial filter diagnostic/alignment tower structures.
- The optomechanical systems.

Laser Bay and Switchyard Support Structures

The function of the laser bay and switchyard structural support systems is to mechanically support the laser beam optics, optics vessels, beam enclosures, diagnostics systems, and utilities. The beam transport system also provides optical stability and seismic restraint and access pathways for service and maintenance. Optical stability is the controlling requirement in these areas.

The Title I design for the laser bay features hybrid concrete-steel structures for stability and ease of construction (Figure 2). These structures draw on the

advantages of each material. Concrete's advantages are that it has higher mechanical damping properties, higher thermal inertia, and lower cost for simple shapes. The advantages of steel are that it is faster to install, easier to physically design around the laser, and easier to handle if the laser configuration changes, or if the laser is decommissioned, and it has a higher stiffness-to-weight ratio for structures.

Below, we describe the structural support systems for the laser bay and the switchyard. We begin with the major structural support subsystems of the laser bay, grouped as follows (see Figure 3):

- The LM1 support structure.
- The amplifier support structures (main amplifier support and power amplifier support).
- The periscope support structure.
- The spatial filter support structures (center-vessel supports and end-vessel supports for the cavity spatial filter and transport spatial filter, as well as the preamplifier support).

This section ends with the switchyard support structures.

FIGURE 2. The hybrid concept uses concrete up to the height of the beamlines and steel surrounding the beamlines. (40-00-0298-0194pb01)

Vessels and beam tubes

Steel supports

Concrete pedestals
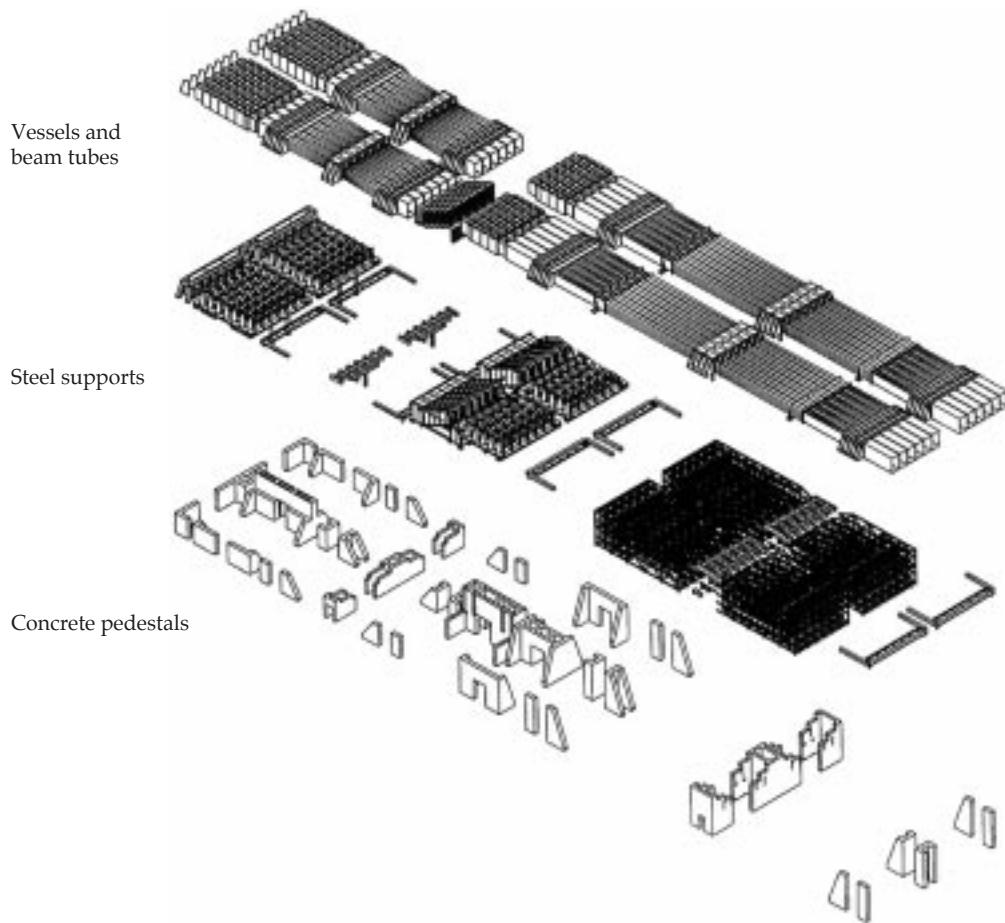
FIGURE 3. Layout of the nine major structural support subsystems in the laser bay. (40-00-1097-2292pb01)

LM1 support

Main amplifier support

CSF center support

Periscope support

TSF center support

CSF end supports

Power amplifier support

Preamp supports

TSF end supports
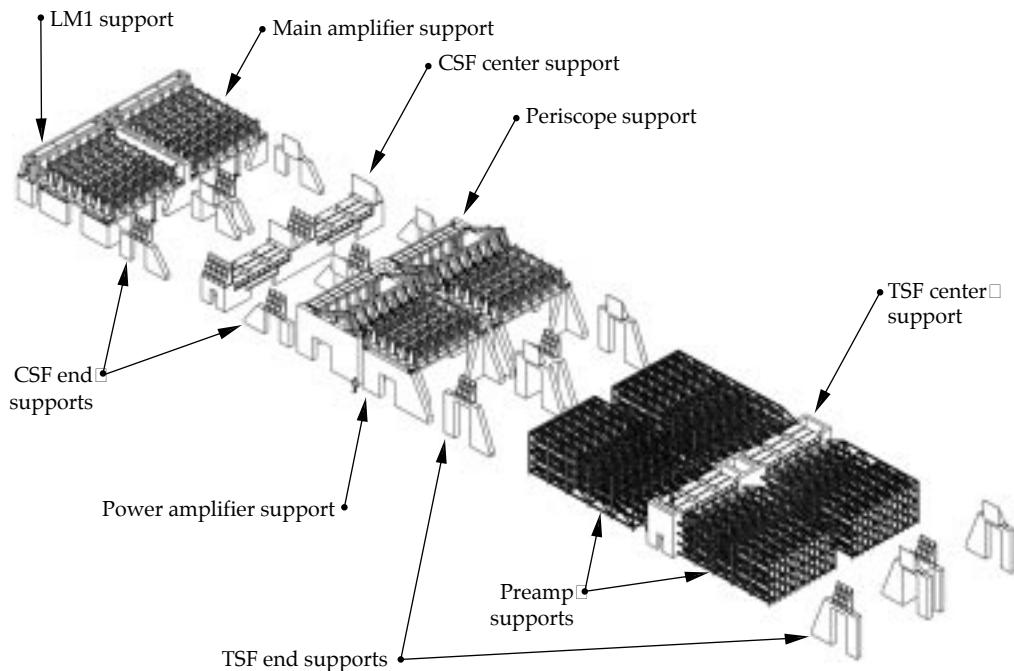
LM1 Support Structure

The support structure for the deformable mirror LM1 must provide pointing stability of ±0.42 µrad for the mirror and a stable mount for beam centering reference light sources used by the alignment system.

The structural design includes reinforced concrete shear walls and steel box beams, a welded modular construction, and an attachment to the superstructure through steel interface plates to the concrete shear walls. For each cluster, the concrete shear walls are 113 metric tons (m.t.), the steel superstructure is 34 m.t., and the cassettes with optics are 6 m.t. The structure is designed using standard catalog structural steel shapes and 61-cm-thick concrete shear walls with embedded steel interface plates. The optical LRUs are supported directly by the superstructure—separate array frames are unnecessary—and the welded module size will consist of one-half of the superstructure, to minimize bolted joints and on-site assembly time. Gas enclosure plates are attached to the superstructure to provide added stiffness, and main utility runs and interstage enclosures are supported by the structure. The optical LRUs are attached to supports on the superstructure through adjustable kinematic mounts. Electric motor and fiber-optic connections attached to the bottom enclosure plates provide for cassette mirror movement, mirror deformation, and deformed shape feedback. Figure 4 shows front and side views of the LM1 support structure, along with its components.

To meet cleanliness requirements, all carbon steel is painted, bundles have partitions between them to prevent any possible cross-contamination, and a slight positive pressure is maintained inside the enclosure to prevent room air intrusion. Outside the enclosure, LRU operations provide sealing to the bottom grid plate to maintain internal cleanliness, and interstage enclosures maintain cleanliness between the optical structures.

Amplifier Support Structures

The amplifier design includes two support structures: one each for the main and power amplifiers. The amplifier support structure must support the amplifiers, flashlamps, utilities, flashlamp cooling system, amplifier nitrogen system, and power cables. The structure must provide a translational stability limit of 500.0 µm, and a rotational stability limit of 2000.0 µrad. There must be a cleared area on the floor, 193 × 193 cm, centered under each LRU cassette position in the amplifier to allow clearance for the LRU transporter and a vertical clearance of 325 cm for the bottom

(a)

(b)
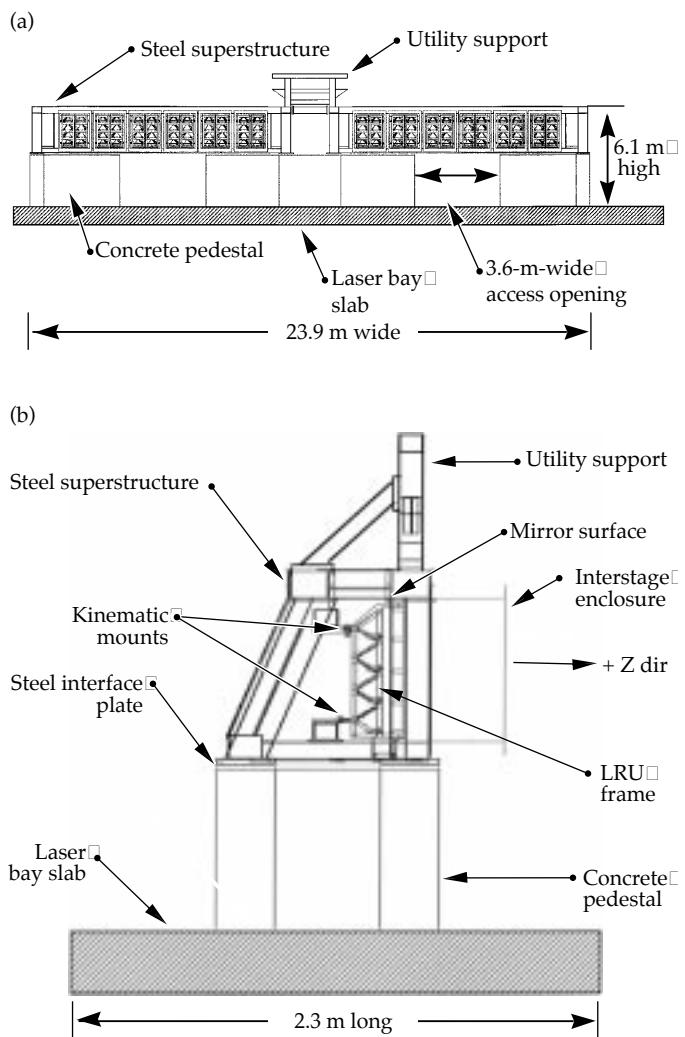
FIGURE 4. The LM1 support structure is 23.9 m wide, 6.1 m high, and 2.3 m long in the beam direction. Two views, (a) front and (b) side, show the components of this structure. (40-00-1097-2293pb01)

loader. In addition to meeting the standard seismic requirement, this support must do so with no breaking glass, falling hardware, or colliding components.

The hybrid concrete-steel design for the amplifiers uses a total of 1005 m.t. of reinforced concrete for the pedestals and 363 m.t. of structural steel for the superstructures. The reinforced concrete shear walls are 56 and 61 cm thick and are integral with the facility's floor slab. The structural steel consists of wide-flange and tube-steel sections in a welded modular construction; the dimensions of the support system for the main and power amplifiers are shown in Figures 5(a) and 5(b), respectively. This design permits top loading for the initial installation and bottom loading for the amplifier cassettes during normal maintenance. It also allows a

FIGURE 5. Dimensions for (a) the main amplifier support structure and (b) the power amplifier support structure. All distances are in millimeters. (40-00-1097-2294pb01)
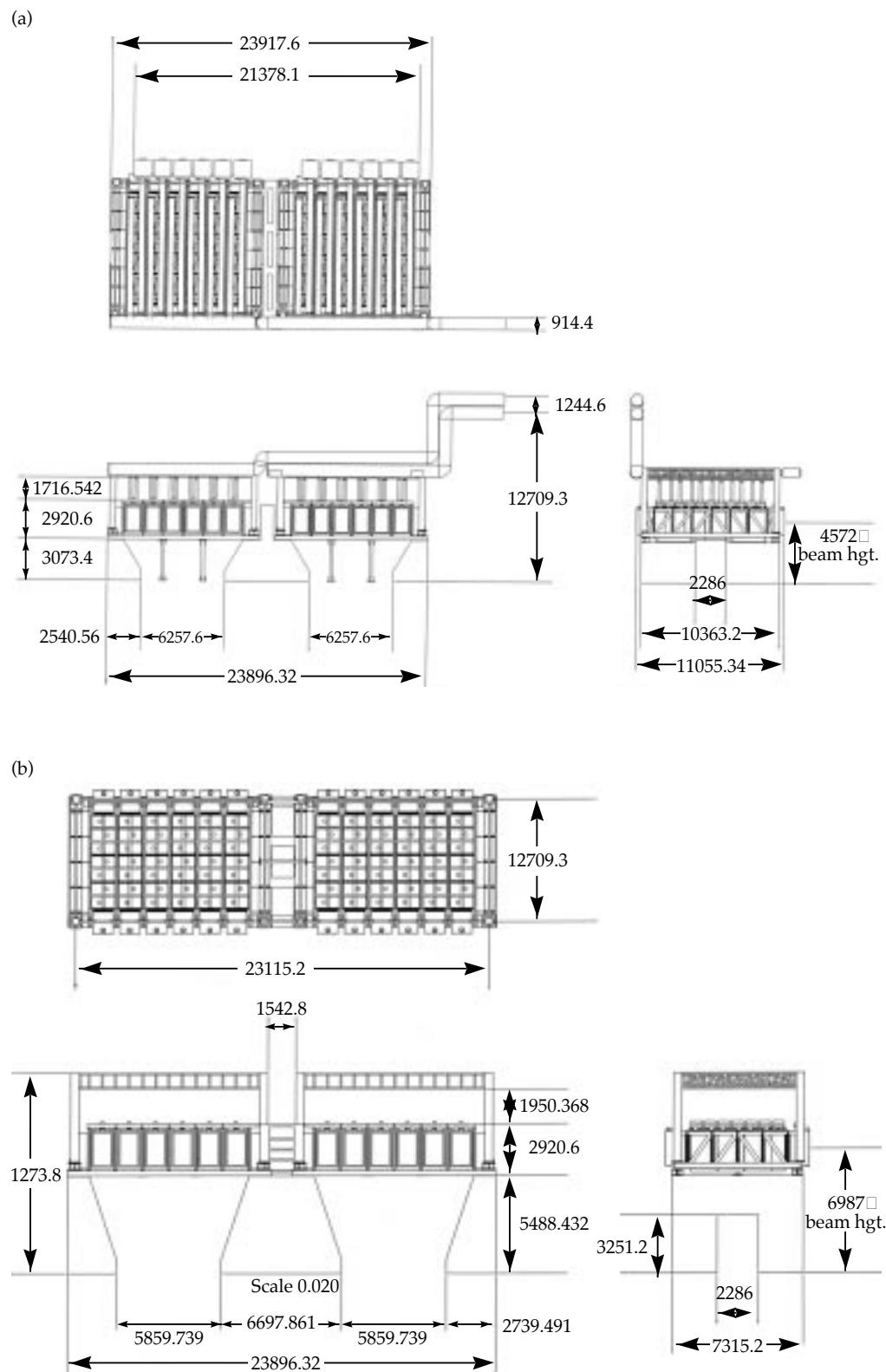
single frame-assembly unit (FAU) to be removed and replaced. The amplifier top plate is a structural element for the support structure, and the amplifier bundles are electrically isolated from each other and the support structure.

Periscope Support Structure

The periscope support structure supports the plasma electrode Pockels cell (PEPC), the polarizer, the LM2 and LM3 mirrors, the reference point sources for centering, and interstage beam enclosures. It must provide ≤0.60 μrad pointing stability for double reflections from LM3 and the polarizer, and ≤0.70 μrad pointing stability for a single reflection from LM2.

The design uses standard steel structural shapes, and 56- and 61-cm-thick concrete shear walls. The structure is 23.9 m wide, 8.9 m high, and 9.3 m long in the beam's direction. Its total weight, including the concrete walls, optics, superstructure, array frames, utilities and interstage enclosures is 697 m.t. To meet cleanliness requirements, we will paint the steel, provide partitions between optic bundles, and provide a slight positive pressure inside the enclosure. The PEPC, LM3/polarizer, and LM2 LRUs are attached to the superstructure through kinematic mounts. The reference light source is mounted onto the superstructure; PEPC utility-line interfaces are provided on the structure; and main utility runs for the building interface to the periscope center structure. Two views of the structure are shown in Figure 6.

Spatial Filter Support Structures

The spatial filter support structures, located at opposite ends of the laser bay, support the spatial filter lenses, the pinhole and diagnostics/alignment towers, the vacuum vessels, the beam enclosures, the injection and diagnostics systems, and the utilities. There are three separate structures in each spatial filter support system—a center-vessel support structure and two end-vessel support structures. The center-vessel support structure holds the center vacuum vessel and pinhole towers, utilities, and beam tubes (the TSF also has a space frame to support the preamplifier system). On either end of the center structure, two end-vessel support structures hold the spatial filter end vessels, utilities, and beam tubes.

The cavity spatial filter (CSF) lenses, SF1 and SF2, require a centering stability ≤6 μm; the transport spatial filter lenses, SF3 and SF4, require centering stability ≤0.7 mm. The structures must provide a 193 × 193-cm clear footprint and a 325-cm vertical clearance for the bottom loader.

The design uses the hybrid concrete-steel concept for all support structures except the preamplifier support, which is entirely structural steel. We use a total of 1673 m.t. of concrete in the pedestals and 725 m.t. of steel in the superstructures. The reinforced concrete shear walls are 56 and 61 cm. thick, integral with the facility's slab. The steel frame is of welded construction and uses standard catalog structured steel shapes. The structure is welded in truckable units at the fabricator's facilities and assembled on-site with bolted moment-resisting joints. Figures 7 and 8 show the plan and elevation of the TSF and CSF support structures.

The close-packed array of preamplifier modules requires an all-steel spaceframe (Figure 9). The structures are fabricated in truckable modules and assembled on-site with bolted moment-resisting joints. The steel frame is of welded construction and uses standard catalog structured steel shapes. The maximum module size is 6 × 2.4 × 3 m and the maximum weight is 3.5 m.t.. The total weight of the PAM support structures is 562 m.t.

Switchyard Support Structures

Each of the two switchyards has one 544-m.t. steel spaceframe (Figure 10). The spaceframes are attached to and stabilized by the target building concrete walls and the switchyard shield walls. The Title I steel switchyard structures are designed for a six-tier laser beam layout. The 27.4-m-tall spaceframe is coupled to the concrete building to optimize stiffness and cost. The spaceframe must accommodate the laser beam layout in the target and laser bays; must allow correct placement of LM4 and LM5 mirror assemblies, beam enclosures, and laser diagnostics; must not preclude a secondary target chamber; must provide <0.7 μrad angular and ≤1 mm translational stability over two hours for the mirrors.

The spaceframe design for each switchyard has eight levels and 20 columns and uses standard 12 × 20-in. tubular-steel horizontal members and 12 × 12-in. tubular-steel columns. The box on p. 154, "The Eight Levels of the Switchyards," provides more information about the layout of each floor.

THE EIGHT LEVELS OF THE SWITCHYARDS

As the figure in this box shows, the eight levels of the two switchyards are similar in layout, but not identical. The first two levels are below floor level.

Level 1 (elevation –6.6 m) in each switchyard has a concrete floor with 20 columns of 12×12 in. structural tubes. Twelve quads are mounted in three tiers: five quads mounted to the floor above, four quads mounted to the floor above and concrete floor below, and three quads mounted to the concrete floor. Nine quads in each switchyard at this level require platforms for maintenance purposes. There is a 1.8-m-wide access pathway to all quad locations, and there are collimators in 3.6-m-thick concrete walls at beam tube locations.

Level 2 (elev –1.1 m) has the largest area of grating. Twelve vertical beam tubes are in each switchyard at this level. Five LM5 quads in each switchyard are mounted immediately below this level. The spaceframe connects to the concrete building in five places at the target bay, two places at the switchyard stairwell, and two places at the switchyard corners. The precision diagnostics vessel is located in switchyard #2 at this level.

Level 3 (elev +2.4 m) has concrete mezzanine floors, which are part of the target bay, for classified electronics racks. Lateral supports for 12 vertical beam tubes are in each switchyard, and maintenance platforms provide access to the bottom of the LM4s located on the floor above.

Level 4 (elev +5.3 m) has 24 LM4 quads mounted in two tiers in each switchyard. This level also includes the roving pick-off mirror enclosures. The spaceframe connects to the concrete building in the same manner as on level 2.

Level 5 (elev +9.0 m) has LM4 maintenance platforms and provides access to 12 LM4 quads mounted immediately below. It is also the top of the roving pick-off mirror enclosures. The spaceframe connects at this level in the same manner as at levels 2 and 4.

Layout of the eight levels in the switchyards.   (40-00-1097-2312pb01)

Level 6 (elev +12.2 m) has concrete mezzanine floors for classified electronics racks. It also has lateral supports for 12 vertical beam tubes in each switchyard.

Level 7 (elev 15.4 m) has 12 LM5 quads mounted in three tiers: three quads mounted to the floor above, four mounted to the floor above and the level 7 floor, and five mounted to the level 7 floor. Seven quads in each switchyard require platforms for mirror maintenance. There are also collimators in 3.6-m-thick concrete walls at the beam-tube locations. The spaceframe connects to the concrete building in the same manner as at levels 2, 4, and 5.

Level 8 (elev +20.9 m) has three LM5 quads mounted immediately below. This level has no access and no grating. The spaceframe connects to the concrete building in the same manner as at levels 2, 4, 5, and 7.

(a)

Interstage
enclosure
(SF side)

Reference point
diagnostic

Array frame

Interstage
enclosure
(PA side)

947.45

LM3

882.39

LM2

LM2 LRU

PEPC LRU

LM3/polarizer
LRU

325

Polarizer

Bottom enclosure

Target building

Outer portions of the steel and concrete structure not shown
(Dimensions in centimeters)

FIGURE 6. (a) An elevation
view of the periscope structure
and (b) a view showing the con-
crete and steel outer structure.
(40-00-1097-2295pb01)

(b)

Reference point
diagnostics (120)

Top enclosure
(12 of 14 shown)

LTAB utilities

Plasma
pulser
cabinet
(12)

Inner partitions

Array frame (14)

LM3/polarizer LRU
(10 of 120 shown)

Outer
enclosure
panels

Interstage enclosure
(12 of 24 shown)

Concrete
shear walls

PEPC LRU (24)

Maintenance and
personnel access way

Target building
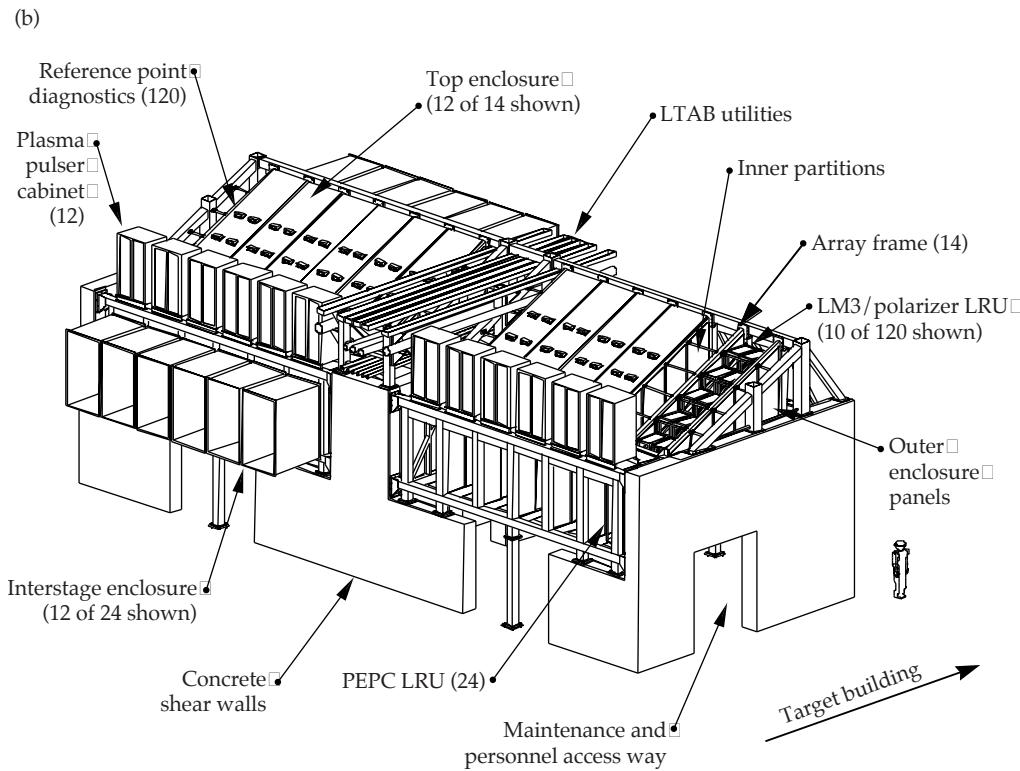
FIGURE 7. Plan and elevation of the TSF support structure. All distances are in millimeters. (40-00-1097-2296pb01)

Plan View

Pinhole area

Front View

Plan View

Pinhole area

Front View
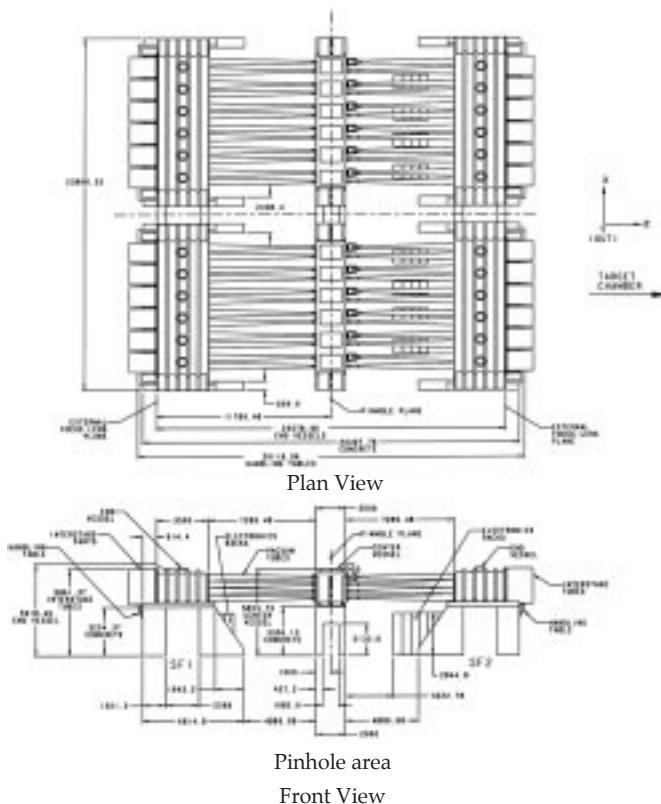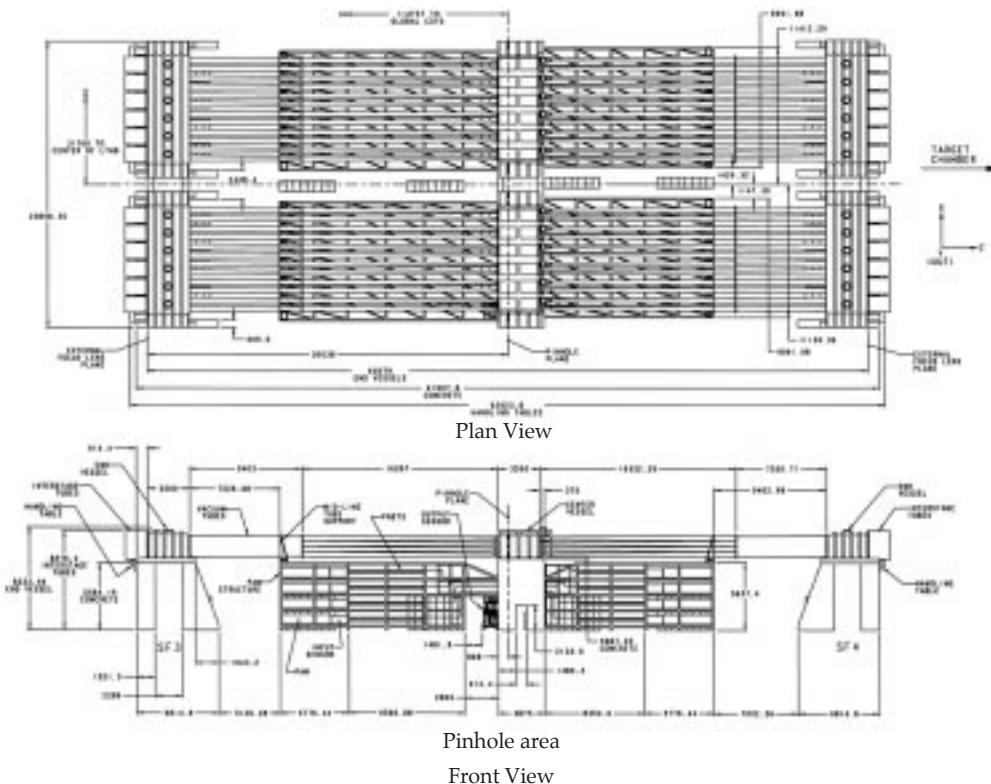
FIGURE 8. Plan and elevation of the CSF support structure. (40-00-1097-2297pb01)

Vacuum Vessels and Beam Enclosures

The vacuum vessels and beam enclosures are a major part of the NIF laser system infrastructure. They contain propagating laser beams and optomechanical hardware in a contamination-controlled environment in the facility and are positioned to allow top and bottom access (Figures 11 and 12). The primary functions of the enclosures and vessels are to safely contain laser beams within the required environment, allow access for removing LRUs, provide interfaces for preamplifier beam injection and laser diagnostics, achieve position and stability requirements within budgeted tolerances, and provide independent bundle operation. In our design, we also considered the surface finish—for cleanliness and ease of cleaning—and the size and weight of the pieces to meet transport and installation requirements.

The spatial filters are stainless steel vacuum vessels interconnected by tapered beam tubes with bellows at the center vessels (Figure 13). The tapered tube/bellows arrangement allows air flow to minimize thermal gradients. Each 60-m transport spatial filter cluster is nearly 275 m.t. of stainless steel. The
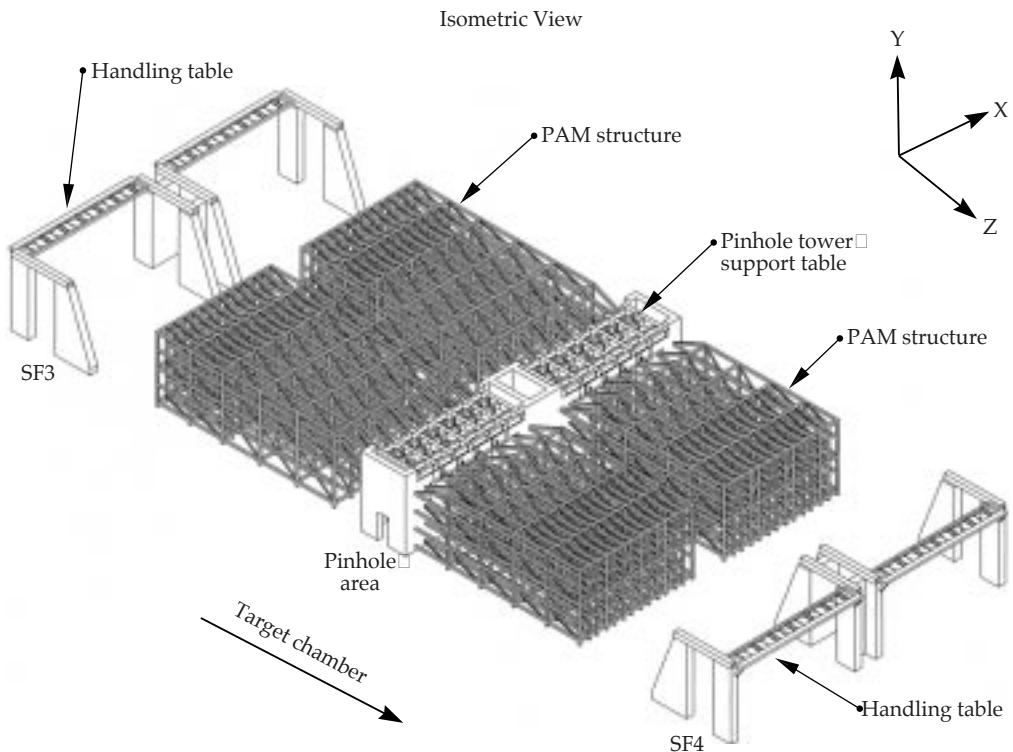
Isometric View
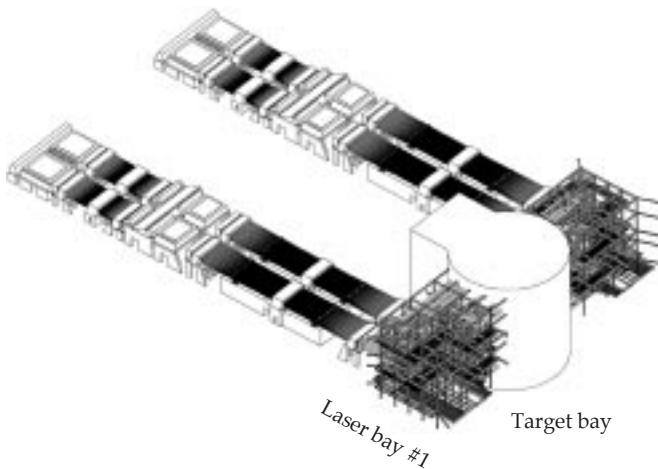
Figure 10. The switchyards in relation to the laser bays and target bay. (40-00-1097-2299pb01)

23.5-m cavity spatial filter cluster has a smaller center vessel and weighs 142 m.t. The TSF and CSF end vessels are identical. The end vessels are optics benches for 4×1 lens arrays; each array provides a vacuum boundary. The center vessels allow top loading of the pinhole/diagnostic tower LRU (see next section on tower structures).

Beam enclosures include the special tapered tubes between the center and end vessels; the interstage beam enclosures between the amplifiers, vessels, and so on; and the beam enclosures in the switchyard.

The tapered stainless steel tubes between the center and end vessels were designed to minimize mass, to increase system stability, to reduce costs, and to allow 10-mm minimum clearance between the tube inner diameter and the full-aperture beam. In addition, the beam spacing within each bundle limited our design configuration. The limited vertical space between laser beams required rectangular tubes at the TSF end vessels. For this, we use 8-mm 304 stainless steel sheet, which is brake-formed into tapered U-shapes and welded together to form bundles. Circular tapered beam tubes are used in areas without space constraints. We used finite-element analysis to evaluate the stress and deflection due to the vacuum load and found that the spatial filter vessel and tapered beam tube designs are within allowable stress and deflection limits.

Interstage beam enclosures (IBEs) enclose the beams in bundles between the amplifiers, vessels, and so on. The IBEs are rib-stiffened, welded stainless-steel sheet-metal enclosures. They are made of 12-gage stainless-steel sheet, with carbon steel external stiffeners, and have shielded elastometric 50-mm bellows/expansion

FIGURE 11. Location of the spatial filter vacuum vessels, interstage beam enclosures, and switchyard enclosures.
(40-00-1097-2300pb01)

Spatial filter vacuum vessels

Switchyard enclosures

Interstage beam enclosures
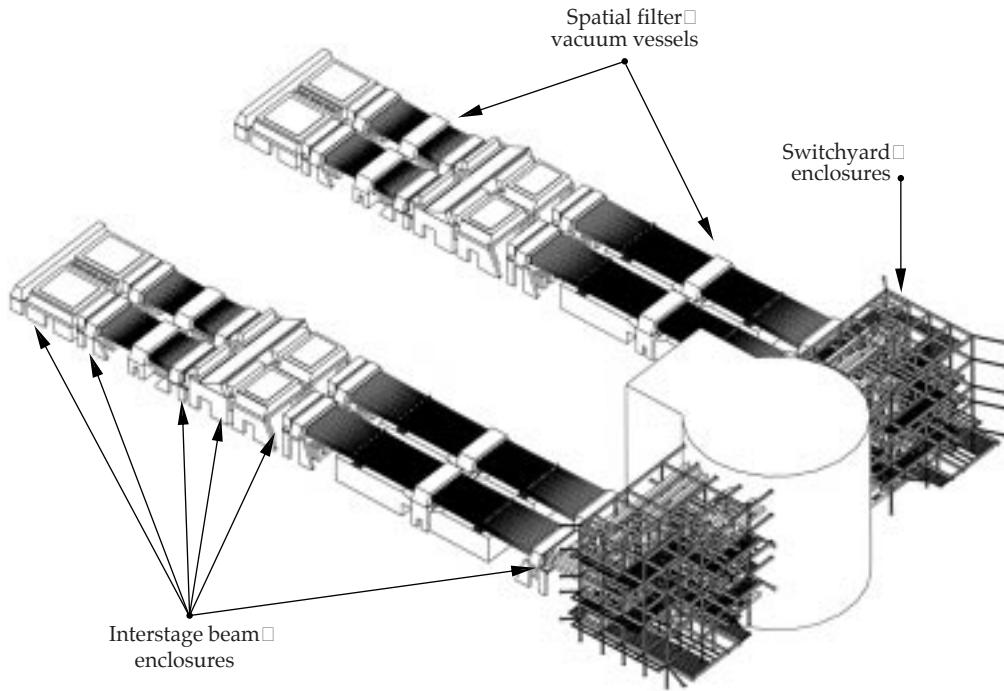
FIGURE 12. Enclosures and vacuum vessels are positioned to allow bottom access.
(40-00-1097-2301pb01)

Laser Bay Elevation

LM1

Main amplifier

Cavity spatial filter

Pockels cell periscope/LM2

3.25 m to top of concrete

5.9 m to top of enclosures

Transport spatial filter

8.3 m to top of enclosures

Boost amplifier

Interstage enclosures

PAM/PABTS

5.6 m to top of concrete
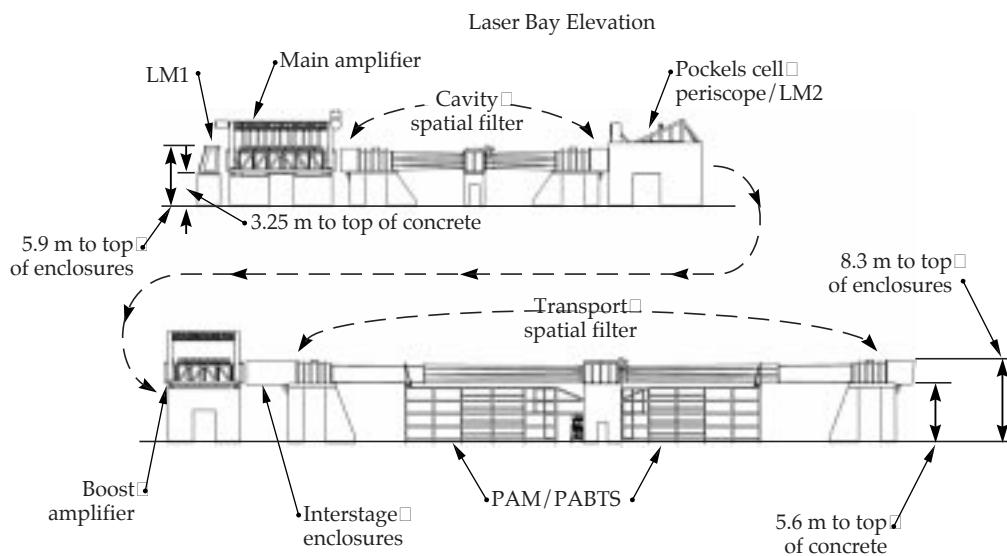
joints. An "eggcrate" baffle divides the beamlines within the IBEs.

Rib-stiffened sheet-metal beam enclosures also contain the laser beams in the switchyard area. In the switchyard alone, nearly 2000 m of sheet-metal beam enclosures provide a clean, argon-filled atmosphere for the beams. Each unique beamline has a different enclosure configuration (Figure 14). These enclosures also provide the interface with the LM4 and LM5 turning mirror boxes.

Spatial Filter Diagnostic/Alignment Tower Structures

We use similar tower structure designs in the transport and cavity spatial filters (Figure 15). These designs are based on an isolated kinematic mount design that meets alignment and stability requirements. An external "optic bench," located under the center vacuum vessel, provides

(a)

Interstage tubes

End vessel

Vacuum tubes

Handling table

Center vessel

End vessel

SF1

Electronics racks

Pinhole area

Interstage tubes

Electronics racks

SF2

Handling table

Y

X

Z

Target chamber

Isometric View
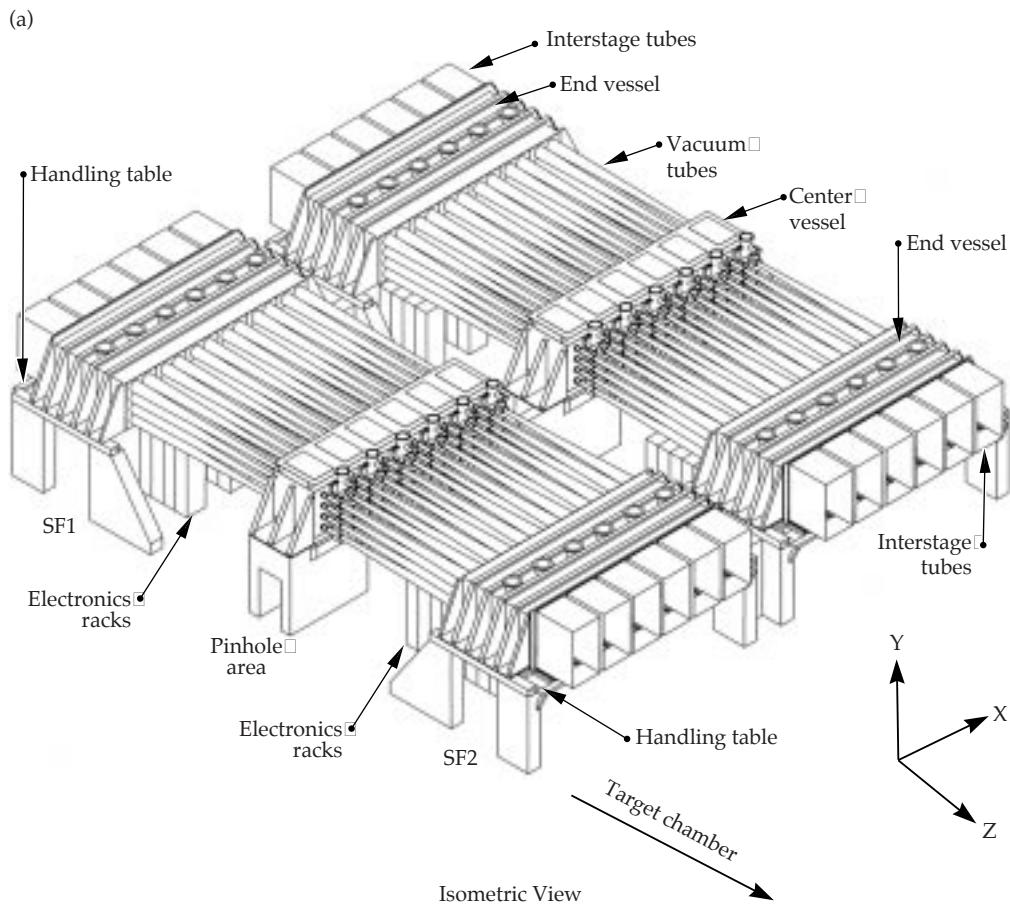
FIGURE 13. Layout of (a) the CSF support structure and (b) the TSF support structure. The CSF structure is a modified design of the TSF structure. (40-00-1097-2302pb01)

(b)

Interstage tubes

Handling table

End vessel

Vacuum tubes

Midtube support

Center vessel

End vessel

SF3

Electronics racks

PAM structure

Pinhole area

Interstage tubes

Target chamber

PAM structure

SF4

Electronics racks

Handling table

Isometric View

Bundle enclosure

Quad enclosure

1.3 m

2.48 m

3 m

1.2 m

0.9 m

3 m

Estimated mass 775 kg/m (107 lb/ft)

Estimated mass 525 kg/m (73 lb/ft)

Cross enclosure

1.5 m

3 m   1.5 m

Turning mirror enclosure

FIGURE 14. Some of the beam-enclosure configurations in the switchyard.   (40-00-1097-2303pb01)
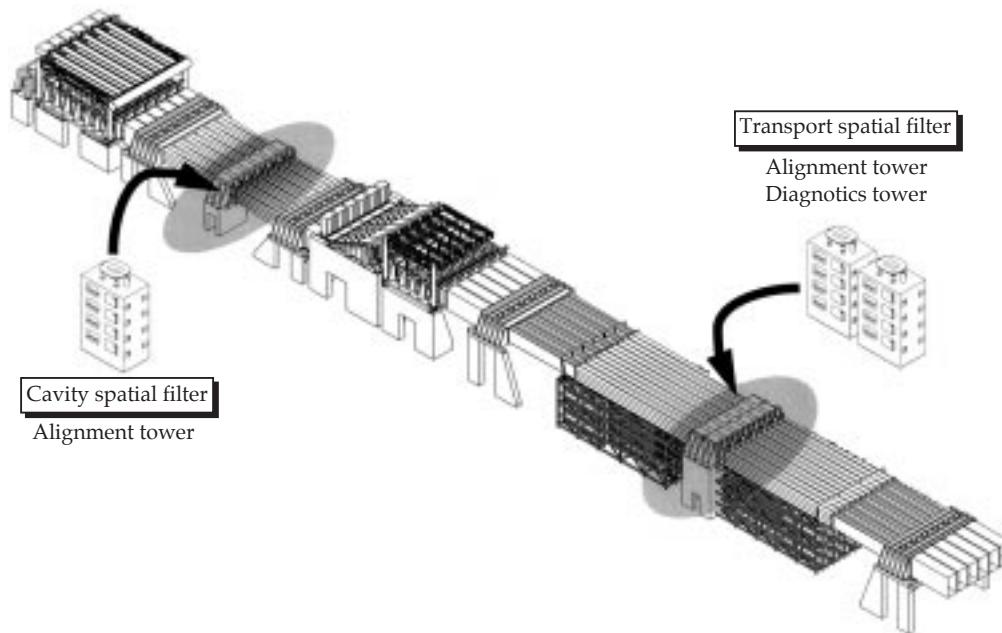
stable mounts for kinematic supports. The mounts are isolated from the vessel wall with bellows. The kinematic mounts provide a registered location for LRUs and will have either a cone-vee-flat or three-vee configuration. These mounts allow the towers to be decoupled from vacuum vessel pumpdown deflections (Figure 16). The spatial filter tower structures are designed for stiffness, with stainless-steel welded spaceframes, shear panels, and 25-mm-thick aluminum mounting plates that are individually shimmed and fastened.

Optomechanical Systems

NIF's optomechanical systems are located in the laser bays, switchyards, and target area (Figure 17). These systems consist of more than 2500 optical mounts: 384 cavity end mirror mounts, 384 polarizers and elbow mirror mounts, 768 spatial filter lens mounts, 192 spatial filter lens mounts, 192 injection mirror and telescope assemblies, 816 transport mirror mounts, and 192 shutter and beam dumps. These optomechanical systems must satisfy a number of diverse requirements. Multipass mirrors must have rotational stabilities of 0.6 μrad; CSF lenses must have translational stabilities of 6 μm; mirror-mount assemblies must have an angular adjustment step size of 0.1 μrad; and optical mount assemblies in LRUs must

FIGURE 15. Tower structure locations and design for the CSF alignment tower and the TSF alignment and diagnostic towers.   (40-00-1097-2304pb01)

Transport spatial filter

Alignment tower
Diagnotics tower

Cavity spatial filter

Alignment tower
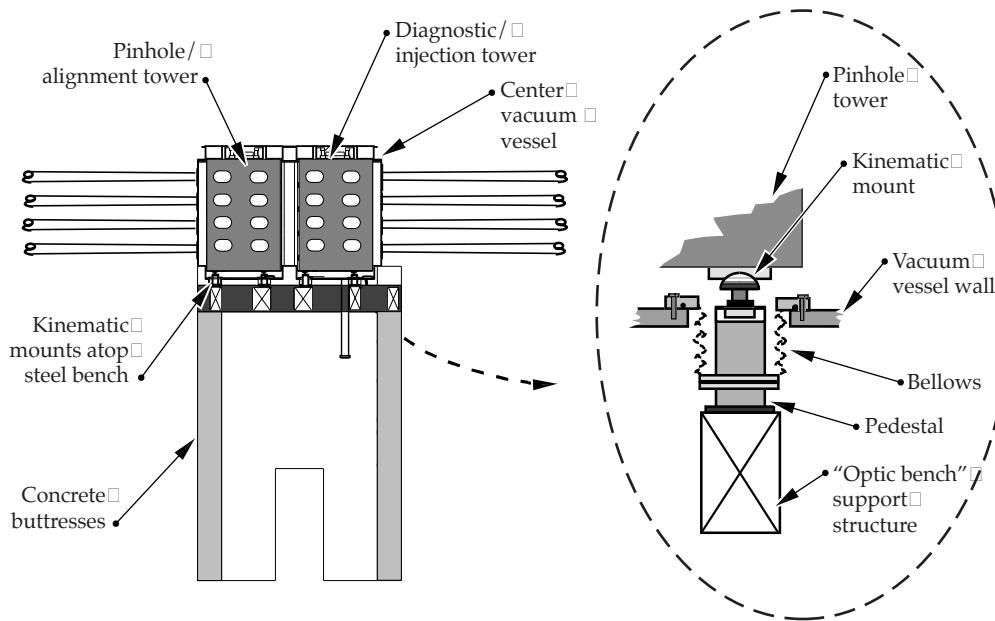
FIGURE 16. Towers are decoupled from vacuum vessel pumpdown deflections. (40-00-1097-2305pb01)
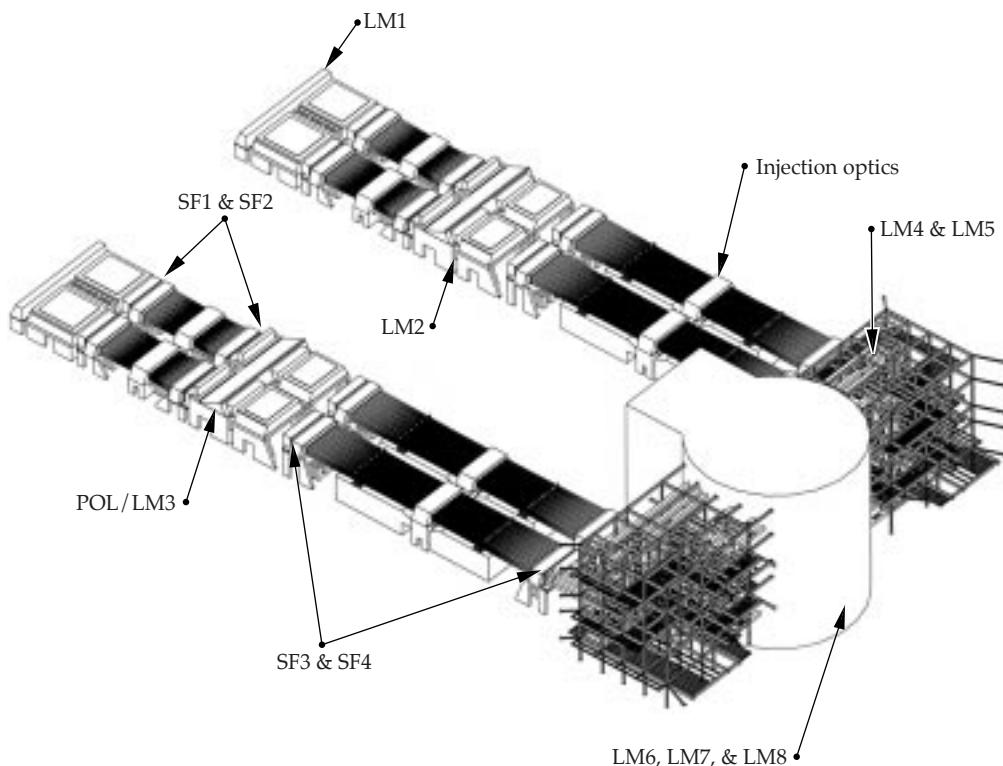
FIGURE 17. Location of NIF's optomechanical systems. (40-00-1097-2306pb01)

161

meet cleanliness and maintenance requirements. In the rest of this section, we describe the mounting designs for the cavity mirrors and periscope assembly, the spatial filter optics, and the switchyard and target area optics.

Cavity Mirrors and Periscope Assembly Mounting

The LM1 and periscope structures hold LM1, LM2, LM3, and the polarizers, and have the most critical stability requirements in the laser bay. All of these optics have tip-tilt adjustments to steer the beams through the chain.

The LM1 structure for each cluster supports twelve LM1 LRUs, each containing four LM1s. The periscope structure supports twelve LM2 LRUs and 30 LM3/ polarizer LRUs. The mounts for the cavity and

periscope LRUs are gravity loaded and based on accepted kinematic principles (see box "Laser Bay LRU Kinematic Mounts" below). These mounts have pneumatic pins that retract for loading and a seismic restraint that retracts when lifted.

The LM1 deformable mirrors are on the front face of the LM1 LRU. Pigtails with pin connectors route through the frame to a panel below. The panel is accessible from the laser bay to plug in pin connectors and to splice the fiber optic.

The close spacing of LRUs means limited space for LRU mounts, mirror mounts, cover seals, and clearance for insertion. The LM2 mirrors install from the front, and Fresnel lenses mount in the frames that attach to the LRU. The LM3/polarizer optics install from each end: the LRU is inclined so that the optics install vertically. Each of the three optics has a tip-tilt

LASER BAY LRU KINEMATIC MOUNTS

The laser bay LRU kinematic mounts—which evolved from a typical three-vee kinematic coupling—have been designed to constrain exactly six degrees of freedom with six theoretical points of contact as shown in the figure. The LRUs hang from two upper vees and brace against one lower vee for six-point support. A pneumatic pin engages two ball swivels to form the upper vee constraint, while the widely spaced spherical pads that form the lower vee passively engage upon insertion. For the upper vee, a molded Teflon seal and low-outgassing grease minimize contamination.

(a)
(b)
2 pts
2 pts
1 pt
1 pt
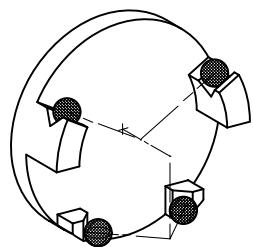
(a) A NIF LRU mount; the lower widely spaced pads form the lower vee.
(40-00-1097-2313pb01)
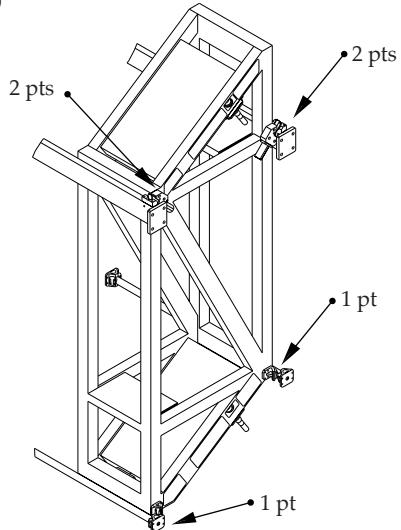
(b) LRUs hang from the two upper vees and brace against one lower vee for six-point support.
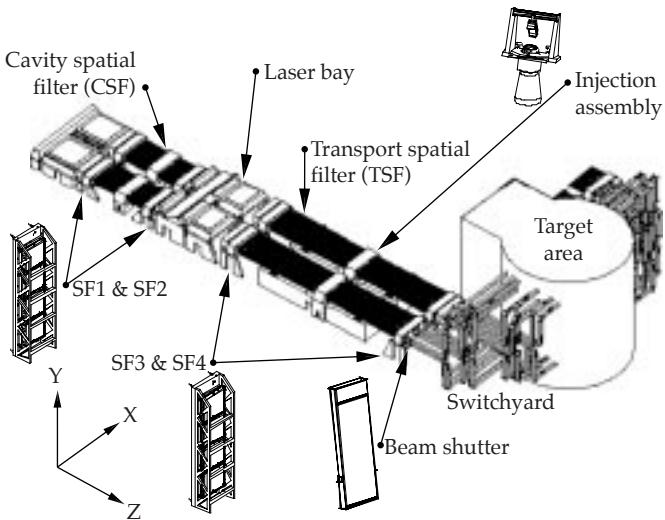
FIGURE 18. The location of the spatial filter optomechanical systems. (40-00-1097-2307pb01)

mirror mount that supports the optic at three points with ball pivot connections. Each ball pivot constrains two degrees of freedom (DOF). These optics show an insignificant amount of gravity-induced deformation.

Spatial Filter Optics Mounting

There are 768 spatial filter lenses, 192 injection mirrors, and 24 beam shutters within NIF (Figure 18). For the spatial filter lens LRUs, the fixed-optic center spacing and lens dimensions leave little space for mounting hardware. For spatial filters SF1 through SF3, the tight vertical lens spacing drives the design; SF4 has an additional design challenge of an optical/mechanical center offset (Figure 19) to avoid ghost-beam back reflections. In addition, the mechanical clear aperture of each lens is limited and is a factor in the mount design. Finally, each spatial filter lens position has a challenging set of positioning accuracy requirements. The positioning requirements for
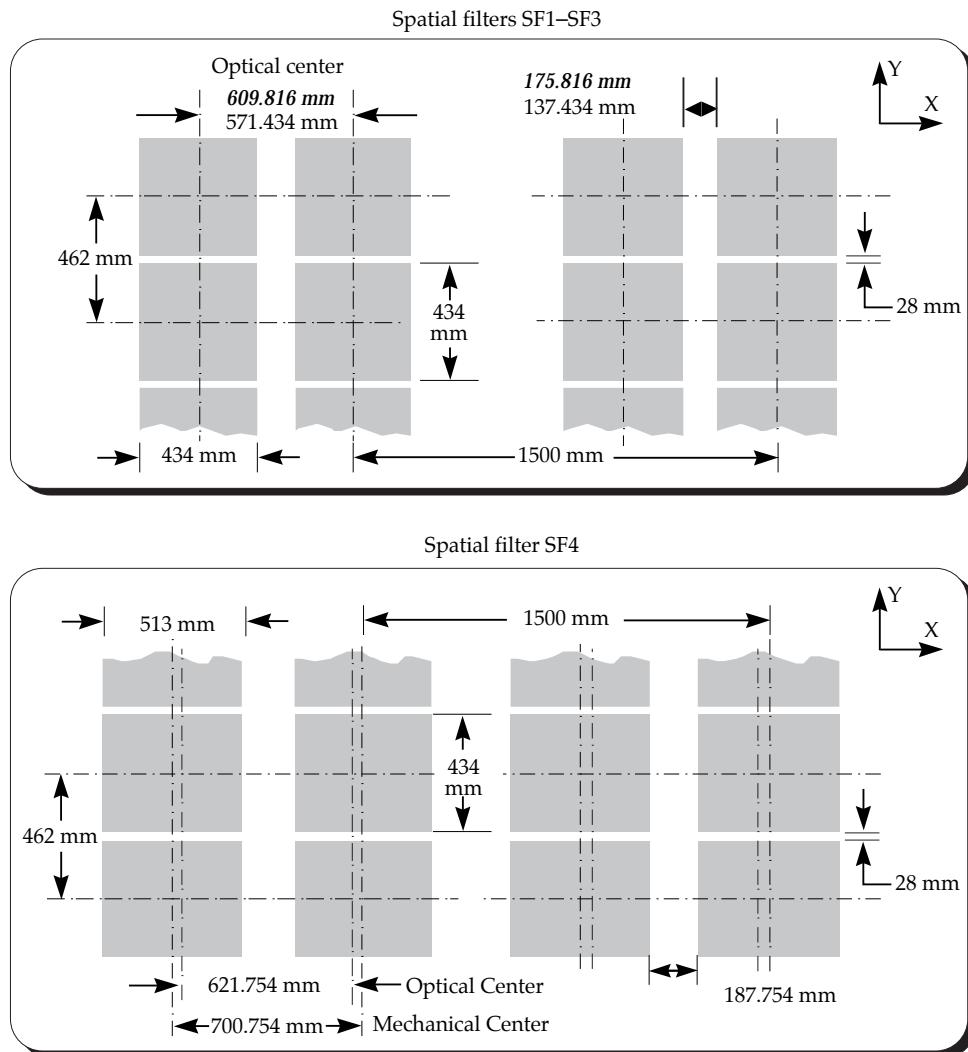
FIGURE 19. Fixed-optic center spacing and lens dimensions leave little space for mounting hardware for the four spatial filters. Italics denotes SF1 and SF2 values. (40-00-1097-2308pb01)

SF1 through SF3 are met by maintaining fabrication toler-ances. After assembly, only the SF4 cassette requires addi-tional tip/tilt alignment, using a bellows and adjustment bolts.

The injection mirror and beam shutter are two of the many optomechanical devices located in the TSF area. We added an injection telescope to the injection mirror (Figure 20) to maintain relay planes and the proper cone angles. It must accept a full-aperture beam, with-stand a full-fluence shot, contain debris, detour back-reflection off-axis, be remotely inserted and removed without releasing beam tube gases, and fit within a small area. Figure 21 shows the layout of the shutter. An array frame contains eight beam shutter cells to block a laser bundle. Each shutter cell has a 2° tilt to send any back-reflections onto additional beam blocks. The array frame is connected to a linear translator within an air-tight enclosure, and the cell array is enclosed to preserve cleanliness and to contain beam-line gases. The beam shutter enclosure is secured in position by two supports: brackets are bolted to the floor frame and the shutter spool is bolted to the struc-ture frame.

Switchyard and Target Area Optical Mounts

In the switchyard, mirrors LM4 and LM5 transport the beams from the laser bay through the switchyard to the target bay. The LM4 quads direct the beam up or down; LM5 quads direct the beam horizontally to the target chamber. In the target bay, mirrors LM6 through LM8 direct the beam to the final optics assembly at the target chamber. The switchyard and target area mirrors share many requirements: the total wavefront distortion from gravity and mounting must be <1/4 wave; the step size for angular adjustment must be ≤0.1 µrad; and the angu-lar stability must be ≤ 0.7 mrad over two hours. For LM4, 5, 7, and 8, the tip/tilt angular range is ±7.5 mrad, and alignment positioning linearity must be 3%. LM6 does not require active alignment during normal operation.

The switchyard and target area mirror-mount designs are the same (Figure 22). In this design, the isolating mounts provide stiff mirror support, yet flex to accommodate different coefficients of thermal expansion. The positioning flexures act as hinges for tip or tilt and as stiff members for mirror support.

FIGURE 20. Layout for the injection telescope optics and hardware.   (40-00-1097-2309pb01)

(a)

(b)
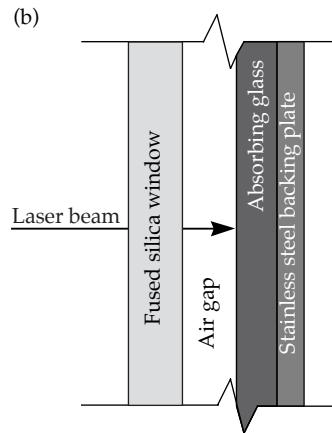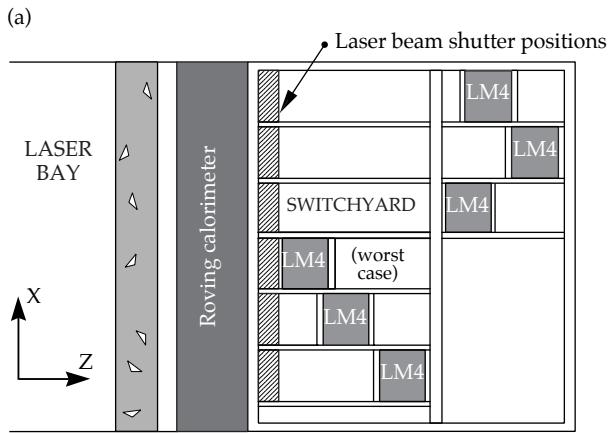
FIGURE 21. (a) The only position available to insert the laser beam shutters between the roving pick-off mirror/calorimeter enclosure and the switchyard mirror LM4. This view shows one cluster only. (b) The primary beam shutter components. (40-00-1097-2310pb01)
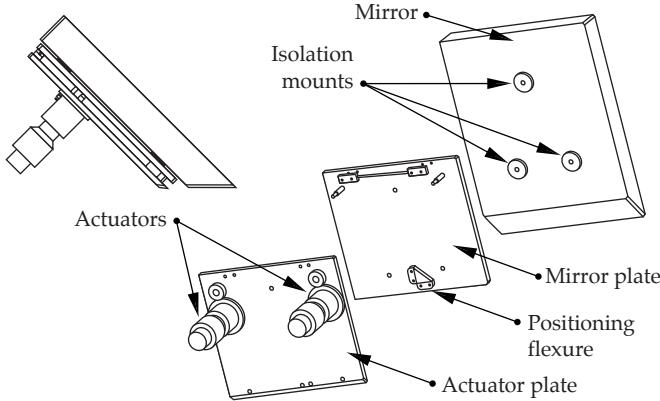
FIGURE 22. In addition to the mirror, a subassembly includes isolation mounts, positioning flexures, plates, and actuators. (40-00-1097-2311pb01)

All of these mirrors are mounted on kinematic equivalents to three-vee mounts. In the target area, LRUs are arranged in 1×2s for the LM6, 2×1s for the LM7, and 1×1s for the LM8. The LM6 LRUs are all identical; the mirrors are in plane and all have a 45° use angle. Six of these LRUs are in the upper mirror chamber and six are in the lower. The LRU enclosures are connected to the target area beam tubes to maintain cleanliness. There are 24 different LRUs for the LM7, with varying mirror offsets and use angles. The mirrors in each LRU have linear and angular offsets from each other. The mirror assemblies use a spacer frame to establish these offsets. The LM8 has eight different LRUs with eight different use angles. The LM8 mirrors are shimmed for use at eight different angles—from 18.8° to 34.4°—in the upper and lower mirror rooms.

Title II Activities

As Title II begins for NIF's beam transport system, we are ready to detail thousands of tons of structures, mechanisms, and vacuum vessels. Among our specific Title II activities, we will begin to procure materials that require a long lead time; prototype, fabricate, and test the LRUs' stability and maintainability; assess cleaning techniques and effects on fabrication; analyze how weather will affect switchyard stability during construction; and update the TSF to accommodate the 96-PAM baseline design. We will also complete details of LRU extraction and cavity closures, finalize mass production techniques for optics mounts, and freeze the interfaces with the target area beam layout. We will verify all analyses for the detailed design, as well.

For more information, contact
Joel M. Bowers
Beam Transport System Engineer
Phone: (925) 423-6877
E-mail: bowers2@llnl.gov
Fax: (925) 424-3763

Target Area Systems

V. Karpenko

C. Adams

J. Chael*

P. Dohoney

R. Foley

W. Gibson†

W. Hibbard

W. Horton

J. Latkowski

D. Lee

A. McDonald*

W. Miller

W. Olson

L. Parietti**

C. Patel

L. Pittenger

P. Pittman**

T. Reitz

D. Trummer

H. Walther*

R. Wavrik*

W. Weed*

K. Wong

*T*itle I designs are complete for the NIF target area systems, including the final optics assembly, the target chamber, the target positioner, the target diagnostics, and the structures. The main function of the final optics assembly is to convert the 1ω light to 3ω and focus it on the target. Following a beam through the assembly, it passes through a vacuum window, the conversion crystals, the final focus lens, a diffractive optic plate, a debris shield, and a 3ω detector. The target chamber acts primarily as a vacuum chamber and provides neutron and gamma ray shielding to the target area. Target chamber systems include the vacuum chamber, neutron/gamma ray shielding, the first wall, vacuum systems, and support structures. The primary functions of the target positioner are to mount, insert, position, and maintain targets for illumination by the laser beams. The target diagnostic system provides the optical, x-ray, and nuclear diagnostics required to support the NIF experimental plan. The NIF project is responsible for locating nearly 90 detectors for 20 experiments on the vacuum chamber and for designing the diagnostic instrument manipulator and three diagnostic systems—the time-resolved x-ray imaging system, the static x-ray imaging system, and the x-ray streak slit camera. The target area structural supports provide a stable vibrational and thermal environment for the mirrors, diagnostics, target positioner, and target chamber. Components of the target area structures are mirror structures, beam tubes, guillotines, passive damping structures, and catwalks and platforms.

Introduction

The NIF target area provides the capability for conducting ICF experiments. Our preliminary design meets NIF's system requirements by integrating the target area subsystems, providing optomechanical stability, incorporating target diagnostics, managing laser light and target energies, protecting the optics, and providing radiation shielding. The target area systems must also meet demanding requirements before, during, and after a shot. The systems include the final optics assemblies, the target chamber, the target positioner, the target diagnostics, and the structures. The requirements and Title I design of each subsystem are covered in this article.

Final Optics Assembly

The final optics assembly (FOA) is the last element of the main laser system and the first of the target area systems. NIF's 192 beamlines feed into the 48 FOAs mounted to the surface of the target chamber. The FOAs have a number of design challenges. They must be mounted at eight different angles to the vertical; the optics must be carefully mounted in a very clean, temperature controlled, mechanically stable assembly to meet NIF's performance requirements; 3ω damage to optics must be mitigated; and the operational access is limited.

The optical configuration requirements result in the design shown in Figure 1. Four beams are routed from the laser bay to an FOA. The vacuum window is located in the 1ω beam to reduce the likelihood of its damage. The conversion crystals are mounted and precisely aligned to the beamline. The lens focuses the light to the target location, and a beam-smoothing phase plate is located with the debris shield for ease of changeout. In this way, the FOAs provide a vacuum barrier for the target chamber, convert 1ω to 3ω light, focus the 3ω light to target center, allow for beam smoothing, allow for 3ω power measurement, and provide a protective shield from the target debris.
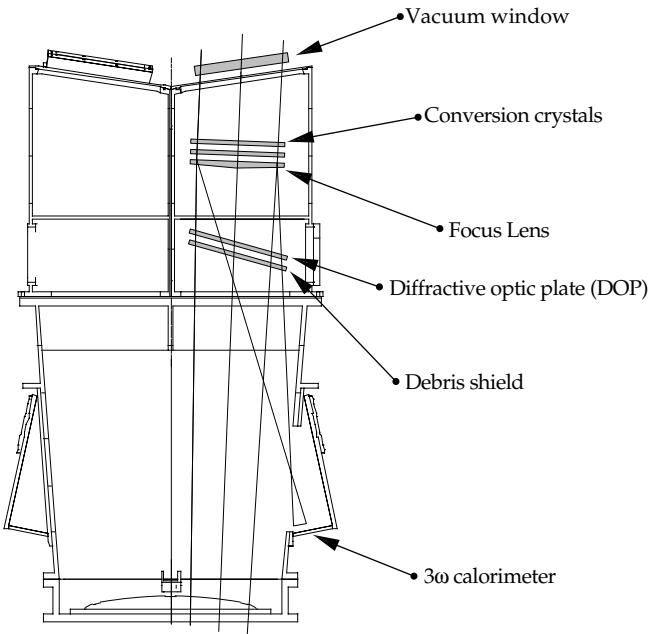
FIGURE 1. The optical design requires the final optics assembly to support a number of key optical components.   (40-00-1097-2268pb01)

and the vacuum isolation valve—each of which is discussed in the following paragraphs.

The IOM is the line-replaceable unit (LRU) that holds the FOA's optical elements. Each IOM 1100 mm × 670 mm × 650 mm, weighs 350 kg, and will be constructed of welded or cast aluminum. Stress and deflection calculations show this design meets stability and stress requirements.

The final optics cell (FOC) is a precision optomechanical mount. It is kinematically mounted within the IOM, and it is the final element in the optics train for aligning and diagnosing the beamline. It holds the crystals, the final focus lens, and a diffractive optic. To meet the frequency conversion efficiency requirements, the FOC must provide full-edge support to the crystals. (In past laser systems, these crystals have only been supported at the corners.) The FOC must also provide flat surfaces (less than 5 μm) for mounting the crystals and for alignment. All optics must be referenced to each other within ±10 μrad, and it is desirable that the FOC be as small as possible. The manufacture and assembly of the FOC are critical design drivers for the system. Table 1 shows the specifications for position, alignment, and resolution of the FOC. Figure 3 shows a cross section of the FOC components. The FOC adjustment system has a full range of motion for focus and for angular adjustment with respect to the beam axis. Translation of the FOC accommodates targets at locations other than at chamber center. Finely

Figure 2 shows the integrated optomechanical design package, including the main subsystems: the integrated optics modules (IOMs), which hold the final optics cells and debris shield cassettes; the 3ω calorimeter chamber;
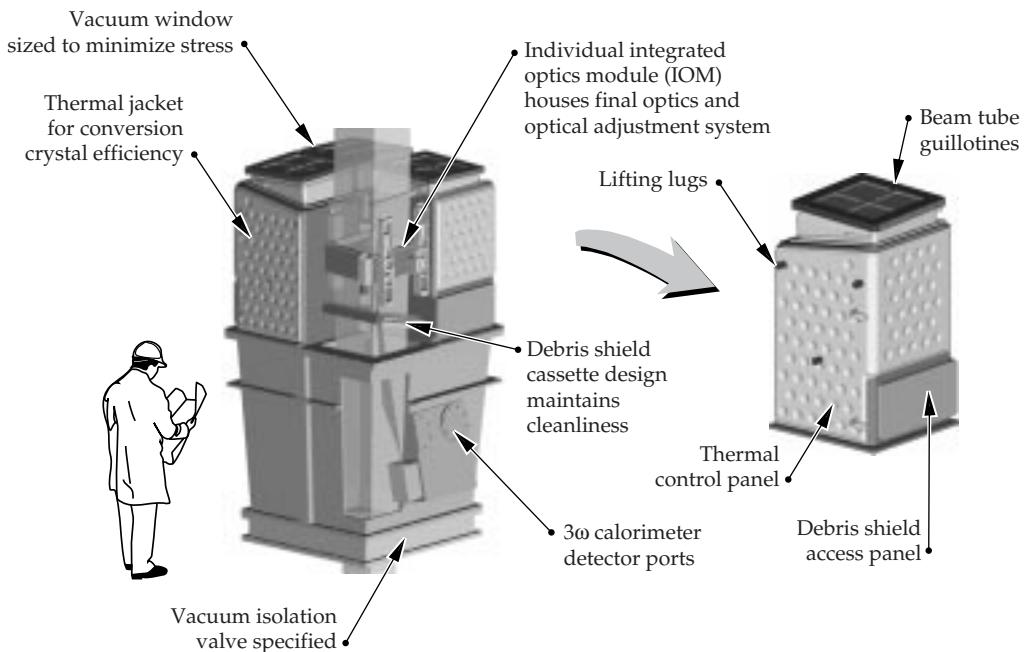
FIGURE 2. The final optics assembly is an integrated optomechanical design package. (40-00-1097-2269pb01)

TABLE 1. The specifications for position, alignment, and resolution of the final optics cell.

Mounting/position for final optics						
	±Tolerance (mm or µrad)					
Optical component	x	y	z	θx	θy	θz
Vacuum window	3	3	3	5000	5000	5000
SHG	2	2	2	20	20	5000
THG	2	2	2	20	20	5000
Final focus lens	0	0	0	0	0	5000
Diffractive optic	3	3	3	10000	10000	10000
Debris shield	3	3	3	30000	30000	30000

Alignment table for final optics						
	±Accuracy (mm or µrad)					
Optical component	x	y	z	θx	θy	θz
Final optic cell	0.1^4	0.1^4	0.3	5	5	n/a

	±Resolution (mm or µrad)					
Optical component	x	y	z	θx	θy	θz
Final optic cell	n/a	n/a	0.1	2	2	n/a

resolved angular motion is needed to achieve high crystal conversion efficiency.

The debris shield cassette is an LRU within the IOM LRU. This cassette is designed to be an independent unit, since all 192 cassettes must be changed weekly when NIF is operational. Within the FOA, the debris shield is tilted relative to the beamline for ghost control. The cassette contains two glass plates, the debris shield, and the diffractive optics plate.

Laser diagnostic requirements impact the FOA design in two areas. First, a 1ω-beam centering fiducial must move into and out of the beam for alignment. The fiducial mounts for the FOC must be centered with respect to the FOC aperture within 0.2 mm, or 0.05% of the beam aperture. Second, for each beamline, a 3ω power measurement requires that a 3ω sampling grating be placed on the plano surface of the final focus lens. The calorimeter detector is located off-axis. These diagnostics affect the aperture of the detector—which must be sized to accommodate a range of target locations—and the orientation of the lens. During Title I, we developed a concept for this fiducial, including an arm, mounted to the FOC, that swings ~45° into the beamline during alignment.

As shown in Figure 4, the vacuum isolation valve interfaces directly with the target chamber. This valve provides operational flexibility, allowing the debris shield

FIGURE 3. The final optics cell, includes the following features: (a) A stiff and stable one-piece cell for mounting and referencing all the optical elements. (b) Three precision surfaces for mounting the optics. (d) A built-in wedge of 10 mrad, between the lens and the crystals. (e) Spacers and compliant elements to load and hold the optics in the cell. (f) Absorbing glass, which also suppresses stimulated Raman scattering. The final optics cell will be kinematically mounted to the actuation system with three ball-and-vees. (40-00-1097-2270pb01)

FIGURE 4. The vacuum isolation valve interfaces directly with the target chamber. (40-00-1097-2271pb01)

cassette and IOM to be removed with the chamber at vacuum. This aluminum valve is 1300 mm × 1300 mm × 205 mm, with an 800-mm-square aperture.

Title II Activities

We have a preliminary design of the FOA that accommodates the NIF design requirements. During Title II, we will complete the design of the IOM handling features, conduct a detailed analysis of the stability performance of the entire FOA, design and analyze vacuum housings to satisfy cleanliness and stress requirements, and build and test the thermal control system for the crystals. The design for the 1ω-beam centering fiducial will also be further developed and tested in a full-scale FOA prototype. This prototype will enable us to evaluate key aspects of cleanliness and operability. Our first Title II priority for the FOC is to optimize the kinematic mount locations to minimize deflections and induced stress to the cell. We will optimize the cell design based on a detailed analysis of the cell in all operational orientations and based on the details of the optics/cell interfaces.

Target Chamber

The target chamber has the following major subsystems: the vacuum chamber, the neutron/gamma ray shielding, the "first wall," the vacuum systems, and the support structures (Figure 5).

Vacuum Chamber and Neutron/Gamma Ray Shielding

The vacuum chamber must provide the mechanical interface between the target and the building environment, provide a vacuum environment for the target, provide mounting points and supports for the FOAs, satisfy general alignment requirements for the FOAs, and contain target debris. The vacuum chamber must maintain a 10^{-6} Torr vacuum, support DT yields totaling 1200 MJ/y, and accommodate test objects up to 2.5 m in diameter, 7 m long, and weighing up to 4500 kg. It also has to incorporate FOA and diagnostics ports, provide support for the neutron/gamma ray shielding, and be made of low activation material.

The vacuum chamber is designed to be a welded aluminum sphere, with an inner diameter of 10 m (±0.05 m) and walls nominally 10 cm thick. The chamber has 72 FOA ports, 48 of which are used at a time (the configuration depends on whether indirect- or direct-drive illumination is being done). These ports have inner diameters

of 116 cm. There are also 85 diagnostic ports with inner diameters varying from 15 to 70 cm, and a 1.5-m-diam port for studying weapons effects (Figure 5). The aluminum chamber has an outer layer of borated concrete that provides neutron and gamma-ray shielding. The concrete is applied in place over steel rebar tied to the chamber.

The chamber's design takes into account the lateral movement of the FOA due to the rise in target chamber temperature from laser and target energies after a shot. The lateral motion results in a change in the location of the focal point relative to the target building and the target positioner. We determined that the lateral motion is acceptable; for the worst FOA (which is 50° from the pole) the repeating shot sequence with a four-hour shot period results in a lateral motion of 2.5 μm in the two-hour alignment period. For an eight-hour shot period, the motion is 1.2 μm. These motions are only a small portion of the total FOA lateral motion allowed (6 μm). The target chamber temperature may require regulation to thermally control the FOAs and the target positioner.
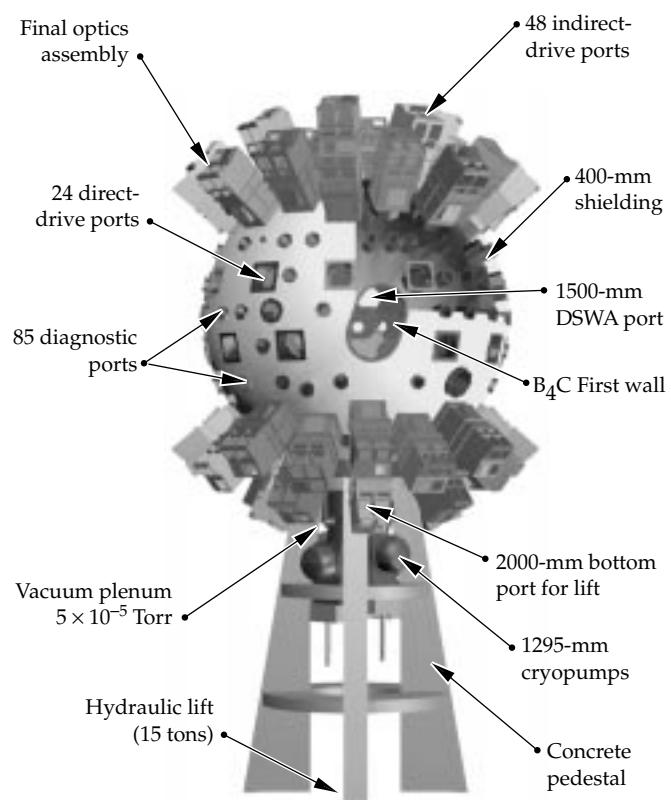
FIGURE 5. The target chamber with its ports and five major subsystems. (40-00-1096-2482pb02)

The elevated temperature has a detrimental effect on the KDP crystal temperature regulation and on the target positioner's thermal stability.

The neutron/gamma ray shielding on the chamber must limit the radiation intensity to personnel in the target building and be made from low-activation materials. The shielding design calls for 40 cm of concrete containing 1% boron to be applied to the exterior of the vacuum chamber. The exterior of the concrete will be sealed with an epoxy paint; no other protective coating is needed. The concrete shield serves a dual purpose: it reduces worker radiation exposures from the chamber and reduces neutron activation of the equipment outside the chamber. Time-motion studies indicate that, three days following a 20-MJ yield, the chamber and shield should contribute <5 mrem/h to the total dose equivalent rate. Although the vacuum chamber will be designed to carry the shield as a dead-weight load, the shield is designed to be self-supporting and to transmit its load to the pedestal. To make the shell self-supporting, three layers of 3/4-in.-diam steel rebar will be attached to the vacuum chamber with welded studs.

Title II Activities

During Title II, we will complete the procurement process for the chamber, detail lateral support attachments and complete their stress analysis, complete details of the plenum attachment to the chamber, evaluate the design consequences of using shielding as a structural member, complete the detail design and specification of shielding and the method of support by the pedestal, and complete the detailed design of the chamber adjusting mechanism.

First Wall and Beam Dumps

The first wall's primary function is to prevent damage to the optics due to ablation of the target chamber. There are several threats to the first wall, including x rays, shrapnel, scattered 3ω laser light, vacuum outgassing, and energetic ions and neutrons. Tests on potential materials indicate that boron carbide (B_4C) is the best overall material for the first wall. It is least removed by x rays, tolerates the scattered 3ω light and may also work as a beam dump. B_4C particles also tend to be blown off optics by laser light without inducing damage, thereby reducing the need to clean the debris shields. B_4C can be applied as a plasma spray on aluminum with low enough porosity to meet outgassing and cleaning erosion criteria.

The first wall will be a mosaic pattern of 348 panels, consisting of eight basic shapes (Figure 6); there are 240 variations on the eight basic shapes. Panels will consist of an aluminum backing plate, plasma-sprayed with B_4C. There are 1/4-in. gaps between panels, and the panels have square laser entrance holes. The gaps will allow for manufacturing and robot placement, but will require flashing in the forms of B_4C strips between panels.

The unconverted light absorbers, or beam dumps, must meet stringent performance requirements (Table 2).
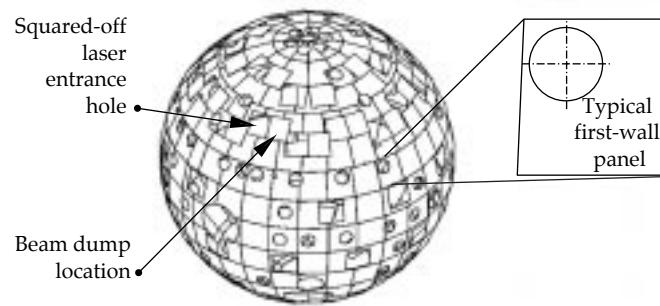
FIGURE 6. The first wall is a mosaic pattern of eight basic shapes. (40-00-1097-2274pb01)

TABLE 2. Performance requirements for unconverted light absorbers.

Area	Criteria	Set by
X-ray, 1ω and 2ω response	<0.3 g particulate and condensable mass removal from first wall for <5 MJ shot, and <2 g of mass removal for >5 MJ shot (total for first wall and beam dumps)	Debris shield laser damage
Absorbance of 1ω and 2ω light	<1% collimated light back up the beam path, 80% absorbance desired, and transmission of 0.03 J/cm^2 or less to back surface of beam dump	Ghost reflection requirements and ablation of target chamber, upstream amplifier components
3ω response	Survive full-energy 3ω shot without catastrophic failure	Life-cycle cost and secondary damage
Shrapnel response	One-year lifetime	Debris shield laser damage and life-cycle cost

The average fluence of 14 J/cm^2 on the beam dump depends on an overlap of the first- and second-order images. The 1ω contributes from 2.3 to 11.9 J/cm^2 to this fluence, and the 2ω ranges from 0.3 to 1.7 J/cm^2. The peaks, caused by beam modulation and inefficient conversion at the edges of the beam, are 40 to 50 J/cm^2 for 1ω and 12 J/cm^2 for 2ω. The baseline design for the beam dumps consists of louvered B_4C panels in boxes with Teflon film covers. There will be one beam dump for each set of four beamlines, approximately 90 cm × 90 cm, when full-beam steering is possible (Figure 7a). The louvered B_4C will be plates of boron carbide that absorb laser light. The plates will be angled at 60° to the incoming laser, and ablated material will be deposited on the backs of adjacent louvers (Figure 7b). The Teflon film cover will transmit laser light as well as contain the ablated material. These covers will be mounted on rollers to allow replacement after single shots.
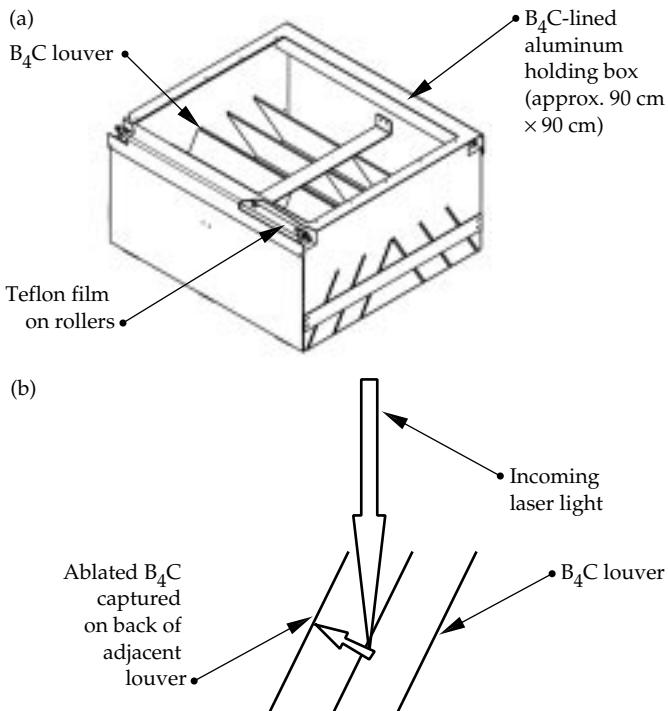
FIGURE 7. (a) Louvered B_4C concept for beam dumps. (b) Capture of ablated B_4C. (40-00-1097-2275pb01)

Title II Activities

Title II activities for the first wall include testing to determine the acceptable thickness and porosity of B_4C. We will assess the shrapnel threat, minimize the cost of plasma-sprayed B_4C while increasing its performance, and prototype a full-scale panel. For the beam dumps, we will conduct further testing to determine

which design is best: B_4C louvers and Teflon film or absorbing glass. We will also prototype a beam dump assembly, possibly on Nova.

Vacuum System

The vacuum system for the target chamber performs two major functions. It evacuates the chamber to the pressure required for target shots, and it evacuates the FOAs before their isolation valves open. It must also be able to handle off-normal events, such as recovery from a ruptured cryogenic tritium-filled target. It must be capable of pumping down the chamber pressure to $< 5 \times 10^{-5}$ Torr for noncryogenic targets and $< 5 \times 10^{-6}$ Torr for cryogenic targets. It must bring the chamber from atmospheric pressure to 5×10^{-5} Torr in less than two hours. It must also use pumps and components to prevent oil backstreaming and minimize oil input to the tritium processing system. The vacuum system must minimize vibration input to the target chamber, and cryogenic pumps and valves must fit onto the chamber plenum.

Figure 8 shows the location of the subsystems that form the vacuum system. An oil-free roughing pump will pump 2700 L/s, using cascaded Roots blowers for pressures between 760 and 10^{-3} Torr. The final stage of the roughing pump will be located in the target bay at the –1.1-m level to minimize conductance losses. Other stages, located in a sheltered utility pad, will have pumps in parallel. Three turbodrag pumps—each capable of pumping 1500 L/s at pressures of 1 to 10^{-7} Torr—will provide intermediate pumping between the rough and high vacuum, if required. Four cryogenic pumps, a net pumping speed of 180,000 L/s of water vapor from 0.2 to 10^{-7} Torr, will be the primary high-vacuum pumps. Each pump will use 4 gal/h of liquid nitrogen. The vacuum system uses three at any one time, leaving an extra for maintenance or regeneration. The four aluminum cryogenic pump gate-valves have 48-in. apertures. Four oil-free off-normal roughing
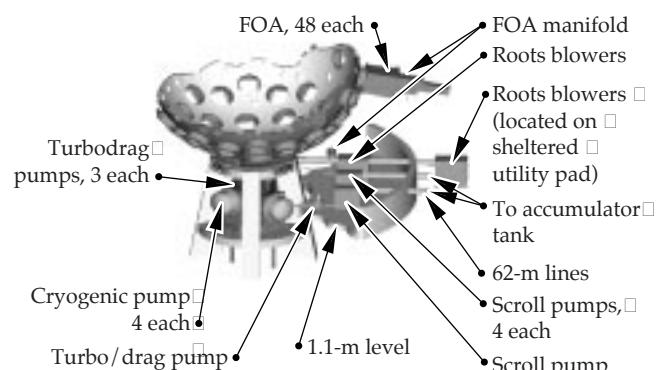
FIGURE 8. Locations of the vacuum system equipment for the target chamber. (40-00-1097-2276pb01)

pumps, each of which pumps 8 L/s from 760 to 10^{-3} Torr, will be used to evacuate the chamber, FOAs, and/or diagnostic tubes in the event that the total pressure rises to $>10^{-2}$ Torr. The four pumps are in parallel for reliability.

The subsystems also include a number of total and partial pressure gauges, including convectrons (covering the range from 760 to 10^{-3} Torr) located on the chamber, pumps and selected piping, a capacitance manometer (1000 to 0.1 Torr) located on the chamber, ionization gauges on the chamber and pumps (10^{-2} to 10^{-7} Torr), and a partial pressure analyzer (760 to 10^{-7} Torr) that provides an option to differentially pump through a variable conductance valve to the chamber. There are also scroll and turbodrag pumps in series, which help regenerate the cryopumps The gases from the regeneration cycle are sent to an accumulator tank for tritium processing. A chamber leak detection system can detect a leak rate as low as 10^{-3} atm-cc/s and can detect leaks at pressures from 1 atm to 10^{-7} Torr. There is a similar system on the FOA ports to detect leaks. The target area vacuum systems and FOA vacuum isolation valves will have real-time controls.

This vacuum system design meets the functional requirement of 5×10^{-5} Torr in two hours, with a half-hour margin. The design is governed by the use of parallel pumps to prevent single point failures. None of the pumps use oil, to avoid oil contamination of the chamber and tritium contamination of the oil. The pressure measurement sensors and locations will allow enhanced troubleshooting capability.

Title II Activities

Our Title II priorities for the vacuum system involve defining the gas loads more accurately, refining the equipment requirements and specifications, refining vacuum and venting aspects of the FOAs, and producing detailed component layout drawings as well as detailed pipe routing drawings.

Mechanical Structures

Two types of structures—the pedestal and the lateral supports—support the vacuum chamber. The pedestal must support a vertical static load of ~650 tonnes (t), remain elastic under a seismic event, provide a center opening that is at least 1.85 m in internal diameter and extends ~3 m high, and provide access where the vacuum system connects to the cryopump and turbo-pump systems. The lateral supports must provide coupling between the chamber and the passive damping system and minimize the stress on the chamber wall. Figure 9 shows the pedestal design configuration. The pedestal is made of reinforced concrete and is tied-in to the LTAB floor and support floors.
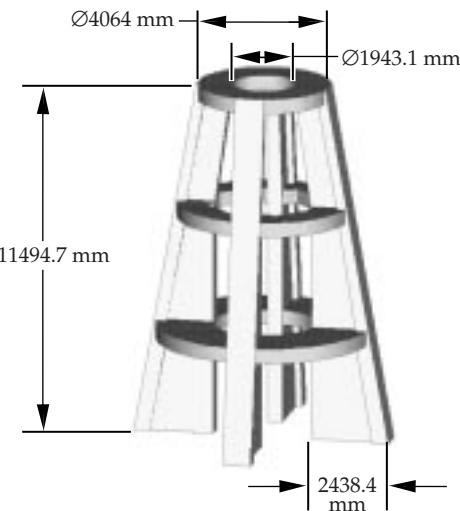
FIGURE 9. Pedestal design configuration. (40-00-1097-2277pb01)

Title II Activities

The lateral support system will be designed during Title II. We plan to complete the preliminary stress analysis by January 1997 for inclusion in the vacuum chamber wall thickness requirements, and complete the detail design by June 1997 for inclusion in the vacuum chamber manufacturing process.

Target Positioner

The primary functions of the target positioner are to mount, insert, position, and maintain targets at specified positions and within specified tolerances for illumination by the laser beams. An identical positioner is also required to mount, insert, and position the target alignment system for coordination of target positioning and laser aiming in concert with the chamber-center reference system. Table 3 shows the most significant requirements for the positioner. In brief, it must have precision location capability at the end of a very long cantilever. It must extend a target assembly (up to 50-cm diam and 200-kg mass) 6 m into the chamber, and position it with ~1-μm accuracy. It also needs to hold the assembly stable to within ±6 μm. The positioner must operate in an extreme environment that includes ultraviolet, neutron, and x-ray radiation. Figure 10 shows the overall design of the positioner. Figure 11 shows the forward boom section entering the target chamber; Figure 12 shows the boom tip, including the angular positioning mechanisms and the blast mitigation ablator (an aluminum foam disc). The boom will be made of graphite fiber-reinforced carbon (GFRC), with a diameter of 520 mm. The outer surface will have an opaque shield to provide protection from ultraviolet light. The boom will be filled with borated polyethylene to protect the regions

TABLE 3. Most significant requirements for the target positioner.

Most significant SSDRS	
Parameter	Requirement
Positional accuracy	6 µm
Stability (vibrational, thermal)	6 µm
Rotational resolution	1 mrad
Translational DOF	3
Rotational DOF	2
Target assembly mass	Up to 200 kg
Target assembly size	Up to 2 m long × 500 mm dia
Environment	X-ray, neutron, thermal, vacuum
Operational	Minimize adverse effects on debris shields, vacuum system
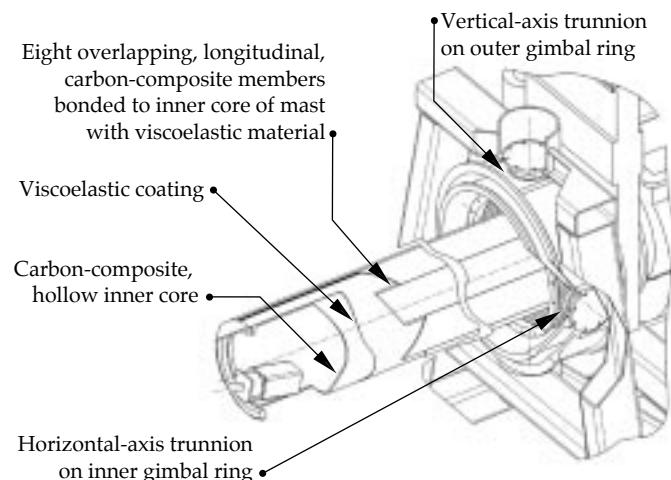
FIGURE 11. Forward boom section of the target positioner.
(40-00-1097-2279pb01)
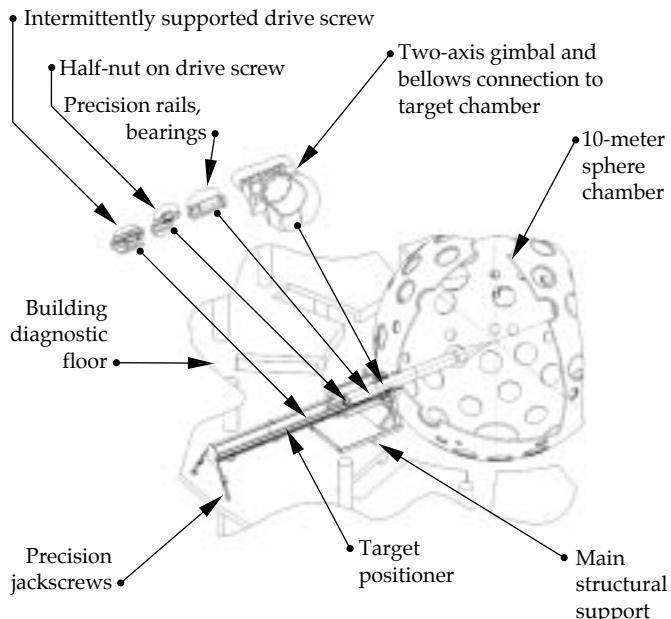
FIGURE 10. Target positioner design and components.
(40-00-1097-2278pb01)

FIGURE 12. (a) Boom tip angular positioning mechanisms.
(b) A typical (noncryogenic) target assembly, with a blast mitigation/ablator foam disc in place. (40-00-1097-2280pb01)

outside the positioner's open valve from neutrons. "Barrel staves" bonded by viscoelastic material to the boom will provide passive vibration damping. The design includes two-axis articulation aft of the target assembly mount for angle adjustments (Figure 13). The portion of the target assembly that is <100 mm from the target will be protected from the shock effects of cold x rays and debris by a shield consisting of a <1-mm B_4C ablative layer over an aluminum foam pad. These shields

are throw-away items inserted in holders between the targets and the structure of the target assemblies.

Title II Activities

The target/target alignment sensor positioner design is fairly mature. Our Title II activities for the positioner include selecting precision components from among suitable alternatives, completing the detailed design,
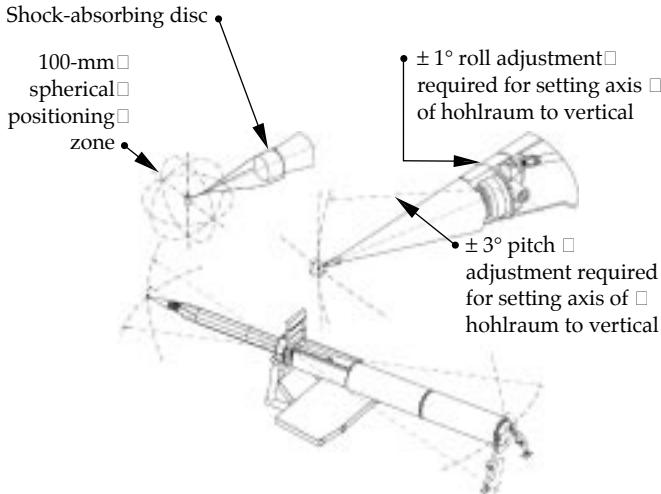
FIGURE 13. Two-axis articulation produces displacement and angulation. (40-00-1097-2281pb01)
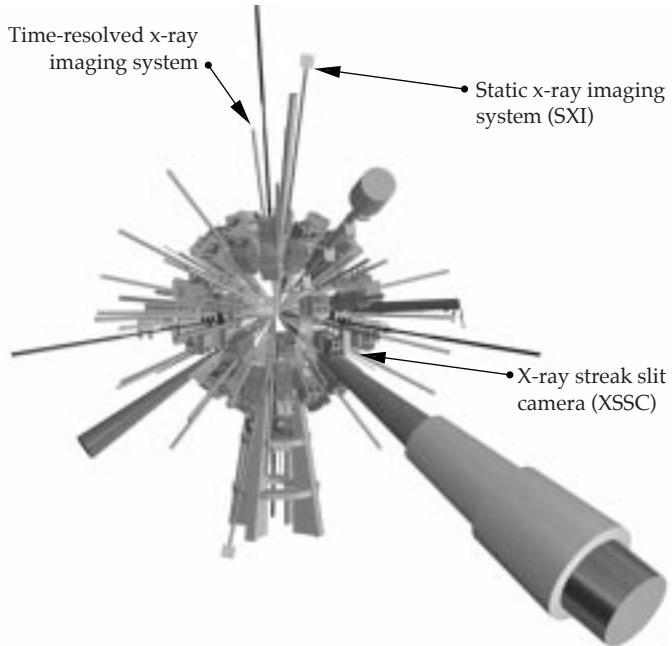
FIGURE 14. Location of diagnostics on the target chamber. (40-00-1097-2282pb01)

and designing shielding against neutrons and gamma-rays for the retracted target alignment sensor. We will also perform structural, vibration, and thermal analyses, and perform ablation shock-loading experiments on prototype shock-absorbing discs to verify behavior under a NIF-like impulse.

Target Diagnostics

The suite of target diagnostic systems includes optical, x-ray, and nuclear diagnostics required to support the NIF experimental plan. This experimental plan includes laser system performance and verification tests on target, ignition, and weapons physics experiments; radiation effects tests; and other applications and tests as required. As of Title I, there are 20 diagnostic experiments identified at 36 locations around the target chamber. Approximately 90 individual detectors will be needed for these experiments. The types of signals to be recorded and processed include images from gated imagers and streak cameras, high-speed transient signals, and single value measurements. Figure 14 shows the preliminary layout of the identified diagnostics and other components on the target chamber. See "Placing Diagnostics on the Chamber" (next page) for the general procedure used to determine the location of these instruments. In this section, we discuss the three target diagnostics whose design is part of the construction project: the time-resolved x-ray imaging system, the static x-ray imaging system, and the x-ray streak slit camera. These three diagnostics are required for the first phase of the experimental plan, laser system performance, and verification tests on target. We also describe the design for the diagnostic instrument manipulator and briefly address the other diagnostics which are not part of the NIF construction project.

The time-resolved x-ray imaging system (TRXI) provides very high frame rate images of the target. This information will initially be used to determine beam pointing, beam focusing, and spot motion performance of the laser. These functions are part of the NIF's laser system performance and verification tests. The TRXI is similar to the gated x-ray imagers (GXI and FXI) currently used on Nova. The proposed TRXI, shown in Figure 15, provides 5- to 10-µm spatial resolution, 50- to 100-ps temporal resolution, a sensitivity range to x rays with energies 3 to 10 keV, a 300- to 3000-µm field of view, a dynamic range of 100, better than
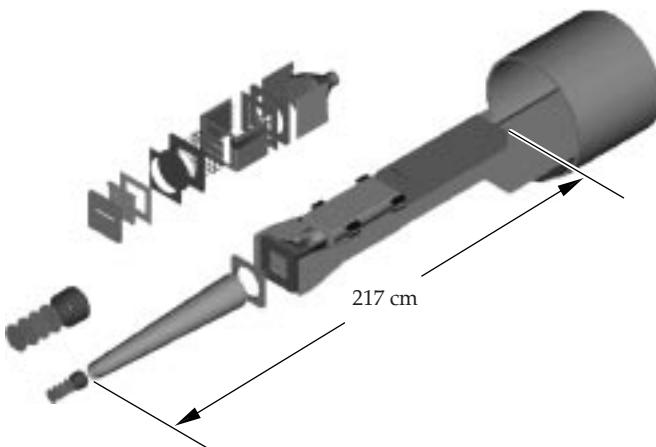
FIGURE 15. Design of the time-resolved x-ray imaging system. (40-00-1097-2283pb01)

Placing Diagnostics on the Chamber

To determine where the nearly 90 detectors should be placed on the target chamber, we began with the layout developed for the conceptual design review. We then determined the size and position requirements for each diagnostic instrument, positioned the diagnostic on the chamber, and checked for interferences with other systems and structures. If there was a conflict, we moved the diagnostic when possible. If moving the diagnostic was not possible, we changed the structure's design. We also located extra ports, as space permitted, to accommodate possible future experiments. During this process, we had to take into account the 72 laser beam ports, the location of beam dumps on the inside of the target chamber, and the required minimum spacing between the various components mounted on the target chamber. Such components include the final optics assemblies, target positioner, target alignment system, and the diagnostic ports. Several examples of the procedure used to determine port positions follows.

Ports were usually arranged in pairs, one directly on the opposite side of the chamber from the other. This is so the opposite ports may be used for alignment purposes. The target positioner had the requirement of being located at the waist. A position halfway between two direct drive laser ports was selected. A last example is the neutron spectrometer (NS), which is a very large diagnostic. Its envelope is a cone, starting at the target chamber center. This cone is 90 cm in diameter at the target chamber wall and 40 m long. It is about 7.2 m in diameter at the end. The NS was required to angle down beneath the ground for radiation shielding purposes. The position selected puts the NS pointing down at about 26° and pointing out between the switchyard and the diagnostic building.

All in all, we have positioned 105 ports—excluding the laser beam ports—on the target chamber. This includes two for the target positioner, four for the target alignment system, one side access port for weapons effects uses, 48 assigned diagnostic ports, and 50 unassigned diagnostic ports.

50-μm alignment capability, compatibility with the diagnostic instrument manipulator, and the ability to operate in the NIF EMI/EMP and radiation environment. The proposed TRXI generates up to 30 images, with 5 images/strip for 6 strips, a magnification from 2 to 20, and continuous temporal coverage of 4.4 ns (or 733 ps/strip). The TRXI has variable gain and filtering, a charge-coupled device (CCD) readout with a film option, and computer-controlled electrical functions.

The x-ray streaked slit camera (XSSC), also required for laser system performance and verification, will make beam synchronization measurements on target. Similar to the streaked slit camera used on Nova, the XSSC is designed to produce time-resolved streak images of target emissions with energies 0.1 to 10 keV. It must have spatial resolution of 500 μm, a temporal resolution of 10 ps, and a field of view of 2 cm to diagnose the laser beam's synchronization at the target. The XSSC will also be used to measure beam smoothing, x-ray-pulse wave shape, and beam spot movement. The spatial and temporal resolutions will be upgraded for ignition and weapons physics experiments. Figure 16 shows the various components of the XSSC.

The static x-ray imager (SXI) provides time-integrated beam pointing and spot size measurements. It will operate on all shots, viewing both ends of the hohlraum. The SXI is required to produce time-integrated images of
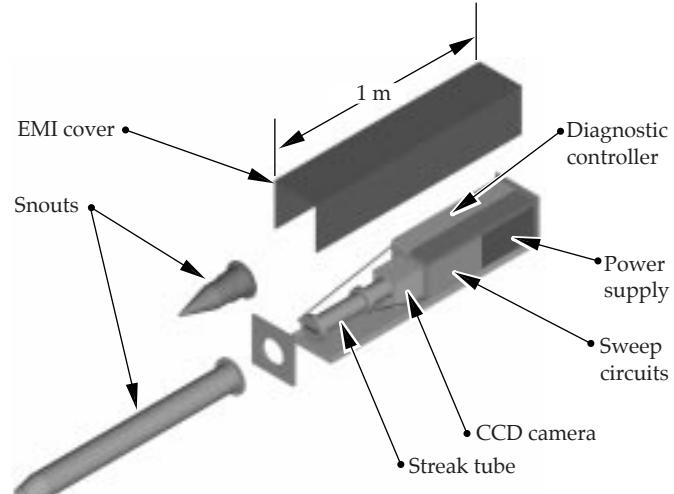
FIGURE 16. Design of the x-ray streaked slit camera. (40-00-1097-2284pb01)

x-ray emissions with energies from 2 to 3 keV and with a spatial resolution better than 25 μm. The field of view of the SXI will be at least 1 cm. The SXI needs to be located within 20° of the chamber's poles. Figure 17 shows the basic setup for the SXI.

The ignition and weapons physics diagnostics as of Title I are listed in Table 4. These diagnostics are not part
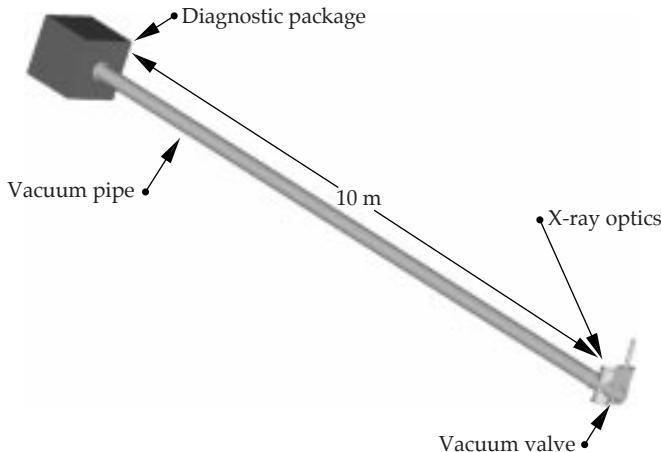
FIGURE 17. Design of the x-ray imager. (40-00-1097-2285pb01)

TABLE 4. Ignition and weapons physics diagnostics.

Soft X-Ray Imaging System (SXRI)

Soft X-Ray Power Diagnostic System (SXPD)

X-Ray Power Diagnostic (DANTE)

Passive Shock Breakout Diagnostic System (PSBO)

Active Shock Breakout Diagnostic System (ASBO)

Filter Fluorescer Diagnostic System (FFLEX)

Total Neutron Yield Diagnostic System—High (NYH)

Total Neutron Yield Diagnostic System—Low (NYL)

Neutron Time-of-Flight Diagnostic System (NTOF)

Neutron Imaging System Diagnostic System (NI)

Full Beam Laser Backscatter System (FABS)

Neutron Spectrometer Diagnostic System (NS)

Bang-Time and Burn Duration Diagnostic System (BTBD)

Neutron Coded Aperture Microscope Diagnostic System (NCAM)

Gamma Ray Spectrometer Diagnostic System (GRS)

Weapons Effects Experimental System (DSWA)

package to this port. The maximum size of this diagnostic package is set at 2.6 m high, 2.8 m wide, and 7 m long. The maximum weight is 4500 kg.

The diagnostic instrument manipulator (DIM) inserts and retracts a variety of instruments into and out of the target chamber (Figure 18). It must operate correctly when installed in any standard diameter diagnostic port and provide precision radial positioning, pointing, and alignment capabilities. The major design requirements for the DIM include a radial positioning accuracy of $<\pm0.25$ mm, a translational pointing accuracy of ±25 µm at target chamber center, and an angular pointing range capability of $\pm3°$ at the mounting point on the chamber wall. The DIM must also be able to accommodate a diagnostic package that is 300 mm in diameter, 3000 mm in length, and a maximum mass of 125 kg. The DIM must be completely retractable from the target chamber, include the appropriate utilities, and have a clear optical aperture of 100 mm through its center.

The data acquisition system is part of the overall NIF Integrated Computer Control System. For a general discussion of the type of data acquisition system (DAS) used throughout NIF, see "Integrated Computer Control System" in this *Quarterly* (p. 198). The Target Diagnostic DAS has the requirement to be able to handle both unclassified and classified data. The box "Dealing with Classified Data" on facing page discusses some of the issues involved with handling classified information generated by classified target area experiments.

Title II Activities

In Title II, we will finalize design to support target diagnostics, develop a prototype of the DIM and complete designs for the TRXI, XSSC, and SXI systems.

of the NIF project; however, NIF's design must allow for their installation at a later date. To fulfill this "not to preclude" requirement for these diagnostics, we collected preliminary physics performance requirements, assigned dedicated ports on the target chamber, specified stayout zones, and if required, modified the building structure to permit future installation.

Similar accommodations were made for weapons effects experiments. For these experiments, we provide a 1.5-m-diam port on the target chamber and provide capabilities to receive and transport a large diagnostic

FIGURE 18. Design of the diagnostic instrument manipulator. (40-00-1097-2286pb01)

DEALING WITH CLASSIFIED DATA

The NIF is required to be able to conduct unclassified and classified experiments. The data acquisition system (DAS) for the target diagnostics is being designed to handle both types of data. The proposed design of the target diagnostics DAS has preliminary approval to handle both types of data. The following guidelines lay the foundation for the basic design. Experiments are divided into two groups: those that are always unclassified and those that are sometimes classified. The diagnostics that are always unclassified are handled with the standard method. For those diagnostics that may be classified, the DAS has a separate cable tray system that is lockable and only worked on by Q-cleared personnel. All computers will be designed with removable disk systems, and chassis will be provided with seals to indicate tampering. A special switch will be used to connect the target area DAS to either the unclassified control system or to the classified supervisory data acquisition system. Portions of the target area will be able to "swing" back and forth between an open or a limited-access area. The main classified control room is the only area in the NIF that will always be classified and the only area where classified conversations will be permitted.

Target Area Structural Supports

The target area structures provide the structural mounting and support for the mirrors, diagnostics, target positioner, and target chamber. The structures must provide structural support and vibration damping, and maintain stability for a two-hour interval after the beam alignment and before a laser shot. The structures must also provide lateral structural support to the target chamber and be constructed from low-activation materials.

We also must provide platforms and catwalks and shielding for the diagnostics. We provide thermal stability by a horizontal flow of air from the heating, ventilation, and air conditioning system (HVAC) at each floor. Vibrational stability and accessibility in the mirror rooms is provided by structural concrete floors, radial ribs, and columns. Finally, lateral supports provide passive damping and seismic restraint. Figure 19 shows the various structural supports for the target area.

Among the components of the structure are mirror structures, beam tubes, guillotines, passive damping structures, and, finally, catwalks and platforms. The design for each is briefly discussed below.

The mirror structures must support the mirror structure enclosures on kinematic mounts, provide stability to ±0.7 µrad rotation and ±0.28°C, and allow accessibility for maintenance. The structures are welded from square aluminum tubing, 6 in. on a side and 0.500 in. thick, into an open space-frame structure with mounting plates. These structures come in various sizes with different attachments for the LM6, LM7 and LM8 mirrors. Figure 20 shows a typical mirror structure with transport mirror modules.
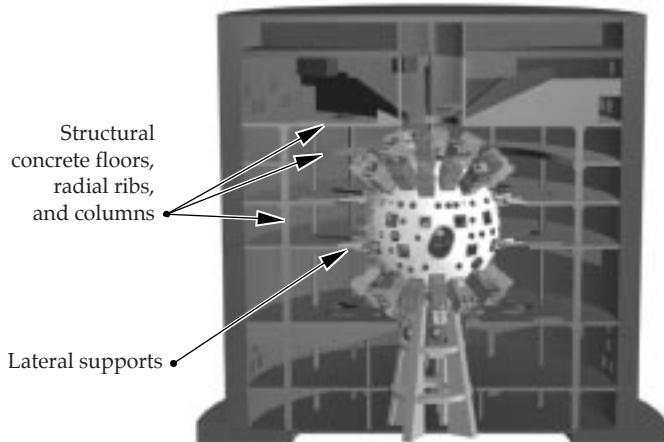
FIGURE 19. The target area structural supports.
(40-00-1097-2287pb01)
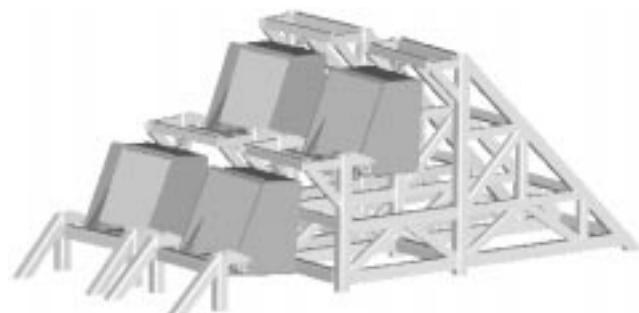
FIGURE 20. Typical mirror structure with transport mirror modules.
(40-00-1097-2288pb01)

The beam tubes must maintain argon gas at a positive pressure of 250 Pa and resist damage from stray light. The tubes must maintain a Class 100 clean-room environment, be made of low-activation materials, and provide accessibility to adjacent or attached equipment. There are three kinds of tubes: one for 1×1 beams, and two for 2×2 beams. The retractable, 1×1 beam tubes are located at some mirror enclosures and at FOAs. The retraction allows access for removing optics enclosures for maintenance. One variety of 2×2 beam tubes, used throughout the switchyard and target area, has rigid, flanged ends; the other, retractable for equipment access, is located in mirror halls on or near floors. All of the beam tubes are made of aluminum or Lexan. The rigid tubes require a flexible section for alignment and removal. Rigid tubes have aluminum end flanges and use O ring seals, and have painted external surfaces. The treatment of the internal surfaces will be decided in Title II. There is also an internal aluminum shield for 1ω light. The retractable beam tube sections have flexible outer sleeves to cover the sliding surfaces and keep them clean. Figure 21(a) shows the beam tubes located between the FOAs and the mirror room floors, and Figure 21(b) shows a 2×2 section connecting to a 1×1 section.

Guillotines cover and seal the optical surfaces during maintenance. They must seal gas pressures of 250 Pa, maintain clean-room level 50 cleanliness, and be easily removed by one person. The exposed surfaces that remain in the beam enclosure must be resistant to 1ω light. There are two types of guillotines: (1) a single-beam type for interfaces between an IOM and a beam tube as well as between a mirror enclosure and a beam tube, and (2) a 2×2 beam type for retractable sections near the target room wall. The 1×1 guillotine is made of stainless-steel removable plates and aluminum guide rails. The assembly consists of two nested sealing plates; the large plate seals off the beam tube, and the nested plate seals off the optic assembly. The nested plates are held together by a locking cam. For the 2×2 guillotines, a thin film of kapton covers the beam tube opening. The sealing surface is formed by an inflatable gasket pressing on this film. The kapton film is on rollers on each side of the array; the roll of film has alternating panels of solid film and panels with holes for passing the laser beams.

The passive damping structures connect the target area floors to the target chamber and provide stability and seismic restraint for the target chamber, while reducing the vibration levels to below ambient levels. There are two truss structures—one attaches to the target chamber, the second attaches to the building floors at two levels near the target chamber's waist [Figure 22(a)]. Each truss supports a "sandwich" of visco-elastic material between steel plates [Figure 22(b)].

The catwalks and platforms must support a dead load of 10 lb/ft^2 and a live load of 150 lb/ft^2. These steel structures provide access for equipment installation and maintenance, operational flow paths, and safety egress. Many levels of platforms will be required to access the FOA, diagnostics, and mirror enclosures.

Title II Activities

During Title II, we will work with the conventional facilities to refine the final design of the columns, ribs, trusses, and HVAC ducting. Other activities include optimizing the passive damping schemes, refining support structures to reduce costs, and testing a prototype guillotine. We will also perform thermal analysis for the target area building, an acoustic vibration analysis, and a total vibration analysis at mirror locations.
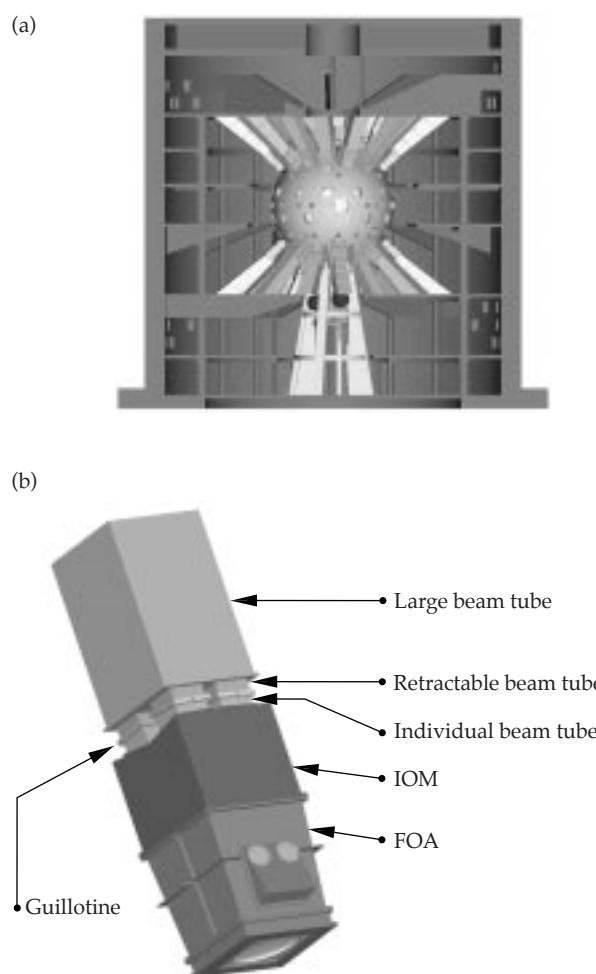
FIGURE 21. (a) Beam tube location between the FOAs and the mirror room floors. (b) A 2×2 section connecting to a retractable 1×1 section. (40-00-1097-2289pb01)

(a)

(b)

Visco-elastic material

Truss structure

Target area building floors
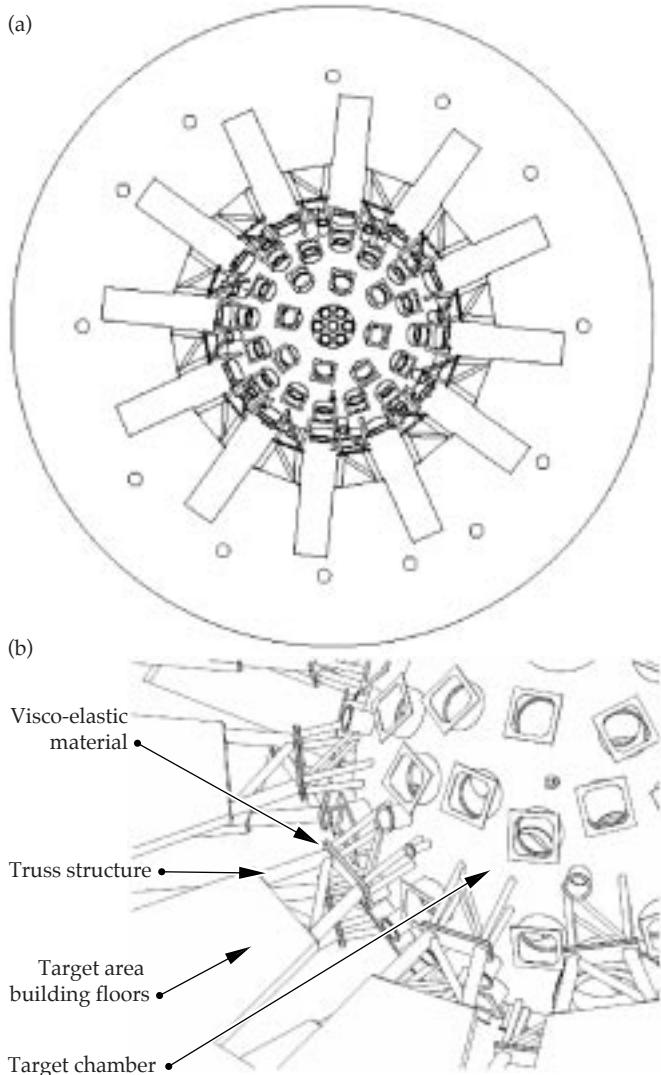
Target chamber

FIGURE 22. (a) The passive damping structures connect the target area building to the floors of the target chamber, a view from the top of the chamber. (b) Truss structures support a sandwich of steel plates and visco-elastic material. (40-00-1097-2290pb01)

For more information, contact
Victor A. Karpenko
System Engineer for Target Area Systems
Phone: (925) 422-9256
E-mail: karpenko1@llnl.gov
Fax: (925) 424-3763

LASER CONTROL SYSTEMS

E. Bliss

D. Davis

F. Holdener

T. Salmon

J. Severyn

R. Zacharias

*T**he laser control systems for the NIF align the laser beam, diagnose the beam, and control the beam's wavefront. Accomplishing these tasks requires approximately 12,000 motors and other actuators, 700 cameras and other detectors, and 192 wavefront sensors and deformable mirrors. Many of the systems perform multiple functions and share components to reduce costs and space requirements. All laser control systems have completed Title I designs and are proceeding with prototyping and detailed design.*

Introduction

System control components are located throughout each beamline as illustrated in Figure 1. Each of NIF's numerous laser control systems serves one or more of the following three functions: laser beam alignment,

12,000 motors & actuators
700 cameras & detectors
2,000 closed loops

Target alignment sensor
Pulse sync system
Final optics assembly
Chamber center ref. system
TSF diagnostics tower
TSF pinhole & alignment tower
CSF tower
LM3
LM1
LM2
PAM
Deformable mirror
Output sensor
Input sensor
Precision diagnostics
Optics inspection system
3ω
1ω

Alignment
Diagnostics
Wavefront

FIGURE 1. Major beam control components for a single NIF beam-line.   (40-00-1097-2260pb01)

beam diagnostics, or wavefront control. We designed many of the control systems to perform more than one function, in order to meet NIF's cost and space constraints. For instance, the input sensors both align and diagnose the initial laser pulse.

The specific requirements for alignment include positioning the 192 beams within the 40-cm apertures of the laser components, focusing them accurately through the far-field pinholes of the amplifier chain spatial filters, and delivering them to the precise locations specified on the target. All alignment functions are accomplished automatically by recording video images of reference light sources (see "Fiber-Optic Light Sources" on facing page) and beams, calculating what adjustments will achieve the desired relative positions of the imaged objects, and sending the corresponding commands to system motors.

Requirements on the laser diagnostic systems are to measure the beam energy, power versus time, and the near-field transverse profile. The detectors that monitor these parameters are calorimeters, fast photodiodes, streak cameras, and charge-coupled device (CCD) video cameras. Requirements for accuracy and reliability are very high.

Wavefront systems measure optical aberrations on the laser output beams and use a deformable mirror in the four-pass amplifier of each beamline to compensate. The resulting improvement in beam quality leads to higher frequency conversion efficiency and provides better focusing characteristics in the target chamber.

For the sake of clarity, this article is organized by function. Thus, the input sensor components that handle alignment appear in the laser beam alignment section, whereas the input sensor's diagnostic components appear in the beam diagnostics section. Discussion of the front-end processors, which are another important element of laser control, appears in "Integrated Computer Control System" (see p. 198).
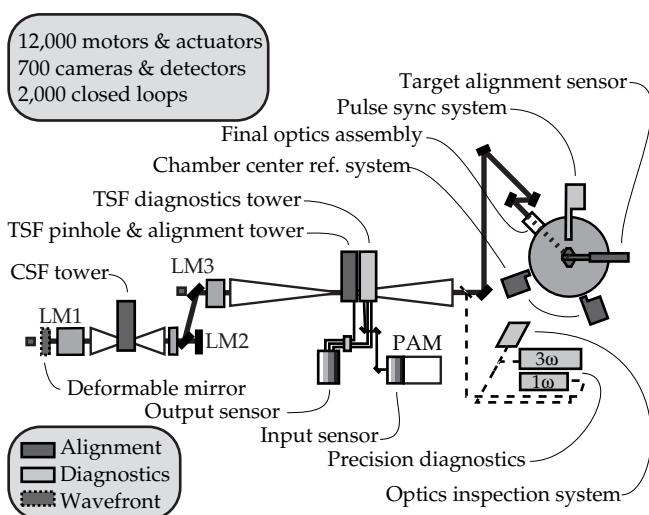
Fiber-Optic Light Sources

Fiber optics are important to NIF's beam control systems, both in distribution networks that transport light from auxiliary lasers to multiple locations in the beamlines and in fiber bundles that transport light from sampling points in the beamlines to detectors in sensor packages. In the former case, depending on what optics are combined with them, fiber sources can provide full-aperture alignment or optics inspection beams, alignment references for beam centering, or diffraction-limited wavefront reference beams. The table summarizes the location, function, and number of NIF light sources.

Summary by location and function of the light sources required by the NIF Title I design.

Location (see Figure 1)	Function	# Locations	Channels per laser	# of lasers
Input sensor	Alignment, optics inspection, and wavefront control beam	48	16	4
LM1	Reference for beam centering	192	256	2
LM3	Reference for beam centering	192	256	2
TSF alignment tower	Reference for beam pointing and wavefront	192	128	2
TSF diagnostic tower	3ω target alignment optics and inspection beam	192	56	4
Final optics assembly	Reference for beam centering	192	256	2
Total		**1008**		**16**

The figure shows a generic fiber launch platform for NIF alignment light sources. This design derives a large number of channels from a single laser by dividing its power many ways while still meeting the power requirements of particular light source functions. The output power from a laser with a favorable cost per watt value is typically too large to couple directly into an optical fiber. Therefore, the power is first divided several times by small dielectric-coated beam-splitters. Then each beam is focused into the input leg of a fiber-optic splitter that also incorporates a monitoring channel for confirming the proper alignment and power level. The net efficiency of the distribution process is such that about 40% of the laser output is ultimately delivered to light source destinations.
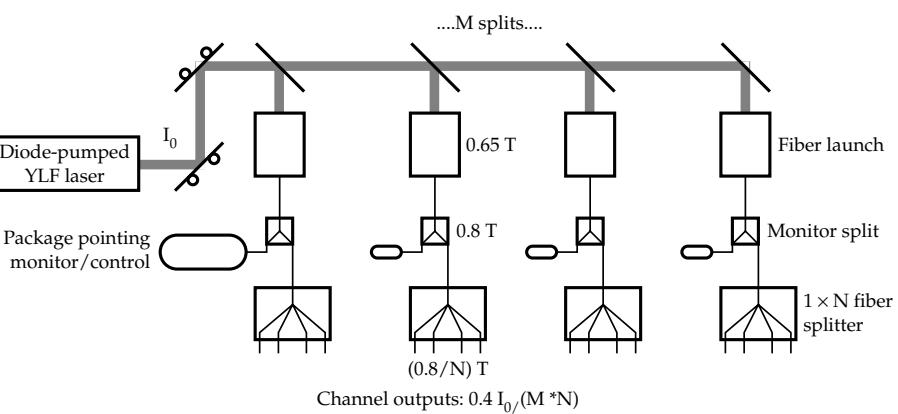
Schematic illustration of a NIF fiber-optic light source distribution platform.
(40-00-1097-2243-pb01)

Title II Activities

In Title II, our priorities are to characterize and choose specific fibers for each light source, based on transmission, power limits, and speckle pattern uniformity and stability. We plan to prototype a 3ω 60-channel fiber-optic fanout, determine power limitations of the splitters, integrate fiber-optic switching requirements into the design, and design and prototype a stable fiber-optic-launch breadboard.

Laser Beam Alignment

In NIF, laser beam alignment is performed in the following areas:

- Input sensor.
- Spatial filter towers.
- Output sensor.
- Target area.

We discuss the design and Title II activities of the alignment components in each of these areas below.

Input Sensor Alignment Functions

The input sensor is located at the output of the preamplifier module (PAM) of the optical pulse generator. For alignment purposes, the input sensor must measure beam pointing and centering, provide alignment references, and provide a beam for alignment through the rest of the system. The sensor must monitor the output at three points within the PAM: the regenerative amplifier, the smoothing by spectral dispersion (SSD) unit, and the multipass amplifier (for the design of these components, see p. 132). The optical design for this alignment system was driven by three factors: (1) resolution and field-of-view requirements, which are directly related to performance of the sensor's function; (2) cost, which limited the number of optical elements and control points; and (3) space, which required that the sensor package fit within the transport optics design footprint. Figure 2 shows isometric views of the multipass and regen sides of the input sensor.

The sensor includes a CCD camera that measures both the near-field and far-field intensity profile of the

FIGURE 2. Isometric views of the input sensor for the (a) regen side and (b) multipass side. NF and FF mean near field and far field, respectively. (40-00-1097-2244pb01)
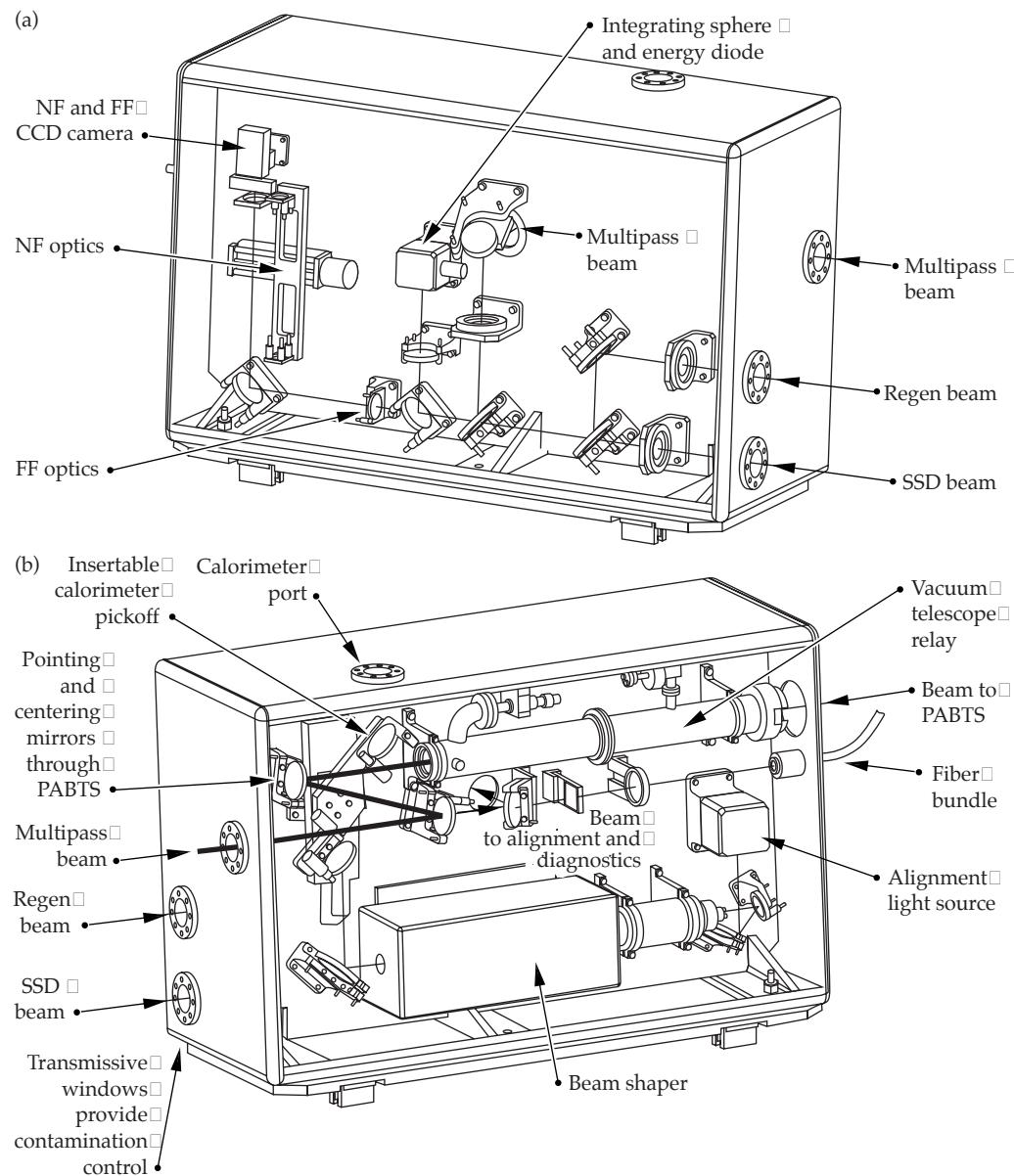
beams. For the far field, the camera measures beam pointing and provides a pointing reference for the PAM control points. Figure 3(a) shows the Title I far-field optical design, which meets all of the performance requirements. The same camera is used to produce a near-field image for beam-centering alignment. We had

to design this camera to perform its near-field imaging without disrupting the far-field pointing reference. In other words, we had to add insertable lenses to the fixed far-field lens element and camera. Figure 3(b) shows the near-field camera design.

The continuous-wave (cw) alignment light source shown in Figure 2 is used to align the rest of the system. It provides a beam of the same wavelength as the regenerative amplifier (regen) beam. Although the regen beam itself can also be used, it is not always available between shots, and then only at the rate of one pulse per second. The cw alignment beam goes through the input-sensor beam shaper, where it is shaped into a 22.5-mm-square beam.

Title II Activities

In Title II, we will add a fixed centering reference behind the first input-sensor mirror and reoptimize the input-sensor design to match the anticipated evolution of the PAM and the preamplifier beam transport system (p. 136) layout. Finally, we will complete detailed drawings for fabrication.

(a)

768 mm

2000 mm

Positive lens element

Input beam

Pupil plane

(b)

Beam representation

Image plane

Imaging representation

CCD camera

Far-field lens

Near-field lenses

FIGURE 3. (a) The far-field camera design for the input sensor includes a biconvex, 50.8-mm-diam singlet lens. The 6.6-mrad field of view is defined by the active area of the CCD. (b) The near-field camera design uses the far-field optic, as well as three additional spherical biconvex lenses. Inserting and controlling these lenses does not disturb the far-field system. For this function, the field of view is 34 × 34 mm (50% larger than the actual beam), and the object plane is the preamplifier beam shaping aperture (see p. 135).   (40-00-1097-2245pb01)

Spatial Filter Tower Alignment Functions

The spatial filter towers are line-replaceable units (LRUs) that are installed from above at the center of the cavity spatial filter (CSF) and transport spatial filter (TSF) (Figure 4). These towers are complex structures that serve multiple functions, as shown in Figure 5. They provide a stable base for injection optics, diagnostic optics, pinhole assemblies, and beam dumps. Figure 6 shows the general
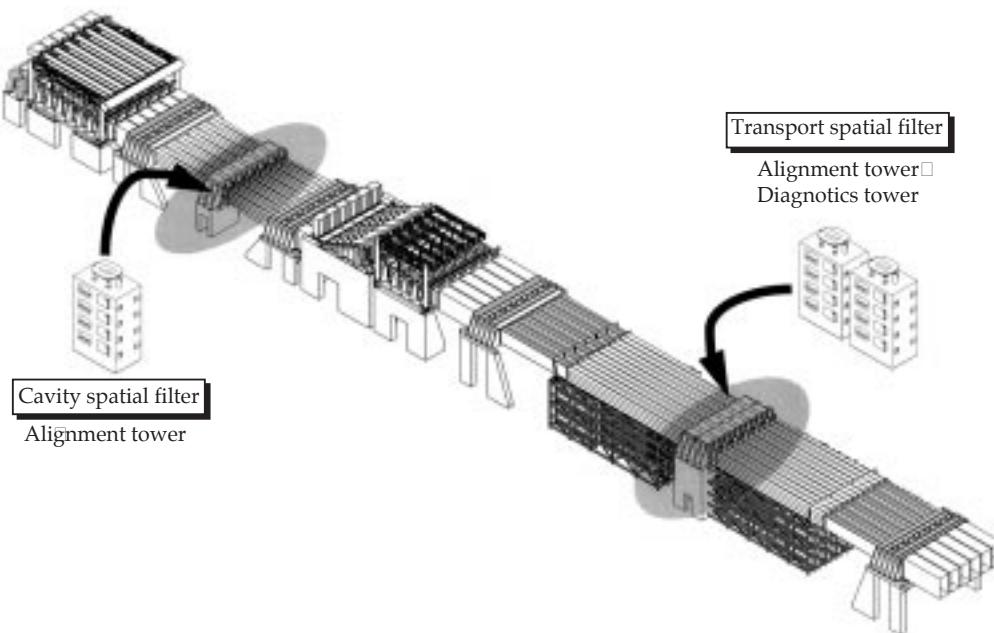
FIGURE 4. Location of the three NIF spatial filter towers. (40-00-1097-2304pb02)

Transport spatial filter

Alignment tower
Diagnotics tower

Cavity spatial filter

Alignment tower

Figure 5. A schematic view of the TSF alignment and diagnostic tower components for one beam. The CSF tower performs some of the same functions. (40-00-1097-2247pb01)

TSF tower #1 - Alignment tower

Alignment beam to output sensor

Precision rotary wheel assembly holds shot pinholes and beam pointing reticles

Beam dump pass #2 & #3 contained within tower #1

Insertable 1ω light source on same rotary stage as baffle

Illuminator

FOA 1ω alignment reticle

3ω target chamber alignment light source

(Schematic top view)

TSF tower #2 - Diagnostic tower

3ω KDP diagnostic beam to output sensor

Input to pass #1 from PABTS

1ω SF4 diagnostic beam to output sensor

SF4 lens reflection

Pass 4 to target

FOA reflection

FOA beam dump

(Schematic top view)

Special splitter/cube reflector shuttles to 3 positions:
(1) direct pass #1
(2) direct pass #4
(3) direct view reticle-KDP

● = Stepping motor

Insertable 10° reflector with attached dump for 3ω diagnostic beam withdrawn from beam for alignment as well as for optical inspection

Reticle illuminator

Pinhole assembly with baffles and 1ω light source

Beam dumps
• Fixed
• Prealigned

Motorized insertable mirrors for directing alignment beams to output sensor

TSF tower also has CCD cameras

Figure 6. The general design of the TSF alignment tower with most of the tower structural elements omitted. (40-00-1097-2248pb01)

design of the TSF tower #1. Each tower has a pinhole assembly—with baffles and a 1ω light source—which positions datums for beam pointing and positions shot-time pinholes. A reticle illuminator backlights reticles to locate pointing references, and pointing images are relayed to the output sensor for the TSF. In the CSF, the reticles are viewed directly by local cameras on the tower. Fixed and prealigned beam dumps absorb energy from faults or leakage from the Pockels cell and from target back-reflections. Alignment optics are removed from the beam path to fire the laser.

The pinhole assembly includes a pinhole wheel with a repeatable reticle inserter, an 80-mm clear aperture, and multiple shot pinholes—10 for the TSF and 30 for the CSF. There are also special pinhole combinations for inspecting optics. A swinging baffle opens for reticle viewing and optics inspection, and closes for shots.

The TSF tower #2 contains some alignment components as well, as shown in Figure 5. It has a 3ω light-source for aligning the laser output to the target and injection optics to establish the correct cone angle for the input beam and to point the beam to pinhole #1. A splitter and absorbing beam dump are removed to align the 1ω reflection from the final optics assembly (FOA) at the pinhole plane. In shot mode, tower #2 directs the reflected beam from the FOA focus lens to the output sensor for diagnostic purposes.

Title II Activities

During Title II, we will evaluate the present tower designs to accommodate the change from 192 to 96

output sensors. We will build and test a prototype tower to verify the structural stability of the tower and its kinematic mounts. We will also finalize the specifications of the components. We plan to prototype critical components—including the pinhole assembly—evaluate alternate beam dump options, and add baffles to the towers as needed to stop stray reflections. Title II will conclude with completion of the detail drawing packages.

Output Sensor Alignment Functions

The output sensor and relay optics packages are located beneath the TSF center vessel, as shown in Figure 7. The sensor and relay optics view the following, for alignment purposes:
- The injection beam at pass 1 for injection pointing.
- Pass 1 in near field for beam centering at the final optics.
- Pass 4 in far field for output pointing.
- Pass 4 in near field for beam centering.
- The reflection from the final optics at the pinhole plane to adjust the angle of the KDP frequency-conversion crystals.

These systems are required to center beams within 0.5% of the beam dimension, center the beams on shot pinholes within 5% of the pinhole diameter, position beams on target within 50 μm rms, and adjust the KDP crystal angle within ±20 μrad over a field of view of ±200 μrad. Light for these tasks is intercepted by a moving beam-splitter cube pickoff near the TSF pinhole plane on the alignment tower (see Figure 5).

Light for all these functions travels to the output sensor along a single path per beam. The pickoffs, relay optics, and transport mirrors are staggered to multiplex the eight beams spatially for each bundle (a bundle is a 4×2 array of beams). Two beams per bundle "time share" each output sensor, using beam-splitters and shutters in the transport paths. The nominal beam size in the relays is 20 mm.

Figure 8 shows the output sensor layout and components. Only the 1ω camera is used for alignment. It has two lens systems for near-field and far-field viewing and a motorized focus adjustment. The near-field lens system is shared with diagnostics (see the diagnostics discussion on p. 188), and the far-field lens system performs focused beam and reticle viewing functions. Both cameras have motorized, continuously variable attenuators.

FIGURE 7. The output sensor packages and associated relay optics are located below the center part of the TSF.
(40-00-1097-2249pb01)
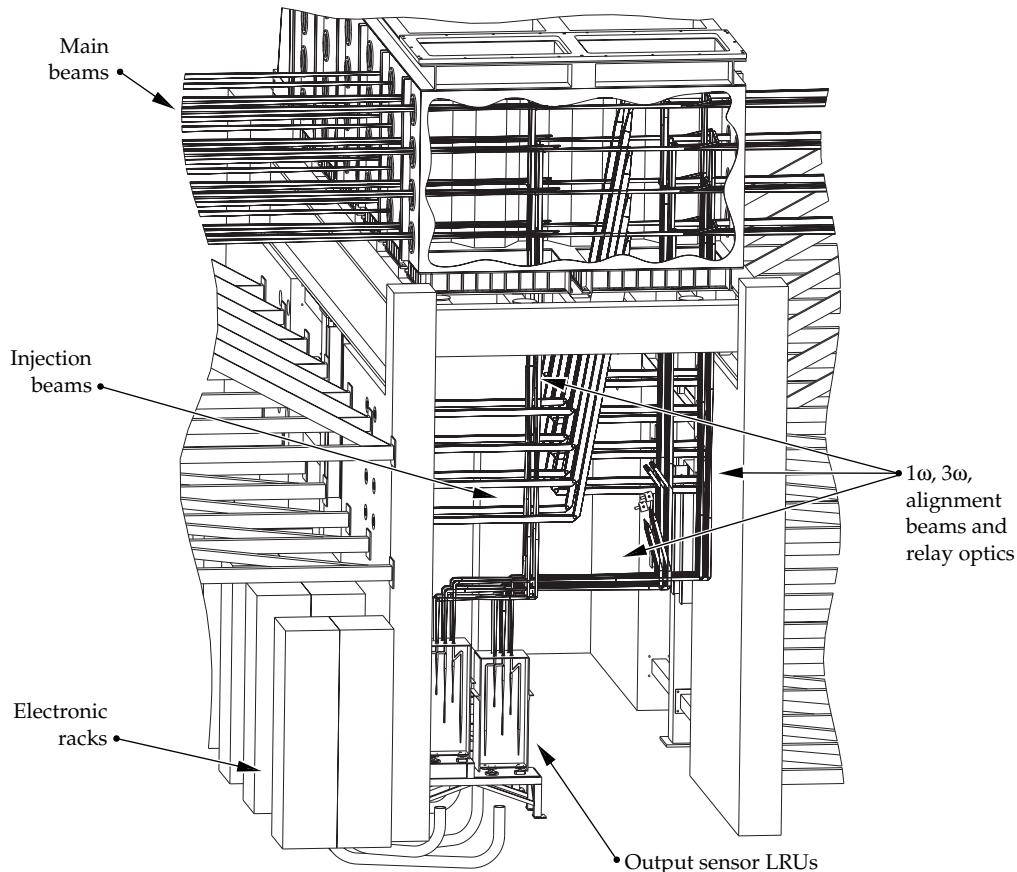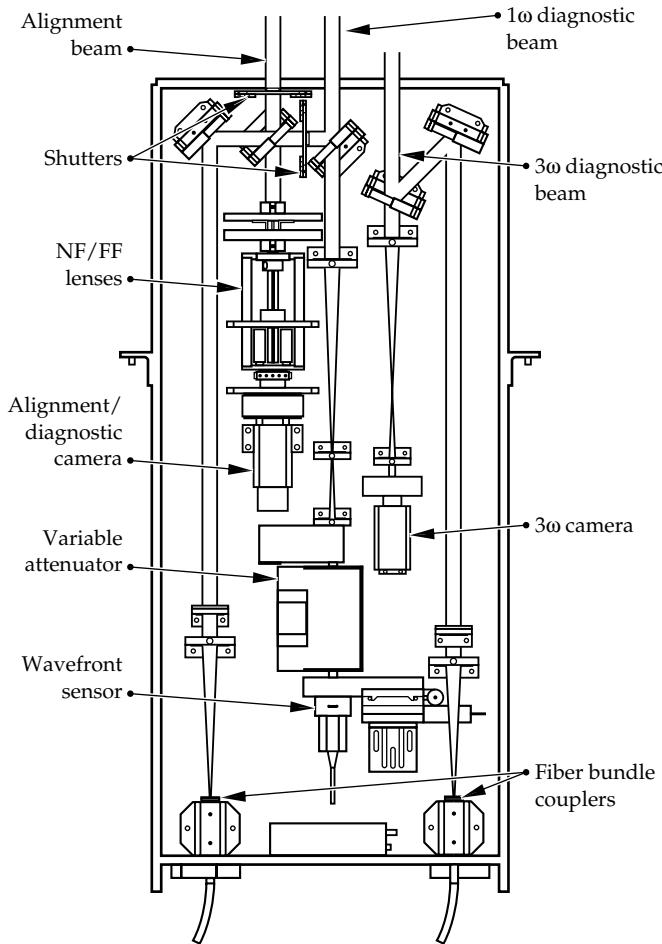
Figure 8. Output sensor design, showing components and beams. The output sensor performs both alignment and diagnostic functions. An identical set of components is located on the other side of the same mounting surface. (40-00-1097-2250pb01)

Title II Activities

In Title II we will be evaluating other options for combining the beams at the output sensors and investigating other options for alignment pickoffs. We will also look into simplifying relay configurations by using simple lenses. We will finalize our light level analysis and specify the transmission of the beam splitters and attenuators. Finally, we will examine the designs with an eye to minimizing costs and complete the detail drawing packages.

Target Area Alignment Functions

We have two main alignment systems in the NIF target area: the chamber center reference system (CCRS) and the target alignment sensor. Figure 9 shows the layout of these two systems within the target chamber. The target alignment sensor inserter uses the same positioner design as the target inserters (see p. 172). These inserters, the CCRS modules, and target

diagnostics are mounted on the same platform to minimize the relative motion among them. At shot time, the sensor is removed and protective baffles are positioned in front of the CCRS port windows.

The CCRS must provide a stable position reference system in the target bay and be able to position targets repeatably within the narrow field of view (FOV) of the target diagnostics. Its long-term stability must be ≤30 μm, and its FOV must be ±5 cm from the target chamber's center. Figure 10 shows how the CCRS positions target chamber components.

The target alignment sensor positions beams in the target plane and adjusts the final focus lenses to set the spot size. The total deviation for all beams must be ≤50 μm rms, a single beam must deviate no more than 200 μm, and the sensor must achieve a specified central lobe size to ±50 μm. The sensor must operate everywhere within 5 cm of the target chamber center. Figure 11 shows the setup for the target alignment sensor. The sensor has two CCDs, which see both the target and the beams. The assemblies that reflect the beams were designed for minimal deflection and high natural frequency.

Title II Activities

In Title II we will conduct a finite element analysis of the CCRS and target alignment sensor to extend our preliminary mechanical and optical analysis. Prototypes will be built to validate the detailed design.

Beam Diagnostics

NIF's beam diagnostics characterize the beam at key locations in the beamline (Figure 12). These systems are as follows:
- Input sensor.
- Output sensor.
- Calibration calorimeters and final optics diagnostics.
- Temporal diagnostics.
- Optics inspection system.
- Target chamber diagnostics.
- Roving assemblies.
- Trombones.
- Precision diagnostics.

We briefly discuss the requirements, design, and Title II activities of each of these diagnostic systems below.

Input Sensor Diagnostic Functions

The input sensor, in addition to providing certain alignment functions (see p. 182), characterizes the PAM by sampling at the regenerative amplifier, the SSD unit, and the multipass rod amplifier. The sensor measures beam energy, near-field images, and temporal pulse shape. The imaging resolution is 1%

Target alignment sensor

Target chamber (upper half removed)

Chamber center reference system No. 1

Target positioner assembly

Target alignment sensor assembly No. 1

Target alignment sensor assembly No. 2

Chamber center reference system No. 2

Light source

Source reticle at relay lens focus

Relay lens

CCD

Image of target reticle on reference position reticle (camera travels in x & y, assembly in z)

CCD

Image of source reticle on reference angle reticle

Target chamber wall

Target mirror with reticle
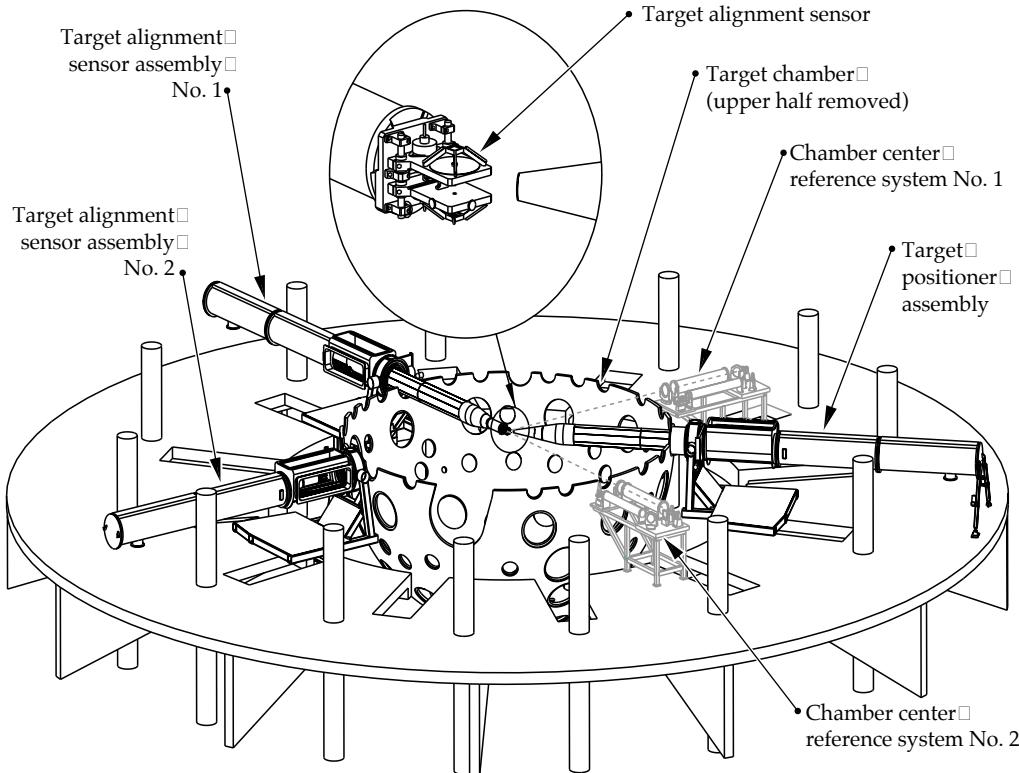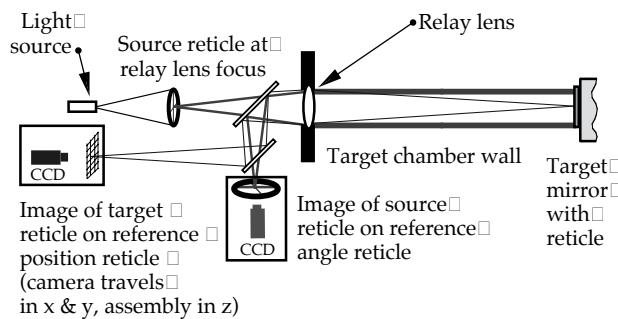
FIGURE 10. The chamber center reference system (CCRS) has two simultaneous modes of operation. It measures a component's target position by imaging its reticle, and measures its orientation by monitoring the direction of light reflected from the reticle. Two CCRS instruments mounted on orthogonal chamber axes precisely locate and orient the target chamber components anywhere within 5 cm of the chamber center. (40-00-1097-2252pb01)

- CCDs see both the target and the beams

- The target is viewed from three sides

- No light hits the target

- Design will vary for different targets

Incoming beams

CCD

CCD
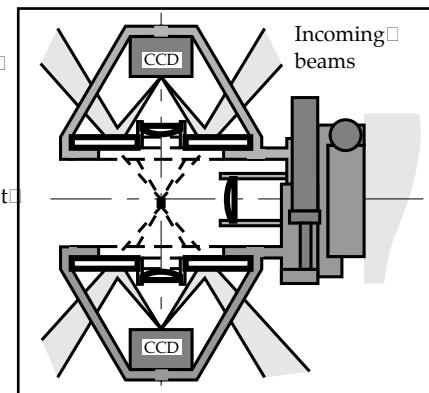
FIGURE 11. The target alignment sensor detects beam positions relative to the target. Two of the three CCDs in the sensor see both the target and the beams, because the images are superimposed. However, no light actually hits the target. (40-00-1097-2253pb01)

of the beam dimension and 2% of the maximum intensity. Figure 2 shows isometric views of the sensor; a schematic of the sensor with its components appears in Figure 13.

Diagnostic samples are obtained from a 1% partial reflector for the regenerative amplifier and through leaky mirrors for the SSD unit and multipass amplifier. The coatings on these mirrors provide adequate signal levels to the energy diagnostics, as well as to the alignment diagnostics.

The energy from the regen, SSD module, or four-pass amplifier is measured with an integrating sphere and photodiode followed by a charge integrator and digitizer. Shutters select which sample is measured and a CCD camera obtains near-field images for each beam prior to or during a shot. An optical fiber bundle sends a sample of the multipass output to the power sensor (see p. 190), where it is time multiplexed with other signals. The PAM output beam can also be diverted to a calorimeter to periodically calibrate the multipass energy diagnostic.

FIGURE 12. Location of the laser diagnostics for NIF. (40-00-1097-2254pb01)
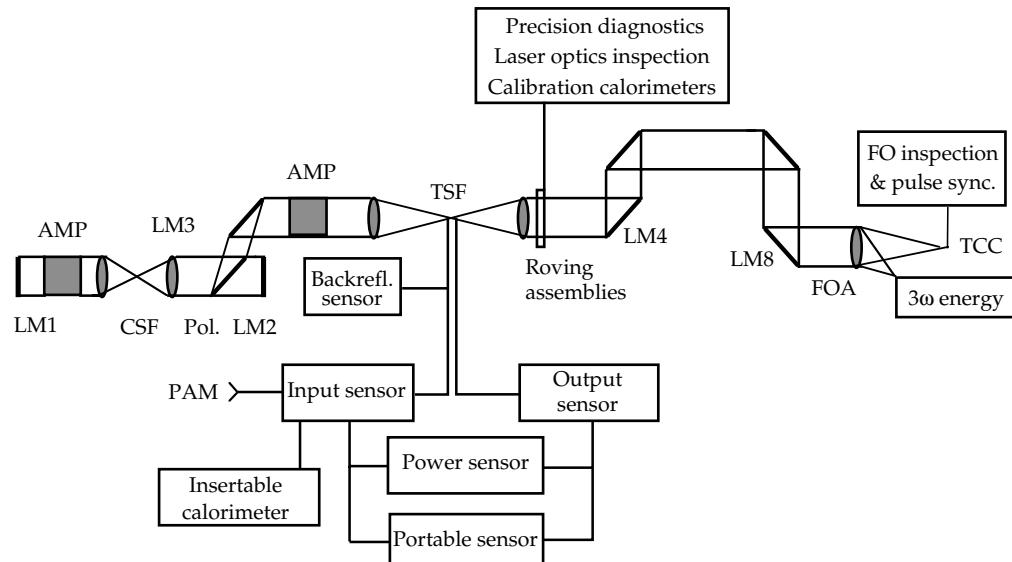
Title II Activities

We have a Title I optical design that meets performance requirements. During Title II, we plan to optimize the coating design, balancing the sampling stability requirements against the desire for high beam-transport throughput. We will also complete the detailed specifications and modeling of the fiber-optic bundle coupling that transmits the multipass output sample. A prototype package will be built from completed detail drawings.

Output Sensor Diagnostic Functions

The output sensor performs many diagnostic tasks in addition to its alignment functions (for alignment discussion, see p. 185). The sensor characterizes the 1ω output (energy, near-field fluence profile, temporal pulse shape, and wavefront) and 3ω output (near-field fluence profile and temporal pulse shape). The 1ω output energy must be measured within 3%, and the 1ω and 3ω temporal pulse shapes must be measured within 2%. The 1ω beam wavefront must be measured within 0.1 waves, and the 3ω output beam must be imaged at the plane of the conversion crystal with a spatial resolution of 2.7 mm. Figure 8 shows the output sensor's general design, and Figure 14 shows a schematic for the output sensor's diagnostic functions.

FIGURE 13. Input sensor schematic for beam diagnostics. NF means near field.   (40-00-1097-2255pb01)
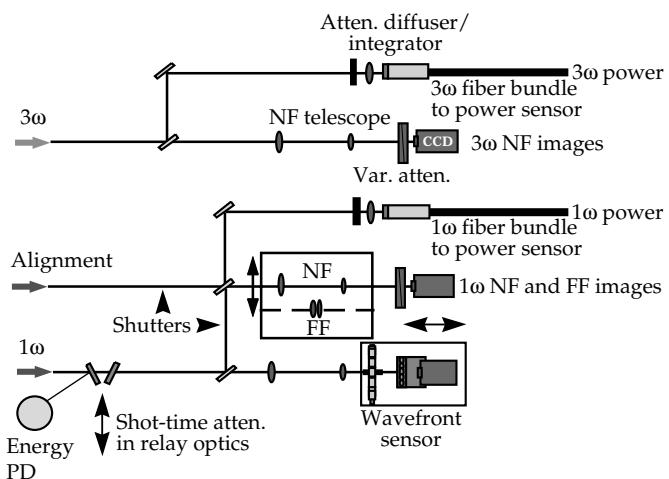
FIGURE 14. Output sensor schematic for beam diagnostics. NF and FF mean near field and far field, respectively.   (40-00-1097-2256pb01)

Reflections from existing optics supply samples of the 1ω and 3ω beams. The 1ω sample reflects from the flat exit surface of the transport spatial filter output lens. This surface is coated with a solgel antireflection coating, (nominally 0.1% R). The lens is tilted by 0.8 mrad to offset the reflected sample from the pass #4 path. The 3ω sample reflects from the flat entrance surface of the target chamber lens in the final optics assembly. This lens is also tilted by 0.6 mrad to offset the reflected sample beam from TSF pass #4 path, and its coating is similar to that on the SF4 lens sampling surface. Because the 3ω sample beam propagates at a small angle relative to the TSF output beam, it becomes decentered. The clear apertures of SF4, LM4, and LM5 must be increased to clear both pass #4 and the 3ω beam. Pickoffs for the beam samples are near the focus in the TSF. Pickoff optics for 1ω and 3ω sample beams are located on TSF tower #2, as shown in Figure 5. Relay optics transport the beams from the TSF to the output sensors beneath the TSF center vessel. For preshot wavefront control, two diagnostic beams per bundle "time share" each output sensor, using beam splitters in the transport paths. One beam from each pair of beams is diagnosed for each shot. The 1ω energies are measured on all beams for each shot.

The output sensor has three CCD cameras, each with continuously variable attenuators. One camera—shared with the alignment functions—images the 1ω near-field profile, the second images the 3ω near-field profile, and the third is the detector array for a Hartmann wavefront sensor (see p. 194 for a discussion of the Hartmann sensor). The 1ω energy is measured by an integrating sphere with a time-integrated photodiode, which is inserted at shot time. Power samples are sent to the power sensor (see p. 190) using two optical fiber bundles.

Title II Activities

For the output sensor diagnostic systems, our Title II priorities include evaluating other options for combining beams at the output sensor, optimizing the fiber coupler for maximum transmission, possibly simplifying relay configurations, completing specifications for the SF4 sampling surface, finalizing our light level analysis, and specifying transmission of the beam splitters and attenuators. We will also analyze the stray light, and specify baffles, stops, and wavelength selective filters. An initial set of drawings will be used to build a prototype.

Calibration Calorimeters and Final Optics Diagnostic Functions

Calorimeters, which measure beam energy, are used in three areas of NIF: the input sensor, the output sensor, and the final optics diagnostics. Each input sensor has a port for manual mounting of a 5-cm calorimeter to calibrate the sensor's energy diode without opening the beamline [Figure 2(b)]. The output energy diodes are calibrated using two groups of eight roving bundles of 50-cm calorimeters—one for each laser bay. Each group can be remotely positioned to intercept the outputs from one eight-beam bundle at a time. Finally, 192 10-cm calorimeters in the final optics diagnostics measure a fraction of each beam's 3ω energy as it propagates toward the target.

We use calorimeters similar to those on Nova. The 5-cm calorimeters are an off-the-shelf design, and the 50-cm and 10-cm calorimeters are scaled versions of the 40-cm ones used in the Nova target chamber. These calorimeters can meet the NIF requirements.

The final optics diagnostics uses a diffractive splitter to obtain a sample for the 3ω calorimeter (Figure 15). This calorimeter calibrates the 3ω power for each shot. It must operate in a vacuum, and have a damage threshold >3 J/cm^2 at 351 nm, a 10×10 cm aperture, a 1–60 J energy range, a repeatability of <1% at the 30 J level, and a linearity of <1% over a range of 50:1. The sampling grating on the flat surface of the focus lens will have a solgel antireflective coating, a transmission of >98% for the zeroth order of 3ω, and a 40×40 cm aperture. It must also focus the sampled beam in 1.5 m. The diffractive splitter design will be demonstrated on the final optics test assembly on Beamlet; however, we have evaluated the calorimeter/diffractive splitter system as a whole and know it can meet NIF's system requirements.

Title II Activities

After testing aspects of the 3ω final optics diagnostic design on Beamlet, we will produce the final design drawings to complete Title II.
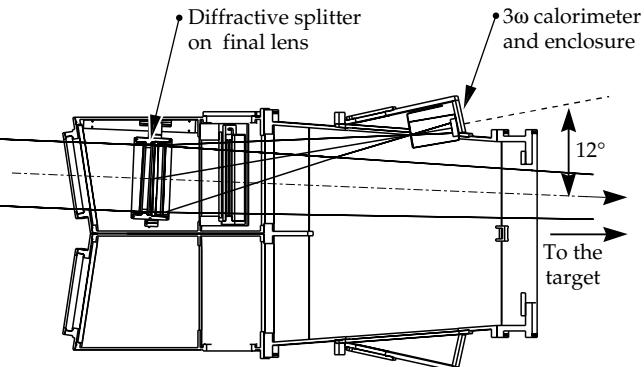
FIGURE 15. The final optics diagnostics uses a diffractive splitter and volume-absorbing calorimeter. (40-00-1097-2257pb01)

Temporal Beam Diagnostics

Temporal diagnostics includes two portable sensors, rack-mounted power sensors near the input and output sensors, and a back-reflection sensor. NIF will have two portable streak cameras, mounted on carts, that can each be used in place of a normal power sensor for one beam at a time. The streak cameras must have a time resolution of 10 ps, a dynamic range of 1000:1, and multiple channels, and must be easily movable among the other sensor packages. Each camera can handle 19 sample inputs—1ω or 3ω—through fiber-optic bundles. One of four sweep times can be selected—1.5 ns, 5 ns, 15 ns or 50 ns—with resolutions from 10 ps (for 1.5 ns) to 250 ps (for 50 ns).

Each power sensor must have a dynamic range of 5000:1, a record length of 22 ns, an accuracy of 2% over a 2-ns interval, and a rise time of 250 ps. It takes samples on fiber bundles from the output and input sensors, and time multiplexes 12 signals to minimize costs. Figure 16 shows a schematic of the Title I design. The transient digitizer in the sensor is a commercial technology with a long record length. One photodiode detects signals from four input sensors and eight output sensors—a total of eight 1ω signals and four 3ω signals. Time separation is achieved using the propagation time through the laser and optical fiber delay lines for signals close in time. The dynamic range of the eight-bit digitizer is extended using four channels, each with a different sensitivity. The 12 signals are multiplexed into the long-record digitizer.

Title II Activities

During Title II, we will analyze both optical and electronic reflections to ensure there is no interference with the data. We will also evaluate the availability, transmission, and cost of the fiber used for the 3ω signals. The diagnostic fiber system must transmit enough light to the photodiode for measurement and provide correct timing for beam diagnostics sharing.
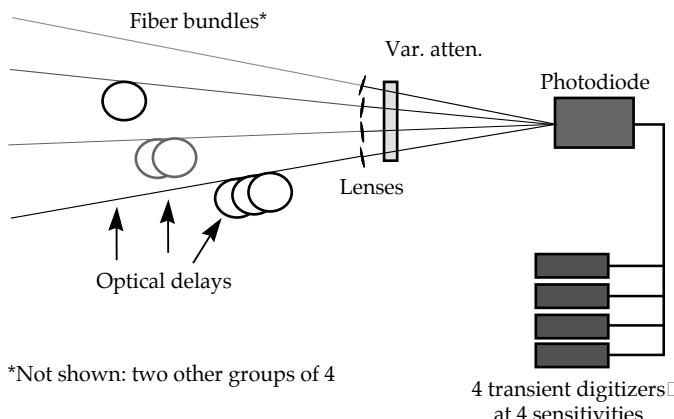
On-Line Optics Inspection

One on-line optics inspection system is located in each switchyard, and one more at target chamber center. These systems have access to each beamline through a set of translatable mirrors described later (p. 192). The requirement for main-beam optics is to detect flaws ≥5 mm, which is 1/4 of the critical flaw size. Our goal is that these systems detect defects ≥0.5 mm. We considered a number of issues when designing these systems. First, we selected dark-field imaging since damage spots appear best against a dark background. This allows us to detect spots below the resolution limit. Our imaging scheme is to backlight the large optics with apodized and collimated laser illumination sources. Undisturbed light is intercepted by a stop in the dark-field optics, but light diffracted from damage spots is imaged onto a CCD camera. Second, the systems' resolution will be limited by one of two factors: the far-field aperture in the TSF or the number of pixels in the cameras' CCD arrays. We must properly account for these limitations in the design. Third, depth of field will be short enough to isolate all but the most closely spaced optics. Fourth, use of different pinhole combinations in the CSF and careful image processing can "strip away" any overlaid images.

The laser bay optics are inspected with the high-resolution cameras located in each switchyard. Figure 17

FIGURE 16. Schematic diagram of a power sensor in which time-multiplexed optical pulses are combined on a common photodiode, and the electrical outputs drive multiple channels in transient digitizers. (40-00-1097-2258pb01)
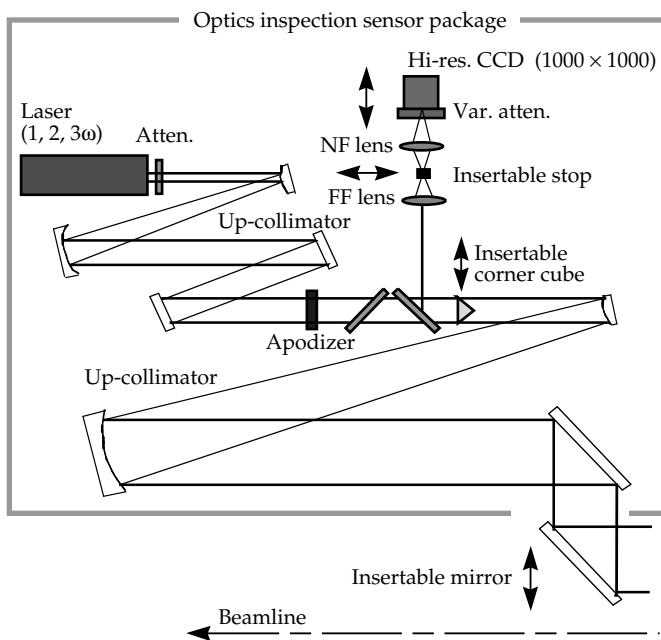
FIGURE 17. Inspection scheme for all but the final optics. One such inspection system resides in each switchyard. NF and FF mean near field and far field, respectively. (40-00-1097-2259pb01)

shows the layout of a switchyard inspection package. For optics LM1 through SF4 in the main laser cavity, the illumination source is the alignment laser located in the input sensor. This alignment beam is injected into the TSF along pass 1, and LM1 is aligned to return the beam along pass 4. The inspection package captures dark-field images at each plane containing an optic. Image subtraction software will help detect the changes from previous inspections.

For inspecting LM4 through the first surface of the final focus lens, the switchyards' 1ω source will be injected toward the target using the outward-looking roving mirror (p. 192). The first surface of the final focus lens will be aligned to retroreflect a portion of this beam. Dark-field images will be captured by the inspection system in the switchyard at each plane containing an optic.

For inspecting the final optics, we will image through the kinoform phase plate (KPP) at 3ω using a damage inspection package inserted at the target chamber center (described further in the next section). This viewer will have a sufficiently short depth of field to discriminate between the closely spaced final optics elements.

Title II Activities

Our priorities during Title II include obtaining dark-field images from Beamlet using the NIF on-line inspection approach, and modeling and validating the preliminary optics designs for the switchyard and target chamber optics inspection systems. We will also design a reflective-optics up-collimator for the switchyard inspection packages and start evaluating image processing strategies.

Target Chamber Beam Diagnostics

Target chamber diagnostics include the pulse synchronization detector module and the target optics inspection system. Both are located at the center of the target chamber at the end of the diagnostic instrument manipulator, as shown in Figure 18(a). Similar adjustments are required for both the pulse synchronization and final optics inspection modules. They can be oriented to any beam position, including direct drive. Translation commands for the diagnostic manipulator and angle commands for the modules come from the CCRS (p. 186). The maximum move time to intercept light from a different four-beam quad is 5 s; the typical time is <0.8 s.

Figure 18(b) shows the components of the synchronization module. The pulse arrival times at target chamber center must be set with 30-ps relative accuracy. The module must simultaneously capture signals from the four beams of a final optics assembly quad and position each focused beam on the end of a separate fiber bundle with an accuracy of <100 μm. The fiber bundles carry the optical signals to a streak camera where their relative times of arrival are compared. The signal is obtained by firing a rod shot and capturing the leakage of 1ω radiation through the conversion crystals.

The final optics damage inspection module, also located at target chamber center, is shown in Figure 18(c). The module examines the closely spaced final optics that are not observable by other means. The final optics are backlit with collimated 3ω radiation. A high-pass filter,
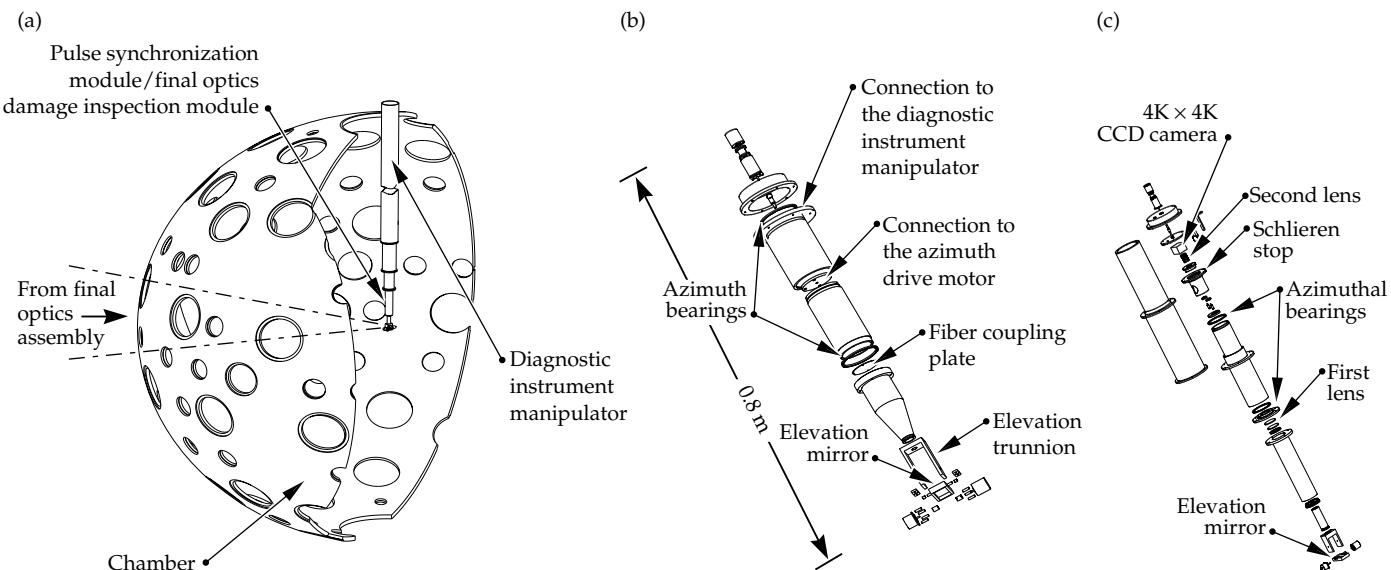
FIGURE 18. (a) The pulse synchronization detector module and final optics damage inspection module can be attached to the end of the diagnostic instrument manipulator and inserted into the center of the target chamber. (b) An exploded view of the pulse synchronization module. (c) An exploded view of the final optics damage inspection module. (40-00-1097-2261pb01)

with a central schlieren stop placed at the focus, removes those rays that are not deviated by flaws. A CCD camera captures data from the full-aperture image. The camera, lenses, schlieren stop, and filters rotate as a unit in the azimuthal direction.

Title II Activities

Our Title II engineering priorities for these systems are to determine the mechanical and electrical interface of both modules with the manipulator, and implement a design for the rapid installation and removal of the modules from the manipulator. We will also complete the detailed design for many of the components and interfaces of the two systems.

Supplemental Beam Diagnostics

As described above, the NIF design includes signifi-cant diagnostic capabilities on each beamline.

However, it will be important to be able to calibrate some of these measurements, to verify that they are operating correctly, or to collect more detailed informa-tion. For this purpose, additional diagnostics that can be used on one or a few beams at a time are located in each switchyard. They include full-aperture calibration calorimeters and a suite of precision diagnostics.

Figure 19 shows the layout of components related to supplemental diagnostics in one of the switchyards. An array of eight calorimeters, the "roving calorimeter assembly," travels on horizontal rails to any of the 12 bundle locations. If desired, each of the eight calorimeters can collect the output from the corre-sponding beam in that bundle. However, any of the eight calorimeters can also be rotated toward the laser on its outside vertical edge so that it allows the beam to pass. Beams that are allowed to pass continue on to the target chamber or are directed to the precision diagnostics as described below.

FIGURE 19. Supplemental diag-nostics for calibration and for a variety of detailed measure-ments are located in the switch-yard.   (40-00-0398-0381pb01)
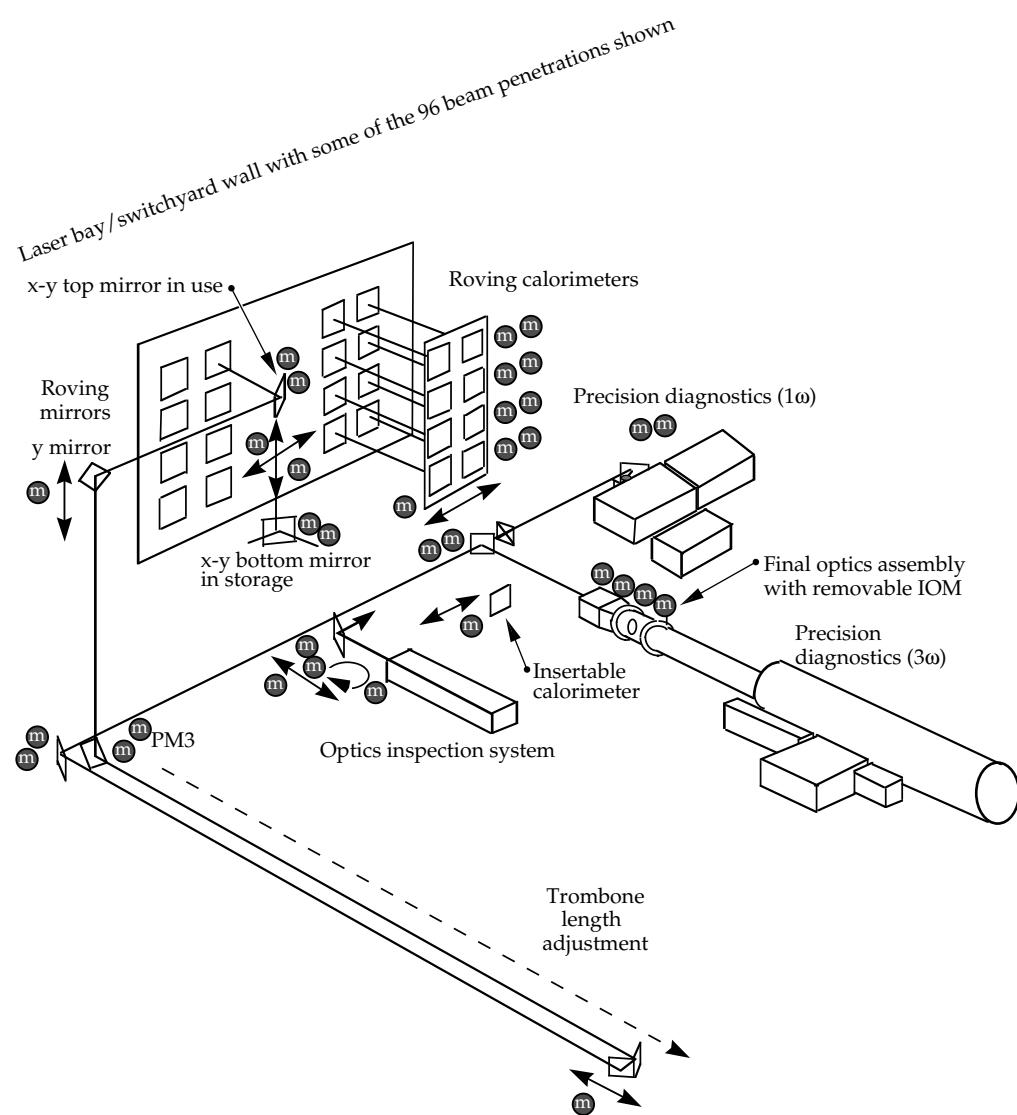
The optical-mechanical system designed to intercept any one beam in each switchyard and send it toward the precision diagnostics is called the "roving mirror system." It comprises an additional pair of parallel horizontal rails, two pairs of parallel vertical rails, and three translatable mirrors. The x-y top mirror [Figure 20(a)] in combination with the y mirror picks off a beam and diverts it toward the precision diagnostics and optics inspection package (see p. 190 and Figure 17). The x-y bottom mirror, combined with the y mirror, provides a path from the optics inspection package to the target chamber [Figure 20(b)].

Each of the roving calorimeter and x-y mirror assemblies weighs about 1000 lb. The assemblies are belt-driven by motors fixed at the target bay end of the enclosure. The drive packages include stepper motors, incremental encoders, and fail-safe breaks. The time to move from one beam to an adjacent beam is estimated at 16 s. All of the components reside within an enclosure that maintains a sealed argon gas environment, and the mechanisms must be designed to avoid production of particles that might contaminate the nearby optics.

The precision diagnostic stations are shared diagnostics that measure laser output performance one beam at a time using more extensive instrumentation than that found in the output sensors (see Table 1). During installation and activation, the precision diagnostics will be used to verify the performance of each beam, including its dedicated diagnostic packages. The 3ω precision diagnostics, illustrated in Figure 21, will measure frequency conversion characteristics of the selected beam using a separately selected integrated optics module (IOM). Each IOM comprises the set of optics, including frequency conversion crystals and final focus lens, that is normally mounted at each beam's entrance to the target chamber. The precision diagnostics provide the only capability for simultaneously measuring high-power 3ω beam properties at the full 40-cm near-field aperture and in a far-field plane equivalent to the target chamber focus. Once NIF is operational, the station will be available for diagnosing beamline and component problems and for performing laser science experiments.

The precision diagnostic station will be able to measure the following aspects of the 3ω laser pulse:

- Energy, with an accuracy of 3%.
- Power vs time, with a dynamic range of ≥50:1, an accuracy of 4%, a rise time of 250 ps, and a record length of 22 ns.
- Focused spot size and smoothness, with 30-μm spatial resolution and 10-ps temporal resolution for a selected 1.5-ns period.
- Near-field spatial profile in the frequency conversion crystal plane, with 2.7-mm resolution.
- Prepulse energy, at levels $\leq 0.25 \times 10^8$ W/cm^2 in equivalent target plane.

(a) Laser bay to precision diagnostics
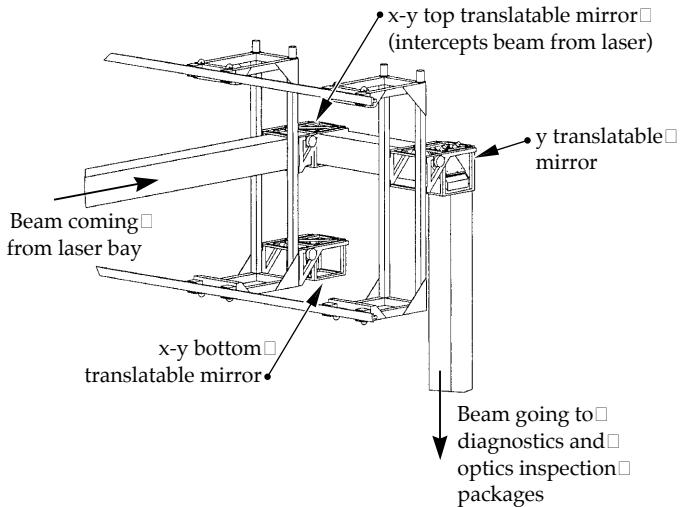
(b) Inspection diagnostics to target chamber
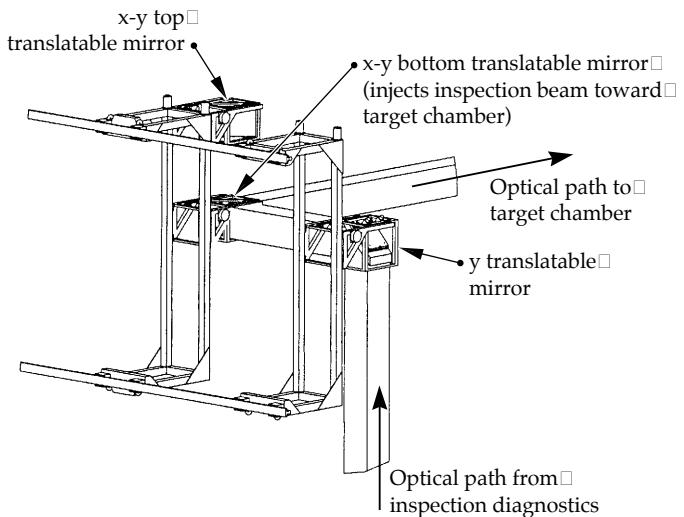
FIGURE 20. Two roving mirror system configurations provide (a) a path from the laser bay to the precision diagnostics station and (b) a path from inspection diagnostics to the target chamber. (40-00-1097-2262pb01)

Title II Activities

As we complete the design, we will specify transport mirror sizes and coatings, design a modified final optics assembly 3ω calorimeter spool, choose an effective method for mounting the IOM, and develop procedures for independent alignment of the supplemental diagnostics modules. We must also analyze thermal and vibration characteristics to verify that they meet the same stability requirements as the corresponding main beamline components.

Wavefront Control

During preparations for a pulsed shot, the wavefront control system monitors the wavefront of each alignment laser at the beamline output and automatically

TABLE 1. The 1ω measurement capabilities of the precision diagnostic station compared to those of the output.

Measurement	Precision diagnostic	Output sensor
Energy		
Range	To 20 kJ	To 20 kJ
Accuracy	Better than 1.5%	3%
Power resolution	<40 ps or 100 ps	250 ps
Far-field imaging FOV	±180 μr (best)	None
Near-field imaging resolution	~1.4 mm and/or	1.6 mm
(in main beam)	~300 μm	
Wavefront		
Hartmann precision	Better than λ/20	λ/10
Radial shearing interferometer precision	~0.1 λ (16× reference)	None
Schlieren		
Energy balance	Better than 15%	None
Power resolution	~10 ps and/or 100 ps	None
Far-field imaging FOV	±800 μr	None
Near-field imaging resolution	~1.6 mm (in main beam)	None
Prepulse sensitivity (3ω equiv.)	Better than 0.25×10^8 W/cm^2	None
Flexibility	Versatile	Fixed

FIGURE 21. The precision diagnostics measure the characteristics of a full-power NIF beamline. The larger vacuum chamber is necessary to avoid high-intensity air breakdown and to expand the beam enough that it doesn't damage beam-splitting optics.
(70-00-0796-1536pb01)

Integrated optics module

Lens

Target plane

Multiple wavelength calorimeter

1-m aperture primary mirror

7.7 m

Frequency converters

Beam dump

Energy balance (1, 2, 3ω)
Pulse shape (1, 2, 3ω)
Alignment (1ω)

Near-field imaging
(3ω resolution <100 μm)
WFOV calorimetry (3ω)

Far-field imaging
(3ω FOV 4 × 4 mm at focal plane)
Apertured calorimetry (3ω)
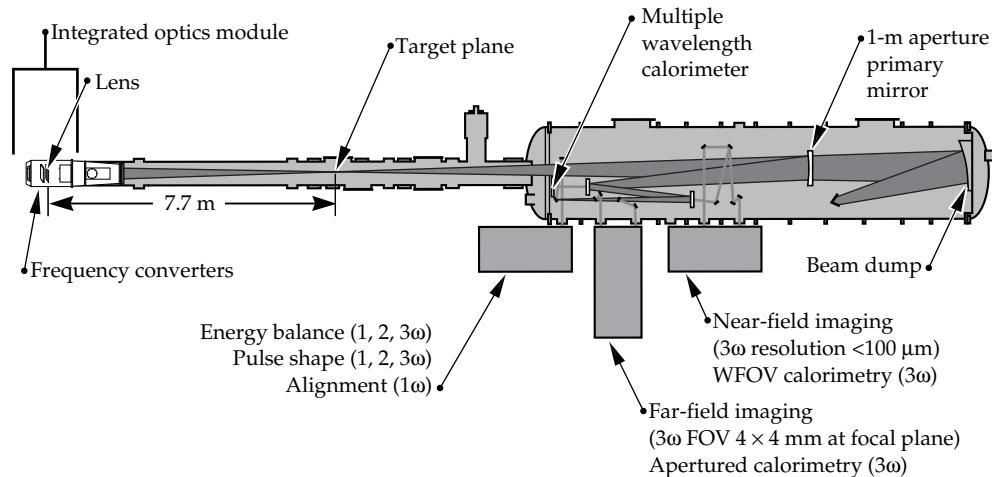
compensates for measured aberrations using a full-aperture deformable mirror. In the last few minutes before a shot, the controlled wavefront is biased to include a precorrection for the estimated dynamic aberrations caused by firing the flashlamp-pumped amplifiers. One second before a shot, closed-loop operation is interrupted, and the Hartmann wavefront sensor is configured to measure the pulsed wavefront. The measured pulsed wavefront error provides additional information for setting precorrection wavefronts prior to the next shot.

Requirements for the system include operation at 1 Hz closed-loop bandwidth and reduction of low spatial frequency angles in the beam to less than 20 μrad. The range

of the system measured at beamline output must be at least 15 waves for simple curvature (second-order correction) and 4 waves of fourth-order correction on both horizontal and vertical axes. Figure 22 shows the location of system components. The three main components are the Hartmann wavefront sensor, the deformable mirror, and the computer controller.

Hartmann Sensor

The Hartmann sensor, illustrated schematically in the Figure 23 inset, includes a 2-D array of lenslets and a CCD video camera. The output sensor (Figure 24)
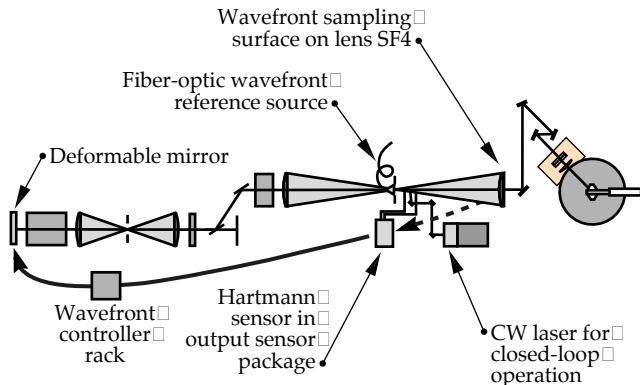
FIGURE 22. General location of the primary wavefront control components—the Hartmann sensor, the deformable mirror, and the wavefront controller. Lens SF4 provides a wavefront sampling surface. (40-00-1097-2265pb01)

delivers a demagnified image of the output beam to the lenslet array. Each lenslet collects light from a specific part of the beam and focuses it on the CCD. The focal length must correspond accurately to the distance from the lenslet to the CCD, and this result is obtained using an index-matching fluid sealed between the lenslets and an optical flat. The lateral position of the focused spot are a direct measure of the direction of the light entering the lenslet. Directional data from the 77 hexagonally packed lenslets of the NIF sensor are processed to determine the output wavefront with an accuracy of ≤0.1 wave and a spatial resolution of 4.5 cm in the 40-cm beamline aperture.

Title I hardware specifications for the Hartmann sensor include a frame-capture video camera with 1.3-cm format, a pixel array of at least 512×480, and a dynamic range of 200:1. The camera should operate on 0.75 μW of continuous 1-μm light or a pulse energy of 12 nJ and be available in a remote-head configuration to minimize heat generation within the output sensor package. Higher input signals will be reduced with high-optical-quality variable attenuators. To minimize stray light, the lenslet array assembly will be antireflection-coated on both sides, and all parts of the input aperture falling between lenslets will be blocked with an opaque mask.

Title II Activities

During Title II, we will optimize the variable attenuator design, qualify a vendor for the lenslet arrays, and evaluate options for using the sensor on two beams at shot time. We also plan to build a prototype unit.

Deformable Mirror

The NIF design includes 192 large-aperture deformable mirrors for wavefront control in the main laser cavity. The required optical clear aperture is
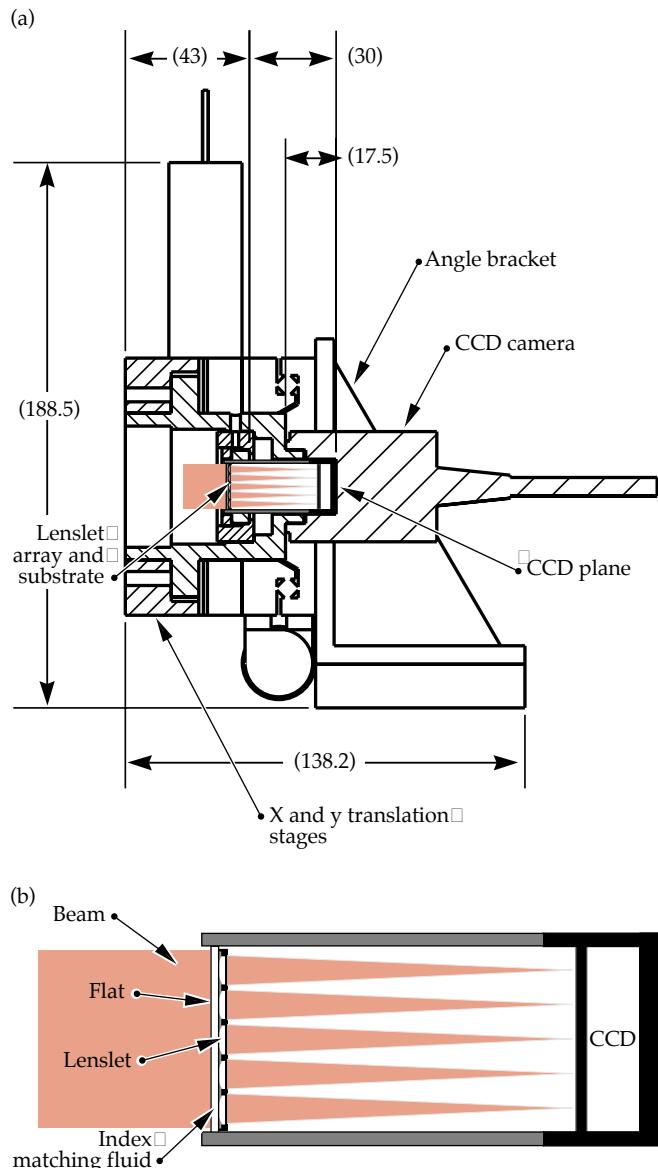
FIGURE 23. (a) A sectional view of the Hartmann sensor. (b) The Hartmann sensor works as an array of pointing sensors with a shared CCD detector. (40-00-1097-2266pb01)

approximately 400×400 mm square. The mirror shape will be determined by the displacements of 39 replaceable actuators spaced 80 mm apart. The actuators have numerous requirements, as listed in Table 2. The residual mirror surface error over the clear aperture must be no more than 0.05 waves rms, and each mirror is an integral part of an LM1 cavity-mirror mount.

During Title I, we assembled 39-actuator "prototype" deformable mirror that met most of the NIF requirements and tested it on Beamlet. The prototype substrate material is BK7, with a hard dielectric coating having a reflectivity of ≥ 99.5% and a 1ω transmission of 0.2–0.5% at an angle of incidence of 0°. Figure 25 is a photograph of the assembled mirror.

Fast neutral
density filter
wheel

Variable
attenuator
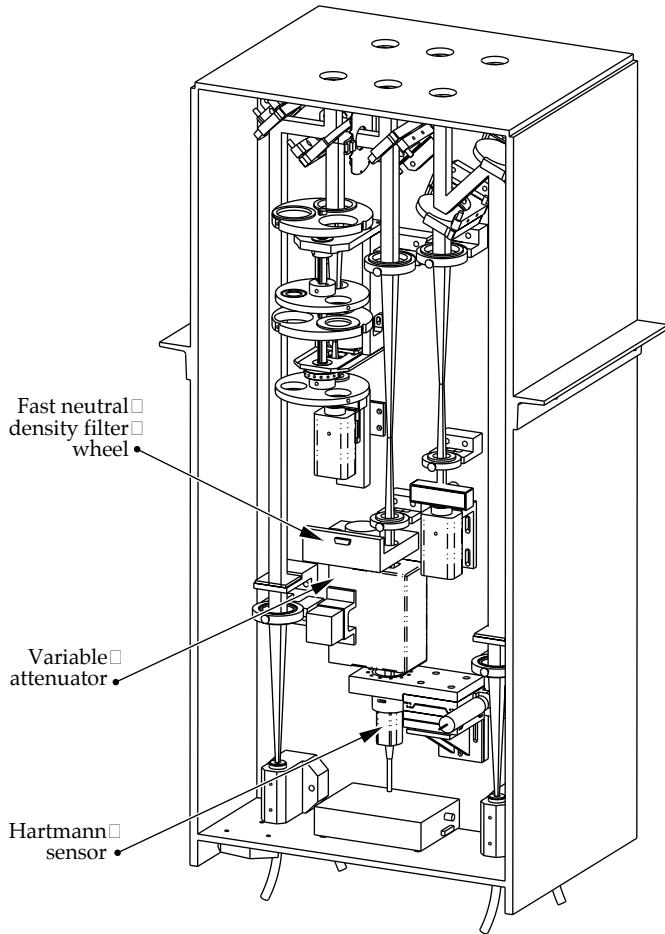
Hartmann
sensor

FIGURE 24. Location of the Hartmann sensor in the output sensor.
(40-00-0398-0387pb01)

FIGURE 25. An LLNL 40×40 cm prototype deformable mirror has been assembled and tested.   (40-00-1097-2267pb01)

TABLE 2. Actuator requirements for the NIF large-aperture deformable mirror.

Actuator requirements	
Stroke	15 μm (0.0006 in.) @ max. voltage
Material	PMN (electrostrictive formulation)
Electrodes	Platinum
Young's modulus	>102 GPa (14 Mpsi)
Tensile strength	>24.1 MPa (3500 psi)
Stiffness	>250 N/μm
Hysteresis	<5%
Creep (max after 24)	<2%
Voltage range	0–200 V
Capacitance	15–30 μF (size dependent)
Frequency	>100 Hz (small amplitude)
Lifetime	$>10^9$ cycles

Title II Activities

In Title II, we will incorporate lessons learned from our prototype fabrication, assembly, and Beamlet operation. We plan to reduce the residual errors after assembly, if possible, and identify design changes that will reduce the cost without changing the performance. We will also work on improving the actuators, to increase their reliability at full voltage. In addition, we will begin qualifying vendors for production of the LLNL or equivalent design.

Wavefront Controller

The wavefront controller function is accomplished by systems that are modular at the eight-beam-bundle level. Each wavefront controller comprises computer hardware and software to periodically calibrate the associated Hartmann wavefront sensors and deformable mirrors, operate the automatic wavefront correction loops during preparations for a shot, and capture pulsed wavefront measurement data during a shot. In the moments immediately prior to a shot, the system is generally operated under closed-loop control to an offset wavefront value. This is because the

flashlamp-pumped amplifiers introduce a dynamic wavefront change when they are fired, and the wavefront system must be set to anticipate that change.

Since the Hartmann sensor data is in video format, the controller incorporates image processing capabilities appropriate for recognizing and tracking the position of the 77 focused spots from each Hartmann image. The image processing code attains maximum accuracy by automatic adjustment of software parameters for grayscale and brightness. The controller also measures and applies the influence matrix for the deformable mirror actuators and the amplifier precorrection file in accordance with the mirror control algorithm. When operating in closed-loop, the controller is intended to maintain a closed-loop bandwidth of approximately 1 Hz on each beam.

The NIF wavefront controller hardware will use VME industrial computer bus and multiprocessor architecture designed to make maximum use of standard components and to accommodate replacement of modular elements as microprocessors and other computer electronics continue to evolve. The system will be attached to the Integrated Computer Control System network using CORBA ().

Title II Activities

During Title II we will complete the hardware design including VME rack and laser bay wiring details, final circuit board layouts, and plans for production quantity procurement. The software specifications and controller design documents will be completed, and initial versions of the software will be written. Wavefront controller hardware and software will be tested both in a simulation system and in the wavefront control laboratory with the other components of the wavefront system.

For more information, contact
Erlan S. Bliss
System Control System Engineer
Phone: (925) 422-5483
E-mail: bliss1@llnl.gov
Fax: (925) 422-0940

INTEGRATED COMPUTER CONTROL SYSTEM

P. VanArsdall

R. Bettenhausen

F. Holloway

M. Miller

B. Reed

J. Spann

J. Wiedwald

*D*uring Title I, we defined the general software approach and hardware systems for NIF's integrated computer control system (ICCS). The ICCS design incorporates CORBA—common object request broker architecture—into a distributed, client–server network. The ICCS is a layered architecture consisting of supervisory systems that coordinate front-end processors. The supervisory systems provide centralized operating controls and status for laser systems such as the Pockels cell, alignment controls, and optical pulse generation. The supervisory system also handles data archiving and integration services. Front-end processors provide the distributed services needed to operate the approximately 36,000 control points in the NIF. During Title II, we will refine our design and begin the actual software coding, an activity that will continue throughout Title III.

Introduction

NIF's complex operation, alignment, and diagnostic functions will be controlled and orchestrated using the ICCS. The ICCS must integrate about 36,000 control points, operate continuously around the clock, and be highly automated and robust. The system architecture also must be flexible; typically, control systems for complex facilities such as the NIF must be able to absorb significant changes in requirements late in project construction. To mitigate risks to the infrastructure, the ICCS design incorporates modularity, segmentation, and open systems standards. This design allows components and subsystems to be replaced at designated interface points, if necessary. Risks to the control system software are managed through a modern, object-oriented software framework that is used to construct all the applications. This framework is extendable and maintainable throughout the project lifecycle. This framework also offers interoperability among computers and operating systems by leveraging CORBA—a "common object request broker architecture" (see "What Is CORBA?" on facing page).

During NIF's 30-year lifetime, the operation of the facility will evolve and computer technology will change. We are planning for this evolution by adhering to existing industry standards, such as UNIX for the operating system; a structured query language (SQL) for the database technology; Ada for the programming language; X-Windows and Motif for the user interface; and CORBA for the distributed software.

In this article, we summarize the ICCS's general architecture, the computer system, the supervisory software system, the application front-end processors, the integrated timing system, and the industrial controls system, as well as the integrated safety system.

System Architecture

The ICCS architecture was created to address the general problem of providing distributed controls for a large-scale scientific facility that does not require significant real-time capability within the supervisory software. Figure 1 shows a simple view of the entire NIF computer system. The ICCS is a layered architecture with a supervisory system (i.e., the upper-level computers) controlling the front-end processors (FEPs). The supervisory layer, which is hosted on UNIX workstations, provides centralized operator controls and status, data archiving, and integration services. The FEPs are constructed from VME-bus or VXI-bus crates of embedded controllers and interfaces that attach to the control points. FEP software provides the distributed services needed by the supervisory system to operate the control points.

Eight supervisory and 13 FEP applications are used to implement the specific requirements of the NIF control system, as shown in Figure 2. The topmost layer is the Shot Director supervisory application, which coordinates the supervisory subsystems to provide shot integration.

WHAT IS CORBA?

CORBA is a standard developed by a consortium of major computer vendors (The Object Management Group) that addresses the need for interoperability among hardware and software products. The best way to think of CORBA is as the universal "software bus." CORBA is a series of sophisticated, but standard sockets into which software objects can "plug and play" to interoperate with one another. Even when made by different vendors at different times, the object interfaces are standard enough to coexist and interoperate. By design, CORBA objects operate across languages, operating systems, networks, and tools.

When objects interact, it is convenient to label one "the client" (that is, the object that initiates the interaction), and the other "the server" (the object that responds to the initiative). CORBA provides tools for building both clients and servers, and allows an object to be a client in some interactions and a server in others. Historically, the interface between clients and servers were separately defined and developed for each application, type of machine, and computing environment. It was unusual to find much in common. By meeting the interface definition of CORBA, the clients and servers of applications can now easily communicate with one another.

The figure shows a greatly simplified diagram of CORBA's major parts. The object request broker (the "ORB" in CORBA) establishes the client–server relationships between objects. Using an ORB, a client can invoke a method on a server object. The ORB intercepts the call and is responsible for finding an object that can implement the request, pass to it the parameters, invoke its method, and return the results. The interface types and methods provided by the servers and used by the clients are defined by an industry-standard Interface Definition Language (IDL). The IDL compiler examines the interface specification and generates the necessary interface code and templates into which user-specific code is added. The code in the client that makes use of CORBA objects is written as if the server were locally available and directly callable— CORBA takes care of all the rest.

CORBA "brokers" between client and server software systems using objects as the common components. In traditional client/server interactions, the client must be programmed to send requests directly to the server. (40-00-0298-0341pb01)
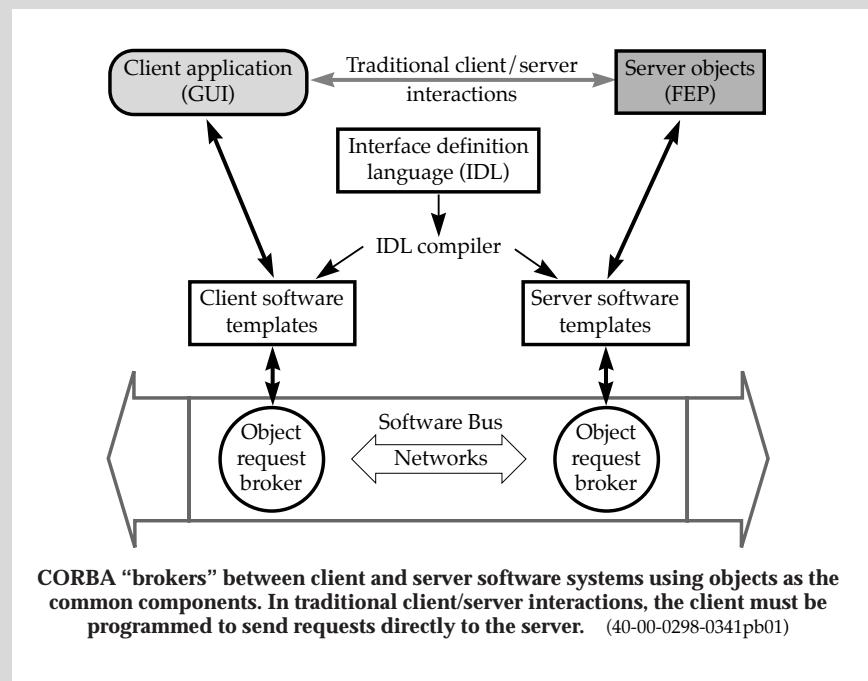
Seven other supervisory applications provide operator control and status. In the next level, application FEPs introduce the capability for autonomous control, provide services to the upper layers, and use the services from the layer below. These application FEPs control ten applications: wavefront, power conditioning, laser energy, laser power, master oscillator room (MOR), automatic alignment, preamplifier module, plasma-electrode Pockels cells (PEPCs), target diagnostics, and industrial controls. The bottom layer comprises FEPs that provide device control services to the upper layers. These server FEPs control three "server" applications: alignment controls, timing, and video.

This architecture is generally applicable to event-driven control systems where client–server tactics are appropriate, as in the case of NIF. For NIF, the shot timeline occurs over several hours and can be suspended if necessary. Some real-time control is necessary; this is handled by the specific subsystems, such as the Integrated Timing System (see p. 208), or at the edges of the architecture. The ICCS client–server architecture will meet NIF's shot timeline requirements, as shown in Figure 3.
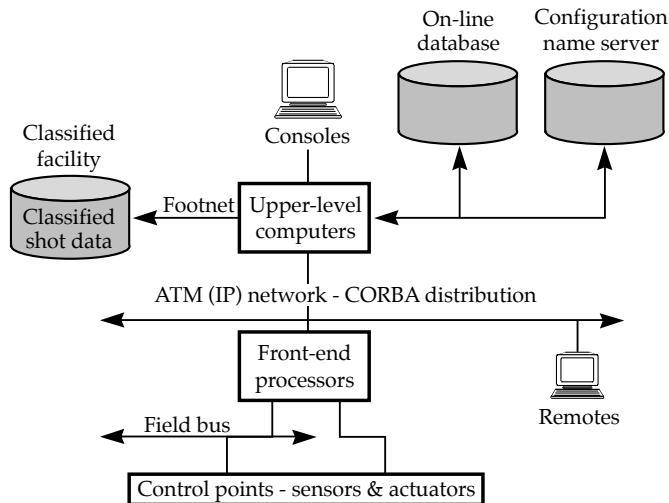
FIGURE 1. The NIF computer system includes upper-level (supervisory) computers, which are connected to consoles in the NIF control room, front-end processors, and remote consoles in the NIF laser bay and target area. The system also includes an on-line database, a configuration name server, and a classified facility for storing classified shot data. (40-00-0298-0323pb01)

Title II Activities

During Title II, we will complete hardware designs and propose plans for procurement, assembly, and installation. Simulation of key parts of the control system will be conducted to ensure adequate capacity and performance of the ICCS infrastructure. We are taking an itera-

tive approach to software development. Our general strategy is to deliver the most needed functionality first, adapt to changing requirements when they become known, and add increasing detail in later releases. During Title II, we plan to activate a production prototype of the software, a year before the first NIF bundle. The prototype will demonstrate the capability of this software design to meet key NIF requirements. Most of the detailed software coding will be done during Title III.

Computer System

The NIF computer system can be divided into two broad areas: the software engineering and the operations computer systems. The software engineering computer system includes software development tools, development and testbed computers, and software targets. The operations computer system includes file servers and run-time commercial software, control room and remote operator consoles, and the graphical user interface (GUI).

The software engineering computer system will be used to develop software for the facility (see "Developing NIF Software" facing page). This system supports both supervisory computers and FEPs. Most FEP targets are PowerPCs. For the supervisory applications, we picked the Solaris operating system. The hardware includes a Sun Ultra-SPARC file server, "Sun SPARC 5" workstations, a switched Ethernet local area network, and an asynchronous transfer mode (ATM) switch. The software development tools include a Rose object-oriented design

FIGURE 2. NIF supervisory and front-end processor software subsystems. (40-00-0298-0324pb01)
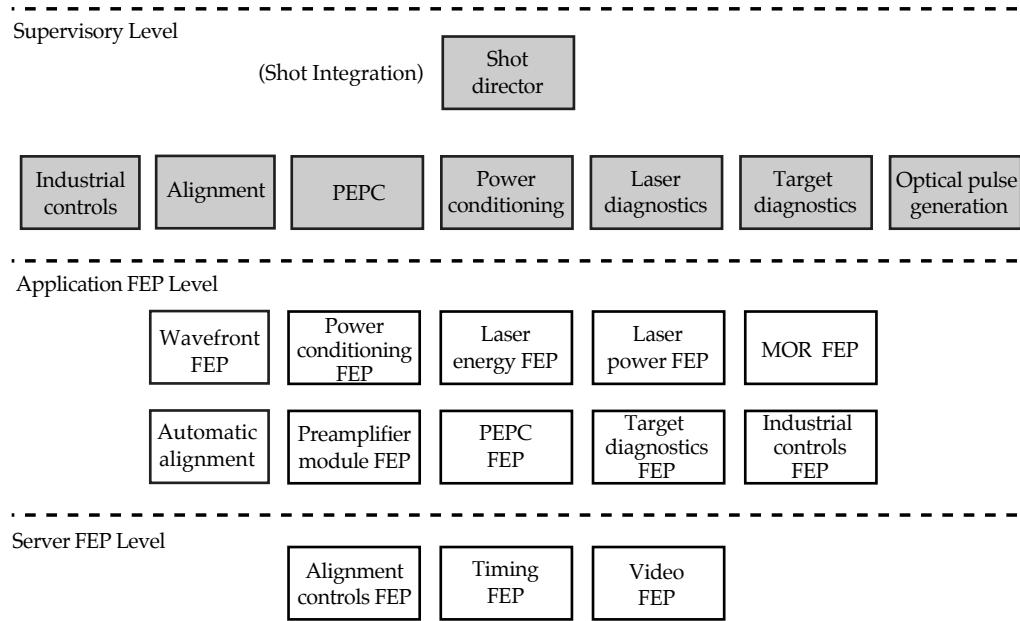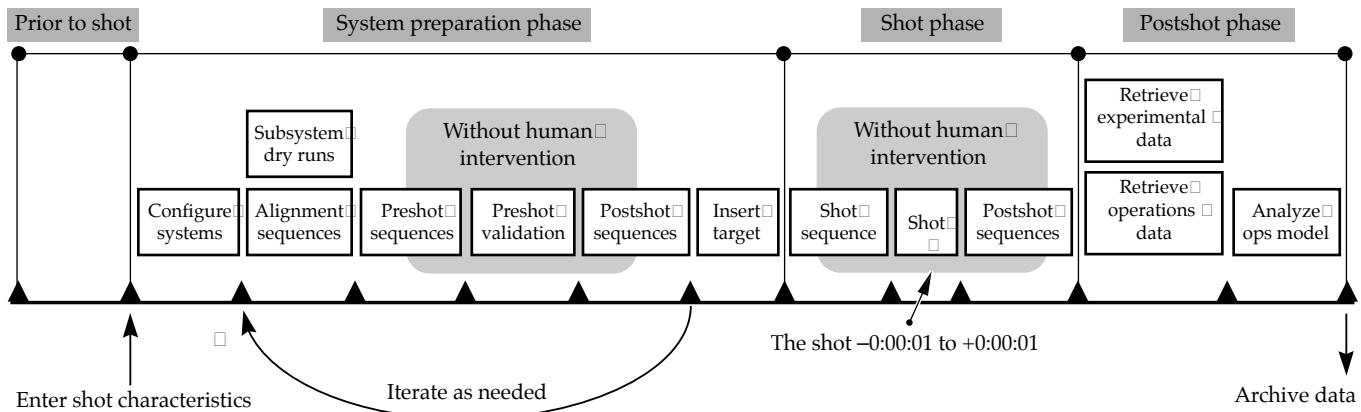
FIGURE 3. The shot timeline. Because the sequence can hold indefinitely, by iterating through the system preparation phase, event-driven techniques are appropriate. A "real-time" NIF shot lasts about 2 s. Other operating modes include computer start-up, maintenance, and commissioning.   (40-00-0298-0325pb01)

tool, Ada 95 and C++ integrated compilers, and an Apex development environment. Other software tools include Objective Interface Systems CORBA for Ada 95, a UIM/Orbix graphical user interface tool, and an Oracle relational and object-oriented database. For the FEP targets, we use VxWorks Tornado real-time UNIX. Figure 4 shows an early Title II design for the software engineering computer system.

Figure 5 shows the Title I operations computer system (i.e., the computers that control the NIF) and network. In the computer room, a pair of file servers provides disk storage and archival databases for the entire system. The file servers also host centralized management and naming services necessary for coordinating the facility operation. Each server has two central processing units (CPUs), expandable to four, and 512 Mbytes of memory, expandable to 30 Gbytes. Servers also have hot-swappable components, redundant power, and redundant cooling. The storage array has 75 Gbytes of memory, expandable to 300 Gbytes, and hot plug disk drives.

Developing NIF Software

ICCS software development is managed under a software quality assurance plan that covers the entire life cycle of the software design, production, and maintenance. Central to the software development are documentation standards for requirement specifications (SRSs) and software design descriptions (SDDs). These documents are essential to the long-term maintainability of the software in view of the periodic software upgrades and staffing turnover expected over the 30-y life of the NIF.

First, we analyze the SRSs and use the Rose tool to obtain object-oriented designs. We then examine classes, or sets of objects that share common structures and common behaviors, to find any abstractions and patterns. Rose then generates code specifications in Ada and Interface Definition Language (IDL)—these specifications form the design description for the software. The software engineers write detailed codes, according to the code specifications. The resulting code is compiled, linked, and debugged. If the code is for supervisory applications, it is compiled by an Apex Ada 95 self-compiler and linked for the Solaris target. If the code is for an FEP, it is compiled through an Ada 95 cross-compiler, before linking to a Power PC VME target (or others) existing in a VxWorks Tornado real-time environment. The working software is finally reverse-engineered to capture any specification changes back into the original Rose model.
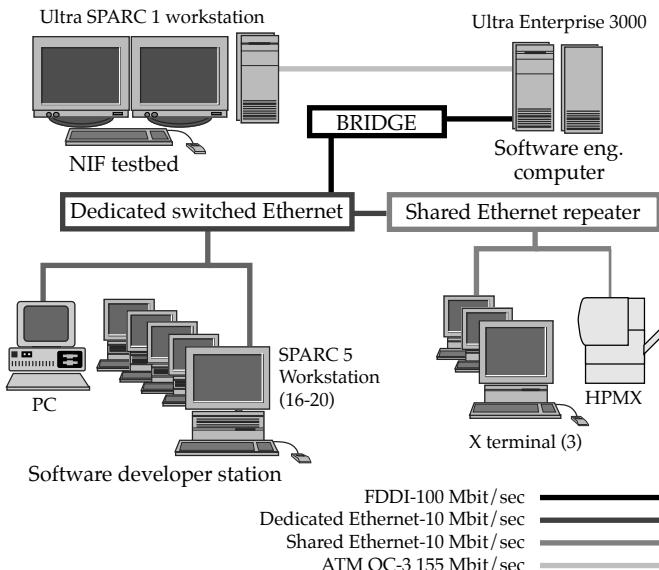
FIGURE 4. Software engineering computer system layout.
(40-00-0298-0326pb01)

The network backbone is built from ATM switches capable of carrying digital motion video as well as standard Internet protocol (TCP/IP). TCP/IP is used for most communications. FEPs are generally attached to shared Ethernet, switched Ethernet, or Fast Ethernet depending on the bandwidth requirements of the control devices and supervisory communication. Some FEPs and all workstations and file servers are attached directly to ATM for maximum communications performance.

Figure 6 shows the main control room layout. The seven graphic consoles include one dedicated to the shot director and six operator consoles. The shot director's console has three color monitors and an Ultra-SPARC 1 with 256 Mbytes of memory. Each operator console has two workstations with two color monitors per workstation. Figure 7 shows where the remote consoles will be located in the facility. There are 13 video-capable consoles and four X-terminal consoles.

Title II Activities

Early on in Title II, we will procure and activate the remaining software engineering computer tools and components. We will also support the first phase of software framework construction. This construction includes demonstrating the integration of vendor-supplied

FIGURE 5. NIF computer system and network
(40-00-0298-0327pb01)
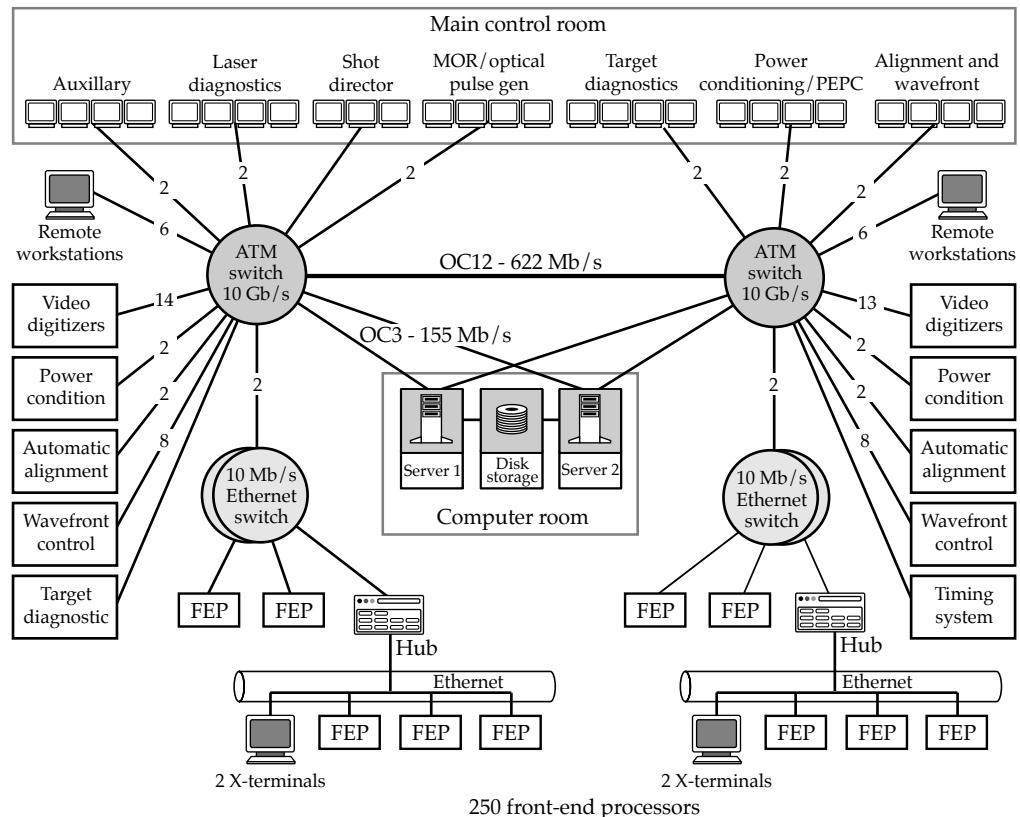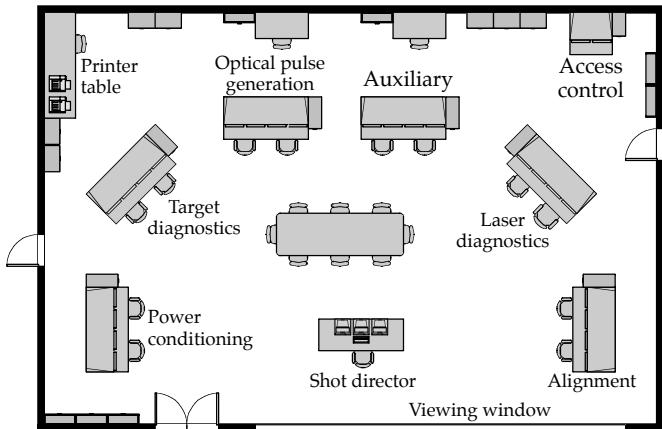
FIGURE 6. Operator control room layout.   (40-00-0298-0328pb01)

software tools, improving our understanding of CORBA performance scaling, and constructing a sample FEP to demonstrate how the tools work. During Title II, we will also develop a more detailed model for guiding computer sizing and software deployment.

Supervisory Software System

The supervisory controls must provide semiautomated sequencing of NIF shots, GUI operator controls, event-driven status reporting for broad-view status displays, shot-data processing, reporting, and archiving, and time-stamped logging and abnormal event ("exception") handling.

The ICCS supervisory software provides integrated control for NIF's seven supervisory applications—alignment controls, the PEPC, power conditioning, target diagnostics, optical pulse generation, laser diagnostics, and industrial controls. It also provides manual operator controls for maintenance; acquires, displays, archives, and reports laser and target-area shot data; configures laser and target-area sensors using FEP capabilities; and provides control room interface for facility environmental monitor, access control, and safety interlocks.

We derived the performance requirements for the supervisory systems from the operators' needs for timely information and interactive responses. The broad-view status update must complete in 10 s, and some GUIs require 10 updates/s. The software is event-driven: status information is propagated from the laser to updates on the graphic user screens. Some process controls are encapsulated in the FEPs and are not part of the supervisory system, notably wavefront control, automatic alignment, and capacitor charging.

The supervisory system is divided into application software—including a database management system—and frameworks, as follows.

Application Software

Application systems perform NIF functions—they execute operator commands, report on machine status, and manage operational and archival data. These supervisory applications play major roles in the life cycle of a NIF shot. While setting up a plan
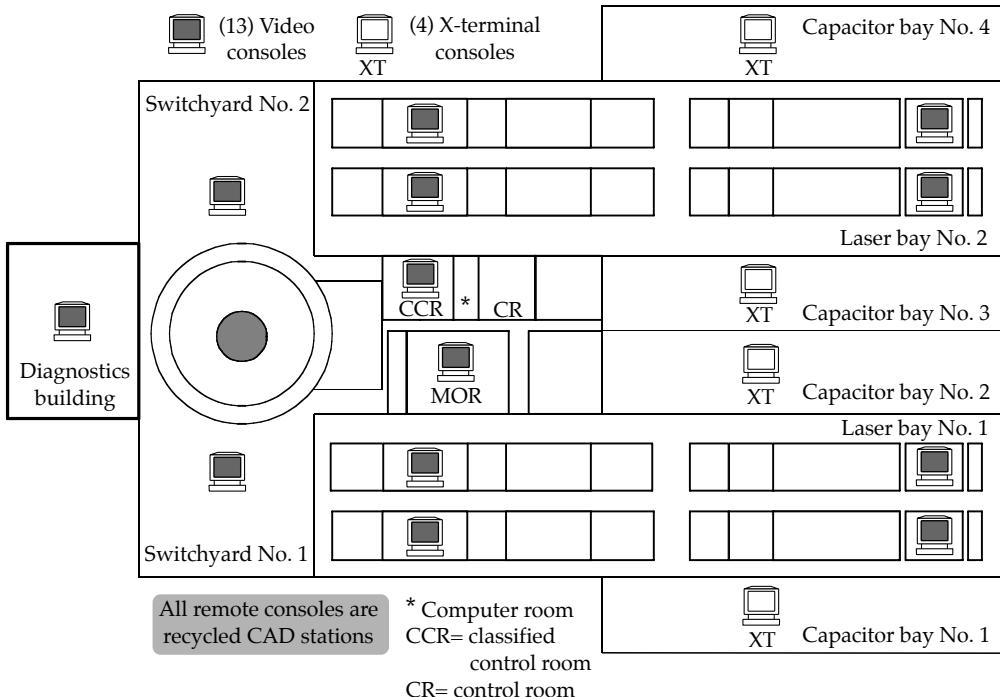
FIGURE 7. Location of the remote consoles in NIF. Graphical user interface controls and motion video are available through these consoles.   (40-00-0298-0329pb01)

for a "system shot" (a shot when the laser is fired to satisfy a set of experiments), experiments may be added or removed, or experimental goals may be changed. There are also nonsystem shots, including the preamplifier module shot, the target alignment sensor shot, and the dry-run shot. As a result of these nonsystem shots, some setup plan parameters are adjusted. Finally, when the system shot is taken, the results are archived and the shot is complete. During this life cycle, there are six ICCS software control phases, as follows:

- Phase I—pick the experiments that will make up the shot.
- Phase II—derive values for the laser hardware to accomplish the shot, perform laser model calculation, and refine the experiments.
- Phase III—set the derived values in the laser hardware to accomplish the shot.
- Phase IV—ensure that the hardware is properly set up and disable changes.
- Phase V—perform the final, time-critical setup, and pass control to the integrated timing system.
- Phase VI—save the information for later analysis.

Figure 8 shows approximately where these phases occur in the timeline of a NIF shot. In "real time," the NIF shot lasts about 2 seconds.

Database Management System

The supervisory applications will draw upon and create an enormous amount of data that must be stored and archived. To manage this data, we are designing an object-relational database management system. This database system will include:

- A configuration database, which stores persistent information pertaining to control system operation, such as device parameters.
- Experiment data sheets, which store experiment goals. Each NIF shot may involve many sheets.
- The shot setup plan, which stores parameters that describe setup conditions for executing a shot. The plan is the collective goals of all experiment data sheets for a particular shot.
- The shot data archive, which temporarily stores data associated with a shot. Each subsystem will likely have its own archive application program, and a record of what is put into each archive package is stored in the database.
- Machine history, which will store the history for each NIF component of interest (e.g., motors, photodiodes, cameras, switches). This history will be used to characterize performance, schedule preventive maintenance, trigger calibration, etc.

For our database design, we are assuming that we will keep online one year's worth of experiment data

FIGURE 8. Estimate of where the six ICCS software control phases will occur in the timeline of a NIF shot. This figure also shows that setup parameters are readjusted after a nonsystem shot.   (40-00-0298-0330pb01)
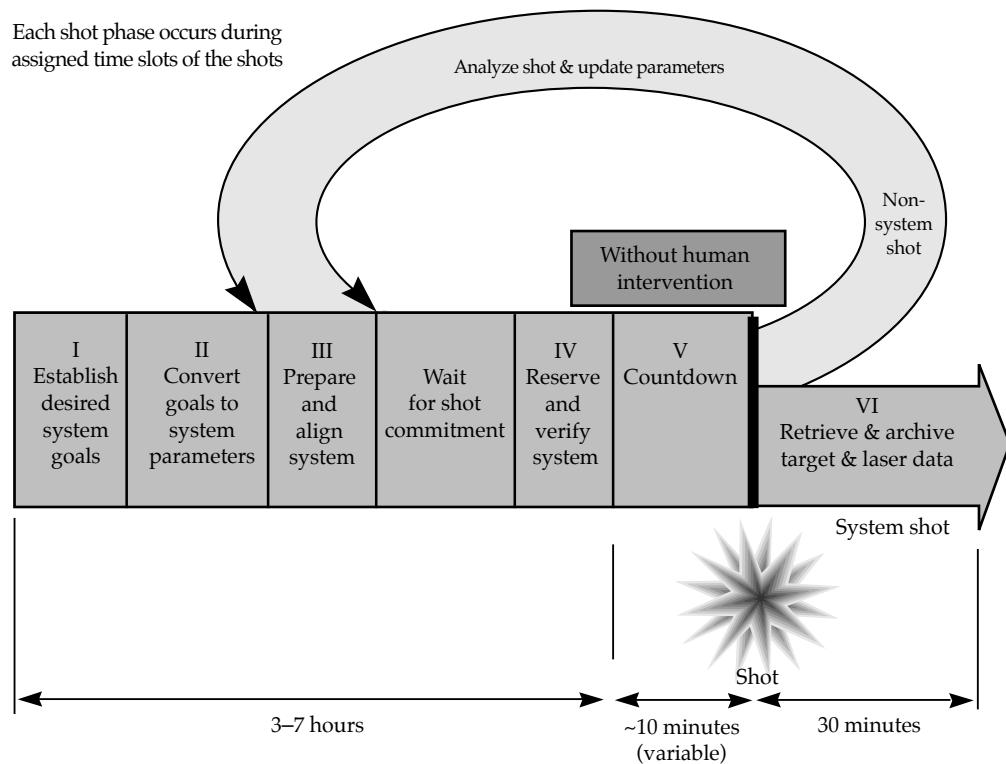
sheets and shot setup plans, 20 shots' worth of shot archive data, machine history for 100,000 components, two weeks' worth of optics inspection data, and configuration data for 50,000 components. We are estimating that we will need a total of 1278 database tables, and about 66.7 Gbytes of disk space.

Frameworks

The ICCS supervisory software framework is a collection of collaborating abstractions used to construct the application software. A framework reduces the amount of coding needed by providing prebuilt components that can be extended to accommodate specific additional requirements. A framework also promotes code reuse by providing a standard model and interconnecting backplane that is shared from one application to the next.

Components in the ICCS framework plug into the CORBA bus. The ten frameworks that form the basis of the ICCS supervisory software are as follows.

The *configuration framework* provides a hierarchical organization for the static data that define the hardware control points accessible to the ICCS. Configuration provides a taxonomic or hierarchical "naming" system that is used as the key by which clients locate devices and other software services on the CORBA bus.

The *status monitor framework* provides generalized services for broad-view operator display of device status information. The status monitor observes devices and notifies other parts of the system when the status changes by a significant amount.

The *sequence control language (SCL) framework* is used to create custom scripting languages for the NIF applications. The SCL service automates sequences of commands executed on the distributed control points or other software artifacts.

The *GUI framework* ensures that the GUIs displayed upon the control room consoles or X terminals are consistent across the applications. The GUI framework is based upon the X Windows system and Motif policies.

The *message log framework* provides event notification and archiving services to all subsystems or clients within the ICCS. A central server collects incoming messages and associated attributes from processes on the network, writes them to appropriate persistent stores, and also forwards copies to interested observers (primarily GUI windows on the screens of operators' consoles).

The *reservation framework* manages access to devices by giving one client exclusive rights to control or otherwise alter the device. The framework uses a lock-and-key model; reserved devices that are "locked" can only be manipulated if and when a client presents the "key." Read access to obtain status is not affected by the reservation.

The *system manager framework* provides services essential for the integrated management of the hundreds of computers on the ICCS network. This framework ensures that necessary processes and computers are operating and communicating. Services include parameterized system start-up, shutdown, and process watchdog monitoring.

The *machine history archive framework* collects information that originates within the ICCS about the performance and operation of the NIF. This data is used in analyzing the NIF operation to improve efficiency and reliability.

The *generic FEP framework* pulls together the distributed aspects of the other frameworks (in particular, system manager, configuration, status monitor, and reservation) by adding unique "classes" for supporting device and controller interfacing. The generic FEP also defines a common hardware basis including the target processor architecture, backplane, I/O boards, device drivers, and field-bus support. (See "Front-end Processors" below for more information about the generic FEP.)

The *shot data archive framework* allows collecting the data from the diagnostics, making the data immediately available for "quick look" analysis, and delivering the data to an archive. The framework contains a server working with the system manager to assure that requested shot data are delivered to a disk staging area. The archive server is responsible for building a table-of-contents file and then forwarding the table and all data files to the archive.

Title II Activities

During Title II, we will begin designing detailed object models of substantial portions of the frameworks for the supervisory software. We will use the ICCS testbed to demonstrate control integration in FY98, and deliver basic supervisory software services when the first NIF bundle is activated in FY00.

Front-end Processors

We currently estimate that NIF will have over 293 FEPs to integrate control points such as sensors and actuators. These control points attach to interface boards plugged into the FEP backplane. In many cases, control points are handled by intelligent components such as stepping motor controllers, photodiode detectors, and power supply controls. These components incorporate local microprocessors operated by small fixed programs (called embedded controllers). In a few cases, remote devices attach to FEP units by using a low-cost network of microcontrollers known as a "field bus."

(a) Control points

(b) Applications

Preliminary information
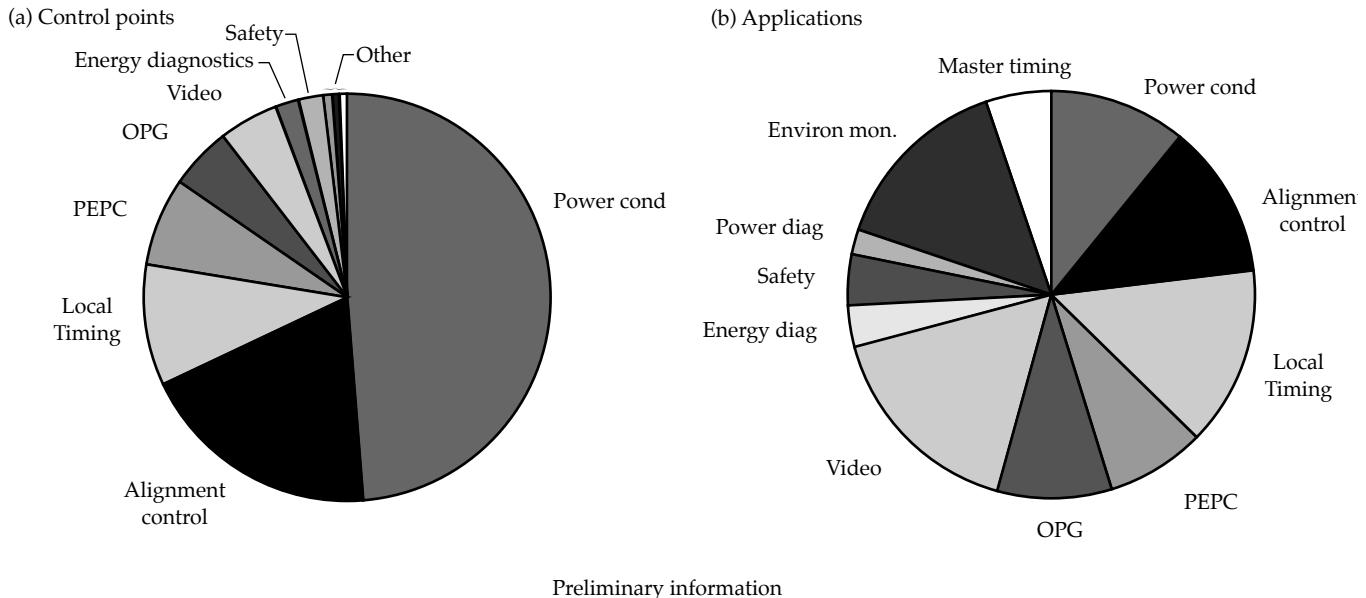
FIGURE 9. Charts showing relative amounts of (a) control points and (b) applications for the various NIF systems (preliminary information, based on Title I design). The present design has 35,826 control points for 96 kinds of devices. These device types are used in 461 different applications. (40-00-0298-0331pb01)

Every control point or device has a unique control-system name, called a "taxon." The elements of that taxon identify where the device is in the NIF system (i.e., what major system it resides on and the "area" within that system), the equipment that contains it [i.e., the container— sometimes a line-replaceable unit (LRU)—and the package within the container], and what kind of device it is (whether a gimbal, shutter, etc., and which particular gimbal or shutter). For Title I, our preliminary information shows that there are about 36,000 control points of 96 kinds of devices in 461 applications (see Figure 9).

Our goal is to build the FEPs with as many common elements as possible to reduce software development and risk. To that end, we are developing a generic FEP, which we will provide to the FEP designers. Figure 10 shows the contents of a generic FEP. It will include frameworks (those software codes that call up services common to all FEPs); a common design; common tools and operating environment; common start-up and control methods; common hardware, where possible; and common test software. At the top of Figure 10 are the frameworks including the user interface, the message log and alert, and the system manager. Each FEP will also contain code to support the device reservation and status monitor frameworks. There are also specific FEP applications. Each FEP will include a device simulation code that allows a supervisory-level system to simulate that FEP's activity, if needed. Each FEP will also have a real-time operating system and drivers that go out to the hardware devices and echo back. For an example of a specific FEP design, see "Automatic Alignment Front-end Processor" on facing page.
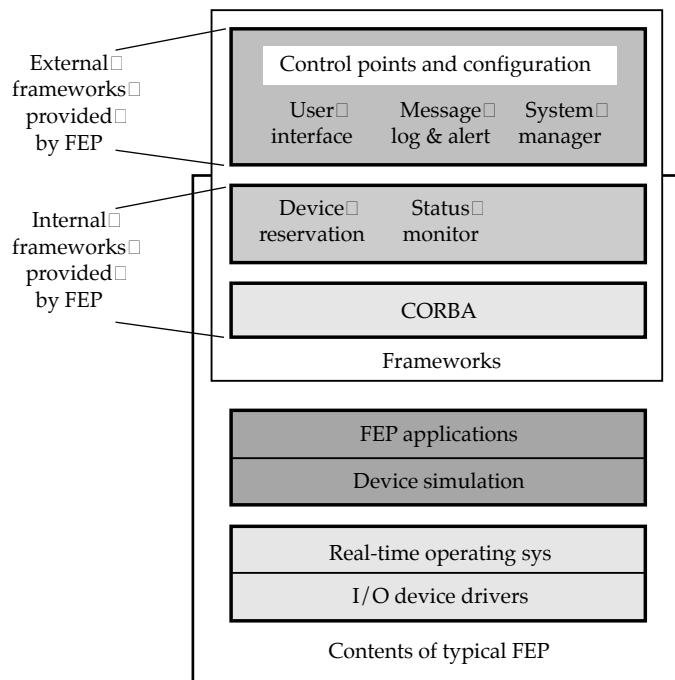
FIGURE 10. A generic front-end processor. (40-00-0298-0332pb01)

Title II Activities

During Title II, we will establish uniform terminology and control point taxons throughout the design materials and drawings and will complete input and addition of information on the control

AUTOMATIC ALIGNMENT FRONT-END PROCESSOR

The requirements imposed on the FEPs for automatic alignment reflect the requirements on the alignment system. This system must automatically align NIF within 30 minutes, point the beam to align with the pinholes, center the beam to align apertures of several optical sections, adjust the beam's 3D orientation, focus the beam onto the target, adjust the KDP angle to match beam pointing, and balance the spatial power distribution of the serrated aperture.

As a result of these requirements, the FEPs have many functions. The primary function is to align the beamlines from the front end of NIF to the target. With more than 3000 devices to align, timely alignment would be impossible without an automated system. The automatic alignment software system must perform electro-optical characterizations, making measurements with video images; determine cross-coupling of some groups of devices; and determine pixel (image) to steps (motors) scale factors. Finally, it must accommodate classified targets, using a classified FEP to align the beamlines. An actuator control translator provides the required control information from the classified computer to the unclassified devices.

To accomplish these tasks, the automatic alignment FEPs interact with the alignment controls supervisor and laser diagnostics supervisor, as well as the service-level FEPs for video and alignment controls. The generic control loop used to align a single beam is shown in the figure at right. There are four basic types of alignment control loops—pointing, centering, rotation, and focusing. The pointing loop must compare beam images with reference reticles; the centering loop compares centroids from two pairs of light sources; the rotation loop compares orientation of two pairs of light sources; and the focusing loop adjusts the spot size of the beam on the target.

Our Title I hardware design is based on Sun's Enterprise 3000 system, which uses Ultra-SPARC processors. To meet the performance requirements, we will have four automatic alignment FEPs to align the 192 beamlines. Alignment will require 17 control loops per beamline: 8 for pointing, 6 for centering, 2 for rotation, and 1 for focusing. We anticipate four iterations per control loop to reach tolerance.
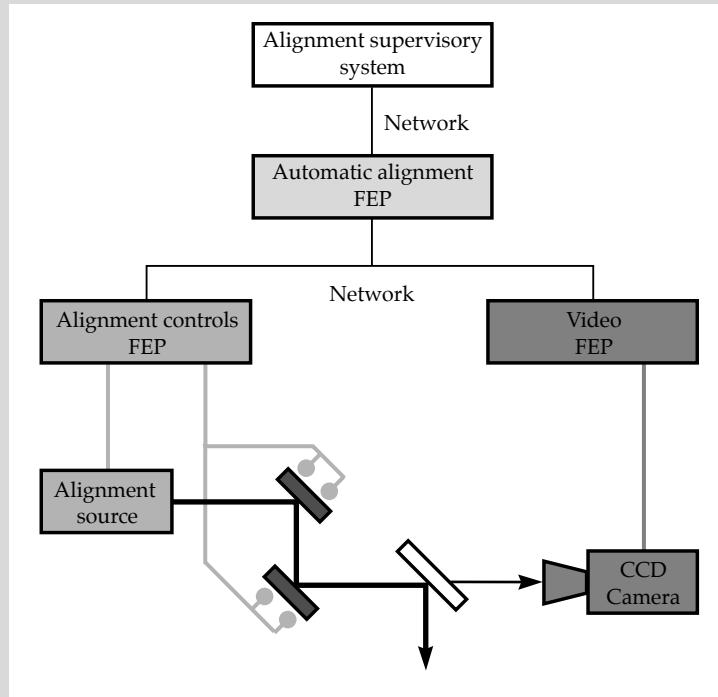
In the generic control loop, the automatic alignment FEP accepts alignment sequence commands from the supervisory system. The FEP sets up the beamline, commanding the alignment controls FEP to select the source, set the shutters, set filters, etc. It requests and acquires a video image from the video FEP, processes the image, and determines the alignment error by comparing the alignment attributes from the image with a stored reference. It adjusts the component by commanding the alignment controls FEP to manipulate optical devices. Finally, the automatic alignment FEP iterates by reacquiring the image, determining alignment error, etc., until the measurement is within tolerance. Over 3000 of these loops must be closed before each shot. (40-00-0298-0343pb01)

devices. We will also identify and assign taxons to the electronic equipment, computers, networks, and computer interfaces as well. We will review the software catalog for common approaches or any unnecessary devices, and initialize the structure of the configuration database. During Title II, we will also complete the design of a generic FEP, and build the first release, which will support the Title II-level frameworks discussed in the section on supervisory software. Finally, we will deliver this version of a generic FEP to the FEP designers, who are developing FEPs for the various NIF systems.

Integrated Timing System

The integrated timing system (ITS) provides triggering and timing signals to several client systems: the optical pulse generation system, the power conditioning system, the amplifier flashlamps, the PEPCs, laser diagnostics, and target diagnostics. The ITS has specific operational and performance requirements. Operationally, it must provide client control of all relevant parameters, support activation and maintenance activities by clients, quickly detect and recover from a hardware failure, and remain functional over NIF's 30-year lifetime. For performance, it must supply 1200 triggers while satisfying clients' range and stability requirements. We are providing three ITS performance levels to provide timing signals (Figure 11).

ITS has three subsystems: cross timing (fiducial distribution), local timing distribution, and facility timing distribution (Figure 12). The facility timing distribution system uses a standard, two-way time-transfer technique

FIGURE 11. Three ITS performance levels complement the ICCS network to provide timing signals. The extended-range fast timing level (100-ns resolution and stability) has 250 channels; the fast timing level (1-ns resolution and stability) has 900 channels; and the precision timing level (30-ps resolution and stability) has 50 channels. (40-00-0298-0333pb01)
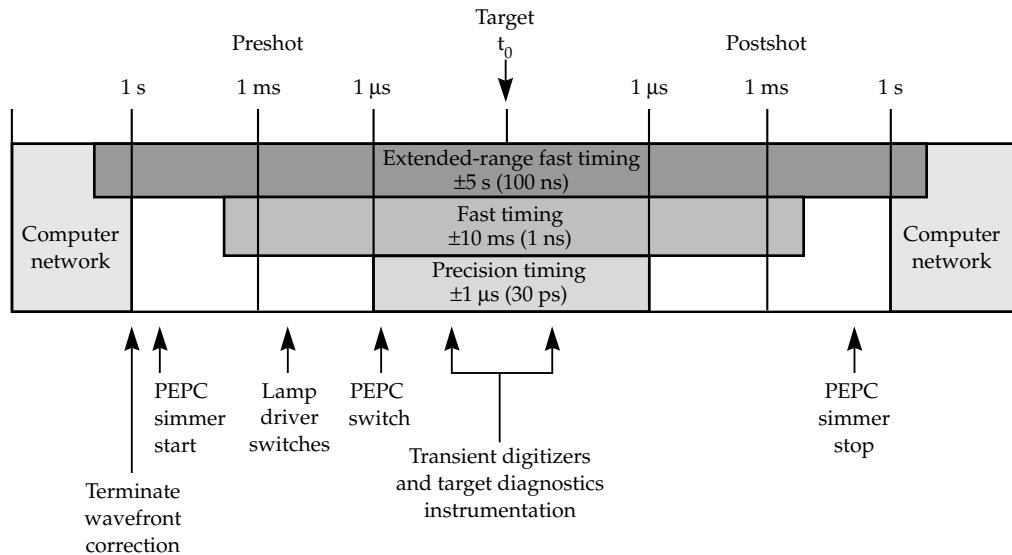
FIGURE 12. Three subsystems make up the integrated timing system, which supplies coordinated trigger and fiducial signals to NIF equipment. (40-00-0298-0334pb01)
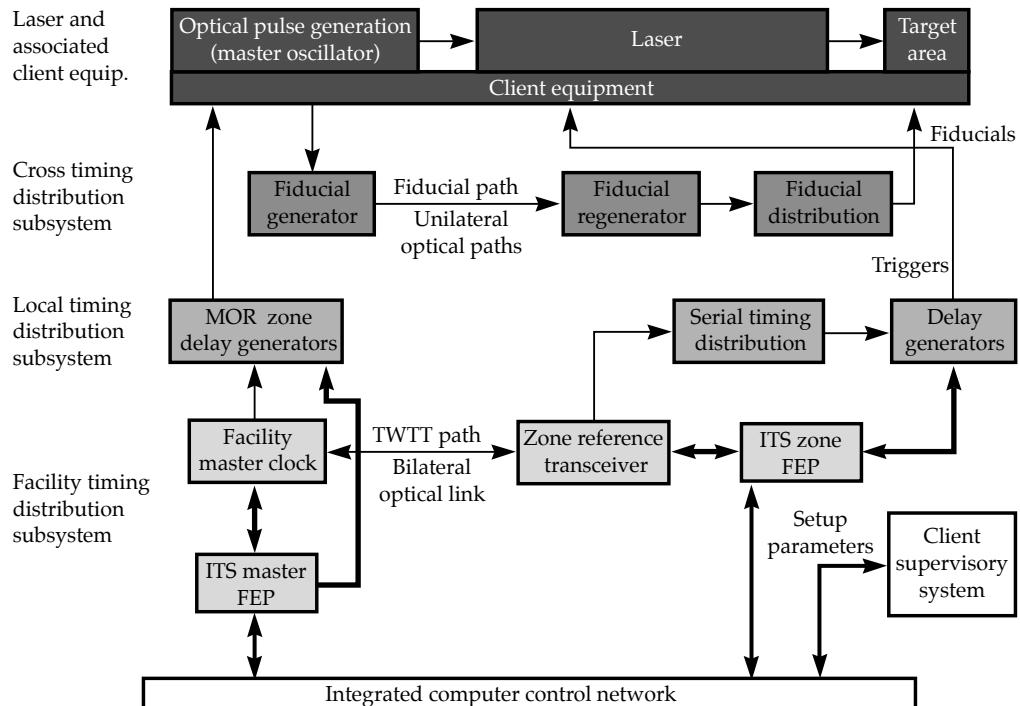
(TWTT) which continuously monitors and compensates for transmission pathlength changes. TWTT will service 11 remote clocks, distributed throughout the Laser and Target Area Building (LTAB) (Figure 13). Each clock will serve a zone with several timing clients. For instance, one of the clocks in laser bay No. 1 will provide timing for preamplifier modules, energy diagnostics, power diagnostics, and imaging diagnostics. Within each zone, the local timing distribution can be easily expanded.

The broadcast serial encoded data—which travels from the zone master clock through the 1:8 splitters to the hex-delay generator—carries all the timing information needed, including epochs, gates, and a phase-critical reference clock. Epochs generate triggers at a fixed repetition rate. We have several specified epoch rates between 0.2 Hz and 960 Hz to support current needs, and have at least two others available for special needs and future growth. Gates generate single-shot triggers. Two gates are reserved for the shot director application—one for dry run/rod shots, the other for system shots. Clients can reserve other gates for use as diagnostic tools and so on. When a client is done, the gate is released for use by others. Finally, a high-frequency, phase-critical reference clock (155.52 MHz) is recovered in each delay generator.

The ITS software provides the link between client requests and generated triggers, and a number of databases provide information needed to operate and maintain the ITS. For instance, two databases are maintained by clients: the shot setup database, which contains client setup parameters, and the laser pathlength database, which keeps track of optical path lengths. The ITS-maintained databases are used to generate control bit patterns. For instance, the local t_0 database computes local t_0s for each client, based on contents of the laser pathlength database. The ITS timing path database contains data on internal ITS pathlengths to correct for detected changes and accelerate recovery due to hardware replacement.

The ITS and the master oscillator maintain a critical timing relationship; the master oscillator room maintains the fiducial in sync with the ITS reference, and the transmitted beams in sync with the fiducial. The ITS also provides optical and electrical fiducials to cross-time diagnostics.

Title II Activities

We have ordered a demonstration facility timing system consisting of a master clock and single remote clock; we anticipate the system will have a timing stability of ~200 ps. We will evaluate and enhance this system early in Title II to reach precision performance levels. A delay generator that will meet NIF precision performance goals is not currently available, but we are working with industry to modify existing designs to enhance stability and meet NIF goals. We also plan to be compatible with the French Laser Megajoule (LMJ) project timing system, so that each of us will have an alternate delay generator source.
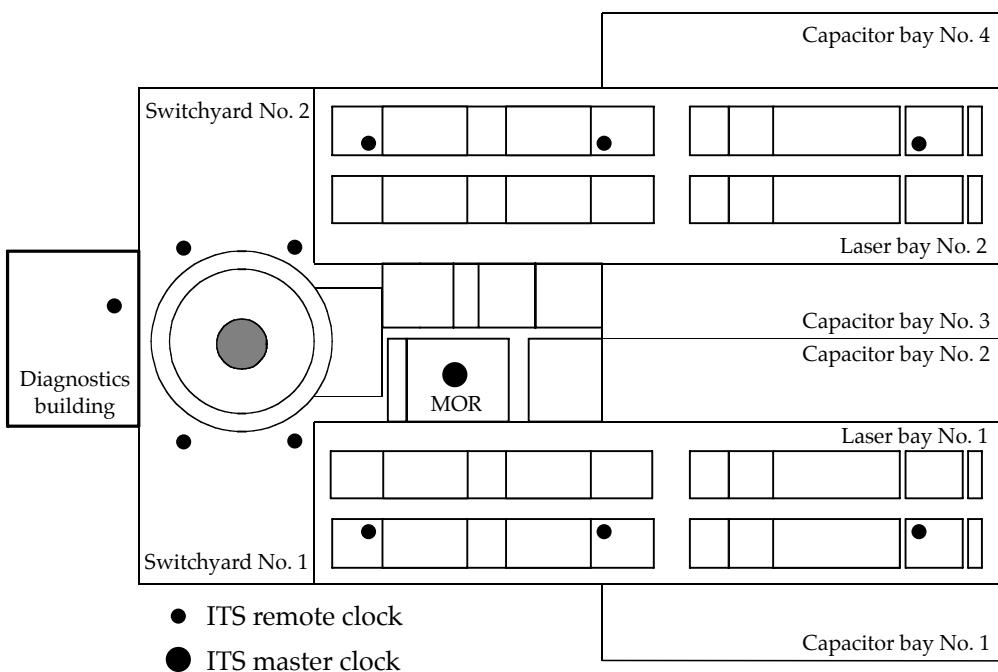
FIGURE 13. Location of the remote clocks and master clock in the NIF buildings. (40-00-0298-0335pb01)

Industrial Controls System

The industrial controls system (ICS) includes the industrial control FEPs, the facility environmental monitor, the communications system, and the integrated safety system. Figure 14 shows a block diagram of the ICS.

Industrial Controls FEP, Facility Environmental Monitor, and Communications System

The two ICS FEPs interface 12 separate industrial controls application areas to the supervisory system:
- The amplifier cooling system.
- The beam transport vacuum system.
- Beam transport gas system.
- Facility environmental monitor.
- Target chamber vacuum system.
- Environmental protection system.
- Tritium processing system.
- Personnel, safety, and occupational access.
- Final optics assembly (FOA) thermal control system.
- Safety interlock system.
- Access control system.
- t-1 abort system.

The last three systems, which form the integrated safety system, are discussed separately in the "Integrated Safety System" section (p. 211).

Programmable logic controllers (PLCs) individually control all but one of these application areas. (The access control system is controlled by a personal computer.) Communications between the ICS FEP and the various subsystems will occur over the ICCS Ethernet network, while communications to the supervisory layer will occur over the ICCS network via CORBA. The industrial controls FEP is scoped to be a SPARC 5 processor in a VME crate running the Solaris UNIX operating system. There are interfaces for control and monitoring, and others for monitoring only (see Table 1).

The environmental monitor must measure and display facility environmental parameters affecting the laser's performance, i.e., temperature, relative humidity, oxygen content, vacuum, argon flow, and nitrogen flow. It must also archive environmental parameters, provide trending displays and reports, and provide machine interlocks to prevent damage to equipment or loss of shot data due to improper operating conditions. This monitor acquires facility environmental data from network data acquisition modules located throughout the facility and acquires additional environmental data from the amplifier cooling system, the spatial filter
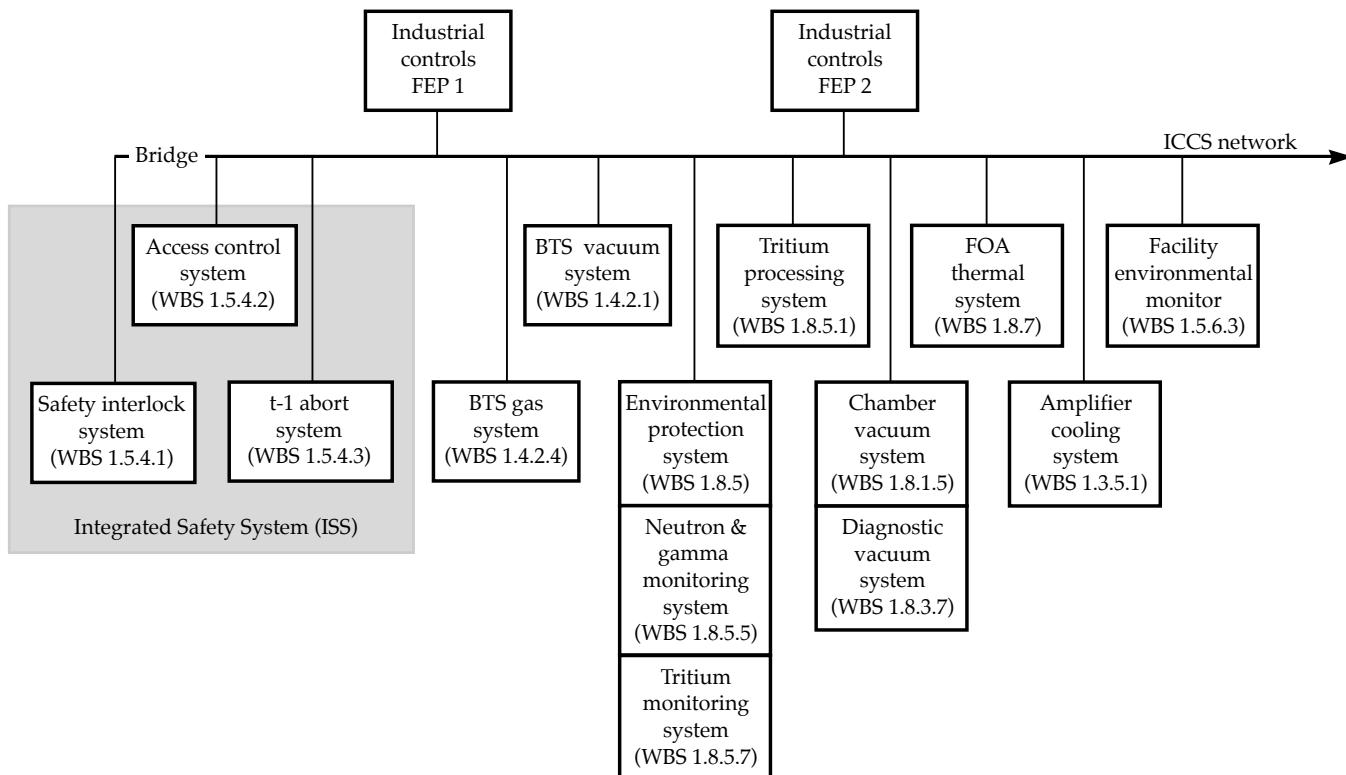
FIGURE 14. Block diagram of the industrial controls system (ICS). (40-00-0298-0336pb01)

TABLE 1. Industrial controls interfaces for control and monitoring, and for monitoring only.

Controlling and monitoring	Monitoring only
Beam transport vacuum control system	Facility enviornmental monitor(data acquired via network data acquisition modules)
Beam transport gas control system	Safety interlock system
Amplifier cooling system	Access control system
FOA thermal control system	t-1 abort system
Target chamber vacuum control system	Envionmental protection system

The communications system provides radio communications throughout the facility as well as a video surveillance system. Radio communications includes 50 hand-held transceivers and the necessary repeaters. The video surveillance system consists of 32 surveillance cameras, which may be manually selected for viewing or scanned sequentially. A time-lapse recording system records the camera images.

Title II Activities

For the industrial controls system, our high-priority Title II tasks are to finalize designs for the FEPs and facility environmental monitor, make the final sensor selections, complete enumeration of the machine interlocks, and complete final surveillance system design and camera location assignments.

Integrated Safety System

The integrated safety system (ISS) consists of the safety interlock system (SIS), the access control system (ACS) and the t-1 abort system.

The SIS requirements include providing and controlling the laser and target area status panels. It must determine the hazards from laser light, ionizing radiation, high voltage, and oxygen depletion, and provide and control audible alarms—such as klaxons and

vacuum system, the target chamber vacuum system, and the gas control system. Figure 15 shows the type of sensors employed by the monitor and their location in the facility. The facility environmental monitor provides machine interlocks for situations such as too high a vacuum in the spatial filter, too high an oxygen content for the amplifiers, and out-of-range temperatures in the KDP crystals.
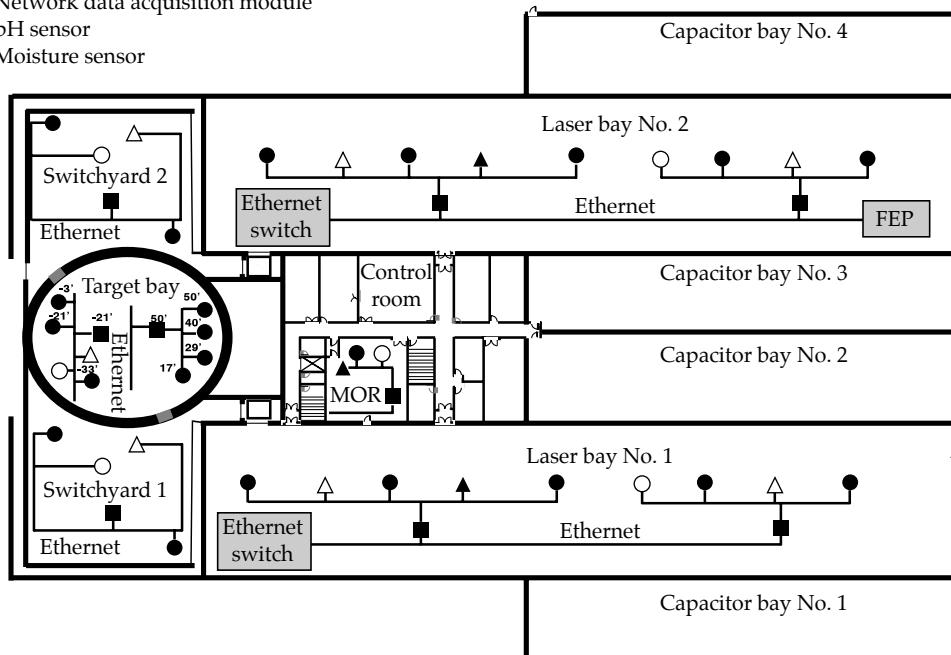
FIGURE 15. Sensor locations for the NIF facility environmental monitor. (40-00-0298-0337pb01)

horns—as well as automatic voice annunciation of hazard-level changes. The system is also required to monitor door positions, crash buttons, and shutter positions, and provide permissives to power conditioning and safety shutters. The SIS must be modular to support partial system operation. It must also provide operator control and status screens, and must fail to a safe condition (be "fail-safe") if there is a loss of AC power.

The SIS distributed system is based on four PLCs. Three PLCs control interlocks in the major areas of the facility, while the fourth "master" PLC oversees the others. As required, the SIS will be capable of functioning in a stand-alone mode, apart from the industrial control FEP or the rest of the ICCS. The SIS is a "safety shutdown" system, not a "mitigating" system. That is, when an abnormal situation is detected, the SIS shuts down the affected system or systems, rather than trying to mitigate the hazard and continue operation. The SIS is designed to be fail-safe, in that it will (1) shut down if there is a communications loss or power loss, (2) allow unrestricted egress from the facility, (3) act as a "watchdog" for the timers that are part of the I/O drops, (4) provide feedback monitoring of all critical outputs, and (5) use internal diagnostics. Although the SIS does not perform process control functions, it does issue control "permissives" allowing interlocked systems to operate. The master PLC performs comparative error checking on the other PLCs in the system. We expect the scan time for the SIS to be about 70 to 100 ms. The SIS monitors and controls 28 "controlled" doors, 80 "monitored" doors, 125 run-safe boxes, 83 status display panels, 28 oxygen monitors, 18 radiation monitors, and 278 outputs (permissives, shutters, etc.). Figure 16 shows the safety devices in a typical NIF beamline; Figure 17 shows the approximate locations of selected devices in the facility.

The ACS must monitor entry and egress of all personnel through the major access points, use names and training records to identify personnel and approve their access, log all monitored access point transactions, and display a summary status. The ACS is designed to function with the SIS and an on-line database of qualified personnel to control access into the NIF. The system allows entry and egress through monitored doors by sensing special badges that will be carried by all personnel and visitors. All movement into, out of, and within the facility will be recorded into a transaction log available to the higher-level ICCS systems. As of Title I, we plan to base the ACS on a personal computer system. The ACS will be able to function as a stand-alone system, without intervention from the industrial controls FEP or other ICCS components. We plan to purchase the ACS as a "turn-key" system, based on a performance specification.

The t-1 abort system is required to work with the ITS to monitor selected components in each beamline before allowing a system shot. The t-1 abort system will abort a shot if the selected components in the active beamlines do not reach their shot configuration positions during the final seconds. We will also be able to configure the abort system to choose which beams to monitor. The components monitored during the last second of the countdown are (1) the output sensor, as 192 mirrors move into the beam path and 96 filter wheels move into position, (2) the input sensor, as 48 alignment laser mirrors move out of position [excluding the preamplifier beam transport system (PABTS) alignment laser and allowing the four-pass to the PABTS], and (3) the cavity spatial filter, as 192 wave plates move out of the beam path. At t-1, the system will begin monitoring the input and output sensors. As of Title I, the abort system is scoped as a PLC-based system.
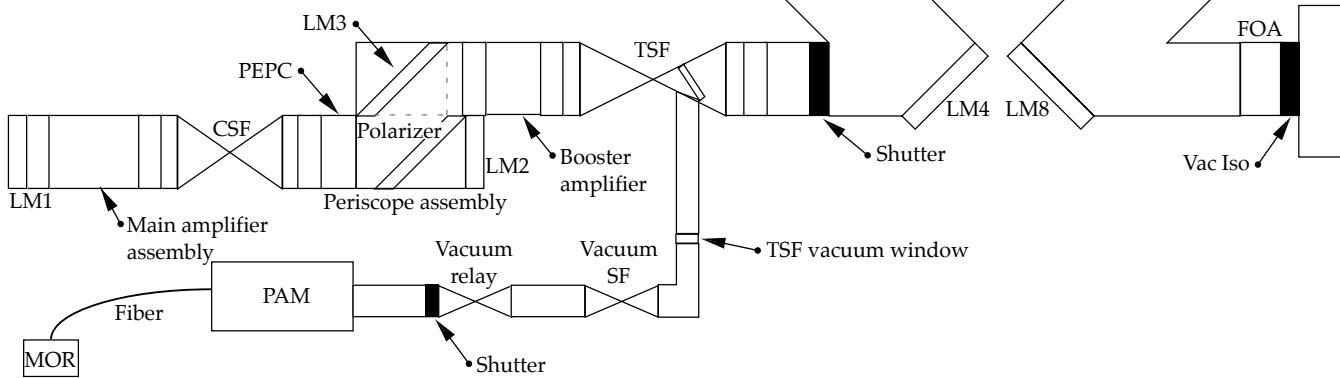
FIGURE 16. Location of safety devices (colored black) in a typical NIF beamline.   (40-00-0298-0338pb01)
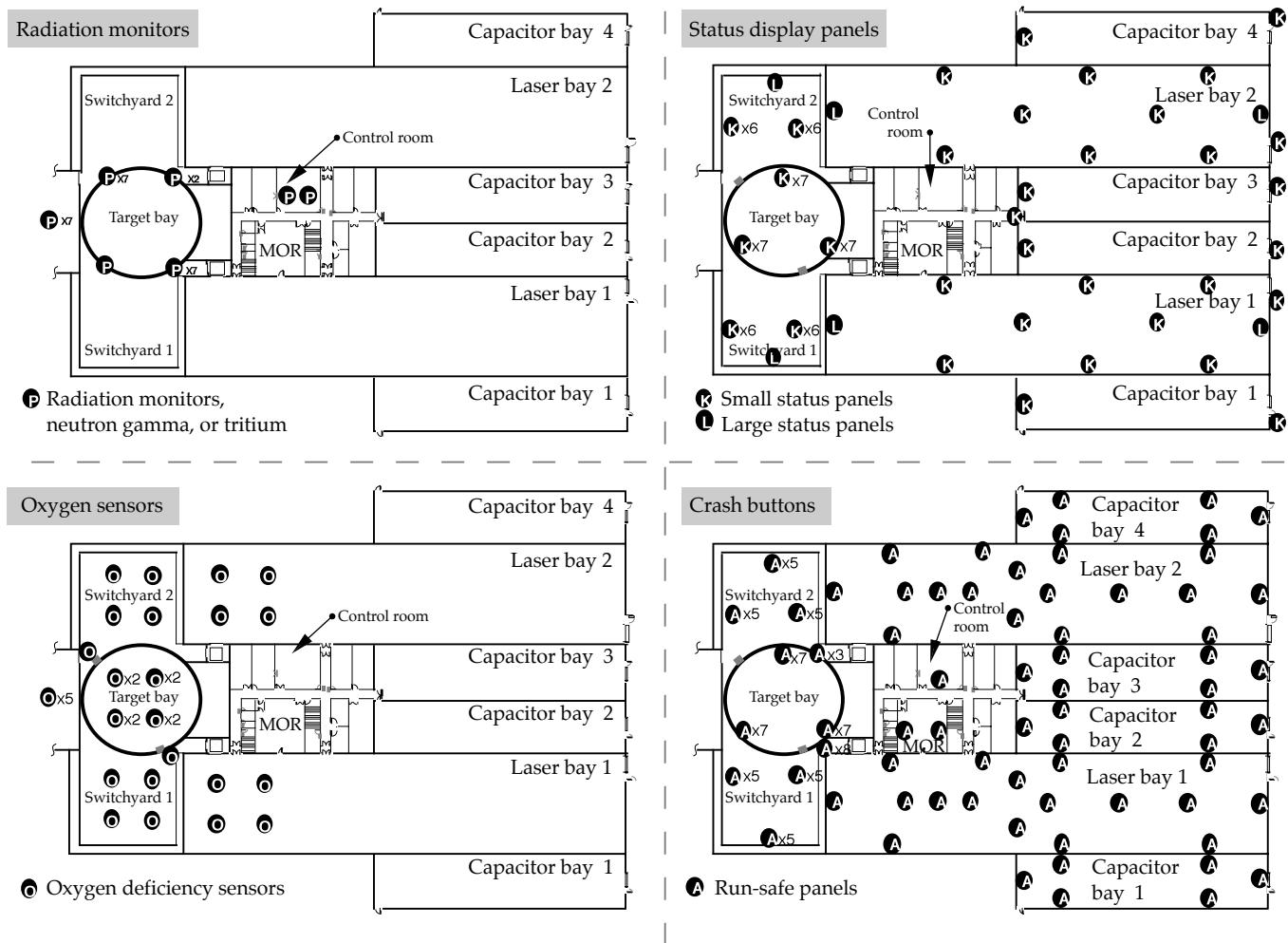
FIGURE 17. The approximate locations of radiation monitors, status display panels, oxygen sensors, and crash buttons for the NIF's safety interlock system (SIS).   (40-00-0298-0339pb01)

Title II Activities

Our high-priority Title II tasks for the ISS are to select a PLC vendor, complete a detailed SIS I/O layout, complete the design of run-safe and status panels, complete design of the SIS interlock strings, complete ISS test plans, and complete ACS procurement specifications.

For more information, contact
Paul J. VanArsdall
Integrated Computer Control System Lead Engineer
Phone: (925) 422-4489
Email: vanarsdall1@llnl.gov
Fax: (925) 422-1930

TRANSPORT AND HANDLING

E. Grasz

M. McDaniel

A. Rowe*

D. Silva

D. Tiszauer

S. Yakuma

*T*he NIF Transport and Handling (T&H) Team has the key mission of rapidly replacing optic line-replaceable units (LRUs) (see "Line-Replaceable Units" below) to ensure reliable laser operations. The three-part transportation process involves transporting the precision prealigned optical LRU from the Optics Assembly Building (OAB), the preamplifier module maintenance area, or the airlock to the beamline position; docking the delivery system to the structure or hand-off hardware; and inserting the optic LRU or optic enclosure into the beamline and locking the LRU into position. This must be accomplished while preserving the cleanliness of the optics during the delivery process and preserving the LRU functionality and precision alignment.

LINE-REPLACEABLE UNITS

The design philosophy for the NIF Project is to modularize the laser subsystem components. The line-replaceable unit (LRU) is the key to maximized modularity and efficient operations. Each laser component will be packaged into an LRU for assembling, transporting, installing, and removing the component in an efficient, safe, and cost-effective manner. An LRU is typically composed of a mechanical housing, laser optics (i.e., lenses and mirrors), utilities, and actuators (if necessary).

The use of LRUs provides considerable advantages in terms of time, efficiency, cost, and reliability. Because one of our major goals is to keep the NIF operating continuously, we want to minimize any activities carried out in the beamline that will slow down the process. Taking the modules off-line for maintenance and repair minimizes down time, which results in fewer and shorter maintenance tasks in the beamline. The LRU also enables localized and off-line assembly and alignment activities and allows for more thorough inspections with fewer time constraints, which makes the laser more reliable.

Inventories can be simplified by using LRUs because of reduced part counts, and storage flexibility can be increased with the use of standardized packaging. We are trying to make each package as similar as possible to minimize the number of spare parts needed. In addition, it simplifies storage to have standardized slot sizes for each module. Another advantage of this standardization is that employees become more effective if they deal with fewer types of motors, for example, rather than having to learn the intricacies of 20 different types.

The use of LRUs also minimizes the exposure of beamlines to the laser bay environment, which is far less clean, and it maximizes the cleanliness of the beamline by reduced operator contact. The interior of the beamline is maintained as Class 100 to protect the optics inside from particles. Minimizing the contact of the beamline with outside environments or operators also helps reduce the possibility of damage to the laser's optical components.

*TRW Space and Defense, Redondo Beach, CA

Introduction

There are five types of delivery systems (Figure 1) needed for the NIF Project: bottom loading, side loading, top loading, switchyard loading, and target bay loading, depending on the requirements of the LRU type, its physical location, structural and other constraints, and the interface requirements. T&H is responsible for installing 34 different types (Figure 2) of optic LRUs that have various locations in the laser bay, the switchyards, and the target area (Figure 3).

The design requirements for T&H include developing delivery system designs for the optic LRUs; building and testing the first-off systems; procuring, fabricating, and assembling the NIF LRU delivery system hardware; inspecting and verifying delivery systems hardware; and delivering optic LRUs according to the plan for start-up activities and long-term operations

Transporter

The laser bay transporter is the "get it there" part of the LRU delivery system (Figure 4). One laser bay transporter design is the basis for all three LRU insertion systems (bottom, top, and side loading) in the laser bay. The transporter transports, lifts, and positions the canister or skid at docking points on the laser structure. It must deliver LRUs to over 2,700 specific locations inside the concrete structures.

Due to clearance, alignment, and weight requirements, the transporter must be customized. The size requirements of the loads in combination with the facility opening dimensions require that the transporter lift on the outside of the canister instead of from the bottom, that it have a 6-ft fork spacing, and that it have a transport guidance system. The tight transporter clearance with the structure in some LRU locations limits the outside dimensions of the transporter as well. In the Title II Design phase, we are working closely with vendors to develop the optimum solution to transporter requirements.

Title II Activities

Title II engineering priorities include completing transporter specifications, evaluating tradeoffs between guidance systems, finalizing docking and alignment designs, down-selecting transporter

FIGURE 1. Five T&H delivery systems. (40-00-0997-2078pb01)

Laser bay bottom-loading delivery

Laser bay top-loading delivery

Laser bay side-loading delivery

Switchyard delivery

Target area delivery

FIGURE 2. The 34 types of optic LRUs (many of the 20 types shown have multiple orientations, making a total of 34 distinct types). (40-00-0997-2079pb01)

FIGURE 3. The optical LRU delivery locations. (40-00-0496-0996pb03)

FIGURE 4. The laser bay transporter. (40-00-0997-2081pb01)

The docking mechanism will use kinematic mounts to align the canister under the laser beam structure. There are three different types of installation processes: single-stage, periscope multistage, and spatial filter three-axis installation (Figure 6). The process for bottom-loading single-stage LRU installation is as follows:

An LRU is inserted into the BLDS canister from the OAB. It is then moved by an automated self-guided vehicle (AGV) transporter to the LRU's insertion location under the laser beam structure. The AGV then lifts the canister to within a few millimeters of the structure and activates its compliance system. Continuing with the lift, the canister docks to the structure by having its kinematic docking balls self-align to the receivers in the structure. The canister's pneuma seal (inflatable seal) is activated, sealing around the laser beam structure cover. The cover is removed by the cover removal system in the canister. The vertical ball screw insertion system then lifts the LRU to a height in the beam structure where the internal kinematic mounts activate and hold the LRU in place. The carriage of the insertion system then lowers down into the canister. The cover removal system replaces the cover in the structure and seals the canister. The pneuma seal is deflated, and the canister is lowered and returned to the OAB.

The spatial filter installation requires the "y" axis transaction of the single-stage lift followed by a translation in the "x" axis to complete the installation.

The periscope installation assembly, the most complex type, requires the use of spacers to lift the LRUs to the required heights (Figure 7). After the periscope LRU is lifted by the carriage to the top of the canisters, a shelf mechanism is activated to capture the LRU. The carriage is lowered back down, and the first spacer is translated onto it. The spacer, with the LRU above it, is then lifted to the shelf mechanism, which holds it. When the carriage is lowered again, a second spacer is inserted and lifted, extending the LRU to the height required for installation inside the beam enclosure.

The Amplifier Module Prototype Laboratory (AMPLAB) is currently testing a prototype vehicle referred to as the maintenance and transport vehicle (MTV). Although the MTV is not configured to transport and install all bottom-loaded LRUs, T&H is leveraging off the experience from the MTV and will gain useful cleanliness data from the insertion and removal of the amplifier and flashlamp LRUs.

Analyses are being done on all critical elements of the delivery system. Prototyping and testing will verify and validate all principles. A Class 100 environment will be maintained inside the canister, so cycle testing for cleanliness will be an integral part of the prototyping effort. The alignment of the delivery system to the beam enclosure

vendors, developing a controls interface, evaluating safety and egress issues, and determining storage and maintenance locations.

Bottom-Loading Delivery System (BLDS)

The requirement of the BLDS is to transport and install 18 different types (with a total of 2,736) of bottom-loaded optic LRUs. Each LRU has a unique geometry (Figure 5) with different footprints and insertion envelopes. The LRUs have different beamline gas environments, vertical travels, kinematic mounts, and utilities connections. All but the flashlamp require a cleanliness level of 50. All LRUs require a bundle spacing of 1,500 mm.

There are three BLDS canisters: universal, amplifier, and flashlamp. All three will use the same lifting systems and virtually the same canister frame design.

Laser mirror 1

Amplifier central
and side flashlamps

Amplifier slabs

Plasma-electrode
Pockels cell

Spatial filters 1–4

Periscopes a–e

LM2

LM1
single-stage
installation

Periscope
multistage
installation

Spatial filter
three-axis
installation

Shelf
mechanism

Periscope LRU

Spacers
(second
stage lift)

Periscope
carriage

Guide rails inside the periscope enclosure
may be required for a successful installation

structures and designing the insertion mechanism are two important challenges for Title II Design.

Title II Activities

During Title II, we will build and test prototype subsystems, including the canisters, insertion mechanisms, control systems, and the AGV transporter. As a result of our prototyping efforts, analysis, and interface issues, we will refine and complete the delivery system design.

Top-Loading Delivery System

Top-loading (TL) LRUs are located in the transport spatial filter and the cavity spatial filter center vacuum vessels. These are top loaded to optimize the use of space in the laser bays.

TL LRUs are all the same size, require a Class 100 clean environment, and use the same transporter as the bottom- and side-loading systems (Figure 8). The laser bay transporter moves the TL canister from the OAB to the laser bay; the laser bay crane lifts and docks the canister to the vacuum vessel; and the canister cleanly transfers the LRU into and out of the vacuum vessel.

Labels: Laser bay crane lifting sling; TL canister alignment pin; Laser bay transporter; LRU; TL canister (2727 kg with LRU); TL canister control panel; Jackstand 4 places
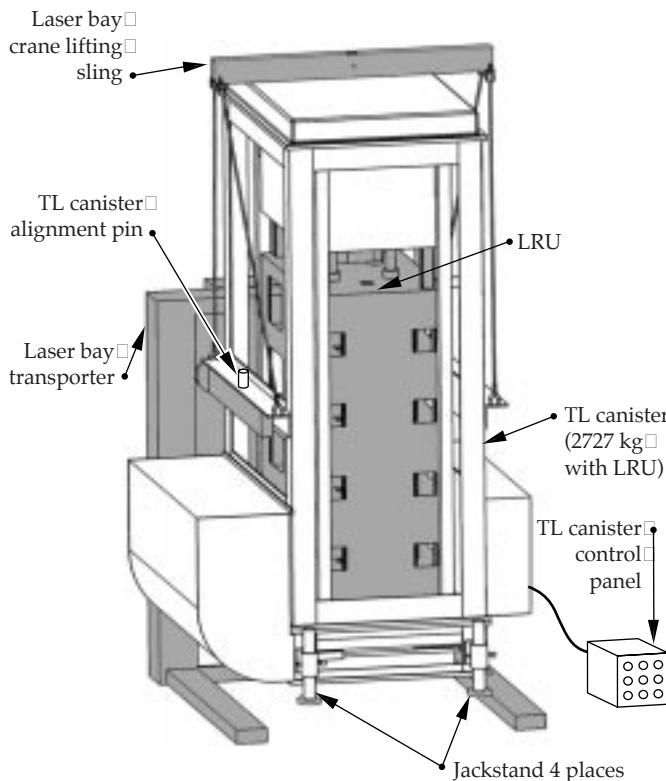
FIGURE 8. The top-loading delivery system.
(40-00-0997-2085pb01)

The vacuum cover removal mechanism must translate and rotate due to the cover size. The latching mechanism (protruding from the canister bottom cover) engages the vacuum vessel cover as the canister is docked, and then a scissors mechanism lifts the vacuum vessel and canister covers (simultaneously) prior to translation and rotation. The LRUs are lowered onto kinematic mounts at the bottom of the vacuum vessel, the vacuum vessel covers are replaced, the canister covers are disengaged, and the TL canister is undocked.

During Title I , we have developed an initial TL delivery system design, quantified vibration and shock requirements, defined personnel safety issues, and developed a scheme to deal with delivery system failures during transport.

Title II Activities

During Title II, the TL canister mechanisms will be prototyped and tested to mitigate risks. Structural and dynamic analyses will be performed. We will analyze the TL delivery system to meet LLNL seismic safety standards. We will support the specification and procurement of the laser bay transporter.

Side-Loading Delivery System

All side-loading (SL) LRUs are located in the transport spatial filter area. There are three SL LRUs and two different delivery systems (Figure 9): the output sensor delivery system and the SL delivery system.

The output sensor transporter is a commercially available manual lift truck with custom-designed lifting forks. It lifts and positions the output sensor for installation. The output sensor is then manually positioned onto its kinematic mounts, and the utilities are connected at the bottom after installation.

The SL delivery system, which consists of the laser bay transporter and the SL skid, is used to load LRUs into and out of the preamplifier module (PAM) support structure (PASS). The laser bay transporter positions and aligns the SL skid for docking to the PASS. The docking mechanism engages the PASS for alignment and support. The SL skid is used to transfer the LRUs on and off the precision LRU support rails.

Title II Activities

During Title II, the SL skid will be prototyped and tested to ensure reliable performance. Structural and dynamic analyses will be performed to ensure

SL LRUs

493 mm

825 mm

1210 mm

4178 mm

914 mm

Power
conditioning
unit (PCU)

PAM optics

457 mm

410 mm

530 mm

1210 mm

PAM (1182 kg)

Input sensor (318 kg)

Output sensor (274 kg)

SL delivery systems

PAM and input-sensor delivery system

Output-sensor delivery system
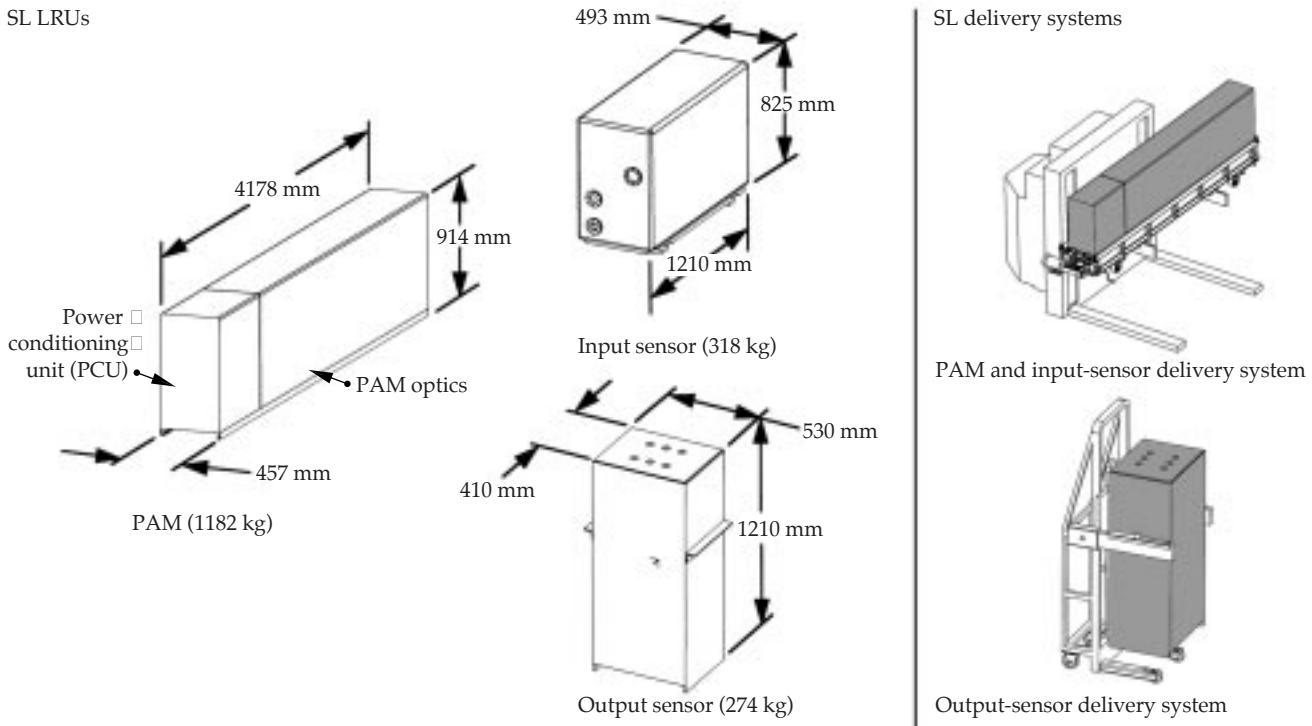
FIGURE 9. Three side-loading LRUs and two side-loading delivery systems.   (40-00-0997-2086pb01)

compliance with LLNL seismic safety standards. We will support the specification and procurement of the laser bay transporter.

Switchyard Delivery System

The LRU positions within the switchyard structure require access to most of the switchyard levels (Figure 10). The handling concepts use as much "off the shelf" hardware as possible to minimize complexity and increase reliability in the T&H task (Figure 11). The powered transporter is based on commercially available designs. The original concept of using bridge cranes has been changed to use monorail systems, which allows access through each switchyard level, thus minimizing floor loading requirements for the switchyard structure. The handling components, such as the shock-mounted skid assembly, may be used in other T&H efforts, reducing risk and design costs and increasing commonality.

The flexible design of the switchyard delivery system skid allows for multiple orientations of the laser mirror (LM) 4 and LM5 optics, which differ slightly in

LM5 mirrors

To target

Target bay

From laser bay

LM4 mirrors

Laser
beam

LM5 mirrors

(Switchyard structure has been removed for clarity)
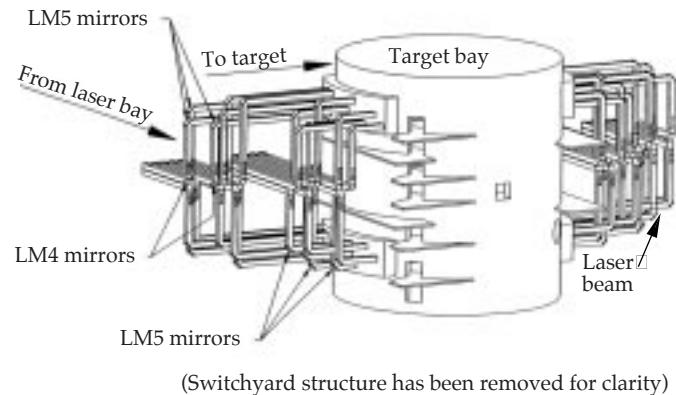
FIGURE 10. The optic positions on the switchyard levels. (40-00-0997-2087pb01)

configuration and direction of insertion. The lift carriage design also adapts to safely support each configuration of the LM optics.

In addition to the laser mirrors, other LRUs within the switchyard include roving mirror optics, precision diagnostics, and beam dump shutters.
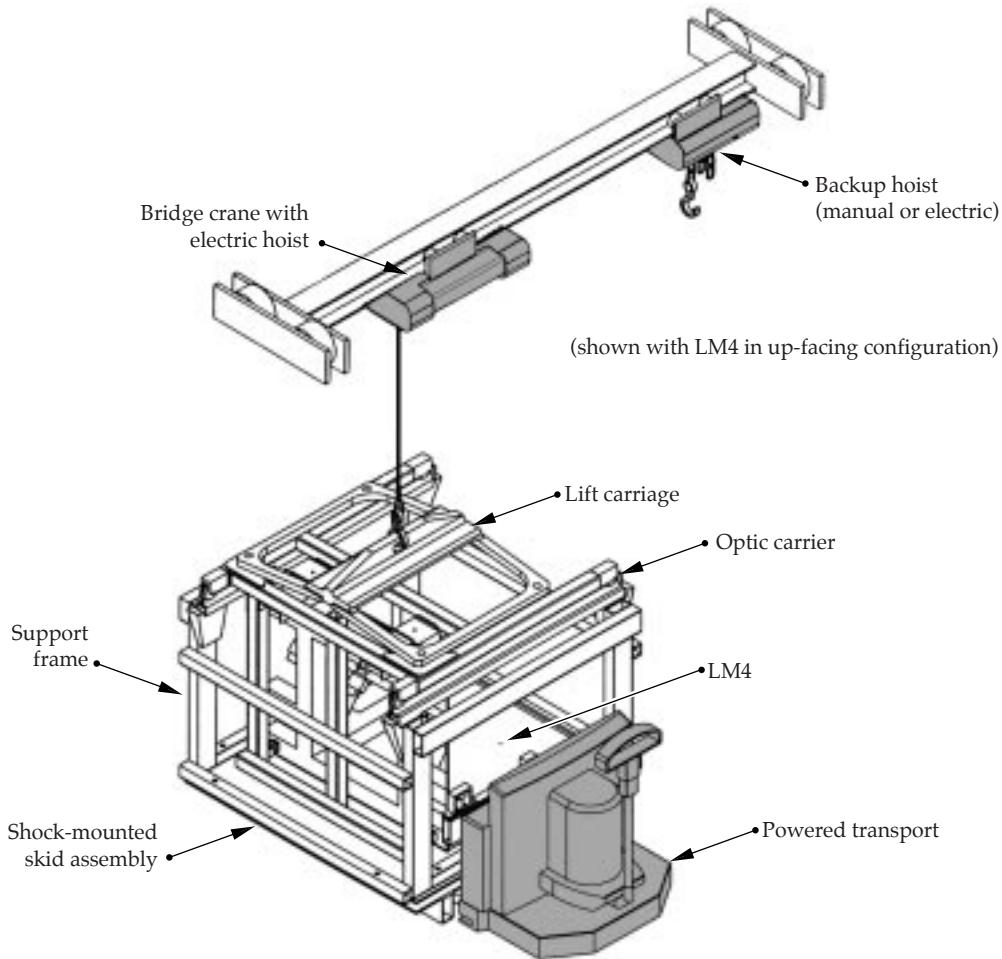
FIGURE 11. Off-the-shelf hardware in the switchyard delivery system. (40-00-0997-2088pb01)

Backup hoist (manual or electric)

Bridge crane with electric hoist

(shown with LM4 in up-facing configuration)

Lift carriage

Optic carrier

Support frame

LM4

Shock-mounted skid assembly

Powered transport

Each of the delivery systems for these LRUs uses the same transporter and skid. Uniqueness in the design is in the support frame, capturing the LRU during transport. The roving mirror LRUs also require an enclosure to preserve Class 100 cleanliness levels for the optics during transport and installation.

Title II Activities

Title II tasks include OAB transfer to delivery systems, detail design of each of the delivery systems, prototype testing of the LM4 up-facing delivery system, concept and design of a Standard Mechanical Interface-type optic enclosure for the roving mirror optics, and the determination of operating procedures for each of the handling tasks.

Target Area Delivery System

The target area optics include the following: LM6, LM7, and LM8 (Figure 12); integrated optics modules (IOMs) and several debris shields (Figure 13). The handling concepts for these optics are very similar: a skid assembly that includes a shock-mounted deck is used along with a transporter. The optics are firmly fastened to the skid deck. Shock and vibration levels are below the maximums as established by each of the LRU engineers.

Title II Activities

The Title II effort will focus on the detail design of each LRU handling system. The main emphasis will be on commonality of the systems and reliability.

FIGURE 12. Target area optics. (40-00-0997-2089pb01)

LM6
2 × 1 optic
Weight <400 kg

LM7
2 × 1 optic
Weight <400 kg

LM8
1 × 1 optic
Weight <200 kg
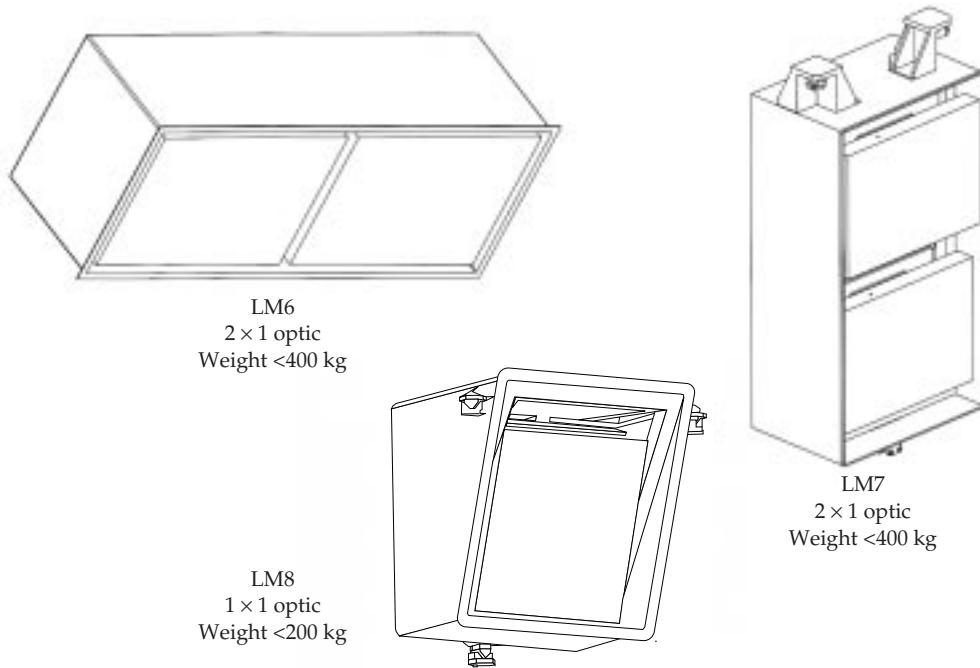
FIGURE 13. Integrated optics module (IOM) and debris shield. (40-00-0997-2090pb01)

Mounting lug
(3 places)

Debris shield
50 × 480 × 480 mm
14 kg

IOM
680 × 650 × 1200 mm
300 kg
Transported on side with lifting provisions on top surface
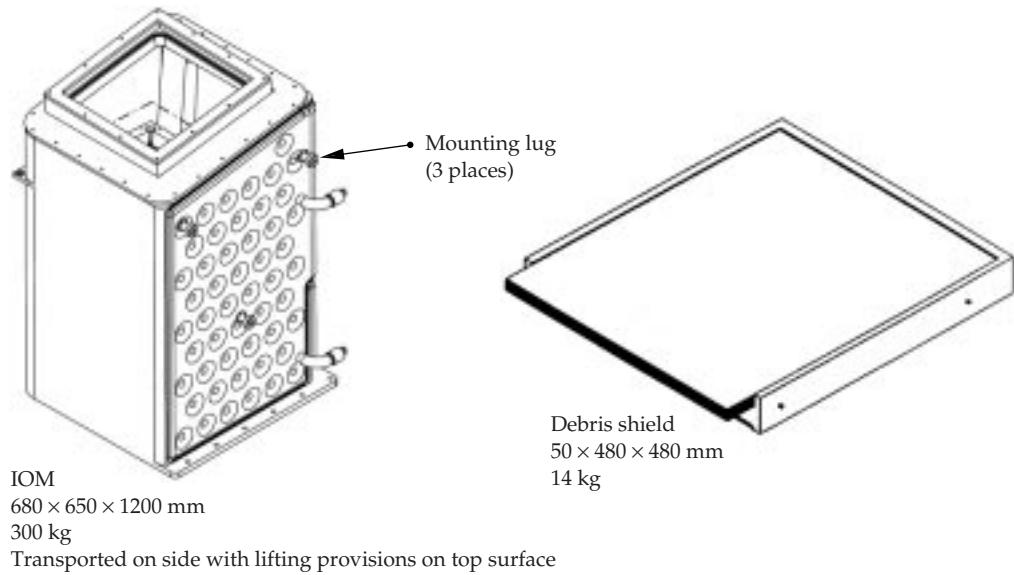
For more information, contact
Erna Grasz
Operations Engineering Deputy
Phone: (925) 423-6556
E-mail: grasz1@llnl.gov
Fax: (925) 423-7390

RAPID GROWTH OF LARGE-SCALE (40–50-CM) KDP CRYSTALS

N. P. Zaitseva   L. M. Carman   R. B. Rozsa

J. J. De Yoreo   M. R. Dehaven   H. R. Spears

W. R. Bell   D. L. James   R. L. Vital

Introduction

Work on rapid growth of KDP-type crystals, mainly KH_2PO_4 (KDP) and $K(D_xH_{1-x})_2PO_4$ (DKDP), was initiated in the early 1980s because the Nova laser at Lawrence Livermore National Laboratory (LLNL) needed large-aperture single-crystal plates. Several rapid growth techniques[1–3] were developed, and a project was started at LLNL[4] with a goal of growing KDP-type crystals at more than an order of magnitude faster than the traditional technique. As a result, rapidly grown crystals of about 10 cm were obtained. Nevertheless, the frequency conversion arrays on Nova were constructed from 27- × 27-cm KDP single-crystal plates grown using traditional slow-growth techniques.

The baseline design for Nova's successor—the National Ignition Facility (NIF)[5]—incorporates about 600 41- × 41-cm Pockels cell, doubler, and tripler crystals. Depending on the type of frequency conversion used for the NIF, the boules that would yield crystal plates of this size must be about four times the size of the Nova boules (see Figure 1). Conventionally grown crystals usually grow 1–2 mm/day for KDP crystals and not faster than 1 mm/day for DKDP. At these rates, it can take more than two years to grow a crystal with the size required for NIF. This slow rate and high risk associated with traditional crystal growth techniques stimulated new work on KDP rapid growth at LLNL about four years ago.[6] Here we describe recent progress in this work including the growth of KDP and DKDP crystals up to 50×50 cm^2 in cross section and grown at rates in excess of 10 mm/day.

Figure 2(b) shows that the final size of a traditionally grown boule is approximately twice as long as it is wide because the regenerated seed and the material with high density of dislocations originating at the seed cap occupy the large portion of the crystal. Additionally, at the low
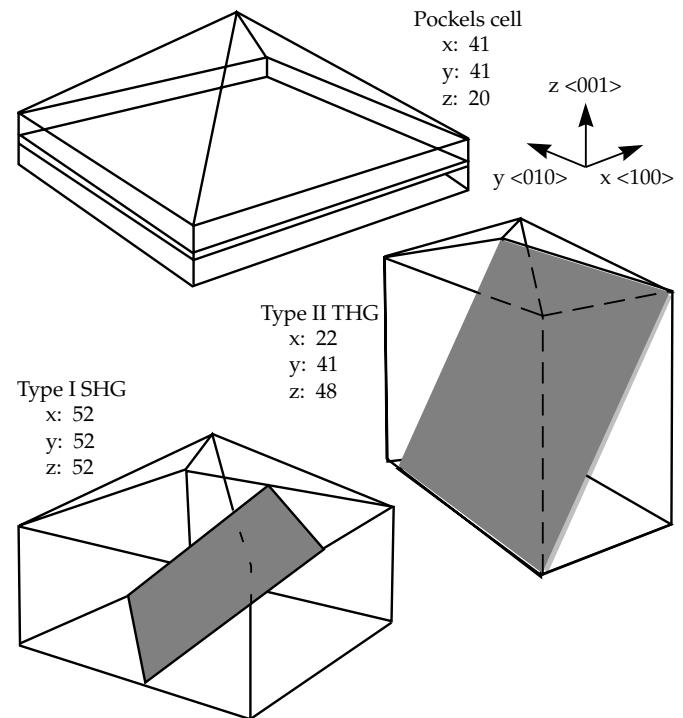
FIGURE 1. The minimum size (centimeter) of KDP single-crystal boules required to obtain Pockels cell and harmonic generation plates of different types for the NIF project.   (40-00-0697-0989pb01)

growth rate used in conventional growth, impurities in the starting salt generate a "dead zone,"[7] a term used to describe an area where growth rates along the <100> and <010> directions are near zero. Attempts to increase growth rates often resulted in the formation of defects on prismatic {100} faces, which start growing at supersaturations just above the "dead zone." As a result, conventional crystals are grown only in the <001> direction, and the growth of the boule must be preceded by the complicated process of obtaining seeds that have the

cross section of the final crystal [see Figure 2(a)]. This process significantly increases the production time.

The use of very pure salts can reduce the width of the "dead zone." We have shown[8,9] that if growth is performed in a regime where the growth rates along <100> and <010> are sufficiently high and comparable to that along <001>, defects on those faces do not form, and crystals have high optical quality both in the prismatic and pyramidal sections. For example, the 37-cm crystal plates currently used on Beamlet, the NIF prototype, were grown by the traditional method. Until last year, the size of rapidly grown crystals did not exceed 15–20 cm.

With our work on KDP rapid growth, we now report that we can grow KDP crystals rapidly with up to 50×50 cm^2 in cross section. We used a method based on the use of the "point seed."[10] In this method the size of the seed does not depend on the final size of the crystal because the crystal grows uniformly on both prismatic {100} and pyramidal {101} faces [see Figures 2(c) and 2(d)]. While the presence of the prismatic faces and the resulting polysectorality can be a potential source of optical inhomogeneity, our measurements showed the following: crystals grown by this technique (to sizes of 10–15 cm) using high-purity salts and at growth rates of 10–15 mm/day have good optical uniformity. In addition, the entire volume of the crystal can be used for obtaining high-quality plates.[9]

Apparatus

Figure 3 is a schematic of the full-scale rapid growth system, and Figure 4 is a photograph of the same system. The system consists of a 1000-L glass tank submerged in a controlled-temperature water bath. The crystal is grown on a square, 60- $\times$ 60-cm^2 acrylic platform; it is rotated alternately in two directions on a symmetrically programmed schedule with controlled acceleration, deceleration, and rotation rates. A seed protector, specially developed for this work, is inserted within the platform shaft where it can freely move up and down, allowing us to keep the 1-cm^3 seed sealed at room temperature while the crystallizer temperature is manipulated. Here, solution treatments, such as filtration and overheating, are executed for any desired length of time while the seed is perfectly preserved under the seed protector. When the solution is ready for growth, the seed protector is raised, and the growth
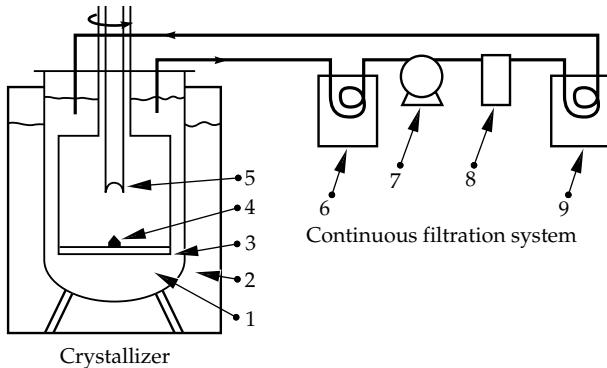
FIGURE 3. Schematic of the 1000-L crystallizer: (1) 1000-L glass growth tank; (2) temperature-controlled water bath; (3) platform; (4) seed; (5) seed protector; (6) heater; (7) pump; (8) filter; (9) cooler. (40-00-0796-1482pb02)

FIGURE 2. Schematic of traditional seed (a) and final traditional crystal (b) compared to rapid-growth point seed (c) and final point-seed crystal (d) with length H for cutting plate. (40-00-0796-1483pb03)
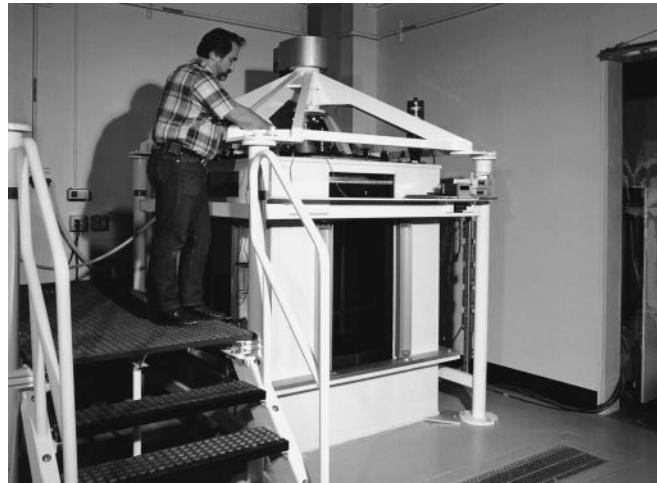
FIGURE 4. Photograph of the 1000-L crystal growth system. (40-00-0697-1068pb01)

process begins. The seed protector can also be used if the crystal needs to be remelted. Once the crystal is melted to the size of the initial seed, it can then be covered by the seed protector, and solution processing can be repeated. In this way, the growth process can be repeated several times without introducing a new seed.

Previously, Montgomery and Milanovich[11] showed that high laser-damage thresholds could be obtained in conventionally grown KDP by continuously filtering the solution during growth. The same continuous filtration system was developed in this work for filtration growth solutions at high supersaturation (see Figure 3). Our system contains three temperature-controlled sections: a superheater, a filter (both operating at 80°C), and the third section, where the filtered solution is cooled to the growth temperature. This system has been used to grow KDP and DKDP crystals in small 20-L crystallizers up to a size of 17 cm. This system was also tested in 1000-L tanks, where it will be used after the first 55-cm crystals have been grown.

Solution Stability and Crystal Growth

KDP crystals grow on vicinal hillocks formed by dislocations.[7] The normal growth rate R of a crystal face growing by this mechanism is given by

$$R = pV \ , \tag{1}$$

where p is the slope of the dislocation hillock and V is the tangential speed of the elementary steps. According to this formula, there are two ways to increase the growth rate: steepening the hillocks or increasing the step speed. In the kinetic limit, the step speed V has been shown both theoretically[12,13] and, for many systems, experimentally[14–16] to be given by

$$V = \omega \beta \, \Delta C \ , \tag{2}$$

where ω is the volume per molecule in the solid, $\Delta C = (C - C_0)$ is the absolute supersaturation, C and C_0 are the actual and equilibrium concentrations, respectively, and β is the kinetic coefficient that must take into account the kinetic barriers associated with the multistage process of moving solute from the solution into the steps.

The slope of the dislocation hillock in Eq. (1) is given by[7]

$$p = h\varepsilon \ , \tag{3}$$

where h is the height of the elementary step, and ε is the activity of the dislocation source. The activity ε of

the dislocation source is a function of both the critical radius r_c and the structure of the dislocation source. In the simple case of an isotropic growth spiral, $\varepsilon = m/(19r_c + 2L)$, where m is the number of unit step heights in the dislocation source and $2L$ is the length of the perimeter of the region enclosing all dislocations within $19r_c$ of one another.[7] In the case of polygonal, anisotropic growth hillocks such as those of KDP, the prefactor of r_c also depends on the relative sizes of the kinetic coefficients for each step direction of the polygon but is independent of the absolute value of β.

The critical radius r_c is given by[17]

$$r_c = \frac{\omega \alpha_{2D}}{kT\ell \, nS} \ , \tag{4}$$

where α_{2D} is the step-edge free energy per unit step height and S is the ratio of the actual to the equilibrium mole fraction of the crystallizing material. ε and, hence, p can be increased by raising ΔC or temperature, T, or by changing the dislocation structure. Furthermore, atomic-force-microscopy investigations[18, 19] of growth spirals on KDP {101} surfaces have shown that for $\sigma \gtrsim 5\%$, the slopes of growth hillocks on the {101} face are limited by the presence of strain-induced dislocation cores.[19] The details of the effect of these cores on step structure near the core has been investigated theoretically,[20,21] and the experimental results and complimentary analysis[19] show that the hillock slope is nearly independent of both supersaturation and dislocation structure because these cores are present. As a result, the growth rate along Z can only be increased significantly by raising ΔC to increase V. The effect of these cores was not observed on the {100} face where m and L vary depending on seed regeneration conditions. These conditions allow us to create dislocation sources of varying activity, thereby obtaining different growth rates on the {100} face at the same temperature and supersaturation. It is possible to vary the ratio of the crystal dimension along Z to that in X and Y,[10] which is practically important for crystal growth of the sizes in Figure 1.

Our data also show that in our regime of growth, the solution flow can slightly affect the growth rate. While the temperature, dislocation structure, and hydrodynamic conditions can also slightly affect growth rates, increasing the supersaturation to increase V is the only effective way to significantly increase growth rates. However, crystal growth in the region of high supersaturations is not a simple practical task because extraneous crystals from the growth solution tend to precipitate. This condition usually leads to the deterioration of the main crystal and termination of the growth run. This makes the problem of solution stability one of the most important challenges for rapid growth. We define solution stability as the ability of the supersaturated solutions to remain free from spontaneous nucleation during

an induction time τ, which must be, obviously, longer than the growth period.

Our previous work[22] in small 5–20-L crystallizers showed that KDP and DKDP supersaturated solutions can be stable against spontaneous nucleation for induction time periods of months at undercoolings of up to 30°C. In addition, during continuous cooling, supersaturations σ of up to 100–130% can be reached. For practical measurements, we used relative supersaturation σ = (C − C_0)/C_0, where C and C_0 are expressed in weight fraction. We showed that the actual stability of growth solutions is much higher than needed for practical crystal growth (Figure 5). The absence of spontaneous nucleation in small crystallizers (5–20 L in volume) during crystal growth at rates of 10–40 mm/day proves that growth solutions are stable. The seed protector device in 20-L crystallizers allows us to grow KDP crystals at growth rates up to 60–70 mm/day. The growth terminates at

high rates usually because of defects and cracks in the growing crystal, not because of spontaneous nucleation from the solution. We believe that these cracks and defects are caused by impurities or hydrodynamic conditions. These results show that, at the supersaturations needed for practical growth rates (usually not faster than 20 mm/day) in well filtered and overheated solutions, spontaneous nucleation in the solution itself is not a problem. From our observations, any extraneous crystals that appear in the shaded region of Figure 5 are caused by the main crystal either through cracking or moving relative to the crystal holder. Faulty equipment, such as dry surfaces or poorly bonded joints on the platforms, can also cause extraneous crystals to appear.

Our measurements in the 1000-L tanks in Figure 6 gave solution stability of the same order of magnitude: during continuous cooling, σ of about 50% was reached, and the induction time τ in a stirred solution saturated at 65°C was more than 1.5 months at σ = 6%. (The run was interrupted to continue crystal growth experiments.) These results furthered our knowledge of the absolute level of the solution stability. We have previously shown[22] that we could not measure the induction time in 5-L tanks at σ = 6% because, practically, it was infinite. But if we assume that the probability of homogeneous nucleation is proportional to the volume of the solution, the calculation from a τ of more than 45 days obtained in 1000-L tanks leads us to a τ in 5-L vessels of at least 25 years.

According to the classical nucleation theory,[23] homogeneous nucleation from the solution can start when, as a result of fluctuation, some certain number of molecules create an aggregate with the size of r_c. Simple calculations allow us to estimate the size of a critical nucleus at the values of σ used during growth.

From Eq. (4), using ω = 9.68 × 10^{-2}/nm^3 per molecule, α = 12.9 mJ/m^2 (Ref. 22) at T = 30°C, and S = 1.7, or σ = 57% (the point when mass crystallization from solution occurs), we obtain r_c = 1.1 nm. At σ = 6% (S = 1.07), the same calculation gives us r_c = 8.6 nm. r_c = 1.1 nm corresponds to a critical nucleus containing about 60 KDP molecules ($4\pi r^3/3\omega$), while r_c = 8.6 nm corresponds to one with about 30,000 molecules. The latter is unlikely to form spontaneously on any time scale, which leads us to conclude that at the relatively low supersaturations used in the rapid growth process, homogeneous nucleation in the bulk cannot take place.

Figure 6 shows one of the large KDP crystals grown in a 1000-L crystallizer compared to a typical 12-cm crystal grown in a 10-L crystallizer. The weight of the large crystal is about 130 kg compared to 1.5 kg for the smaller one. Both crystals were grown on point seeds of the same size. The dimensions of the large crystal are about 45 cm in all X, Y, and Z directions. The entire period of growth was 30 days.
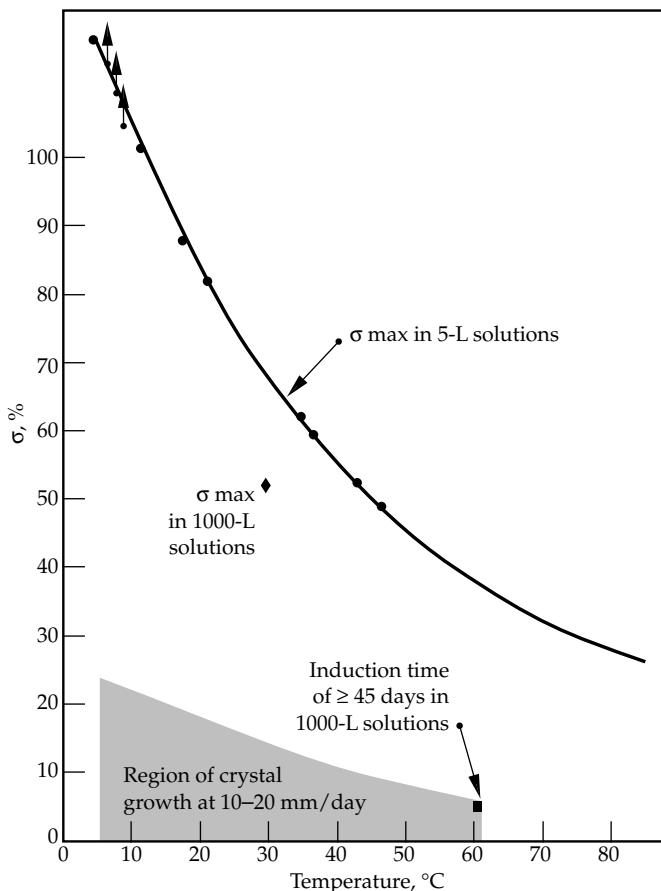
FIGURE 5. Maximum stability obtained in KDP solutions in comparison to the region used for crystal growth. (40-00-0796-1481pb02)
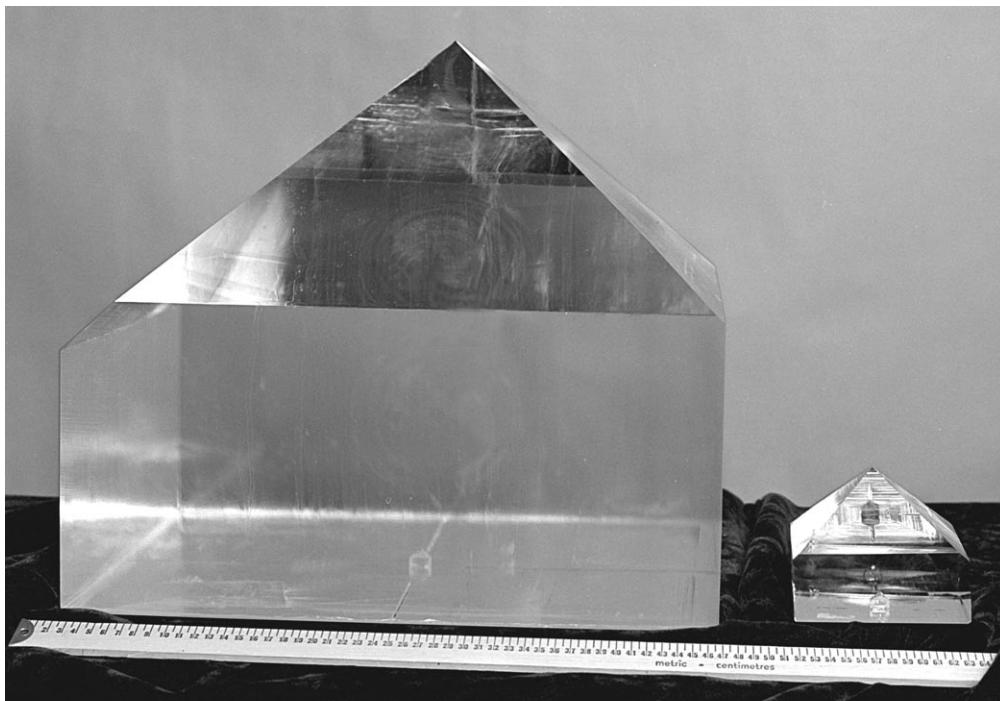
FIGURE 6. Photograph of KDP crystals grown in 1000- and 10-L crystallizers.
(40-00-0796-1582pb01)

More than 20 KDP and DKDP crystals with sizes of about 40–50 cm in all directions have been grown. The initial saturation temperature of the solutions in different growth runs varied from 60 to 68°C. According to our calculations, the saturation temperature does not have to exceed 70°C to obtain full-size crystals of about 55 cm on a side and 250 kg in weight from solution volumes of 1000 L. Crystals were grown at rates of 10–25 mm/day along the Z axis and 5–12 mm/day along the X–Y directions. Supersaturation and required cooling rate were controlled by measuring growth rates and crystal dimensions during the growth process.

In the case of the DKDP crystal (Figure 7), the initial saturation point of the solution was 60–66°C, and the deuteration level of the solution was about 92%. The growth rate along the Z axis was about 14 mm/day, and each prismatic face grew at a rate of 10–12 mm/day. Precipitation of the monoclinic phase was never observed during the growth of the tetragonal crystal, which further demonstrates the high stability of the growth solutions against spontaneous nucleation.

At present, the main obstacles in obtaining crystals of the larger size are related to mechanical problems resulting from the large size of the equipment. These problems include deformation of the platform-crystal holder caused by the flow of the solution (1000 kg in mass) and the increasing mass of the crystal as it grows. Though we are working on solving these problems, we are currently growing crystals of sufficient size to provide Z-plates for the NIF.

Depolarization loss (%)

0.02   0.05   0.08   0.1
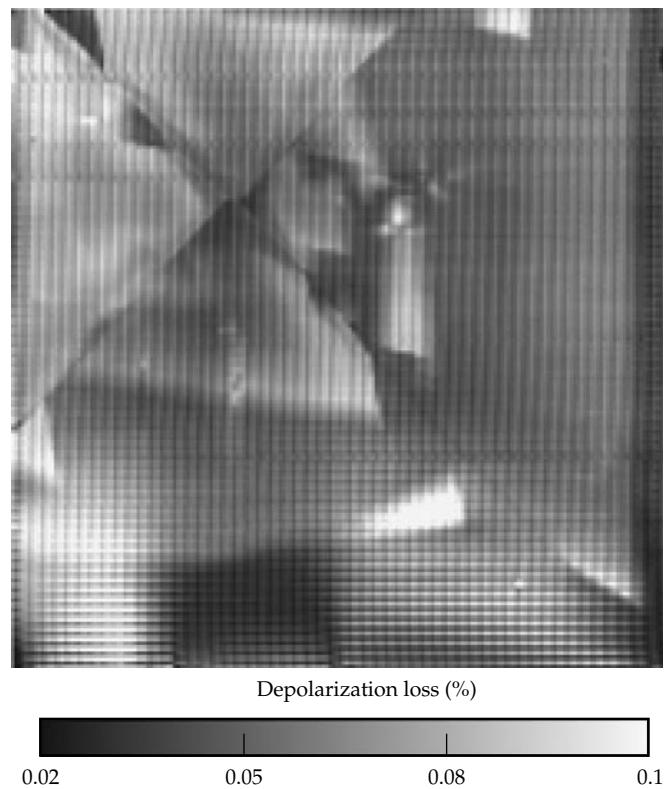
FIGURE 7. Photograph of DKDP crystal with the deuteration level about 92%. The size in cross section is 50×50 cm^2. (40-00-0697-0987pb01)

Crystal Quality

Only preliminary measurements have been performed on the crystals grown in 1000-L crystallizers. Some crystals had no visible defects, though in many crystals, solution inclusions appeared randomly on both the prismatic and pyramidal faces. These defects were typically slight on the prismatic {100} faces and much more pronounced on the top of the pyramidal {101} faces. The nature of these defects is not yet clear and is a subject of current investigations.

The surface structure of the crystals did not differ from that typically observed in the small crystals: each prismatic face had only one growth hillock clearly seen in reflected light from the beginning to the end of growth. Growth hillocks on the pyramidal faces changed more often. One or two hillocks with intervicinal boundaries could be observed at any time on the same face, which is also typical for small crystals.[24]

One of the large crystals which had a cross section of 44×44 cm^2 was cut into Z <001> plates from which two 41- $\times$ 41- $\times$ 1-cm Pockels cell crystals were fabricated (see Figure 1). Measurements of anomalous birefringence and transmitted wavefront distortion on these plates, as well as measurements of the laser-induced damage threshold on witness samples taken from adjacent positions in the boule, show that the optical quality of these crystals meets the NIF requirements.

Figure 8 is a profile of the depolarization loss measured in a 29- $\times$ 29-cm section of one plate. The average loss is 4×10^{-2}%, and the maximum loss is about 0.1%. These numbers are five to ten times smaller than those specified for the NIF. Figure 9 shows the distortion of the transmitted wavefront due to index variations in the bulk of this plate. The peak-to-valley distortion is $<\lambda/4$, and the maximum gradient is $<\lambda/10$ cm^{-1}. These values meet the NIF specifications. The measured laser-conditioned damage threshold at the first harmonic (1064 nm) using 7.6-ns pulses is 32 J/cm^2. When scaled to 3 ns, this value exceeds the NIF requirement for both the Pockels cell and the second harmonic generator. Our preliminary measurements also show no direct dependence of the damage threshold on sectorial structure of the crystals grown on the point seeds. These findings demonstrate that the presence of the prismatic sectors and sector boundaries are not the obstacles for obtaining large single-crystal plates of high optical quality, as was expected many years ago when this work began.[25]
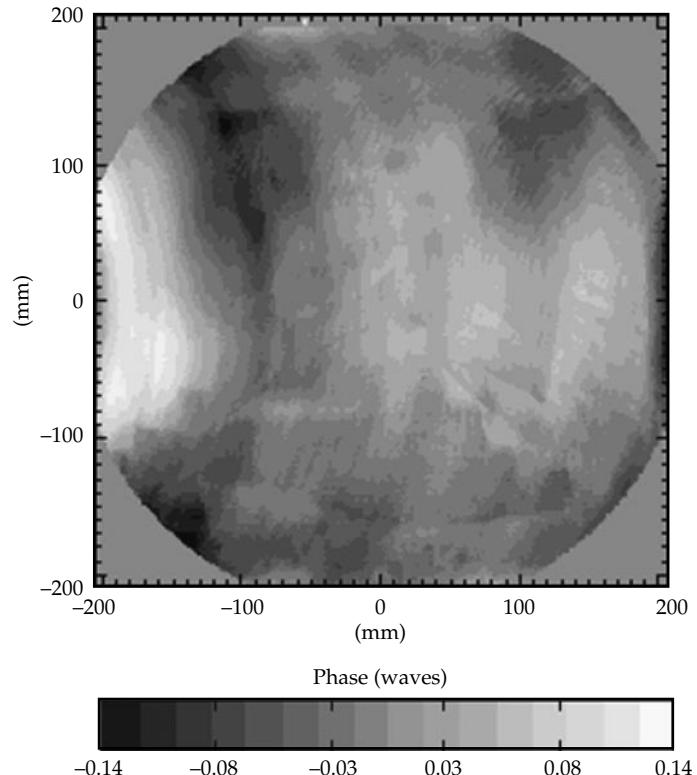
FIGURE 8. Profile of the depolarization loss in a 29- $\times$ 29-cm section of a 41- $\times$ 41-cm plate. Sector boundaries and growth hillock boundaries are clearly visible but result in only minor depolarization losses.   (40-00-0697-0988pb01)
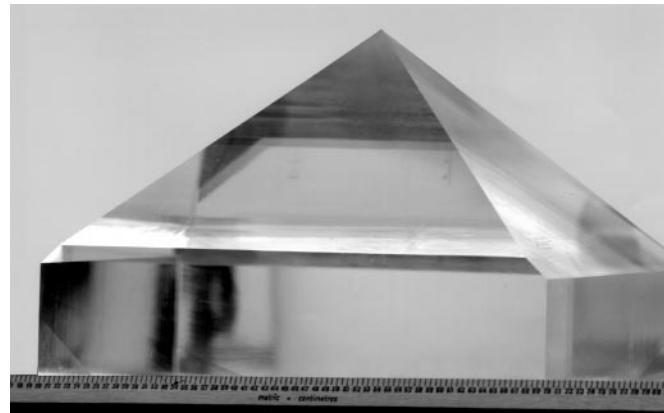
FIGURE 9. Profile of wavefront distortion in a 40-cm circular section of the 41- $\times$ 41-cm plate described in Figure 7. Although sector and growth hillock boundaries are visible, the distortion is small. (40-00-0398-0449pb01)

Conclusion

Our results show that large KDP single crystals for laser fusion systems can be grown rapidly using high supersaturations. The next task of this work is to develop a stable technique for obtaining KDP and DKDP crystals of up to 55 cm that have high optical quality and high laser-damage threshold. The high reproducibility of our results on growth and optical quality has given us a predictive understanding of the rapid-growth technique. We have also shown that we can obtain the desired optical quality in our work with small rapidly grown crystals as well as at large scale. Our current findings lead us to believe that the development of the rapid-growth technique initiated more than 10 years ago is close to a successful conclusion.

Acknowledgments

References

1. L. N. Rashkovich, *Vestn. Akad. Nauk SSSR* **9**, 15 (1984).
2. G. M. Loiacono, J. J. Zola, and G. Kostescky, *J. Crystal Growth* **62**, 543 (1983).
3. V. I. Bespalov, V. I. Bredikhin, V. P. Ershov, V. I. Katsman, N. V. Kiseleva, and S. P. Kuznetsov, *Sov. Kvant. Elektron.* **9**, 2343 (1982).
4. J. F. Cooper, M. F. Singleton, and J. Zundelevich, *VIII Int. Congr. on Crystal Growth*, Abstracts with Program (York, England, July 1986) POA1/147.
5. J. Paisner, J. Murray, et al., *ICF Quarterly Report* **7** (3), Lawrence Livermore National Laboratory, Livermore, CA (1998).
6. J. J. De Yoreo, J. Britten, R. Vital, K. Montgomery, N. P. Zaitseva, B. W. Woods, L. J. Atherton, C. A. Ebbers, Z. Rek, *ICF Quarterly Report* **3** (3), Lawrence Livermore National Laboratory, Livermore, CA (1993).
7. L. N. Rashkovich, *KDP Family of Crystals* (Adam-Hilger, New York, 1991).
8. N. P. Zaitseva, F. Sh. Ganikhanov, O. V. Kachalov, V. F. Efimkov, S. A. Pastukhov, and V. B. Sobolev, *Proc. SPIE* **1402,** 223 (1990).
9. J. J. De Yoreo, Z. U. Rek , N. P. Zaitseva, T. A. Land, and B. W. Woods, *J. Cryst. Growth* **166**, 291 (1996).
10. N. P. Zaitseva, I. L. Smolsky, and L. N. Rashkovich, *Krystallografiya* **36**, 198 (1991).
11. K. E. Montgomery and F. P. Milanovich, "High-laser-damage-threshold potassium dihydrogen phosphate crystals," *J. Appl. Phys.* **68**, 15 (1990).
12. A. A. Chernov, *Soviet Phys.* **4**, 116 (1961).
13. G. H. Gilmer , R. Ghez, and N. Cabrera, *J. Cryst. Growth* **8**, 79 (1971).
14. P. Vekilov, Yu. G. Kuznetsov, and A. A. Chernov, *J. Cryst. Growth* **121**, 643 (1992) .
15. A. J. Malkin, Yu. G. Kuznetsov, W. Glantz, and A. McPherson, *J. Phys. Chem.* **100**, 11736 (1996).
16. T. A. Land, J. J. De Yoreo, J. D. Lee, A. J. Malkin, Yu. G. Kuznetsov, and A. McPherson, *Surf. Sci.,* (submitted).
17. W. K. Burton, N. Cabrera, and F. C. Frank, *Royal Soc. London Philos. Trans.* **A243**, 299 (1951).
18. J. J. De Yoreo, T. A. Land, and B. J. Dair, *Phys. Rev. Lett.* **73**(6), 838 (1994).
19. J. J. De Yoreo, T. A. Land, L. N. Rashkovich, T. A. Onischenko, J. D. Lee, O. V. Monovskii, and N. P. Zaitseva, *J. Cryst. Growth* (submitted).
20. B. Van der Hoek, J. P. Van der Eerden, and P. Bennema, *J. Cryst. Growth*, **56**, 621 (1982).
21. B. Van der Hoek, J. P. Van der Eerden, P. Bennema, and I. Sunagawa, *J. Cryst. Growth* **58**, 365 (1982).
22. N. P. Zaitseva, L. N. Rashkovich, and S. V. Bogatyreva, *J. Crystal Growth* **148**, 276 (1995).
23. M. Volmer and A. Weber, *Z. Phys. Chem.* **119 A,** 277 (1926).
24. I. L. Smolsky and N. P. Zaitseva, *Growth of Crystals*, E.I. Givargizov and S. A. Grinberg, eds. (Plenum Publ. Corp., N.Y., 1994), Vol. **19**, pp.173-185.
25. A. T. Amandosov, Z. S. Pashina, and L.N. Rashkovich, *Sov. Kvant. Elektron.* **10**, 469 (1983).

THE PETAWATT LASER SYSTEM

D. M. Pennington

M. D. Perry

B. C. Stuart

J. A. Britten

C. G. Brown

S. Herman

J. L. Miller

G. Tietbohl

V. Yanovsky

Introduction

In this article, we describe the Petawatt laser system as it has developed into FY 1997. In May of 1996, we demonstrated the production of over a petawatt (quadrillion watts) of peak power in the Nova/Petawatt Laser Facility, generating >600 J in ~430 fs. The development of small-scale multiterawatt and now petawatt lasers has opened an entirely new regime of laser–matter interaction to exploration.[1] Applications of these extremely powerful lasers range from enabling new accelerator concepts[2] to new approaches to inertial confinement fusion (ICF).[3]

The Petawatt Laser Project was proposed in a Laboratory Directed Research and Development (LDRD) program in 1992 to develop a laser capable of producing petawatt pulses in order to examine the "fast ignitor" concept for inertial confinement fusion.

Shown schematically in Figure 1, fast ignition requires high pulse energy in addition to the short pulse duration. Conventional ICF relies on creating a hot, uniformly dense central core formed by compression of a deuterium/tritium plasma. The necessity of forming the hot central core requires substantial energy and places severe requirements on implosion symmetry.[4] In the fast ignitor concept, ignition is decoupled from compression. The pellet is assembled cold and, at the point of maximum compression, is ignited by raising a small section of the pellet on the periphery of the dense core rapidly above the ignition temperature. Hot electrons (200 keV < E < 1 MeV) are generated by the interaction of the intense (10^{19}–10^{21} W/cm^2) light with plasma. The hot electrons rapidly equilibrate in the dense fuel, raising the overall ion temperature to 5 to 20 keV, which initiates fusion burn. The fusion burn then propagates throughout the compressed fuel

FIGURE 1. Diagram of "fast ignitor" concept in inertial confinement fusion. (70-00-0298-0179pb01)

Laser energy

Inward transported thermal energy

Atmosphere formation
Laser or particle beams rapidly heat the surface of the fusion target forming a surrounding plasma envelope.

Compression
Fuel is compressed by rocket-like blowoff of the surface material.

Ignition
At the moment of maximum compression a short (1–10 ps) high-intensity (10^{19} W/cm^2) pulse ignites the capsule.

Burn
Thermonuclear burn spreads rapidly through the compressed fuel, yielding many times the driver input energy.

before the hydrodynamic disassembly time of the pellet. In order to transfer enough energy to the ions in a small, well-defined volume faster than hydrodynamic disassembly, the energy must be deposited directly in the dense fuel, in a volume less than ~4000 μm^2 and a duration $\tau \leq 10$ ps, dependent on the density, convergence ratio, etc.,

$$\left(\tau \approx \frac{R_{\text{spot}}}{v_{\text{s}}} \leq 10 \text{ ps} \right) \ .$$

High laser pulse energy is required in order to produce enough hot electrons to heat the plasma sufficiently to initiate a self-sustaining fusion burn. In addition, nearly perfect beam quality is required in the laser in order to achieve a small spark region. The fast ignitor concept offers the possibility of high target gain at substantially reduced total drive energy than conventional ICF. However, unlike conventional ICF, this approach relies on untested physics in a completely new regime of laser–matter interaction.

In addition to testing the concept of fast ignition, the extreme conditions produced by the Petawatt open a new regime of laser–matter interactions to study. The short pulse duration, coupled with the enormous light pressure (>300 Gbar) and high irradiance, makes possible the production of extremely dense matter at kilovolt to megavolt temperatures. Focused irradiance above 10^{20} W/cm^2 is required to achieve the simultaneous conditions of hot (>1 keV), dense (~10^{24} cm^{-3}) matter of relevance to equation of state and hydrodynamic measurements. With an irradiance >10^{21} W/cm^2, the absorption physics enter a new regime where it may be possible to achieve high temperatures at solid density. The Petawatt will also enable the production of copious amounts of hard (10 keV to >10 MeV) x rays, which can serve as a high-energy backlighter for Nova or NIF implosions, as well as other radiographic applications.

To meet the conditions necessary to address the numerous issues associated with the fast ignitor *and* serve as a general facility for experiments in intense laser–matter interaction, the Petawatt laser was designed to produce 1-kJ pulses with a pulse duration adjustable between 0.5 and 20 ps and sufficient beam quality to produce an irradiance greater than 10^{21} W/cm^2 when focused at $f/3$.

Several new advances in technology enabled the production of petawatt pulses. One was the development of broadband laser materials for solid-state laser systems, such as Ti:sapphire. Another was the application of the chirped-pulse amplification (CPA) technique to solid-state lasers.[5-7] By stretching the pulse prior to amplification, the limitation on pulse energy imposed by beam filamentation due to small-scale self-focusing can be overcome. The CPA technique has

been applied to existing, large-scale Nd:glass laser systems at CEA, Limeil,[8,9] the Rutherford-Appleton Laboratory,[10] ILE Osaka,[11] and at LLNL.[12,13]

Manufacture of pulse compression gratings of sufficient size and quality to permit the demonstration of a petawatt-scale laser was considered to be one of the most challenging tasks of the Petawatt Laser Project. To address this issue, a facility was built at LLNL, and unique processing techniques were developed to enable the fabrication of high-efficiency diffraction gratings with high laser-damage thresholds and a uniform submicron period over a length scale approaching 1 meter.[14] The final Petawatt laser design utilizes a hybrid Ti:sapphire/Nd:glass laser system in order to provide sufficient bandwidth to achieve the shortest pulse duration, large-scale diffraction gratings to compress the pulse after amplification, and compression in vacuum to avoid beam distortion and self-phase modulation resulting from the nonlinear refraction of air.

Laser System

The Petawatt laser begins with a commercial Kerr-lens mode-locked Ti:sapphire oscillator that produces transform-limited 100-fs, 1054-nm pulses. A single pulse is selected from the mode-locked train and stretched to 3 ns in a single-grating, single-lens pulse stretcher. This pulse is amplified to 6 to 7 mJ in a linear, TEM$_{00}$, Ti:sapphire regenerative amplifier operating at 1054 nm.[15] Further amplification to 50 mJ is achieved in a Ti:sapphire ring regenerative amplifier with a larger mode size to prevent the onset of nonlinear effects, such as self-phase modulation (SPM) and self-focusing. Up to this point, the system runs at 10 Hz with an energy stability of 3%. A pulse slicer eliminates pulse leakage from the regenerative amplifier, while a half-wave slicer switches a single pulse from the 10-Hz pulse train into the Nd:glass amplifier stage of the system. The remaining pulses are compressed to 320 fs in air for use in subterawatt level experiments[16,17] and Nova x-ray diagnostic characterization.

The pulse selected for further amplification is spatially tailored to give a near-uniform top-hat spatial profile for efficient energy extraction in mixed phosphate glass rod amplifiers, producing a spectrally shaped pulse up to 12 J in energy.[12] The beam can be propagated either to the 100-TW laser system in the Nova two-beam chamber[13] or through an image-relayed beamline, which injects the beam into Nova beamline 6 for further amplification. A 37-actuator deformable mirror will be installed in the beam at the output of the 45-mm amplifier in the master oscillator room (MOR) to precorrect for pump-induced and thermal aberrations in the Nova disk-amplifier section.

The component schematic for the Petawatt laser system is shown in Figure 2. The Nova preamplifier system has multiple stages of amplification and magnification. These optics represent a significant source of
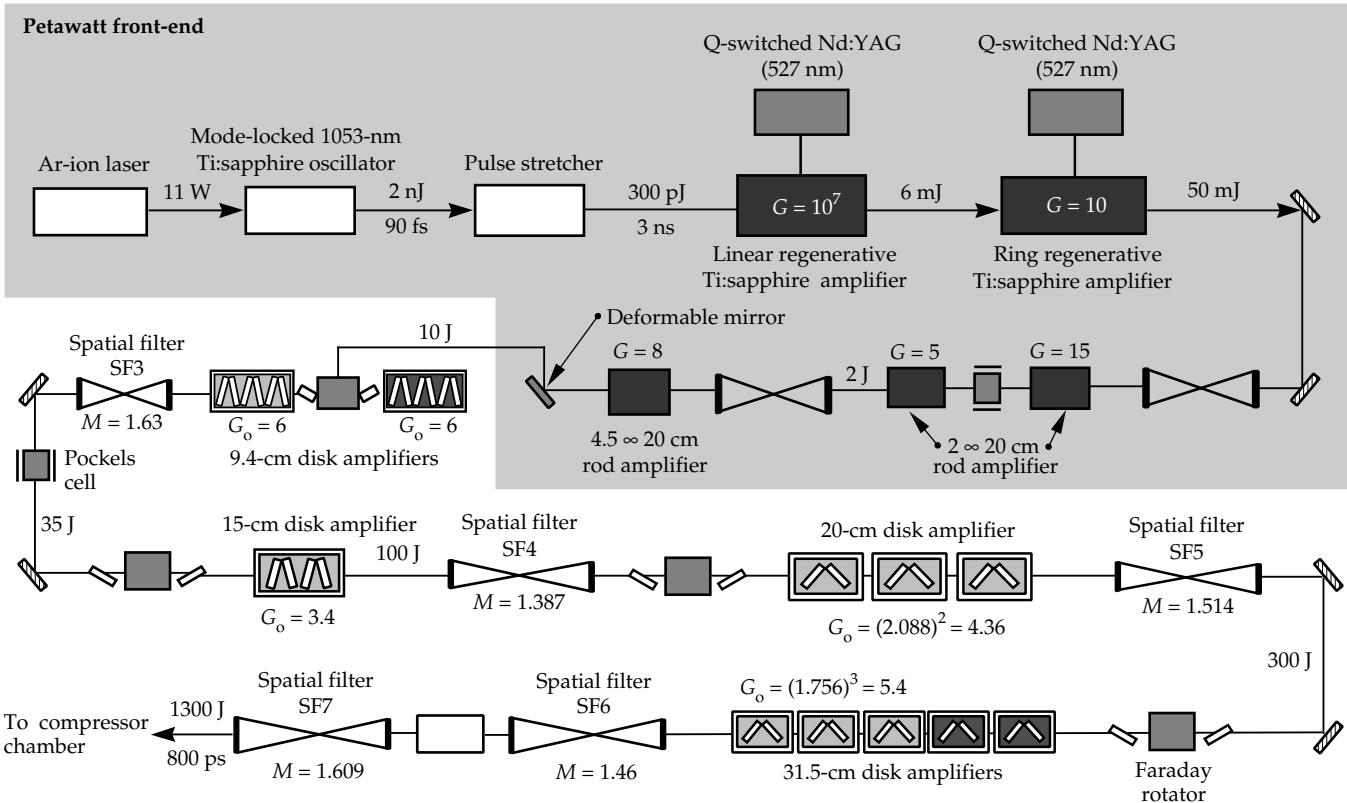
FIGURE 2. Layout of the Petawatt laser system. (70-00-0298-0180pb02)

spectral gain narrowing due both to amplification and bandwidth limiting optical components. In order to minimize the gain narrowing of the spectrum caused by high gain amplification of the laser pulse, we chose to inject the beam as far along the Nova amplifier chain as possible. Near diffraction-limited beam quality is achieved by limiting the beam to the central 80% of these amplifiers, minimizing edge effects in the disk amplifiers. A gain of only a few hundred is needed from Nova to reach the Petawatt maximum expected energy of ~1 kJ (allowing for passive transmission losses). As a result, a limited number of sets of Nova disk amplifiers provide the necessary energy, as indicated in Figure 2. The Nova 46-cm disk amplifiers are removed from the chain for Petawatt shots, as they produce a twofold problem. First, the amplifiers are split into two halves, preventing parasitic oscillations in the amplifier slab, but also destroying the coherence between the two halves of the beam. Second, the two halves of the 46-cm disks thermally distort in opposite directions when fired, steering the two halves of the beam away from each other. Together, these effects would limit the peak focal plane irradiance to much less than the diffraction limit.

Gain narrowing in the phosphate glass amplifiers reduces the spectral width to 4.0 nm and reduces the pulse duration to 800 ps. Figure 3 shows the progression of spectral gain narrowing at the output of the

compressor as amplifiers were sequentially fired. The output of the two regenerative amplifiers in the Petawatt MOR is nominally Gaussian, with 65 Å bandwidth full width at half maximum (FWHM). When the two 19-mm and the 45-mm Nd:glass amplifiers in the Petawatt MOR are fired, this spectrum narrows to approximately 53 Å FWHM, producing an 18% decrease in the total bandwidth. As the beam is progressively amplified in the Nova amplifier chain, the bandwidth continues to narrow, but the spectrum remains Gaussian in shape. Addition of the 9.4-cm and 15-cm disk amplifiers reduces the spectrum by an additional 19%. In order to obtain sufficient energy out of the laser chain, all three 20-cm disk amplifiers are fired, producing another 7% reduction in bandwidth. The final three 31-cm amplifiers reduce the bandwidth by 5%. The total spectral gain narrowing observed with all amplifiers fired is ~41% from the output of the regenerative amplifiers to the output of the Nova chain.

Additional energy could be extracted from the disk amplifier section at the price of degraded spatial quality and temporal contrast upon recompression.[18] Above an intensity length product of ~100 GW/cm^2, nonlinear effects begin to degrade the beam quality, due to the intensity-dependent refractive index $n = n_0 + n_2 I$, where I is the intensity of the pulse, and n_0 and n_2 are the linear and nonlinear refractive indices, respectively.

(a)

Nova target chamber

Vacuum
compressor
chamber

Minichamber

Gratings
(ϕ94 cm)

Output beam
to parabola

Input beam
to compressor

(b)
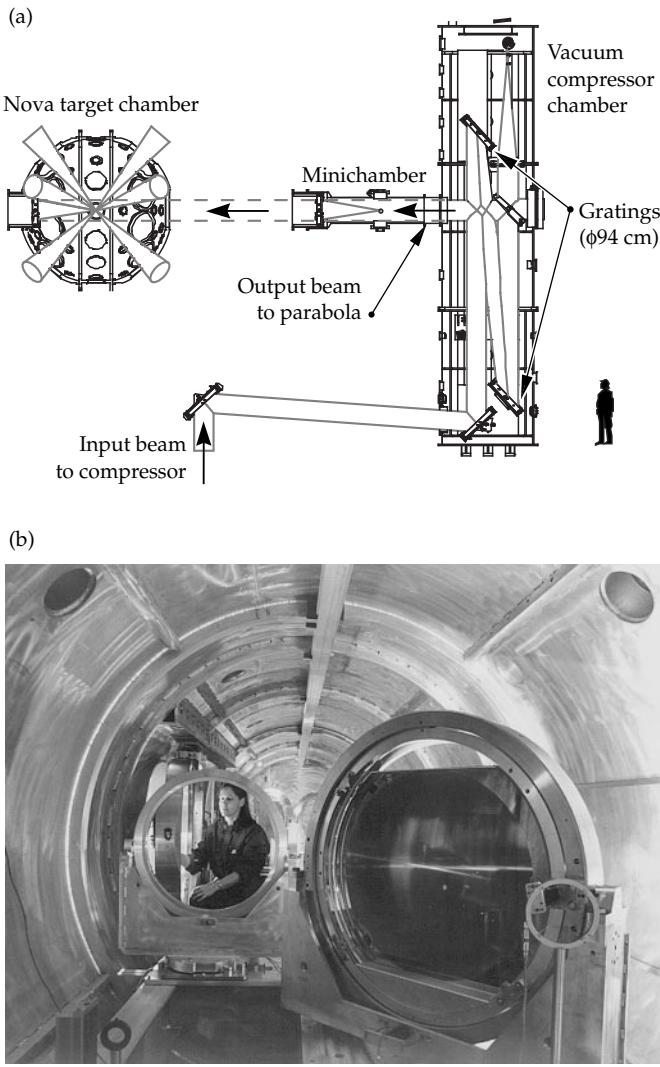
FIGURE 3. After amplification, the chirped pulse is temporally compressed in a single-pass grating compressor, then focused onto a target in an independent target chamber or integrated with Nova in the 10-beam chamber. The optical layout of the compressor is shown in (a), while a photograph of the interior of the compressor chamber (b) provides a sense of scale.   (70-00-0298-0181pb03)

This intensity-dependent refractive index produces a nonlinear phase retardation that results in wavefront distortion and eventually beam filamentation.[19,20] The nonlinear phase retardation, or *B*-integral, is given by

$$B = \frac{2\pi}{\lambda} \int_0^\ell n_2 I(z)dz \quad ,$$

where ℓ is the propagation length.

As an example, a laser pulse propagating through 10 cm of fused silica at a power density of 10 GW/cm^2 accumulates 2 radians of nonlinear phase. The technique of CPA was developed specifically to overcome the limitations imposed by this nonlinear phase by

stretching the pulse prior to amplification, thereby reducing the peak power in the amplifiers. However, economic factors dictate that petawatt-class lasers will almost always be operated at the maximum *B*-integral allowable in the laser system even with CPA. To achieve high-quality petawatt pulses on Nova, we limit the total *B*-integral to 1.0 in the Nova driver section and 1.52 in the power section, corresponding to $\Delta B \sim 2.5$ in the amplifier section.

In addition to *B*-integral, SPM in the amplifier chain can degrade the quality of the compressed pulse in CPA systems, ultimately limiting the pulse contrast.[18] This effect is easily seen by observing the increase in bandwidth of an intense, ultrashort laser pulse upon passage through a nonlinear medium according to

$$\omega(t) = \omega_0(t) - \frac{\partial B}{\partial t} \quad .$$

Spatial phase modulation is determined by the value of the nonlinear phase while frequency modulation is determined by the time-derivative. For a conventional (near transform-limited) laser pulse with the duration equal to the stretched pulse in a petawatt-class laser (500–1000 ps), the self-phase modulation effect would be negligible. However, the pulse in CPA systems is strongly chirped (i.e., exhibits a time-dependent frequency). As a result, the central part of the pulse (near the carrier frequency) experiences a greater phase retardation than the early or later part of the pulse where the intensity is less. This limits the ability to recompress the pulse and often results in temporal wings appearing on either side of the compressed pulse.[18]

Following amplification in Nova, the chirped pulse is compressed to a pulse duration which can easily be adjusted from 0.43 to 30 ps. Pulse compression occurs in a vacuum chamber with a pair of large aperture diffraction gratings arranged in a single-pass geometry, as shown in Figure 4. At the input to the compressor, the frequency components of the beam are dispersed in time from red to blue. As the beam propagates to the second grating, the blue components catch up with the red components. The second grating stops the dispersion process, producing a temporally compressed pulse. The optical throughput of the compressor was determined to be 84%. The compressed beam is reflected off a full-aperture beamsplitter to an on-axis parabolic mirror, located in a target chamber adjacent to the compressor chamber.

In small-scale CPA systems, the beam ellipticity and spatial chirp associated with a single-pass compressor geometry would be intolerable. However, in the limit that the diameter of the beam is much larger than the dispersed length, these effects are negligible. Currently, the Petawatt operates with a 46-cm beam and a dispersion length of ($c\tau_{str} \cdot \cos\theta_{compressor}$) ~20 cm. This

FIGURE 4. Progression of spectral gain narrowing (measured at the output of the compressor) as amplifiers were sequentially fired. (70-00-0298-0182pb01)
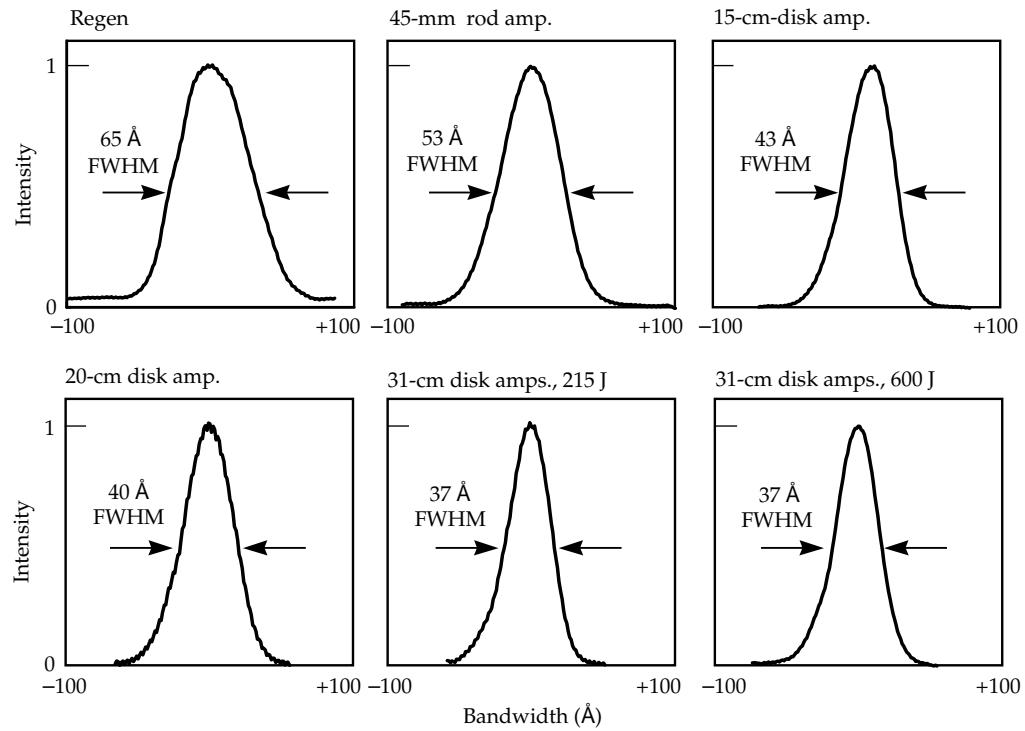
system is limited to a maximum pulse energy of 650 J due to the use of subaperture (74 cm) diffraction gratings. These gratings exhibit a diffraction efficiency of 95%, a diffracted wavefront quality of better than 0.1 μm (peak to valley) and a damage threshold of 0.42 J/cm^2 for 1054 nm pulses at 200 fs.[14] These gratings are currently being exchanged for full 94-cm size gratings, which will allow operation of the Petawatt at >900 J with a 58-cm-diameter beam in January 1998.

Most CPA laser systems are designed to produce the minimum pulse duration upon recompression. This is accomplished by setting the compressor to cancel the dispersion of the stretcher and optical material. Since the compressor cannot cancel the dispersion of the stretcher and optical material in the laser system exactly, the system is designed to minimize the residual phase, $\delta = \phi_{com}(\omega) + \left[\phi_{str}(\omega) + \phi_{mat}(z, \omega)\right] = 0$. These phase functions are often written in a Taylor series expansion,

$$\phi_{mat}(z, \omega) = \beta_1(\omega - \omega_0)z + \frac{\beta_2(\omega - \omega_0)^2}{2!}z$$

$$+ \frac{\beta_3(\omega - \omega_0)^3}{3!}z + \frac{\beta_4(\omega - \omega_0)^4}{4!}z + \dots$$

where $\beta_n = (\partial n_k / \partial \omega^n)\omega = \omega_0$. The stretcher/compressor combination in the Petawatt laser are designed to correct for chromatic aberration and material dispersion in the system up to third-order (i.e., only the fourth-order terms in δ remain). This is sufficient for pulses of duration greater than 100 fs.

Diagnostics are located throughout the laser system to characterize and optimize its performance. Spectra, energy, pulse length measurements, and near-field irradiance are obtained in the MOR at the output of the 45-mm amplifier, in the Nova output sensor diagnostic, and at the output of the Petawatt compressor. A low-energy beam sample transmitted through the final beam splitter allows laser diagnostic measurements following compression. Parameters measured on each shot include energy, near-field irradiance, far-field irradiance, second-order autocorrelation, spectrum, and prepulse measurements. A Hartmann sensor for measuring the wavefront of the beam at low power is also located in the diagnostic station at the output of the compressor. Output pulse characteristics of the Petawatt beam under current operational conditions are shown in Figure 5. The fine-scale structure in this figure is the result of individual elements of the charge-coupled device (CCD) array used to record the data. For the Gaussian spectrum shown in Figure 5(a), the compressed pulse width is near transform limited, with a time-bandwidth product of $\Delta\nu\Delta\tau \sim 0.43$. The autocorrelation shown in Figure 5(b) indicates that on the order of a few percent of the energy is in the temporal wings of the pulse. The highest peak power achieved to date with the Petawatt laser is 1.23 PW, with 680 J out of

(a) Spectrum

(b) Autocorrelation

(c) Near-field irradiance

(d) Focused irradiance without debris shield

(e) Horizontal profile

(f) Vertical profile
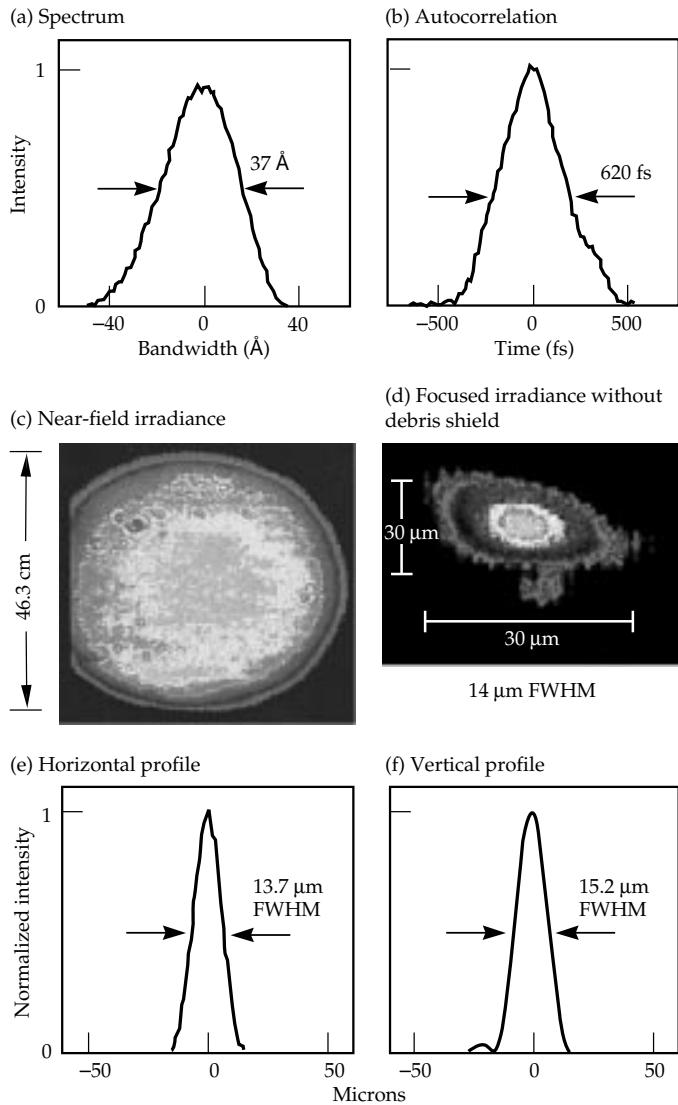
FIGURE 5. A representative sample of the Petawatt (a) spectrum, (b) autocorrelation, and (c) near-field irradiance measured on each shot in the Petawatt diagnostic station. (d) shows the focal plane distribution measured at target chamber center at 10 Hz. Intensity line-outs of this focal spot shown in (e) and (f) indicate the spot is approximately 14 µm FWHM. (70-00-0298-0183pb01)

the Nova chain and a pulse width of ~430 fs FWHM. The near-field irradiance is shown in Figure 5(c). No evidence of optical damage was observed on the gratings at this power level, or for fluences up to 400 mJ/cm^2.

Targeting System and Experiments

Target experiments with petawatt pulses will be possible either in an independent target chamber or with the Nova laser system for integrated fast ignition experiments. A one-beam chamber has been installed in between the Petawatt compressor and the 10-beam chamber to allow single-beam experiments. The primary target chamber focusing optic is an on-axis parabolic mirror, nominally $f/3$. The entire parabola assembly is transferable between the one-beam and 10-beam chambers for integrated experiments with the Petawatt beam and Nova at some point in the future.

A microscope and reticle assembly are used to measure the focal spot size at the target chamber center. A representative image of the focal spot measured at the target chamber center at 10 Hz is shown in Figure 5(d). We have measured a primary focus directly off the parabolic mirror as small as 14 µm FWHM [Figure 5(e)]. Change in the stresses applied by the grating mounts has caused a gradual degradation of grating wavefront over time, resulting in a current focal spot on the order of 26×38 µm FWHM. These wavefront distortions will be corrected with the implementation of the deformable mirror. Thermal distortion of the amplifier disks due to repeated firing throughout the day causes the focal distribution to broaden by a factor of 2 to 3, as expected. These pump-induced aberrations can also be compensated with the use of the deformable mirror wavefront correction system, which will be operational in early 1998. Experiments on the Beamlet laser have shown that deformable mirror pre-correction can produce a nearly diffraction-limited focal spot.[21] With the deformable mirror system, the Petawatt laser system should achieve a near diffraction-limited focal spot with a high shot rate.

For long-pulse (5–20 ps) fast ignitor physics experiments, the parabola is protected from target debris by a full-aperture debris shield. For short-pulse experiments, however, a conventional 1-cm-thick fused silica debris shield would produce an unacceptable accumulation of nonlinear phase retardation, ~28 radians double-passed! To protect the parabola from line-of-sight debris without incurring a large nonlinear phase retardation, a secondary "plasma mirror" is used in conjunction with the primary parabola, as shown in Figure 6.[22] For irradiances $> 2 \times 10^{14}$ W/cm^2, short-pulse radiation creates a critical-density plasma on the surface of a dielectric substrate. For incident pulses on the order of 500 fs, the plasma has insufficient time to undergo hydrodynamic expansion, producing a density-scale length less than the incident wavelength. This produces a reflecting plasma with a reflected wavefront comparable in quality to that of the initial surface. Reflectivities exceeding 90% have been achieved. Small-scale measurements made with the Petawatt front-end are in good agreement with the theoretical calculations shown in Figure 7. This novel targeting system enables the production of high-contrast

(a)

Target

Incident pulse

Debris shield

(b)

Target

Incident pulse

On-axis parabolic
reflector

Secondary "mirror"
(fused silica with λ/2
HfO$_2$ overlayer)

Target

HfO$_2$ overlayer
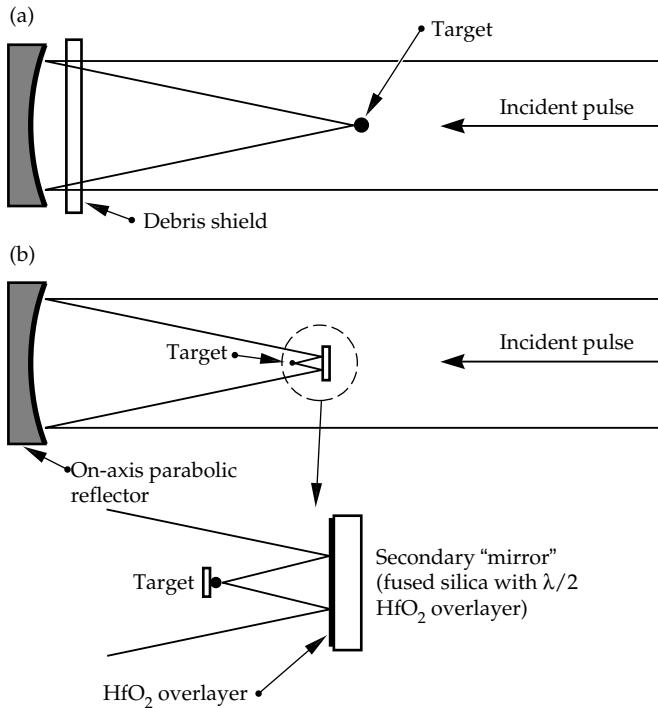
FIGURE 6. (a) A conventional debris shield cannot be used in the Petawatt targeting system for short pulses. The accumulated nonlinear phase retardation for double-pass through a 1-cm-thick fused silica debris shield would produce 28 radians of *B*. (b) Line-of-sight debris can be eliminated by focusing with a spherical plasma mirror in conjunction with an incident target shield. (70-00-0298-0184-pb01)
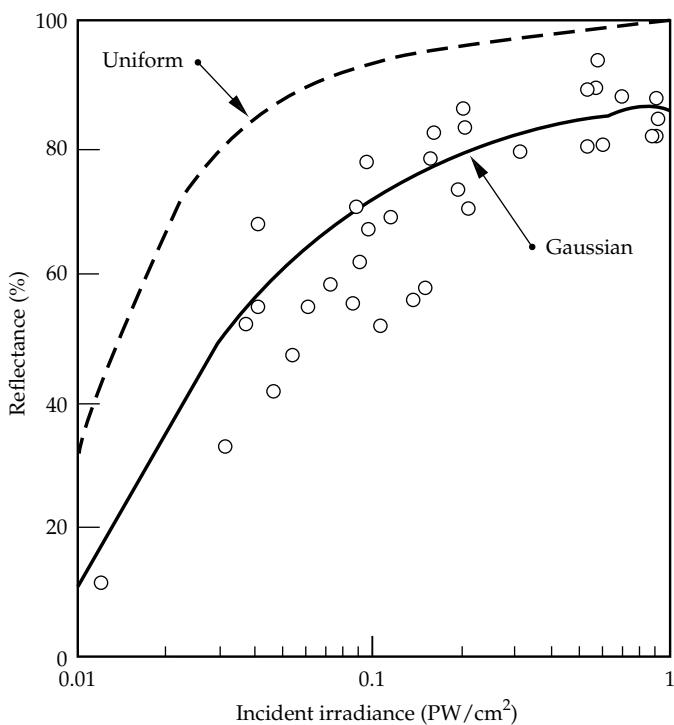
FIGURE 7. Small-scale experiments done at the output of the Petawatt front-end indicate that greater than 90% reflectivity can be achieved with good reflected wavefront quality. Measurements are in good agreement with the theoretical calculations. (70-00-0298-0185pb01)

pulses (10^7), when an antireflection-coated substrate is used. In addition, by using a curved plasma mirror, the effective focal length of the system can be easily varied. Initial experiments with the plasma mirror on gold targets showed molten gold from the target hit the mirror surface, and splattered back onto the parabolic mirror. Future experiments will prevent this by placing the target inside a large disk to protect the parabola from line-of-sight debris, or by using an off-axis geometry. Currently all experiments with the Petawatt are performed in the one-beam chamber.

Two classes of experiments have been performed to date using the Petawatt laser. Long-pulse (~20 ps) experiments address fast ignitor physics, while initial short-pulse (~500 fs) experiments were designed to demonstrate the potential use of the Petawatt as a source for laser-driven radiography. Figure 8 shows a photographic image of a long-pulse beam target experiment with the Petawatt laser. The laser pulse is entering from left. The background green light is the result of second harmonic emission from the target. Particles emerging from the back of the target can be observed in a series of jets at right. K-α fluorescence induced in a molybdenum layer buried in a solid aluminum target provides a measure of the conversion efficiency of laser light to electrons. Up to 35% conversion to electrons of mean energy 1 MeV at 2×10^{19} W/cm^2 has been measured.[23]

Recent short-pulse experiments delivered up to 330 J on target with pulse length 420–500 fs, for a peak irradiance of 1.7×10^{20} W/cm^2. These experiments examined the creation of hot (0.1–1 MeV) electrons by high-irradiance pulses. By changing the
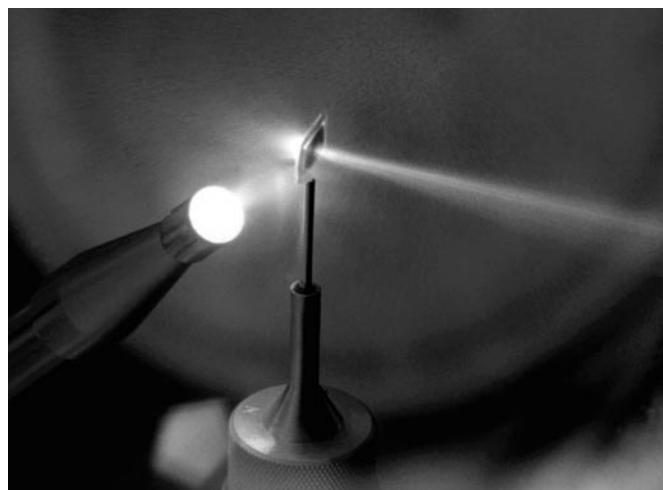
FIGURE 8. Photographic image of single-beam target experiment with the Petawatt laser taken by G. Stone. The laser pulse is entering from left. The background light is green resulting from second harmonic emission from the target. Particles emerging from the back of the target can be observed in a series of jets at right. (70-60-0597-0766.4pb01)

experimental conditions, the electron spectrum can be shifted towards higher energy (10–100 MeV), even in solid-density plasmas. High-field magnetic dipole spectrometers were fielded at 30º and 95º off the laser axis to measure the electron spectrum (from 0.1 to 150 MeV) emerging from the back of the target and orthogonal to the laser axis. The dispersed electron spectrum is recorded as tracks in a standard emulsion. A representative electron spectrum produced from a 0.5-mm-thick gold target shot at near normal incidence is shown in Figure 9. Electrons were observed at energies extending above 90 MeV; however, the bulk of the distribution was in the range of ~5 to 15 MeV, where the emission was found to be forward directed with about ten times more flux observed at 30º, with respect to the laser propagation direction, as compared to the flux at 95º.

High-energy bremsstrahlung x rays generated by the electrons in the gold target produced photo-nuclear reactions in both the gold and surrounding copper target-holder. These reactions produced activation and transmutation to platinum and nickel daughter isotopes. Some specific reactions observed include $^{197}Au(\gamma,n)^{196}Au$, identified by the decay of the ^{196}Au to ^{196}Pt emitting nuclear gamma rays at 356 and 333 keV, and $^{63}Cu(\gamma,n)^{62}Cu$ and $^{65}Cu(\gamma,n)^{64}Cu$, which were identified by their subsequent beta decay to ^{62}Ni and ^{64}Ni with half-lives of 9.7 minutes and 12.7 hours, respectively. The threshold gamma-ray energy for photo-activation of the gold and copper is ~8 and ~11 MeV, respectively, indicating a large flux of high-energy bremsstrahlung. A gamma spectrum and decay curve are shown in Figure 10. Neutron spectra and other high-energy x-ray spectra are also routinely measured. Together, these diagnostics are providing us the first glimpse into this new regime of laser–matter interactions.

FIGURE 10. Photonuclear activation spectrum taken on a short-pulse Petawatt target.   (70-00-0298-0188pb01)

Summary

The overall performance of the Petawatt laser to date has exceeded expectations. We have demonstrated the production of 1.23 petawatt of peak power in the Nova/Petawatt Laser Facility, generating >600 J in <500 fs. Currently, this system is limited to 600-J pulses in a 46.3-cm beam. Expansion of the beam to 58 cm, with the installation of 94-cm gratings, will enable >900-J operation. Focusing the beam onto a target is accomplished using an on-axis parabolic mirror with a debris shield for 5- to 20-ps pulse length, or in conjunction with a plasma mirror for pulse lengths <5 ps. Recent short-pulse experiments (with pulse length 420–500 fs) delivered up to 330 J on target, for a world-record peak irradiance of 1.7×10^{20} W/cm². With the installation of the full-aperture gratings and deformable mirror, an irradiance of 10^{21} W/cm² should be achievable. Target experiments with petawatt pulses have concentrated on the demonstration of fast ignitor physics and the potential use of the petawatt-class lasers as a source for laser-driven radiography.

FIGURE 9. Electron spectrum produced in 0.5-mm gold target at 1.1×10^{20} W/cm².   (70-00-0298-0187pb01)

Acknowledgments

References

1. M. D. Perry and G. Mourou, *Science*, **264**, 917–924 (1994).
2. C. Joshi and P. B. Corkum, *Physics Today* (1996).
3. M. Tabak, J. Hammer, M. E. Glinsky, W. L. Kruer, S. C. Wilks, J. Woodworth, E. M. Campbell, M. D. Perry, and R. J. Mason, *Phys. Plasmas*, **1**, 1626–1634 (1994).
4. J. Lindl, *Phys. Plasmas*, **2**, 3933–4024 (1995).
5. C. E. Cook, *Proc. IRE*, **48**, 310–316 (1960).
6. R. A. Fisher and W. K. Bischel, *IEEE J. Quantum Electron.*, **QE-11**, 46–52 (1975).
7. D. Strickland and G. Mourou, *Opt. Comm.*, **56**, 219–221 (1985).
8. C. Sauteret, D. Husson, G. Thiell, S. Seznac, et al., *Opt. Lett.*, **16**, 238 (1991).
9. C. Rouyer, E. Mazataud, I. Allais, A. Pierre, S. Seznac, C. Sauteret, and G. Mourou, *Opt. Lett.*, **18**, 214–216 (1993).
10. C. N. Danson, L. Barzanti, Z. Chang, A. Damerell, et al., *Opt. Comm.*, **103**, 392–397 (1993).
11. K. Yamakawa, H. Shiraga, and Y. Kato, *Opt. Lett.*, **16**, 1593 (1991).
12. M. D. Perry, F. G. Patterson, and J. Weston, *Opt. Lett.*, **15**, 381–383 (1990).
13. B. C. Stuart, M. D. Perry, J. Miller, G. Tietbohl, S. Herman, J. A. Britten, C. Brown, D. Pennington, and V. Yanovsky, *Opt. Lett.* (1997).
14. R. Boyd, J. Britten, D. Decker, B. W. Shore, B. C. Stuart, M. D. Perry, and L. Li, *Appl. Opt.*, **34**, 1697–1706 (1995).
15. B. C. Stuart, S. Herman, and M. D. Perry, *IEEE J. Quantum Electron.*, **31**, 528–538 (1995).
16. B. C. Stuart, M. D. Feit, A. M. Rubenchik, B. W. Shore, and M. D. Perry, *Phys. Rev. Lett.*, **74**, 2248–2251 (1995).
17. B. C. Stuart, M. D. Feit, A. M. Rubenchik, B. W. Shore, and M. D. Perry, *Phys. Rev. B*, **53**, 1749–1761 (1996).
18. M. D. Perry, T. Ditmire, and B. C. Stuart, *Opt. Lett.*, **19**, 2149–2151 (1994).
19. Y. R. Shen, *The Principles of Nonlinear Optics* (Wiley, New York, NY, 1984).
20. W. Koechner, *Solid-State Laser Engineering*, 3rd ed. (Springer–Verlag, New York, NY, 1990).
21. B. M. V. Wonterghem, E. S. Bliss, J. A. Caird, R. G. Hartley, M. W. Kartz, J. T. Salmon, and P. J. Wegner, paper presented at Solid-State Lasers for Application to Inertial Confinement Fusion, Paris, France, 1996.
22. M. D. Perry, V. Yanovsky, M. Feit, and A. Rubenchik, *Phys. Plasmas*, to be submitted, 1997.
23. K. Wharton, *Phys. Rev. Lett.*, to be submitted, 1997.

HIGH-AVERAGE-POWER, HIGH-BRIGHTNESS ND:GLASS LASER TECHNOLOGY

C. B. Dane

L. A. Hackel

Introduction

In this report, we discuss the design and performance of a 100-J-per-pulse, solid-state laser with a repetition rate of 5 Hz resulting in an average output power of 500 W. The laser can also be operated with 10-Hz bursts of up to 50 pulses.

The system shown in Figure 1 consists of a single master oscillator and four separate amplifier chains, which are coupled by a single, stimulated Brillouin scattering (SBS), phase conjugate mirror. The laser demonstrates for the first time reliable phase locking of multiple laser amplifiers in separate optical beam lines into a single output beam with high pulse energy and high average output power. The laser has high brightness with near-diffraction-limited beam quality and, importantly, has the ability to be operated with pulse

FIGURE 1. Photograph of the completed 100-J-per-pulse, four-amplifier laser system. Pictured are Jim Wintemute and Balbir Bhachu, two key contributors to the design, construction, and operation of the laser system. (70-00-0298-0151pb01)

durations between 10 ns and 1 μs. The longer pulses are achieved by employing a special oscillator configuration involving amplification of the exponentially rising edge of a free-running master oscillator pulse. The shorter pulses are generated by amplifying more conventional Q-switched oscillator pulses. The laser employs zigzag laser slab technology with highly uniform pumping excitation and efficient heat extraction. In addition to providing phase locking of the individual laser beams, the SBS mirror also corrects thermally induced distortions introduced in the glass amplifier slabs. A self-pumped, Brillouin-enhanced, four-wave mixing configuration provides the nonlinear thresholds that are sufficiently low for efficient operation at the long pulse widths and prevents temporal phase fluctuations, which can interfere with the phase-locking process. The laser's high output-beam quality enables efficient second-harmonic conversion with measured full average power efficiencies that range from 65% for 500-ns pulses to more than 80% for 10-ns pulses.

We are developing this laser technology for several important applications. One application is to provide the U.S. Air Force with an illuminator for high-resolution imaging of space objects. Another is to provide high-rate damage testing of optics, protective coatings, and beam-blocking materials that are being developed for the National Ignition Facility (NIF). In the commercial sector, the unique high energy and high average power of the laser will enable the first high-throughput, commercial system for improving the fatigue lifetime of metals by laser shock processing.

High-Average-Power Lasers with Large Pulse Energy

Pulsed solid-state lasers with output energies exceeding 10 J have historically been limited to low repetition rates and, consequently, low average output

power. Although the Nova laser can produce single pulse energies of up to 120 kJ at a wavelength of 1 µm, it is limited to firing about once every two hours for an equivalent average power of only 17 W. Commercial solid-state lasers with outputs of 10 to 100 J, when available, are generally limited to repetition rates of one shot each 20 minutes, for a maximum average power of less than 100 mW.

The thermal loading of the laser gain media is a major limitation to the available average power that can be extracted from a solid-state laser. As the repetition rate is increased, the thermal loading increases correspondingly and generates stress and strain in the gain medium. The stress and strain lead to wavefront aberrations and depolarization that can cause damage to laser optical components by distorted extraction beams as well as seriously degraded output power performance. At the upper limit of thermal loading, the gain medium will fracture. We have shown that SBS phase conjugation, which corrects the thermal aberrations of concern, can allow full-power, high-quality laser output up to the mechanical limit of the gain medium. Furthermore, SBS phase conjugation enables a practical means of increasing system output by combining multiple beams.

The single-pulse energy of the laser is limited by the physical size of the amplifier slab and the saturation fluence and optical damage threshold of the gain medium. Increasing the height of the zigzag slab quickly becomes impractical because of the cost of large optics required to accommodate the extraction beams and increased difficulty in fabricating the slab. The length of the slab is limited by the maximum gain allowed by amplified

spontaneous emission (ASE) and, for short laser pulses, by the maximum glass path length allowed by nonlinear self-focusing. Increasing the zigzag slab thickness, the dimension through which cooling takes place, proportionally decreases the pulse repetition frequency. However, by phase locking multiple amplifier apertures, the pulse energy can be scaled to larger values without any compromise in repetition rate. The beams from each of the amplifiers are combined to form a single, spatially coherent beam that propagates as if it were generated in a single, diffraction-limited aperture.

Laser Architecture

The laser system architecture employs a single oscillator, the output of which is divided into four injection beams that propagate through separate amplifier chains. After being reflected from the phase conjugate mirror, the beams retrace their path through their respective amplifiers and are rejoined in the near field. The resulting output beam consists of four side-by-side beams with corrected wavefronts and with no piston phase offset between each beam. The beams therefore coherently sum in the far field, yielding a single, diffraction-limited peak.

Master Oscillator–Power Amplifier Architecture

Figure 2 shows a simplified conceptual drawing of the master oscillator–power amplifier (MOPA) architecture. The master oscillator uses a 4-mm-diameter,

FIGURE 2. Schematic of the master oscillator–power amplifier architecture using multiple phase-locked amplifiers. Faraday rotators provide passive switching within the amplifier to allow for amplification of pulses of arbitrary duration. The SBS phase conjugator provides correction of wavefront aberrations and phase locks the multiple apertures.
(70-00-0298-0152pb01)

Amplified output

Oscillator input beam

Polarizing beam splitter

Faraday isolators

Four-pass Nd:glass amplifiers

SBS phase conjugator
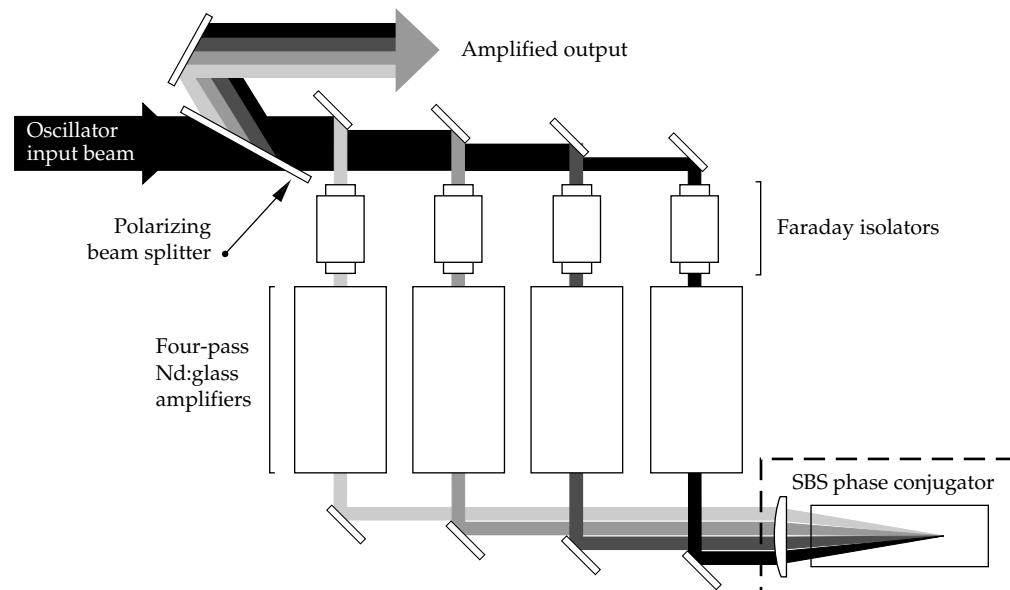
neodymium-doped yttrium lithium fluoride (Nd:YLF) rod configured in a resonator to generate single-frequency pulses at 1.053 μm. It produces a near-diffraction-limited beam, which is then amplified to 250 mJ by two Nd:YLF preamplifiers. The output of the oscillator is sheared into four separate beams by four spatially offset mirrors. Each beam is directed into a power amplifier chain configured to provide four passes through a Nd:glass zigzag slab. At this point, the four beams are brought together side-by-side and focused into the SBS phase conjugate mirror. The phase conjugator acts on the beams such that each beam is exactly retroreflected for a reverse trip through the optical system, making four more amplifier passes. Because of its non-linear threshold characteristics, the SBS process also provides gain isolation between the first four and

second four amplification passes. The polarization rotation of the beam by large-aperture Faraday rotators in each amplifier arm isolates the counterpropagating output beam from the input, allowing it to be extracted in transmission through the injection polarizer. Figure 3 is a more detailed drawing of the laser design showing the actual beam paths in a scale layout.

Zigzag Slab Technology

Each zigzag slab amplifier consists of a rectangular slab of APG-1 Nd:glass (Schott Glass Technologies, Inc.). Each slab has dimensions of $1 \times 14 \times 40$ cm and is doped to 2.7% Nd by weight. The amplifiers have two flashlamp/reflector assemblies and appropriate plumbing to allow water cooling of the slab faces.
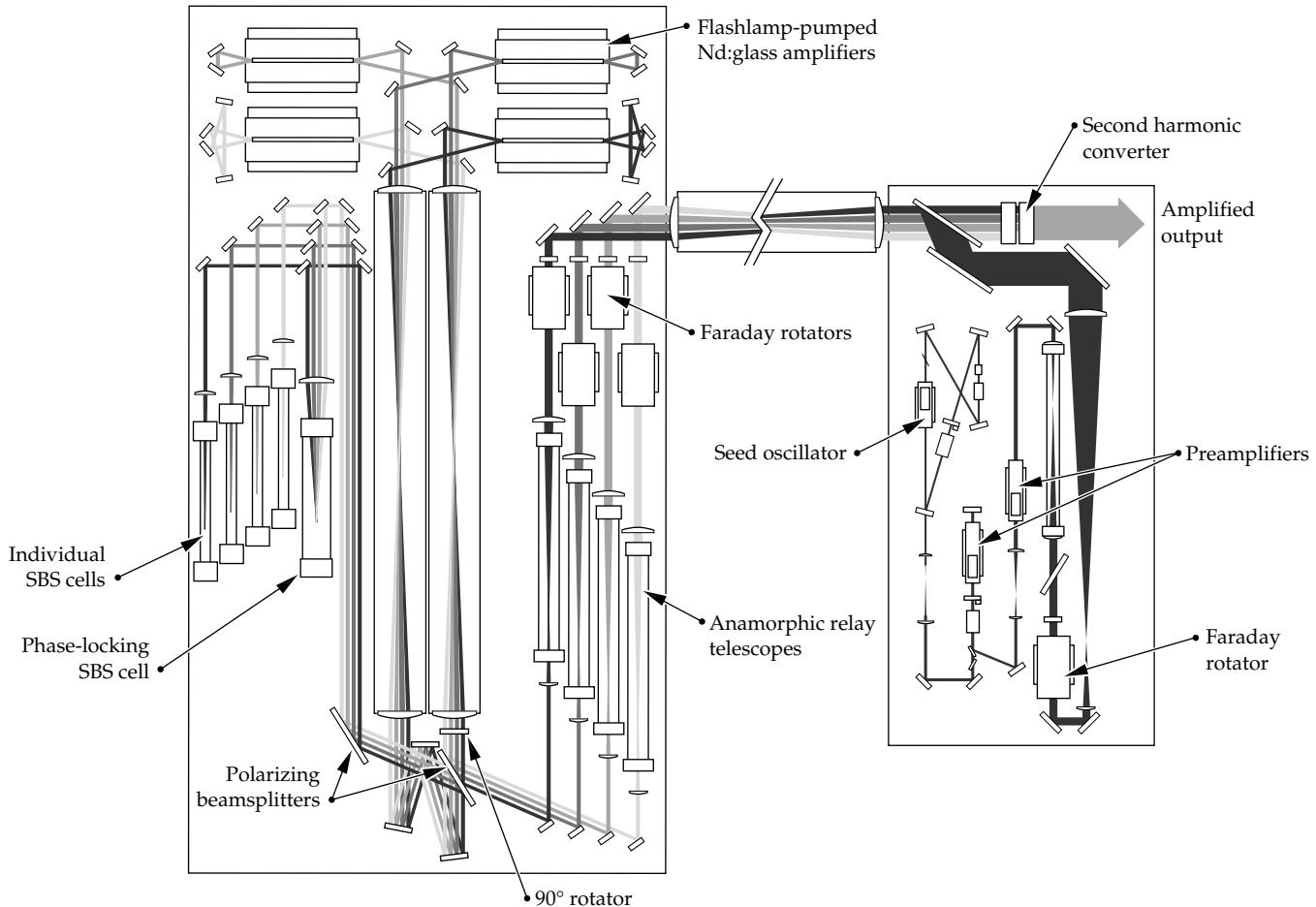
FIGURE 3. Schematic of the actual laser layout showing the master oscillator, relaying and formatting optics, power amplifiers, and phase conjugation. The system can be operated with four nonphase-locked outputs by using the individual SBS cells or, in a phase-locked mode, by combining the beams in a single conjugator cell.   (70-00-0298-0153pb01)

Figure 4 is a schematic diagram of a single amplifier unit. The slab is held in the center of the assembly and has a water cooling channel along both sides, which is formed by the slab face and a reflector assembly window. Two flashlamps on each side pump the slab through the cooling channels. Diffuse reflectors surround the flashlamps. By appropriate shaping, these reflectors provide uniform optical pumping of the slab. The thin (1-cm) dimension of the glass slab provides a short path for high heat conduction from the slab center to the cooling water. The resulting heat transfer efficiently removes heat buildup in the slab and increases the repetition-rate capability of the laser. Very uniform optical pumping from the reflector assembly results in uniform energy distribution from top to bottom in the slab. At high repetition rates, the primary thermal gradient that develops in the direction of heat conduction is across the thin dimension. However, laser light propagates through a slab in a zigzag path, reflecting from side to side across the thin dimension, resulting in nearly complete cancellation of aberrations induced by the strong thermal gradient.
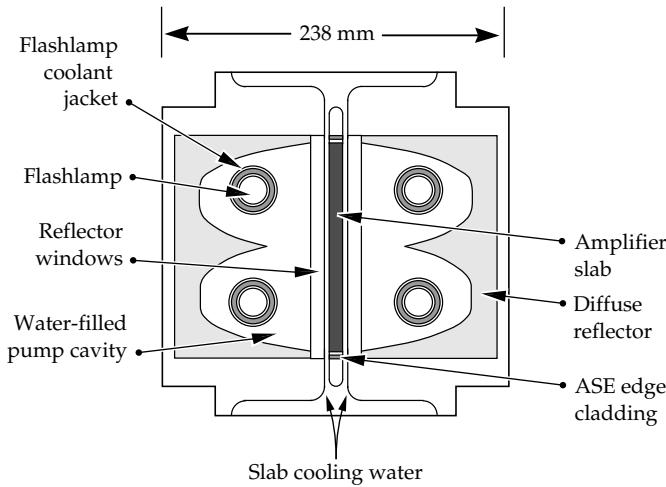
FIGURE 4. Cross-sectional view of the Nd:glass laser amplifier. Flashlamp light, tailored for highly uniform illumination by diffuse reflectors, provides the excitation to the slab. The thin (1-cm) dimension of the slab allows for efficient heat extraction into the water flow. The laser light zigzags through this thin dimension, averaging wavefront distortions.   (70-00-0298-0154pb01)

Wavefront Correction with SBS Phase Conjugation

Phase conjugators are becoming widely used in high-performance, solid-state laser systems. However, there has been no previous demonstration showing that multiple beams amplified in separate optical pathways can be successfully phase locked and reliably operated at high average power. The phase locking of beams enables the scaling of pulse energy and average power output because the laser is no longer limited by the energy or thermal performance of a single-amplifier aperture. In the present case, we are able to combine the 25-J outputs of four amplifiers into a coherent, 100-J laser with four times the average power output of a single head.

As shown in Figure 5, the SBS mirror uses a Brillouin-enhanced, four-wave-mixing, loop geometry. Without such a geometry, adequate phase locking stability of the four beams cannot be achieved. The loop geometry also supports conjugation of lasers with long pulse duration or low pulse energy, where the peak power of the laser at the conjugator is below the threshold for a conventional, single-focus SBS mirror, also shown in Figure 5. The input to the SBS cell is directed through three foci in the SBS medium. The first and third foci overlap to generate a self-pumped, four-wave mixing interaction, which eliminates temporal phase instabilities and frequency drift that can lead to inadequate phase locking and spectral broadening of the laser output. The 25-J beams are rejoined in the near field to form a single beam consisting of the four, approximately square, 25-mm beams with ~1-mm interbeam gaps.

Figure 6 shows near-field intensity profiles for the four-beam set and the measured far fields for one, two, three, and four beams at full pulse energy. Phase locking of the multiple beams is clearly evident: the far-field horizontal divergence narrows with the addition of each beam, finally reaching one fourth the width of that for a single beam. The profiles are very nearly the expected Fourier transforms of the rectangular near-field patterns. The measured divergence in each case is well below 1.5 times the diffraction limit for each near-field distribution.

Technique for Long-Pulse Amplification

The extraction scheme used to generate long pulses (>200 ns) in solid-state lasers is significantly different than that normally used for short pulses. Typical Q-switched laser systems operate with pulse widths of 5 to 30 ns. Free running, long-pulse operation of a solid-state laser results in a long train of pulses caused by the phenomenon of relaxation oscillation (spiking) with only a fraction of the total energy in each subpulse. Several different approaches have been taken to solve the problem of generating long pulses, including the closed-loop variable Q-switch, the open-loop variable Q-switch, and saturable absorber Q-switches. These methods typically result in very poor pulse-to-pulse stability in pulse duration, shape, and energy, and they have only been demonstrated at low output energies.

In our high-average-power system, we amplify the

Conventional SBS mirror

SBS loop geometry

Confocal lens pair

HR

HR

Top view showing multiple input beams
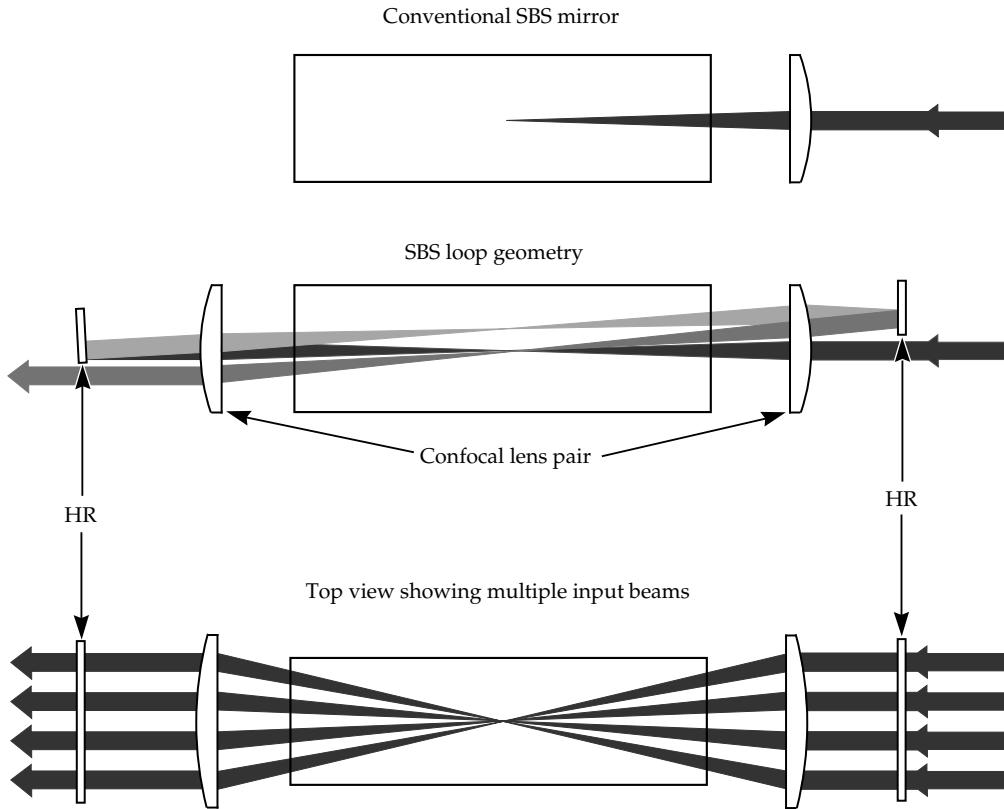
FIGURE 5. The use of an SBS loop is required to achieve high-performance phase locking of multiple apertures and narrow spectral bandwidth. This geometry (center and bottom) is compared to a conventional, single-focus, SBS phase conjugate mirror (top). (70-00-0298-0155pb01)

leading edge of a free-running oscillator to produce a near-rectangular output pulse. We have recognized that by using the exponentially rising edge of the laser pulse, the amplitude of the amplified output is a function of only the exponential time constant of the oscillator buildup; therefore, increasing gain in the amplifier does not increase the peak power, but extends the length of the pulse.

In operation, the oscillator output is allowed to build up at a slow rate determined by the growth rate of the first relaxation oscillation. This initial rate is controlled by introducing a small optical loss of 5 to 10% using a Pockels cell within the oscillator cavity. Once the SBS phase conjugator in the amplifier reaches threshold, the loss is removed, increasing the buildup rate to the level required for the desired amplifier output level. This yields the lowest possible SBS threshold and generates a near-constant output power determined by the exponential time constant of the oscillator buildup.

Figure 7 shows a typical input pulse and corresponding output pulse at 600 ns. As the gain of the amplifiers is increased, the output pulse power reaches a saturated level. Further increases in output energy do not increase the peak power, but extend the pulse duration. Note that in this case, a 240-ns injection pulse is amplified to generate an output pulse with a width of 540 ns, and that the output pulse occurs well before the peak of the input pulse.

Applications

Advanced Imaging

An important application for our laser system will be its use as an illuminator for advanced imaging of space objects. LLNL is building the first 100-J, infrared (or 65-J, green), 500-ns pulse duration laser system for the U.S. Air Force. At the Starfire Optical Range, the Phillips Laboratory's Imaging Directorate will use the device as a space object illuminator. In addition to specifications of long pulse duration and high pulse energy, the laser is required to have transform-limited coherence length. We have shown that temporal phase errors during the 500-ns pulse can be held to less than 10 milliwaves, peak to valley. In addition, the use of four separate amplifiers allows the laser to be configured with either a single phase conjugator (phase locking all beams as described here) or with up to four separate phase conjugators. By slightly shifting the pressure in the conjugator cells—hence tuning the Stokes frequency shift of the conjugated return—the frequency output of the individual amplifier channels can be offset by known and controlled amounts. Such tuning allows for imaging work involving heterodyne detection. The four-amplifier laser system will be installed at the Starfire Optical Range in early 1998.

Near-field image
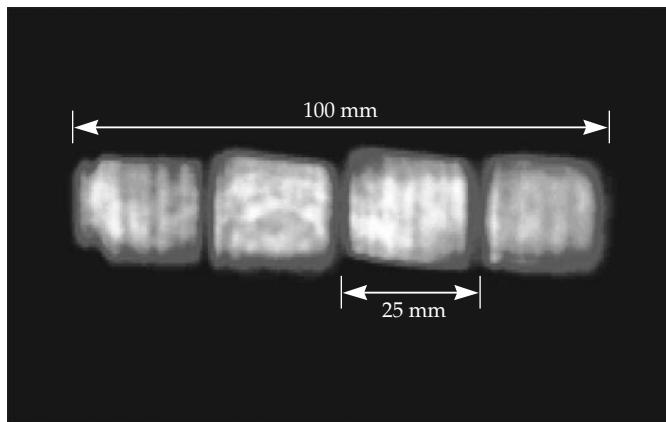
Horizontal cross section
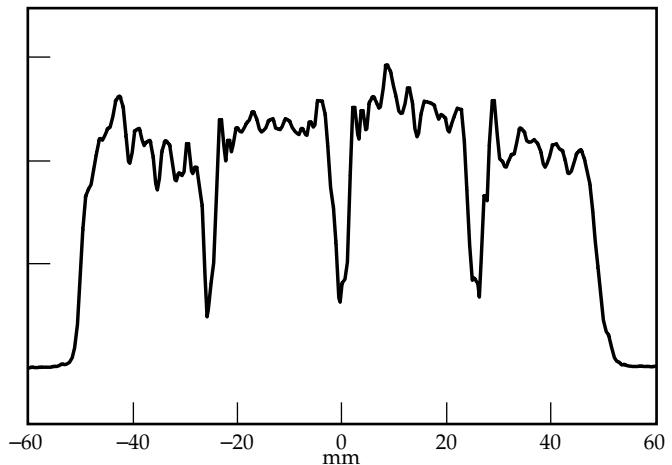
Far-field images
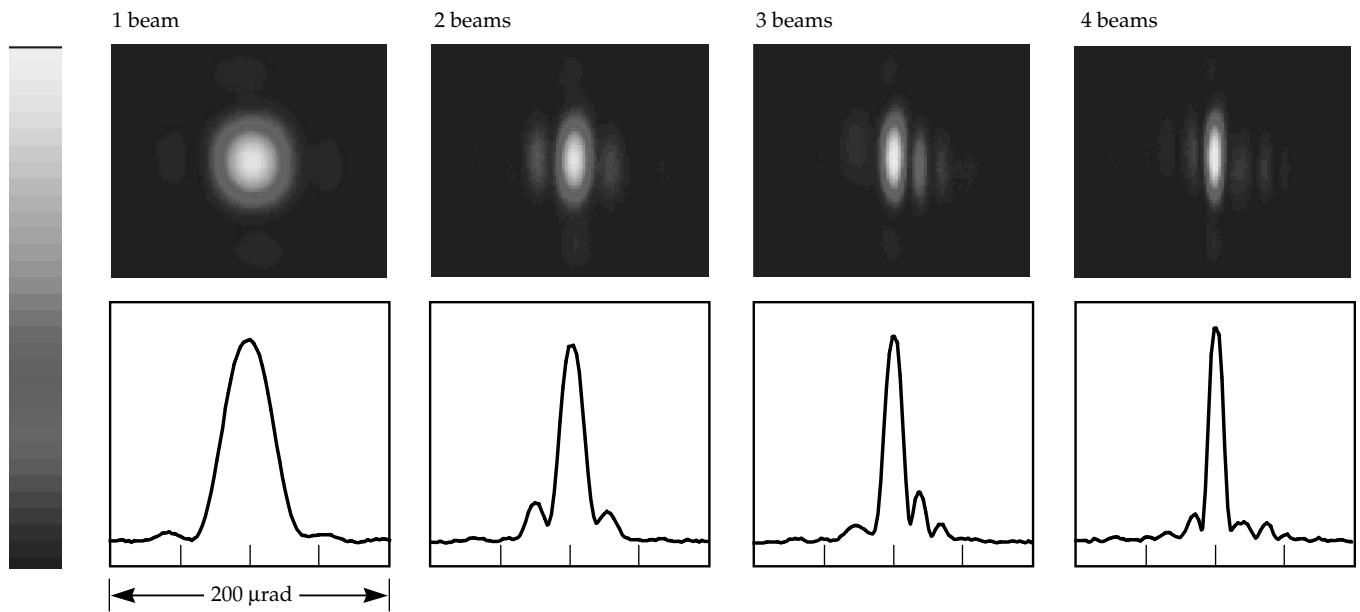
FIGURE 6. Experimental data showing the near-field beam profiles and resulting far-field laser output. The data illustrate how the far-field spot size narrows as multiple beams are phase locked using SBS phase conjugation, demonstrating excellent wavefront correction with no beam-to-beam piston phase offset errors.   (70-00-0298-0156pb01)

Laser Shock Processing

Used in a 30-ns pulse width configuration, the high-energy Nd:glass laser technology described in this report is proving to be an ideal source for inducing intense and deep residual compressive stresses in metal surfaces. For some time, it has been known that controlled inducement of residual stress in a metal surface, called peening, increases the life expectancy of metal by preventing cracks arising from fatigue and corrosion. The deeper the residual stress, the better. Shocks induced with our laser have been shown to impart residual compressive stresses that are deeper and more intense than those in conventional shot peening.

In this application, our laser creates a plasma shock of 10 to 30 kbar at a metal surface. A thin layer of black paint on the metal surface provides an absorber to initiate the plasma formation and to prevent ablation of the metal. A confining or tamping material, such as a 1-mm film of water, covers the surface layer and provides an inertial barrier, which increases the intensity of the shock directed into the metal.

Figure 8 shows an x-ray diffraction measurement of the more intense and much deeper stress obtained in a titanium alloy when treated by laser shock processing in our laboratory. Deeper residual stress is important in high-stress mechanical components, such as the turbine blades of jet engines. Foreign object debris (FOD)

Single beam output profiles
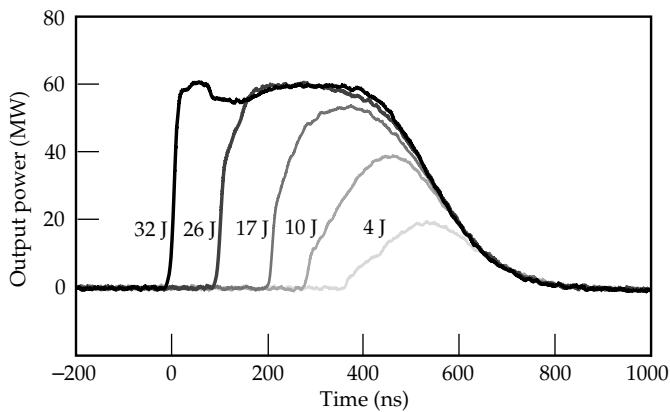
FIGURE 7. The 540-ns output pulse of the laser is generated by amplifying the exponentially rising portion of a much shorter relaxation-oscillation input pulse. The bulk of the output energy occurs well before the peak of the input. As the rise of the leading edge of the oscillator pulse falls away from exponential growth, the output pulse power falls to zero. Increases in pulse energy do not increase the output power beyond its saturation level, but result in an increased pulse duration. (70-00-0298-0157pb01)

FIGURE 8. Using the high energy per pulse available from the Nd:glass laser, a more intense residual stress can be impressed into metal surfaces at a greater depth, compared to that available from conventional shot peening. (70-00-0298-0158pb01)

picked up in operation can often generate damage sites that penetrate a thinner compressive layer and, hence, become an initiation point for fatigue cracks. In testing the laser shock-processing treatment, engine blades that have deeper residual stress have been shown to exhibit significantly superior performance. However, until our recent development of high-pulse-energy, high-average-power, solid-state lasers, no system has produced both sufficient energy and repetition rate to achieve production throughput at an affordable cost. This new high-energy, high-average-power technology is expected to take laser shock processing from laboratory demonstrations into commercial production.

Summary

We have developed a class of laser system at the 100-J level with average power capability approaching 1 kW. The new technology includes uniformly pumped, zigzag slab gain media, passively switched MOPA architectures, and phase conjugation to minimize the problems associated with thermal loading. The demonstrated technique of phase locking of multiple apertures allows us to pursue new applications, such as coherent imaging and laser shock processing of materials, both of which require high pulse energies with high-average-power output.

DIODE-PUMPED REGENERATIVE AMPLIFIER FOR THE NIF LASER SYSTEM

J. K. Crane

M. Martinez

R. J. Beach

S. Mitchell

F. Penko

D. Browning

R. Wilcox

Introduction

The National Ignition Facility (NIF) laser pulse is born in the Master Oscillator Room (MOR) at very low energy (up to 1-nJ output). The energy increases as the laser pulse passes through the regenerative amplifier (up to 10-mJ output) and the 4-pass amplifier (up to 22-J output). Finally, in the full-aperture optics, up to 10 kJ of 351-nm light is reached on target.

To achieve ignition, the laser energy on target must be in the form of specifically tailored, high-fidelity temporal shape with a precise frequency spectrum. The optical pulse generation (OPG) system, or front end of the NIF laser system, consists of the MOR and the preamplifier modules (PAMs). The MOR produces the initial laser pulse in a Q-switched, single-mode, fiber, ring-laser oscillator. This laser pulse, which is reproduced 960 times per second, is shaped, modulated, amplified, and multiplexed to feed pulses to the 48 individual PAMs using fiber and integrated optical components.

The first laser system in a NIF beamline is the PAM. The input to the PAM is a 1-nJ shaped pulse that is delivered via single-mode, polarization-preserving fiber. The output is a 22-J pulse that is spatially shaped to meet the requirements of the main laser amplifiers. Figure 1 is a block diagram of a PAM showing its five component subsystems, namely, fiber injection, diode-pumped

regenerative amplifier, spatial beam shaping, smoothing by spectral dispersion (SSD), and the 4-pass amplifier. The five subsystems are housed in a modular, I-beam-supported structure that is about $4.3 \times 1.0 \times 0.7$ m in size and contains all of the power, control, and diagnostic systems to make each PAM a complete system.

The PAMs produce the largest optical gain of the entire NIF laser system, boosting 1-nJ pulses from the MOR to 22 J. The performance specifications for the PAM and its component laser systems were determined as a flowdown from the output performance specifications of the overall NIF laser system, which are based on target requirements for ignition.[1,2] These specifications, listed in Table 1, include performance descriptions for both the regenerative and 4-pass amplifiers that are derived from the overall requirements of a PAM. We are allowed some flexibility to adjust the internal PAM parameters to produce the optimum design.

This article describes the current baseline diode-pumped regenerative amplifier and the results of a comprehensive series of measurements of its performance. In conjunction with these measurements, we have developed models allowing us to evaluate improvements to the baseline that will provide an additional margin to increase the performance of the entire preamplifier system.
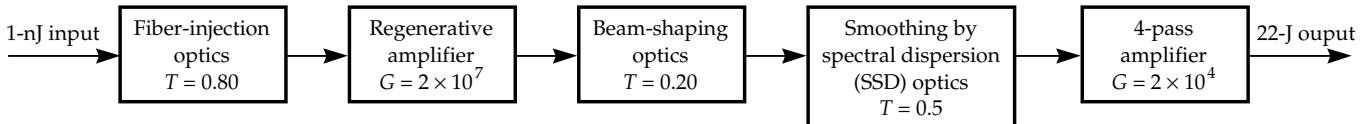
FIGURE 1. Block diagram showing the major subsystems within the NIF preamplifier modules (PAMs). *G* is gain; *T* is transmission loss. (70-00-0298-0159pb01)

TABLE 1. PAM output specifications based on flowdown from the NIF laser system and target requirements.

	Parameter	Value
1.	Minimum PAM shaped energy	14.5 J
2.	Design energy*	22 J
3.	Peak power*	8.8 GW
4.	4-pass amplifier injection energy	1.0 mJ
5.	Regenerative amplifier output energy	10 mJ
6.	Pulse duration	21 ns
7.	Square-pulse distortion (regen)	1.2
8.	Square-pulse distortion (4-pass amplifier)	2.3
9.	Temporal contrast at PAM input	275:1
10.	Temporal contrast at PAM output	100:1
11.	Spatial profile	2:1
12.	Prepulse contrast	10^5–10^6
13.	Near-field spatial contrast	< 5%
14.	RMS energy fluctuation	<0.03

*Energy and power in a flat-top beam with a 90% fill factor

Description of the Regenerative Amplifier

In large, complex, solid-state laser systems, a regenerative amplifier (or regen) is often used to boost the output energy of the laser oscillator to a level that is suitable for injection into the larger power amplifiers. In this way, a regen is analgous to a high-fidelity preamplifier used in conventional radio frequency (rf) systems, such as stereos. A laser regen is an optical cavity with gain into which a low-energy laser pulse is injected, amplified by several orders of magnitude, then switched out of the cavity. For example, if the net gain per round trip in the cavity G_{net} is 3.0, and the pulse is allowed to circulate for $k = 15$ round trips, then the total unsaturated gain of the regen is

$$G_{total} = (G_{net})^k = (3.0)^{15} = 1.4 \times 10^7 . \qquad (1)$$

The total gain is ultimately limited by the amount of stored energy that can be extracted from the amplifier. If a substantial amount of the stored energy in the amplifier is removed, then G_{net} drops below 1.0 (G_{net} is the product of the gain in the amplifier G and the transmission losses in a single round trip T, such that $G_{net} = GT$), and G_{total}

decreases as a function of round trip because the amplifier gain is saturated.

The MOR generates pulses up to 21 ns long with a particular temporal shape determined by the target requirements. This specially shaped pulse must be amplified with a high degree of fidelity to ensure that the desired shape is preserved to the end of the laser chain. Based on its method of operation, the regen cavity must be long enough to contain an entire 21-ns pulse without a temporal overlap between the beginning and end of the pulse. Two types of regen cavities are found in the Laser Programs: space ring cavities[3,4] and linear cavities.[5] Each type has certain advantages over the other.

In a ring cavity, the pulse circulates in one direction in a closed path. The perimeter of the ring must be longer than the pulse length; that is, perimeter $>c(T_{pulse} + T_{switch})$, where c is the speed of light. Some additional length, cT_{switch}, provides time for a Pockels cell to switch the polarization of the light pulse and trap it in the cavity. This additional switching time is 3–5 ns, depending on the rise time of the Pockels cell. The linear cavity can be approximately half as long as the perimeter of the ring cavity because the pulse can partially overlap itself in the cavity as long as the front and tail ends of the pulse do not overlap in the Pockels cell during switching.

Figure 2 shows the current prototype regen. The cavity is a folded linear design with a diode-pumped rod amplifier at either end. A pulse propagating in the cavity double-passes through each rod amplifier. A rod amplifier has a single-pass gain of 1.5; thus the gain per round trip is $(1.5)^4T$, where T is the round trip transmission of the cavity. A 2.0-m focal length lens in the center gives the cavity a stability value of $g^2 = 0.02$, and an adjustable iris is used to limit the spatial modes to one. In the current design, the cavity has a round trip time of 30 ns, allowing us to cleanly switch a pulse as long as 24 ns into and out of the cavity.[6]

FIGURE 2. Baseline regenerative amplifier with optics for seeding the cavity from a single-mode fiber. (70-00-0298-0160pb01)

The seed pulse from the MOR is introduced into the cavity by reflection from a thin-film polarizer. A two-lens telescope, which is part of the optics for seeding the regen, is designed to match the output mode from the fiber to the eigenmode of the cavity. In the first cavity round trip [Figure 3(a)], both Pockels cells are off, and the s-polarized pulse is converted to p polarization upon double passing a quarter-wave plate. After the tail of the pulse passes [Figure 3(b)], the Q-switch Pockels cell fires, trapping the p-polarized pulse in the cavity. The quarter-wave plate and Pockels cell produce equal retardation, so the pulse is trapped in the cavity for the desired number of round trips, whereupon the cavity-dump Pockels cell fires, and the amplified pulse is ejected [Figure 3(c)].
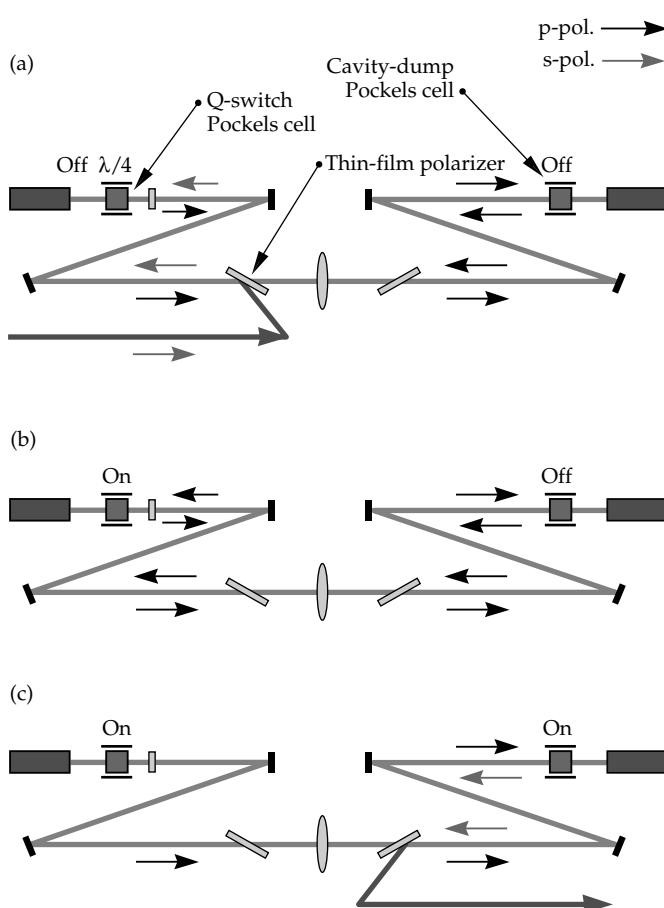
FIGURE 3. Polarization states in the regenerative amplifier. (a) When injecting the seed, both polarizers are off. (b) When Q-switching or trapping the pulse in the cavity, the Q-switch Pockels cell is on. (c) During switchout of the amplified pulse, the cavity-dump Pockels cell is turned on. Gray arrows represent s-polarization; black arrows represent p-polarization. (70-00-0298-0161pb01)

Diode-Pumped Rod Amplifiers

The diode-pumped rod amplifiers used in the regen are similar in design to several others developed by LLNL's Solid-State Laser Group and are described in detail in several publications.[6,7] Figure 4 shows a picture of the head with labels for each of the key components. In the currently operating regen, the pump light in each head is produced by a diode array, consisting of forty-eight 100-W diode bars stacked in an array with 1-mm spacing between bars. Spectra Diode Labs (SDL) makes the diode bars. The laser light from each bar is conditioned by a cylindrical microlens to produce a far-field cone with angular dimensions of 80 × 240 mrad. The diode light is collected by a tapered lens duct that funnels the pump light into the end of the amplifier rod. The rod is 5 mm in diameter by 50 mm long and made of Nd-doped phosphate glass (LG760 or APG1). The end of the rod adjacent to the lens duct is coated to efficiently pass the pump light but reflect the 1053-nm wavelength light. This surface is the back mirror of the regen cavity. The Nd doping of the rod is specified to provide a single-pass absorptivity of 1.5 at the absorption peak near 800 nm. The diode array, lens duct, and rod are packaged as shown in the Figure 4. The rod is mounted with a surrounding plenum that allows for dry nitrogen cooling to reduce temperature gradients. Nitrogen exhausted from the rod plenum flows over a fin-shaped structure that thermally contacts the diode array and provides some cooling to the diodes themselves.
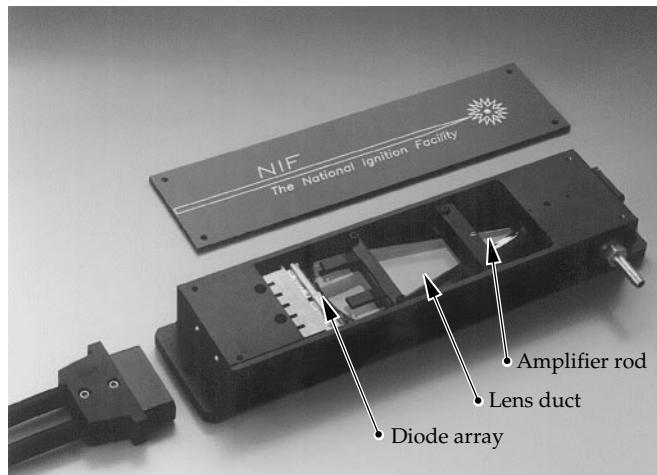
FIGURE 4. A 48-bar diode array with microlenses end pumps a 5- × 50-mm rod. The lens duct focuses light from the array into the rod. (70-00-0298-0162pb01)

Performance Measurements

Diode Pumping

The diode arrays were initially characterized before being assembled into the diode-pumped rod amplifier packages. Light energy out of the diodes, after the microlensing and at the output of the lens duct, was measured as a function of diode-driver current using an integrating sphere. Figure 5 shows the results of
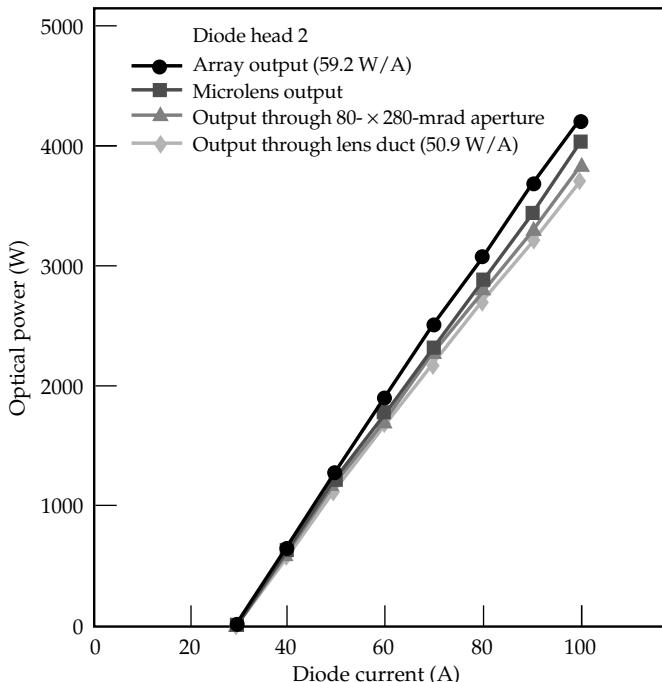
FIGURE 5. Measured optical power from one of the two diode arrays in the regen amplifier heads. (70-00-0298-0163pb01)

FIGURE 6. Normalized emission spectrum from diode head number 1 (DH1) (gray curve) and LG760 absorptivity (black curve). (70-00-0298-0164pb01)

measurements for one of the two diode heads used in the current regen. The data show that the array has a slope of 59.2 W/A; at 100 A of current, the optical pump power at the input to the laser rod is 3.6 kW. The efficiency for collecting and transporting diode-pump light to the end of the rod is 86%. For a 350-μs-long square pulse, the optical pump energy at the rods is 1.12 and 1.26 J for head one and two, respectively.

As part of the initial characterization of the diode arrays, we measured their output spectrum using a quarter-meter spectrometer with a camera at the output. Figure 6 shows the output emission spectrum

from the diodes along with the absorption spectrum of the laser glass, LG760. Each diode package for a rod amplifier consists of two arrays that are mounted side-by-side on a single heat sink. The single Gaussian-shaped emission indicates that the separate arrays closely overlap in wavelength.

From the data on diode emission and glass absorption, we can determine the absorption efficiency of diode pumping. We define a diode-emission spectral power density $\rho_{\text{diode}}(\lambda)$ such that the output power of the diode array is

$$P_{\text{diode}} = \int_{-\infty}^{\infty} \rho_{\text{diode}}(\lambda)d\lambda \quad . \tag{2}$$

The transmission of the Nd-doped glass is given by

$$T(\lambda) = \exp[-\alpha(\lambda)2d] \, , \tag{3}$$

where $\alpha(\lambda)$ is the absorptivity per unit length of laser medium, and d is the rod length. Figure 7 shows the normalized diode-emission power density $\rho_{\text{diode}}(\lambda)$ and glass transmission $T(\lambda)$ as well as the fraction of the diode emission that is absorbed and transmitted after two passes through the rod. The ratio of power absorbed to diode power emitted gives the absorption efficiency η_{abs} as follows

$$\eta_{abs} = 1 - \frac{\int_{-\infty}^{\infty} \rho_{diode}(\lambda) \exp[-\alpha(\lambda)2d]d\lambda}{\int_{-\infty}^{\infty} \rho_{diode}(\lambda)d\lambda} \quad . \qquad (4)$$

For the data shown in Figure 7, the absorption efficiency is 90%. This value could be increased by shifting the wavelength of the diodes to better overlap the peak of the absorption curve, or by increasing Nd^{3+} doping to provide increased absorption.

$$G^2(\lambda,t) = S_{sig}(\lambda,t)/S_{ref} \quad . \qquad (5)$$

The square-root of the detector signal ratio yields the single-pass gain. The wavelength λ and time-dependence are important to note. We used a narrow-band, Nd-doped yttrium lithium fluoride (Nd:YLF) probe laser whose wavelength is centered on the regen gain spectrum; alternatively, we can use the MOR pulse to probe the regen gain. We measured the gain at the end of the 350-μs pump pulse where it is at a maximum value and, consequently, when we Q-switch the regen.

FIGURE 7. Normalized emission at rod input, output emission after double passing through rod, amount absorbed, and transmission function of LG760 glass. (70-00-0298-0165pb01)
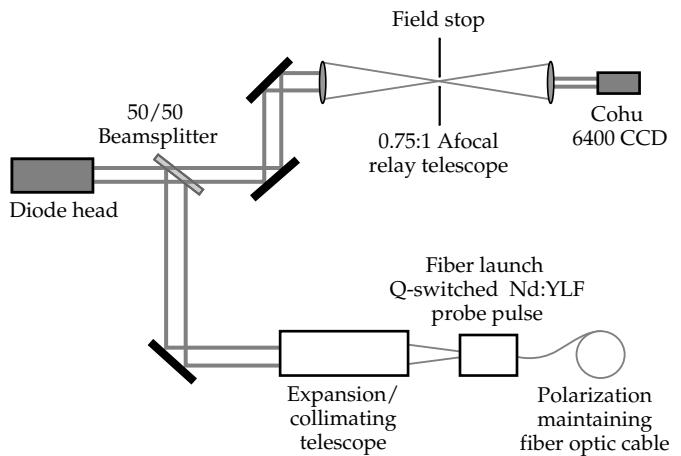
FIGURE 8. Optical layout for measuring spatial gain profiles. (70-00-0298-0166pb01)

An important step toward understanding the energetics of the regen is to characterize the gain in the diode-pumped rod amplifiers. We measured double-pass gain through the rod amplifier using a small probe laser, as shown in Figure 8. (Recall that the rod amplifier is end pumped, so there is only access at one end of the rod for measurements.) We can vary the arrangement shown Figure 8 to probe either a small volume in the center of the rod or to measure gain over the entire rod diameter. For probing a small volume in the center of the rod, we use photodiodes as reference and signal detectors. The double-pass gain is the ratio of the detector signals:

Figure 9(a) shows the measured, single-pass gain G_1 as a function of diode-driver current using the YLF laser as a probe. In Figure 9(b), we converted the gain data to stored energy using the relation $E_{stored} = AJ_{sat}\ln(G)$ and plotted stored energy vs diode current, as shown. The solid line plotted with the data represents a simple model for stored energy vs diode pump power

$$P_{pump} = \frac{E_{stored}}{\eta_{ext}\eta_{del}\eta_{abs} \; QD \left(1 - e^{\tau_P/\tau_0}\right)} \; \frac{1}{\tau_0} \quad , \qquad (6)$$

where η_{ext}, η_{del}, and η_{abs} are the efficiencies for producing diode emission, delivering the emission to the rod, and absorbing the energy into the upper laser level of the glass, respectively; QD is the quantum defect of the upper laser transition; τ_p is the pump period; and τ_0 is the spontaneous emission lifetime of the upper laser level. Values for the constants in Eq. (6) are:

$\eta_{del} = 0.75$
$\eta_{ext} = 0.83$
$\eta_{abs} = 0.90$
$QD = 0.76$
$\tau_0 = 320$ μs and
$\tau_p = 350$ μs.

The data depart from the model at about 80-A diode current, or $G = 1.48$ to 1.50. Several different explanations could account for the rolloff in gain. For example, the diode-emission frequency could be changing frequencies (chirping) away from the absorption line center of the glass at the end of the current pulse. If the amount of

chirp increases with increasing diode current, then the absorption efficiency η_{abs} would decrease, causing the stored energy described by Eq. (6) to roll over, as shown in Figure 9(b). Another contributor could be amplified spontaneous emission that is quenching the stored energy in the upper laser level, causing the gain to roll over with increasing current as shown. The amplifier rods have highly polished barrels to permit total internal reflection (TIR) of pump light and help homogenize the spatial gain distribution. Unfortunately, the polished sides can also support long-pathlength propagation at the laser wavelength, such as whisper modes, that effectively clamp the gain and reduce pump efficiency.

Regen Gain and Loss Measurements

As part of our comprehensive characterization of the laser system, we made a series of careful measurements of gain, loss, output energy, and power from our baseline regen. In conjunction with these measurements, we developed a model that accurately reproduces the measured results and that can now be used to help optimize the current design.

Figure 10 shows the layout of the regen with its seeding optics and several diagnostics used in the measurements. We recorded the temporal pulse shapes at the input and output to the regen, and by looking at the pulse buildup in the cavity immediately before the output thin-film polarizer. We measured the output energy from the regen with Molectron calorimeters (the choice of calorimeter depends on the energy range being measured). The measured energy value at the calorimeter is divided by the value of the measured optical transmission between the output of the regen and the location of the calorimeter to give a value that is equivalent to the regen output energy. For a single regen shot, we recorded the three photodetector signals and the calorimeter reading. We converted the temporal signals $S(t)$ from the output and cavity buildup detectors to power $P(t)$ vs time by dividing the integrated detector signal by the measured energy E, according to

$$P(t) = \frac{ES(t)}{\int S(t)dt} \quad . \tag{7}$$

The input calorimeter was calibrated separately by placing a J3S calorimeter head directly after the input thin-film polarizer. We then compared the integrated temporal signal from the input photodetector to the calorimeter value to obtain a calibration factor to convert the temporal signal to power. In this way, we can record on any shot the power at the regen input and output, and the power buildup inside the cavity for each pass.

(a)

(b)
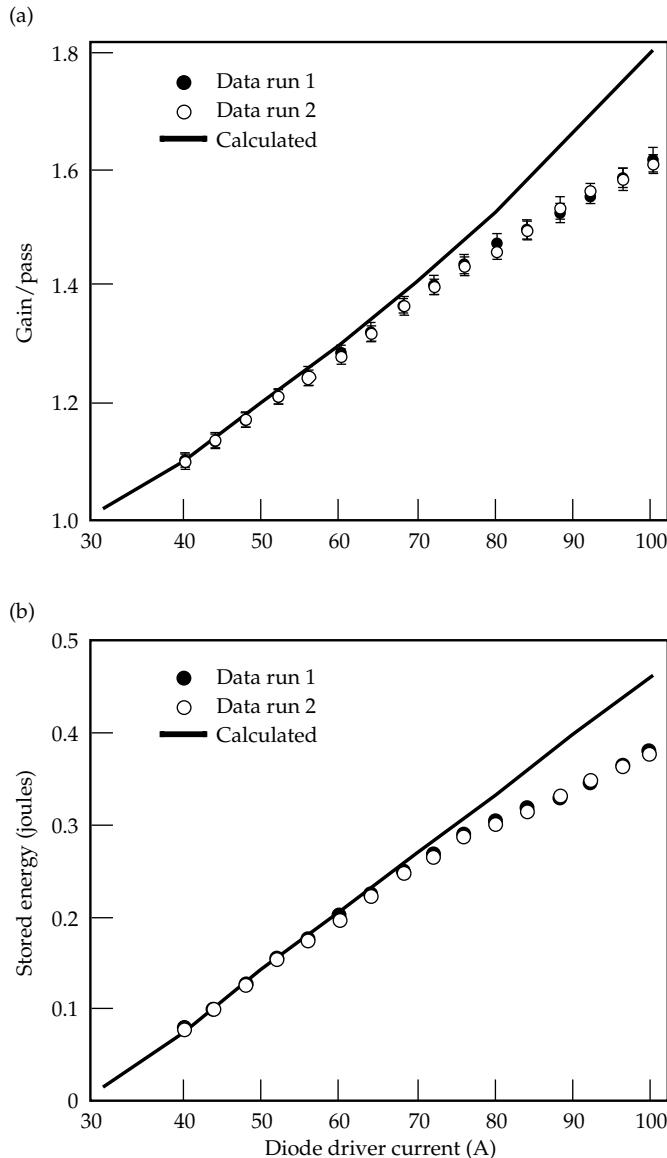
FIGURE 9. (a) Gain per pass and (b) stored energy for diode-pumped rod amplifiers with LG760 glass. The solid line is the model prediction. (70-00-0298-0167pb01)
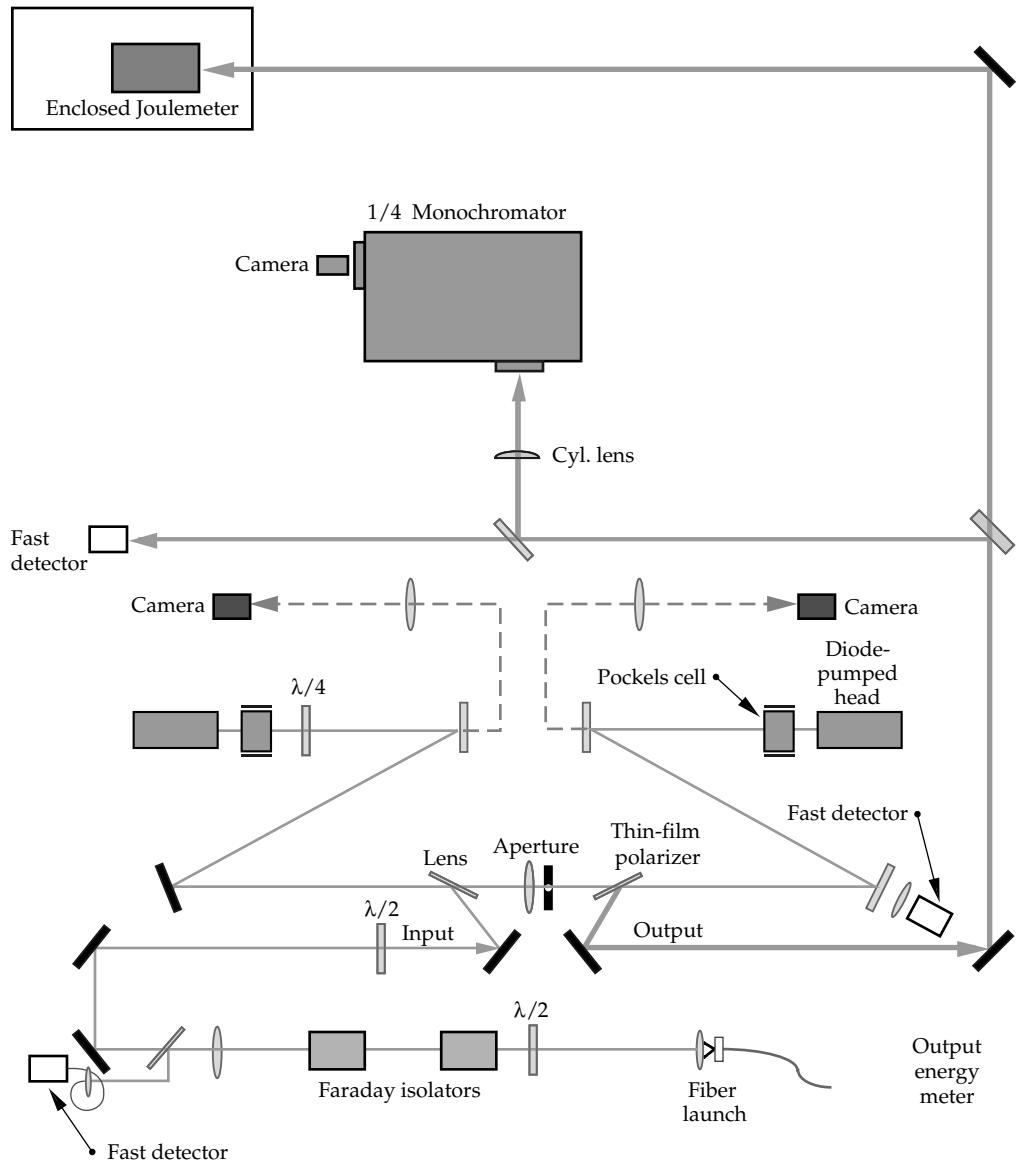
In addition to the power and energy from the regen, we measured the spectral overlap between the seed from the MOR and the gain spectrum of the regen. We also measured and recorded the spatial extent of the laser mode on each rod by imaging the mode at the rod input onto a calibrated charged-coupled device (CCD) camera that is part of a Big Sky beam-profiling system. The spatial information allows us to convert the measured power and energy for each round trip into irradiance $I(r,t)$ in the gain medium according to

$$I(r,\theta,t) = \frac{P(t)R(r)\Theta(\theta)}{\int R(r)\Theta(\theta)rdrd\theta} \rightarrow \frac{P(t)R(r)}{2\pi\int R(r)rdr} \quad , \qquad (8)$$

where $R(r)$ is the radial dependence, and the azimuthal dependence $\Theta(\theta)$ is assumed to be constant for a TEM_{00} mode.

To complete our suite of energetics measurements for the regen, we measured the cold transmission of the laser pulse for one round trip in the cavity. We made this measurement using three different techniques that yield similar answers. The easiest way to measure cavity transmission is to measure the relative intensity of a continuous wave (cw) beam that is sent into the cavity through the same seed optics so that it is mode-matched to the cavity. We used this technique as a diagnostic to look for problems, such as bad coatings, clipping in the cavity, or stress-induced birefringence.

The second technique for measuring cavity transmission is to switch in a seed pulse with the rod amplifiers turned off, switch it out after successive numbers of round trips, and measure the "ringdown" or attenuation of the pulse per round trip. The ringdown technique, which is dynamic and includes switching losses from the Pockels cells, indicates seeding of multiple roundtrips, which is undesirable. Figure 11 shows the data for a ringdown measurement as well as the value for the static transmission measured with a cw beam.

The third technique is to measure the output of the regen after the first few round trips with the amplifiers

FIGURE 12. Small signal gain in the regen for different values of pump-diode current. (70-00-0298-0170pb01)

FIGURE 11. Cold-cavity ringdown measurement of regenerative amplifier round-trip transmission. (70-00-0298-0169pb01)

on. We repeated the measurement for different values of pump-diode current, and measured a net gain per round trip, as shown in Figure 12. Using the values of gain per pass measured for the rod amplifiers (see Figure 9), we obtained a value of round-trip transmission that includes any additional losses from the energized rod amplifiers, where $T = G_{net}/(G_1{}^2 G_2{}^2)$. These three different techniques for measuring the round-trip cavity transmission in the current design yield values that range between $T = 0.59$–0.65. We are working on alternative cavity designs that will increase the value of cavity transmission by eliminating one Pockels cell and thin-film polarizer (TFP) and using the remaining TFP in reflection rather than transmission.

Saturated Gain Measurements

Description of the 2-D Model

We developed a time-dependent model to describe the gain $G(t)$ and circulating irradiance $I(t)$ in the regen. The current version is based on the time-dependent equation for gain[8]

$$G(r,t) = \frac{1}{1 - \left[1 - \dfrac{1}{G(r,0)}\right]\exp\left[\dfrac{-U(r,t)}{J_{sat}}\right]} \quad , \qquad (9)$$

where J_{sat} is the saturation fluence of the laser transition, $G(r,0)$ is the initial gain as a function of radius in the rod, and

$$U(r,t) = \int_0^t I(r,t')dt' \quad . \qquad (10)$$

The radial dependence of the cavity eigenmode is included to more accurately describe spatial saturation in the amplifier rod. If the mode is treated as an equivalent flat top with equal energy and peak irradiance, then the model predicts a much faster falloff of energy after full saturation. In the two-dimensional (2-D) model, we use the measured Gaussian cavity mode, providing a radial dependence to the gain saturation. However, because the regen is a seeded oscillator with a single-cavity spatial eigenmode, we renormalize the spatial dependence of the irradiance to this mode after each round trip.

The current regen has end-pumped, diode-pumped rod amplifiers at either end of the cavity; consequently, the laser pulse folds back on itself temporally in the gain medium. As a result of the pulse overlap, the trailing portion of the pulse is more strongly saturated than in the case of no overlap, as in a ring cavity, and square-pulse distortion (SPD) will be more severe.

The modeling and data analysis were both performed using a software package called IGOR developed by WaveMetrics, Inc., Lake Oswego, Oregon. The model inputs describing the regen energetics include the input pulse (power vs time), gain in each amplifier, mode size in each rod, round-trip cavity transmission, saturation fluence of the laser transition (we used the value of 3.99 J/cm^2 for LG760 from Ref. 9), and the number of round trips. The model calculates the time-dependent gain $G(r,t)$ and irradiance $I(r,t)$ on each pass using Eq. (9). From these two quantities, the model determines the power, energy, and square-pulse distortion at the regen output, the power and energy buildup in the cavity, and the spatial and temporal gain saturation in the amplifiers. We can then compare these model results with the data.

Comparisons of Model and Data

Figure 13 shows a measurement of output energy from the regen as a function of round trips for a fixed value of diode pump power. The measurement was made over the full dynamic range of the regen, that is, eight decades. Four different calorimeters were used to cover the full range. When we were close to the upper limit of one calorimeter, we repeated the measurement with a less sensitive calorimeter and used reference photodiodes as cross checks. The solid line in Figure 13 shows the model prediction for the input parameters given in the caption. The radial dependence of the mode in the rod must be included for the model to replicate the slow rolloff in the energy after the gain peak. The peak energy extracted is 22 mJ, corresponding to 63% of the stored energy in the mode volume of both amplifiers and consistent with the cavity transmission that falls between 59 and 65%.

Figure 14 shows model predictions of output power vs time for a pulse switched out of the cavity after 12 round trips. In Figure 14(a), we calculate an input
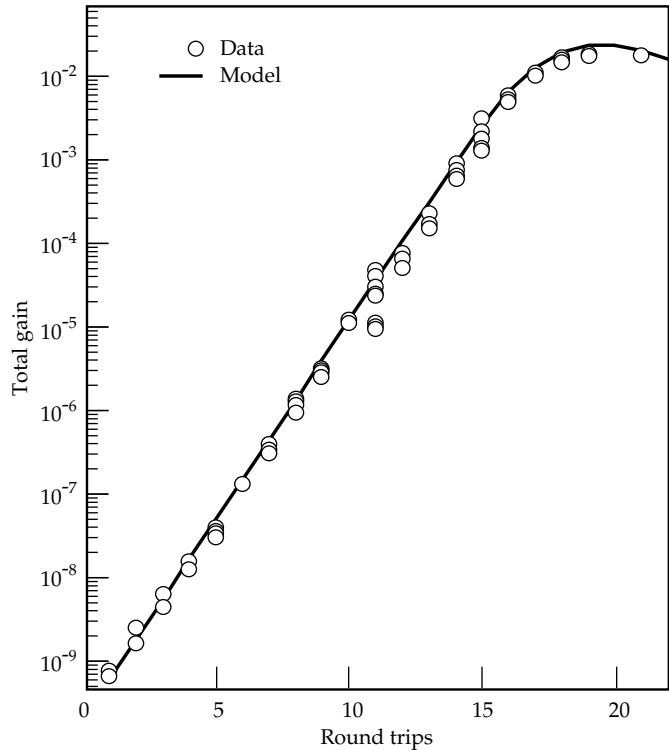
FIGURE 13. Comparison between 2-D Frantz–Nodvik model and data for regen output energy. Model parameters are $G_1 = G_2 = 1.50$; round-trip cavity transmission $T = 0.60$; beam waist $w_0 = 0.80$ cm, and input energy $E_{in} = 177$ pJ.   (70-00-0298-0171pb01)

square pulse that is equal in energy and peak power to the measured input pulse, and propagate that pulse using our model. This procedure facilitates the calculation of square-pulse distortion (SPD). With only 79 µJ extracted from the available 35 mJ, the gain saturation is negligible, and SPD = 1.003. Figure 14(b) compares the measured output pulse and the model output using the measured input pulse as the model input. The amplitude modulation on the real pulse appears at both regen input and output and arises from mode beating in the fiber master oscillator.

Figure 15 shows a 12.0-mJ output pulse switched out of the regen after 17 round trips. We repeated the comparison between the measured output pulse and a modeled square pulse, and the measured input pulse propagated through the model. We still find good agreement between the model pulses and the actual measured pulses, although they do not overlay exactly as in the lower-energy pulse in Figure 14. The output detector has a lower bandwidth than that of the input detector, so there may be some distortion of the sharper features. Comparing the square pulse output to the actual output pulse, we see that the break points at the peak of the pulse and in the dropoff portion of the pulse agree in amplitude, so the value of SPD = 1.54 is accurate.

(a)

(a)

(b)
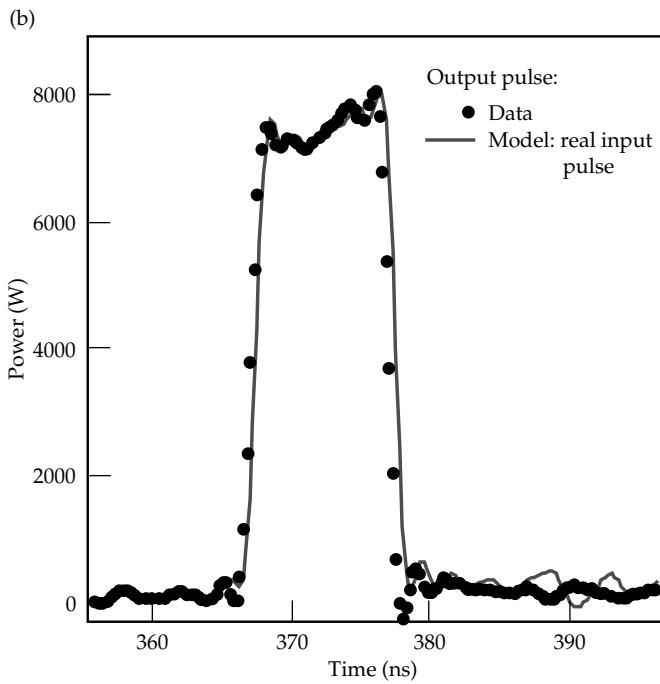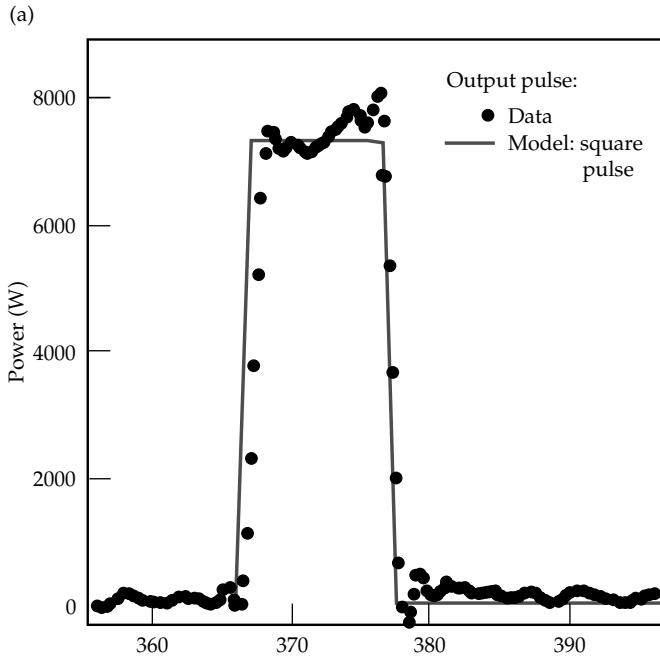
FIGURE 14. Model vs measured regen output pulse, where E_{in} = 147 pJ, E_{out} = 79 μJ, 12 round trips, G_1 = 1.495, G_2 = 1.50, cavity transmission T = 0.60, and SPD = 1.003. (70-00-0298-0172pb01)

(b)

FIGURE 15. Comparison between model and data for a 12.0-mJ pulse. (a) Equivalent square pulse plus measured pulse. (b) Real pulse input to model compared with measured output pulse: SPD = 1.54. (70-00-0298-0173pb01)

Comparisons between the energy and power data from the regen and the model shown in Figs. 13 through 15 demonstrate very good agreement. Our goal was to develop a model that accurately predicts the output power, energy, and gain saturation of the

NIF regenerative amplifier for a given set of inputs, and to use this model to examine ways to improve the performance of the regen. Features such as radial gain saturation and temporal pulse overlap in the amplifiers were added to the original, time-dependent saturation model

to accurately reproduce the slow rolloff in energy output after the peak, and to replicate the large amount of temporal pulse distortion observed in the data.

Signal-to-Noise Measurements

The ability to control the temporal pulse shape, hence pulse power of the laser system, resides in the OPG up to the output of the regen slicer. The remainder of the laser system consists of large amplifiers that can distort the pulse and add noise, but they cannot be used to affect controlled changes to the pulse shape. The noise added by the regen and MOR tend to set the upper acceptable limit for the entire laser system; thus, it is important that we measure and understand these sources of noise. The original specifications for the regen include a signal-to-noise ratio (S/N) of 10^4 for a 500-pJ input and a prepulse contrast between 10^5 and 10^6 (Refs. 3 and 4).

To determine the S/N at the output, we measured the noise power at the output photodiode with the input seed blocked and unblocked. This technique requires a detector that can accurately measure two signals that differ in amplitude by 4 to 5 orders of magnitude. We used a Hamamatsu vacuum photodiode and calibrated neutral-density filters to provide a known amount of attenuation. Figure 16 shows the output power of the regen with the input seed blocked and unblocked. An 18.6-mJ pulse is switched out after 18 round trips, and the peak power of the 10-ns pulse is 2.7 MW. When the seed is blocked, the output power

drops to 160 W. The trapezoidal shape of this pulse reveals the switching window of the regen and is the shape of the noise pedestal atop which the amplified seed pulse rides. This measurement technique underrates the S/N value because the seeded regen is saturated, whereas the unseeded measurement is still in the small-signal regime. With fewer round trips, we cannot detect the regen output when the seed is blocked.

To determine the noise-equivalent power (NEP) at the input of the regen, we used our 2-D model. First, we constructed a square pulse of equivalent energy and peak power as the measured input pulse. We used this pulse as an input to the model and propagated it for the actual number of round trips, 18, that corresponds to the data. We adjusted the values of single-pass gain until we accurately reproduced the measured output pulse. A comparison between the measured and modeled output pulse is shown in Figure 16(b). Next, we constructed a trapezoidal-shaped input pulse to represent the noise pulse. We used the same values of gain per rod and transmission as required to reproduce the seeded output pulse, and adjusted the input energy of the noise pulse until we reproduced the measured output pulse shown in Figure 16(b). Figure 16(a) compares the model input pulses that were required to duplicate the measured output pulses using the model. From Figure 16(a), we obtained the energy and power S/N referenced to the input of the regen. Here, S/N (energy) = 1.29×10^4, S/N (power) = 1.75×10^4, and the NEP at the input of
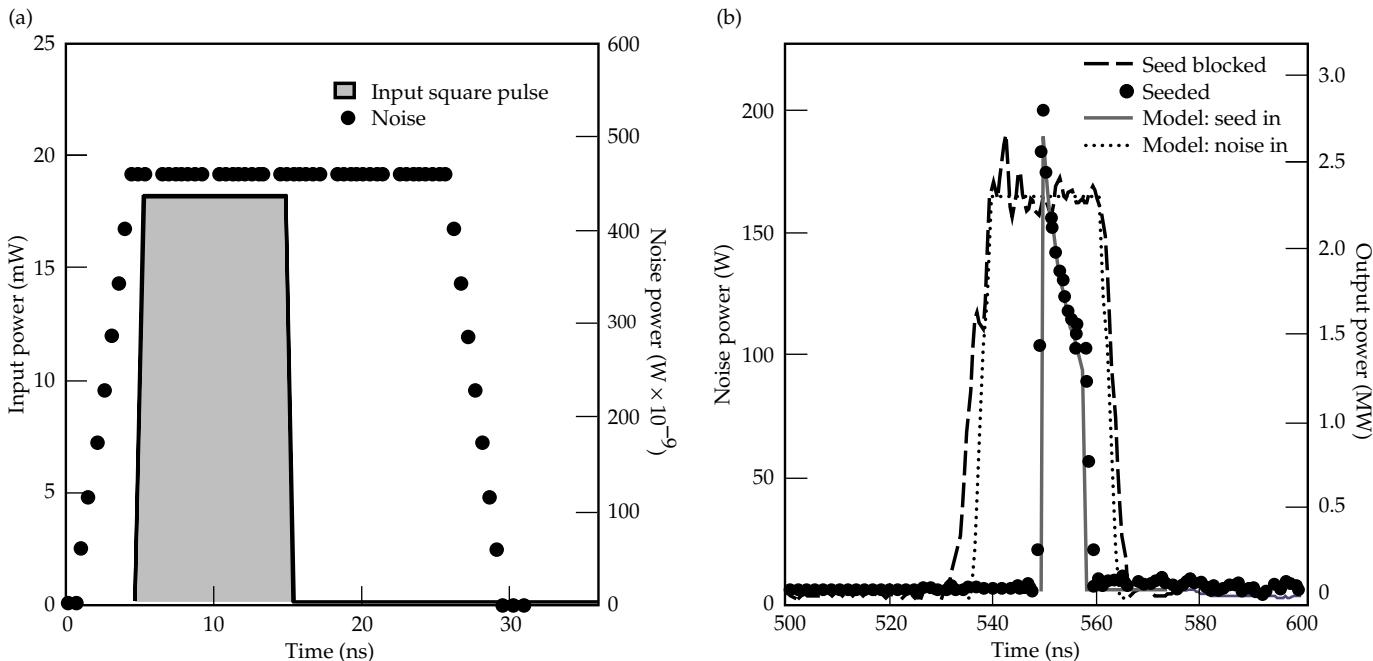
FIGURE 16. (a) Model input pulses consisted of a 181-pJ square pulse and 14-fJ noise pulse. (b) Comparison between measured output pulses and model results using the input pulses shown in (a). (70-00-0298-0174pb01)

the regen is 460 nW. As expected, the power S/N referenced to the input of the regen is larger than the ratio obtained by measuring the power ratio of the output pulses, where saturation must be considered.

To compare this measured noise value with the fundamental quantum limit, we seeded our regen model with a single spontaneous-emission photon per cavity mode over the full emission bandwidth of the laser transition in LG760. The noise energy E_{noise} is given by[10]

$$E_{noise} = \frac{h\nu}{2} \ N_{mode} = \frac{h\nu}{2} \Delta\nu_{SE}\left(\frac{2L}{c}\right) \quad , \tag{11}$$

where $h\nu$ is the photon energy, N_{mode} is the number of cavity modes, $\Delta\nu$ is the spontaneous emission bandwidth, L is the regen cavity length, and c is the speed of light. The spontaneous emission bandwidth $\Delta\nu_{SE}$ for LG760 corresponds to a FWHM of 20 nm. The number of noise photons is reduced by one-half in Eq. (11) because of the polarization selectivity of the cavity. To compare the quantum-limited noise energy with the measured value in Figure 16, we propagated the noise input spectrum, given by Eq. (11) for 18 round trips, using a Lorentzian-shaped gain spectrum for the amplifiers

$$g(\nu) = \frac{g(\nu_0)\left(\Delta\nu_{1/2}\right)^2}{\left(\Delta\nu_{1/2}\right)^2 + \left(\nu - \nu_0\right)^2} \quad , \tag{12}$$

where the peak centerline gain $g(\nu_0) = 4\ln G = 1.62$, and $\Delta\nu_{1/2} = \Delta\lambda_{1/2}c/\lambda^2$ is the FWHM of the exponential gain spectrum of LG760 (here, $\Delta\lambda_{1/2} = 20$ nm; that is, it is easier to think of bandwidth for broad spectral lines in terms of nm rather than Hz). After 18 round trips, the initially broad spectrum narrows to the 2.7-nm amplified noise spectrum shown in Figure 17. To determine the noise-equivalent energy (NEE) referred to the input, we divide the output energy by the total gain from 18 round trips, where $G_{total} = (G^4T)^{18} = 4.8 \times 10^8$. The quantum-limited NEE, referenced to the input of the regen, is 2.28 fJ as shown in Figure 17. The quantum-limited NEP for the trapezoidal-shaped power pulse that is characteristic of the regen noise shown in Figure 17 is 84 nW.

Gain Stability

Uniformity of target illumination, whether hohlraum or spherical target, flows down to a power-balance requirement for each of the 192 beamlines and, further, to the 48 PAMs. The current requirement for pulse-to-pulse fluctuation out of a preamplifier is 3% rms. This 3% value for the preamplifier output represents the total variation in output for one beamline of the OPG and must further be
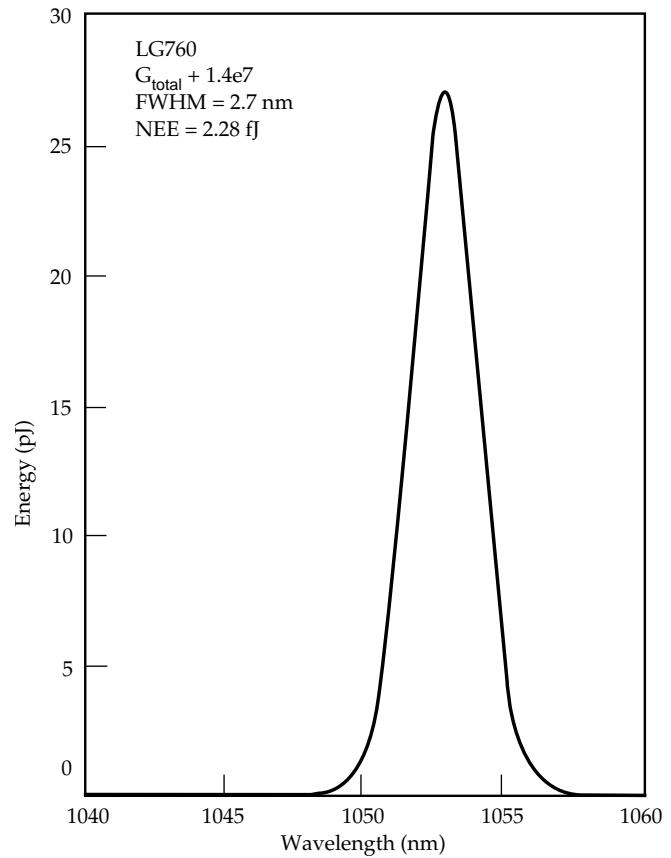
FIGURE 17. Quantum-limited noise spectrum for the regen with LG760 glass. (70-00-0298-0175pb01)

apportioned to the various subsystems, including the MOR, regenerative amplifier, and 4-pass amplifier. One of the early motivations for developing a diode-pumped regen was to reduce the pulse-to-pulse gain variation that is observed in flashlamp-pumped amplifiers.

To understand the source of fluctuations, we performed a simple differential analysis and then measured the individual contributors. The variation in output energy from the regen ΔE_{out} can be written as

$$\frac{\Delta E_{out}}{E_{out}} = \frac{\Delta E_s}{E_s} + \frac{\Delta T_s}{T_s} + \frac{k\Delta T_c}{T_c} + 2k\left(\Delta g_1 + \Delta g_2\right) \quad , \tag{13}$$

where T_s and T_c are the seed and cavity transmission, respectively, E_s is the input pulse energy from the MOR, k is the number of round trips, and g_1 and g_2 are the single-pass exponential gains of the diode-pumped amplifiers. These individual contributions to the overall variation in output energy of the regen can be grouped into high- and low-bandwidth effects. Low-bandwidth contributions include mechanical drift in optical mounts, mechanical vibrations that cause fluctuations in the polarization of the light emerging from

TABLE 2. Summary of regenerative amplifier performance.

Laser characteristic	NIF specification	Measured performance
1. Maximum output energy	—-	22 mJ
2. Required energy	10 mJ	10 mJ
3. Input energy	500 pJ	180 pJ
4. Total gain	2×10^7	5.5×10^7
5. Round trips	13–15	15
6. Cavity length (s)	—	30.5 ns
7. Cavity length (cm)	—	458 cm
8. Cavity configuration	—	linear, TEM_{00}
9. Cavity stability	—	$g^2 = 0.019$
10. Far-field beam profile	$1.5 \times$ D.L.	$1.1 \times$ D. L.
11. Near-field spatial amplitude modulation	<5%[a]	<1%
12. Pointing stability	<35 μrad[a]	<12 μrad
13. Gain stability	<0.03[a]	<0.014
14. Pulse repetition rate	1 Hz	1 Hz
15. Wavelength	1053 nm	1052.9 nm
16. Diode-pumped amplifiers	2	2
17. Diode driver current	—	92 A/head
18. Total electrical power to diodes	—	18.4 kW
19. Pump pulse length	—	350 μs
20. Total pump energy (optical)	—	2.1 J[b]
21. Total pump power at rods	—	6 kW[b]
22. Amplifier glass	—	LG760
23. Rod dimensions	—	5 mm (diam) $\times$ 50 mm
24. Stimulated emission cross section	—	4.67×10^{-20}
25. Saturation fluence	—	3.99 J/cm^2
26. Nd^{3+} doping	—	1%
27. Gain/pass/head	—	1.5[c]
28. Optical stored energy in rods	—	526 mJ[b]
29. Mode size in rod ($1/e^2$ radius), w_0	—	0.083 cm
30. Effective mode area/rod $A_{mode} = \pi w_0^2/2$	—	1.08×10^{-2}
31. Fill factor = A_{mode}/A_{rod}	—	0.055
32. Stored energy in mode	—	35 mJ[b]
33. Maximum extraction efficiency	—	0.62
34. Extraction efficiency at 10 mJ	—	0.29
35. Fraction of total stored energy extracted	—	1.9×10^{-2}
36. Optical effic. of regen = energy out/pump power	—	4.76×10^{-3}
37. Total wall-plug efficiency	—	1.55×10^{-3}
38. Square-pulse distortion (SPD) at 10-mJ output	1.2	1.17[d]
39. SPD at maximum output energy	—	—
40. Prepulse contrast ratio	10^5–10^6	4.8×10^5
41. Energy signal-to-noise ratio for 500-pJ input	10^4	3.56×10^4

[a]Specifications for the OPG. The flowdown has not yet been done for the regenerative amplifier.
[b]Combined value for both amplifiers.
[c]Average value of the two amplifiers .
[d]Achieved with recent upgrade to current design using single-diode head.

the single-mode fiber, and thermal drift in the temperature of the pump-diodes, causing a shift in the diode emission wavelength. We have solved most of these causes of slow drift of the regen output energy. For example, variations in diode temperature have been reduced by working with the manufacturer to improve heat sinking in the diode package, and by using a Nd:doped glass with a broader absorption spectrum that is less sensitive to the small changes in the diode wavelength. Higher-bandwidth contributions to gain fluctuations in Eq. (13) include pulse-to-pulse variations in the diode-driver current or voltage, and frequency chirp of the diode-emission frequency during the diode current pulse.

To identify sources of faster, pulse-to-pulse variations in the regen energy, we set up diagnostics to measure changes in those parameters that affect, or are related to, the gain in the rod amplifiers. In one experiment, we determined that the diode-current spontaneous emission from the rods, along with the regen output energy, all correlated on a shot-to-shot basis with small fluctuations in the voltage gate that controls the diode current. Figure 18 is a histogram showing the variation in regen output energy for 3000 shots. The solid line is a Gaussian fit to the data that yields a value of 1.4% for the rms variation of the output energy. This value is well within the 3% total variation for the preamplifier, but it does not allow much margin for variation in gain of the larger 4-pass amplifier. We are currently investigating ways to actively control the output energy of the regen to reduce energy fluctuations to less than 1% rms using high-bandwidth, feed-forward and feed-back techniques.

Summary of Regenerative Amplifier Performance

Table 2 is a summary of the measured performance and operating conditions for the current regen prototype. For comparison, we include the specifications derived from a flowdown of the entire laser system. In all cases, the current design meets or surpasses the NIF performance specifications.
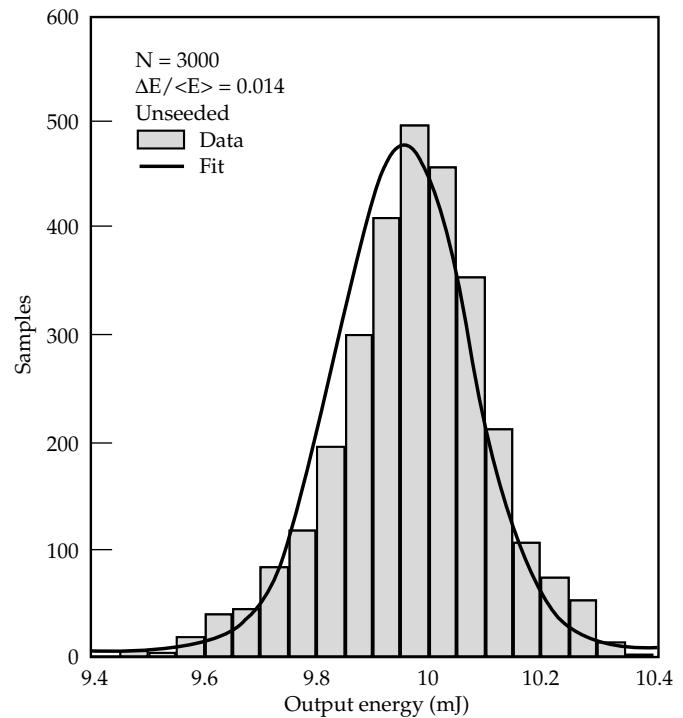
FIGURE 18. Histogram of the shot-to-shot variation in regen output energy. (70-00-0298-0176pb01)

Conclusions

The diode-pumped regenerative amplifier is the highest-gain laser system in the NIF laser chain. It acts as a high-fidelity preamplifier to boost the output pulses from the MOR to an energy level for injection into the large laser power amplifiers that form the rest of a NIF laser chain. Our current design meets or surpasses all of the performance specifications derived from a flowdown of the entire laser system. Our principal activity in the near future will be to combine this prototype regen with the completed 4-pass amplifier and MOR in an integrated OPG testbed, and to assemble a similar regenerative amplifier in the first PAM prototype. The OPG testbed will be operated for the next year as a facility for demonstrating all performance requirements for the NIF OPG system.

Notes and References

1. J. Davin, *SSDR 1.3.1, Optical Pulse Generation Subsystem*, Lawrence Livermore National Laboratory, Livermore, CA, NIF-0000058-02, WBS 1.3.1 (1996).

2. *National Ignition Facility Conceptual Design Report*, *Vol. 2*, Lawrence Livermore National Laboratory, Livermore, CA, UCRL-PROP-117093, Version 2 (1994).

3. B. M. Van Wonterghem, J. T. Salmon, and R. W. Wilcox, "Beamlet Pulse Generation and Wavefront Control System," *ICF Program Annual Report 1995*, Lawrence Livermore National Laboratory, Livermore, CA, UCRL-LR-105820-95, 42–51 (1995).

4. F. G. Patterson, M. D. Perry, and J. T. Hunt, "Design and Performance of a Multiterawatt, Subpicosecond Neodymium:Glass Laser," *J. Opt. Soc. Am. B* **8**, 2384 (1991).

5. J. K. Crane, M. Martinez, R. J. Beach, S. Mitchell, G. Pratt, and J. J. Christensen, "Ultra-Stable, Diode-Pumped Nd-Doped Glass Regenerative Amplifier for the National Ignition Facility (NIF)," Conference on Lasers and Electrooptics (CLEO), Anaheim, CA, May 1996.

6. R. Beach et. al., "Scalable Diode-End-Pumping Technology Applied to a 100-mJ Q-Switched Nd^{3+}:YLF Laser Oscillator," *Opt. Lett.* **18**, 1326 (1993).

7. R. Beach, "Scalable Diode Pumping for End-Pumped Laser Systems," *Laser Tech. Briefs* **2**(1), 32–36 (1994).

8. This equation appears in many forms in most laser texts and is derived from the classical coupled atom-field equations. The time-integrated version of Eq. (9) is commonly called the Frantz–Nodvik equation. The particular form shown here can be found in A. E. Siegman, *Lasers* (University Science Books, Mill Valley CA, 1986), ch. 10.

9. R. Page and G. Wilke (private communication).

10. A. Yariv, *Quantum Electronics*, 2nd ed. (J. Wiley, New York, 1975).

NIF GLOSSARY

adaptive optics Optical components whose shape can be actively changed to compensate for optical wave-front distortions. NIF uses thin, electrically controlled, deformable mirrors for this function.

amplifier slab As used in NIF, a neodymium-doped phosphate glass slab that is set in the beam at Brewster's angle and pumped by xenon-filled flash-lamps. The light from these flashlamps excites the neodymium ions to a higher energy state that leads to amplification of light beams at a small range of wavelengths around 1053 nm.

amplitude modulation Changing the amplitude of a signal without affecting its phase.

anode The positive electrode of an electronic device.

apodizer A variable-transmission filter that puts a smoothly varying irradiance profile on the edge of a beam in order to suppress diffractive ripples

architectural design The process of defining a collection of hardware and/or software components, their functions, interfaces, and key characteristics to establish a framework for system development.

architecture The logical and physical structure of a system forged by all the strategic and tactical decisions applied during development. Software architecture deals with abstraction, with decomposition and composition, with style and esthetics.

asynchronous transfer mode network (ATM) A cell-based switched network capable of carrying time-critical data such as video.

backlighter/backlighting Many NIF experiments will require that some of the beams be used to generate a source of x rays that is used to photograph the main experiment. This source is usually called a "back-lighter."

beam dump An optical component that disposes of an unwanted beam safely.

birefringence A material has this property if its index of refraction differs for different light polarizations.
An input light beam is then separated into two beams that take slightly different paths through the material.

blast shield As used in NIF, a glass shield that protects amplifier slabs from contamination generated by flashlamps.

borosilicate float glass A high-quality window glass manufactured by floating molten glass on a liquid metal support.

boule An "as-grown" synthetic crystal before finishing.

Brewster's angle A beam of light incident on a slab of optical glass at this angle (about 57º to the surface normal) has zero reflection for one of the polarization components of the beam.

Brillouin scattering Stimulated Brillouin scattering (SBS) is an interaction between light and sound waves in a material that leads to the growth of the sound wave and a second, scattered light wave. It is an undesirable effect in large lasers.

bundle A NIF "bundle" is an array of beams stacked four high and two across. The bundle is the basic building block of the laser system.

calorimeter A device used for measuring the energy of a laser pulse by measuring the temperature rise of an absorber.

canister A protective cover "box" in which a line-replaceable unit (LRU) is placed for transport to a desired location.

cathode The negative electrode of an electronic device.

cavity spatial filter (CSF) The spatial filter within the NIF main laser multipass cavity.

centering Positioning a beam in the center of an optical aperture when the beam is at full size (near field). See pointing.

charge-coupled device (CCD) A type of image sensor used in TV cameras.

class In software parlance, a class is a set of objects that share a common structure and a common

behavior. Typically classes are static; their existence, semantics, and relationships are fixed prior to the execution of a program.

clear aperture That portion of the aperture of an optical component that we allow the laser beam to occupy. See hard aperture.

client An object acts as a client in an interaction with another object (the server) if it initiates the interaction.

client/server computing Client/server computing encompasses a decentralized architecture that enables end users to gain access to information transparently within a multivendor environment of heterogeneous hardware and software platforms.

cluster A NIF "cluster" is an assembly of six bundles. The NIF laser contains four clusters, each containing 48 beams.

color separation grating (CSG) As used on NIF, a kinoform that transmits 3ω with no deflection, but diffracts 1ω and 2ω away from the target.

common object request broker architecture (CORBA) An *ad hoc* industry standard for software objects that communicate across processors in a network.

configuration A framework that is a collection of classes that all subsystems use to maintain the complete as-built description of the devices that they control.

dark-field imaging See schlieren technique.

datum A precise position reference.

diffractive optic See kinoform.

doubler A frequency conversion crystal that converts 1ω to 2ω.

event-based A system organizing concept (from the software programmer's point of view) wherein an application program is notified of outside occurrences by events.

far field A position in an optical train that is very far from an image. In NIF, the far fields occur at the focal planes of lenses in the spatial filters or the target chamber.

Faraday rotator An optical device that uses Faraday's magneto-optic effect to rotate the plane of polarization of a light beam.

filamentation See nonlinear index.

final optics assembly (FOA) A NIF assembly that includes the target chamber vacuum window, final optics cell, diffractive optics plate, debris shield, and some laser diagnostics.

final optics cell (FOC) The final optics cell is an assembly that holds and positions the two frequency conversion crystals and the target focus lens.

first wall The inside wall of the NIF target chamber. It must be highly resistant to x rays, other target radiation and debris, and laser light.

flashlamp As used in NIF, a xenon-filled quartz gas-discharge lamp that is used to pump amplifier slabs.

fluence The energy per unit area (generally J/cm^2) in a beam of light.

framework A large-scale software building block. A framework provides architectural guidance by partitioning the design into abstract classes and defining their responsibilities and collaborations.

freeboard The difference between the maximum expected aperture occupied by a beam and the actual clear aperture of an optical component.

Fresnel lens A thin lens constructed with stepped setbacks so as to have the optical properties of a much thicker lens; also an example of a "kinoform."

front-end processor (FEP) The low-level computer that implements device control.

fused silica A glassy, noncrystalline form of quartz (SiO_2). The fused silica used in NIF is usually a high-purity form that is manufactured by chemical vapor deposition (CVD).

Gaussian beam The beam generated by a laser that is forced to operate in a single, lowest-order mode.

ghost beam, ghost focus, ghost reflection Optical components that transmit laser beams in NIF are antireflection coated, but these coatings are never perfect so some very small laser energy is reflected at each of these surfaces. Although the energy in these beams is small, it is important to manage carefully where it goes in the system. If these beams come to a focus, for example, they can easily reach fluences that cause severe damage to components located near that focus.

half-wave plate A thin section of a birefringent crystal cut so that it rotates the polarization of light passing through it when the crystal is rotated around its optical axis.

hard aperture The aperture set by the mechanical mounting hardware for an optical component. The beam must not strike this hardware, consequently the hard aperture is larger than the clear aperture.

Hartmann sensor, Hartmann wavefront sensor A sensor that uses an array of small lenses to measure local wavefront tilts on a beam. The lenses generate an array of far-field spots on a charge-coupled device (CCD) camera, and image-processing software uses the positions of these spots to reconstruct the wavefront of the beam.

HEPA High-efficiency particulate air. A type of air filter using paper elements that is commonly used in clean rooms.

hierarchy A ranking or ordering of abstractions where the lowest common denominator is placed at the top and from this base all other classifications arise.

image relay An arrangement of optical components that forms a real image of a beam-defining aperture at several points ("relay image planes") through an optical system. Effective optical propagation distances are reset to zero at each image, so an image-relayed system has less beam modulation from diffraction than an unrelayed system.

injection system A NIF system that takes the input beam from the preamplifier beam transport system (PABTS) to the pinhole plane of the transport spatial filter.

input sensor A NIF system that diagnoses the output of the preamplifier module (PAM) before it is injected into the main laser cavity.

Integrated Computer Control System (ICCS) The system of computers and software which control NIF and stores information about its history and operation.

integrated optics module (IOM) An assembly that holds and positions the target chamber vacuum window, final optics cell (FOC), diffractive optics plate, and debris shield for a single beam of NIF. The IOM is a line-replaceable unit. (See final optics assembly.)

irradiance The power per unit area (generally W/cm^2) in a beam of light. Sometimes called "intensity;" however, the official SI definition of intensity includes a measure of the divergence of the beam.

KDP, KD*P Potassium dihydrogen phosphate crystal (KH_2PO_4). Thin plates of this crystal and its deuterated analog KD*P (KD_2PO_4) are used as the active optical elements in the NIF PEPC and frequency converter.

kinematic mount A mount designed so that components placed on it are forced to come to rest in a very precise location.

kinoform An optical component with fine phase structure that changes the phase of a beam ("diffractive optic").

laser entrance hole (LEH) An aperture in a hohlraum target through which the laser beam enters the hohlraum.

line-replaceable unit (LRU) A self-contained package, containing multiple laser components, that can be assembled and tested off-line in a clean room and then installed on the laser as a unit while preserving its highly clean and prealigned state. LRUs are installed on prealigned kinematic mounts in the NIF laser. Examples include the preamplifier module (PAM), a column of four amplifier slabs in the amplifier; a cassette of flashlamps in the amplifier; a column of four spatial filter lenses; and an integrated optics module (IOM) in the final optics assembly.

machine history Data that are saved by the integrated computer control system (ICCS) software that are pertinent to the operation and maintenance of NIF.

message log A framework that stores and retrieves text messages from many software components for the purpose of constructing an audit trail of system action.

near field A position in an optical train that is close to an image. In NIF, these are the regions where the beam is at its full size.

nonlinear index, nonlinear phase shift Optical materials have an index of refraction, which is the ratio of the speed of light in a vacuum to the speed in the optical material. At very high irradiance the index of refraction increases, or the speed of light is reduced in the material. Local regions of high irradiance travel more slowly, so the optical wavefront becomes concave near them. A concave wavefront is a focusing wavefront, so the local irradiance grows even larger as the diameter of the local hot spot decreases. This process amplifies any irradiance noise on the laser beam and can ultimately lead to "filamentation." In filamentation, the local region of high intensity collapses to an extremely intense spike that damages the material along a track a few microns in diameter. A few micron-sized damage tracks of this sort cause no particular harm, but a large density of them can obscure parts of the beam and can initiate further optical damage.

object A software entity that the system can act upon.

optical damage High laser irradiance and fluence can heat small defects in the bulk or on the surface of an optical component. These defects then explode and can cause damage (such as a pattern of small fractures) to the component. These damage sites may grow to a size that affects the laser's operation on subsequent shots, and the component must then be replaced. Components for a high-fluence laser such as the NIF must have a low density of defects and must also be kept very clean so that dirt particles that might initiate damage are very infrequent.

optical pulse generation system (OPG) The low-energy, small-aperture parts of the NIF laser that shape and amplify the laser pulses before they are injected into the main laser cavity.

output sensor A NIF assembly that diagnoses the output beam from the laser.

periscope As used in the NIF, the structure that supports the plasma-electrode Pockels cell (PEPC), polarizer, and two laser mirrors—LM2 and LM3.

periscope installation assembly A type of line-replaceable unit (LRU) installation structure that requires the use of spacers to lift LRUs to the required heights for installation.

phase modulation Changing the phase (or frequency) of a signal while the amplitude is held constant.

pinhole As used in NIF, an aperture in the focal plane of a spatial filter. The main laser pulse goes through the aperture, while stray light and high-spatial-frequency noise hit the edge of the aperture and are removed from the beam.

plasma-electrode Pockels cell (PEPC) A Pockels cell that uses tenuous helium plasmas as electrodes to apply a voltage to the active element.

plenum A chamber used to connect a gas supply or a vacuum pump to other volumes that require these services.

Pockels cell An electro-optic switch that rotates the polarization of a light beam passing through a mate-

rial when an electric field is applied to the material in the direction of beam travel (Pockels effect).

pointing Positioning a beam to the correct angle as it passes through an optical component at full size (near field). Pointing can also be described as centering a beam focal spot on the pinhole in a spatial filter pinhole plane (far field). See centering.

polarizer An optical element that separates the two polarization states of a light beam. The polarizers used on NIF are thin-film polarizers consisting of a specially designed multilayer coating applied to an optical glass substrate.

preamplifier beam transport system (PABTS) An optical system that transports the beam from the preamplifier module to the injection system in the transport spatial filter.

preamplifier module (PAM) A NIF component that is a self-contained package (LRU) that amplifies a shaped input pulse from an optical fiber to a level of about 10 J. The output from the PAM is split four ways into the four beams of a 2×2 quad.

pupil relay system See relay imaging.

pyrolitic graphite A highly pure form of graphite manufactured by chemical vapor deposition.

quad A "quad" is a 2×2 array of NIF beams. It is the basic building block of both the PAM and the beam transport system from the laser to the target chamber. Each bundle contains two quads, one routed to the top of the target chamber and the other to the bottom.

Raman scattering Stimulated Raman scattering (SRS) is an interaction between light waves and molecular vibrations or rotations in a material that leads to the growth of the molecular vibration or rotation and a second, scattered light wave. It is an undesirable effect in large lasers.

regen See regenerative amplifier.

regenerative amplifier A multipass amplifier having a large number of passes. As used in NIF, an amplifier stage in the preamplifier module.

relay imaging, relay plane See image relay.

relay telescope See spatial filter and image relay.

reservation A framework that assures orderly access to shared equipment.

reticle A pattern inserted into an optical path to aid in measuring angles or positions.

rod amplifier An amplifier whose active element is in the shape of a glass rod (cylinder). See amplifier slab.

Roots blower A type of high-volume vacuum pump.

schlieren technique A technique for emphasizing light scattered from small structures on an optical component. The main beam is blocked at a focal plane, and the only light remaining is the high-spatial-frequency noise on the beam that lies outside the main focal spot. This is the inverse of the usual pinhole spatial filtering.

sequence control language (SCL) A framework that implements a sequencing language used to execute user-defined and SCL-defined commands within a subsystem. Each subsystem determines which of its commands may be executed by SCL sequences.

serrated aperture A type of apodizer. See apodizer.

server An object is a server in an interaction with another object (the client) if it is the passive object which is invoked by a subprogram call.

smoothing by spectral dispersion (SSD) A technique for beam smoothing in which a diffraction grating disperses a broad-band beam through a slight angle. This causes motion of the small-scale speckle structure in the spot on the target and tends to average over intensity nonuniformities in the spot.

software tool A computer program used to help develop, test, analyze, or maintain another computer program or its documentation; for example, automated design tool, compiler, test tools, maintenance tool.

solgel As used here, a technique for applying anti-reflection coatings to optical elements. The coating is composed of ~50-nm particles of silica (SiO_2) deposited from an alcohol solution.

spatial filter An arrangement of two lenses, separated by the sum of their focal lengths, with an aperture at the common focus to restrict the range of angles in a beam of light.

speckle Random irradiance fluctuations in a beam caused by interference of randomly phased small areas.

status monitor A framework that defines strategy to acquire status information from various NIF components.

streak camera An instrument for measuring very fast events. A slit allows a one-dimensional strip of a light beam to strike a photosensitive cathode. Electrons emitted by the cathode are manipulated to form a two-dimensional image in which one dimension is the strip and the other dimension is time.

taxon the name applied to a taxonomic group in a formal system of nomenclature. In NIF, the taxonomic name of a NIF device classifies it according to its location within the hierarchy of the laser assembly.

Title I, II, III Project stages as defined by the Department of Energy in DOE Order 4700.1 or the DOE Glossary. In brief, the completion of Title I means that the project design is completed to a level of detail that allows a reliable cost estimate, and the completion of Title II means that drawings and procurement packages are completed to a stage that they can be sent for procurement of the buildings and components. Title III activities

are project activities that follow procurement and occur before the facility is turned over to operations personnel. These include acceptance tests, installation, and any engineering modifications that are required.

transporter A forklift-type device for moving LRUs to different locations.

transport spatial filter (TSF) In NIF, the 60-m-long spatial filter that lies between the laser and the target area.

trigger pulse A signal that commands an instrument to start.

tripler A frequency conversion crystal that sums 1ω and 2ω beams to give 3ω.

trombone An optical path of adjustable length used to equalize the propagation distance of two or more beams.

turbomolecular drag pump A type of high-vacuum pump.

vacuum manifold See plenum.

VME bus Versa Module Eurocard bus—an industry standard bus for embedded systems.

wavefront error The phase error on an optical beam caused by the accumulation of small errors in optical components (fabrication uncertainty, inhomogeneous material, mounting distortions, etc.)

1ω The fundamental frequency of a neodymium glass laser, corresponding to an infrared wavelength of 1053 nm (commonly called "red").

2ω The second harmonic of a neodymium glass laser, corresponding to a visible wavelength of 527 nm ("green").

3ω The third harmonic of a neodymium glass laser, corresponding to an ultraviolet wavelength of 351 nm (commonly called "blue").

NIF ACRONYMS

ACS	access control system	**GXI**	gated x-ray imager
AGV	automated self-guided vehicle	**HEPA**	high-efficiency particulate air
AMPLAB	Amplifier Module Prototype Laboratory	**HVAC**	heating, ventilation, and air conditioning
ATM	asynchronous transfer mode network	**IBE**	interstage beam enclosure
BK7™	a standard borosilicate optical glass (Borosilikat Kron 7)	**ICCS**	integrated computer control system
		ICF	inertial confinement fusion
BLDS	bottom loading delivery system	**ICS**	industrial controls system
CEA	*Commissariat a l'Energie Atomique* (French Atomic Energy Commission)	**IDL**	interface definition language
		IOM	integrated optics module
CCD	charge-coupled device	**ISS**	integrated safety system
CCI	Cleveland Crystals, Inc.	**ITS**	integrated timing system
CCRS	chamber-center reference system	**KDP**	KH_2PO_4 crystal (potassium dihydrogen phosphate)
CD	conceptual design		
CDR	conceptual design report or review	**KD*P**	KD_2PO_4 crystal (potassium dideuterium phosphate)
CORBA	common object request broker architecture		
CPU	central processing unit	**KPP**	kinoform phase plate
CSF	cavity spatial filter	**LANL**	Los Alamos National Laboratory
CSG	color separation grating	**LEH**	laser entrance hole
CS&T	core science and technology (LLNL laser research not part of the NIF project)	**LLE**	Laboratory for Laser Energetics, University of Rochester, NY
		LLNL	Lawrence Livermore National Laboratory
CVD	chemical vapor deposition	**LM**	laser mirror
CW *or* **cw**	continuous wave	**LMJ**	*Laser Megajoule* (laser project in France comparable to the NIF)
DAS	data acquisition system		
DIM	diagnostic instrument manipulator		
DOF	degrees of freedom	**LM1**	laser mirror 1 (a deformable mirror)
EMI	electromagnetic interference	**LRU**	line-replaceable unit
EMP	electromagnetic pulse	**LTAB**	Laser and Target Area Building
FAU	frame assembly unit	**MA**	Main amplifier
FEM	facility environmental monitor	**MOR**	master oscillator room
FEP	front-end processor	**MTV**	maintenance transport vehicle
FF	far field	**NF**	near field
FOA	final optics assembly	**NIF**	National Ignition Facility
FOC	final optics cell	**NS**	neutron spectrometer
FOV	field of view	**OAB**	Optics Assembly Building
FXI	framing x-ray imager	**OPG**	optical pulse generator
GFRC	graphite fiber-reinforced carbon	**P–V**	peak-to-valley
GUI	graphical user interface	**PA**	power amplifier

PABTS	preamplifier beam transport system		**SQL**	structured query language
PAM	preamplifier module		**SRS**	stimulated Raman scattering
PAMMA	preamplifier module maintenance area		**SSD**	smoothing by spectral dispersion
PASS	preamplifier module support structure		**SXI**	static x-ray imager
PEPC	plasma-electrode Pockels cell		**SY/TA**	switchyard and target area
PLC	programmable logic controller		**T&H**	transport and handling
RP0	relay plane zero		**TCP/IP**	standard internet communication protocol
SBS	stimulated Brillouin scattering		**TL**	top loading
SCL	sequence control language		**TRXI**	time-resolved x-ray imaging system
SF	spatial filter		**TSF**	transport spatial filter
SIS	safety interlock system		**TWTT**	two-way time-transfer technique
SL	side loading		**VME**	Versa Module Eurocard (bus)
SNL	Sandia National Laboratories		**XSSC**	x-ray streaked slit camera

Monthly Highlights

September 1997

Nova as a "20-Beam" Laser. We have effectively doubled the number of beamspots on Nova by propagating two different pulse shapes on each half of the 10 Nova beamline split-glass amplifiers. Using a single lens, the pulses from each half are partially defocused at the target plane to provide two adjacent beam spots with a continuously adjustable power ratio. Applied to a cylindrical hohlraum target, this "20-beam" Nova variant provides a NIF-like two-ring irradiation geometry for testing advanced symmetry control concepts required for achieving ignition.

NIF AMPLAB. We have performed gain measurements on a full-size 4-slab-high × 2-slab-wide × 1-slab-long prototype amplifier with a flashlamp pump cavity nearly identical to the NIF baseline amplifier design. The results, which were in excellent agreement with 2D ray-trace code predictions, are consistent with the NIF amplifiers achieving an aperture-average gain coefficient of 5%/cm. The prototype amplifier, shown below, had a full complement of laser glass and was outfitted with specially shaped flashlamp reflectors and antireflective coatings on the blastshields to increase pumping efficiency.

The assembled amplifier seen from the north mirror tower.

NIF Construction. NIF construction packages for the site preparation, foundations, the laser building shell, and the optics assembly building were awarded on schedule. The first contract (under $1M) was awarded to Red Top Construction of Hayward, California. Digging the "big hole" was done by Teichert Construction of Stockton, California, in a contract under $2M. The third contract, of $4.2M (to do the foundation and concrete slab work) was awarded to Walsh Pacific of Monterey, California. The $11.4M contract for constructing the laser building shell was awarded to Neilson Dillingham of Pleasanton, California. Preparations for the remaining construction contracts are proceeding on schedule.

NIF KDP Rapid-Growth Program. Over the last few months, a great deal of progress has been made in the rapid growth of KDP and KD*P (deuterated) crystals for the NIF. Shown below is a KDP boule measuring $57 \times 57 \times 47$ cm, which is the minimum size required for NIF second-harmonic-generation crystals. Larger, crack-free, and higher-optical-quality crystals resulted from thermal expansion coefficient matching of the growth-platform base plate to the crystal material. An additional KDP boule measuring $55 \times 55 \times 38$ cm was grown with a continuous filtration system installed and operating for the duration of the run. Crystals grown in small tanks with continuous filtration have been tested and show a significant improvement in damage threshold over those grown without constant filtration.

A KD*P boule measuring $52 \times 51 \times 38$ cm has also been grown, but it does not have sufficient height to yield a third-harmonic-generation plate. Experiments are under way to increase the aspect ratio of these crystals. We have demonstrated NIF damage thresholds in small KD*P boules, but have not yet evaluated the 52-cm boule. The large crystals still contain some inclusions, so work continues on improved system design and process optimization.
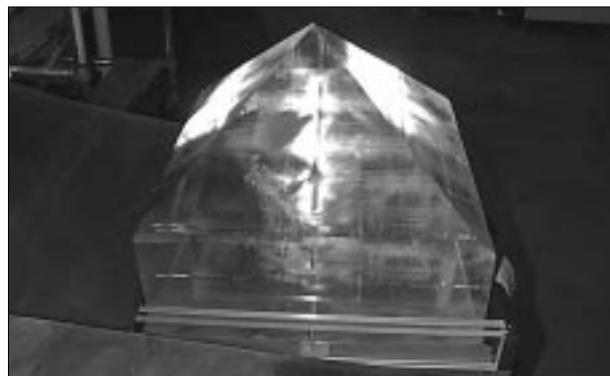
$57 \times 57 \times 47$-cm KDP crystal.

NOVA/BEAMLET/NIF UPDATES
APRIL–JUNE 1997

G. Hermes/R. Speck/A. Clobes

Nova Operations

During this quarter, Nova Operations fired a total of 176 system shots resulting in 205 experiments. These experiments were distributed among ICF experiments, Defense Sciences experiments, X-Ray Laser experiments, Laser Sciences, and facility maintenance shots.

Smoothing by spectral dispersion (SSD) on all 10 beamlines of Nova was activated during this quarter. In addition to the activation of the SSD system in the preamp section of the laser, this change also included the installation of double debris-shield holders on all focus lens assemblies of the 10-beam chamber. The double debris-shield holders contain both the kinoform phase plates (KPPs) and a debris shield to protect them from target debris resulting from a shot. Activation required several days of beam propagation evaluation and system performance verification. The application of SSD and KPPs produces an improvement in spatial smoothness of the focal spot on target.

We have started the installation of the 4ω probe beam for the 10-beam target chamber. This beamline will be created by a "pick-off" mirror installed into the center obstruction of beamline 8 in the switchyard. This subaperture, 1ω beam will be propagated to the 10-beam chamber where it will be converted to 4ω and used as a target diagnostic probe beam. Installation will continue through this quarter, with system activation scheduled for next quarter.

The Los Alamos Full Aperture Back Scatter Imager was installed on beamline 7 in the target area. The primary purpose of this instrument is to provide time-resolved target-plane images of the stimulated Raman (SRS) and stimulated Brillouin (SBS) backscatter emission. In addition, the instrument will measure the energy and time-integrated near-field pattern of the SRS and SBS backscattered light.

In continuing support of the Petawatt project, the Petawatt minichamber was received and is being cleaned and prepared for installation in January of 1997. This minichamber will be used during the initial Petawatt demonstration to measure system performance and beam focusability. The 32-in. gate valve between the compressor chamber and the minichamber was installed. The fabrication of the parabolic mirror system vacuum housing, extension tube, and gimbal rings by Bechtel Nevada was completed and received. The parabolic mirror is due in early February of 1997. The details of the Target Alignment Viewer and Target Inserter have been completed, and fabrication of these systems has started. The backscatter diagnostic table and enclosure were also installed. These systems will be installed and activated on the minichamber late next quarter.

Tests comparing the performance of a Princeton Instruments charge-coupled device (CCD) camera to film was completed. The results show that the CCDs compare favorably with film. The details of this evaluation are being compiled, and a report will soon be available. Further comparisons of CCDs and film coupled to a microchannel plate on an x-ray source are continuing.

We have started planning for the decommissioning of the Nova Two-Beam Target Area. The hardware in this area will be disassembled and removed for salvage or storage as appropriate. Experiments in the Two-Beam area will end in September of 1997. The area must be clear for activation of the National Ignition Facility (NIF) optics processing facility by mid-December of 1997.

Beamlet

Beamlet continues to provide the test bed to validate the laser physics foundations of the National Ignition Facility (NIF) and to check laser engineering concepts and components proposed for the NIF. During the first quarter of FY 1997, activities on

Beamlet included the following:

1. Reactivation of the laser following the lens implosion caused by side-scattered stimulated Brillouin scattering (SBS) during the long-pulse campaign in September of 1996.
2. Installation and activation of beam smoothing by one-dimensional smoothing by spectral dispersion (1-D SSD) on the Beamlet preamplifier.
3. Initial detailed beam-quality characterization of the injected near field.
4. Installation and alignment of NIF prototype square spatial filter lenses.
5. Recalibration of existing wavefront sensors and installation of additional higher-resolution sensors in preparation for detailed wavefront characterization shots, planned for January 1997.

The prevention of vacuum barrier optics damage and implosion is critical for the NIF design. Analysis of failed lenses has shown that a significant reduction of the internal stress can prevent formation of multiple cracks, in addition to increasing the critical flaw size. Modifications were completed to install tilted square lenses in all Beamlet spatial filters. These have a stress significantly lower than the original round lenses, and are comparable to Nova spatial filter lenses (<900 psi). The tilted lens design required a complex alignment procedure to maintain the overall static aberration below two waves peak-to-valley.

An operational readiness review and fault analysis were completed before reactivating the laser. Several measures were implemented to reduce the SBS sidescatter risk, including real-time bandwidth sensors for the master oscillator room and regenerative amplifier. An optical fail-safe system is being designed and tested, and will be installed in the Beamlet Master Oscillator later in FY 1997, complementing the existing electronic fail-safe system.

While system reactivation activities took place on the main laser, several campaigns were completed to characterize the Beamlet injection beam. This information is required to complete the Beamlet propagation model and noise analysis by the NIF Project. Near-field measurements were performed using an additional diagnostic system and confirmed a contrast level of 5%, consistent with model predictions of Beamlet output noise level and preamplifier modeling.

Beam smoothing is an important requirement to optimize target irradiation on the NIF, and Beamlet will test the proposed scheme using 3- to 5-Å bandwidth, critically dispersed in one axis using a grating in the preamplifier (1-D SSD). A first step towards this test was the installation of the preamplifier dispersive optical system and a verification of its operation at the injection plane. Near-field, far-field, and time-resolved power measurements confirmed predicted behavior. Speckle smoothing was tested with a small phase plate in the test setup.

National Ignition Facility

The principal activity for the NIF Project during this quarter was the completion of the Title I Review process, which included the Independent Cost Estimate (ICE). The Title I Design Review (i.e., for Preliminary Design) was completed November 22, 1996. No issues were identified by the review committee that would preclude starting Title II Design (i.e., Final Design) and long-lead procurements. The ICE Review draft report was completed as scheduled on December 6, with overall estimates in excellent agreement (within about 1%) with the project estimate. The Project requested and DOE/OAK granted approval to initiate Title II design and long-lead procurements. Title II design and long-lead procurements are underway, and progress has been made in all areas.

Title I Design Review

The Title I Design Reviews were completed in accordance with the *NIF Title I Review Plan*. Formal presentations were made by the Project to the Review Committee consisting of external and internal reviewers with significant expertise in their areas of review.

The review was divided into these main areas:

- Conventional Facilities.
- Optical Design and Laser Performance.
- Laser System.
- Beam Transport System.
- System Control.
- Target Experimental System.
- Optical Components.
- Operations Engineering.
- Integrated Computer Control System.
- The Conventional Facilities Design Review covered the site improvements, Laser and Target Area Building (LTAB), and OAB. Based upon the presentations and the review of numerous design documents provided, the committee submitted extensive comments. While there were numerous important findings, the Committee determined that the NIF Conventional Facilities Title I Design meets the system requirements and is the minimum platform to meet the NIF functional requirements. The Committee recommended proceeding to Title II design.
- The Laser System reviews included the amplifier, Plasma Electrode Pockels Cell (PEPC), power conditioning, and auxiliary subsystems. Three areas of concern (optical pulse generation, pulse-power switch, and amplifier blast shield/seal) were identified by the Review Committee as requiring management attention early in Title II Design.

The majority of the Title I Design reviews turned up no significant items to resolve before Title II. Following the review, the summary recommendation of the Review Team was "to accept the designs with comment, and

proceed with Title II Design." Title II Design started following DOE/OAK approval. There are, however, three areas of concern (optical pulse generation, pulse power switch, and amplifier) that will be addressed in initial Title II Design. As each area of the Project completed its Title I Review, the engineering effort in that area switched to Title II Design.

Based on the Title I Design Review, the *Primary Criteria and Functional Requirements* (PC/FR) for Title II and the *Project Data Sheet* were updated and approved by the Level 1 Baseline Change Control Board (BCCB1) in Washington, D.C. An update of the Title II design criteria based on Title I Design Review results was completed and incorporated in two proposed Baseline Change considerations: (1) Title I update of *Primary Criteria and Functional Requirements* (BCP97-001) and (2) *Project Data Sheet* update (BCP97-002). These proposals were approved by the BCCB1 on December 20, 1996. The *Project Data Sheet* update was submitted to the Secretary of Energy for consideration.

The Title I planning included an accelerated transition to operations in support of the user community. The Title I schedule and planning define the basic strategy for the NIF Project and the ICF Program to implement a smooth transition between construction and operations to support Defense Programs' Stockpile Stewardship and Management Program (SSMP).

Other Activities

In the Beam Transport System, the design was modified to reflect an optimized 48-PAM structure (not to preclude 96 units). In collaboration with Conventional Facilities, the height of the switchyard concrete building was decreased by 2.5 ft from the Title I design as a cost saving measure. The switchyard space-frame column and mirror-support locations were revised, and dynamic analysis verified that the stability meets specification. Analyses have been completed to support a change to increase the spatial filter lens thickness, thereby reducing the lens stress to 500 psi (from 700 psi) in order to provide an increased safety margin.

In reworking the Preamplifier System for the new 48-PAM design, the functions and design specifications for the splitter section of the Preamplifier Beam Transport System (PABTS) were refined. (The reduction in number of PAMs necessitates a beam-splitter section to inject light from 48 PAMs into 192 beams.) Specifically, the requirements for optical-path-length adjustability and energy-splitting adjustability were developed further based on comments from the Title I review. In addition, the merits of splitting a single PAM's output into a single quad were evaluated.

Significant advances were made in preparation for the Conventional Facilities construction:

• The Project Labor Agreement with national, state, and local labor unions that reduces sched-

ule risks and cost impacts due to potential labor disputes during Conventional Facilities construction was finalized by the Parsons negotiators. The agreement has been signed by the Union Representatives and is awaiting Project Office approval.

• The Owner-Controlled Insurance Program has been approved. This initiative reduces conventional facility construction bid costs and improves site construction safety.

• An updated, integrated schedule for Conventional Facilities construction packages was prepared and distributed. The Conventional Facilities construction management plan was developed.

• The Title II design for the first construction package, Site Preparation, is nearing completion and is on schedule for completion to meet the project milestones leading to the beginning of Site Preparation on March 11, 1997.

During this quarter significant progress has also been made in various areas of the Core Science and Technology (CS&T) Program, which supports the NIF Project:

• Selected design details of the 40-cm deformable mirror are being reevaluated following experience gained from assembly and testing of a full-scale prototype mirror built in the CS&T Program. In particular, it may be possible to simplify the method of attachment of the actuator assemblies on the back side of the substrate.

• The 4×2 NIF prototype amplifier activation in AMPLAB has made good progress.

• Assembly of a NIF prototype 2×1 PEPC was completed in collaboration with CS&T, and testing started. This unit validates most of the important design features in the NIF design, including a two-aperture-long plasma charging two crystals in parallel; validation of anodized Al as a PEPC housing; and integration of vacuum and electrical interfaces at the end of the 2×1 PEPC, thereby allowing close-packing of PEPC Line Replaceable Units (LRUs) in the NIF.

Advances in power conditioning development included the following:

• In collaboration with CS&T, half-current (250-kA) testing of the ST-300 spark gap switch was completed, and full-current testing began. Flashlamp triggering tests at American Control Engineering validated the flashlamp triggering strategy for the NIF pulse-power system.

• A NIF prototype power conditioning module operated (SNL-Albuquerque) for over 400 shots at full specified voltage and current (25 kV, 500 kA).

- A spark-gap switch was operated (SNL-Albuquerque) for 100 shots. The measured resistance was higher than expected. Reduced delivered energy (~5%) will be addressed if the measurements are validated.
- Power conditioning system testing is continuing at American Controls Engineering. Reliable triggering of flashlamps was demonstrated at a favorable 12 kV, which is one-half the specified voltage.

Permitting and assurance activities included the following:

- The Record of Decision (ROD) for the *Programmatic Environmental Impact Statement on Stockpile Stewardship and Management* was published by DOE on December 11, 1996, establishing LLNL as the NIF site. The ROD was a critical-path constraint on start of construction, procurement, environmental permits, and Critical Decision 3.
- Environmental permit applications were completed and submitted to the regulatory agencies following release of the ROD. These permits are required prior to the beginning of site preparation.
- A significant effort was directed to complete the draft of the *Construction Safety Program* document, which is the overall safety document for construction and special equipment subcontractors and Laboratory personnel at the LLNL site. The activity involves Conventional Facilities, Hazards Control, and Project Assurances.

- The second Public ES&H Working Group meeting was held on October 7, 1996. The briefing included seismic design, decontamination and decommissioning for Nova and NIF, and bounding accidents.

Optics activities included the following:

- The first full-scale NIF crystals were obtained from a rapid-growth KDP crystal. The two 41-cm Z plates met the NIF transmitted-wavefront specification. Witness samples from the crystal met the 1ω damage requirement. A photothermal deflection technique as a diagnostic for precursor to KDP bulk damage was demonstrated.
- Two out of four full-sized mirror substrates were manufactured to NIF specifications using the NIF manufacturing process. Coated mirrors will be demonstrated on Beamlet in 3Q FY97. Also, spatial filter lenses that meet NIF power-spectral-density and roughness specifications were manufactured using NIF processes.
- The large-aperture optics drawing package (80 drawings in total) was delivered to the NIF Optics Production group for use in their preparation for long-lead optics procurements. These drawings, which were developed to a near-Title II level of completeness and detail, contain near-final specification information for procurement of the over 7,000 large optical components in the NIF.

Nova/Beamlet/NIF Updates January–March 1997

R. Ehrlich/P. Wegner/S. Kumpan

Nova

Nova Operations performed 201 full system shots, resulting in 213 experiments during this quarter. These experiments supported efforts in ICF, defense sciences, university collaborations, laser sciences, and Nova facility maintenance. The Nova shot rate continues to be impacted by facility funding reductions. The process of moving Nova Operations personnel into National Ignition Facility (NIF) related positions will continue, eventually resulting in Nova operating 1.5 shifts per day. Also impacting the shot rate for the quarter was a three-week period during which the first shift of each day was dedicated to facility maintenance. The Nova Operations personnel efficiently used the added maintenance time to perform deferred maintenance tasks and to expedite progress on system upgrades and additions.

The first series of implosion experiments was performed with kinoform phase plates (KPPs) on all ten beamlines. We were successful in maintaining the accuracy of precision pointing and power balance with the KPPs at levels sufficient to produce symmetric implosions. The first target-shot series with smoothing by spectral dispersion and KPPs on all ten beamlines was also successful. We achieved the desired bandwidth (2.4 Å at 1ω) with acceptable levels of temporal and spatial modulation on all beamlines.

The Petawatt Project efforts concentrated on preparing for the first series of shots into the new Petawatt target chamber in late April. The target chamber was cleaned, assembled, and installed early in the quarter. By the end of the quarter, the target chamber had been integrated into the Nova vacuum system with new hardware and software, then pumped down to a satisfactory vacuum level. The parabolic mirror, beam alignment, target insertion, target alignment, and target diagnostic systems were installed. Tests of these systems will be performed in early April.

The 4ω probe beam was successfully installed on the ten-beam target chamber. Off-line testing of the frequency conversion system has been completed. On-line testing and tuning will commence early next quarter. Plans are being formulated to use this beamline, which uses light taken from the center obscuration of beamline 8, as a probe beam for experiments in the Petawatt target chamber.

The preparations for decommissioning the Nova two-beam target area continue. The system will continue to operate until mid-November to allow for the completion of 100-TW and equation-of-state experiments. The area will be clear by mid-January, when we will begin work to convert it into a NIF optics processing area.

Beamlet

Beamlet continues to provide a testbed for validating the laser physics foundations of the National Ignition Facility (NIF) and for evaluating laser engineering concepts and components proposed for the NIF. During the second quarter of FY 1997 activities on Beamlet included the following:

1. Characterization of beam quality at the output of the Beamlet front end to validate noise propagation models and to support the development of optical specifications for the NIF preamplifier module.
2. Optimization of the laser wavefront using the Beamlet adaptive optics system to gauge compliance with NIF focusability requirements and to provide a baseline for testing a prototype NIF deformable mirror.

3. Successful testing of a 40-cm NIF prototype deformable mirror inside the main amplifier cavity.

4. Propagation of full system shots with angularly dispersed bandwidth to test the 1.06-μm laser requirements for producing 1D beam smoothing at NIF targets.

Modifications to the facility included a safety upgrade to dual-camera inspection systems for all four spatial filter lenses, as well as the removal of the frequency converter enclosure at the output of Beamlet to make way for installation of the final optics test mule.

The measurements performed on the Beamlet front end confirmed that the beam injected into the main amplifier is of high quality. In the absence of active wavefront correction, the injected beam is near-diffraction limited, with 80% of the power contained inside a divergence half angle of 4.3 μrad (for a 34-cm beam). The distortion of the measured wavefront is 0.1 wave rms, and the calculated Strehl ratio is 0.7. Amplitude modulation in the near field was measured to have an irradiance contrast of 5%, confirming model predictions that the small amount of modulation observed in the output beam at low power is driven by contributions from the front end.

Beam divergence at the output of the laser was characterized with the Beamlet adaptive optics system (AOS) optimized to correct for wavefront distortions incurred in the main amplifier. Emphasis of the tests was on establishing best attainable divergence at low power in the angular regime below 20 to 30 μrad to help ascertain wavefront gradient requirements for NIF optical components. Performance was monitored with radial shearing interferometers that measured near-field wavefront at the input and output of the main amplifier with a spatial resolution of 1 cm, and with cameras that measured the corresponding intensity distributions in the far field with an angular resolution of 0.3 μrad. Test results show that pumping the Beamlet amplifiers induces 1.8 waves of long scale-length distortion over the 34-cm beam that is fully correctable with the Beamlet AOS. Passive distortions in the system total ~2 waves peak to valley and are only partially correctable, resulting in a residual error of 1 wave peak to valley, 0.2 wave rms. The resulting output beam has 80% of the power contained inside a divergence half angle of 10 to 11 μrad, and a Strehl ratio of 0.5.

A prototype 40-cm deformable mirror and controller were provided by the NIF Wavefront Controls and U-AVLIS Adaptive Optics groups. The mirror was installed and tested in the multipass cavity at an end mirror position adjacent to the amplifier modules. No evidence of coating damage or degradation to the actuator assemblies was observed for the 11 shots in which the mirror was exposed to flashlamp radiation. Output wavefront was not as good as that obtained

with the Beamlet deformable mirror because of a figure error of 1 wave peak to valley in the large mirror that was incurred during fabrication. The advantages of distributing large wavefront correction over two passes of the cavity were addressed by examining the pass 2 focal spot in the cavity spatial filter. With 3 waves of correction, an approximate 25% reduction in spot size was observed over the case where the correction is applied in the front end, although the irradiance level at the edges of the pinhole was not measured.

1D beam smoothing by spectral dispersion (SSD) was successfully tested for the 1.06-μm part of the laser at output powers up to 3.5 TW in 1-ns pulses. Bandwidth of 2 Å was generated with a 6.7-GHz phase modulator and angularly dispersed in the Beamlet front end to produce an output divergence of 25 μrad, consistent with NIF indirect-drive requirements. Testing was performed with the pinhole in the transport spatial filter removed to better observe nonlinear growth of beam modulation in the laser. For B integrals in the booster amplifier stage of 1.4 rad corresponding to the maximum power tested, measurements showed a high-quality output beam with no increase in near-field modulation over the non-SSD case.

National Ignition Facility

The primary focus of the NIF Laboratory Project Office for the second quarter of FY 1997 was to complete the revision of the project baseline in accordance with the directives of the DOE Headquarters (HQ) Level 1 Baseline Change Control Board (BCCB1). This activity, namely in the form of the FY 1998 Project Data Sheet, was approved and forwarded to the Secretary of Energy in December 1996; it culminated in a proposed new baseline to be documented in an updated *Project Execution Plan*.

Critical Decision 3, Approval to Begin Construction, was signed by the Acting Secretary of Energy on March 7, 1997. This top-level milestone for the NIF Project was achieved ahead of schedule, allowing the Project to proceed with construction activities at the selected site, Lawrence Livermore National Laboratory (LLNL).

The Notice to Proceed for the first Construction Subcontract Package, Site Preparation, was given on March 18, 1997. After the notification was issued, site work began on March 31, 1997, with preparation of the construction laydown area (Kirschbaum Field) for the installation of the construction management trailers.

Key activities supporting construction and completed as scheduled include the following:

• Execution of the NIF Project Labor Agreement, a key to the construction strategy.

• Implementation of a Project-specific *Construction Safety Program*, which was included in the first construction package.

- Completion of a traffic survey.
- Approval of an Owner Controlled Insurance Program.
- Award of a broker contract.

The final *Independent Cost Estimate Report* was completed and released, and all action items were completed.

Revision 1.6 of the *Primary Criteria and Functional Requirements* was completed in accordance with the Level 1 Baseline Change Control Action, and a description of the process for developing the ES&H criteria using DOE's *Work Smart Standards* was prepared.

At the request of the BCCB1, the NIF Laboratory Project Office prepared and submitted to DOE's Oakland office (DOE/OAK) the *NIF Project Completion Criteria*. This document specifies the criteria for completion of the NIF Project and for achieving Critical Decision 4 in September 2003, consistent with the Project baseline revision effort. The overall strategy for completion enables the ICF Program to begin experimental operations in support of Stockpile Stewardship and other programmatic missions at the earliest possible date, as NIF performance capability is building up toward the eventual goals set out in the *Primary Criteria and Functional Requirements*.

The NIF *Mitigation Action Plan* (MAP) has been formally transmitted by DOE/OAK. The MAP's purpose is to describe how to mitigate environmental impacts identified in the *Record of Decision* and the *Final Programmatic Environmental Impact Statement for Stockpile Stewardship and Management*. The first MAP action was placing public notices of the start of construction in all local papers and the *San Francisco Chronicle*.

Working with the NIF System Integration team and DOE/OAK and using the DOE guidelines for Necessary and Sufficient (Work Smart) Standards, the NIF Project Assurances team developed the final draft of a document describing the process for preparing the *Primary Criteria and Functional Requirements*. This and revision 1.6 of the *Primary Criteria and Functional Requirements* were signed at DOE/HQ.

Site and Conventional Facilities

The Project began the transition to the construction phase for the NIF Conventional Facilities. The first construction subcontract package was awarded as scheduled, and construction began on Construction Subcontract Package 1: "Duct Bank Relocation and Parking Lot Relocation." The construction laydown area where the construction management complex is located (Kirschbaum Field) was prepared for construction management trailers.

In addition, the Title II design for Conventional Facilities saw the completion of several design review packages:
- The "Target Building Mat and Laser Bay Foundation" (Construction Subcontract Package 3) was received for Title II 100% review.

- The "Target Area Building Shell" (Construction Subcontract Package 6) 65% review comments were received.
- The "Laser Building Buildout, Site, and Central Plan" (Construction Subcontract Package 9) was received for Title II 65% review.

Special Equipment

- The optomechanical layout of the pre-amplifier module (PAM) has been updated to reflect the optical component design currently under analysis. The beam size in the multipass amplifier section has been increased from 23 mm to approximately 27 mm. As a result, several of the 50-mm optics will need to be increased to 75 mm.
- The 50-mm Nova rod amplifier head has been installed and activated in the preamplifier integration testbed. Gain, gain uniformity, and birefringence measurements under full loading have been completed. The 4-pass amplifier cavity has been set up and extraction experiments begun. Results will be available for the Technical Management Plan review scheduled in April.
- The impact of the optomechanical layout for the 1:4 beamsplitting assembly following the PAM and the location of the separate PAM power conditioning unit (PCU) with respect to the pre-amplifier support structure (PASS) in the beam transport system were evaluated. The PAM PCU will now be located on the Laser and Target Area Building floor beneath the PASS.
- After careful comparison between air and nitrogen, the amplifier cooling gas working group recommended that the amplifier flashlamp cooling gas be changed from air to nitrogen.
- The Power Conditioning development team worked to validate the NIF system design and answer Title I issues. Effort was concentrated on switch testing. The first full-energy, 1000-shot run was completed on the prototype module at Sandia National Laboratories (SNL) using the Physics International switch in self-break mode. Results showed that the 6-mm spark-gap erosion observed in initial tests grew to 18 mm after 1000 shots. Although the gap erosion rate exceeded that predicted by the manufacturer, this experiment demonstrated the feasibility of using the spark-gap switch in the NIF application.
- The Beam Transport design team concluded that a graded approach on spatial-filter interior surface finish should be used. This means that polished plate will be used for end and center vacuum vessels (near optics) and that bead-

blasted surfaces will be used in the vacuum beam tubes. This decision allows the placement of the long-lead mill order after the vessel configuration is frozen.

- The Integrated Computer Controls System (ICCS) team developed the *Hardware Control Emulation Plan* to help guide the planning for the first of the ICCS software prototypes. Prototype frameworks for the configuration, system manager, generic front-end processor, status monitor, message log, and sequence control will be demonstrated in May. Four design reviews on these framework components were held in March. The object-oriented models for the prototype are complete, and coding of the associated software packages has commenced.

- The ICCS team developed a first-draft software test package that contains the essential elements of a full-scale benchmark test. The plan is to subject the NIF components, software tools, and networks (in a repeatable fashion) to simulated performance stresses expected during operation. A 'client' within the test package can exercise CORBA services that are used in the ICCS framework. Scale testing of the software is accomplished by operating any number of objects in any number of servers on any number of computers. Timing, memory usage, and results of sample calculations are measured. Initial tests of functionality and speed of performance were made.

- After problems associated with the behavior of an updated version of a third-party-supplied module were corrected, the two-way time transfer system was shipped to Jet Propulsion Laboratories (JPL). Measurements made at the supplier indicate that the timing performance meets expectations. Following JPL evaluation, the unit will be further evaluated at LLNL, and efforts to enhance performance to meet integrated timing system precision requirements will begin. The master clock source, which will serve both as a two-way time transfer system timing input and a network time server, has been ordered.

- A decision has been made by the Diagnostics design team that a set of four output sensors will not share the input of quads (of four beams) from adjacent bundles. The decision not to share was made due to the concomitant complexity of the relay optics and the lack of space that would be available for installation and alignment. Other methods of data sharing between the quads of adjacent bundles are being considered.

- A proposal was made by the Diagnostics design team to use each output sensor diagnostic camera simultaneously for two beams. Options for beam sizes and beam combination techniques were evaluated. A preliminary analysis was made of the performance of the 1ω diagnostic near-field camera with the required larger aperture. Options for 1ω diagnostic tower and relay beam layouts were considered; a layout was chosen as a compromise between minimizing potential damage problems and equalizing relay lengths. This new configuration eliminates the crossover beams, simplifying the component mounting requirements under the TSF vessel and improving access.

- The prototype large-aperture deformable mirror (DM) was tested on Beamlet this quarter. The purpose of the Beamlet tests was fourfold: (1) Assure that the DM survives flashlamp exposure with no adverse prompt effect due to electromagnetic interference (EMI) or thermal expansion and with no structural or cleanliness degradation due to flashlamp ultraviolet exposure to the epoxy. (2) Acquire data from which a Beamlet propagation model can be validated for wavefront and focus spot performance. This validated model can later be extrapolated to the NIF configuration and beam size. (3) Investigate the focus spot performance in the early cavity pinholes. (4) Test the NIF wavefront controller prototype on Beamlet. The DM was inspected after 12 Beamlet shots and showed no apparent degradation or discoloration. Also, the DM showed no evidence of adverse prompt effects due to EMI or thermal expansion.

- The target chamber Request for Proposal was released on January 27, 1997, to five potential offerors. Updating of drawings is ongoing through the Title II engineering phase, with the goal of releasing the package to the successful bidder in June. Vendor bids are due April 23, 1997.

- Further redesign of the target chamber has been done to accommodate last-minute requests for more diagnostic ports and an access port for the first-wall-servicing robot.

- Continuing work was done on assessing the cost and performance of hot-pressed B_4C and Al-B_4C cermet (metalized ceramic) for the first wall. A small R&D contract was developed with a potential cermet manufacturer to develop a cermet that meets NIF cost and performance criteria. X-ray fluorescence analysis was done on new cermets and hot-pressed B_4C to quantify whether they would meet performance specifications.

- We completed a preliminary investigation into the effects of the proposed new color separation grating on beam dumps. The current locations for the beam dumps appear to be satisfactory, and a nominal size of 1 m $\times$ 1 m (possibly just

over 1 m in one direction and just under 1 m in the other) should handle the first five orders of 1ω and 2ω light.

Optics Technology

- Schott Glass Technologies completed the construction of a 13,000-ft^2 building to house the NIF-size prototype of the continuous melter and installed melting and annealing equipment. A melting campaign is scheduled to begin in late April, with results available in the summer. A full-size BK-7 analog, continuously melted and formed, met NIF specifications.
- Hoya Optics completed fine annealing of continuously melted laser glass formed at half-scale; all properties except homogeneity met NIF specifications. Hoya received a building permit from the city of Fremont for its NIF laser glass facility and is moving ahead with the design. Facility construction will begin this summer and will be completed in FY 1998.
- LLNL grew a 51-cm KDP boule using rapid growth technology, demonstrating the size needed for the NIF second-harmonic generation crystals (i.e., Pockels cell crystals demonstrated in FY 1996). Improved platform design to improve crystal quality and minimize stresses is continuing and will be demonstrated in July.
- The Optics Technology group demonstrated new coating source material at each of the coating vendors, which will improve the spectral performance of polarizers. The damage threshold has been qualified on subscale parts; full-scale parts will be tested beginning in late April.

Upcoming Major Activities

During the third quarter of FY 1997, the NIF Project will begin its transition from strictly design to the initiation of Conventional Facility site work, the start of Special Equipment procurement, and the start of vendor facilitization in Optics. Site Preparation work will begin in April and should be completed in July, and the Site Excavation contractor was mobilized in June. In Special Equipment, the selection of the contractor for the Target Chamber should be completed, and award is planned for early August. In Optics, the facilitization contract for the amplifier slab fabrication facilitization should be awarded. Plans are also taking shape for the NIF Groundbreaking Ceremony, which will be held in May to mark the beginning of construction on the NIF site.

Nova/Beamlet/NIF Updates April–June 1997

R. Ehrlich/S. Burkhart/S. Kumpan

Nova Operations

Nova Operations performed 258 full system shots, resulting in 289 experiments during this quarter. These experiments supported efforts in ICF, defense sciences, university collaborations, laser sciences, and Nova facility maintenance. The shot rate was significantly above average this quarter, primarily due to increased reliability as a result of added maintenance time in January. Nova Operations was able to maintain a high shot rate while lending personnel to Beamlet and National Ignition Facility (NIF) to assist in the completion of project milestones.

Installation of the hardware required for "beam phasing" on Nova was completed in preparation for the initial experiments in early July. Beam phasing will provide the capability to irradiate indirectly driven Nova targets with two rings of beam spots on each side for studies of time-dependent second-Legendre and time-integrated fourth-Legendre flux asymmetry control. The timing and pulse shape of the outer rings of beams illuminating the targets will be controlled independently from those of the inner rings. This is achieved by propagating the pulse from the back-lighter pulse shaping system down one spatial half of each beamline, while propagating the main pulse shape down the other half. When slightly defocused on target, the beam halves make two separate rings of spots on each side of the target.

The Petawatt project successfully completed the first two series of shots onto targets in the new Petawatt target chamber during this quarter. These shots placed up to 520 J of light on target in 5–20-ps pulses with a focal spot diameter of approximately 14 µm FWHM (for the Fast Ignitor project). Diagnostics on the Petawatt target chamber worked well. The sources of hot electrons and their heating effects were explored with x-ray spectroscopic and neutron production measurements. The peak irradiance achieved during these shots was about 10^{19} W/cm^2. Peak irradiances of up to an order of magnitude higher are expected in the next quarter with pulses as short as 500 fs.

Two significant target diagnostic capabilities for experiments in the ten-beam chamber were added this quarter. The 4ω probe beam was successfully tested and implemented on target shots. Also, the capability to delay beamlines 7 and 8 for up to 100 ns for x-ray backlighting of targets was added and successfully used.

Beamlet Operations

Beamlet completed a total of 61 system shots during 33 shot-days this quarter, with experiments on 1D beam smoothing by spectral dispersion (1D-SSD), spatial filter pressure tests, and pinhole closure. These experiments are all directed towards resolving scientific and engineering issues for the NIF. In addition, a number of system upgrades were completed. The highlights of these experiments are as follows:

- Concluded the 1D-SSD campaign that began in the second quarter of FY 1997. We reached 70% of the NIF red-line B-Integral with 1D-SSD, observing no unexpected effects. The experiments were concluded at this level to limit the fluence within the laser cavity until improved spatial filter lenses could be installed.
- Performed measurements on the allowable spatial filter background pressure for NIF. The Beamlet beam was resized to the correct $f/\#$ to simulate both the NIF cavity and transport filters.
- Made detailed pinhole closure measurements for various types of pinholes, including the standard "washer" type, offset leaf, and cone pinholes. This was done using time-resolved diagnostics, including a streaked pinhole interferometer and a gated optical near-field imager.

- Activated the NIF prototype wavefront controller, using the same hardware and software used in the second quarter for the large deformable mirror tests.
- Mounted a major engineering effort to conclude the final optics "Test Mule" installation. Initial thermal tests were completed with the Test Mule at vacuum.

Early in the quarter, we completed 6 shots on 1D-SSD at high power, using 200-ps and 1-ns pulses. B-Integral effects during SSD operation were not observed to be a problem, although we only reached 70% of the NIF red-line fluence, which is below where we expect to see major problems. The testing was concluded to avoid damaging the temporary lenses on the system, which were installed until we could obtain the replacement high-damage lenses.

In April, we installed the upgraded NIF deformable mirror controller in place of the original one that was on Beamlet since initial activation. The new system has advantages in maintenance and reliability and gives the NIF design engineers experience with the controller on a NIF prototypical system (i.e., Beamlet).

We performed 25 shots investigating effects of spatial filter pressure on output beam quality. The purpose for this series was to set the requirements for background pressure in the NIF cavity and transport spatial filters. The experiments were performed by bleeding air into Beamlet's transport spatial filter to reach specified background pressures in the range from 10^{-5} Torr to 10^{-3} Torr. At each pressure we fired a series of square 1-ns shots at increasing energy and determined beam perturbation by inspecting the output near-field beam profile. Simulating the NIF cavity spatial filter was simple; it has nearly the same $f/\#$ as Beamlet. However, to perform experiments relevant to the NIF transport cavity, we inserted a special beam apodizer in the front-end to shrink the beam to an effective $f/80$ on Beamlet. Beam breakup threshold for the NIF cavity and transport were measured at 6 mTorr and 2 mTorr, respectively.

Following the background pressure tests, Beamlet performed an 18-shot series on pinhole closure and backscatter. The goals for this pinhole series were as follows:
1. Determine the pinhole loading.
2. Measure closure time and phase shift at closure for the offset leaf pinhole.
3. Perform initial experiments on cone type pinholes.
4. Compare planar, offset-leaf, and cone pinholes with regard to back reflections.

Offset-leaf pinholes are a longitudinal dispersed variant of a square pinhole, where the four sides are offset to prevent plasma interaction between each of the sides. They were tested in both the square and diamond orientations using Ta blades. The ±150-μrad square oriented

pinhole remained open for a 0.3-TW, square, 20-ns pulse, but closed at ~18 ns into a 0.43-TW pulse. The ±100-μrad, square-oriented offset-leaf closed at 10 ns during a 0.05-TW pulse, while the same pinhole, diamond oriented, remained open for 20 ns at 0.10 TW.

The most promising pinhole is the cone pinhole, which has a cone angle of about twice the converging beam. The ±100-μrad cone pinhole stayed open for 20 ns at 0.14 TW, although it closed when the power was increased to 0.17 TW. The NIF foot pulse is between 0.14 and 0.17 TW. A dramatic advantage of the cone pinhole is its near-total lack of back reflection, as discussed further below.

The pinhole backscatter experiments were performed with the following goals:
1. Determine the source of back reflections.
2. Compare the different pinhole geometries for backscatter performance.

Previous data suggested that the source of back reflection was the pinhole edges, especially if the final pinhole edges could be imaged back through the cavity pinholes. For diagnostic purposes, the pinhole plane was imaged in the west cavity diagnostics, and we clearly observed pinhole edge back reflection. The cone pinholes suppressed this by more than a factor of 10. Back-reflected energy from the cone remained insignificant at 3.5 TW, the highest power tested, which is a great advantage to injection mirror longevity. However, we did observe a large back reflection from the on-axis region of the pinhole for minor postpulses, underscoring the importance of controlling postpulses on the NIF.

May through mid-June was an intense period of activity to complete the "Test Mule," in which we will test NIF prototype final optics to high fluence and determine cleanliness requirements. The Mule consists of a temperature- and cleanliness-controlled vacuum chamber with a large access door and internal optical table for supporting the integrated optics module and final optics cell. While the chamber was put in place in April, a significant amount of work was required to install thermal controls, vacuum systems, and clean rooms. This was completed in June, and the system was successfully pumped down with window installed. Initial tests were performed on thermal performance, including direct and infrared camera measurement of the vacuum window temperature. The final week of June was spent on focal plane diagnostic alignment. We plan to install the final optics in early July, closely followed by system shots.

National Ignition Facility

During the third quarter of FY 1997, the NIF Project began its transition from strictly design to the initiation of conventional facility site work, the start of special equipment procurement, and the start of vendor faciliti-

zation in optics. Site preparation work began in April and will be completed in July, and the site excavation contractor was mobilized in June. The selection of the contractor for the target chamber was nearly completed, and will be awarded in July. The contract for the amplifier slab fabrication facilitization was awarded to Zygo Corp. in May.

There were no Level 0,1,2,3 milestones due during the third quarter. There were twelve Department of Energy/Oakland Office (DOE/OAK) Performance Measurement Milestones due; ten were completed within the quarter; and the other two (target area building shell, 100% design submittal, and optical design mid-Title II 65% review) have been completed as of the writing of this report.

The *NIF Project Execution Plan* (PEP) was updated, and the draft, including the updated project data sheet, is now being reviewed by DOE. The PEP is now consistent with the Level 0 Baseline Change Control Board (Secretary of Energy) action of January 1997, and with the detailed Project rebaseline prepared during the second quarter of FY 1997.

The major event for the third quarter was the Ground Breaking Ceremony, led by the Secretary of Energy and attended by approximately 2000 interested individuals, including distinguished members of Congress, the Department of Energy, the Department of Defense, the scientific community, the University of California, LLNL management, the Mayor of Livermore, national ICF Program managers, NIF Project personnel and their family members, and members of nongovernmental organizations.

The key assurance activities for the third quarter—to resolve the *Fire Hazards Analysis* recommendations, conduct the *Preliminary Safety Analysis Report* audit, conduct contractor audits, and oversee construction safety—are on schedule. Work on permits and National Environmental Policy Act determinations for soil reuse, along with the monitoring of the *Mitigation Action Plan* commitments, continues. As a special assignment, NIF Assurances supported DOE/HQ on the litigation of the *Programmatic Environmental Impact Statement for Stockpile Stewardship and Management*.

Site and Conventional Facilities

Progress to date is satisfactory on Title II design and bid and construction activities for Construction Subcon-tract Packages (CSPs) 1 through 4. Title II Conventional Facility design is critical path, driven by conventional facility construction package bid and award schedules, and special equipment technical performance requirements as described in interface control documents.

Construction is proceeding on schedule and within budget. The site preparation contractor will complete in July, and the excavation contractor is mobilized on-

site and working. Implementation of the Owner Controlled Insurance Program has proceeded successfully on schedule, in budget, and to the performance standards established for this service.

Laser and Target Area Building (LTAB) Design. The following activities were completed during the quarter:
- Delivered CSP-3 (Target Building Mat and Laser Bay Foundations) and CSP-4 (Laser Building Shell) bid documents to Procurement.
- Completed Title II 65% design review for CSP-6 (Target Area Building Shell) and Title II 65% design review for CSP-9 (Laser Building Buildout, Site and Central Plant).
- Received Title II 100% design documents for CSP-9.

Optics Assembly Building Design. The Project completed Title II 100% design review for CSP-5.1 (Optics Assembly Building).

Construction Packages. There are many construction packages in various stages of completion as of this quarter:
- Construction on CSP-1 (Site Preparation) is currently 90% complete and planned to complete on schedule in July.
- Parking lots associated with the work were turned over on schedule to allow completion of the fencing of the construction site as planned.
- The contract for CSP-2 (Site Excavation) was bid and awarded this quarter, and the Notice to Proceed given on May 28.
- The excavation contractor mobilized on-site on June 19, and that work is currently 5% complete.
- The Invitation for Bid packages for CSP-3 (Target Building Mat and Laser Bay Foundations) and CSP-4 (Laser Building Shell) were issued.
- Two addenda have been issued for CSP-3, and bids are due late in July.
- CSP-4 bids are due early in August.

Special Equipment

The third quarter included much activity in the special equipment area.

Optical Pulse Generation. Commercially produced fiber amplifiers were received and characterized during this quarter. After some modifications by LLNL scientists, the commercial units demonstrated the critical NIF performance characteristics. Major procurements were placed for the prototype preamplifier module, including laser diodes, power electronics, and most commercial off-the-shelf hardware. An updated multipass amplifier cavity design was operated successfully with single-pass gain in excess of 25, exceeding the NIF requirements.

Amplifier. Dramatic progress was made during this quarter on the amplifier prototype laboratory activation. Preliminary tests were completed to assess the cleanliness performance of the NIF bottom-loading concept for the first time, using full-scale hardware and flashlamp light exposure. The results are very promising and indicate that there are no fundamental flaws in the amplifier installation and maintenance strategy. In addition, the first gain measurements were completed on the prototype amplifier in an effort to activate the large-area diagnostic system.

Pockels Cell. The 2×1 plasma electrode Pockels cell prototype was activated during this quarter, and its performance exceeded NIF requirements. The use of external currents to improve the plasma uniformity was demonstrated, and found to be crucial to meeting the NIF switching efficiency requirements. This system of "plasma spreading" is now being incorporated into the NIF baseline design. Drawings were completed and hardware ordered for the 4×1 mechanical and physics prototypes. The mechanical prototype will be used for testing maintenance strategies, kinematic mounting and alignment techniques, as well as transport interfaces.

Power Conditioning. Initial tests were completed during this quarter to validate the 500-kA switch (ST-300 from Primex Physics International). Four switches were tested, each with slight modifications to the design, in order to identify performance sensitivity. The results were quite positive: the switch appears to survive 1000 to 2000 shots at full power before requiring refurbishment, and no prefires were experienced other than those induced to gather safety factor data. A second switch design, from a different manufacturer, was also tested for 2500 shots at NIF operating conditions. The switch performed flawlessly, and inspection indicates that its lifetime might exceed 10,000 shots. Other design progress included a preliminary design of a solid-state trigger generator for the switch, which was also prototyped and operated successfully. The strategy for grounding the amplifier support structure to provide good bonding during a failure of the amplifier frame assembly unit insulation was investigated. Initial designs of this bonding system required increasing the mesh frequency in the LTAB slab to reduce the inductance of the system. Recent analysis indicates that enclosing the cables in the cable tray would have better performance than an improved slab ground grid. Therefore, a change to the LTAB design to increase the grounding mesh density in the slab is not likely to be required.

Beam Transport Systems. Mid-Title II (65%) design was formally reviewed by an independent team of engineers from within and outside the NIF project. All four subsystems were presented in separate sessions, and action items were recorded. No issues were identified that would result in a delay of Title II design activities. A postreview effort was initiated to aggressively pursue all remaining interfaces to facilitate the completion of Title II. The long-lead procurement of stainless steel for spatial filter vacuum vessels was initiated with the on-schedule release of the first Request for Proposal. A recent engineering change to improve target irradiation symmetry during shots with subsets of beams has been incorporated into structural details without affecting the design schedule; the change affected the location of switchyard mirrors.

Integrated Computer Controls System (ICCS). There has been excellent progress in Title II design of the ICCS. The first of the Mid-Title II (65%) reviews, the supervisory software frameworks 65% design review, was completed in June and featured results obtained from the prototype. The review covered the development process, the object-oriented architecture, important CORBA test results, and the simulation program plan. Review documentation featured the first releases of seven (of about 30) software design descriptions to be prepared for the project. The next iteration of the software will incorporate database functionality and advanced error detection and recovery. Comments from the review team are pending. An overview document called the *Integrated Computer Control System Architectural Overview* (NIF-0002479) was prepared to assist the 65% review team in understanding the model-driven approach used in the ICCS. Sections of the document introduce the layered control system model, NIF software applications, computer and network hardware infrastructure, common object request broker architecture distribution, software development tools and environment, the abstract supervisory software framework, and software deployment. This overview document will be published on the LLNL-intranet and updated periodically to incorporate the latest summary information.

Integrated Timing System. The Two-Way Time Transfer Demonstration System has undergone environmental testing and a manufacturer-supplied upgrade while at Jet Propulsion Laboratory. The temperature effects on both transmission path length and terminal equipment were characterized. Upgrades addressing the long-term stability are planned for next quarter. In support of Local Timing Distribution development, measurements were made to characterize commercial delay generators operating in a clock-synchronous trigger mode. Results were excellent, with jitters less than 10 ps RMS and 15-hr stability of 20 ps RMS. The system will be delivered to LLNL in early July for continued development and testing.

Mirror Mounts. Testing continued this quarter to determine the mounting details for switchyard and target area mirrors that need to be supported from the

backside. The specifications and cost of designs that are robust enough to withstand the target-backscattered UV light are being investigated.

Optical System Modeling. A detailed optical model (using commercial lens design software) has been completed. The model is wholly consistent with the optical configuration and includes the capability to simulate the alignment system operation. The model allows verification of such things as clear apertures, end-to-end wavefront error, and installation sensitivities.

Laser System Ghost Analysis. A nonsequential ray trace model for the main laser system with spatial filter beam tubes and vessel walls has been constructed. This model was used to calculate the ghost-reflection beam fluences inside the spatial filter beam tubes and to determine the locations of baffles and absorbers. The spatial filter vessel design is very compatible with the stray light management approach.

Final Optics Assembly. An engineering change request was approved in May for the final optics configuration. This changes the focal length of the focus lens from 7 m to 7.7 m, which enables the mechanical design to accommodate a line-replaceable unit (LRU) for a single beamline instead of an entire quad (four beams). This will greatly improve maintenance and cleanliness of the LRU. In addition, a contract for a prototype integrated optics module (IOM) was awarded. The IOM is the LRU for final optics, and includes a vacuum housing, vacuum window mount, and the interface to the beam tube and the water-based thermal control system. Initially this hardware will allow for testing of the pump-down and evacuation concept as well as the thermal stabilization system. Follow-on testing will include integration of this hardware with the final optics cell and its actuation system.

Target Chamber Review. A portion of the Mid-Title II (65%) Design Review for the target chamber will be held on July 10, 1997. This review covers the design for the aluminum chamber so that it can proceed to fabrication. The 65% review for the remaining portions of the target chamber task (e.g., the first wall and the beam dumps) is scheduled for November 1997.

Target Chamber Procurement. During this period, the target chamber proposals were received from four companies. The proposals were reviewed by a technical evaluation team. Two vendors were selected for negotiations, and a final selection was made. A contract was placed with Pitt-Des Moines, Inc., in early July.

Neutron Spectrometer. An engineering change request for the neutron spectrometer (NS) was accepted by the Level 4 (Engineering) Change Control Board. This request added to the project construction all portions of the NS (cone) that are interior to the switchyard and target bay area, and that portion of the construction exterior to the building that is needed to not preclude the construction of the external portion of the NS. This was accomplished with no increase in cost and no impact to the schedule. A much simpler design for the interior and exterior portions of the NS was developed and was the driving factor in accomplishing the request.

Data Acquisition System. The layout of cable trays and penetrations in the shield wall and floors for the Data Acquisition System is proceeding. Penetration information for present and future diagnostics has been included in the penetration spread sheets and turned in to the architect/engineers (Parsons). The classification report by Parsons' consultant was reviewed, and comments were returned. Details on the security interface control document are being worked out with the appropriate people at Parsons. A preliminary schedule from the British Atomic Weapons Establishment has been received; they are generating a detailed schedule for the diagnostic manipulator. Work has continued toward finishing the target area portion of the *NIF Grounding and Shielding Plan*.

Start-Up Activities

Beam Symmetry. An engineering change was proposed by the Start-up team and approved by the Level 4 (Engineering) Change Control Board. It modifies the arrangement of a few beam tubes and mirrors in the switchyards and target area. This will allow maximum flexibility in the use of subsets of laser beams during initial NIF testing and long-term facility operations by users, thus permitting the increase of shot rate on target with beam subsets while maintaining symmetrical irradiation.

Operability Model. A status review of the operability model, a discrete-event simulation model, was held during May. Initial estimates of LRU random failure rates and scheduled maintenance requirements are provided as inputs to the simulation. Using these estimates, preliminary simulation results from the Operability Model address two facility issues: (1) estimation of the operations staff that correlates to the maintenance rates and (2) assessment of shot availability versus staffing. During Title II, the model will incorporate updated information on reliability, availability, and maintainability; updated timeline information; identification of types of people for each task; and more detailed characterization of failures and their impact on the shot cycle.

Operating Procedures. A draft *Procedure for Writing NIF Operating Procedures and Training Documents* has been prepared and is being reviewed by start-up personnel. The document outlines a proposed process for developing written operations procedures and training qualifica-

tion documents for NIF. It includes a description of the approach chosen, a plan for implementation, and estimates of time and resources required. Examples of document templates, titles, and contents are given. Operations personnel at Lawrence Berkeley National Laboratory and Stanford Linear Accelerator Center were consulted during preparation of this draft.

Optics Technology

Optics Vendor Facilitization. The schedule for bidding and negotiating the optics facilitization contracts has been maintained with respect to the NIF schedule. Moore Tool Company was awarded a contract in June for the NIF crystal diamond turning. Negotiations for the fused silica facilitization contract began in June, and are expected to be completed in July. Negotiations for the mirrors, windows, and polarizers flats finishing and lens finishing contracts continued through June, and are expected to be completed in July. Work is continuing on the glass melting facility at Hoya, which is scheduled to be completed in October. Zygo Corp. was awarded the contract for amplifier slab finishing facilitization in May.

KDP Crystals. In the KDP rapid growth program, conditions have been identified in subscale tanks that produce the needed aspect ratio for NIF-size boules. The first test at full size will begin in July, with the results available in August. Rapid-growth KDP crystals grown from ultrapure material and continuous filtration at subscale yielded damage thresholds equivalent to the best Beamlet crystals, and above the NIF requirement. Continuous filtration has been added to a full-size tank; the run is scheduled to be complete in early August.

Optical Fabrication Development. The first of the Beamlet Mule focus lenses was produced in June, and damage tests at full aperture are scheduled for July. The second lens is still on schedule to be delivered in July. Initial damage tests of small, inspection-polished cerium-doped mirror substrates were encouraging. Subscale parts will be coated for damage testing in the first fiscal quarter of 1998. Full-size prototype mirrors from three U.S. sources were laser conditioned to the NIF fluence requirement for the transport mirrors. These mirrors will be installed in Beamlet in August.

Educational Outreach. LLNL signed an agreement with Monroe Community College in Rochester, New York, to begin a certificated optics fabrication program this Fall. This is expected to be a significant benefit to the NIF; it will provide trained workers that are needed in the optics fabrication businesses that supply components to the project.

Upcoming Major Activities

During the fourth quarter of FY 1997, the NIF Project will continue its transition from strictly design to the start of conventional facility site-work, special equipment procurement, and vendor facilitization in optics. Site excavation work will begin in August and will continue for several months. Also, the contracts for the start of building construction will be placed. In special equipment, several Mid-Title II (65%) design reviews will be held, and the contract for the target chamber will be placed, along with a contract for large stainless steel plates for the spatial filters. In optics, the contracts for the amplifier slab fabrication facilitization and for lens and window fabrication will be awarded.

Nova/Beamlet/NIF Updates
July–September 1997

R. Ehrlich/S. Burkhart/S. Kumpan

Nova Operations

Nova Operations performed 239 full system shots, resulting in 246 experiments during this quarter. These experiments supported efforts in ICF, Defense Sciences, university collaborations, Laser Sciences, and Nova facility maintenance. The Nova Operations group continued to transfer manpower to support NIF project efforts and to prepare for reduction from a 2- to a 1.5-shift operation at the beginning of the next quarter. With Nova operating from 6:30 a.m. to 8:30 p.m., Monday through Thursday, we expect to achieve an annualized rate of over 700 experiments.

Plans to reduce the routine optical power limits on Nova were formulated and agreed upon by a group of Nova users and operations management. To reduce the rate of optical damage to optics in the laser chain and the target chamber, we reduced the maximum optical power from 6.75 to 5.5 TW per beamline at the first harmonic starting at the beginning of September. The resulting decrease in damage rate will allow us to continue to operate Nova until the proposed July 1999 shutdown with a budget that is continuing to decrease.

Reducing the optical damage will also help us to comply with the anticipated new Laboratory guidelines for operating systems with vacuum-loaded optics without seriously reducing our shot rate. These new guidelines will decrease the size of allowable damage sites on vacuum-loaded optics. In response, we have increased the rate at which we inspect optics for damage and changed the procedures for which personnel access areas near vacuum-loaded optics on Nova. Gate valves were installed on the cryogenic vacuum pumps on the final spatial filter of each beamline; this increases the efficiency with which we can pump the filters after venting to allow safe access near the vacuum-loaded lenses.

Three weeks of successful Petawatt experiments were conducted during this quarter. In addition to use in experiments related to fast ignitor physics, the Petawatt laser demonstrated success in high-resolution radiography of dense objects ($\rho r \geq 150$ g/cm^2) with photons >1 MeV. The extreme brightness and short duration of the Petawatt pulses offer a tool that may be a new alternative to conventional electron accelerator bremsstrahlung hard x-ray sources. Experiments will continue to determine the maximum achievable photon flux.

The Nova laser facility drew many thousands of visitors during the Laboratory's two-day family open house. Visitors toured through the laser bay, switchyard, ten-beam target bay, and diagnostics loft during what will likely be the last time that the public will be able to view Nova. The disassembly of the Nova two-beam target bay has been scheduled to start in mid-November, with a target time of early January to turn over the facility to the NIF project.

Beamlet Operations

Beamlet completed a total of 60 system shots during 30 shot days this quarter, completing Phase I of the "Test-Mule" frequency-conversion experiments. These were the first large-aperture frequency-conversion experiments in vacuum using the NIF prototype final optics assembly. In addition to those tests, Beamlet began a series of spatial filter pinhole-closure experiments with a 20-ns square and shaped NIF laser pulse propagated through a final 100-μr cone-type pinhole. The operations and experimental highlights are as follows:

- Completed installation and alignment of the Test-Mule vacuum vessel within which we test the scientific prototypes and concepts for NIF final optics. The 2-m-diam by 2-m-long vessel,

including a 1-m-square window, emulates the NIF integrated optics module.

- Completed Test Mule thermal stability measurements demonstrating ±0.1°C and a Test Mule window cooling $1/e$ time of 120 m.

- Installed the final optics cell (FOC), which contains a KDP doubler crystal and a deuterated KD*P tripling crystal. For the Phase I tests, we continued to use the wedged final focus lens in a separate mount as it was used in previous frequency-conversion campaigns. Subsequent experiments (Phase II) will utilize an unwedged (centered) lens mounted in the FOC.

- Demonstrated performance of the frequency converter with full edge support, which is the NIF baseline design. Conducted most of the 50 shots at 200 ps, plus several at 1 ns with drive irradiances to 5 GW/cm². Reduced efficiency relative to theoretical was similar to FY96 experiments where the dominating influence was crystal nonuniformities. Subsequent tests will utilize new KDP from NIF production boules.

- Performed the first 10 of the Pinhole closure tests with 100-μr and 150-μr spatial filter pinholes. The first experiments were performed up to 3.6 kJ at 20 ns through a 100-μr stainless-steel cone. The purpose for this series was to obtain scaling for pinhole closure between temporally square and shaped pulses.

The Beamlet Test Mule was completed in June, and we successfully pumped it to high vacuum near the end of the month. The first task was to verify the thermal stability because frequency conversion with KDP is quite sensitive to temperature variations. To maintain the Test Mule at a constant temperature, it was painstakingly wrapped in Q3 with a maze of aluminum piping with controlled-temperature water circulation and then wrapped with an insulating blanket. Mule surface and water temperature were shown to maintain well within ±0.1°C, the engineering requirement.

The NIF physics prototype FOC and integrated optics module (IOM) were successfully tested under vacuum conditions in the Test Mule. The FOC is designed to hold the doubling and tripling crystals and the final focus lens, although for these tests the lens was mounted external to the cell. The cell resides in the IOM with stepper motors for alignment, and is the first LLNL use of full-edge-supported KDP crystals of this size. This series of experiments required two months during this quarter, much of it associated with diagnostic calibration and reactivation of the focal plane diagnostics (FPD).

Following IOM installation and pumpdown, we quickly found that the IOM stepper motors that control

FOC alignment put a great deal of heat into the FOC, up to +4°C in 48 hours, even though the three motors collectively dissipate no more than 1 W at idle. This is because of the radiative-dominated heat flow to the FOC in vacuum. We performed rod shot rocking curves to verify doubler alignment, then pumped the Test Mule to vacuum for diagnostic calibration. Numerous issues were uncovered during the calibration, as the FPD had not been operated for some time, most notable being contamination on some sol-gel antireflective coatings, which affected the energy balance. With diagnostic issues resolved, we took 16 shots for 1ω calibration, 23 shots for 2ω calibration and doubling efficiency measurement, and 19 shots for 3ω efficiency measurements. We used KDP and KD*P crystals fabricated for the original Beamlet campaigns in 1996, and measured doubling and tripling efficiencies similar to the previous campaign, efficiency-dominated by known crystal nonuniformities. Future frequency-conversion experiments will test crystals grown for NIF, including fast-growth crystals. Finally, we measured the 3ω focal spot, which was within 15% of meeting the the the U.S. DOE's Stockpile Stewardship and Management Program requirements.

During this quarter, we replaced the last of the Beamlet fused quartz spatial filter lenses with fused silica versions, some of which were cut from the original round lenses to square, which nearly doubles their resistance to laser induced fracture. Even these lenses are temporary, as we are fabricating thicker (46-mm vs 35-mm) lenses to replace them in early FY98. Beamlet can now operate with no special fluence/intensity restrictions.

The design and fabrication of the offset mirror tower is proceeding towards installation in FY98 first quarter. The Beamlet FPD was designed to accept a beam from a wedged final focus lens, but the NIF baseline is an untilted lens that requires us to offset the beam in order to test that configuration. The beam will be offset and pointed by 2.2° to maintain the FPD alignment with minimal disruption. Concurrent with this is the testing of high-damage-threshold transport mirrors relevant to NIF mirror development.

The final week in FY97 fourth quarter was spent testing new pinhole concepts for NIF. We inserted a 100-μr cone-style pinhole and propagated square pulses up to 3.9 kJ to measure the onset of pinhole closure. Measurements were made using both a pinhole plasma-detecting interferometer and a gated near-field optical imager to understand the extent and effect of pinhole plasma on the propagated laser beam. These tests will continue into FY98, including experiments with NIF shaped pulses to higher fluences.

National Ignition Facility

Overall progress on the National Ignition Facility (NIF) Project remained satisfactory for the fourth quarter of FY 1997. The major site excavation work was completed nearly on schedule, despite unexpected site conditions, and the contractor was demobilized until needed for the backfilling operations. Awards were made for Conventional Facilities Construction Subcontract Packages 3, 4, and 5 at bids several million dollars less than budgeted. In Special Equipment, five Mid-Title II (65%) Design Reviews were held during the fourth quarter, and two major procurement contracts were awarded, for the target chamber and the spatial filter stainless steel. The optics vendor facilitization contracts for laser glass melting, fused silica, and lens and window fabrication were awarded in the fourth quarter also.

There were no Level 0, 1, 2, 3 milestones due during the fourth quarter. There were 13 Department of Energy/Oakland Office (DOE/OAK) Performance Measurement Milestones due, and all were completed. All 34 DOE/OAK Performance Measurement Milestones due in FY 1997 were also achieved. The FY 1998 DOE/OAK Performance Measurement Milestone plan was submitted to DOE/OAK in late September. It specifies approximately 100 milestones covering all aspects of the NIF Project in FY 1998.

Revision 1 of the *NIF Project Execution Plan* (PEP) was approved at Level 1 and issued to controlled distribution in August. The revision contains the revised baseline cost and schedule plans according to the Level 1 directives of January 1997.

Key assurance activities to support litigation activities and the NIF Construction Safety Program, to initiate the *Final Safety Analysis Report*, to conduct assurance audits (e.g., construction safety, *Preliminary Safety Analysis Report* commitments), to prepare for the DOE-EH Assessment, and to support environmental permits are on schedule.

Site and Conventional Facilities

The Title II design effort on Conventional Facilities peaked during the fourth quarter, with all Construction Subcontract Packages (CSPs) at either 100% Issue For Bid or already awarded, with the exception of CSP-6/10, Target Area Building Shell and Buildout, and CSP-11, Landscaping. Title II design on CSPs 1, 2, 3, 4, and 5 have been offered for bid and contracts awarded. CSP-9, Laser Building Buildout & Central Plant, which is the largest of the NIF construction packages, will be issued for bid in October and awarded in December. CSP-6 and CSP-10 will be bid as one contract (CSP-6/10) in February 1998.

NIF site construction has proceeded with a nominal schedule slippage of two weeks due to unforeseen soil and site conditions: (1) more soil was hauled off site than planned because it was not suitable for stringent NIF requirements for load-bearing compaction, and (2) dumped capacitors were encountered in the excavation of the NIF building footprint.

Construction Packages. The construction work and project management of prequalified contractors has proven to be reliable and predictable to date, and the NIF continues to base construction success on selecting the best contractors. The site preparation contractor (CSP-1) has completed work and was demobilized. The site excavation contractor (CSP-2) completed the major excavation for the NIF in this quarter and was also demobilized until required for backfilling work. The Target Building Mat and Laser Bay Foundations contractor (CSP-3) is mobilized and working on major, underground concrete structures that will support NIF buildings.

Special Equipment

The Title II design continued in the fourth quarter, with the completion of five Mid-Title II (65%) reviews. Also, major procurements began with the award of contracts for the target chamber and stainless steel for the spatial filters.

Optical Pulse Generation. The optical pulse generation software subsystem design requirements (1.3.1) were revised to reflect the existence of the 1:4 split in the preamplifier beam transport section of the beamline and to update the design code requirements. The performance of the redesigned multipass amplifier cavity in the preamplifier module was validated, including the extraction of a >25-J pulse with temporal distortion, meeting the NIF requirements. Title II design efforts to package this design consistent with the NIF space constraints are in progress.

The ring oscillator prototype has been assembled and initial testing has begun. High losses in components and connections must be identified and corrected in order for the system to demonstrate all requirements.

Amplifier. The Amplifier Module Prototype Laboratory (AMPLAB) prototype facility was activated over the past quarter, including obtaining gain measurements over the full aperture of the 1×4 column amplifier. Initial results indicate that the amplifier gain requirement is achievable. Activation of the wavefront measurement system is under way, including the use of a Hartmann sensor and Twyman Green interferometer in place of the CEL-V-provided CILAS interferometer, which is delayed. Initial results indicate that the gas motion in the beam path adds a substantial wavefront error and that "double-pulse" interferometry will be required to distinguish the pump-induced aberration in the slabs from the effects of turbulence in the cavity.

Testing of prototype lamps with doped electrodes on both ends demonstrated substantially reduced sputtering. The flashlamp specification will be modified to require this feature. Blast-shield seal tests accumulated over 7500 full-fluence shots with only minor degradation to the seal and no change in leak rate. This data provides confidence in the proposed approach, which will be tested at full scale in FY 1998.

Pockels Cell. Parts for the 4×1 plasma electrode Pockels cell (PEPC) prototype have nearly all arrived, and assembly is in progress for the cell and the diagnostic system. The prototype plasma pulsers have been assembled and tested and perform as expected. The commercial hardware and software selection process for the PEPC controls is complete. The architecture has changed since Title I from a remote I/O-based design to one that uses centralized front-end processors to house the interface hardware. This will reduce the number of required I/O channels and, ultimately, the cost of the system.

Power Conditioning. Assembly of the prototype capacitor module is nearly complete, with full-power testing scheduled to begin in October. Preliminary tests are in progress, including characterization of switch trigger voltage distribution in the ballast enclosure. A seismic analysis of the capacitor module was completed, which validated the rack design but indicated that changes are required in the design of the floor connection details. Switch testing highlights included a 1431 shot run on a PRIMEX ST-300 switch with a 0.242-in. initial gap and a steel housing. This implies that the switch might last nearly two years on the NIF without refurbishment. The Maxwell rotating arc gap switch accumulated over 4000 shots without a misfire, and efforts are under way to determine the relative cost of this potential backup. Testing of development capacitors resumed in late July. Second-version capacitor tests (from all manufacturers that have supplied second versions) have also been completed. The control and monitor system design was completed, and the custom waveform digitizers were fabricated and tested.

Beam Transport System (BTS). Significant detail design progression, several innovative design solutions, and value-engineering efforts marked progress in this quarter. Interface control documents were frozen following the Mid-Title II (65%) review, and drawing production began. The checking process has begun on the first complete detail drawings.

BTS led the integration of a 1-in. rise in the entire laser bay chain from laser mirror (LM)1 to LM4 to provide additional clearance for optics handling. All long-lead material orders for FY 1997 have been placed on time and under budget. Despite an increase of 300 tons over Title I design estimates, steel cost was contained through creative use of alternate lower-cost steel production

methods, without sacrificing quality. A major innovation on the switchyard structure mirror support resulted in a design that now accommodates a potential 1-in. settlement of the building while increasing the stability margin of the mirrors by 30%. Cost estimates for site preparation of the two construction lay-down areas were reduced, and environmental assessments indicated that these areas are suitable for use by BTS. A laser bay crane utilization study was completed recommending an additional bridge crane in each laser bay. An Energy Change Request proposing an additional bridge crane in each laser bay was approved at Level 3 (Project Office). A major optimization study of the amplifier upper support structure resulted in a lower-cost system that is easier to fabricate and maintain.

Integrated Computer Control System (ICCS). Title II design progress is satisfactory. The Mid-Title II (65%) Reviews for work breakdown structure (WBS) 1.5.1 (Computer System) and WBS 1.5.6.1 (Video Distribution System) were completed in a joint session; no major issues were raised by reviewers. The Mid-Title II (65%) Review for WBS 1.5.5 (Automatic Alignment System) was also completed; the review committee's summary report is expected in October. The supervisory application status review milestone was completed via a comprehensive presentation of the NIF shot life cycle. A status review was also held for the Integrated Timing System.

Distributed Control System Simulation. Preliminary results were obtained from the first of a series of performance and resource utilization simulations: a discrete-event simulation model of the computer system during system start-up. Scenarios of planned activity for system start-up from all software components are being constructed and assembled into a single stream. The scenario comprises the first complete draft of the deployment view that shows how all the ICCS software is distributed onto the computers. Beginning with power-up on the computers, all the steps necessary to initialize ICCS service on all the computers and related services are listed, and the dependencies among them are documented. Measurements will be taken on ICCS prototypes to derive data for validating the evolving simulation. Conclusions from computerized simulation runs will expose potential bottlenecks and allow refinements of interactions among planned software, hardware, and network resources so that the system requirements can be met. The ICCS simulation project status was described during the Computer Systems & Network Mid-Title II (65%) Design Review.

Optomechanical Systems. The prototype spatial filter (SF)4 lens cassette was released for fabrication in early September; a November delivery is projected. This prototype package will be used to verify that the mechanical design meets several of its key design

requirements (e.g., structural stability, cleanliness). Several vacuum seal concepts will be evaluated for ease of assembly, vacuum compatibility, and cleanliness.

Optical Design. The Mid-Title II (65%) review for optical design was presented during three one-half day sessions on July 14–15. Detailed information for main laser design, switchyard and target area transport mirrors, optics specifications, and large optics drawings were presented. Also discussed were the final optics, stray light control, and the injection system and other aspects of the optical pulse generation system.

The optical design model for the Preamplifier Beam Transport System (PABTS) was completed. There are 16 configurations because of the slight variations in path length under the transport spatial filter and in the switchyard. Significant progress was also made in finalizing the multipass amplifier layout in the PAM. Successful experimental results (reported under WBS 1.3.1) led to scientific and engineering consensus on the optomechanical layout and packaging. The optical configuration drawing should be ready for approval in the first quarter of FY 1998.

Detailed tables documenting the analysis of clear apertures and mirror sizes for the switchyard and target area mirror system were transmitted in August to LLNL for review by the optical design, optics manufacturing, and mirror mount design teams. Optical design models for all 192 beam paths have been created, which include 832 mirrors. Determination of final mirror sizes is ongoing based on the results of this analysis.

The optical design of the output sensor was presented at a Mid-Title II (65%) review on September 19; the relay optics system was also reviewed. This design is closely coupled with efforts in System Control (WBS 1.7) to build a prototype output sensor.

Final Optics Assembly. The integrated optics module (IOM) prototype (conventionally machined) was received in September. Also, a fabrication contract was awarded for an IOM manufactured by a casting process, which will be compared to the conventionally machined prototype. Objectives of the prototype testing include the vacuum outgassing characteristics of cast aluminum, suitability of surface finish for cleanliness control, operation of the thermal control system, and manufacturing cost.

The prototype IOM vacuum housing holds the vacuum window and the final optics cell (FOC), which is the precision mount for the harmonic conversion crystals and the focus lens. Objectives of the prototype testing include cleanliness, vacuum pump rates, thermal control system, and manufacturability.

Laser Control. Emphasis is shifting from discussion and evaluation of design options to making decisions for the final design and producing detail drawings. Only a few informal 30% or "status" reviews remain, and the first of the more formal Mid-Title II (65%) reviews was presented. Some prototype components are being tested, while others are in fabrication. Laboratory space is being prepared for assembly and testing of additional prototype components, and planning has started for eventual handling of production hardware.

An analytical modeling effort of the adaptive optic systems was begun. One goal of the work is to develop better computation models of the principal components in the wavefront correction systems, i.e., the deformable mirror, wavefront sensor, and closed-loop controller. The other main goal is to apply the optimized models to simulations of the entire laser system. This will enable the laser performance to be more accurately predicted and will enhance the ability to identify ways in which existing components can be improved, or additional components can be added, to obtain better overall performance. It has already been established that increasing the number of deformable mirror actuators or adding an appropriate fixed corrector in each beamline will reduce the attainable focused spot size. However, technology and cost constraints are also important considerations that must be evaluated.

Target Experimental Systems. The Title II design effort for the Target Experimental Systems has progressed satisfactorily during the past quarter. A significant accomplishment is the ordering of the aluminum by Pitt-Des Moines Inc. (PDM) for the fabrication of the NIF target chamber. The material will be shipped from the mill directly to France for forming. Forming is scheduled for mid-November.

Operations Special Equipment. Operations Special Equipment successfully completed nine informal reviews of prototyping procurements during this quarter. Several significant pieces of clean-room hardware were delivered and installed in the B432 prototyping clean room. The line-replaceable unit prototype canisters have arrived and are being installed for testing.

Start-up Activities

Integrated Project Schedule (IPS) Management. The IPS database has increased from 1200+ activities to over 9000 activities. The file has significantly more detail than the March 1997 rebaselined IPS. The Integrated Schedule team is in the process of integrating the Project milestones into the appropriate areas of the schedule based upon responsibility. The team also continued to work with Cost Account Plan (CAP) managers to finalize the detailed schedules required to support the CAP planning completion.

Start-up Planning. Recently, start-up planning has focused on the coordination of ICCS planning with start-up planning. A list of development laboratories is being generated for the purpose of ensuring that the computer controls have maximum opportunity for prototype testing of the controls system with actual

NIF hardware. The Optical Pulse Generation Lab and the Laser Alignment Lab plans were reviewed, and in both cases additional opportunities were identified for maximizing readiness for start-up. Another result has been an increased emphasis by the Front-End Processor Working Group to identify common equipment in their designs.

A draft list of operability and maintainability issues has been identified that could be used by operations personnel who are participating in the Title II design teams. Issues include assembly, installation and contamination control, electrical racks and cabling, transport vehicles, temperature stability requirements, and operational support facilities.

Optics Technology

The schedule for bidding and negotiating the optics facilitization contracts has been maintained, with minor slips having little or no impact on the overall NIF schedule. Following negotiations in July, Corning and Tinsley were awarded contracts in September for the fused silica and lens finishing facilities respectively (both were DOE/OAK Performance Measurement Milestones). Proposals for coatings facilities are due in October, with awards expected in the first quarter of FY 1998. Work is continuing on the glass melting facility at Hoya, which is scheduled to be completed in October, and the Schott development run will take place in November.

In potassium dihydrogen phosphate (KDP) rapid growth, significant success has been achieved with the growth of a 55-cm (lateral) crystal. The final 10 cm of growth showed no inclusions, proving out the most problematic part of the process. Additional crystals based on the new aluminum platform design will be grown in the first quarter of FY 1998.

Damage thresholds at 3ω continue to fall short of expectations for fused silica parts, despite significant advantages achieved in metrology and in finishing technology. While parts can consistently be manufactured to 6 in. in diameter with high-damage thresholds, problems still exist, and damage thresholds for full-size optics are lower than anticipated. Further work, focused on Tinsley Laboratories in Richmond, will be done in the first quarter of FY 1998 at both 6 in. and full scale.

Laser Glass. Raw materials (many tons) were shipped to Germany for powder processing in preparation for the Schott melting campaign. The development run is now scheduled for the first quarter of FY 1998.

KDP Crystals. The KDP Rapid Growth program achieved a major milestone by growing the largest rapid-growth crystal ever. The crystal was grown on an ultra-stiff teflon-coated aluminum platform. It grew to full size, even growing into the vertical support bars without spoiling the crystal or "crashing" the solution. All crystal surfaces were clear of inclusions for the final 10 cm of growth. While the crystal still does not have the internal quality needed for the NIF, the favorable results during the last, and most problematic, part of the growth phase were extremely encouraging. Additional aluminum platforms of large size to accommodate full-size NIF boules are currently being constructed. Analysis of optical absorption dependence on impurity level was completed, which showed that all absorption near the third harmonic is due to iron. This means that for optical performance, work must now be done on controlling the impurity level of a single element.

Color Separation Grating. The first full-scale color separation grating (CSG), which was made back in July, demonstrated a problem when it was coated with a sol-gel AR. The sol-gel degrades the optical performance by ~4%, causing 3ω light to be diffracted in a similar manner to the 1ω and 2ω light. A second full-scale CSG fabrication has now been completed, and etch depths appear ideal (the first part was off by 20 nm). New sol-gel coating techniques are being evaluated; the second full-scale part is to be used for the Beamlet Mule campaign in October.

Upcoming Major Activities

During the first quarter of FY 1998, Conventional Facilities construction will officially begin with placement of concrete in October. Also, the architect/engineer, Parsons, will complete all of the Title II design packages for Conventional Facilities. The Notice-to-Proceed for CSP-5 for the Optics Assembly Building will be issued in October. In Special Equipment, six Mid-Title II (65%) Design Reviews and two Title II (100%) Design Reviews will be completed. In Optics, the activities for bidding and negotiating the optics facilitization contracts will continue.

Publications and Presentations
October–December 1996

A

Anderson, A. T., and Peterson, P. F., "Experimental Methods for Measuring X-Ray Ablation Response of Surfaces," Lawrence Livermore National Laboratory, Livermore, CA, UCRL-JC-125352 (1996). Submitted to *Experimental Heat Transfer*.

Anderson, A. T., Burnham, A. K., Tobin, M. T., and Peterson, P. F., "Modeling and Experiments of X-Ray Ablation of National Ignition Facility First Wall Materials," Lawrence Livermore National Laboratory, Livermore, CA, UCRL-JC-123553; *Fusion Tech.* **30**(3), 757–763 (1996).

B

Back, C. A., Landen, O. L., Turner, R. E., Koch, J. A., Hammel, B. A., MacFarlane, J. J., Cohen, D., and Nash, T. J., *Experiments and Analysis of Soft X-Ray Emission from Laser-Produced Nova Plasmas Using a Grating Spectrometer,* Lawrence Livermore National Laboratory, Livermore, CA, UCRL-JC-126319 ABS. Prepared for *13th Intl Conf on Laser Interactions and Related Plasma Phenomena,* Monterey, CA, Apr 13–18, 1997.

Banks, P. S., and Perry, M. D., *High Intensity Third Harmonic Generation in Single Crystal BBO,* Lawrence Livermore National Laboratory, Livermore, CA, UCRL-JC-126063. Prepared for *Conf on Lasers & Electro-optics,* Baltimore, MD, May 18–23, 1997.

Berning, M., Rubenchik, A., Glendinning, S. G., and Remington, B. A., *Comparative Studies of the Weakly Nonlinear Evolution of Hydrodynamic Interface Instabilities in 2D and 3D,* Lawrence Livermore National Laboratory, Livermore, CA, UCRL-JC-126314 ABS. Prepared for *13th Intl Conf on Laser Interactions and Related Plasma Phenomena,* Monterey, CA, Apr 13–18, 1997.

Budil, K. S., Remington, B. A., Weber, S. V., Peyser, T. A., Mikaelian, K. O., Perry, T. S., and Rubenchik, A. M., *Investigation of the Multimode Classical Rayleigh–Taylor Instability,* Lawrence Livermore National Laboratory, Livermore, CA, UCRL-JC-124548 ABS Rev. 1. Prepared for *13th Intl Conf on Laser Interactions and Related Plasma Phenomena,* Monterey, CA, Apr 13–18, 1997.

C

Caird, J. A., Nielsen, N. D., Patton, H. G., Seppala, L. G., Thompson, C. E., and Wegner, P. J., *Beamlet Focal Plane Diagnostic,* Lawrence Livermore National Laboratory, Livermore, CA, UCRL-JC-124872. Prepared for *2nd Annual Intl Conf on Solid-State Lasers for Application to Inertial Confinement Fusion,* Paris, France, Oct 22–25, 1996.

Collins, G. W., Da Silva, L. B., Celliers, P., Budil, K. S., Cauble, R., Holmes, N. C., Barbee, T. W., Hammel, B. A., Kilkenny, J. D., Wallace, R. J., Ross, M., Ng, A., and Chiu, G., *Equation of State Measurements of Deuterium up to 200 GPa,* Lawrence Livermore National Laboratory, Livermore, CA, UCRL-JC-125982 ABS. Prepared for *1997 March Mtg of the American Physical Society,* Kansas City, MO, Mar 17–21, 1997.

Collins, G. W., Bittner, D. N., Monsler, E., Letts, S., "Infrared Distribution of D_2 and HD Layers for Inertial Confinement Fusion," Lawrence Livermore National Laboratory, Livermore, CA, UCRL-JC-122449; *J. Vac. Sci. & Tech A* **14**(5), 2897–2900 (1996).

Crane, J. K., Martinez, M., Moran, B., Laumann, C., Davin, J., Beach, R., Golick, B., Jones, R., Braucht, J., Perry, M., Skulina, K., Penko, F., Herman, S., Burkhart, S., and Mitchell, S., *Description and Performance of the Preamplifier for the National Ignition Facility (NIF) Laser System,* Lawrence Livermore National Laboratory, Livermore, CA, UCRL-JC-124517. Prepared for *2nd Annual Intl Conf on Solid-State Lasers for Application to Inertial Confinement Fusion,* Paris, France, Oct 22–25, 1996.

D

De Yoreo, J. J., Land, T. A., Lee, J. D., Malkin, A. J., Kuznetsov, Y. G., and McPherson, A., *In Situ Investigation of Canavalin Crystallization Kinetics,* Lawrence Livermore National Laboratory, Livermore, CA, UCRL-JC-126077. Submitted to *Surface Science.*

De Yoreo, J. J., Land, T. A., and Lee, J. D., *Limits on Surface Vicinality and Growth Rate due to Hollow Dislocation Cores on KDP [101],* Lawrence Livermore National Laboratory, Livermore, CA, UCRL-JC-126088. Submitted to *Phys. Rev. Lett.*

Dixit, S. N., Feit, M. D., Perry, M. D., and Powell, H. T., "Designing Fully Continuous Phase Screens for Tailoring Focal Plane Irradiance Profiles," Lawrence Livermore National Laboratory, Livermore, CA, UCRL-JC-123842; *Opt. Lett.* **21**(21), 1715–1717 (1996).

Drake, R. P., Remington, B. A., Estabrook, K. G., Glendinning, S. G., London, R., Rubenchick, A. M., Liang, E. P., McCray, R., and Max, C. E., *Laboratory Simulation of the Interaction of the Ejecta and the Blue Supergiant Wind from Supernova 1987 A,* Lawrence Livermore National Laboratory, Livermore, CA, UCRL-ID-126083.

E

Emanuel, M. A., Skidmore, J. A., and Carlson, N. W., "High-Efficiency AlGaAs-Based Laser Diode at 808 nm with Large Transverse Spot Size," Lawrence Livermore National Laboratory, Livermore, CA, UCRL-JC-124003; *IEEE Photonics Tech. Lett.* **8**(10), 1291–1293 (1996).

Erlandson, A. C., Lambert, H., Zapata, L. E., Pedrotti, L., Larson, D. W., Rotter, M. D., Dallum, W. J., Seznec, S. E., LeTouze, G., Grebot, E., Carbourdin, O., Fornerod, J. C., and Bosch, P., *Effect of Amplifier Component Maintenance on Laser System Availability and Reliability for the U.S. National Ignition Facility,* Lawrence Livermore National Laboratory, Livermore, CA, UCRL-JC-124911. Prepared for *2nd Annual Intl Conf on Solid-State Lasers for Application to Inertial Confinement Fusion,* Paris, France, Oct 22–25, 1996.

F

Feit, M. D., and Rubenchik, A. M., *Laser Intensity Modulation by Nonabsorbing Defects,* Lawrence Livermore National Laboratory, Livermore, CA, UCRL-JC-124536 Rev. 1. Prepared for *2nd Annual Intl Conf on Solid-State Lasers for Application to Inertial Confinement Fusion,* Paris, France, Oct 22–25, 1996.

Feit, M. D., Rubenchik, A. M., Faux, D. R., Riddle, R. A., Shapiro, A., Eder, D. C., Penetrante, B. M., Milam, D., Genin, F. Y., and Kozlowski, M. R., *Surface Contamination Initiated Laser Damage,* Lawrence Livermore National Laboratory, Livermore, CA, UCRL-JC-126326. Prepared for *2nd Annual Intl Conf on Solid-State Lasers for Application to Inertial Confinement Fusion,* Paris, France, Oct 22–25, 1996.

G

Glendinning, S. G., Dixit, S. N., Hammel, B. A., Kalantar, D. H., Key, M. H., Kilkenny, J. D., Knauer, J. P., Pennington, D. M., Remington, B. A., Wallace, R. J., and Weber, S. V., "Measurements of Laser-Speckle-Induced Perturbations in Laser-Driven Foils," Lawrence Livermore National Laboratory, Livermore, CA, UCRL-JC-123082; *Phys. Rev. E* **54**(4), 4473–4475 (1996).

Glendinning, S. G., Arnett, W. D., Drake, R. P., Estabrook, K., Kane, J., Liang, E., London, R., McCray, R., Remington, B. A., and Rubenchik, A., *Supernova-Relevant Hydrodynamics Instability Experiments on the Nova Laser,* Lawrence Livermore National Laboratory, Livermore, CA, UCRL-JC-121488 ABS Rev. 1. Prepared for *13th Intl Conf on Laser Interactions and Related Plasma Phenomena,* Monterey, CA, Apr 13–18, 1997.

Glenzer, S. H., Back, C. A., Suter, L. J., Blain, M. A., Landen, O. L., MacGowan, B. J., Stone, G. F., Turner, R. E., and Wilde, B. H., *Thomson Scattering from Inertial Confinement Fusion Hohlraum Plasmas,* Lawrence Livermore National Laboratory, Livermore, CA, UCRL-JC-126320 ABS. Prepared for *13th Intl Conf on Laser Interactions and Related Plasma Phenomena,* Monterey, CA, Apr 13–18, 1997.

H

Hinkel, D. E., Berger, R. L., Langdon, A. B., Lasinski, B. F., Still, C. H., and Williams, E. A., *Backscatter, Laser Light Smoothing and Channeling in Underdense Plasmas,* Lawrence Livermore National Laboratory, Livermore, CA, UCRL-JC-126306 ABS. Prepared for *2nd Intl Workshop on Laser Plasma Interaction Physics,* Banff, Alberta, Canada, Feb 18–22, 1997.

K

Kalantar, D. H., Remington, B. A., Budil, K. S., Collins, G. W., Colvin, J. D., Weber, W. V., Griswold, D., Lee, R., Hauer, A., and Wark, J. S., *Hydrodynamic Instability Experiments in the Solid State,* Lawrence Livermore National Laboratory, Livermore, CA, UCRL-JC-126313 ABS. Prepared for *13th Intl Conf on Laser Interactions and Related Plasma Phenomena,* Monterey, CA, Apr 13–18, 1997.

Kane, J., Arnett, W. D., Remington, B. A., Glendinning, S. G., and Rubenchik, A., *Simulations of Supernova-Relevant Hydrodynamics Experiments on the Nova Laser,* Lawrence Livermore National Laboratory, Livermore, CA, UCRL-JC-126311 ABS. Prepared for *13th Intl Conf on Laser Interactions and Related Plasma Phenomena,* Monterey, CA, Apr 13–18, 1997.

Kania, D. R., Gaines, D. P., Sweeney, D. S., Sommargren, G. E., "Precision Optical Aspheres for Extreme Ultraviolet Lithography," Lawrence Livermore National Laboratory, Livermore, CA, UCRL-JC-123033; *J. Vac. Sci. & Tech. B* **14**(6), 3706–3708 (1996).

Kirkwood, R. K., Moody, J. D., Montgomery, D. S., Afeyan, B. B., MacGowan, B. J., Glenzer, S. H., Estabrook, K. G., Berger, R. L., and Williams, E. A., *Saturation of Stimulated Langmuir Waves by Ion Wave Decays in Ignition Relevant Plasmas,* Lawrence Livermore National Laboratory, Livermore, CA, UCRL-JC-126308 ABS. Prepared for *13th Intl Conf on Laser Interactions and Related Plasma Phenomena,* Monterey, CA, Apr 13–18, 1997.

Koch, J. A., Back, C. A., Brown, C., Hammel, B. A., Hatchett, S. P., Key, M. H., Landen, O. L., Lee, R. W., Moody, J., Offenberger, A., Pennington, D., Perry, M. D., Tabak, M., Yanovsky, V., Wharton, K. B., and Wilks, S. C., *Generation and Characterization of keV, High-Density Plasmas Produced by 100 TW and PW Short-Pulse Lasers,* Lawrence Livermore National Laboratory, Livermore, CA, UCRL-JC-126309 ABS. Prepared for *13th Intl Conf on Laser Interactions and Related Plasma Phenomena,* Monterey, CA, Apr 13–18, 1997.

Kozioziemski, B. J., Collins, G. W., and Bernat, T. P., *Single Crystal Growth of Solid D_2,* Lawrence Livermore National Laboratory, Livermore, CA, UCRL-JC-125981 ABS. Prepared for *1997 March Mtg of the American Physical Society,* Kansa City, MO, Mar 17–21, 1997.

Kruer, W. L., and Afeyan, B. B., *Fluctuation-Induced Stimulated Raman Scattering,* Lawrence Livermore National Laboratory, Livermore, CA, UCRL-JC-126318 ABS. Prepared for *2nd Intl Workshop on Laser Plasma Interaction Physics,* Banff, Alberta, Canada, Feb 18–22, 1997.

L

Land, T. A., Ferguson, J., and De Yoreo, J. J., *Diffusion Controlled Surface Morphology during Solution Growth of KH_2PO_4,* Lawrence Livermore National Laboratory, Livermore, CA, UCRL-JC-126327 ABS. Prepared for *Intl Conf on Crystal Growth XI,* The Hague, Netherlands, Jun 16–28, 1995.

Land, T. A., Lee, J. D., and De Yoreo, J. J., *Real Time AFM Observations of Step-Pinning during Growth of KH_2PO_4 from Solution,* Lawrence Livermore National Laboratory, Livermore, CA, UCRL-JC-126328 ABS. Prepared for *Intl Conf on Crystal Growth XI,* The Hague, Netherlands, Jun 16–28, 1995.

Latkowski, J. F., Sanz, J., Vujic, J. L., and Tobin, M. T., "Sequential Charged-Particle and Neutron Activation of Flibe in the HYLIFE-II Inertial Fusion Energy Power Plant Design," Lawrence Livermore National Laboratory, Livermore, CA, UCRL-JC-123558; *Fusion Tech.* **30**(3), 1475–1479 (1996).

Latkowski, J. F., Sanz, J., and Vujic, J. L., "The Impact of Pulsed Irradiation Upon Neutron Activation Calculations for Inertial and Magnetic Fusion Energy Power Plants," Lawrence Livermore National Laboratory, Livermore, CA, UCRL-JC-123559; *Fusion Tech.* **30**(3), 1470–1474 (1996).

London, R. A., Glinsky, M. E., Zimmerman, G. B., Bailey, D. S., Eder, D. C., and Jacques S. L., "LATIS: A Program for Laser-Tissue Interaction Modeling," Lawrence Livermore National Laboratory, Livermore, CA, UCRL-JC-125974 (1996). Submitted to *J. of Applied Opt*.

M

Meier, W. R., and Logan, B. G., "Developing Inertial Fusion Energy—Where Do We Go from Here?" Lawrence Livermore National Laboratory, Livermore, CA, UCRL-JC-123079; *Fusion Tech*. **30**(3), 1279–1285 (1996).

Moir, R. W., "IFE Power Plant Design Strategy" Lawrence Livermore National Laboratory, Livermore, CA, UCRL-JC-123287; *Fusion Tech*. **30**(3), 1613–1623 (1996).

Moody, J. D., Brown, C., Hammel, B. A., Hatchett, S. P., Hinkel, D. E., Key, M. H., Koch, J. A., Lasinski, B., Langdon, A. B., MacGowan, B. J., Offenberger, A., Pennington, D., Perry, M. D., Tabak, M., Yanovsky, V., Wharton, K. B., and Wilks, S. C., *Experimental Studies of Hole-Boring in Thin Solid and Foam Targets,* Lawrence Livermore National Laboratory, Livermore, CA, UCRL-JC-126322 ABS. Prepared for *13th Intl Conf on Laser Interactions and Related Plasma Phenomena,* Monterey, CA, Apr 13–18, 1997.

Moody, J. D., MacGowan, B. J., Berger, R. L., Hinkel, D. E., Kruer, W. L., and Williams, E. A., *Fluctuation Measurements in Nova Gasbag Targets Using Near Forward Scattering,* Lawrence Livermore National Laboratory, Livermore, CA, UCRL-JC-126321 ABS. Prepared for *13th Intl Conf on Laser Interactions and Related Plasma Phenomena,* Monterey, CA, Apr 13–18, 1997.

Moran, M. J., *PROTEX: a Proton-Recoil Detector for ICF Fusion Neutrons,* Lawrence Livermore National Laboratory, Livermore, CA, UCRL-JC-125996 ABS. Prepared for *1997 Institute of Electronic and Electrical Engineers Intl Conf on Plasma Science,* San Diego, CA, May 19–22, 1997.

O

Orzechowski, T. J., Rosen, M. D., Kornblum, H. N., Porter, J. L., Suter, L. J., Thiessen, A. R., and Wallace, R., "The Rosseland Mean Opacity of a Composite Material at High Temperatures," Lawrence Livermore National Laboratory, Livermore, CA, UCRL-JC-123579; *Phys. Rev. Lett*. **77**(17), 3545–3548 (1996).

P

Page, R. H., Skidmore, J. A., Schaffers, K. I., Beach, R. J., Payne, S. A., and Krupke, W. F., *2150–2800 nm Coverage and Diode Pumping with ZnSe:Cr^{2+} Lasers,* Lawrence Livermore National Laboratory, Livermore, CA, UCRL-JC-126302 ABS SUM. Prepared for *Conf on Lasers and Electro-Optics/Pacific Rim '97*, Chiba, Japan, Jul 14–18, 1997.

Paisner, J. A., and Hogan, W. J., "Progress in the Title I Design of the National Ignition Facility," Lawrence Livermore National Laboratory, Livermore, CA, UCRL-JC-123560; *Fusion Tech*. **30**(3), 475–485 (1996).

Payne, S. A., Beach, R. J., Bibeau, C., Ebbers, C. A., Emanuel, M. A., Honea, E. C., Marshall, C. D., Page, R. H., Schaffers, K. I., Skidmore, J. D., Sutton, S. B., and Krupke, W. F., *Diode Arrays, Crystals, and Thermal Management for Solid-State Lasers,* Lawrence Livermore National Laboratory, Livermore, CA, UCRL-JC-126323. Submitted to *IEEE Special Issue on Selected Topics*.

Perry, M. D., Pennington, D. M., Stuart, B. C., Boyd, R., Britten, J. A., Brown, C. G., Herman, S., Miller, J. L., Nguyen, H., Shore, B., Tietbohl, G., and Yanovsky, V., *Design and Performance of the Petawatt Laser System,* Lawrence Livermore National Laboratory, Livermore, CA, UCRL-JC-126317 ABS & SUM. Prepared for *Conf on Lasers & Electro-Optics/Quantum Electronics and Laser Science Conf '97*, Baltimore, MD, May 18–23, 1997.

Perry, M. D., Yanovsky, V., Feit, M. D., and Rubenchik, A., *Plasma Mirrors,* Lawrence Livermore National Laboratory, Livermore, CA, UCRL-JC-125376. Submitted to *Science.*

R

Remington, B. A., Kane, J., Drake, R. P., Glendinning, S. G., Estabrook, K., London, R., Wallace, R. J., Arnett, D., Liang, E., McCray, R., and Rubenchik, A., *Supernova Hydrodynamics Experiments Using the Nova Laser,* Lawrence Livermore National Laboratory, Livermore, CA, UCRL-JC-126312 ABS. Prepared for *13th Intl Conf on Laser Interactions and Related Plasma Phenomena*, Monterey, CA, Apr 13–18, 1997.

Rothenberg, J. E., *Improved Beam Smoothing with SSD Using Generalized Phase Modulation,* Lawrence Livermore National Laboratory, Livermore, CA, UCRL-JC-124508. Prepared for *2nd Annual Intl Conf on Solid-State Lasers for Application to Inertial Confinement Fusion,* Paris, France, Oct 22–25, 1996.

Rothenberg, J. E., *Electro-Optic Deflectors as a Method of Beam Smoothing for ICF,* Lawrence Livermore National Laboratory, Livermore, CA, UCRL-JC-124507. Prepared for *2nd Annual Intl Conf on Solid-State Lasers for Application to Inertial Confinement Fusion,* Paris, France, Oct 22–25, 1996.

Rothenberg, J. E., Moran, B., Henesian, M., and Van Wonterghem, B., *Evaluation of Smoothing by Spectral Dispersion on the Beamlet Laser for the National Ignition Facility,* Lawrence Livermore National Laboratory, Livermore, CA, UCRL-JC-125988 ABS & SUM. Prepared for *1997 Conf on Lasers & Electro-Optics,* Baltimore, MD, May 18–23, 1997.

Rothenberg, J. E., Moran, B., Henesian, M., and Van Wonterghem, B., *Performance of Smoothing by Spectral Dispersion (SSD) on Beamlet,* Lawrence Livermore National Laboratory, Livermore, CA, UCRL-JC-124506. Prepared for *2nd Annual Intl Conf on Solid-State Lasers for Application to Inertial Confinement Fusion,* Paris, France, Oct 22–25, 1996.

Rothenberg, J. E., and Weber, S. V., *Impact of Beam Smoothing Method on Direct Drive Target Performance for the NIF,* Lawrence Livermore National Laboratory, Livermore, CA, UCRL-JC-124509 Rev. 1. Prepared for *2nd Annual Intl Conf on Solid-State Lasers for Application to Inertial Confinement Fusion,* Paris, France, Oct 22–25, 1996.

S

Schirmann, D., and Tobin, M., "Target Conceptual Design Issues of the French Laser Megajoule Facility (LMJ)," Lawrence Livermore National Laboratory, Livermore, CA, UCRL-JC-123563; *Fusion Tech.* **30**(3), 512–519 (1996).

Sharp, W. M., and Kamin, G. W., *Transverse-Control Algorithms for a Small Recirculating Heavy-Ion Accelerator,* Lawrence Livermore National Laboratory, Livermore, CA, UCRL-JC-125998 ABS. Prepared for *1997 Particle Accelerator Conf,* Vancouver, BC, Canada, May 12–16, 1997.

Smolski, I., De Yoreo, J. J., Zaitseva, N. P., Lee, J. D., and Land, T. A., "Oriented Liquid Inclusions in KDP Crystals," Lawrence Livermore National Laboratory, Livermore, CA, UCRL-JC-122011; *J. Crystal Growth* **169**(4), 741–746 (1996).

Snavely, R. A., Da Silva, L. B., Eder, D. C., Matthews, D. L., and Moon, S. J., *Traveling Wave Pumping of Ultra-Short Pulse X-Ray Lasers,* Lawrence Livermore National Laboratory, Livermore, CA, UCRL-JC-125992 ABS. Prepared for *Society of Photo-Optical Instrumentation Engineers '97 Conf,* San Diego, CA, Jul 27–Aug 1, 1997.

Still, C. H., Berger, R. L., Estabrook, K. G., Hinkel, D. E., Langdon, A. B., Williams, E. A., and Young, P. E., *Simulating Beam Deflection and Channel Formation with F3D,* Lawrence Livermore National Laboratory, Livermore, CA, UCRL-JC-126304 ABS. Prepared for *2nd Intl Workshop on Laser Plasma Interaction Physics,* Banff, Alberta, Canada, Feb 18–22, 1997.

T

Tobin, M., Karpenko, V., Kauffman, R., Anderson, A., Simonson, G., Kruger, H., Davis, J., and Hoover, T., "Utility of the National Ignition Facility for Inertial Fusion Energy and Radiation Sciences Experiments," Lawrence Livermore National Laboratory, Livermore, CA, UCRL-JC-123568; *Fusion Tech.* **30**(3), 452–456 (1996).

Tobin, M., Karpenko, V., Burnham, A., and Peterson, P., "Target Area Design Issues for Implementing Direct Drive on the National Ignition Facility," Lawrence Livermore National Laboratory, Livermore, CA, UCRL-JC-124479; *Fusion Tech.* **30**(3), 457–463 (1996).

Tobin, M., Karpenko, V., Foley, D., Anderson, A., Burnham, A., Reitz, T., Latkowski, J., and Bernat, T., "Confinement of Ignition and Yield on the National Ignition Facility," Lawrence Livermore National Laboratory, Livermore, CA, UCRL-JC-123562; *Fusion Tech.* **30**(3), 504–511 (1996).

Tokheim, R. E., Seaman, L., Cooper, T., Lew, B., Curran, D. R., Sanchez, J., Anderson, A., and Tobin, M., "Calculating the Shrapnel Generation and Subsequent Damage to First Wall and Optics Components for the National Ignition Facility," Lawrence Livermore National Laboratory, Livermore, CA, UCRL-JC-124947; *Fusion Tech.* **30**(3), 745–751 (1996).

V

Van Wonterghem, B. M., Wegner, P. J., Lawson, J. K., Auerbach, J. M., Henesian, M. A., Barker, C. E., Thompson, C. E., Widmayer, C. C., and Caird, J. A., "Recent Performance Results of the National Ignition Facility Beamlet Demonstration Project," Lawrence Livermore National Laboratory, Livermore, CA, UCRL-JC-123080; *Fusion Tech.* **30** (3), 642–647 (1996).

Van Wonterghem, B. M., Murray, J. E., Burkhart, S. C., Penko, F., Henesian, M. A., Auerbach, J. A., Wegner, P. J., and Caird, J. A., *High Fluence 1.05 µm Performance Tests Using 20 ns Shaped Pulses on the Beamlet Prototype Laser,* Lawrence Livermore National Laboratory, Livermore, CA, UCRL-JC-124865. Prepared for *2nd Annual Intl Conf on Solid-State Lasers for Application to Inertial Confinement Fusion*, Paris, France, Oct 22–25, 1996.

W

Weber, S. V., Budil, K. S., Colvin, J. D., Glendinning, S. G., Griswold, D. L., Kalantar, D. H., and Remington, B. A., *Simulations of Rayleigh–Taylor Growth for Direct Drive and with Material Strength,* Lawrence Livermore National Laboratory, Livermore, CA, UCRL-JC-125995 ABS. Prepared for *6th Intl Workshop on the Physics of Compressible Turbulent Mixing*, Marseille, France, Jun 18–21, 1997.

Weber, S. V., Glendinning, S. G., Kalantar, D. H., Key, M. H., Remington, B. A., Rothenberg, J. E., Wolfrum, E., Verdon, C. P., and Knauer, J. P., *Simulations of Laser Imprint for Nova Experiments and for Ignition Capsules,* Lawrence Livermore National Laboratory, Livermore, CA, UCRL-JC-124547 Rev. 1. Prepared for *38th Annual Mtg of the American Physical Society Div of Plasma Physics*, Denver, CO, Nov 11–15, 1996.

Wegner, P. J., Van Wonterghem, B. M., Dixit, S. N., Henesian, M. A., Barker, C. E., Thompson, C. E., Seppala, L. G., and Caird, J. A., "Characterization of Third-Harmonic Target Plane Irradiance on the National Ignition Facility Beamlet Demonstration Project," Lawrence Livermore National Laboratory, Livermore, CA, UCRL-JC-123070; *Fusion Tech.* **30**(3), 539–547 (1996).

Wegner, P. J., Barker, C. E., Caird, J. A., Dixit, S. N., Henesian, M. A., Seppala, L. G., Thompson, C. E., and Van Wonterghem, B. V., *Third-Harmonic Performance of the Beamlet Prototype Laser,* Lawrence Livermore National Laboratory, Livermore, CA, UCRL-JC-124529. Prepared for *2nd Annual Intl Conf on Solid-State Lasers for Application to Inertial Confinement Fusion,* Paris, France, Oct 22–25, 1996.

Wharton, K., Brown, C., Hammel, B., Hatchett, S., Koch, J., Moody, J., Offenberger, A., Perry, M., Tabak, M., Wilks, S., Yanovsky, V., and Zakharenkov, Y., *Characterization of Hot Electrons Produced by 5×10^{19} W/cm^2 Laser–Plasma Interactions,* Lawrence Livermore National Laboratory, Livermore, CA, UCRL-JC-126310 ABS. Prepared for *13th Intl Conf on Laser Interactions and Related Plasma Phenomena*, Monterey, CA, Apr 13–18, 1997.

Widmayer, C. C., Auerbach, J. M., Ehrlich, R. B., Henesian, M. A., Hunt, J. T., Lawson, J. K., Milam, D., Renard, P. A., Speck, D. R., Wegner, P. J., Weiland, T. L., Williams, W. H., Wolfe, C. R., Van Wonterghem, B. M., "Producing National Ignition Facility (NIF)-Quality Beams on the Nova and Beamlet Lasers," Lawrence Livermore National Laboratory, Livermore, CA, UCRL-JC-124937; *Fusion Tech.* **30**(3), 464–470 (1996).

Wilks, S. C., Wharton, K., Hatchett, S., Tabak, M., Key, M., and Kruer, W. L., *Recent 100 Terawatt K_α Experiments at LLNL: Hot Electron Production for the Fast Ignitor,* Lawrence Livermore National Laboratory, Livermore, CA, UCRL-JC-126307 ABS. Prepared for *2nd Intl Workshop on Laser Plasma Interaction Physics*, Banff, Alberta, Canada, Feb 18–22, 1997.

Williams, E. A., Cohen, B. I., and Berger, R. L., *Ion Wave Parametric Decay and Related Instabilities,* Lawrence Livermore National Laboratory, Livermore, CA, UCRL-JC-126305 ABS. Prepared for *2nd Intl Workshop on Laser Plasma Interaction Physics*, Banff, Alberta, Canada, Feb 18–22, 1997.

Z

Zaitseva, N. P., De Yoreo, J. J., Dehaven, M. R., Vital, R. L., Montgomery, K. E., Richardson, M., and Atherton, L. J., "Rapid Growth of Large-Scale (40–55 cm) KH_2PO_4 Crystals," Lawrence Livermore National Laboratory, Livermore, CA, UCRL-JC-125387 (1996); submitted to *J. Crystal Growth*.

Publications and Presentations
January–March 1997

A

Afeyan, B. B., Chou, A. E., and Kruer, W. L., *Physical Mechanisms That Give Rise to Anti-Correlation between SBS and SRS Reflectivities,* Lawrence Livermore National Laboratory, Livermore, CA, UCRL-JC-126515 ABS. Prepared for *2nd Intl Workshop on Laser Plasma Interaction Physics,* Banff, Alberta, Canada, Feb 18–22, 1997.

Amendt, P. A., Strauss, M., London, R. A., Glinsky, M. E., Maitland, D. J., Celliers, P. M., Visuri, S. R., Bailey, D. S., Young, D. A., and Ho, D., *Modeling of Bubble Dynamics in Relation to Medical Applications,* Lawrence Livermore National Laboratory, Livermore, CA, UCRL-JC-126961. Prepared for *Society of Photo-Optical Instrumentation Engineers Photonics West '97 Symp,* San Jose, CA, Feb 8–14, 1997.

Amendt, P., London, R. A., Strauss, M., Glinsky, M. E., Maitland, D. J., Celliers, P. M., Visuri, S. R., Bailey, D. S., Young, D. A., Ho, D., and Kelly, M. W., *Simulation Studies of Vapor Bubble Generation by Short-Pulse Lasers,* Lawrence Livermore National Laboratory, Livermore, CA, UCRL-JC-126822 ABS. Prepared for *Society of Photo-Optical Instrumentation Engineers BiOS Europe '97,* San Remo, Italy, Sept 4–8, 1997.

Auerbach, J. M., Eimerl, D., Milam, D., and Milonni, P. W., *A Perturbation Theory for Electric Field Amplitude and Phase Ripple Transfer in Frequency Doubling and Tripling,* Lawrence Livermore National Laboratory, Livermore, CA, UCRL-JC-124005; *Applied Optics: Lasers, Photonics, & Environ. Optics* **36**(3), 606–612 (1997).

B

Back, C. A., Glenzer, S. H., Landen, O. L., MacGowan, B. J., and Shepard, T. D., *X-Ray Diagnostics of Hohlraum Plasma Flow,* Lawrence Livermore National Laboratory, Livermore, CA, UCRL-JC-123283; *Rev. Sci. Inst.* **68**(1), 831–833 (1997).

Back, C. A., Landen, O. L., Turner, R. E., Koch, J. A., Hammel, B. A., MacFarlane, J. J., Cohen, D., and Nash, T. J., *Experiments and Analysis of Soft X-Ray Emission from Laser-Produced Nova Plasmas Using a Grating Spectrometer,* Lawrence Livermore National Laboratory, Livermore, CA, UCRL-JC-126319 ABS. Prepared for *13th Intl Conf on Laser Interactions and Related Plasma Phenomena,* Monterey, CA, Apr 13–18, 1997.

Bailey, D. S., London, R. A., and Alley, E. A., *Hard Tissue Ablation Simulations Using the LATIS Computer Code,* Lawrence Livermore National Laboratory, Livermore, CA, UCRL-JC-126962 ABS. Prepared for *Society of Photo-Optical Instrumentation Engineers BiOS Europe '97,* San Remo, Italy, Sept 4–8, 1997.

Banks, P. S., and Perry, M. D., *High Intensity Third Harmonic Generation in Single Crystal BBO,* Lawrence Livermore National Laboratory, Livermore, CA, UCRL-JC-126063. Prepared for *Conf on Lasers & Electro-optics,* Baltimore, MD, May 18–23, 1997.

Berning, M., Rubenchik, A., Glendinning, S. G., and Remington, B. A., *Comparative Studies of the Weakly Nonlinear Evolution of Hydrodynamic Interface Instabilities in 2D and 3D,* Lawrence Livermore National Laboratory, Livermore, CA, UCRL-JC-126314 ABS. Prepared for *13th Intl Conf on Laser Interactions and Related Plasma Phenomena,* Monterey, CA, Apr 13–18, 1997.

Bibeau, C., Beach, R., Ebbers, C., and Skidmore, J., *CW and Q-Switched Performance of a Diode End-Pumped Yb:YAG Laser,* Lawrence Livermore National Laboratory, Livermore, CA, UCRL-JC-124042 Rev 1. Prepared for *12th Topical Mtg on Advance Solid-State Lasers,* Orlando, FL, Jan 27–29, 1997.

Britten, J. A., *Moving-Zone Marangoni Drying Process for Critical Cleaning and Wet Processing,* Lawrence Livermore National Laboratory, Livermore, CA, UCRL-JC-126549. Submitted to *Solid State Technol.*

Budil, K. S., Remington, B. A., Perry, T. S., Rubenchik, A. M., Berning, M., Peyser, T. A., Louis, H., Demiris, T., and Wallace, R., *A Novel Method for Diagnosing the Growth of Subresolution-Scale Perturbations,* Lawrence Livermore National Laboratory, Livermore, CA, UCRL-JC-124033; *Rev. Sci. Instrum.* **68**(1), 799–801 (1997).

Budil, K. S., Remington, B. A., Weber, S. V., Peyser, T. A., Mikaelian, K. O., Perry, T. S., and Rubenchik, A. M., *Investigation of the Multimode Classical Rayleigh–Taylor Instability,* Lawrence Livermore National Laboratory, Livermore, CA, UCRL-JC-124548 ABS Rev 1. Prepared for *13th Intl Conf on Laser Interactions and Related Plasma Phenomena,* Monterey, CA, Apr 13–18, 1997.

Budil, K., Perry, T. S., Alvarez, S. A., Hargrove, D., Mazuch, J. R., Nikitin, A., and Bell, P. M., *Point Projection Radiography with the FXI,* Lawrence Livermore National Laboratory, Livermore, CA, UCRL-JC-123135; *Rev. Sci. Instrum.* **68**(1), 796–798 (1997).

C

Cable, M. D., Barbee, T. W., Koch, J. A., Lerche, R. A., Moran, M. J., Ognibene, T., Ress, D. B., Sangster, T. C., Trebes, J. E., Phillips, T. W., Hicks, D., Li, C. K., Petrasso, R. D., and Seguin, F., *Diagnostics for High Density Implosions at Nova and the National Ignition Facility,* Lawrence Livermore National Laboratory, Livermore, CA, UCRL-JC-126844 ABS. Prepared for *9th Natl Topical Conf on High-Temperature Plasma Diagnostics*, St. Petersburg, Russia, Jun 2–4, 1997.

Caird, J. A., Nielsen, N. D., Patton, H. G., Seppala, L. G., Thompson, C. E., and Wegner, P. J., *Beamlet Focal Plane Diagnostic,* Lawrence Livermore National Laboratory, Livermore, CA, UCRL-JC-124872. Prepared for *2nd Annual Intl Conf on Solid-State Lasers for Application to Inertial Confinement Fusion,* Paris, France, Oct 22–25, 1996.

Celliers, P., Barbee, T. W., Cauble, R., Da Silva, L. B., Decker, C. D., Kalantar, D. H., Key, M. H., London, R. A., Moreno, J. C., Snavely, R., Trebes, J. E., Wan, A. S., and Weber, F., *Probing High Density Plasmas with Soft X-Ray Lasers,* Lawrence Livermore National Laboratory, Livermore, CA, UCRL-JC-126541 ABS. Prepared for *Society of Photo-Optical Instrumentation Engineers' 1997 Intl Symp on Optical Science, Engineering, and Instrumentation*, San Diego, CA, Jul 27–Aug 1, 1997.

Celliers, P., Estabrook, K., Wallace, R. J., Murray, J. E., Da Silva, L. B., MacGowan, B. J., Van Wonterghem, B. M., and Manes, K. R., *Novel Spatial Filter Pinhole for High Energy Pulsed Lasers,* Lawrence Livermore National Laboratory, Livermore, CA, UCRL-JC-124029. Submitted to *J. of Appl. Optics: Lasers, Photonics and Environment Optics.*

Cohen, B. I., Langdon, A. B., Lasinski, B. F., and Williams, E. A., *BZOHAR Simulations of Ponderomotively Driven Ion Waves,* Lawrence Livermore National Laboratory, Livermore, CA, UCRL-JC-126300 ABS. Prepared for *2nd Intl Workshop on Laser Plasma Interaction Physics,* Banff, Alberta, Canada, Feb 18–22, 1997.

Collins, G. W., Da Silva, L. B., Celliers, P., Budil, K. S., Cauble, R., Holmes, N. C., Barbee, T. W., Hammel, B. A., Kilkenny, J. D., Wallace, R. J., Ross, M., Ng, A., and Chiu, G., *Equation of State Measurements of Deuterium up to 200 GPa,* Lawrence Livermore National Laboratory, Livermore, CA, UCRL-JC-125982 ABS. Prepared for *1997 March Mtg of the American Physical Society*, Kansas City, MO, Mar 17–21, 1997.

Collins, G. W., Da Silva, L., Celliers, P., Budil, K., Cauble, R., Holmes, N. C., Barbee, T. W., Hammel, B. A., Kilkenny, J. D., Wallace, R. J., Ross, M., Ng, A., and Chiu, G., *Equation of State Measurements of Deuterium up to 2 Mbar,* Lawrence Livermore National Laboratory, Livermore, CA, UCRL-JC-126340 ABS. Prepared for *1997 Joint April American Physical Society/American Assn of Physics Teachers' Mtg and Canadian Assn and Mexicana '97,* Washington, DC, Apr 18–21, 1997.

Crane, J. K., Martinez, M., Moran, B., Laumann, C., Davin, J., Beach, R., Golick, B., Jones, R., Braucht, J., Perry, M., Skulina, K., Penko, F., Herman, S., Burkhart, S., and Mitchell, S., *Description and Performance of the Preamplifier for the National Ignition Facility (NIF) Laser System,* Lawrence Livermore National Laboratory, Livermore, CA, UCRL-JC-124517. Prepared for *2nd Annual Intl Conf on Solid-State Lasers for Application to Inertial Confinement Fusion,* Paris, France, Oct 22–25, 1996.

D

Da Silva, L. B., Celliers, P., Collins, G. W., Budil, K. S., Holmes, N. C., Barbee Jr., T. W., Hammel, B. A., Kilkenny, J. D., Wallace, R. J., Ross, M., Cauble, R., Ng, A., and Chiu, G., *Absolute Equation of State Measurements on Shocked Liquid Deuterium up to 200 GPa (2 Mbar),* Lawrence Livermore National Laboratory, Livermore, CA, UCRL-JC-124445 Rev 1; *Phys. Rev. Lett.* **78**(3), 483–486 (1997).

Dalton, A. C., *Modeling the Arm II Core in Microcap IV,* Lawrence Livermore National Laboratory, Livermore, CA, UCRL-ID-126189.

De Yoreo, J. J., Land, T. A., and Lee, J. D., *Limits on Surface Vicinality and Growth Rate due to Hollow Dislocation Cores on KDP [101],* Lawrence Livermore National Laboratory, Livermore, CA, UCRL-JC-126088. Submitted to *Phys. Rev. Lett.*

De Yoreo, J. J., Land, T. A., Lee, J. D., Malkin, A. J., Kuznetsov, Y. G., and McPherson, A., *In Situ Investigation of Canavalin Crystallization Kinetics,* Lawrence Livermore National Laboratory, Livermore, CA, UCRL-JC-126077. Submitted to *Surf. Sci.*

Decker, C. D., and London, R. A., *Designs for a Compact Ni-like Tungsten X-Ray Laser,* Lawrence Livermore National Laboratory, Livermore, CA, UCRL-JC-126334. Submitted to *Phys. Rev. Lett.*

Decker, C., Turner, R. E., Landen, O. L., Suter, L. J., Amendt, P., Kornblum, H. N., Hammel, B. A., Murphy, T. J., Wallace, J., Hauer, A. A., Knauer, J., Marshall, F. J., Bradley, D., Seka, W., and Soures, J. M., *Hohlraum Radiation Drive Measurements on the Omega Laser,* Lawrence Livermore National Laboratory, Livermore, CA, UCRL-JC-126959. Submitted to *Phys. Rev. Lett.*

Drake, R. P., Remington, B. A., Estabrook, K. G., Glendinning, S. G., London, R., Rubenchick, A. M., Liang, E. P., McCray, R., and Max, C. E., *Laboratory Simulation of the Interaction of the Ejecta and the Blue Supergiant Wind from Supernova 1987 A,* Lawrence Livermore National Laboratory, Livermore, CA, UCRL-ID-126083.

E

Ehrlich, R. B., Amendt, P. A., Dixit, S. N., Hammel, B. A., Kalantar, D. H., Pennington, D. M., and Weiland, T. L., *Developing Beam Phasing on the Nova Laser,* Lawrence Livermore National Laboratory, Livermore, CA, UCRL-JC-124513. Prepared for *2nd Annual Intl Conf on Solid-State Lasers for Applications to Inertial Confinement Fusion,* Paris, France, Oct 22–25, 1997.

Emanuel, M. A., Skidmore, J. A., and Beach, R. J., *High-Power Laser Diodes at Various Wavelengths,* Lawrence Livermore National Laboratory, Livermore, CA, UCRL-JC-126513. Prepared for *Society of Photo-Optical Instrumentation Engineers Photonics West '97 Symp,* San Jose, CA, Feb 8–14, 1997.

Erlandson, A. C., Lambert, H., Zapata, L. E., Pedrotti, L., Larson, D. W., Rotter, M. D., Dallum, W. J., Seznec, S. E., LeTouze, G., Grebot, E., Carbourdin, O., Fornerod, J. C., and Bosch, P., *Effect of Amplifier Component Maintenance on Laser System Availability and Reliability for the U.S. National Ignition Facility,* Lawrence Livermore National Laboratory, Livermore, CA, UCRL-JC-124911. Prepared for *2nd Annual Intl Conf on Solid-State Lasers for Application to Inertial Confinement Fusion,* Paris, France, Oct 22–25, 1996.

F

Feit, M. D., and Rubenchik, A. M., *Laser Intensity Modulation by Nonabsorbing Defects,* Lawrence Livermore National Laboratory, Livermore, CA, UCRL-JC-124536 Rev 1. Prepared for *2nd Annual Intl Conf on Solid-State Lasers for Application to Inertial Confinement Fusion,* Paris, France, Oct 22–25, 1996.

Feit, M. D., Garrison, J. C., Komashko, A. M., Musher, S. L., Rubenchik, A. M., and Turitsyn, S. K., *Relativistic Laser Pulse Channeling,* Lawrence Livermore National Laboratory, Livermore, CA, UCRL-JC-126337 ABS. Prepared for *13th Intl Conf on Laser Interactions and Related Plasma Phenomena,* Monterey, CA, Apr 13–18, 1997.

Feit, M. D., Rubenchik, A. M., Faux, D. R., Riddle, R. A., Shapiro, A., Eder, D. C., Penetrante, B. M., Milam, D., Genin, F. Y., and Kozlowski, M. R., *Surface Contamination Initiated Laser Damage,* Lawrence Livermore National Laboratory, Livermore, CA, UCRL-JC-126326. Prepared for *2nd Annual Intl Conf on Solid-State Lasers for Application to Inertial Confinement Fusion,* Paris, France, Oct 22–25, 1996.

G

Genin, F. Y., Michlitsch, K., Furr, J., Kozlowski, M. R., and Krulevitch, P., *Laser-Induced Damage of Fused Silica at 355 and 1064 nm Initiated at Aluminum Contamination Particles on the Surface,* Lawrence Livermore National Laboratory, Livermore, CA, UCRL-JC-124878. Prepared for *28th Annual Symp on Optical Materials for High Power Lasers,* Boulder, CO, Oct 7–9, 1996.

Genin, F. Y., Stolz, C. J., and Kozlowski, M. R., *Growth of Laser-Induced Damage during Repetitive Illumination of HfO$_2$-SiO$_2$ Multilayer Mirror and Polarizer Coatings,* Lawrence Livermore National Laboratory, Livermore, CA, UCRL-JC-124877. Prepared for *28th Annual Symp on Optical Materials for High Power Lasers,* Boulder, CO, Oct 7–9, 1996.

Genin, F. Y., Stolz, C. J., Reitter, T., Kozlowski, M. R., Bevis, R. P., and Vongunten, M. K., *Effect of Electric Field Distribution on the Morphologies of Laser-Induced Damage in Hafnia-Silica Multilayer Polarizers,* Lawrence Livermore National Laboratory, Livermore, CA, UCRL-JC-124873. Prepared for *28th Annual Symp on Optical Materials for High Power Lasers,* Boulder, CO, Oct 7–9, 1996.

Glendinning, S. G., Amendt, P., Hammel, B. A., Landen, O. L., Suter, L. J., Lafitte, S., Desenne, D., and Jadaud, J. P., *Time-Resolved Hohlraum Drive Symmetry Measurements Using Foam Spheres as Surrogate Implosion Targets,* Lawrence Livermore National Laboratory, Livermore, CA, UCRL-JC-126345. Submitted to *Phys. Rev. Lett.*

Glendinning, S. G., Arnett, W. D., Drake, R. P., Estabrook, K., Kane, J., Liang, E., London, R., McCray, R., Remington, B. A., and Rubenchik, A., *Supernova-Relevant Hydrodynamics Instability Experiments on the Nova Laser,* Lawrence Livermore National Laboratory, Livermore, CA, UCRL-JC-121488 ABS Rev 1. Prepared for *13th Intl Conf on Laser Interactions and Related Plasma Phenomena,* Monterey, CA, Apr 13–18, 1997.

Glenzer, S. H., Back, C. A., Estabrook, K. G., and MacGowan, B. J., *Thomson Scattering in the Corona of Laser-Produced Gold Plasmas,* Lawrence Livermore National Laboratory, Livermore, CA, UCRL-JC-123282; *Rev. Sci. Instrum.* **68**(1), 668–671 (1997).

Glenzer, S. H., Back, C. A., Estabrook, K. G., Kirkwood, R. K., Wallace, R., MacGowan, B. J., Hammel, B. A., Cid, R. E., and De Groot, J. S., *Thomson Scattering from Two-Species Laser-Produced Plasmas,* Lawrence Livermore National Laboratory, Livermore, CA, UCRL-JC-123752; *Rev. Sci. Instrum.* **68**(1), 641–646 (1997).

Glenzer, S. H., Back, C. A., Suter, L. J., Blain, M. A., Landen, O. L., MacGowan, B. J., Stone, G. F., Turner, R. E., and Wilde, B. H., *Thomson Scattering from Inertial Confinement Fusion Hohlraum Plasmas,* Lawrence Livermore National Laboratory, Livermore, CA, UCRL-JC-126320 ABS. Prepared for *13th Intl Conf on Laser Interactions and Related Plasma Phenomena,* Monterey, CA, Apr 13–18, 1997.

Glenzer, S. H., Back, C. A., Suter, L. J., Blain, M. A., Landen, O. L., MacGowan, B. J., Stone, G. F., Turner, R. E., and Wilde, B. H., *Thomson Scattering from Inertial Confinement Fusion Hohlraum Plasmas,* Lawrence Livermore National Laboratory, Livermore, CA, UCRL-JC-126320. Submitted to *Phys. Rev. Lett.*

Glenzer, S. H., Wrubel, Th., and Kunze, H.-J., *Investigation of a Short-Wavelength Laser Plasma of a Gas-Liner Pinch Discharge,* Lawrence Livermore National Laboratory, Livermore, CA, UCRL-JC-124886; *Phys. Rev. Lett. E* **55**(1), 939–946 (1997).

H

Hammel, B. A., *Recent Results from the Nova Laser,* Lawrence Livermore National Laboratory, Livermore, CA, UCRL-JC-126952 ABS. Prepared for *13th Intl Conf on Laser Interactions and Related Plasma Phenomena,* Monterey, CA, Apr 13–18, 1997.

Hinkel, D. E., Berger, R. L., Langdon, A. B., Lasinski, B. F., Still, C. H., and Williams, E. A., *Backscatter, Laser Light Smoothing and Channeling in Underdense Plasmas,* Lawrence Livermore National Laboratory, Livermore, CA, UCRL-JC-126306 ABS. Prepared for *2nd Intl Workshop on Laser Plasma Interaction Physics,* Banff, Alberta, Canada, Feb 18–22, 1997.

J

Jancaitis, K. S., Haney, S. W., Munro, D. H., Le Touze, G., and Cabourdin, O., *3-Dimensional Ray-Trace Model for Predicting the Performance of Flashlamp-Pumped Laser Amplifiers,* Lawrence Livermore National Laboratory, Livermore, CA, UCRL-JC-125290. Prepared for *2nd Annual Intl Conf on Solid State Lasers for Application to Inertial Confinement Fusion,* Paris, France, Oct 22–25, 1996.

K

Kalantar, D. H., Budil, K. S., Hammel, B. A., Landen, O. L., and Keane, C. J., *X-Ray Backlit Imaging to Measure the In-Flight Pusher Density of an Indirect Drive Capsule Implosion Core,* Lawrence Livermore National Laboratory, Livermore, CA, UCRL-JC-123285; *Rev. Sci. Instrum.* **68**(1), 814–816 (1997).

Kalantar, D. H., Cauble, R. C., Chandler, E., Colvin, J., Lee, R., Remington, B. A., Wiley, L., Hauer, A., Wark, J. S., Woolsey, N. C., Meyers, M., and Ravichandran, G., *Transient X-Ray Diffraction Used to Diagnose High Pressure Shocked Solids,* Lawrence Livermore National Laboratory, Livermore, CA, UCRL-JC-126831 ABS. Prepared for *1997 Annual Mtg of the American Crystallographic Assn,* St. Louis, MO, Jul 19–25, 1997.

Kalantar, D. H., Da Silva, L. B., Glendinning, S. G., Weber, F., Remington, B. A., Weber, S. V., Key, M. H., Neely, D., Wolfrum, E., Demir, A., Lin, J., Smith, R., Kim, N., Zhang, J., McPhee, A., Warwick, J., and Knauer, J. P., *Extreme Ultraviolet Probing of Laser Imprint in a Thin Foil Using an X-Ray Laser Backlighter,* Lawrence Livermore National Laboratory, Livermore, CA, UCRL-JC-123284; *Rev. Sci. Instrum.* **68**(1), 802–805 (1997).

Kalantar, D. H., Remington, B. A., Budil, K. S., Collins, G. W., Colvin, J. D., Weber, W. V., Griswold, D., Lee, R., Hauer, A., and Wark, J. S., *Hydrodynamic Instability Experiments in the Solid State,* Lawrence Livermore National Laboratory, Livermore, CA, UCRL-JC-126313 ABS. Prepared for *13th Intl Conf on Laser Interactions and Related Plasma Phenomena,* Monterey, CA, Apr 13–18, 1997.

Kane, J., Arnett, W. D., Remington, B. A., Glendinning, S. G., and Rubenchik, A., *Simulations of Supernova-Relevant Hydrodynamics Experiments on the Nova Laser,* Lawrence Livermore National Laboratory, Livermore, CA, UCRL-JC-126311 ABS. Prepared for *13th Intl Conf on Laser Interactions and Related Plasma Phenomena,* Monterey, CA, Apr 13–18, 1997.

Key, M. H., *Edward Teller Medal Lecture—High Intensity Lasers and the Road to Ignition,* Lawrence Livermore National Laboratory, Livermore, CA, UCRL-JC-126846 ABS. Prepared for *13th Intl Conf on Laser Interactions and Related Plasma Phenomena,* Monterey, CA, Apr 13–18, 1997.

Kirkwood, R. K., Back, C. A., Glenzer, S. H., MacGowan, B. J., Montgomery, D. S., and Moody, J. D., *Imaging Back Scattered and Near Back Scattered Light in Ignition Scale Plasmas,* Lawrence Livermore National Laboratory, Livermore, CA, UCRL-JC-124041; *Rev. Sci. Instrum.* **68**(1), 636–640 (1997).

Kirkwood, R. K., MacGowan, B. J., Montgomery, D. S., Afeyan, B. B., Kruer, W. L., Pennington, D. M., Wilks, S. C., Moody, J. D., Wharton, K., Back, C. A., Estabrook, K. G., Glenzer, S. H., Blain, M. A., Berger, R. L., Hinkel, D. E., Lasinski, B. F., Williams, E. A., Munro, D., Wilde, B. H., and Rousseaux, C., *Observation of Multiple Mechanisms for Stimulating Ion Waves in Ignition Scale Plasmas,* Lawrence Livermore National Laboratory, Livermore, CA, UCRL-JC-124651 Rev 1. Prepared for *38th Annual Mtg of the American Physical Society Div of Plasma Physics,* Denver, CO, Nov 11–15, 1997.

Kirkwood, R. K., Moody, J. D., Montgomery, D. S., Afeyan, B. B., MacGowan, B. J., Glenzer, S. H., Estabrook, K. G., Berger, R. L., and Williams, E. A., *Saturation of Stimulated Langmuir Waves by Ion Wave Decays in Ignition Relevant Plasmas,* Lawrence Livermore National Laboratory, Livermore, CA, UCRL-JC-126308 ABS. Prepared for *13th Intl Conf on Laser Interactions and Related Plasma Phenomena,* Monterey, CA, Apr 13–18, 1997.

Koch, J. A., Back, C. A., Brown, C., Hammel, B. A., Hatchett, S. P., Key, M. H., Landen, O. L., Lee, R. W., Moody, J., Offenberger, A., Pennington, D., Perry, M. D., Tabak, M., Yanovsky, V., Wharton, K. B., and Wilks, S. C., *Generation and Characterization of keV, High-Density Plasmas Produced by 100TW and PW Short-Pulse Lasers,* Lawrence Livermore National Laboratory, Livermore, CA, UCRL-JC-126309 ABS. Prepared for *13th Intl Conf on Laser Interactions and Related Plasma Phenomena,* Monterey, CA, Apr 13–18, 1997.

Koch, J. A., Landen, O. L., Hammel, B. A., Seely, J., Brown, C., Bennet, G., Celliers, P., Collins, G., Da Silva, L., Kalantar, D., Feldman, U., Hauer, A., Hsing, W., Kilkenny, J., Marshall, F., and Weber, F., *High-Energy X-Ray Imaging Instrumentation and Applications for the National Ignition Facility,* Lawrence Livermore National Laboratory, Livermore, CA, UCRL-JC-126818 ABS. Prepared for *9th Natl Topical Conf on High Temperature Plasma Diagnostics,* St. Petersburg, Russia, Jun 2–4, 1997.

Kozioziemski, B. J., Collins, G. W., and Bernat, T. P., *Single Crystal Growth of Solid D_2,* Lawrence Livermore National Laboratory, Livermore, CA, UCRL-JC-125981 ABS. Prepared for *1997 March Mtg of the American Physical Society,* Kansas City, MO, Mar 17–21, 1997.

Kruer, W. L., and Afeyan, B. B., *Fluctuation-Induced Stimulated Raman Scattering,* Lawrence Livermore National Laboratory, Livermore, CA, UCRL-JC-126318 ABS. Prepared for *2nd Intl Workshop on Laser Plasma Interaction Physics,* Banff, Alberta, Canada, Feb 18–22, 1997.

Kruer, W. L., and Hammer, J. H., *Laser Beam Deflection in Nonlinearly-Steepened Flow Profiles,* Lawrence Livermore National Laboratory, Livermore, CA, UCRL-JC-124447; *Comments on Plasma Phys. and Controlled Fusion* **18**(2), 85–93 (1997).

L

Land, T. A., Ferguson, J., and De Yoreo, J. J., *Diffusion Controlled Surface Morphology during Solution Growth of KH_2PO_4,* Lawrence Livermore National Laboratory, Livermore, CA, UCRL-JC-126327 ABS. Prepared for *Intl Conf on Crystal Growth XI,* The Hague, Netherlands, Jun 16–28, 1995.

Land, T. A., Lee, J. D., and De Yoreo, J. J., *Real Time AFM Observations of Step-Pinning during Growth of KH_2PO_4 from Solution,* Lawrence Livermore National Laboratory, Livermore, CA, UCRL-JC-126328 ABS. Prepared for *Intl Conf on Crystal Growth XI,* The Hague, Netherlands, Jun 16–28, 1995.

Langer, S. H., Scott, H. A., Keane, C. J., Landen, O. L., and Marinak, M. M., *Yield and Emission Line Ratios from ICF Target Implosions with Multi-Mode Rayleigh–Taylor Perturbations,* Lawrence Livermore National Laboratory, Livermore, CA, UCRL-JC-124484. Submitted to *J. Quant. Spectros. Radiat. Transfer*.

Lasinski, B. F., Cohen, B. I., Langdon, A. B., and Williams, E. A., *Stimulated Brillouin Scatter in PIC-Fluid Simulations,* Lawrence Livermore National Laboratory, Livermore, CA, UCRL-JC-124457 ABS Rev 2. Prepared for *2nd Intl Workshop on Laser Plasma Interaction Physics,* Banff, Alberta, Canada, Feb 18–22, 1997.

Lawson, J., *Fourier Analysis,* Lawrence Livermore National Laboratory, Livermore, CA, UCRL-ID-126849.

Lerche, R A., *Neutron-Induced Noise in NIF-Class Diagnostic Instruments,* Lawrence Livermore National Laboratory, Livermore, CA, UCRL-JC-123556; *Rev. Sci. Instrum.* **68**(1), 628–631 (1997).

Lindl, J. D., *Target Physics Basis for Inertial Confinement Fusion (ICF) Ignition and the Path to Potential Energy Applications,* Lawrence Livermore National Laboratory, Livermore, CA, UCRL-JC-126342 ABS. Prepared for *Princeton Plasma Physics Laboratory,* Princeton, NJ, Feb 12, 1997.

Liu, J. C.-C., *Experimental and Numerical Investigation of Shock Wave Propagation through Complex Geometry, Gas Continuous, Two-Phase Media,* Lawrence Livermore National Laboratory, Livermore, CA, ID-116871.

Logan, B. G., Perry, M. D., and Caporaso, G. J., *Concept for High-Charge-State Ion Induction Accelerators,* Lawrence Livermore National Laboratory, Livermore, CA, UCRL-JC-126828. Prepared for *Intl Atomic Energy Agency Technical Committee Mtg on Drivers and Ignition Facilities for Inertial Fusion,* Osaka, Japan, Mar 10–14, 1997.

M

Malkin, A. J., Kuznetsov, Yu. G., Land, T. A., De Yoreo, J. J., and McPherson, A., *Mechanisms of Growth for Protein and Virus Crystals,* Lawrence Livermore National Laboratory, Livermore, CA, UCRL-JC-126341. Submitted to *Nature Structural Biology*.

Meier, W. R., Moir, R. W., and Abdou, M. A., *Chamber Technology Concepts for Inertial Fusion Energy—Three Recent Examples,* Lawrence Livermore National Laboratory, Livermore, CA, UCRL-JC-126817. Prepared for *4th Intl Symp on Fusion Nuclear Technology,* Tokyo, Japan, Apr 6–11, 1997.

Moir, R. W., *Protection of Final Optics with Cryogenic Liquid Droplets,* Lawrence Livermore National Laboratory, Livermore, CA, UCRL-JC-126820 ABS. Prepared for *13th Intl Conf on Laser Interaction and Related Plasma Phenomena,* Monterey, CA, Apr 13–18, 1997.

Moody, J. D., Brown, C., Hammel, B. A., Hatchett, S. P., Hinkel, D. E., Key, M. H., Koch, J. A., Lasinski, B., Langdon, A. B., MacGowan, B. J., Offenberger, A., Pennington, D., Perry, M. D., Tabak, M., Yanovsky, V., Wharton, K. B., and Wilks, S. C., *Experimental Studies of Hole-Boring in Thin Solid and Foam Targets,* Lawrence Livermore National Laboratory, Livermore, CA, UCRL-JC-126322 ABS. Prepared for *13th Intl Conf on Laser Interactions and Related Plasma Phenomena,* Monterey, CA, Apr 13–18, 1997.

Moody, J. D., MacGowan, B. J., Berger, R. L., Hinkel, D. E., Kruer, W. L., and Williams, E. A., *Fluctuation Measurements in Nova Gasbag Targets Using Near Forward Scattering,* Lawrence Livermore National Laboratory, Livermore, CA, UCRL-JC-126321 ABS. Prepared for *13th Intl Conf on Laser Interactions and Related Plasma Phenomena,* Monterey, CA, Apr 13–18, 1997.

Moon, S. J., and Eder, D. C., *Back-Side Emission from Filtered Gold Targets,* Lawrence Livermore National Laboratory, Livermore, CA, UCRL-JC-126347 ABS. Prepared for *Society of Photo-Optical Instrumentation Engineers 1997 Intl Symp on Optical Science, Engineering, and Instrumentation,* San Diego, CA, Jul 27–Aug 1, 1997.

Moran, M. J., and Hall, J., *Nuclear Diagnostics in Support of Inertial Confinement Fusion Experiments,* Lawrence Livermore National Laboratory, Livermore, CA, UCRL-JC-124232; *Rev. Sci. Instrum.* **68**(1), 521–526 (1997).

Moran, M. J., *PROTEX: a Proton-Recoil Detector for ICF Fusion Neutrons,* Lawrence Livermore National Laboratory, Livermore, CA, UCRL-JC-125996 ABS. Prepared for *1997 Institute of Electronic and Electrical Engineers Intl Conf of Plasma Science,* San Diego, CA, May 19–22, 1997.

O

Orzechowski, T. J., Rosen, M. D., Kornblum, H. N., Porter, J. L., Suter, L. J., Thiessen, A. R., and Wallace, R. J., *Rosseland Mean Opacity of a Mixture of Gold and Gadolinium at High Temperatures,* Lawrence Livermore National Laboratory, Livermore, CA, UCRL-JC-123318-ERR. Submitted to *Phys. Rev. Lett.*

P

Page, R. H., Bartels, R. A., Beach, R. J., Sutton, S. B., Furu, L. H., and LaSala, J. E., *1-Watt Composite-Slab Er:YAG Laser,* Lawrence Livermore National Laboratory, Livermore, CA, UCRL-JC-125351 Rev 1. Prepared for *12th Topical Mtg on Advanced Solid-State Lasers,* Orlando, FL, Jan 27–29, 1997.

Page, R. H., Schaffers, K. I., DeLoach, L. D., Wilke, G. D., Patel, R. D., Tassano, J. B., Payne, S. A., and Krupke, W. F., *Cr^{2+}-Doped Zinc Chalcogenides as Efficient, Widely-Tunable Mid-Infrared Lasers,* Lawrence Livermore National Laboratory, Livermore, CA, UCRL-JC-123768 Rev 1. Submitted to *J. of Quantum Electronics.*

Page, R. H., Skidmore, J. A., Schaffers, K. I., Beach, R. J., Payne, S. A., and Krupke, W. F., *2150–2800 nm Coverage and Diode Pumping with $ZnSe:Cr^{2+}$ Lasers,* Lawrence Livermore National Laboratory, Livermore, CA, UCRL-JC-126302 ABS SUM. Prepared for *Conf on Lasers and Electro-Optics/Pacific Rim '97,* Chiba, Japan, Jul 14–18, 1997.

Page, R. H., Skidmore, J. A., Schaffers, K. I., Beach, R. J., Payne, S. A., and Krupke, W. F., *Demonstrations of Diode-Pumped and Grating-Tuned $ZnSe:Cr^{2+}$ Lasers,* Lawrence Livermore National Laboratory, Livermore, CA, UCRL-JC-125353 Rev 1. Prepared for *12th Topical Mtg on Advanced Solid-State Lasers,* Orlando, FL, Jan 27–29, 1997.

Payne, S. A., Beach, R. J., Bibeau, C., Ebbers, C. A., Emanuel, M. A., Honea, E. C., Marshall, C. D., Page, R. H., Schaffers, K. I., Skidmore, J. D., Sutton, S. B., and Krupke, W. F., *Diode Arrays, Crystals, and Thermal Management for Solid-State Lasers,* Lawrence Livermore National Laboratory, Livermore, CA, UCRL-JC-126323; *IEEE Special Issue on Selected Topics* **3**(1), 71–81 (1997).

Pennington, D. M., Milam, D., and Eimerl, D., *Gain Saturation Studies in LG-750 and LG-770 Amplifier Glass,* Lawrence Livermore National Laboratory, Livermore, CA, UCRL-JC-124504. Prepared for *2nd Annual Intl Conf on Solid-State Lasers for Applications to Inertial Confinement Fusion,* Paris, France, Oct 22–25, 1996.

Pennington, D. M., Perry, M. D., Boyd, R., Britten, J. A., Brown, C. G., Herman, S., Horner, J., Miller, J. L., Nguyen, H., Shore, B., Stuart, B. C., Tietbohl, G., and Yanovsky, V., *Petawatt Laser and Targeting System,* Lawrence Livermore National Laboratory, Livermore, CA, UCRL-JC-126336 ABS. Prepared for *13th Intl Conf on Laser Interactions and Related Plasma Phenomena,* Monterey, CA, Apr 13–18, 1997.

Pennington, D. M., Perry, M. D., Stuart, B. C., Boyd, R., Britten, J. A., Brown, C. G., Herman, S., Miller, J. L., Nguyen, H., Shore, B., Tietbohl, G., and Yanovsky, V., *Petawatt Laser System,* Lawrence Livermore National Laboratory, Livermore, CA, UCRL-JC-124492. Prepared for *2nd Annual Intl Conf on Solid-State Lasers for Applications to Inertial Confinement Fusion,* Paris, France, Oct 22–25, 1996.

Perry, M. D., Pennington, D. M., Stuart, B. C., Boyd, R., Britten, J. A., Brown, C. G., Herman, S., Miller, J. L., Nguyen, H., Shore, B., Tietbohl, G., and Yanovsky, V., *Design and Performance of the Petawatt Laser System,* Lawrence Livermore National Laboratory, Livermore, CA, UCRL-JC-126317ABS&SU. Prepared for *Conf on Lasers & Electro-Optics/Quantum Electronics and Laser Science Conf '97,* Baltimore, MD, May 18–23, 1997.

Phillips, T. W., Cable, M. D., Hicks, D. G., Li, C. K., Petrasso, R. D., and Seguin, F. H., *A Study of CR-39 Track Response to Charged Particles from Nova Implosions,* Lawrence Livermore National Laboratory, Livermore, CA, UCRL-JC-124231; *Rev. Sci. Instrum.* **68**(1), 596–598 (1997).

R

Reiser, K. M., Small, W., Maitland, D. J., Heredia, N. J., Da Silva, L. B., Matthews, D. L., and Last, J. A., *Laser Welding and Collagen Crosslinks,* Lawrence Livermore National Laboratory, Livermore, CA, UCRL-JC-126841. Prepared for *Society of Photo-Optical Instrumentation Engineers Intl Symp on Optical Applied Science and Engineering,* San Jose, CA, Feb 8, 1997.

Remington, B. A., Kane, J., Drake, R. P., Glendinning, S. G., Estabrook, K., London, R., Wallace, R. J., Arnett, D., Liang, E., McCray, R., and Rubenchik, A., *Supernova Hydrodynamics Experiments Using the Nova Laser,* Lawrence Livermore National Laboratory, Livermore, CA, UCRL-JC-126312 ABS Rev 1. Prepared for *5th Cerro Tololo Inter-American Observatory/European Southern Observatory Workshop,* La Serena, Chile, Feb 22–28, 1997.

Remington, B. A., Kane, J., Drake, R. P., Glendinning, S. G., Estabrook, K., London, R., Wallace, R. J., Arnett, D., Liang, E., McCray, R., and Rubenchik, A., *Supernova Hydrodynamics Experiments Using the Nova Laser,* Lawrence Livermore National Laboratory, Livermore, CA, UCRL-JC-126312 ABS. Prepared for *13th Intl Conf on Laser Interactions and Related Plasma Phenomena,* Monterey, CA, Apr 13–18, 1997.

Rhodes, M. A., and Fochs, S., *Two-Aperture Plasma-Electrode Pockels Cell,* Lawrence Livermore National Laboratory, Livermore, CA, UCRL-JC-126571. Submitted to *R&D Magazine.*

Rothenberg, J. E., and Weber, S. V., *Impact of Beam Smoothing Method on Direct Drive Target Performance for the NIF,* Lawrence Livermore National Laboratory, Livermore, CA, UCRL-JC-124509 Rev 1. Prepared for *2nd Annual Intl Conf on Solid-State Lasers for Application to Inertial Confinement Fusion,* Paris, France, Oct 22–25, 1996.

Rothenberg, J. E., *Electro-Optic Deflectors as a Method of Beam Smoothing for Inertial Confinement Fusion,* Lawrence Livermore National Laboratory, Livermore, CA, UCRL-JC-124507. Prepared for *2nd Annual Intl Conf on Solid-State Lasers for Appplication to Inertial Confinement Fusion,* Paris, France, Oct 22–25, 1996.

Rothenberg, J. E., *Improved Beam Smoothing with SSD Using Generalized Phase Modulation,* Lawrence Livermore National Laboratory, Livermore, CA, UCRL-JC-124508. Prepared for *2nd Annual Intl Conf on Solid-State Lasers for Application to Inertial Confinement Fusion*, Paris, France, Oct 22–25, 1996.

Rothenberg, J. E., Moran, B., Henesian, M., and Van Wonterghem, B., *Evaluation of Smoothing by Spectral Dispersion on the Beamlet Laser for the National Ignition Facility,* Lawrence Livermore National Laboratory, Livermore, CA, UCRL-JC-125988 ABS & SUM. Prepared for *1997 Conf on Lasers & Electro-Optics,* Baltimore, MD, May 18–23, 1997.

Rothenberg, J. E., Moran, B., Henesian, M., and Van Wonterghem, B., *Performance of Smoothing by Spectral Dispersion (SSD) on Beamlet,* Lawrence Livermore National Laboratory, Livermore, CA, UCRL-JC-124506. Prepared for *2nd Annual Intl Conf on Solid-State Lasers for Application to Inertial Confinement Fusion,* Paris, France, Oct 22–25, 1996.

S

Sacks, R. A., Williams, W. W., Henesian, M. A., Orth, C. D., Haney, S. W., Trenholme, J. B., Auerbach, J. M., and Lawson, J. K., *Propagation Modeling in Two Transverse Dimensions of the National Ignition Facility Baseline Performance,* Lawrence Livermore National Laboratory, Livermore, CA, UCRL-JC-125292. Prepared for *2nd Annual Intl Conf on Solid-State Lasers for Application to Inertial Confinement Fusion,* Paris, France, Oct 22–25, 1996.

Schaffers, K. I., Bayramian, A. J., Marshall, C. D., Tassano, J. B., and Payne, S. A., *Analysis of Sr_5-$Ba(PO_4)_3F$:Yb^{3+} Crystals for Improved Laser Performance with Diode-Pumping,* Lawrence Livermore National Laboratory, Livermore, CA, UCRL-JC-126339. Prepared for *12th Topical Mtg on Advanced Solid-State Lasers,* Orlando, FL, Jan 27–29, 1997.

Schaffers, K., and Payne, S. A., *Crystal Growth of Optical Materials for Advanced Lasers,* Lawrence Livermore National Laboratory, Livermore, CA, UCRL-ID-126458.

Sharp, W. M., and Kamin, G. W., *Transverse-Control Algorithms for a Small Recirculating Heavy-Ion Accelerator,* Lawrence Livermore National Laboratory, Livermore, CA, UCRL-JC-125998 ABS. Prepared for *1997 Particle Accelerator Conf,* Vancouver, BC, Canada, May 12–16, 1997.

Shestakov, A. I., Dubois, P. F., Furnish, G., Gentile, N. A., Milovich, J. L., Motteler, Z., Prasad, M. K., Painter, J. F., and Yang, T.-Y. B., *The ICF3D Code,* Lawrence Livermore National Laboratory, Livermore, CA, UCRL-JC-124448. Submitted to *J. Comp. Physics.*

Shore, B. W., Li, L. F., and Feit, M. D., *Poynting Vectors and Electric Field Distributions in Simple Dielectric Gratings,* Lawrence Livermore National Laboratory, Livermore, CA, UCRL-JC-123297; *J. Modern Optics* **44**(1), 69–81 (1997).

Small IV, W., Maitland, D. J., Heredia, N. J., Eder, D. C., Celliers, P. M., Da Silva, L. B., London, R. A., and Matthews, D. L., *Investigation of Laser Tissue Welding Dynamics via Experiment and Modeling,* Lawrence Livermore National Laboratory, Livermore, CA, UCRL-JC-126842. Submitted to *J. Clinical Laser Med. & Surg.*

Small IV, W., Celliers, P. M., Da Silva, L. B., Matthews, D. L., and Soltz, B. A., *Two-Color Infrared Thermometer for Low-Temperature Measurement Using a Hollow Glass Optical Fiber,* Lawrence Livermore National Laboratory, Livermore, CA, UCRL-JC-126840. Prepared for *Society of Photo-Optical Instrumentation Engineers Intl Symp on Optical Applied Science and Engineering,* San Jose, CA, Feb 8, 1997.

Snavely, R. A., Da Silva, L. B., Eder, D. C., Matthews, D. L., and Moon, S. J., *Traveling Wave Pumping of Ultra-Short Pulse X-Ray Lasers,* Lawrence Livermore National Laboratory, Livermore, CA, UCRL-JC-125992 ABS. Prepared for *Society of Photo-Optical Instrumentation Engineers '97 Conf,* San Diego, CA, Jul 27–Aug 1, 1997.

Still, C. H., Williams, E. A., Young, P. E., Estabrook, K. G., Hinkel, D. E., Langdon, A. B., and Berger, R. L., *Simulating Beam Deflection and Channel Formation with F3D,* Lawrence Livermore National Laboratory, Livermore, CA, UCRL-JC-126304 ABS. Prepared for *2nd Intl Workshop on Laser Plasma Interaction Physics,* Banff, Alberta, Canada, Feb 18–22, 1997.

Stuart, B. C., Perry, M. D., Feit, M. D., Da Silva, L. B., Rubenchik, A. M., Neev, J., Herman, S., Nguyen, H., and Armstrong, P., *Femtosecond Laser Materials Processing,* Lawrence Livermore National Laboratory, Livermore, CA, UCRL-JC-126064. Prepared for *Applications of High Field and Short Wavelength Sources 7th Topical Mtg,* Santa Fe, NM, Mar 19–22, 1997.

Suter, L. J., Thiessen, A. R., Ze, F., Kauffman, R., Price, R. H., Rupert, V. C., Slivinsky, V. W., and Wang, C., *Use of Thin Wall Imaging in the Diagnosis of Laser Heated Hohlraums,* Lawrence Livermore National Laboratory, Livermore, CA, UCRL-JC-116323; *Rev. Sci. Instrum.* **68**(1), 838–841 (1997).

Sutton, S., Marshall, C., Petty, C., Smith, L., Van Wonterghem, B., and Mills, S., *Thermal Recovery of NIF Amplifiers,* Lawrence Livermore National Laboratory, Livermore, CA, UCRL-JC-124528. Prepared for *2nd Annual Intl Conf on Solid-State Lasers for Application to Inertial Confinement Fusion,* Paris, France, Oct 22–25, 1996.

V

Van Wonterghem, B., Murray, J. E., Burkhart, S. C., Penko, F., Henesian, M. A., Auerbach, J. A., Wegner, P. J., and Caird, J. A., *High Fluence 1.05 µm Performance Tests Using 20 ns Shaped Pulses on the Beamlet Prototype Laser,* Lawrence Livermore National Laboratory, Livermore, CA, UCRL-JC-124865. Prepared for *2nd Annual Intl Conf on Solid-State Lasers for Application to Inertial Confinement Fusion,* Paris, France, Oct 22–25, 1996.

Van Wonterghem, B., Murray, J. R., Campbell, J. H., Speck, D. R., Barker, C. E., Smith, I. C., Browning, D. F., and Behrendt, W. C., *Performance of a Prototype, Large-Aperture Multipass Nd-Glass Laser for Inertial Confinement Fusion,* Lawrence Livermore National Laboratory, Livermore, CA, UCRL-JC-125150 Rev 1. Submitted to *Appl. Opt.*

W

Weber, F. A., Barbee, T. W., Cauble, R., Celliers, P., Da Silva, L. B., Decker, C. D., London, R. A., Moreno, J. C., Snavely, R., Trebes, J. E., and Wan, A. S., *High Density Plasma Probing with Soft X-Ray Lasers,* Lawrence Livermore National Laboratory, Livermore, CA, UCRL-JC-126505 ABS. Prepared for *Society of Photo-Optical Instrumentation Engineers 1997 Intl Symp on Optical Science, Engineering, and Instrumentation,* San Diego, CA, Jul 27–Aug 1, 1997.

Weber, F. A., Barbee, T. W., Celliers, P., Da Silva, L. B., Tanaka, K., Kodama, R., and Takahashi, K., *Soft X-Ray Laser Based Moire Deflectometry of Dense Plasmas,* Lawrence Livermore National Laboratory, Livermore, CA, UCRL-JC-126506 ABS. Prepared for *Society of Photo-Optical Instrumentation Engineers 1997 Intl Symp on Optical Science, Engineering, and Instrumentation,* San Diego, CA, Jul 27–Aug 1, 1997.

Weber, F. A., Da Silva, L. B., Barbee, T. W., Ciarlo, D., and Mantler, M., *Quantification of Carbon in a Binary System by the Fundamental Parameter Method,* Lawrence Livermore National Laboratory, Livermore, CA, UCRL-JC-126507 (1997). Submitted to *Adv. in X-ray Analysis 40.*

Weber, S. V., Budil, K. S., Colvin, J. D., Glendinning, S. G., Griswold, D. L., Kalantar, D. H., and Remington, B. A., *Simulations of Rayleigh–Taylor Growth for Direct Drive and with Material Strength,* Lawrence Livermore National Laboratory, Livermore, CA, UCRL-JC-125995 ABS. Prepared for *6th Intl Workshop on the Physics of Compressible Turbulent Mixing,* Marseille, France, Jun 18–21, 1997.

Weber, S. V., Budil, K. S., Colvin, J. D., Kalantar, D. H., Peyser, T. A., and Remington, B. A., *Simulations of Rayleigh–Taylor Growth at Imbedded Interfaces and with Material Strength,* Lawrence Livermore National Laboratory, Livermore, CA, UCRL-JC-126970 ABS. Prepared for *27th Annual Anomalous Absorption Conf,* Vancouver, BC, Canada, Jun 1–5, 1997.

Weber, S. V., Glendinning, S. G., Kalantar, D. H., Key, M. H., Remington, B. A., Rothenberg, J. E., Wolfrum, E., Verdon, C. P., and Knauer, J. P., *Simulations of Laser Imprint for Nova Experiments and for Ignition Capsules,* Lawrence Livermore National Laboratory, Livermore, CA, UCRL-JC-124547 Rev 1. Prepared for *38th Annual Mtg of the American Physical Society Div of Plasma Physics,* Denver, CO, Nov 11–15, 1996.

Wegner, P. J., Barker, C. E., Caird, J. A., Dixit, S. N., Henesian, M. A., Seppala, L. G., Thompson, C. E., and Van Wonterghem, B. V., *Third-Harmonic Performance of the Beamlet Prototype Laser,* Lawrence Livermore National Laboratory, Livermore, CA, UCRL-JC-124529. Prepared for *2nd Annual Intl Conf on Solid-State Lasers for Application to Inertial Confinement Fusion*, Paris, France, Oct 22–25, 1996.

Wharton, K., Brown, C., Hammel, B., Hatchett, S., Koch, J., Moody, J., Offenberger, A., Perry, M., Tabak, M., Wilks, S., Yanovsky, V., and Zakharenkov, Y., *Characterization of Hot Electrons Produced by 5×10^{19} W/cm^2 Laser–Plasma Interactions,* Lawrence Livermore National Laboratory, Livermore, CA, UCRL-JC-126310 ABS. Prepared for *13th Intl Conf on Laser Interactions and Related Plasma Phenomena,* Monterey, CA, Apr 13–18, 1997.

Wilks, S. C., Wharton, K., Hatchett, S., Tabak, M., Key, M., and Kruer, W. L., *Recent 100 terawatt k_α Experiments at LLNL: Hot Electron Production for the Fast Ignitor,* Lawrence Livermore National Laboratory, Livermore, CA, UCRL-JC-126307 ABS. Prepared for *2nd Intl Workshop on Laser Plasma Interaction Physics,* Banff, Alberta, Canada, Feb 18–22, 1997.

Williams, E. A., Cohen, B. I., and Berger, R. L., *Ion Wave Parametric Decay and Related Instabilities,* Lawrence Livermore National Laboratory, Livermore, CA, UCRL-JC-126305 ABS. Prepared for *2nd Intl Workshop on Laser Plasma Interaction Physics,* Banff, Alberta, Canada, Feb 18–22, 1997.

Woods, B., Runker, M., Yan, M., Staggs, M., Zaitseva, N., Kozlowski, M., and De Yoreo, J., *Investigation of Damage in KDP Using Light Scattering Techniques,* Lawrence Livermore National Laboratory, Livermore, CA, UCRL-JC-125368. Prepared for *28th Annual Symp on Optical Materials for High Power Lasers '96,* Boulder, CO, Oct 7–9, 1996.

Y

Yan, M., Torres, R., Runkel, M., Woods, B., Hutcheon, I., Zaitseva, N., and De Yoreo, J., *Impurity and Laser-Induced Damage in the Growth Sectors of Rapidly Grown KDP Crystals,* Lawrence Livermore National Laboratory, Livermore, CA, UCRL-JC-126804. Prepared for *28th Annual Symp on Optical Materials for High Power Lasers '96,* Boulder, CO, Oct 7–9, 1996.

Z

Zaitseva, N. P., De Yoreo, J. J., Dehaven, M. R., Vital, R. L., Carman, L. M., and Spears, H. R., *Rapid Growth of Large-Scale (40–55 cm) KDP Crystals,* Lawrence Livermore National Laboratory, Livermore, CA, UCRL-JC-126805. Prepared for *2nd Annual Intl Conf on Solid-State Lasers for Application to Inertial Confinement Fusion,* Paris, France, Oct 22–25, 1996.

PUBLICATIONS AND PRESENTATIONS
APRIL–JUNE 1997

A

Afeyan, B. B., Chou, A. E., Kruer, W. L., Schmitt, A. J., and Town, R., *Nonlinear Evolution of Stimulated Raman and Brillouin Scattering in Inhomogeneous and Nonstationary Plasmas,* Lawrence Livermore National Laboratory, Livermore, CA, UCRL-JC-127119-ABS. Prepared for the *27th Annual Anomalous Absorption Conf,* Vancouver, BC, Canada, Jun 1–5, 1997.

Amendt, P., Glendinning, S. G., Hammel, B. A., Landen, O. L., Murphy, T. J., Suter, L. J., Hatchett, S., Rosen, M. D., Lafitte, S., Desenne, D., and Jaduad, J. P., *New Methods for Diagnosing and Controlling Hohlraum Drive Asymmetry on Nova*, Lawrence Livermore National Laboratory, Livermore, CA, UCRL-JC-124658; *Phys. Plasmas* **4**(5), 1862–1871 (1997).

B

Bailey, D. S., Hatchett, S., and Tabak, M., *Stopping Questions for the Fast Ignitor,* Lawrence Livermore National Laboratory, Livermore, CA, UCRL-JC-127746-ABS. Prepared for the *8th Intl Workshop on Atomic Physics for Ion-Driven Fusion,* Heidelberg, Germany, Sept 22–23, 1997.

Berger, R. L., Kirkwood, R. K., Langdon, A. B., MacGowan, B. J., Montgomery, D. S., Moody, J., Still, C. H., and Williams, E. A., *Interplay among Stimulated Raman and Brillouin Backscattering and Filamentation Instabilities,* Lawrence Livermore National Laboratory, Livermore, CA, UCRL-JC-127133-ABS. Prepared for the *27th Annual Anomalous Absorption Conf,* Vancouver, BC, Canada, Jun 1–5, 1997.

Bibeau, C., Beach, R., Ebbers, C., Emanuel, M., Honea, E., Mitchell, S., and Skidmore, J., *Performance of a Diode-End-Pumped Yb:YAG Laser,* Lawrence Livermore National Laboratory, Livermore, CA, UCRL-JC-127284. Prepared for the *1997 Diode Laser Technical Review,* Albuquerque, NM, Jun 9–12, 1997.

Boone, T., Cheung, L., Cook, R., Nelson, D., and Wilemski, G., *Modeling of Microencapsulated Polymer Mandrel Solidification,* Lawrence Livermore National Laboratory, Livermore, CA, UCRL-JC-127118-ABS. Prepared for *Microsphere-Microcapsules and ICF Targets Technology,* Moscow, Russia, Jun 2–7, 1997.

Britten, J., Boyd, R. D., Ceglio, N. T., Fernandez, A., Hawryluk, A. M., Hoaglan, C. R., Kania, D. R., Nguyen, H. T., Perry, M. D., and Spallas, J. P., *Precision Manufacturing Using Advanced Optical Interference Lithography,* Lawrence Livermore National Laboratory, Livermore, CA, UCRL-ID-127161.

Budil, K. S., Barbee, T. W., Celliers, P., Collins, G. W., Da Silva, L. B., Hammel, B. A., Holmes, N. C., Kilkenny, J. D., Ross, M., and Wallace, R. J., *Absolute Equation of State Measurements of Shocked Liquid Deuterium up to 200 GPa (2 Mbar),* Lawrence Livermore National Laboratory, Livermore, CA, UCRL-JC-124445 Rev 1. Prepared for the *6th Intl Workshop on the Physics of Compressible Turbulent Mixing,* Marseille, France, Jun 18–21, 1997.

Budil, K. S., Perry, T. S., Peyser, T. A., Remington, B. A., and Weber, S. V., *Nonlinear Rayleigh–Taylor Instability Experiments at Nova,* Lawrence Livermore National Laboratory, Livermore, CA, UCRL-JC-127732. Prepared for the *6th Intl Workshop on the Physics of Compressible Turbulent Mixing,* Marseille, France, Jun 18–21, 1997.

Burnham, A., Alford, C. S., Dittrich, T. R., Honeau, E. C., King, C. M., Makowiecki, D. M., Steinman, D., and Wallace, R. J., *Evaluation of B₄C as an Ablator Material for NIF Capsules,* Lawrence Livermore National Laboratory, Livermore, CA, UCRL-JC-125144 Rev 1. Prepared for the *11th Target Fabrication Specialists' Mtg,* Orcas Island, WA, Sept 8–12, 1996.

C

Cable, M. D., Barbee, T. W., Koch, J. A., Lane, S. M., Lerche, R. A., Moran, M. J., Ognibene, T. E., Ress, D. B., Sangster, T. C., and Trebes, J. E., *Diagnostics for High Density Implosions at Nova and the National Ignition Facility,* Lawrence Livermore National Laboratory, Livermore, CA, UCRL-JC-126844. Prepared for the *9th Natl Topical Conf on High-Temperature Plasma Diagnostics,* St. Petersburg, Russia, Jun 2–4, 1997.

Campbell, E. M., Decker, C., Kruer, W. L., Suter, L. J., and Wilks, S. C., *Laser Plasma Physics for Advanced Hohlraums,* Lawrence Livermore National Laboratory, Livermore, CA, UCRL-JC-127745-ABS. Prepared for the *39th Annual Mtg of the American Physical Society Div of Plasma Physics,* Pittsburgh, PA, Nov 17–21, 1997.

Cauble, R., Da Silva, L. B., Perry, T. S., Bach, D. R., Budil, K. S., Celliers, P., Collins, G. W., Ng, A., Barbee Jr,. T. W., Hammel, B. A., Holmes, N. C., Kilkenny, J. D., Wallace, R. J., Chiu, G., and Woolsey, N. C., *Absolute Measurements of the Equations of State of Low-Z Materials in the Multi-Mbar Regime Using Laser-Driven Shocks*, Lawrence Livermore National Laboratory, Livermore, CA, UCRL-JC-125746; *Phys. Plasmas* **4**(5), 1857–1861 (1997).

Cohen, B. I., Lasinski, B. F., Langdon, A. B., and Williams, E. A., *Resonantly Excited Nonlinear Ion Waves,* Lawrence Livermore National Laboratory, Livermore, CA, UCRL-JC-124922; *Phys. Plasmas* **4**(4), 956–977 (1997).

Collins, G. W., Barbee, T. W., Budil, K. S., Cauble, R., Celliers, P., Da Silva, L. B., Gold, D., Hammel, B. A., Holmes, N. C., and Stewart, R., *Equation of State Measurements of Hydrogen and Deuterium up to 2 Mbar,* Lawrence Livermore National Laboratory, Livermore, CA, UCRL-JC-127101-ABS. Prepared for *1997 Topical Conf on Shock Compression of Condensed Matter,* Amherst, MA, Jul 27–Aug 1, 1997.

Colvin, J. D., Chandler, E. A., Kalantar, D. H., Remington, B. A., and Wiley, L. G., *Dispersion Relationship for Solid State Instability Growth and Sensitivity to Equation of State,* Lawrence Livermore National Laboratory, Livermore, CA, UCRL-JC-127496. Prepared for the *6th Intl Workshop on the Physics of Compressible Turbulent Mixing,* Marseille, France, Jun 18–21, 1997.

Colvin, J. D., Griswold, D. L., Kalantar, D. H., and Remington, B. A., *Scaling Relationships for Solid State Instability Growth and Sensitivity to Equation of State,* Lawrence Livermore National Laboratory, Livermore, CA, UCRL-JC-127496-ABS. Prepared for the *6th Intl Workshop on the Physics of Compressible Turbulent Mixing,* Marseille, France, Jun 18–21, 1997.

Cook, R., Gresho, P. M., and Hamilton, K. E., *How Spherical Can We Make Microencapsulated Shells?* Lawrence Livermore National Laboratory, Livermore, CA, UCRL-JC-127149-ABS. Prepared for *Microsphere-Microcapsules and ICF Targets Technology,* Moscow, Russia, Jun 2–7, 1997.

D

Dane, C. B., Bhachu, B., Hackel, L. A., and Wintemute, J. D., *Diffraction-Limited, High Average Power Phase-Locking of Four 30J Beams from Discrete Nd:Glass Zig-Zag Amplifiers,* Lawrence Livermore National Laboratory, Livermore, CA, UCRL-JC-127264. Prepared for the *Conf on Lasers and Electro-Optics/Quantum Electronics and Laser Science Conf '97,* Baltimore, MD, May 18–23, 1997.

De Yoreo, J. J., Land, T. A., Lee, J. D., and Orme, C., *Studying the Surface Morphology and Growth Dynamics of Solution-Based Crystals Using the Atomic Force Microscope,* Lawrence Livermore National Laboratory, Livermore, CA, UCRL-JC-127726-ABS. Prepared for the *Romanian Conf on Advanced Materials '97,* Bucharest, Romania, Nov 24–26, 1997.

Decker, C., Amendt, P., Glendinning, G., Hammel, B. A., Hauer, A. A., Landen, O. L., Murphy, T. J., Suter, L. J., Turner, R. E., and Wallace, J., *Measuring the Hohlraum Radiation Drive on the Omega Laser Using Dante and the Foam Ball Technique,* Lawrence Livermore National Laboratory, Livermore, CA, UCRL-JC-127146-ABS. Prepared for the *27th Annual Anomalous Absorption Conf,* Vancouver, BC, Canada, Jun 1–5, 1997.

Decker, C., Back, C., Davis, J., Grun, J., and Suter, L., *Modeling Multi-keV Radiation Production of Laser Heated Xe Filled Be Cans,* Lawrence Livermore National Laboratory, Livermore, CA, UCRL-JC-127145-ABS. Prepared for the *27th Annual Anomalous Absorption Conf,* Vancouver, BC, Canada, Jun 1–5, 1997.

Dimonte, G., Baumgardner, J. R., Flower-Maudin, E., Gore, R., Nelson, D., Sahota, M. S., Schneider, M., and Weaver, S., *Rheological Characterization of Virgin Yogurt,* Lawrence Livermore National Laboratory, Livermore, CA, UCRL-JC-127477. Submitted to *J. Rheol.*

Dimonte, G., Gore, R., and Schneider, M., *Rayleigh–Taylor Instability in Elastic–Plastic Materials,* Lawrence Livermore National Laboratory, Livermore, CA, UCRL-JC-127495. Submitted to *Phys. Rev. Lett.*

Dorogotovtsev, V. M., Akunets, A. A., Cook, R., Fearon, E., Merkuliev, Y. A., Reibold, R., and Turivnoy, A. P., *Thermal Decomposition of Polystyrene in the High Temperature Fabrication Technology of Hollow Microspheres,* Lawrence Livermore National Laboratory, Livermore, CA, UCRL-JC-125232 Rev 1. Prepared for the *11th Target Fabrication Specialists' Mtg,* Orcas Island, WA, Sept 8–12, 1996, and submitted to *Fusion Technol.*

Drake, R. P., Estabrook, K., and Watt, R. G., "Greatly Enhanced Acoustic Noise and the Onset of Stimulated Brillouin Scattering," *Phys. Plasmas* **4**(5), 1825–1831 (1997).

E

Emanuel, M. A., Jensen, M., Nabiev, R., and Skidmore, J. A., *High Power InAIGaAs/GaAs Laser Diode Emitting near 731 nm,* Lawrence Livermore National Laboratory, Livermore, CA, UCRL-JC-127116. Submitted to the *IEEE Photonics Technol. Lett.*

F

Fearon, E. M., Allison, L. M., Cook, R. C., and Letts, S. A., *Adapting the Decomposable Mandrel Technique to Build Specialty ICF Targets,* Lawrence Livermore National Laboratory, Livermore, CA, UCRL-JC-127113. Prepared for the *11th Target Fabrication Specialists' Mtg,* Orcas Island, WA, Sept 8–12, 1996, and submitted to *Fusion Technol.*

Feit, M. D., Garrison, J. C., Komashko, A., Musher, S. L., Rubenchik, A. M., and Turisyn, S. K., *Relativistic Self-Focusing in Underdense Plasma,* Lawrence Livermore National Laboratory, Livermore, CA, UCRL-JC-I27277. Prepared for the *13th Intl Conf on Laser Interactions and Related Plasma Phenomena,* Monterey, CA, Apr 13–18, 1997.

Fernandez, A., Nguyen, H. T., Britten, J. A., Boyd, R. D., Perry, M. D., Kania, D. R., and Hawryluk, A. M., *The Use of Interference Lithography to Pattern Arrays of Submicron Resist Structures for Field Emission Flat Panel Displays,* Lawrence Livermore National Laboratory, Livermore, CA, UCRL-JC-125953; *J. Vac. Sci. & Tech. B* **14**(5), 729–735 (1997).

Fernandez, J. C., Bauer, B. S., Cobble, J. A., Dubois, D. F., Kyrala, G. A., Montgomery, D. S., Rose, H. A., Vu, H. X., Watt, R. G., Wilde, B. H., Wilke, M. D., Wood, W. M., Failor, B. H., Kirkwood, R., and MacGowan, B. J., "Measurements of Laser-Plasma Instability Relevant to Ignition Hohlraums," *Phys. Plasmas* **4**(5), 1849–1856 (1997).

Furnish, G., *Disambiguated Glommable Expression Templates,* Lawrence Livermore National Laboratory, Livermore, CA, UCRL-JC-126523; *Computers in Physics* **11**(3), 263–269 (1997).

G

Genin, F. Y., Brusasco, R., and Kozlowski, M. R., *Catastrophic Failure of Contaminated Fused Silica Optics at 355 nm,* Lawrence Livermore National Laboratory, Livermore, CA, UCRL-JC-125417. Prepared for the *2nd Annual Intl Conf on Solid-State Lasers for Applications to Inertial Confinement Fusion,* Paris, France, Oct 22–25, 1996.

Genin, F., Feit, M., Kozlowski, M., Rubenchik, A., and Salleo, A., *UV Laser Ablation of Glass Enhanced by Contamination Particles,* Lawrence Livermore National Laboratory, Livermore, CA, UCRL-JC-127483-ABS. Prepared for the *4th Conf on Laser Ablation,* Pacific Grove, CA, Jul 21, 1997.

Glendinning, S. G., Budil, K. S., Marinak, M. M., Remington, B. A., and Wallace, R. J., *Measurements of Rayleigh–Taylor Unstable Growth of a Three-Dimensional Continuous Spectrum of Modes,* Lawrence Livermore National Laboratory, Livermore, CA, UCRL-JC-127115-ABS. Prepared for the *27th Annual Anomalous Absorption Conf,* Vancouver, BC, Canada, Jun 1–5, 1997.

Glendinning, S. G., Dixit, S. N., Hammel, B. A., Kalantar, D. H., Key, M. H., Kilkenny, J. D., Knauer, J. P., Pennington, D. M., Remington, B. A., Wallace, R. J., and Weber, S. V., *Measurement of a Dispersion Curve for Linear-Regime Rayleigh-Taylor Growth Rates in Laser-Driven Planar Targets*, Lawrence Livermore National Laboratory, Livermore, CA, UCRL-JC-124653; *Phys. Rev. Lett.* **78**(17), 3318–3321 (1997).

Glendinning, S. G., Dixit. S. N., Hammel, B. A., Kalantar, D. H., Key, M. H., Kilkenny, J. D., Knauer, J. P., Pennington, D. M., Remington, B. A., and Wallace, R. J., *Comparison of Drive-Seeded Modulations in Planar Foils for 0.35 and 0.53 μm Laser Drive*, Lawrence Livermore National Laboratory, Livermore, CA, UCRL-JC-127617. Submitted to *Phys. of Plasmas.*

Glenzer, S. H., Back, C. A., Blain, M. A., Landen, O. L., MacGowan, B. J., Stone, G. F., Suter, L. J., Turner, R. E., and Wilde, B. H., *Thomson Scattering from Inertial Confinement Fusion Hohlraum Plasmas*, Lawrence Livermore National Laboratory, Livermore, CA, UCRL-JC-126320-ABS Rev 1. Prepared for the *27th Annual Anomalous Absorption Conf,* Vancouver, BC, Canada, Jun 1–5, 1997.

H

Hackel, L. A., and Dane, C. B., *Laser Shock Processing of Metals Techniques and Laser Technology,* Lawrence Livermore National Laboratory, Livermore, CA, UCRL-JC-127731-ABS. Prepared for the *Materials Research Society Fall 1997 Mtg.*, Boston, MA, Dec 1, 1997.

Hamilton, K. E., Buckley, S. R., Cook, R. C., Fearon, E. M., Letts, S. A., Schroen-Carey, D., and Wilemski, G., *Role of Reactant Transport in Determining the Properties of NIF Shells Made by Interfacial Polycondensation,* Lawrence Livermore National Laboratory, Livermore, CA, UCRL-JC-125125. Prepared for the *11th Target Fabrication Specialists' Mtg,* Orcas Island, WA, Sept 8–12, 1996, and submitted to *Fusion Technol.*

Haney, S. W., Bulmer, R. H., Freidberg, J. P., and Pearlstein, L. D., *Vertical Stability Analysis of Tokamaks Using a Variational Procedure,* Lawrence Livermore National Laboratory, Livermore, CA, UCRL-JC-127102. Submitted to *Plasma Phys. Rep.*

Hayden, J. S., Crichton, S., and Tomozawa, M., *Measurement of Water Diffusion in a Series of Phosphate Laser Glasses from below T_g to about 1000°,* Lawrence Livermore National Laboratory, Livermore, CA, UCRL-CR-126976.

Hinkel, D., Langdon, A. B., and Still, C. H., *Channeling and Filamentation of Intense Laser Light in Underdense Plasma,* Lawrence Livermore National Laboratory, Livermore, CA, UCRL-JC-127126-ABS. Prepared for the *27th Annual Anomalous Absorption Conf,* Vancouver, BC, Canada, Jun 1–5, 1997.

Hsu, C. F., Emanuel, M. A., Wu, C. H., and Zory, P. S., *Coulomb Enhancement in InGaAs/GaAs Quantum Well Lasers,* Lawrence Livermore National Laboratory, Livermore, CA, UCRL-JC-127137. Submitted to *IEEE J. Quantum Electron.*

J

Jones, O., Haan, S., Pollaine, S., and Suter, L., *Symmetry Analysis of NIF Hohlraums,* Lawrence Livermore National Laboratory, Livermore, CA, UCRL-JC-127132 ABS. Prepared for the *27th Annual Anomalous Absorption Conf,* Vancouver, BC, Canada, Jun 1–5, 1997.

K

Kalantar, D. H., Chandler, E. A., Colvin, J. D., Griswald, D., Remington, B. A., Weber, S. V., and Wiley, L., *Nova Experiments to Investigate Hydrodynamics Instabilities in the Solid State,* Lawrence Livermore National Laboratory, Livermore, CA, UCRL-JC-125443-DR. Prepared for the *6th Intl Workshop on the Physics of Compressible Turbulent Mixing*, Marseille, France, Jun 18–21, 1997.

Kalantar, D. H., Key, M. H., Da Silva, L. B., Glendinning, S. G., Remington, B. A., Rothenberg, J. E., Weber, F., Weber, S. V., Wolfrum, E., Kim, N. S., Neely, D., Zhang, J., Wark, J. S., Demir, A., Lin, J., Smith, R., Tallents, G. J., Lewis, C. L. S., MacPhee, A., Warwick, J., and Knauer, J. P., *Measurements of Direct Drive Laser Imprint in Thin Foils by Radiography Using an X-Ray Laser Backlighter*, Lawrence Livermore National Laboratory, Livermore, CA, UCRL-JC-124654; *Phys. Plasmas* **4**(5), 1985–1993 (1997).

Kane, J., Arnett, D., Remington, B. A., Glendinning, S. G., Managan, R., Castor, J., Wallace, R., Rubenchik, A., and Fryxell, B., *Supernova-Relevant Hydrodynamic Instability Experiments on the Nova Laser*, Lawrence Livermore National Laboratory, Livermore, CA, UCRL-JC-121488 Rev 2. Prepared for the *13th Intl Conf on Laser Interactions and Related Plasma Phenomena,* Monterey, CA, Apr 13–18, 1997; *Astrophysical J.* **478**(2-2), L75+ (1997).

Kane, J., Berning, M., Fryxell, B. A., Glendinning, S. G., Managan, R., Remington, B. A., Rubenchik, A., and Wallace, R., *Supernova-Relevant 2D-3D Hydro Instability Experiments on the Nova Laser,* Lawrence Livermore National Laboratory, Livermore, CA, UCRL-JC-127148-ABS. Prepared for the *27th Annual Anomalous Absorption Conf,* Vancouver, BC, Canada, Jun 1–5, 1997.

Kirkwood, R. K., Afeyan, B. B., Back, C. A., Blain, M. A., Estabrook, K. G., Glenzer, S. H., Kruer, W. L., MacGowan, B. J., Montgomery, D. S., and Moody, J. D., *Interaction between Stimulated Raman Scattering and Ion Acoustic Waves in Ignition Relevant Plasmas,* Lawrence Livermore National Laboratory, Livermore, CA, UCRL-ID-127616.

Kirkwood, R. K., Afeyan, B. B., Berger, R. L., Estabrook, K. G., Glenzer, S. H., MacGowan, B. J., Montgomery, D. S., Moody, J. D., and Williams, E. A., *Saturation of Stimulated Langmuir Waves by Ion Wave Decays in Ignition Relevant Plasmas,* Lawrence Livermore National Laboratory, Livermore, CA, UCRL-JC-126308-ABS Rev 1. Prepared for *27th Annual Anomalous Absorption Conf,* Vancouver, BC, Canada, Jun 1–5, 1997.

Kirkwood, R. K., MacGowan, B. J., Montgomery, D. S., Afeyan, B. B., Kruer, W. L., Pennington, D. M., Wilks, S. C., Moody, J. D., Wharton, K., Back, C. A., Estabrook, K. G., Glenzer, S. H., Blain, M. A., Berger, R. L., Hinkel, D. E., Lasinski, B. F., Williams, E. A., Munro, D., Wilde, B. H., and Rousseaux, C., *Observation of Multiple Mechanisms for Stimulating Ion Waves in Ignition Scale Plasmas,* Lawrence Livermore National Laboratory, Livermore, CA, UCRL-JC-124651; *Phys. Plasmas* **4**(5), 1800–1810 (1997).

Koch, J. A., Back, C. A., Brown, C., Estabrook, K., Hammel, B. A., Hatchett, S. P., Key, M. H., Kilkenny, J. D., Landen, O. L., and Lee, R. W., *Time-Resolved X-Ray Spectroscopy of Deeply Buried Tracer Layers as a Density and Temperature Diagnostic for the Fast Ignitor,* Lawrence Livermore National Laboratory, Livermore, CA, UCRL-JC-126309. Prepared for the *13th Intl Conf on Laser Interactions and Related Plasma Phenomena,* Monterey, CA, Apr 13–18, 1997.

Koch, J. A., Back, C. A., Brown, C., Hammel, B. A., Hatchett, S. P., Key, M. H., Landen, O. L., Lee, R. W., Moody, J. C., and Offenberger, A., *Production and Characterization of Hot, Dense Matter Produced by 100 TW and Petawatt Ultra Short-Pulse Lasers,* Lawrence Livermore National Laboratory, Livermore, CA, UCRL-JC-127482-ABS. Prepared for the *Intl Workshop on Measurements of the Ultrafast Dynamics of Complex Systems with Short Wavelength Radiation,* Montreal, Canada, Jun 18, 1997.

Kolosov, V. V., London, R. A., Ratowsky, R. P., and Zemlyanov, A. A., *X-Ray Laser Coherence in the Presence of Density Fluctuations,* Lawrence Livermore National Laboratory, Livermore, CA, UCRL-JC-123027. Submitted to *Phys. Rev. A.*

Kozioziemski, B. J., Bernat, T. P., and Colins, G. W., *Crystal Growth and Roughening of Solid D_2,* Lawrence Livermore National Laboratory, Livermore, CA, UCRL-JC-125121. Prepared for the *11th Target Fabrication Specialists' Mtg,* Orcas Island, WA, Sept 8–12, 1996, and submitted to *Fusion Technol.*

Kruer, W. L., Afeyan, B. B., DeGroot, J. S., and Estabrook, K. G., *Saturation of Stimulated Scattering by Secondary Instabilities,* Lawrence Livermore National Laboratory, Livermore, CA, UCRL-JC-127744-ABS. Prepared for the *39th Annual Mtg of the American Physical Society Div of Plasma Physics,* Pittsburgh, PA, Nov 17–21, 1997.

Kruer, W. L., Afeyan, B. B., DeGroot, J. S., Rambo, P. W., and Wilks, S. C., *Saturation Models for Laser Plasma Instabilities,* Lawrence Livermore National Laboratory, Livermore, CA, UCRL-JC-127120-ABS. Prepared for the *27th Annual Anomalous Absorption Conf,* Vancouver, BC, Canada, Jun 1–5, 1997.

Kuznetsov, Y. G., Malkin, A. J., Land, T. A., and De Yoreo, J. J., "Molecular Resolution Imaging of Macromolecular Crystals by Atomic Force Microscopy," *Biophysical Journal* **72**(5), 2357–2364 (1997).

L

Landen, O. L., Amendt, P. A., Bradley, D., Cable, M. D., Hammel, B. A., Kilkenny, J. D., Marshall, F., Suter, L. J., Turner, R. E., and Wallace, R., *Demonstration of Indirect-Drive Time-Dependent Symmetry Control Using Imploding Capsules at Omega,* Lawrence Livermore National Laboratory, Livermore, CA, UCRL-JC-127135-ABS. Prepared for the *27th Annual Anomalous Absorption Conf,* Vancouver, BC, Canada, Jun 1–5, 1997.

Langdon, A. B., Bonnaud, G., Hinkel, D. E., Kruer, W. L., Lasinski, B. F., Lefebvre, E., Still, C. H., and Toupin, C., *Ultra High Intensity Laser Plasma Interactions,* Lawrence Livermore National Laboratory, Livermore, CA, UCRL-JC-127131-ABS. Prepared for the *27th Annual Anomalous Absorption Conf,* Vancouver, BC, Canada, Jun 1–5, 1997.

Langer, S. H., Landen, O. L., and Scott, H. A., *Modeling Line Emission from Nova Rayleigh–Taylor Capsules,* Lawrence Livermore National Laboratory, Livermore, CA, UCRL-JC-127144-ABS. Prepared for the *27th Annual Anomalous Absorption Conf,* Vancouver, BC, Canada, Jun 1–5, 1997.

Lasinksi, B. F., and Langdon, A. B., *PIC Simulations of Hole-Boring,* Lawrence Livermore National Laboratory, Livermore, CA, UCRL-JC-127129-ABS. Prepared for the *27th Annual Anomalous Absorption Conf,* Vancouver, BC, Canada, Jun 1–5, 1997.

Lasinksi, B. F., Baldis, H. A., Cohen, B. I., Estabrook, K. G., Labaune, C., Langdon, A. B., and Williams, E. A., *BZOHAR Simulations of Nonlinear Ion Waves and Stimulated Brillouin Scattering,* Lawrence Livermore National Laboratory, Livermore, CA, UCRL-JC-127130-ABS. Prepared for the *27th Annual Anomalous Absorption Conf,* Vancouver, BC, Canada, Jun 1–5, 1997.

Latkowski, J. F., and Phillips, T. W., *Monte Carlo Prompt Dose Calculations for the National Ignition Facility,* Lawrence Livermore National Laboratory, Livermore, CA, UCRL-JC-127604-ABS. Prepared for the *17th Inst of Electronic and Electrical Engineers/Nuclear and Plasma Sciences Society Symp on Fusion Engineering '97,* San Diego, CA, Oct 6, 1997.

Lefebvre, E., Berger, R. L., Bonnaud, G., Langdon, A. B., Rothenberg, J. E., and Williams, E. A., *Reduction of Laser Self-Focusing in an ICF Plasma by Polarization Smoothing,* Lawrence Livermore National Laboratory, Livermore, CA, UCRL-JC-127128-ABS. Prepared for the *27th Annual Anomalous Absorption Conf,* Vancouver, BC, Canada, Jun 1–5, 1997.

Lefebvre, E., Berger, R. L., Langdon, A. B., Rothenberg, J. E., and Williams, E. A., *Reduction of Laser Self-Focusing in Plasma by Polarization Smoothing,* Lawrence Livermore National Laboratory, Livermore, CA, UCRL-JC-127739. Submitted to *Phys. Rev. Lett.*

M

MacGowan, B .J., Afeyan, B. B., Back, C. A., Berger, R. L., Blain, M. A., Glenzer, S. H., Hinkel, D. E., Kirkwood, R. K., Montgomery, D. S., and Moody, J. D., *Trends and Anomalies in Nova Large Scale Length Plasma Experiments,* Lawrence Livermore National Laboratory, Livermore, CA, UCRL-JC-127106-ABS. Prepared for the *27th Annual Anomalous Absorption Conf,* Vancouver, BC, Canada, Jun 1–5, 1997.

Marshall, C. D., Baldis, H., Bibeau, C., Krupke, W. F., Payne, S. A., and Powell, H. T., *Next Generation Rep-Rated ICF Laser; Technology Development Efforts and Near Term Applications to High Energy Density Physics,* Lawrence Livermore National Laboratory, Livermore, CA, UCRL-JC-127268-ABS. Prepared for the *27th Annual Anomalous Absorption Conf,* Vancouver, BC, Canada, Jun 1–5, 1997.

Marshall, C. D., Speth, J. A., and Payne, S. A., *Induced Optical Absorption in Gamma, Neutron, and Ultraviolet Irradiated Fused Quartz and Silica,* Lawrence Livermore National Laboratory, Livermore, CA, UCRL-JC-122652; *J. Non-Crystalline Solids* **212**(1), 59–73 (1997).

McEachern, R., Alford, C., Cook, B., Makowiecki, E., and Wallace, R., *Sputter-Deposited Be Ablators for NIF Target Capsules,* Lawrence Livermore National Laboratory, Livermore, CA, UCRL-JC-127112. Prepared for the *11th Target Fabrication Specialists' Mtg,* Orcas Island, WA, Sept 8–12, 1996, and submitted to *Fusion Technol.*

Moody, J. D., Afeyan, B. B., Berger, R. L., Glenzer, S. H., Hinkel, D. E., Kirkwood, R. K., Kruer, W. L., MacGowan, B. J., and Williams, E. A., *Effects of Fluctuations of Laser Propagation and Stimulated Interactions in Nova Gasbag Targets,* Lawrence Livermore National Laboratory, Livermore, CA, UCRL-JC-127110-ABS. Prepared for the *27th Annual Anomalous Absorption Conf,* Vancouver, BC, Canada, Jun 1–5, 1997.

Moody, J. D., Brown, C., Hammel, B. A., Hatchett, S. P., Hinkel, D. E., Key, M. H., Koch, J. A., Kruer, W. L., Lasinski, B., and Yanovsky, V., *Experimental Studies of Hole-Boring in Thin Solid Targets,* Lawrence Livermore National Laboratory, Livermore, CA, UCRL-JC-127111-ABS. Prepared for the *27th Annual Anomalous Absorption Conf,* Vancouver, BC, Canada, Jun 1–5, 1997.

N

Nikitenko, A. I., Cook, R. C., and Tolokonnikov, S. M., *Design of the Ballistic Furnace and Initial Microshells Formation Experiments,* Lawrence Livermore National Laboratory, Livermore, CA, UCRL-JC-125432 Rev 1. Prepared for the *11th Target Fabrication Specialists' Mtg,* Orcas Island, WA, Sept 8–12, 1996, and submitted to *Fusion Technol.*

Norton, M., Dane, B., Fisher, P., Gouge, M., and Hackel, L., *Liquid Droplet Generator for X-Ray Lithography,* Lawrence Livermore National Laboratory, Livermore, CA, UCRL-ID-127124.

O

Olson, R. E., Porter, J. L., Chandler, G. A., Fehl, D. L., Jobe, D. O., Leeper, R. J., Matzen, M. K., McGurn, J. S., Noack, D. D., Ruggles, L. E., Sawyer, P., Torres, J. A., Vargas, M., Zagar, D. M., Kornblum, H. N., Orzechowski, T. J., Phillion, D. W., Suter, L. J., Theissen, A. R., and Wallace, R. J., "Inertial Confinement Fusion Ablator Physics Experiments on Saturn and Nova," *Phys. Plasmas* **4**(5), 818–1824 (1997).

P

Page, R. H., Schaffers, K. I., Payne, S. A., and Krupke, W. F., *Dy-Doped Chlorides as Gain Media for 1.3 µm Telecommunications Amplifiers*, Lawrence Livermore National Laboratory, Livermore, CA, UCRL-JC-123544; *J. Lightwave Tech.* **15**(5), 786–793 (1997).

Pennington, D. M., Britten, J. A., Brown, C. G., Herman, S., Horner, J., Miller, J. L., Perry, M. D., Stuart, B. C., Tietbohl, G., and Van Lue, J., *Petawatt Laser and Target Irradiation System at LLNL,* Lawrence Livermore National Laboratory, Livermore, CA, UCRL-JC-127729. Prepared for *Ultrafast Optics 1997*, Monterey, CA, Aug 4–7, 1997.

Pennington, D. M., Britten, J. A., Brown, C. G., Herman, S., Horner, J., Miller, J. L., Perry, M. D., Stuart, B. C., Tietbohl, G., and Van Lue, J., *Petawatt Laser System and Targeting Performance,* Lawrence Livermore National Laboratory, Livermore, CA, UCRL-JC-127271. Prepared for the *Conf on Lasers and Electro-Optics /Quantum Electronics and Laser Science Conf '97,* Baltimore, MD, May 18–23, 1997.

Peterson, P. F., Anderson, A. T., Jin, H., and Scott, J. M., *Final Report for NIF Chamber Dynamics Studies,* Lawrence Livermore National Laboratory, Livermore, CA, UCRL-CR-127738.

R

Remington, B. A., Arnett, D., Drake, R. P., Estabrook, K., Glendinning, S. G., Kane, J., McCray, R., Rubenchik, A., and Wallace, R. J., *Supernova Hydrodynamics Experiments Using the Nova Laser,* Lawrence Livermore National Laboratory, Livermore, CA, UCRL-JC-126312. Prepared for the *5th Cerro Tololo Inter-American Observatory/European Southern Observatory Workshop*, La Serena, Chile, Feb 22–28, 1997.

Remington, B. A., Budil, K. S., Collins, G., Colvin, J., Glendinning, S. G., Haan, S. W., Kalantar, D. H., Marinak, M. M., Wallace, R., and Weber, S. V., *Hydrodynamic Instability Experiments Using the Nova Laser,* Lawrence Livermore National Laboratory, Livermore, CA, UCRL-JC-127742-ABS. Prepared for the *39th Annual Mtg of the American Physical Society Div of Plasma Physics,* Pittsburgh, PA, Nov 17, 1997.

Remington, B. A., Kane, J., Drake, R. P., Glendinning, S. G., Estabrook, K., London, R., Castor, J., Wallace, R. J., Arnett, D., Liang, E., McCray, R., Rubenchik, A., and Fryxell, B., *Supernova Hydrodynamics Experiments on the Nova Laser,* Lawrence Livermore National Laboratory, Livermore, CA, UCRL-JC-124949; *Phys. Plasmas* **4**(5), 1994–2003 (1997).

S

Sanchez, J. J., and Letts, S. A., *Polyimide Capsules May Hold High Pressure DT Fuel without Cryogenic Support for the National Ignition Facility Indirect-Drive Targets,* Lawrence Livermore National Laboratory, Livermore, CA, UCRL-JC-127114. Prepared for the *11th Target Fabrication Specialists' Mtg*, Orcas Island, WA, Sept 8–12, 1996, and submitted to *Fusion Technol*.

Sanford, T. W. L., Nash, T. J., Mock, R. C., Spielman, R. B., Struve, K. W., Hammer, J. H., De Groot, J. S., Whitney, K. G., and Apruzese, J. P., "Dynamics of a High-Power Aluminum-Wire Array Z-Pinch Implosion," *Phys. Plasmas* **4**(6), 2188–2203 (1997).

Shore, B. W., Perry, M. D., Britten, J. A., Boyd, R. D., Feit, M. D., Nguyen, H. T., Chow, R., Loomis, G., and Li, L., *Design of High-Efficiency Dielectric Reflection Gratings*, Lawrence Livermore National Laboratory, Livermore, CA, UCRL-JC-122908 Rev 1; *J. Opt. Soc. Am. A* **14**(5), 1124–1136 (1997).

Simmons, W., Bokor, J., Bucksbaum, P., Byer, R., Davis, R., Peressini, E., Whittenbury, C., Zory, P., *Laser Science and Technology Program Report of the Technical Advisory Committee 1996*, Lawrence Livermore National Laboratory, Livermore, CA, UCRL-ID-127623-96.

Simmons, W., Bokor, J., Bucksbaum, P., Fejer, M., Larson, L., Peressini, E., Whittenbury, C., and Zory, P., *Laser Science and Technology Program Report of the Technical Advisory Committee 1997*, Lawrence Livermore National Laboratory, Livermore, CA, UCRL-ID-127623-97.

Small, W., Celliers, P. M., Da Silva, L. B., Eder, D. C., Heredia, N. J., London, R. A., Maitland, D. J., and Matthews, D. L., *Experimental and Computational Laser Tissue Welding Using a Protein Patch,* Lawrence Livermore National Laboratory, Livermore, CA, UCRL-JC-127608. Submitted to the *J. of Biomedical Opt.*

Small, W., Celliers, P. M., Eder, D. C., Heilbron, M., Heredia, N. J., Hussain, F., Kopchok, G. E., London, R. A., Maitland, D. J., and Reiser, K. M., *In Vivo Argon Laser Vascular Welding and Collagen Crosslinking,* Lawrence Livermore National Laboratory, Livermore, CA, UCRL-JC-127139. Submitted to *Lasers in Surgery and Medicine J.*

Stephens, R. B., and Collins, G., *Analysis of Integrating Sphere Performance for IR Enhanced DT Layering,* Lawrence Livermore National Laboratory, Livermore, CA, UCRL-JC-127476. Prepared for the *11th Target Fabrication Specialists' Meeting,* Orcas Island, WA, Sept 8, 1996, and submitted to *Fusion Technol.*

Still, C. H., Berger, R. L., Estabrook, K. G., Hinkel, D. E., Langdon, A. B., Williams, E. A., and Young, P. E., *Simulating Laser Beam Deflection and Channel Formation Experiments,* Lawrence Livermore National Laboratory, Livermore, CA, UCRL-JC-127127-ABS. Prepared for the *27th Annual Anomalous Absorption Conf,* Vancouver, BC, Canada, Jun 1–5, 1997.

Suter, L. J., Glendinning, S. G., and Kauffman, R. L., *X-Ray Production and Utilization in Laser Heated Hohlraums,* Lawrence Livermore National Laboratory, Livermore, CA, UCRL-JC-127251-ABS. Prepared for the *27th Annual Anomalous Absorption Conf,* Vancouver, BC, Canada, Jun 1–5, 1997.

Suter, L. J., Glenzer, S., Hammer, J., Harte, J. A., and Town, R. J., *Vetting Heat Flow Scenarios in Gas Filled Hohlraums,* Lawrence Livermore National Laboratory, Livermore, CA, UCRL-JC-127150-ABS. Prepared for the *27th Annual Anomalous Absorption Conf,* Vancouver, BC, Canada, Jun 1–5, 1997.

T

Tietbohl, G. L., Horner, J. B., Horton, R. L., Ludwigsen, A. P., Miller, J. L., Olson, W. H., Patel, C. S., Vergino, M. D., and Weiland, T. L., *Engineering the Petawatt Laser into Nova,* Lawrence Livermore National Laboratory, Livermore, CA, UCRL-JC-127749-ABS. Prepared for the *Society of Photo-Optical Instrumentation Engineers Photonics West Conf,* San Jose, CA, Jan 24–30, 1998.

Tokheim, R. E., Curran, D. R., and Seaman, L., *Nova Upgrade Design Support Threats from Radiation Effects in the Proposed Nova Upgrade,* Lawrence Livermore National Laboratory, Livermore, CA, UCRL-CR-127484.

Turner, R. E., Amendt, P., Decker, C., Delamater, N., Landen, O., Morse, S., Murphy , T., Pien, G., and Seka, W., *Absolute Measurements of the Soft X-Ray Drive from Experiments on Omega,* Lawrence Livermore National Laboratory, Livermore, CA, UCRL-JC-127122-ABS. Prepared for the *27th Annual Anomalous Absorption Conf,* Vancouver, BC, Canada, Jun 1–5, 1997.

V

Van Wonterghem, B. M., Barker, C. E., Burkhart, S. C., Caird, J. A., Henesian, M. A., Murray, J. E., Wegner, P. J., and Weiland, T. L., *Laser Performance and Lessons Learned from NIF Beamlet Prototype,* Lawrence Livermore National Laboratory, Livermore, CA, UCRL-JC-127750-ABS. Prepared for the *Society of Photo-Optical Instrumentation Engineers Laser '98 Symp,* San Jose, CA, Jan 24, 1998.

W

Wan, A. S., Barbee, T. W., Cauble, R., Celliers, P., Da Silva, L. B., Moreno, J. C., Rambo, P. W., Stone, G. F., Trebes, J. E., and Weber, F., *Electron Density Measurement of a Colliding Plasma Using Soft-X-Ray Laser Interferometry,* Lawrence Livermore National Laboratory, Livermore, CA, UCRL-JC-123154 Rev 1; *Phys. Rev. E* **55**(5), 6293–6296 (1997).

Weber, S. V., Glendinning, S. G., Kalantar, D. H., Key, M. H., Remington, B. A., Rothenberg, J. E., Wolfrum, E., Verdon, C. P., and Knauer, J. P., *Simulations of Laser Imprint for Nova Experiments and for Ignition Capsules,* Lawrence Livermore National Laboratory, Livermore, CA, UCRL-JC-124547; *Phys. Plasmas* **4**(5), 1978–1984 (1997).

Wegner, P. J., Barker, C. E., Caird, J. A., Dixit, S. N., Henesian, M. A., Seppala, L. G., Thompson, C. E., and Van Wonterghem, B. M., *Characterization of Third-Harmonic Target Plane Irradiance on the National Ignition Facility Beamlet Demonstration Project,* Lawrence Livermore National Laboratory, Livermore, CA, UCRL-JC-123070. Prepared for the *12th Topical Mtg on the Technology of Fusion Energy,* Reno, NV, Jun 16–20, 1996.

Wharton, K. B., Afeyan, B. B., Estabrook, K. G., Glenzer, S. H., Joshi, C., Kirkwood, R. K., and Moody, J. D., *Experimental Studies of Energy Transfer between Laser Beams in Flowing Plasmas,* Lawrence Livermore National Laboratory, Livermore, CA, UCRL-JC-127121-ABS. Prepared for the *27th Annual Anomalous Absorption Conf,* Vancouver, BC, Canada, Jun 1–5, 1997.

Wharton, K. Brown, C., Hammel, B., Hatchett, S., Key, M., Koch, J., Moody, J., Offenberger, A., Perry, M., and Tabak, M., *Characterization of Hot Electrons Produced by 4×10^{19} W/cm^2 Laser–Plasma Interactions,* Lawrence Livermore National Laboratory, Livermore, CA, UCRL-JC-127107-ABS. Prepared for the *27th Annual Anomalous Absorption Conf,* Vancouver, BC, Canada, Jun 1–5, 1997.

Wilks, S. C., Baldis, H., Cowan, T. E., Decker, C., Freeman, R. R., Hagmann, C. A., Hartemann, F., Kerman, A. K., Young , P. E., and van Bibber, K., *Laser–Plasma Acceleration of Electrons Using the Petawatt Laser,* Lawrence Livermore National Laboratory, Livermore, CA, UCRL-JC-126964-ABS Rev. Prepared for the *27th Annual Anomalous Absorption Conf,* Vancouver, BC, Canada, Jun 1–5, 1997.

Williams, E. A., Berger, R. L., and Cohen, B. I., *Kinetic Coupling of Ion Waves,* Lawrence Livermore National Laboratory, Livermore, CA, UCRL-JC-127134-ABS. Prepared for the *27th Annual Anomalous Absorption Conf,* Vancouver, BC, Canada, Jun 1–5, 1997.

Williams, W., Auerbach, J., Henesian, M., Hunt, J., Lawson, L., Manes, K., Orth, C., Sacks, R., Trenholme, J., and Wegner, P., *NIF Optics Phase Gradient Specification,* Lawrence Livermore National Laboratory, Livermore, CA, UCRL-ID-127297.

Woodworth, J. G., and Meier, W. R., *Target Production for Inertial Fusion Energy,* Lawrence Livermore National Laboratory, Livermore, CA, UCRL-JC-117396; *Fus. Tech.* **31**, 280–290 (1997).

Y

Yanovsky, V. P., Brown, C. G., Perry, M. D., and Rubenchik, A., *Plasma Mirrors for Short Pulse Lasers,* Lawrence Livermore National Laboratory, Livermore, CA, UCRL-JC-127730. Prepared for *Ultrafast Optics 1997,* Monterey, CA, Aug 4–7, 1997.

Z

Zaitseva, N. P., Carman, L. M., De Yoreo, J. J., Dehaven, M. R., Spears, H. R., and Vital, R. L., *Large-Scale (41–55 cm) KDP Crystals Grown by Rapid Growth Technique for Laser Fusion Applications,* Lawrence Livermore National Laboratory, Livermore, CA, UCRL-JC-127285-ABS. Prepared for the *6th Intl Workshop on Laser Physics (LPHYS '97)*, Prague, Czechoslovakia, Aug 4–8, 1997.

Publications and Presentations
July–September 1997

A

Afeyan, B. B., Batishchev, O., Kirkwood, R. K., Montgomery, D. S., Russell, D., Schmitt, A. J., and Town, R. P. J., *Theoretical Studies of Optical Mixing Controlled Stimulated Scattering Instabilities*, Lawrence Livermore National Laboratory, Livermore, CA, UCRL-JC-127925 ABS. Prepared for the *39th Annual Mtg of the American Physical Society Div of Plasma Physics*, Pittsburgh, PA, Nov 17, 1997.

Amendt, P., Bradley, D., Delamater, N., Glendinning, S. G., Keck, R., Landen, O., Marshall, F., Murphy, T., Turner, R. E., and Wallace, J., *Modeling for OMEGA Cylindrical Hohlraum Time-Dependent Drive Asymmetry Control Campaign,* Lawrence Livermore National Laboratory, Livermore, CA, UCRL-JC-127950 ABS. Prepared for the *39th Annual Mtg of the American Physical Society Div of Plasma Physics*, Pittsburgh, PA, Nov 17, 1997.

B

Back, C. A., Davis, J. L., Decker, C., Grun, J., Landen, O. L., Suter, L. J., and Wallace, R., *Production of Multi-Kilovolt X-Rays from Laser-Heated Targets,* Lawrence Livermore National Laboratory, Livermore, CA, UCRL-JC-125975. Prepared for the *Intl Symp on Optical Science, Engineering, and Instrumentation*, San Diego, CA, Jul 27, 1997.

Back, C. A., Cohen, D., Hammel, B. A., Koch, J. A., Landen, O. L., MacFarlane, J. J., Nash, T. J., and Turner, R. E., *Spectrally-Resolved Albedo Measurements from Nova Hohlraum Targets,* Lawrence Livermore National Laboratory, Livermore, CA, UCRL-JC-127924 ABS. Prepared for the *39th Annual Mtg of the American Physical Society Div of Plasma Physics*, Pittsburgh, PA, Nov 17, 1997.

Bernat, T. P., Collins, G. W., Duriez, C., and Mapoles, E. R., *Heat-Flux Induced Changes to Multicrystalline D_2 Surfaces,* Lawrence Livermore National Laboratory, Livermore, CA, UCRL-JC-124261 ABS Rev. Prepared for the *39th Annual Mtg of the American Physical Society Div of Plasma Physics*, Pittsburgh, PA, Nov 17, 1997.

Berning, M., Glendinning, S. G., Kane, J., Remington, B. A., and Rubenchik, A., *Comparative Studies of the Weakly Nonlinear Evolution of Hydrodynamic Interface Instabilities in 2D and 3D,* Lawrence Livermore National Laboratory, Livermore, CA, UCRL-JC-126314 ABS Rev. Prepared for the *39th Annual Mtg of the American Physical Society Div of Plasma Physics*, Pittsburgh, PA, Nov 17, 1997.

Bibeau, C., Beach, R., Emanuel, M., Honea, E., Marshall, C., Payne, S., Skidmore, J., and Sutton, S., *High Average Power Diode-Pumped Solid-State Lasers,* Lawrence Livermore National Laboratory, Livermore, CA, UCRL-JC-127944 ABS & SUM. Prepared for the *11th Intl Symp on Gas Flow and Chemical Lasers and High Power Laser Conf*, Edinburgh, Scotland, Aug 25, 1996.

Budil, K. S., Perry, T. S., Remington, B. A., Stry, P. E., and Wan, A., *Ablation Instability Experiments at Nova,* Lawrence Livermore National Laboratory, Livermore, CA, UCRL-JC-128012 ABS. Prepared for the *39th Annual Mtg of the American Physical Society Div of Plasma Physics*, Pittsburgh, PA, Nov 17, 1997.

Burnham, A., Anderson, A., Genin, F., Gerassimenko, M., Hibbard, W., Norton, M., Reitz, T., Sanders, D., Scott, J. M., and Whitman, P., *First Wall and Beam Dumps for the National Ignition Facility Target Chamber,* Lawrence Livermore National Laboratory, Livermore, CA, UCRL-JC-127914 ABS. Prepared for the *17th Institute of Electronic and Electrical Engineers /Nuclear and Plasma Sciences Society Symp on Fusion Engineering '97*, San Diego, CA, Oct 6, 1997.

C

Cable, M. D., Hatchet, S. P., Key, M. H., Koch, J. A., Moran, M. J., Nelson, M. G., Pennington, D. M., Phillips, T. W., Sangster, T. C., and Tabak, M., *Neutron Measurements for Picosecond Laser Experiments,* Lawrence Livermore National Laboratory, Livermore, CA, UCRL-JC-128028 ABS. Prepared for the *39th Annual Mtg of the American Physical Society Div of Plasma Physics*, Pittsburgh, PA, Nov 17, 1997.

Callahan, D. A., and Tabak, M., *Distributed Radiator, Heavy Ion Target with Realistic Ion Beams,* Lawrence Livermore National Laboratory, Livermore, CA, UCRL-JC-127949 ABS. Prepared for the *39th Annual Mtg of the American Physical Society Div of Plasma Physics*, Pittsburgh, PA, Nov 17, 1997.

Callahan, D. A., and Tabak, M., *Distributed Radiator, Heavy Ion Target with Realistic Ion Beams,* Lawrence Livermore National Laboratory, Livermore, CA, UCRL-JC-127949 ABS Rev 1. Prepared for the *Nuclear Explosives Design Physics Conf*, Livermore, CA, Oct 20–24, 1997.

Celliers, P., Barbee, T. W., Cauble, R., Da Silva, L. B., Decker, C. D., Kalantar, D. H., Key, M. H., London, R. A., Moreno, J. C., and Snavely, R., *Probing High Density Plasmas with Soft X-Ray Lasers,* Lawrence Livermore National Laboratory, Livermore, CA, UCRL-JC-126541. Prepared for the *1997 Intl Symp on Optical Science, Engineering, and Instrumentation*, San Diego, CA, Jul 27–29, 1997.

Celliers, P. M., Cauble, R. C., Collins, G. W., Da Silva, L. B., Erskine, D. J., Foord, M. E., Gold, D. M., Hammel, B. A., Stewart, R. E., and Wallace, R. J., *Displacement and Velocity Interferometry for Laser-Driven Shock Wave Experiments,* Lawrence Livermore National Laboratory, Livermore, CA, UCRL-JC-128041 ABS. Prepared for the *39th Annual Mtg of the American Physical Society Div of Plasma Physics*, Pittsburgh, PA, Nov 17, 1997.

Cohen, B. I., Baldis, H. A., Estabrook, K. G., Kirkwood, R., Labaune, C., Langdon, A. B., Lasinski, B. F., Wharton, K. B., and Williams, E. A., *Kinetic Simulations of Stimulated Brillouin Scattering and Nonlinear Ion Waves,* Lawrence Livermore National Laboratory, Livermore, CA, UCRL-JC-127905 ABS. Prepared for the *39th Annual Mtg of the American Physical Society Div of Plasma Physics*, Pittsburgh, PA, Nov 17, 1997.

Collins, G. W., Bernat, T., Bittner, D., Letts, S., Mapoles, E., Moll, G., Monsler, E., and Stevens, R., *Forming and Smoothing D^2 and HD Layers for ICF by Infra-Red Heating,* Lawrence Livermore National Laboratory, Livermore, CA, UCRL-JC-124255 ABS Rev. Prepared for the *39th Annual Mtg of the American Physical Society Div of Plasma Physics*, Pittsburgh, PA, Nov 17, 1997.

Collins, G. W., Barbee, T. W., Budil, K. S., Cauble, R., Celliers, P., Da Silva, L., Foord, M., Gold, D., Holmes, N. C., and Stewart, R., *Hydrogen Equation of State Measurements along the Principle Hugoniot,* Lawrence Livermore National Laboratory, Livermore, CA, UCRL-JC-128039 ABS. Prepared for the *39th Annual Mtg of the American Physical Society Div of Plasma Physics*, Pittsburgh, PA, Nov 17, 1997.

Collins, G. W., Budil, K., Cauble, R., Celliers, P., Da Silva, L., Foord, M., Gold, D., Holmes, N., Ross, M., and Stewart, R., *Equation of State Measurements of D^2 on Nova,* Lawrence Livermore National Laboratory, Livermore, CA, UCRL-JC-128201. Prepared for the *1997 American Physical Society Topical Conf on Shock Compression of Condensed Matter*, Amherst, MA, Jul 27, 1997.

Colston, B. W., Da Silva, L. B., Everett, M. J., Nathel, H., Otis, L. L., and Stroeve, P., *Imaging of Hard and Soft Tissue Structure in the Oral Cavity by Optical Coherence Tomography,* Lawrence Livermore National Laboratory, Livermore, CA, UCRL-JC-127487. Submitted to *Opt. Lett.*

Cook, R. C., Gresho, P. M., and Hamilton, K. E., *Examination of Some Droplet Deformation Forces Related to NIF Capsule Sphericity,* Lawrence Livermore National Laboratory, Livermore, CA, UCRL-JC-128085. Submitted to *J. of Moscow Physical Society*.

D

Dane, C. B., and Hackel, L. A., *A1l Solid-State SBS Phase Conjugate Mirror Using Fused Silica,* Lawrence Livermore National Laboratory, Livermore, CA, UCRL-JC-127939 ABS. Prepared for the *Intl Symp on High-Power Lasers and Applications*, San Jose, CA, Jan 24, 1998.

Decker, C., Turner, R. E., Landen, O. L., Suter, L. J., Amendt, P., Kornblum, H. N., Hammel, B. A., Murphy, T. J., Wallace, J., Hauer, A. A., Knauer, J., Marshall, F. J., Bradley, D., Seka, W., and Soures, J. M., *Hohlraum Radiation Drive Measurements on the Omega Laser*, Lawrence Livermore National Laboratory, Livermore, CA, UCRL-JC-126959; *Phys. Rev. Lett.* **79**(8), 1491–1494 (1997).

Demos, S. G., De Yoreo, J. J., Radousky, H. B., Staggs, M., Woods, B. W., Wu, Z. L., and Yan, M., *Temperature and Spectral Investigation of Bulk KDP below Damage Using 355 nm Laser Irradiation*, Lawrence Livermore National Laboratory, Livermore, CA, UCRL-JC-128357 ABS. Prepared for the *Annual Symp on Optical Materials for High Power Lasers*, Boulder, CO, Oct. 6, 1997.

Dittrich, T. R., Haan, S. W., and Marinak, M. M., *NIF Capsule Design Issues*, Lawrence Livermore National Laboratory, Livermore, CA, UCRL-JC-127912 ABS. Prepared for the *39th Annual Mtg of the American Physical Society Div of Plasma Physics*, Pittsburgh, PA, Nov 17, 1997.

E

Eimerl, D., Auerbach, J. M., Barker, C. E., Milam, D., and Milonni, P. W., *Novel Multicrystal Designs for Efficient Third-Harmonic Generations*, Lawrence Livermore National Laboratory, Livermore, CA, UCRL-JC-127906. Submitted to *Opt. Lett*.

Estabrook, K., Alley, W. E., Bailey, D. S., Glendinning, S. G., Harte, J. H., Kane, J., Munro, D. H., Remington, B. A., Suter, L. J., and Zimmerman, G. B., *LASNEX Simulations of Supernova-Residual Gas Shocks on the Nova Laser*, Lawrence Livermore National Laboratory, Livermore, CA, UCRL-JC-128022 ABS. Prepared for the *39th Annual Mtg of the American Physical Society Div of Plasma Physics*, Pittsburgh, PA, Nov 17, 1997.

Estabrook, K. G., Afeyan, B. B., Glenzer, S. H., Joshi, C., Kirkwood, R. K., Moody, J. D., and Wharton, K. B., *Experimental Studies of Energy Transfer between Crossed Laser Beams in Flowing Plasmas*, Lawrence Livermore National Laboratory, Livermore, CA, UCRL-JC-127917 ABS. Prepared for the *39th Annual Mtg of the American Physical Society Div of Plasma Physics*, Pittsburgh, PA, Nov 17, 1997.

Everett, M. J., Colston, B. W., Da Silva, L., and Schoenenberger, K., *Tissue Birefringence Measurements via Optical Coherence Tomography*, Lawrence Livermore National Laboratory, Livermore, CA, UCRL-JC-128042 ABS. Prepared for *BiOS '98 Intl Biomedical Optics Symp*, San Jose, CA, Jan 24, 1998.

F

Feit, M. D., Campbell, J., Faux, D., Genin, F. Y., Kozlowski, M. R., Riddle, R., Rubenchik, S., Salleo, A., and Yoshiyama, J., *Modeling of Laser-Induced Surface Cracks in Silica at 355 nm*, Lawrence Livermore National Laboratory, Livermore, CA, UCRL-JC-128363 ABS. Prepared for the *Annual Symp on Optical Materials for High Power Lasers*, Boulder, CO, Oct 6, 1997.

Feit, M. D., Da Silva, L. B., Kim, B.-M., Rubenchik, A. M., and Shore, B. W., *Ultrashort Laser Pulse Propagation through Hollow Core Fibers*, Lawrence Livermore National Laboratory, Livermore, CA, UCRL-JC-128094 ABS. Prepared for *BiOS '98 Intl Biomedical Optics Symp*, San Jose, CA, Jan 24, 1998.

Feit, M. D., Garrison, J. C., Komashko, A. M., Musher, S. L., Rubenchik, A. M., and Turitsyn, S. K., *Relativistic Laser Pulse Channeling*, Lawrence Livermore National Laboratory, Livermore, CA, UCRL-JC-126337 ABS Rev. Prepared for the *39th Annual Mtg of the American Physical Society Div of Plasma Physics*, Pittsburgh, PA, Nov 17, 1997.

Feit, M. D., Garrison, J. C., and Rubenchik, A. M., *Channeling of Intense Laser Beams in Underdense Plasmas*, Lawrence Livermore National Laboratory, Livermore, CA, UCRL-JC-125398; *Phys. Rev. E* **56**(3) Part A, R2394–R2397 (1997).

Feit, M. D., Komashko, A. M., Musher, S. L., Rubenchik, A. M., and Turitsyn, S. K., *Electron Cavitation and Relativistic Self-Focusing in Underdense Plasma*, Lawrence Livermore National Laboratory, Livermore, CA, UCRL-JC-127909. Submitted to *Phys. Lett*.

Feit, M. D., Rubenchik, A. M., and Salleo, A., *Pulseshape and Pulselength Scaling of Laser Damage Threshold due to Rate Limiting by Thermal Conduction*, Lawrence Livermore National Laboratory, Livermore, CA, UCRL-JC-128364 ABS. Prepared for the *Annual Symp on Optical Materials for High Power Lasers*, Boulder, CO, Oct 6, 1997.

Fornier, A., Burnham, A., Cordillot, C., Feit, M. D., Genin, F. Y., Rubenchick, A. M., Schirman, D., Whitman, P., and Yoshiyama, J., *Thin Film Contamination Effects on Laser-Induced Damage of Fused Silica Surfaces at 355 nm*, Lawrence Livermore National Laboratory, Livermore, CA, UCRL-JC-128360 ABS. Prepared for the *Annual Symp on Optical Materials for High Power Lasers*, Boulder, CO, Oct 6, 1997.

G

Genin, F. Y., Campbell, J., Salleo, A., Sands , T., and Yoshiyama, J., *Quantitative Damage Morphology Analysis of Laser-Induced Surface Cracks in Fused Silica at 355 nm,* Lawrence Livermore National Laboratory, Livermore, CA, UCRL-JC-128358 ABS. Prepared for the *Annual Symp on Optical Materials for High Power Lasers,* Boulder, CO, Oct 6, 1997.

Genin, F. Y., Dijon, J., Garrec, P., Sheehan, L., and Yoshiyama, J., *Statistical Study of Laser-Induced Damage of UV Grade Fused Silica at 355 nm,* Lawrence Livermore National Laboratory, Livermore, CA, UCRL-JC-128359 ABS. Prepared for the *Annual Symp on Optical Materials for High Power Lasers,* Boulder, CO, Oct 6, 1997.

Glendinning, S. G., Dixit, S. N., Hammel, B. A., Kalantar, D. H., Key, M. H., Kilkenny, J. D., Knauer, J. P., Pennington, D. M., Remington, B. A., and Rothenberg, J., *Comparison of Drive-Seeded Modulations in Planar Foils for 0.35 and 0.53 µm Laser Drive,* Lawrence Livermore National Laboratory, Livermore, CA, UCRL-JC-127617 Rev 1. Submitted to *Phys. Rev. Lett.*

Glendinning, S. G., Cherfils, C., Collins, G. W., Galmiche, D., Haan, S. W., Marinak, M. M., Remington, B. A., Richard, A., Wallace, R. J., and Weber, S. V., *Rayleigh–Taylor Growth of Ablation Front Modulations in Indirectly-Driven Be/Cu Planar Foils,* Lawrence Livermore National Laboratory, Livermore, CA, UCRL-JC-127922 ABS. Prepared for the *39th Annual Mtg of the American Physical Society Div of Plasma Physics,* Pittsburgh, PA, Nov 17, 1997.

Glendinning, S. G., Budil, K. S., Haan, S. W., Marinak, M. M., Remington, B. A., and Wallace, R. J., *Rayleigh–Taylor Evolution of 3D Multimode Modulations in Indirectly-Driven Planar Foils,* Lawrence Livermore National Laboratory, Livermore, CA, UCRL-JC-127942 ABS. Prepared for the *39th Annual Mtg of the American Physical Society Div of Plasma Physics,* Pittsburgh, PA, Nov 17, 1997.

Glenzer, S. H., Back, C. A., Blain, M. A., De Groot, J. S., Estabrook, K. G., Hammel, B. A., Hammer, J. H., MacGowan, B. J., Pollaine, S. M., and Suter, L. J., *Thomson Scattering from Inertial Confinement Fusion Plasmas,* Lawrence Livermore National Laboratory, Livermore, CA, UCRL-JC-128021. Prepared for the *13th Intl Conf on Laser Interactions and Related Plasma Phenomena,* Monterey, CA, Apr 13, 1997.

Glenzer, S. H., Back, C. A., Blain, M. A., Hammer, J. H., Landen, O. L., Lindl, J. D., MacGowan, B. J., and Suter, L. J., *Characterization of Laser-Produced Fusion Plasmas with Thomson Scattering,* Lawrence Livermore National Laboratory, Livermore, CA, UCRL-JC-128040. Prepared for the *8th Intl Symp on Laser-Aided Plasma Diagnostics,* Doorwerth, The Netherlands, Sept 22, 1997.

Glenzer, S. H., Back, C. A., Estabrook, K. G., Lee, R. W., MacGowan, B. J., Rosmej , F. B., Shepard, T. D., and Turner, R. E., *Measurements of Suprathermal Electrons in Hohlraum Plasmas with X-Ray Spectroscopy,* Lawrence Livermore National Laboratory, Livermore, CA, UCRL-JC-128259. Submitted to *Phys. Rev. Lett.*

Glenzer, S. H., Back, C. A., Suter, L. J., Blain, M. A., Landen, O. L., MacGowan, B. J., Stone, G. F., Turner, R. E., and Wilde, B. H., *Thomson Scattering from Inertial-Confinement-Fusion Hohlraum Plasmas,* Lawrence Livermore National Laboratory, Livermore, CA, UCRL-JC-126320; *Phys. Rev. Lett.* **79**(7), 1277–1280 (1997).

Gold, D. M., Budil, K. S., Cauble, R., Cellier, P., Collins, G. W., Da Silva, L. B., Foord, M. E., Stewart, R. E., and Wallace, R. J., *Interferometric Laser Probe for High-Pressure, Laser-Driven Experiments,* Lawrence Livermore National Laboratory, Livermore, CA, UCRL-JC-128539 ABS. Prepared for the *12th Topical Conf on High-Temperature Plasma Diagnostics,* Princeton, NJ, Jun 7, 1998.

H

Hackel, L. A., Daly, J., Dane, C. B., and Harrison, J., *Laser Shot Peening of Metals: Techniques and Laser Technology,* Lawrence Livermore National Laboratory, Livermore, CA, UCRL-JC-128351 ABS. Prepared for the *1997 U.S. Air Force Aircraft Structural Integrity Program Conf,* San Antonio, TX, Dec 2, 1997.

Hackel, L. A., and Dane, C. B., *High Energy, High Average Power Solid State Laser in the ns to µs Range,* Lawrence Livermore National Laboratory, Livermore, CA, UCRL-JC-128606 ABS. Prepared for the *Intl Symp on High-Power Laser Ablation,* Santa Fe, NM, Apr 26, 1998.

Hammel, B., Amendt , P., Cline, B. D., Ehrlich, R. B., Glendinning, S. G., Kalantar, D. H., Landen , O. L., Richard, A., Wallace, R. J., and Weiland, T. J., *Drive Symmetry Experiments with Phased Beams on Nova,* Lawrence Livermore National Laboratory, Livermore, CA, UCRL-JC-127916 ABS. Prepared for the *39th Annual Mtg of the American Physical Society Div of Plasma Physics,* Pittsburgh, PA, Nov 17, 1997.

Henesian, M., Bliss, E., Sacks, R., Trenholme, J., Wegner, P., Williams, W., Winters, S., and Zacharias, R., *Optimization Studies for the NIF Adaptive Optics System,* Lawrence Livermore National Laboratory, Livermore, CA, UCRL-JC-127935-ABS. Prepared for the *Intl Symp on High-Power Lasers and Applications*, San Jose, CA, Jan 24, 1998.

Honea, E. C., Beach, R. J., Sutton, S. B., Speth, J. A., Marshall, S. C., Skidmore, J. A., Emanuel, M. A., and Payne, S. A., "115-W Tm:YAG Diode-Pumped Solid-State Laser," *IEEE J. Quant. Elect.* **33**(9), 1592–1600 (1997).

J

Jones, O., Haan, S., Pollaine, S., and Suter, L., *Radiation Symmetry of NIF Hohlraums,* Lawrence Livermore National Laboratory, Livermore, CA, UCRL-JC-128002 ABS. Prepared for the *39th Annual Mtg of the American Physical Society Div of Plasma Physics*, Pittsburgh, PA, Nov 17, 1997.

K

Kalantar, D. H., Da Silva, L. B., Demir, A., Key, M. H., Kim, N. S., Lewis, C. L. S., Lin, J., MacPhee, A., Neely, D., Remington, B. A., Rothenberg, J. E., Smith, R., Tallents, G. J., Wark, J., Warwick, J., Weber, S. V., Wolfrum, E., and Zhang , J., *X-Ray Laser Measurements of Direct Drive Imprint on Vulcan,* Lawrence Livermore National Laboratory, Livermore, CA, UCRL- ID-128006.

Kalantar, D. H., Chandler, E. A., Colvin, J. D., Griswald, D. L., Remington, B. A., Turner, R. E., Weber, S. V., and Wiley, L. G., *Nova Experiments to Investigate Hydrodynamic Instabilities in the Solid State,* Lawrence Livermore National Laboratory, Livermore, CA, UCRL-JC-125443. Prepared for the *6th Intl Workshop on the Physics of Compressible Turbulent Mixing*, Marseille, France, Jun 18, 1997.

Kalantar, D. H., Boehly, T., Knauer, J., Meyerhofer, D., Remington, B. A., Smalyuk, V., and Weber, S. V., *Direct Drive Laser Imprinting in CH Foils on the Omega Laser,* Lawrence Livermore National Laboratory, Livermore, CA, UCRL-JC-127915 ABS. Prepared for the *39th Annual Mtg of the American Physical Society Div of Plasma Physics*, Pittsburgh, PA, Nov 17, 1997.

Kalantar, D. H., Chandler, E. A., Colvin, J. D., Remington, B. A., Weber, S. V., and Wiley, L. G., *Solid State Material Strength Effects in Hydrodynamic Instability Experiments on the Nova Laser,* Lawrence Livermore National Laboratory, Livermore, CA, UCRL-JC-127923 ABS. Prepared for the *39th Annual Mtg of the American Physical Society Div of Plasma Physics*, Pittsburgh, PA, Nov 17, 1997.

Kalantar, D. H., Chandler, E. A., Colvin, J. D., Failor, B. H., Hauer, A., Lee, R., Remington, B. A., Wark, J. S., Weber, S. V., and Wiley, L. G., *Transient X-Ray Diffraction Used to Diagnose Shock Compressed Solids on the Nova Laser,* Lawrence Livermore National Laboratory, Livermore, CA, UCRL-JC-127927 ABS. Prepared for the *39th Annual Mtg of the American Physical Society Div of Plasma Physics*, Pittsburgh, PA, Nov 17, 1997.

Kane, J., Arnett, W. D., Glendinning, S. G., Remington, B. A., and Rubenchik, A., *Simulations of Supernova-Relevant Hydrodynamic Instability Experiments on the Nova Laser,* Lawrence Livermore National Laboratory, Livermore, CA, UCRL-JC-121487 ABS Rev 2. Prepared for the *39th Annual Mtg of the American Physical Society Div of Plasma Physics*, Pittsburgh, PA, Nov 17, 1997.

Kane, J. O., Boehly, T., Kalantar, D., and Remington, B., *Design of a Direct Drive Low Temperature Rayleigh–Taylor Instability Laser Experiment,* Lawrence Livermore National Laboratory, Livermore, CA, UCRL-JC-128036 ABS. Prepared for the *39th Annual Mtg of the American Physical Society Div of Plasma Physics*, Pittsburgh, PA, Nov 17, 1997.

Kauffman, R. L., Blain, M. A., Dixit, S. N., Glendinning, S. G., Glenzer, S. H., Landen, O. L., MacGowan, B. J., Orzechowski, T. J., Powers, L. V., and Richard, A. L., *Improved Gas-Filled Hohlraum Performance on Nova with Beam Smoothing,* Lawrence Livermore National Laboratory, Livermore, CA, UCRL-JC-128004 ABS. Prepared for the *39th Annual Mtg of the American Physical Society Div of Plasma Physics*, Pittsburgh, PA, Nov 17, 1997.

Kim, B.-M., Da Silva, L. B., Feit, M. D., London, R. A., Perry, M. D., Rubenchik, A. M., and Stuart, B. C., *Therapeutic Ultrashort Pulsed Laser Tissue Ablation,* Lawrence Livermore National Laboratory, Livermore, CA, UCRL-JC-128081 ABS. Prepared for *BiOS '98 Intl Biomedical Optics Symp*, San Jose, CA, Jan 24, 1998.

Kim, B.-M., Da Silva, L. B., Feit, M. D., and Rubenchik, A. M., *Feedback System for Precision Ultra Short Pulse Laser Biotissue Ablation,* Lawrence Livermore National Laboratory, Livermore, CA, UCRL-JC-128095 ABS. Prepared for *BiOS '98 Intl Biomedical Optics Symp*, San Jose, CA, Jan 24, 1998.

Kirkwood, R. K., Afeyan, B. B., Estabrook, K. G., Glenzer, S. H., Kruer, W. L., MacGowan , B. J., Montgomery, D. S., Moody, J. D., Wharton, K. B., and Williams, E. A., *Observation of the Saturation of Langmuir Waves Driven by Ponderomotive Force in a Large Scale Plasma,* Lawrence Livermore National Laboratory, Livermore, CA, UCRL-ID-128007.

Kirkwood, R. K., Estabrook, K. G., Glenzer, S. H., MacGowan, B. J., Moody, J. D., and Williams, E. A., *Experimental Studies of the Scaling of SRS in Large Scale Plasmas,* Lawrence Livermore National Laboratory, Livermore, CA, UCRL-JC-127918 ABS. Prepared for the *39th Annual Mtg of the American Physical Society Div of Plasma Physics*, Pittsburgh, PA, Nov 17, 1997.

Kirkwood, R. K., Afeyan, B. B., Estabrook, K. G., Glenzer, S. H., Kruer, W. L., MacGowan, B. J., Montgomery, D. S., Moody, J. D., Wharton, K. B., and Williams, E. A., *Observation of the Saturation of Langmuir Waves Driven by Ponderomotive Force in a Large Scale Plasma,* Lawrence Livermore National Laboratory, Livermore, CA, UCRL-JC-128298 DR. Submitted to *Phys. Rev. Lett.*

Kirkwood, R. K., Afeyan, B. B., Back, C. A., Kruer, W. L., MacGowan, B. J., Montgomery, D. S., Moody, J. D., Pennington, D. M., Wharton, K., and Wilks, S. C., *Stimulation and Saturation of Plasma Waves in Laser Plasma Experiments,* Lawrence Livermore National Laboratory, Livermore, CA, UCRL-JC-128554 ABS. Prepared for the *1998 Natl Radio Science Mtg*, Boulder, CO, Jan 1, 1998.

Koch, J. A., Barbee, T. W., Bennet, G., Brown, C., Celliers, P., Da Silva, L. B., Glendinning, S. G., Hammel, B. A., Landen, O. L., and Seely, J., *High-Energy X-Ray Microscopy of Laser-Fusion Plasmas at the National Ignition Facility,* Lawrence Livermore National Laboratory, Livermore, CA, UCRL-JC-126818. Prepared for the *9th Natl Topical Conf on High Temperature Plasma Diagnostics*, St. Petersburg, Russia, Jun 2, 1997.

Koch, J. A., Bauer, J. D., Carman, T. S., Landen , O. L., Perry, T. S., Suter, L. J., and Ward, R. A., *Radiation Hydrodynamics Experiments Using Low-Density Silica Aerogel Samples,* Lawrence Livermore National Laboratory, Livermore, CA, UCRL-JC-127921 ABS. Prepared for the *39th Annual Mtg of the American Physical Society Div of Plasma Physics*, Pittsburgh, PA, Nov 17, 1997.

Koch, J. A., Barbee, T. W., Brown, C., Celliers, P., Da Silva, L. B., Glendinning, S. G., Hammel, B. A., Kalantar, D. H., Landen, O. L., and Seely, J., *High-Energy X-Ray Microscopy Techniques for Laser-Fusion Plasma Research at the National Ignition Facility,* Lawrence Livermore National Laboratory, Livermore, CA, UCRL-JC-128448. Submitted to *Appl. Opt.*

Kozlowski, M. R., Camp, D., Carr, J., Hutcheon, I., Sheehan, L., and Yan, M., *Depth Profiling of Polishing-Induced Contamination on Fused Silica Surfaces,* Lawrence Livermore National Laboratory, Livermore, CA, UCRL-JC-128355 ABS. Prepared for the *Annual Symp on Optical Materials for High Power Lasers*, Boulder, CO, Oct 6, 1997.

L

Langdon, A. B., "Clouds-in-Clouds, Clouds-in-Cells Physics for Many-Body Simulation-Introduction," *J. Comp. Physics* **135**(2), 139–140 (1997).

Langdon, A. B., Hinkel, D. E., Lasinski, B. F., and Still, C. H., *Ultra-High Intensity Laser Plasma Interactions,* Lawrence Livermore National Laboratory, Livermore, CA, UCRL-JC-127131 ABS Rev. Prepared for the *39th Annual Mtg of the American Physical Society Div of Plasma Physics*, Pittsburgh, PA, Nov 17, 1997.

Langer, S. H., Landen , O. L., Marinak, M. M., and Scott, H. A., *Comparison of Models and Experimental Data for Line Emission from Nova Rayleigh–Taylor Capsules,* Lawrence Livermore National Laboratory, Livermore, CA, UCRL-JC-127910 ABS. Prepared for the *39th Annual Mtg of the American Physical Society Div of Plasma Physics*, Pittsburgh, PA, Nov 17, 1997.

Lasinski, B. F., and Langdon, A. B., *PIC Simulations of Hole-Boring,* Lawrence Livermore National Laboratory, Livermore, CA, UCRL-JC-127129-ABS Rev. Prepared for the *39th Annual Mtg of the American Physical Society Div of Plasma Physics*, Pittsburgh, PA, Nov 17, 1997.

Latkowski, J. F., and Vujic, J. L., *Inertial Fusion Energy: a Clearer View of the Environmental and Safety Aspects,* Lawrence Livermore National Laboratory, Livermore, CA, UCRL-JC-128089. Submitted to *Fusion Technology.*

Lerche, R. A., Ellis, R. J., Lane, S. M., and Ress, D., *60-µm Penumbral Aperture Imaging Demonstrated Using ICF Fusion Neutrons,* Lawrence Livermore National Laboratory, Livermore, CA, UCRL-JC-127930 ABS. Prepared for the *39th Annual Mtg of the American Physical Society Div of Plasma Physics,* Pittsburgh, PA, Nov 17, 1997.

M

MacGowan, B. J., Afeyan, B. B., Back, C. A., Berger, R. L., Blain, M. A., Glenzer, S. H., Hinkel, D. E., Kirkwood, R. K., Montgomery, D. S., and Moody, J. D., *Trends in Nova Large Scale Length Plasma Experiments,* Lawrence Livermore National Laboratory, Livermore, CA, UCRL-JC-127928-ABS. Prepared for the *39th Annual Mtg of the American Physical Society Div of Plasma Physics,* Pittsburgh, PA, Nov 17, 1997.

Mapoles, E. R., Pipes, J., and Sater, J., *Cryogenic D-T Fuel Layers Formed in l-mm Spheres by Beta-Layering,* Lawrence Livermore National Laboratory, Livermore, CA, UCRL-JC-128031 ABS. Prepared for the *39th Annual Mtg of the American Physical Society Div of Plasma Physics,* Pittsburgh, PA, Nov 17, 1997.

Mapoles, E. R., Pipes, J., and Sater, J., *Smoothing of Deuterium-Tritium Ice in ICF-Scale Geometries by Electrical Heating of the Saturated Vapor,* Lawrence Livermore National Laboratory, Livermore, CA, UCRL-JC-128032 ABS. Prepared for the *39th Annual Mtg of the American Physical Society Div of Plasma Physics,* Pittsburgh, PA, Nov 17, 1997.

Marshall, C. D., Bibeau, C., and Payne, S. A., *Diode-Pumped Solid-State Laser-Driven Inertial Fusion Energy,* Lawrence Livermore National Laboratory, Livermore, CA, UCRL-JC-128605 EXT-ABS. Prepared for the *Intl Atomic Energy Agency Technical Committee Mtg on Innovative Approaches to Fusion Energy,* Pleasanton, CA, Oct 20, 1997.

Martinez, M., Browning, D., Crane, J., and Penko, F., *Optimized, Diode Pumped, Nd:Glass, Prototype Regenerative Amplifier for the National Ignition Facility (NIF),* Lawrence Livermore National Laboratory, Livermore, CA, UCRL-JC-127940 ABS. Prepared for the *Intl Symp on High-Power Lasers and Applications,* San Jose, CA, Jan 24, 1998.

McEachern, R., Alford, C., Cook, B., Makowiecki, E., and Wallace, R., *Tailoring Properties of Sputter-Deposited Be for ICF Target Capsules,* Lawrence Livermore National Laboratory, Livermore, CA, UCRL-JC-128038 ABS. Prepared for the *39th Annual Mtg of the American Physical Society Div of Plasma Physics,* Pittsburgh, PA, Nov 17, 1997.

Moody, J. D., Afeyan, B. B., Berger, R. L., Glenzer, S. H., Hinkel, D. E., Kirkwood, R. K., Kruer, W. L., MacGowan, B. J., Munro, D. E., and Rubenchik, A., *Measurements of Fluctuation Effects on Laser Propagation and Stimulated Interactions in a Laser Plasma Using Near Forward Scattering,* Lawrence Livermore National Laboratory, Livermore, CA, UCRL-JC-127920 ABS. Prepared for the *39th Annual Mtg of the American Physical Society Div of Plasma Physics,* Pittsburgh, PA, Nov 17, 1997.

Moon, S. J., and Eder, D. C., *Back-Side Emission from Filtered Gold Targets,* Lawrence Livermore National Laboratory, Livermore, CA, UCRL-JC-126347. Prepared for the *1997 Intl Symp on Optical Science, Engineering, and Instrumentation,* San Diego, CA, Jul 27–29, 1997.

Moran, B., Crane, J., Dane, C. B., Martinez, M., and Penko, F., *22 joule Nd:Glass Four-Pass Amplifier for the National Ignition Facility (NIF),* Lawrence Livermore National Laboratory, Livermore, CA, UCRL-JC-127938 ABS. Prepared for the *Intl Symp on High-Power Lasers and Applications,* San Jose, CA, Jan 24, 1998.

N

Nilsen, J., Moreno, J. C., Barbee, T. W., and Da Silva, L. B., *Measurement of Spatial Gain Distribution for a Neonlike Germanium 19.6-nm Laser,* Lawrence Livermore National Laboratory, Livermore, CA, UCRL-JC-126739; *Optics Lett*. **22**(17), 1320–1322 (1997).

Norton, M. A., Dane, C. B., and Hackel, L. A., *Efficient Second Harmonic Generation of 1 micron, 600 nsec Pulses,* Lawrence Livermore National Laboratory, Livermore, CA, UCRL-JC-128005 ABS. Prepared for the *Intl Symp on High-Power Lasers and Applications,* San Jose, CA, Jan 24, 1998.

O

Ognibene, T. J., Cable, M. D., Griffith, R. L., Lerche, R. A., and Zuegel, J. D., *Implementation of Neutron Temporal Diagnostic at OMEGA,* Lawrence Livermore National Laboratory, Livermore, CA, UCRL-JC-127913 ABS. Prepared for the *39th Annual Mtg of the American Physical Society Div of Plasma Physics*, Pittsburgh, PA, Nov 17, 1997.

Orth, C., Beach, R., Bibeau, C., Honea, E., Jancaitis, K., Marshall, C., and Sacks, R., *Design Modeling of the LLNL Mercury Laser,* Lawrence Livermore National Laboratory, Livermore, CA, UCRL-JC-127934 ABS. Prepared for the *Intl Symp on High-Power Lasers and Applications*, San Jose, CA, Jan 24, 1998.

P

Pennington, D. M., Britten, J. A., Brown, C. G., Herman, S., Horner, J., Miller, J. L., Perry, M. D., Stuart, B. C., Tietbohl, G., Tsukamoto, M., Van Lue, J., and Yanovsky, V., *The Petawatt Irradiation System at LLNL,* Lawrence Livermore National Laboratory, Livermore, CA, UCRL-JC-127946 ABS. Prepared for *High Power Lasers and Applications Symp*, San Jose, CA, Feb 8–14, 1997.

Pollaine, S., Marinak, M., and Munro, D., *3-D Simulations of Tetrahedral Hohlraums,* Lawrence Livermore National Laboratory, Livermore, CA, UCRL-JC-128001 ABS. Prepared for the *39th Annual Mtg of the American Physical Society Div of Plasma Physics*, Pittsburgh, PA, Nov 17, 1997.

Prasad, M. K., Kershaw, D. S., Milovich, J. L., Shaw, M. J., and Shestakov, A. I., *ICF3D-Hydro: 3D Parallel Finite Element Unstructured Mesh Hydrodymanics Code,* Lawrence Livermore National Laboratory, Livermore, CA, UCRL-JC-128097 ABS. Prepared for the *Intl Conf on Computational Physics: PC97*, Santa Cruz, CA, Aug 25, 1997.

R

Rambo, P. W., Wilks, S. C., and Kruer, W. L., "Hybrid Particle-In-Cell Simulations of Stimulated Brillouin Scattering Including Ion-Ion Collisions," *Phys. Rev. Lett.* **79**(1), 83–86 (1997).

Remington, B. A., Budil, K. S., Estabrook, K., Glendinning, S. G., Kane, J., London, R., Managan, R. A., Rubenchik, A., Ryutov, D., and Wallace, R. J., *Supernova Hydrodynamics Experiments Using the Nova Laser,* Lawrence Livermore National Laboratory, Livermore, CA, UCRL-JC-126312 Rev 1. Prepared for *SuperNova 1987A: Ten Years Later*, La Serena, Chile, Feb 22, 1997.

Remington, B. A., Castor, J., Estabrook, K., Glendinning, S. G., Kane, J., London, R., Munro, D. H., Rubenchik, A., Suter, L., and Wallace, R. J., *Supernovae Hydrodynamics Experiments on the Nova Laser,* Lawrence Livermore National Laboratory, Livermore, CA, UCRL-JC-127140. Submitted to *Phys. of Plasmas*.

Remington, B. A., Estabrook, K., Farley, D., Glendinning, S. G., Kane, J., Lagory, L., London, R., Miller, P., Ryutov, D., and Wallace, R. J., *Supernova Hydrodynamics and Radiative Jet Experiments on the Nova Laser,* Lawrence Livermore National Laboratory, Livermore, CA, UCRL-JC-128268 ABS. Prepared for the *1997 Mtg of the American Astronomy Society High Energy Astrophysics*, Estes Park, CO, Nov 4, 1997.

Rothenberg, J. E., Berger, R., MacGowan, B., and Wilcox, R., *Beam Smoothing for Inertial Confinement Fusion on the National Ignition Facility (NIF),* Lawrence Livermore National Laboratory, Livermore, CA, UCRL-JC-127908 ABS. Prepared for the *Intl Symp on High-Power Lasers and Applications*, San Jose, CA, Jan 24, 1998.

Rothenberg, J. E., "Comparison of Beam-Smoothing Methods for Direct-Drive Inertial Confinement Fusion," *J. Opt. Soc. Am. B* **14**(7), 1664–1671 (1997).

Rubenchik, A. M., Da Silva, L. B., Feit, M. D., Kim, B.-M., Perry, M. D., and Stuart, B. C., *Pressure and Temperature Evolution Induced by Ultra-Short Laser Pulse Ablation,* Lawrence Livermore National Laboratory, Livermore, CA, UCRL-JC-128093 ABS. Prepared for *BiOS '98 Intl Biomedical Optics Symp*, San Jose, CA, Jan 24, 1998.

Runkel, M., De Yoreo, J., Yan, M., and Zaitseva, N., *Effect of Impurities and Stress on the Damage Distributions of Rapidly Grown KDP Crystals,* Lawrence Livermore National Laboratory, Livermore, CA, UCRL-JC-128091 ABS. Prepared for the *Annual Symp on Optical Materials for High Power Lasers*, Boulder, CO, Oct 6, 1997.

Runkel, M., De Yoreo, J., Milam, D., and Sell, W., *Laser Conditioning Study of KDP on the Optical Sciences Laser Using Large Area Beams,* Lawrence Livermore National Laboratory, Livermore, CA, UCRL-JC-128352 ABS. Prepared for the *Annual Symp on Optical Materials for High Power Lasers*, Boulder, CO, Oct 6, 1997.

Ryutov, D., Kane, J., and Remington, B. A., *Similarity Analysis of the Experimental Simulations of the SN 1987A Event,* Lawrence Livermore National Laboratory, Livermore, CA, UCRL-JC-127743 ABS. Prepared for the *39th Annual Mtg of the American Physical Society Div of Plasma Physics*, Pittsburgh, PA, Nov 17, 1997.

Ryutov, D., Kane, J., and Remington, B. A., *Similarity Analysis of Experiments of SN 1987A Hydrodynamics,* Lawrence Livermore National Laboratory, Livermore, CA, UCRL-JC-127931 ABS. Prepared for the *39th Annual Mtg of the American Physical Society Div of Plasma Physics*, Pittsburgh, PA, Nov 17, 1997.

Ryutov, D. D., Kane, J., and Remington, B., *Similarity Criteria for Experiments on SN 1987A Hydrodynamics,* Lawrence Livermore National Laboratory, Livermore, CA, UCRL-JC-128149 ABS. Prepared for the *Institute for Theoretical Physics Conf "Supernova Explosions: Their Causes and Consequences,"* Santa Barbara, CA, Aug 5, 1997.

S

Sacks, R., Auerbach, J., Henesian, M., Lawson, J., Orth, C., Trenholme, J., and Williams, W., *Computer Modeling of the National Ignition Facility Laser,* Lawrence Livermore National Laboratory, Livermore, CA, UCRL-JC-127933 ABS. Prepared for the *Intl Symp on High-Power Lasers and Applications*, San Jose, CA, Jan 24, 1998.

Salleo, A., Feit, M., Genin, F. Y., Kozlowski, M. R., Stolz, C. J., and Yoshiyama, J., *Laser-Induced Damage of Fused Silica at 355 nm Initiated at Scratches,* Lawrence Livermore National Laboratory, Livermore, CA, UCRL-JC-128361 ABS. Prepared for the *Annual Symp on Optical Materials for High Power Lasers*, Boulder, CO, Oct 6, 1997.

Sanchez, J. J., Bernat, T. P., and Giedt, W. H., *Importance of Fill Gas and Capsule Wall Thermal Conductivities in NIF Cryogenic Hohlraums,* Lawrence Livermore National Laboratory, Livermore, CA, UCRL-JC-128030 ABS. Prepared for the *39th Annual Mtg of the American Physical Society Div of Plasma Physics*, Pittsburgh, PA, Nov 17, 1997.

Sangster, T. C., Cable, M. D., Hatchet, S. P., Key, M. H., Koch, J. A., Moran, M. J., Nelson, M. B., Pennington, D. M., Phillips, T. W., and Tabak, M., *Neutron Emission from Short-Pulse Laser Interactions with Matter,* Lawrence Livermore National Laboratory, Livermore, CA, UCRL-JC-128027 ABS. Prepared for the *39th Annual Mtg of the American Physical Society Div of Plasma Physics*, Pittsburgh, PA, Nov 17, 1997.

Sathyam, U. S., Celliers, P. M., and Da Silva, L. B., *Interferometric Technique to Measure Shock- Induced Surface Velocities in Tissues for the Determination of Dynamic Mechanical Properties,* Lawrence Livermore National Laboratory, Livermore, CA, UCRL-JC-128080 ABS. Prepared for *Laser Tissue Interaction IX*, San Jose, CA, Jan 24, 1998.

Sheehan, L. M., Camp, D. W., and Kozlowski, M., *Application of Total Internal Reflection Microscopy for Laser Damage Studies on Fused Silica,* Lawrence Livermore National Laboratory, Livermore, CA, UCRL-JC-128356 ABS. Prepared for the *Annual Symp on Optical Materials for High Power Lasers*, Boulder, CO, Oct 6, 1997.

Small, W., Celliers, P. M., Da Silva, L. B., and Matthews, D. L., *Two-Color Mid-Infrared Thermometer Using a Hollow Glass Optical Fiber,* Lawrence Livermore National Laboratory, Livermore, CA, UCRL-JC-128082. Prepared for the *IEEE Conf on the Engineering Foundation*, Snowbird, UT, Jul 13–18, 1997.

Small, W., Da Silva, L. B., Heredia, N. J., Maitland, D. J., and Matthews, D. L., *Dye-Enhanced Protein Solders and Patches in Laser-Assisted Tissue Welding,* Lawrence Livermore National Laboratory, Livermore, CA, UCRL-JC-128247. Submitted to *J. of Climate Laser Medicine and Surgery.*

Still, C. H., Berger, R. L., Hinkel, D. E., Langdon, A. B., Lasinski, B. F., Williams, E. A., and Young , P. E., *Laser-Plasma Simulation on Multiprocessors,* Lawrence Livermore National Laboratory, Livermore, CA, UCRL-JC-128011 ABS. Prepared for the *39th Annual Mtg of the American Physical Society Div of Plasma Physics*, Pittsburgh, PA, Nov 17, 1997.

Still, C. H., Berger, R. L., and Langdon, A. B., *Three-D Nonlinear Hydrodynamics Code to Study Laser Plasma Interactions,* Lawrence Livermore National Laboratory, Livermore, CA, UCRL-JC-128014. Submitted to *Computer Physics Communications.*

T

Tabak, M., Callahan-Miller, D., Ho, D. D.-M., and Zimmerman, G. B., *Design of a Distributed Radiator Target for Inertial Fusion Driven from Two Sides with Heavy Ion Beams,* Lawrence Livermore National Laboratory, Livermore, CA, UCRL-JC-128366. Submitted to *Phys. Rev. Lett.*

Teng, H. H., De Yoreo, J. J., Dove, P. M., and Orme, C., *Microscopic Characterization of Mechanisms and Fundamental Parameters Governing Calcite Mineralization,* Lawrence Livermore National Laboratory, Livermore, CA, UCRL-JC-128087. Submitted to *J. of Crystal Growth.*

Trebes, J. E., Dolan, K. W., Haddad, W. S., Haskins, J. J., Lerche, R. A., Logan, C. M., Perkins, D. E., Rikard, R. D., and Schneberk, D. J., *High Resolution, Large Area, High Energy X-Ray Tomography,* Lawrence Livermore National Laboratory, Livermore, CA, UCRL-JC-128429. Prepared for the *1997 Intl Symp on Optical Science, Engineering, and Instrumentation*, San Diego, CA, Jul 27, 1997.

Turner, R. E., Amendt , P. A., Decker, C. D., Glendinning, S. G., Kalantar, D. H., Landen, O. L., Morse, S., Murphy , T., Pien, G., and Seka, W., *Indirect Drive ICF Symmetry Experiments on OMEGA,* Lawrence Livermore National Laboratory, Livermore, CA, UCRL-JC-127919 ABS. Prepared for the *39th Annual Mtg of the American Physical Society Div of Plasma Physics*, Pittsburgh, PA, Nov 17, 1997.

V

Van Wonterghem, B., Murray, J. R., Campbell, J. H., Speck, D. R., Barker, C. E., Smith, I. C., Browning, D. F., and Behrendt, W. C., *Performance of a Prototype for a Large-Aperture Multipass Nd:Glass Laser for Inertial Confinement Fusion,* Lawrence Livermore National Laboratory, Livermore, CA, UCRL-JC-125150; *Applied Opt.* **36**(21), 4932–4953 (1997).

W

Wang , L., De Yoreo, J. J., Kozlowski, M., Mohideen, U., Sheehan, L., Siekhaus, W., and Yan, M., *Defects and Laser Damage Studies Using Near Field Scanning Optical Microscopy,* Lawrence Livermore National Laboratory, Livermore, CA, UCRL-JC-128354 ABS. Prepared for the *Annual Symp on Optical Materials for High Power Lasers*, Boulder, CO, Oct 6, 1997.

Weber, S. V., Bailey, D. S., Colvin, J. D., Kalantar, D. H., Remington, B. A., and Wiley, L. G., *Modeling of Material Strength Effects upon Rayleigh–Taylor Instability,* Lawrence Livermore National Laboratory, Livermore, CA, UCRL-JC-127929 ABS. Prepared for the *39th Annual Mtg of the American Physical Society Div of Plasma Physics*, Pittsburgh, PA, Nov 17, 1997.

Wharton, K., Brown, C., Hammel, B., Hatchett, S., Key, M., Koch, J., Moody, J., Offenberger, A., Perry, M., and Tabak, M., *Conversion of High-Intensity Laser Energy into Hot Electrons in Solid Density Targets,* Lawrence Livermore National Laboratory, Livermore, CA, UCRL-JC-127941 ABS. Prepared for the *39th Annual Mtg of the American Physical Society Div of Plasma Physics*, Pittsburgh, PA, Nov 17, 1997.

Wood-Vasey, W. M., Budil, K. S., Peyser, T., Remington, B. A., and Rubenchik, A., *Computational Modeling of Classical and Ablative Rayleigh–Taylor Experiments on Nova,* Lawrence Livermore National Laboratory, Livermore, CA, UCRL-JC-128037 ABS. Prepared for the *39th Annual Mtg of the American Physical Society Div of Plasma Physics*, Pittsburgh, PA, Nov 17, 1997.

Wood-Vasey, W. M., Berning, M., Budil, K. S., Demiris, T., Louis, H., Mikaelian, K. O., Miller, P. L., Peyser, T. A., Remington, B. A., and Rubenchik, A. M., *Computational Modeling of Classical and Ablative Rayleigh–Taylor and Richtmyer-Meshkov Instabilities,* Lawrence Livermore National Laboratory, Livermore, CA, UCRL-JC-128269. Submitted to *Phys. Rev. Lett.*

Woods, B. W., De Yoreo, J. J., Han, Y., Kozlowski, M. R., Radousky, H. B., Wu, Z. L., Yan, M., and Zhao, Q., *Photothermal Mapping of Defects in the Study of Bulk Damage in KDP,* Lawrence Livermore National Laboratory, Livermore, CA, UCRL-JC-128353 ABS. Prepared for the *Annual Symp on Optical Materials for High Power Lasers*, Boulder, CO, Oct 6, 1997.

Woolsey, N. C., Hammel, B. A., Keane, C. J., Asfaw, A., Back, C. A., Moreno, J. C., Nash, J. K., Calisti, A., Mosse, C., Stamm, R., Talin, B., Klein, L., and Lee, R. W., *Evolution of Electron Temperature and Electron Density in Indirectly Driven Spherical Implosions*, Lawrence Livermore National Laboratory, Livermore, CA, UCRL-JC-125756; *Phys Rev E* **56**(2), 2314–2317 (1997).

Wyslouzil, B. E., Cheung, J. L., Wilemski, G., and Strey, R., *Small Angle Neutron Scattering from Nanodroplet Aerosols*, Lawrence Livermore National Laboratory, Livermore, CA, UCRL-JC-127281; *Phys. Rev. Lett.* **79**(3), 431–434 (1997).

Y

Yoshiyama, J., Camp, D., Genin, F. Y., Hutcheon, I., Kozlowski, M. R., Salleo, A., Sheehan, L., and Thomas, I., *Study of the Effects of Polishing, Etching, Cleaving, and Water Leaching on the Laser-Induced Damage of Fused Silica at 355 nm*, Lawrence Livermore National Laboratory, Livermore, CA, UCRL-JC-128362 ABS. Prepared for the *Annual Symp on Optical Materials for High Power Lasers*, Boulder, CO, Oct 6, 1997.

Z

Zaitseva, N. P., De Yoreo, J. J., Dehaven, M. R., Vital, R. L., Montgomery, K. E., Richardson, M., and Atherton, L. J., *Rapid Growth of Large-Scale (40–55 cm) KH_2PO_4 Crystals*, Lawrence Livermore National Laboratory, Livermore, CA, UCRL-JC-125387; *J. Crystal Growth* **180**(2), 255–262 (1997).

1997 ICF
AWARDS, PATENTS, AND REFEREED PUBLICATIONS

The *1997 ICF Annual Report* uses this space to report on the Awards received by, Patents issued to, and Publications by LLNL employees in the ICF Program. The goal is to showcase the distinguished scientific and technical achievements of our employees.

The *Annual Report* is based on the Fiscal Year of 1997, whereas the achievements listed here are based on the Calendar Year of 1997. The reason for this disparity is the fact that a publication or award may not have a precise date other than the particular year it was given.

The awards listed are those granted by recognized organizations outside of LLNL and given to ICF Program employees.

The patents may include work that is afield from ICF but are granted to ICF Program employees. This could include work that is supported from discretionary funds.

The publications listed are those from refereed scientific journals. Therefore, conference proceedings are generally not included unless they are also published in refereed scientific journals. The work in ICF is broad-based at LLNL, and many employees who are not directly in the ICF Program publish ICF-related results; these publications are included. Furthermore, publications are included in which an ICF Program author contributes but is not the lead author.

1997 ICF Program Awards

R&D 100 Awards

Absolute Interferometer—Gary Sommargren, Eugene Campbell, Don Phillion, Frank Snell

Ultra Clean Ion Beam Sputter Deposition System—Don Kania, Patrick Kearney, Richard Levesque, Steve Vernon

Femtosecond Laser Materials Processing—Brent Stuart, Michael Perry, Hoang Nguyen, Steve Herman, Paul Armstrong, Paul Banks, Michael Feit, Alexander Rubenchik, Booth Myers, Howard Powell, Joseph Sefcik

Federal Laboratory Consortium Awards

A Stroke Treatment System to Emulsify Blood-Clots and Quickly Restore Blood Flow Following a Stroke, Based on Fiber-Optic-Delivered, Opto-Acoustic Thrombolysis—Peter Celliers, Luiz Da Silva, Dennis Matthews, Richard London, Duncan Maitland, William Benett, Peter Krulevitch, Abraham Lee, Patrick Fitch

Ultra-Clean Ion Beam Sputter System (IBD-350)—Don Kania, Patrick Kearney, Richard Levesque, Swie-In Tan

Edward Teller Medal Awards

Michael H. Key

George Zimmerman

American Physical Society Fellows

Max Tabak

Charles Verdon

Industry Week's 5th Annual Technology & Innovation Awards
"50 R&D Stars to Watch"

Thomas E. McEwan

Northern California Society for Technical Communication Competition

Award of Distinguished Technical Communication
Experimental Interstage Processing Furnace—Mark McDaniel, Tom McCarville

National Ignition Facility—Sandy Lynn, Scott Dougherty, Jason Carpenter

Nova Laser Facility—Sandy Lynn, Scott Dougherty, Jason Carpenter

Award of Excellence
ICF Quarterly Report 96-2—Jason Carpenter, Al Miguel, Pam Davis, Sandy Lynn, Don Correll, Roy Johnson, Deanna Pennington

Award of Merit
ICF Quarterly Report 96-3—Jason Carpenter, Al Miguel, Sandy Lynn, Don Correll, Roy Johnson

Global Precision Optical Weapon—Mark McDaniel, Victor George

Science and Engineering Fair—Scott Dougherty, Karen Kiernan

Award of Achievement
High Temperature Plasma Diagnostics—Sandy Lynn, Joe Kilkenny

Plasmas for National Security—Sandy Lynn, Don Correll

Document Services—Jason Carpenter, Mark McDaniel, Barbara Zears

International Society for Technical Communication Competition
Nova Laser Facility—Sandy Lynn, Scott Dougherty, Jason Carpenter

1997 ICF Patents

John S. Taylor
Precision Non-Contact Polishing Tool
U. S. Patent 5,591,068
January 7, 1997.

George D. Craig, Robert Glass, and Bernhard Rupp
System and Method for Forming Synthetic Protein Crystals to Determine the Conformational Structure by Crystallography
U. S. Patent 5,597,457
January 28, 1997.

Thomas E. McEwan
Electronic Multi-Purpose Material Level Sensor
U. S. Patent 5,609,059
March 11, 1997.

William J. Benett, Peter A. Krulevitch, Abraham P. Lee, Milton A. Northrup,
James A. Folta
Miniature Plastic Gripper and Fabrication Method
U. S. Patent 5,609,608
March 11, 1997.

Thomas E. McEwan
High Accuracy Electronic Material Level Sensor
U. S. Patent 5,610,611
March 11, 1997.

Lloyd A. Hackel and Patrick Reichert
Faraday Imaging at High Temperatures
U. S. Patent 5,612,538
March 18, 1997.

Raymond J. Beach, William J. Benett, and Steven T. Mills
Fiber Optic Coupling of a Microlens Conditioned, Stacked Semiconductor Laser Diode Array
U. S. Patent 5,617,492
April 1, 1997.

Thomas E. McEwan
Micropower RF Transponder with Superregenerative Receiver and RF Receiver with Sampling Mixer
U. S. Patent 5,630,216
May 13,1997.

James A. Folta
Miniaturized Flow Injection Analysis System
U. S. Patent 5,644,395
July 1, 1997.

Milton A. Northrup, Dino R. Ciarlo, Abraham P. Lee, Peter A. Krulevitch
Microfabricated Therapeutic Actuator Mechanisms
U. S. Patent 5,645,564
July 8, 1997.

Jerald A. Britten
Moving Zone Marangoni Drying of Wet Objects Using Naturally Evaporated Solvent Vapor
U. S. Patent 5,660,642
August 26, 1997.

Thomas E. McEwan
Window-Closing Safety System
U. S. Patent 5,661,385
August 26, 1997.

Thomas E. McEwan
Time-of-Flight Radio Location System
U. S. Patent 5,661,490
August 26, 1997.

Stephen A. Payne and Joseph S. Hayden
Ultrafast Pulsed Laser Utilizing Broad Bandwidth Laser Glass
U. S. Patent 5,663,972
September 2, 1997.

Kathleen I. Schaffers, Laura D. DeLoach, Stephen A. Payne, and Douglas A. Keszler
Ytterbium-Doped Borate Fluoride Laser Crystals and Lasers
U. S. Patent 5,677,921
October 14, 1997.

Thomas E. McEwan
Pulse Homodyne Field Disturbance Sensor
U. S. Patent 5,682,164
October 28, 1997.

C. Brent Dane and Lloyd A. Hackel
Long-Pulse-Width, Narrow Bandwidth Solid State Laser
U. S. Patent 5,689,363
November 18, 1997.

Raymond J. Beach
High Efficiency 2 Micrometer Laser Utilizing Wing-Pumped Tm^{3+} and a Laser Diode Array End-Pumping Architecture
U. S. Patent 5,689,522
November 18, 1997.

Natale M. Ceglio and David A. Markle
Maskless, Reticle-Free Lithography
U. S. Patent 5,691,541
November 25, 1997.

Ralph H. Page, Kathleen I. Schaffers, Stephen A. Payne, William F. Krupke, Raymond J. Beach
Optical Amplifier Operating at 1.3 Micron Useful for Telecommunications and Based on Dysprosium-Doped Metal Chloride Host Materials
U. S. Patent 5,694,500
December 2, 1997.

Sherry L. Baker, Stephen P. Vernon, Daniel G. Stearns
Recovery of Mo/Si Multilayer Coated Optical Substrates
U. S. Patent 5,698,113
December 16, 1997.

1997 ICF Program Refereed Publications

A

B. B. Afeyan and E. A. Williams, "A Variational Approach to Parametric Instabilities in Inhomogeneous Plasmas I: Two Model Problems," *Phys. Plasmas* **4**(11), 3788–3802 (1997).

B. B. Afeyan and E. A. Williams, "A Variational Approach to Parametric Instabilities in Inhomogeneous Plasmas II: Stimulated Raman Scattering," *Phys. Plasmas* **4**(11), 3803–3826 (1997).

B. B. Afeyan and E. A. Williams, "A Variational Approach to Parametric Instabilities in Inhomogeneous Plasmas III: Two-Plasmon Decay," *Phys. Plasmas* **4**(11), 3827–3844 (1997).

B. B. Afeyan and E. A. Williams, "A Variational Approach to Parametric Instabilities in Inhomogeneous Plasmas IV: The Mixed Polarization High-Frequency Instability," *Phys. Plasmas* **4**(11), 3845–3862 (1997).

P. Amendt, S. G. Glendinning, B. A. Hammel, O. L. Landen, T. J. Murphy, L. J. Suter, S. Hatchett, M. D. Rosen, S. Lafitte, D. Desenne, and J. P. Jaduad, "New Methods for Diagnosing and Controlling Hohlraum Drive Asymmetry on Nova," *Phys. Plasmas* **4**(5), 1862–1871 (1997).

M. S. Aouadi, A. Kleinschmidt, G. A. Clarke, and N. R. Osborne, "Inconel/Carbon Multilayers for X-Ray Mirrors," *Thin Solid Films* **303**(1-2), 53–57 (1997).

J. M. Auerbach, D. Eimerl, D. Milam, and P. W. Milonni, "Perturbation Theory for Electric Field Amplitude and Phase Ripple Transfer in Frequency Doubling and Tripling," *Appl. Optics* **36**(3), 606–612 (1997).

B

C. A. Back, T. S. Perry, D. R. Bach, B. G. Wilson, C. A. Iglesias, O. L. Landen, S. J. Davidson, and B. J. B. Crowley, "Opacity Measurements: Extending the Range and Filling the Gaps," *J. Quant. Spectrosc. Radiat. Transfer* **58**(4-6), 415–425 (1997).

C. A. Back, S. H. Glenzer, O. L. Landen, B. J. MacGowan, and T. D. Shepard, "X-Ray Diagnostics of Hohlraum Plasma Flow," *Rev. Sci. Inst.* **68**(1), 831–833 (1997).

H. A. Baldis and C. Labaune, "Interplay Between Parametric Instabilities in the Context of Inertial Confinement Fusion," *Plasma Phys. Control. Fusion* **39**, A51–A57 (1997).

F. N. Beg, A. R. Bell, A. E. Dangor, C. N. Danson, A. P. Fews, M. E. Glinsky, B. A. Hammel, P. Lee, P. A. Norreys, and M. Tatarakis, "A Study of Picosecond Laser–Solid Interactions up to 10^{19} W/cm^2," *Phys. Plasmas* **4**(2), 447–457 (1997).

T. P. Bernat, "Guest Editor's Comments," *Fusion Tech.* **31**(4), **V** (1997).

K. E. Branham, J. W. Mays, G. M. Gray, R. D. Sanner, G. E. Overturf III, and R. Cook, "Reactions of Titanocene Derivatives with Molecular Carboxylic Acids and Copolymers Bearing Carboxylic Acid Groups," *Appl. Organometallic Chem.* **11**, 213–221 (1997).

S. Brereton, L. McLouth, B. Odell, M. Singh, M. Tobin, M. Trent, and J. Yatabe, "Overview of the Preliminary Safety Analysis of the National Ignition Facility," *J. Fusion Energy* **16**(1-2), 85–94 (1997).

J. A. Britten, "A Moving-Zone Marangoni Drying Process for Critical Cleaning and Wet Processing," *Solid State Tech.* **40**(10), 143+ (1997).

K. S. Budil, T. S. Perry, S. A. Alvarez, D. Hargrove, J. R. Mazuch, A. Nikitin, and P. M. Bell, "Point Projection Radiography with the Flexible X-Ray Imager," *Rev. Sci. Inst.* **68**(1), 796–798 (1997).

K. S. Budil, B. A. Remington, T. S. Perry, A. M. Rubenchik, M. Berning, T. A. Peyser, H. Louis, T. Demiris, and R. Wallace, "A Novel Method for Diagnosing the Growth of Subresolution-Scale Perturbations," *Rev. Sci. Inst.* **68**(1), 799–801 (1997).

A. K. Burnham, C. S. Alford, D. M. Makowiecki, T. R. Dittrich, R. J. Wallace, E. C. Honeo, and C. M. King, "Evaluation of B$_4$C as an Ablator Material for NIF Capsules," *Fusion Tech.* **31**(4), 456–462 (1997).

C

D. A. Callahan, A. B. Langdon, A. Friedman, and I. Haber, "The Longitudinal Wall Impedance Instability in a Heavy-Ion Fusion Driver," *J. Appl. Phys.* **81**(8-1), 3398–3409 (1997).

E. M. Campbell, N. C. Holmes, S. B. Libby, B. A. Remington, and E. Teller, "The Evolution of High Energy-Density Physics: From Nuclear Testing to the Superlasers," *Laser and Part. Beams* **15**(4), 607–626 (1997).

R. Cauble, L. B. Da Silva, T. S. Perry, D. R. Bach, K. S. Budil, P. Celliers, G. W. Collins, A. Ng, T. W. Barbee Jr,. B. A. Hammel, N. C. Holmes, J. D. Kilkenny, R. J. Wallace, G. Chiu, and N. C. Woolsey, "Absolute Measurements of the Equations of State of Low-Z Materials in the Multi-Mbar Regime Using Laser-Driven Shocks," *Phys. Plasmas* **4**(5), 1857–1861 (1997).

B. I. Cohen, B. F. Lasinski, A. B. Langdon, and E. A. Williams, "Resonantly Excited Nonlinear Ion Waves," *Phys. Plasmas* **4**(4), 956–977 (1997).

D

A. A. Darinskii, A. V. Ly, F. I. Torchinskii, A. I. Neelov, and R. Cook, "Equilibrium Properties and Relaxation–Time Spectrum of a Polymer Chain in a Quadrupole Field: Computer Simulation," *Polymer Science A* **39**(9), 989–996 (1997).

L. B. Da Silva, P. Celliers, G. W. Collins, K. S. Budil, N. C. Holmes, T. W. Barbee Jr., B. A. Hammel, J. D. Kilkenny, R. J. Wallace, M. Ross, R. Cauble, A. Ng, and G. Chiu, "Absolute Equation of State Measurements on Shocked Liquid Deuterium up to 200 GPa (2 Mbar)," *Phys. Rev. Lett.* **78**(3), 483–486 (1997).

C. Decker, R. E. Turner, O. L. Landen, L. J. Suter, P. Amendt, H. N. Kornblum, B. A. Hammel, T. J. Murphy, J. Wallace, A. A. Hauer, J. Knauer, F. J. Marshall, D. Bradley, W. Seka, and J. M. Soures, "Hohlraum Radiation Drive Measurements on the Omega Laser," *Phys. Rev. Lett.* **79**(8), 1491–1494 (1997).

J. J. De Yoreo, T. A. Land, L. N. Rashkovich, T. A. Onischenko, "The Effect of Dislocation Cores on Growth Hillock Vicinality and Normal Growth Rates of KDP (101) Surfaces," *J. Crystal Growth* **182**(3-4), 442–460 (1997).

J. J. De Yoreo, T. A. Land, and J. D. Lee, "Limits on Surface Vicinality and Growth Rate Due to Hollow Dislocation Cores on KDP [101]," *Phys. Rev. Lett.* **78**(23), 4462–4465 (1997).

G. Dimonte and M. Schneider, "Turbulent Richtmyer-Meshkov Instability Experiments with Strong Radiatively Driven Shocks," *Phys. Plasmas* **4**(12), 4347–4357 (1997).

T. R. Dittrich, S. W. Haan, S. Pollaine, A. K. Burnham, and G. L. Strobel, "NIF Capsule Design Update," *Fusion Tech* **31**(4), 402–405 (1997).

V. M. Dorogotovtsev, A. A. Akunets, Y. A. Merkuliev, A. P. Turivnoy, R. Reibold, E. Fearon, and R. Cook, "Thermal Decomposition of Polystyrene in the High Temperature Fabrication Technology of Hollow Microspheres," *Fusion Tech*. **31**(4), 424–430 (1997).

R. P. Drake, K. Estabrook, and R. G. Watt, "Greatly Enhanced Acoustic Noise and the Onset of Stimulated Brillouin Scattering," *Phys. Plasmas* **4**(5), 1825–1831 (1997).

P. F. Dubois, "The Future of Scientific Computing," *Computers in Physics* **11**(2), 168–173 (1997).

E

V. V. Elisseev, I. Ourdev, W. Rozmus, V. T. Tikhonchuk, C. E. Capjack, and P. E. Young, "Ion Wave Response to Intense Laser Beams in Underdense Plasmas," *Phys. Plasmas* **4**(12), 4333–4346 (1997).

F

E. M. Fearon, S. A. Letts, L. M. Allison, and R. C. Cook, "Adapting the Decomposable Mandrel Technique to Build Specialty ICF Targets," *Fusion Tech*. **31**(4), 406–410 (1997).

M. D. Feit, J. C. Garrison, and A. M. Rubenchik, "Channeling of Intense Laser Beams in Underdense Plasmas," *Phys. Rev. E* **56**(3) Part A, R2394–R2397 (1997).

A. Fernandez, J. Y. Decker, S. M. Herman, D. W. Phillion, D. W. Sweeney, and M. D. Perry, "Methods for Fabricating Arrays of Holes Using Interference Lithography," *J. Vac. Sci. Technol. B* **15**(6), 2439–2443 (1997).

A. Fernandez, H. T. Nguyen, J. A. Britten, R. D. Boyd, M. D. Perry, D. R. Kania, and A. M. Hawryluk, "Use of Interference Lithography to Pattern Arrays of Submicron Resist Structures for Field Emission Flat Panel Displays," *J. Vac. Sci. & Tech. B* **14**(5), 729–735 (1997).

J. C. Fernandez, B. S. Bauer, J. A. Cobble, D. F. Dubois, G. A. Kyrala, D. S. Montgomery, H. A. Rose, H. X. Vu, R. G. Watt, B. H. Wilde, M. D. Wilke, W. M. Wood, B. H. Failor, R. Kirkwood, and B. J. MacGowan, "Measurements of Laser-Plasma Instability Relevant to Ignition Hohlraums," *Phys. Plasmas* **4**(5), 1849–1856 (1997).

G. Furnish, "Disambiguated Glommable Expression Templates," *Computers in Physics* **11**(3), 263–269 (1997).

G

S. G. Glendinning, S. N. Dixit, B. A. Hammel, D. H. Kalantar, M. H. Key, J. D. Kilkenny, J. P. Knauer, D. M. Pennington, B. A. Remington, R. J. Wallace, and S. V. Weber, "Measurement of a Dispersion Curve for Linear-Regime Rayleigh–Taylor Growth Rates in Laser-Driven Planar Targets," *Phys. Rev. Lett.* **78**(17), 3318–3321 (1997).

S. H. Glenzer, C. A. Back, L. J. Suter, M. A. Blain, O. L. Landen, B. J. MacGowan, G. F. Stone, R. E. Turner, and B. H. Wilde, "Thomson Scattering from Inertial-Confinement-Fusion Hohlraum Plasmas," *Phys. Rev. Lett.* **79**(7), 1277–1280 (1997).

S. H. Glenzer, C. A. Back, K. G. Estabrook, B. J. MacGowan, D. S. Montgomery, R. K. Kirkwood, J. D. Moody, D. H. Munro, and G. F. Stone, "Electron Temperature and Density Measurements in Laser-Produced Large-Scale-Length Gas-Bag Plasmas by X-Ray Spectroscopy," *Phys. Rev. E* **55**(1), 927–938 (1997).

S. H. Glenzer, C. A. Back, K. G. Estabrook, and B. J. MacGowan, "Thomson Scattering in the Corona of Laser-Produced Gold Plasmas," *Rev. Sci. Inst.* **68**(1-2), 668–671 (1997).

S. H. Glenzer, C. A. Back, K. G. Estabrook, R. K. Kirkwood, R. Wallace, B. J. MacGowan, B. A. Hammel, R. E. Cid, and J. S. De Groot, "Thomson Scattering from Two-Species Laser-Produced Plasmas," *Rev. Sci. Inst.* **68**(1-2), 641–646 (1997).

S. H. Glenzer, Th. Wrubel, H.-J. Kunze, and L. Godbert-Mouret, "Investigation of a Short-Wavelength Laser Plasma of a Gas-Liner Pinch Discharge," *Phys. Rev. E* **55**(1), 939–946 (1997).

H

K. E. Hamilton, S. A. Letts, S. R. Buckley, E. M. Fearon, G. Wilemski, R. C. Cook, and D. Schroen-Carey, "The Role of Reactant Transport in Determining the Properties of NIF Shells Made by Interfacial Polycondensation," *Fusion Tech.* **31**(4), 391–401 (1997).

D. G. Hicks, C. K. Li, R. D. Petrasso, F. H. Seguin, B. E. Burke, J. P. Knauer, S. Cremer, R. L. Kremens, M. D. Cable, and T. W. Phillips, "Design of an Electronic Charged Particle Spectrometer to Measure $\langle \rho \Re \rangle$ on Inertial Fusion Experiments," *Rev. Sci. Inst.* **68**(1), 589–592 (1997).

E. C. Honea, R. J. Beach, S. B. Sutton, J. A. Speth, S. C. Mitchell, J. A. Skidmore, M. A. Emanuel, and S. A. Payne, "115 W Tm:YAG Diode-Pumped Solid-State Laser," *IEEE J. Quant. Elect.* **33**(9), 1592–1600 (1997).

K

D. H. Kalantar, M. H. Key, L. B. Da Silva, S. G. Glendinning, B. A. Remington, J. E. Rothenberg, F. Weber, S. V. Weber, E. Wolfrum, N. S. Kim, D. Neely, J. Zhang, J. S. Wark, A. Demir, J. Lin, R. Smith, G. J. Tallents, C. L. S. Lewis, A. MacPhee, J. Warwick, and J. P. Knauer, "Measurements of Direct Drive Laser Imprint in Thin Foils by Radiography Using an X-Ray Laser Backlighter," *Phys. Plasmas* **4**(5), 1985–1993 (1997).

D. H. Kalantar, S. W. Haan, B. A. Hammel, C. J. Keane, O. L. Landen, and D. H. Munro, "X-Ray Backlit Imaging Measurement of In-Flight Pusher Density for an Indirect Drive Capsule Implosion," *Rev. Sci. Inst.* **68**(1), 814–816 (1997).

D. H. Kalantar, L. B. Da Silva, S. G. Glendinning, B. A. Remington, F. Weber, S. V. Weber, M. H. Key, N. S. Kim, D. Neely, E. Wolfrum, J. Zhang, J. S. Wark, A. Demir, J. Lin, R. Smith, G. J. Tallents, C. L. S. Lewis, A. MacPhee, J. Warwick, and J. P. Knauer, "Extreme Ultraviolet Probing of Laser Imprint in a Thin Foil Using an X-Ray Laser Backlighter," *Rev. Sci. Inst.* **68**(1) Part 2, 802–805 (1997).

J. Kane, D. Arnett, B. A. Remington, S. G. Glendinning, J. Castor, R. Wallace, A. Rubenchik, and B. Fryxell, "Supernova-Relevant Hydrodynamic Instability Experiments on the Nova Laser," *Astrophys. J.* **478**(2-2), L75+ (1997).

R. K. Kirkwood, B. J. MacGowan, D. S. Montgomery, B. B. Afeyan, W. L. Kruer, D. M. Pennington, S. C. Wilks, J. D. Moody, K. Wharton, C. A. Back, K. G. Estabrook, S. H. Glenzer, M. A. Blain, R. L. Berger, D. E. Hinkel, B. F. Lasinski, E. A. Williams, D. Munro, B. H. Wilde, and C. Rousseaux, "Observation of Multiple Mechanisms for Stimulating Ion Waves in Ignition Scale Plasmas," *Phys. Plasmas* **4**(5), 1800–1810 (1997).

R. K. Kirkwood, C. A. Back, M. A. Blain, D. E. Desenne, A. G. Dolieu, S. H. Glenzer, B. J. MacGowan, D. S. Montgomery, and J. D. Moody, "Imaging Backscattered and Near to Backscattered Light in Ignition Scale Plasmas," *Rev. Sci. Inst.* **68**(12), 636–640 (1997).

B. J. Kozioziemski, G. W. Collins, and T. P. Bernat, "Crystal Growth and Roughening of Solid D_2," *Fusion Tech.* **31**(4), 482–484 (1997).

W. L. Kruer, "Deflection, Spraying and Induced Scattering of Intense Laser Beams in Plasmas," *Plasma Phys. Control. Fusion* **39**, A153–A159 (1997).

W. L. Kruer and J. H. Hammer, "Laser Beam Deflection in Nonlinearly Steepened Flow Profiles," *Comments Plasma Phys. Controlled Fusion* **18**(2), 85–93 (1997).

Y. G. Kuznetsov, A. J. Malkin, T. A. Land, J. J. De Yoreo, "Molecular Resolution Imaging of Macromolecular Crystals by Atomic Force Microscopy," *Biophys. J.* **72**(5), 2357–2364 (1997).

L

C. Labaune, H. A. Baldis, N. Renard, E. Schifano, and A. Michard, "Interplay Between Ion Acoustic Waves and Electron Plasma Waves Associated with Stimulated Brillouin and Raman Scattering," *Phys. Plasmas* **4**(2), 423–427 (1997).

A. B. Langdon, "Clouds-in-Clouds, Clouds-in-Cells Physics for Many-Body Simulation-Introduction," *J. Comp. Physics* **135**(2), 139–140 (1997).

S. H. Langer, H. A. Scott, C. J. Keane, O. L. Landen, and M. M. Marinak, "Yield and Emission Line Ratios from ICF Target Implosions with Multi-Mode Rayleigh–Taylor Perturbations," *J. Quant. Spectrosc. Radiat. Transfer* **58**(4-6), 709–720 (1997).

E. Leboucher-Dalimier, P. Angelo, P. Gauthier, P. Sauvan, A. Poquerusse, H. Derfoul, T. Ceccotti, C. A. Back, T. D. Shepard, E. Forster, I. Uschmann, and M. Vollbrecht, "X-Ray Spectroscopy and Imaging of Hot Dense Plasma Created by Colliding Foils. Simulation of Spectra," *J. Quant. Spectrosc. Radiat. Transfer* **58**(4-6), 721–735 (1997).

R. W. Lee, J. K. Nash, and Y. Ralchenko, "Review of the NLTE Kinetics Workshop," *J. Quant. Spectrosc. Radiat. Transfer* **58**(4-6), 737–742 (1994).

R. J. Leeper, G. A. Chandler, G. W. Cooper, M. S. Derzon, D. L. Fehl, D. E. Hebron, A. R. Moats, D. D. Noack, J. L. Porter, L. E. Ruggles, C. L. Ruiz, J. A. Torres, M. D. Cable, P. M. Bell, C. A. Clower, B. A. Hammel, D. H. Kalantar, V. P. Karpenko, R. L. Kauffman, J. D. Kilkenny, F. D. Lee, R. A. Lerche, B. J. MacGowan, M. J. Moran, M. B. Nelson, W. Olson, T. J. Orzechowski, T. W. Phillips, D. Ress, G. L. Tietbohl, J. E. Trebes, R. J. Bartlett, R. Berggren, S. E. Caldwell, R. E. Chrien, B. H. Failor, J. C. Fernandez, A. Hauer, G. Idzorek, R. G. Hockaday, T. J. Murphy, J. Oertel, R. Watt, M. Wilke, D. K. Bradley, J. Knauer, R. D. Petrasso, and C. K. Li, "Target Diagnostic System for the National Ignition Facility," *Rev. Sci. Inst.* **68**(1), 868–879 (1997).

R. A. Lerche, "Neutron-Induced Noise in National Ignition Facility-Class Diagnostic Instruments," *Rev. Sci. Inst.* **68**(1), 628–631 (1997).

W. K. Levedahl and J. D. Lindl, "Energy Scaling of Inertial Confinement Fusion Targets for Ignition and High Gain," *Nucl. Fusion* **37**(2), 165–173 (1997).

C. K. Li, D. G. Hicks, R. D. Petrasso, F. H. Seguin, M. D. Cable, T. W. Phillips, T. C. Sangster, J. P. Knauer, S. Cremer, and R. L. Kremens, "Charge-Coupled Devices for Charged-Particle Spectroscopy on Omega and Nova," *Rev. Sci. Inst.* **68**(1), 593–595 (1997).

R. A. London, M. E. Glinsky, G. B. Zimmerman, D. S. Bailey, D. C. Eder, and S. L. Jacques, "Laser–Tissue Interaction Modeling with LATIS," *Appl. Optics* **36**(34), 9068–9074 (1997).

M

E. R. Mapoles, J. Sater, J. Pipes, and E. Monsler, "Smoothing of Deuterium-Tritium Ice by Electrical Heating of the Saturated Vapor," *Phys. Rev. E* **55**(3-B), 3473–3480 (1997).

C. D. Marshall, J. A. Speth, and S. A. Payne, "Induced Optical Absorption in Gamma, Neutron, and Ultraviolet Irradiated Fused Quartz and Silica," *J. Non-Crystalline Solids* **212**(1), 59–73 (1997).

R. McEachern, C. Alford, R. Cook, D. Makowiecki, and R. Wallace, "Sputter-Deposited Be Ablators for NIF Target Capsules," *Fusion Tech.* **31**(4), 435–441 (1997).

K. O. Mikaelian, "Finite Larmor Radius Stabilization of the Rayleigh–Taylor Turbulent Mixing Width," *Phys. Plasmas* **4**(2), 499–500 (1997).

M. J. Moran and J. Hall, "Nuclear Diagnostics in Support of Inertial Confinement Fusion Experiments," *Rev. Sci. Inst.* **68**(1), 521–526 (1997).

C. Mosse, A. Calisti, R. Stamm, B. Talin, R. W. Lee, J. Koch, A. Asfaw, J. Seely, J. Wark, and L. Klein, "X-Ray Laser Photopumped Resonance Fluorescence," *J. Quant. Spectrosc. Radiat. Transfer* **58**(4-6), 803–810 (1997).

N

J. Neev, J. S. Nelson, M. Critelli, J. L. McCullough, E. Cheung, W. A. Carrasco, A. M. Rubenchik, L. B. Da Silva, M. D. Perry, and B. C. Stuart, "Ablation of Human Nail by Pulsed Lasers," *Lasers in Surgery and Medicine* **21**(2), 186–192 (1997).

J. D. Ng, Y. G. Kuznetsov, A. J. Malkin, and G. Keith, "Visualization of RNA Crystal Growth by Atomic Force Microscopy," *Nucleic Acids Res.* **25**(13), 2582–2588 (1997).

H. T. Nguyen, B. W. Shore, S. J. Bryan, J. A. Britten, R. D. Boyd, and M. D. Perry, "High-Efficiency Fused-Silica Transmission Gratings," *Optics Lett.* **22**(3), 142–144 (1997).

A. I. Nikitenko, S. M. Tolokonnikov, and R. Cook, "The Design of the Ballistic Furnace and Initial Microshells Formation Experiments," *Fusion Tech.* **31**(4), 385–390 (1997).

J. Nilsen, J. Zhang, A. G. MacPhee, J. Lin, T. W. Barbee, Jr., C. Danson, L. B. Da Silva, M. H. Key, C. L. S. Lewis, D. Neely, R. M. N. O'Rourke, G. J. Pert, R. Smith, G. J. Tallents, J. S. Wark, and E. Wolfrum, "Near-Field Spatial Imaging of a Ni-Like Ag 140-A X-Ray Laser," *Phys. Rev. A* **56**(4), 3161–3165 (1997).

J. Nilsen, J. C. Moreno, T. W. Barbee, and L. B. Da Silva, "Measurement of Spatial Gain Distribution for a Neonlike Germanium 19.6-nm Laser," *Optics Lett.* **22**(17), 1320–1322 (1997).

J. Nilsen, J. C. Moreno, L. B. Da Silva, and T. W. Barbee Jr., "Two-Dimensional Spatial Imaging of the Multiple-Pulse-Driven 196-angstrom Neonlike Germanium X-Ray Laser," *Phys. Rev. A* **55**(1), 827–830 (1997).

O

R. E. Olson, J. L. Porter, G. A. Chandler, D. L. Fehl, D. O. Jobe, R. J. Leeper, M. K. Matzen, J. S. McGurn, D. D. Noack, L. E. Ruggles, P. Sawyer, J. A. Torres, M. Vargas, D. M. Zagar, H. N. Kornblum, T. J. Orzechowski, D. W. Phillion, L. J. Suter, A. R. Theissen, and R. J. Wallace, "Inertial Confinement Fusion Ablator Physics Experiments on Saturn and Nova," *Phys. Plasmas* **4**(5), 818–1824 (1997).

T. J. Orzechowski, M. D. Rosen, H. N. Kornblum, J. L. Porter, L. J. Suter, A. R. Theissen, and R. J. Wallace, "The Rosseland Mean Opacity of a Mixture of Gold and Gadolinium at High Temperatures," [Errata] *Phys. Rev. Lett.* **78**(11), 2273 (1997).

P

R. H. Page, K. I. Schaffers, S. A. Payne, and W. F. Krupke, "Dy-Doped Chlorides as Gain Media for 1.3 mm Telecommunications Amplifiers," *J. Lightwave Tech.* **15**(5), 786–793 (1997).

R. H. Page, K. I. Schaffers, L. D. DeLoach, G. D. Wilke, F. D. Patel, J. B. Tassano Jr., S. A. Payne, W. F. Krupke, K.-T. Chen, and A. Burger, "Cr^{2+}-Doped Zinc Chalcogenides as Efficient Widely Tunable Mid-Infrared Lasers," *IEEE J. Quantum Electron.* **33**(4), 609–619 (1997).

S. A. Payne, R. J. Beach, C. Bibeau, C. A. Ebbers, M. A. Emmanuel, E. C. Honea, C. D. Marshall, R. H. Page, K. I. Schaffers, J. D. Skidmore, S. B. Sutton, and W. F. Krupke, "Diode Arrays, Crystals, and Thermal Management for Solid-State Lasers," *IEEE J. Sel. Topics in QE* **3**(1), 71–81 (1997).

D. W. Phillion, "General Methods for Generating Phase-Shifting Interferometry Algorithms," *Appl. Optics* **36**(31), 8098–8115 (1997).

T. W. Phillips, M. D. Cable, D. G. Hicks, C. K. Li, R. D. Petrasso, and F. H. Seguin, "A Study of CR-39 Track Response to Charged Particles from Nova Implosions," *Rev. Sci. Inst* **68**(1), 596–598 (1997).

S. J. Piet, S. J. Brereton, J. M. Perlado, Y. Seki, S. Tanaka, and M. T. Tobin, "Overview of Safety and Environmental Issues for Inertial Fusion Energy," *J. Fusion Energy* **16**(1-2), 133–140 (1997).

R

P. W. Rambo, S. C. Wilks, and W. L. Kruer, "Hybrid Particle-In-Cell Simulations of Stimulated Brillouin Scattering Including Ion-Ion Collisions," *Phys. Rev. Lett.* **79**(1), 83–86 (1997).

B. A. Remington, J. Kane, R. P. Drake, S. G. Glendinning, K. Estabrook, R. London, J. Castor, R. J. Wallace, D. Arnett, E. Liang, R. McCray, A. Rubenchik, and B. Fryxell, "Supernovae Hydrodynamics Experiments on the Nova Laser," *Phys. Plasmas* **4**(5), 1994–2003 (1997).

H. F. Robey, K. S. Budil, and B. A. Remington, "Spatial Resolution of Gated X-Ray Pinhole Cameras," *Rev. Sci. Inst.* **68**(1) Part 2, 792–795 (1997).

J. E. Rothenberg, "Comparison of Beam-Smoothing Methods for Direct-Drive Inertial Confinement Fusion," *J. Opt. Soc. Am. B* **14**(7), 1664–1671 (1997).

S

J. J. Sanchez and S. A. Letts, "Polyimide Capsules May Hold High Pressure DT Fuel Without Cryogenic Support for the National Ignition Facility Indirect-Drive Targets," *Fusion Tech.* **31**(4), 491–496 (1997).

T. W. L. Sanford, T. J. Nash, R. C. Mock, R. B. Spielman, K. W. Struve, J. H. Hammer, J. S. De Groot, K. G. Whitney, and J. P. Apruzese, "Dynamics of a High-Power Aluminum-Wire Array Z-Pinch Implosion," *Phys. Plasmas* **4**(6), 2188–2203 (1997).

B. W. Shore, M. D. Perry, J. A. Britten, R. D. Boyd, M. D. Feit, H. T. Nguyen, R. Chow, and G. E. Loomis, "Design of High-Efficiency Dielectric Reflection Gratings," *J. Opt. Soc. Am. A* **14**(5), 1124–1136 (1997).

B. W. Shore, L. F. Li, and M. D. Feit, "Poynting Vectors and Electric Field Distributions in Simple Dielectric Gratings," *J. Modern Optics* **44**(1), 69–81 (1997).

B. W. Shore, M. D. Feit, M. D. Perry, A. Rubenchik, and B. Stuart, "Brief Intense Laser Fields in Bulk Matter," *Laser Physics* **7**(1), 119–125 (1997).

R. Solarz, R. Beach, C. Bibeau, E. Campbell, W. Krupke, C. Marshall, R. Page, J. Paisner, S. Payne, M. Perry, K. Schaefer, and K. Scheiber, "Current Research Directions and Topics in the Laser Directorate at Lawrence Livermore National Laboratory," *Laser Physics* **7**(1), 234–238 (1997).

P. T. Springer, K. L. Wong, C. A. Iglesias, J. H. Hammer, J. L. Porter, A. Toor, W. H. Goldstein, B. G. Wilson, F. J. Rogers, C. Deeney, D. S. Dearborn, C. Bruns, J. Emig, and R. E. Stewart, "Laboratory Measurement of Opacity for Stellar Envelopes," *J. Quant. Spectrosc. Radiat. Transfer* **58**(4-6), 927–935 (1997).

R. B. Stephens and G. Collins, "Analysis of Integrating Sphere Performance for IR Enhanced DT Layering," *Fusion Tech.* **31**(4), 485–490 (1997).

B. C. Stuart, M. D. Perry, J. Miller, G. Tietbohl, S. Herman, J. A. Britten, C. Brown, D. Pennington, V. Yanovsky, and K. Wharton, "125-TW Ti:Sapphire/Nd:Glass Laser Systems," *Optics Lett.* **22**(4), 242–244 (1997).

L. J. Suter, A. R. Thiessen, F. Ze, R. Kauffman, R. H. Price, V. C. Rupert, V. W. Slivinsky, and C. Wang, "Use of Thin Wall Imaging in the Diagnosis of Laser Heated Hohlraums," *Rev. Sci. Inst.* **68**(1), 838–841 (1997).

V

B. Van Wonterghem, J. R. Murray, J. H. Campbell, D. R. Speck, C. E. Barker, I. C. Smith, D. F. Browning, and W. C. Behrendt, "Performance of a Prototype for a Large-Aperture Multipass Nd:Glass Laser for Inertial Confinement Fusion," *Applied Optics* **36**(21), 4932–4953 (1997).

W

A. S. Wan, T. W. Barbee, R. Cauble, P. Celliers, L. B. Da Silva, J. C. Moreno, P. W. Rambo, G. F. Stone, J. E. Trebes, and F. Weber, "Electron Density Measurement of a Colliding Plasma Using Soft-X-Ray Laser Interferometry," *Phys. Rev. E* **55**(5), 6293–6296 (1997).

P. Wang, J. J. MacFarlane, and T. J. Orzechowski, "An Investigation of the Opacity of High-Z Mixture and Implications for Inertial Confinement Fusion Hohlraum Design," *Rev. Sci. Inst.* **68**(1), 1107–1110 (1997).

S. V. Weber, S. G. Glendinning, D. H. Kalantar, M. H. Key, B. A. Remington, J. E. Rothenberg, E. Wolfrum, C. P. Verdon, and J. P. Knauer, "Simulations of Laser Imprint for Nova Experiments and for Ignition Capsules," *Phys. Plasmas* **4**(5), 1978–1984 (1997).

F. A. Weber, L. B. Da Silva, T. W. Barbee, Jr., and D. Ciarlo, "Quantification of Carbon in a Binary System by the Fundamental Parameter Method," *Advances in X-Ray Analysis*, **40** (Plenum Publishing Corp., New York, NY). To be published.

C. C. Widmayer, D. Milam, and S. P. deSzoeke, "Nonlinear Formation of Holographic Images of Obscurations in Laser Beams," *Appl. Optics* **36**(36), 9342–9347 (1997).

J. G. Woodworth and W. R. Meier, "Target Production for Inertial Fusion Energy," *Fus. Tech.* **31**, 280–290 (1997).

N. C. Woolsey, B. A. Hammel, C. J. Keane, C. A. Back, J. C. Moreno, J. K. Nash, A. Calisti, C. Mosse, L. Godbart, R. Stamm, B. Talin, L. Klein, and R. W. Lee, "Spectroscopic Line Shape Measurements at High Densities," *J. Quant. Spectrosc. Radiat. Transfer* **58**(4-6), 975–989 (1997).

N. C. Woolsey, B. A. Hammel, C. J. Keane, A. Asfaw, C. A. Back, J. C. Moreno, J. K. Nash, A. Calisti, C. Mosse, R. Stamm, B. Talin, L. Klein, and R. W. Lee, "Evolution of Electron Temperature and Electron Density in Indirectly Driven Spherical Implosions," *Phys Rev. E* **56**(2), 2314–2317 (1997).

B. E. Wyslouzil, J. L. Cheung, G. Wilemski, and R. Strey, "Small Angle Neutron Scattering from Nanodroplet Aerosols," *Phys. Rev. Lett.* **79**(3), 431–434 (1997).

Y

B. K. F. Young, B. G. Wilson, G. B. Zimmerman, D. F. Price, and R. E. Stewart, "Generation and Modeling of Near-LTE Plasmas Using Ultrashort Pulse Laser Heated, Tamped Mid-Z Targets," *J. Quant. Spectro. Radiat. Transfer* **58**(4-6), 991–1000 (1997).

Z

N. P. Zaitseva, J. J. De Yoreo, M. R. Dehaven, R. L. Vital, K. E. Montgomery, M. Richardson, and L. J. Atherton, "Rapid Growth of Large-Scale (40-55 cm) KH_2PO_4 Crystals," *J. Crystal Growth* **180**(2), 255–262 (1997).

F. Ze, S. H. Langer, R. L. Kauffman, J. D. Kilkenny, D. Ress, M. D. Rosen, L. J. Suter, R. J. Wallace, and J. D. Wiedwald, "A Comparative Study of X-Ray Emission from Laser Spots in Laser Heated Hohlraums Relative to Spots on Simple Disk Targets," *Phys. Plasmas* **4**(3), 778–787 (1997).

J. Zhang, A. G. MacPhee, J. Nilsen, J. Lin, T. W. Barbee, Jr., C. Danson, M. H. Key, C. L. S. Lewis, D. Neely, R. M. N. O'Rourke, G. J. Pert, R. Smith, G. J. Tallents, J. S. Wark, and E. Wolfrum, "Demonstration of Saturation in a Ni-Like Ag X-Ray Laser at 14 nm," *Phys. Rev. Lett.* **78**(20), 3856–3859 (1997).

ARTICLES BY AUTHOR